ECSS-E-HB-31-01 Part 14A
5 December 2011

Space engineering

Thermal design handbook - Part 14: Cryogenic Cooling

ECSS Secretariat
ESA-ESTEC
Requirements & Standards Division
Noordwijk, The Netherlands

Foreword

This Handbook is one document of the series of ECSS Documents intended to be used as supporting material for ECSS Standards in space projects and applications. ECSS is a cooperative effort of the European Space Agency, national space agencies and European industry associations for the purpose of developing and maintaining common standards.

The material in this Handbook is a collection of data gathered from many projects and technical journals which provides the reader with description and recommendation on subjects to be considered when performing the work of Thermal design.

The material for the subjects has been collated from research spanning many years, therefore a subject may have been revisited or updated by science and industry.

The material is provided as good background on the subjects of thermal design, the reader is recommended to research whether a subject has been updated further, since the publication of the material contained herein.

This handbook has been prepared by ESA TEC-MT/QR division, reviewed by the ECSS Executive Secretariat and approved by the ECSS Technical Authority.

Disclaimer

Published by: ESA Requirements and Standards Division
ESTEC, P.O. Box 299,
2200 AG Noordwijk
The Netherlands

Table of contents

Figures

Tables

1
Scope

In this part Part 14 cooling methods below 100 K are described. These low temperature levels are mainly required by space borne electronic systems operating under very low noise conditions. Details on the materials used and safety factors are given.

The Thermal design handbook is published in 16 Parts

ECSS-E-HB-31-01 Part 1	Thermal design handbook – Part 1: View factors
ECSS-E-HB-31-01 Part 2	Thermal design handbook – Part 2: Holes, Grooves and Cavities
ECSS-E-HB-31-01 Part 3	Thermal design handbook – Part 3: Spacecraft Surface Temperature
ECSS-E-HB-31-01 Part 4	Thermal design handbook – Part 4: Conductive Heat Transfer
ECSS-E-HB-31-01 Part 5	Thermal design handbook – Part 5: Structural Materials: Metallic and Composite
ECSS-E-HB-31-01 Part 6	Thermal design handbook – Part 6: Thermal Control Surfaces
ECSS-E-HB-31-01 Part 7	Thermal design handbook – Part 7: Insulations
ECSS-E-HB-31-01 Part 8	Thermal design handbook – Part 8: Heat Pipes
ECSS-E-HB-31-01 Part 9	Thermal design handbook – Part 9: Radiators
ECSS-E-HB-31-01 Part 10	Thermal design handbook – Part 10: Phase – Change Capacitors
ECSS-E-HB-31-01 Part 11	Thermal design handbook – Part 11: Electrical Heating
ECSS-E-HB-31-01 Part 12	Thermal design handbook – Part 12: Louvers
ECSS-E-HB-31-01 Part 13	Thermal design handbook – Part 13: Fluid Loops
ECSS-E-HB-31-01 Part 14	Thermal design handbook – Part 14: Cryogenic Cooling
ECSS-E-HB-31-01 Part 15	Thermal design handbook – Part 15: Existing Satellites
ECSS-E-HB-31-01 Part 16	Thermal design handbook – Part 16: Thermal Protection System

2
References

ECSS-S-ST-00-01	ECSS System - Glossary of terms
ECSS-E-HB-31-01 Part 5	Thermal design handbook – Part 5: Structural Materials: Metallic and Composite
ECSS-E-HB-31-01 Part 7	Thermal design handbook – Part 7: Insulations
ECSS-E-HB-31-01 Part 8	Thermal design handbook – Part 8: Heat Pipes
ECSS-E-HB-31-01 Part 9	Thermal design handbook – Part 9: Radiators
ECSS-E-HB-31-01 Part 13	Thermal design handbook – Part 13: Fluid Loops

All other references made to publications in this Part are listed, alphabetically, in the **Bibliography**.

3
Terms, definitions and symbols

3.1 Terms and definitions

For the purpose of this Standard, the terms and definitions given in ECSS-S-ST-00-01 apply.

3.2 Abbreviated terms

The following abbreviated terms are defined and used within this Standard

A	aged
AAD	average absolute deviation
AC	air cooled
	alternating current
Ann	annealed
AnnA	annealed and aged
APS	active phase separator
BLIP	background limited infrared photoconductor
CHRESUS	superfluid helium cryostat for space use
CTFE	polychlorotrifluorethylene
CW	cold worked
DA	double aged
DTA	detect capsule assembly
DC	direct current
EMI	electro magnetic interference
GIRL	German infrared laboratory
GR	generation-recombination

GRS	glass fabric and silicone rubber
HEOA	high energy astronomical observatory
HIP	hot isostatic pressed
IR	infrared
JT	Joule-Thomson
LAIM	low acoustic impedance medium
LNG	liquified natural gas
MLI	multilayer insulation
NDT	nil ductility transition
NEP	noise equivalent power
RMS	root mean square
RRR	residual resistance ratio
SHFE	superfluid helium in zero g set of experiments
OFHC	oxygen free high conductivity
QCM	quartz crystal microbalance
Q	quenched
QA	quenched and aged
RevAnn	reverse annealed
SA	solution annealed
SHFE	superfluid helium in zero g set of experiments
SPT	standard pressure and temperature
SS	stainless steel
ST	solution treated
STA	solution treated and aged
STDA	solution treated and double aged
STQA	solution treated, quenched and aged
STQW	solution treated, water quenched
TEMPER	tempered

VCS	vapor cooled shield
WQ	water quenched
bcc	cubic-body-centered
ccp	cubic-close-packed
ed	electropolishing depth
hcp	hexagonal-close-packed
id	inner diameter
ppm	parts per million

3.3 Symbols

A	Clause 6: insulation area, [m^2] it is measured normally to the main temperature gradient Clause 7: cross-sectional area. [m2] Clauses 7 and 8: Gorter & Mellink constant, [$m.s.kg^{-1}$]
A	Helmholtz potential, [$m^2.s^{-2}$] it is defined in clause 12.1.2.2
A_{FL}	internal cross-sectional area of a Ddct or a porous plug. [m^2]. Also called free flow area. In the case of a porous plug, $A_{FL} = \Phi A_{FR}$.
A_{FR}	frontal area of a porous plug, [m^2]
A_d	detector area, [m^2]
A_p	system area, [m^2]
A_s	support cross-sectional area, [m^2]
B	dimensionless force parameter in Vinen's theory
Bo	bond number, $Bo = \delta\rho g l R/\sigma$
Ca	capillary number, $Ca = \mu V/\sigma$
C_o	Bessel cylinder function of order zero
D	Clauses 6 and 8: diameter, [m] Clause 9: quenching distance, [m]
D_E	equivalent or hydraulic diameter of a duct of non-

	circular cross-section, [m]
D_j	dimensionless heat conduction factor for the insulation layer, it is defined in Eq. (10.11)
D^*	detectivity of a detector, [$m.W^{-1}.s^{-1/2}$]
E	minimum ignition energy, [J]
Ec	Eckert number, $Ec = p/(\rho V^2)$
F	fluid dynamic impedance of a duct, [m.s]
Fr	froude number, $Fr = V^2/(gl)$
F_l	auxiliary function, it is defined in Eq. [7-70]
F_n	friction force per unit volume between the normal fluid and the wall, [$N.m^{-3}$]
F_p	fluid dynamic impedance of a porous plug, [m.s]
F_s	friction force per unit volume between the superfluid and the wall, [$N.m^{-3}$]
F'_s	fs above plus the loss of momentum at the tube exit, [$N.m^{-3}$]
F_{sn}	mutual friction force per unit volume between superfluid and normal component, [$N.m^{-3}$]
Gr	Grashof number, $Gr = Re/Fr$
J	impact energy absorbed, [J]
$J(Cu)$	charpy U - notch impact energy absorbed, [J]
$J(C_V)$	charpy V - notch impact energy absorbed, [J]
J_C	J-integral toughness based on maximum load, [$J.m^{-2}$]
J_{IC}	critical value of J-integral for crack initiation, [$J.m^{-2}$]
J_ν	Bessel function of first kind and order ν
J-integral	integral toughness, [$J.m^{-2}$]
J_i	upper value of subscript j
K	permeability or geometric factor or a porous medium, [m^2]
K_D	dynamic fracture toughness, [$Pa.m^{1/2}$]
K_{IC}	plane strain fracture toughness, [$Pa.m^{1/2}$]

$K_{IC}(J)$	K_{IC} computed from J_{IC}, [Pa.m$^{1/2}$]
K_{TH}	stress intensity factor at crack arrest, [Pa.m$^{1/2}$]
K	stress intensity factor, [Pa.m$^{1/2}$] is is based on the load corresponding to 5% secant line
K_c	fracture toughness, [Pa.m$^{1/2}$]
K_{max}	Stress intensity factor, [Pa.m$^{1/2}$] it is based on the maximum load at failure
K_t	stress concentration factor
L	length, [m]
L_b	bond length, $L_b = [\sigma/(\delta\rho g)]^{1/2}$
L_v	length per unit fluid volume of vortex line in Vinen's theory, [m $^{-2}$]
L_{293}	length at T = 293 K, [m]
M	Clause 7: specific surface of the porous medium, [m^{-1}] it is defined in Table 7-46. Clauses 7 and 8: molar mass, [kg.mol^{-1}]
M_p	refrigerating system mass per unit of refrigeration power, [Kg.W^{-1}]
M_s	specific area of the porous medium, based on the apparent volume of the medium, [m^{-1}] it is defined in Table 7-46.
N	Clause 6: number of shields in an MLI Clause 8: number of layers in a composite material Clause 9: number of load cycles in fatigue
Nu	Nusselt number, $Nu = hD_E/k$
O_p	Ratio of open to total area of a capillary barrier
P	Clause 6: mechanical load, [N] Clause 7: percentage of material between adjacent sieves, it is introduced in Table 7-47.
Pr	Prandtl number, $Pr = \mu c_p/k$
Q	heat transfer rate, [W]
Q_l	heat transfer rate from the heat source, [W] also called

	heat load
Q_m	heat transfer rate through the insulation, [W]
Q_s	heat transfer rate through the supports, [W]
R	Clause 6: characteristic length along the insulation, [m] tank radius, [m]
	Clauses 7 and 8: gas constant of a particular gas, [$m^2.s^{-2}.K^{-1}$]
R_o	local radius of the effective vane profile, [m]
R_1,R_2	principal radii of curvature of an interface, [m]
R	universal gas constant, R = 8,31432 $J.K^{-1}.mol^{-1}$
RA	tensile reduction in area
Re	Reynolds number, $Re = \rho VD/\mu$
S	Cryogen sensibility, $S = [c_p(T_H-T_C)]/h_{fg}$
T	temperature, [K]
T_B	normal boiling temperature, [K]
T_M	melting temperature, [K]
T_b	fluid bulk temperature, [K] it is defined in the list of symbols of ECSS-E-HB-31-01
T_{fl}	flash point, [K]
T_i	Clause 6: temperature of the i-th vapor cooled shield, [K]
	Clause 9: ignition temperature, [K]
T_r	reduced temperature, $T_r = T/T_C$
T_w	wall temperature, [K]
U	Clause 6: ullage
	Clause 7: potential of any conservative body force per unit volume, [$m^2.s^{-2}$]
UPE	unit propagation energy, [$J.m^{-2}$]
V	Clause 5: volume, [m^3]
	Clause 6: mean fluid velocity, [$m.s^{-1}$]

We	Weber number, $We = \rho V^2 L/\sigma$
X,Y	strained coordinates
$X(T)$	bon Mardion et al. function, $X(T) = L(T)q^{3,4}$
Y	inverse dimensionless Stokes layer thickness
Y_ν	Bessel function of second kind and order ν
Z	compressibility factor, it is defined in clause 8.1.2.1
a	crack length, [m]
a_o	Vortex core radius, [m]
b	time constant, [s^{-1}]
c	Clause 4: speed of light in vacuum, c = 2,9978 x 10^8 $m.s^{-1}$
	Clause 8: specific heat of a solid, [$J.kg^{-1}.K^{-1}$]
	Clause 9: coefficient in fatigue crack growth rate equation (Paris equation), [$m^{1-n/2}.Pa^{-n}.cycle^{-1}$]
c_{H2}	Hydrogen content, [$m^3.kg^{-2}$]
c_o	numerical factor in Kozeny's equation Table 7-47.
c_p	constant pressure fluid specific heat, [$J.kg^{-1}.K^{-1}$] for gases c_p is used in distinction to c_v, the constant volume specific heat, for liquids no such distinction is needed, nevertheless c_p will be used
d	Clauses 6 and 7: diameter, [m]
	Clause 7: particle diameter, [m] it is defined in Table 7-46.
d_m	mean particle size, [m] Table 7-47.
d_v	pore diameter, [m]
$\overline{dl}$	vector element of streamline, [m]
f	Clause 4: diameter to focal length ratio of a lens, f^1 is usually known as lens aperture
	Clause 7: force per unit length on a vortex line in Vinen's theory, [$N.m^{-1}$] fanning friction factor, it is defined in ECSS-E-HB-31-01, clause 7.2.2
g	acceleration due to gravity, [$m.s^{-2}$]

h	Clause 15 Planck's constant, h = 1,0545 x 10^{-34} J.s
	Clauses 5 and 8: specific enthalpy, [J.kg^{-1}]
	Clause 6: convective heat transfer coefficient, [W.m^{-2}.K^{-1}]
	Clause 7: thermal conductance of the porous medium plus the fluid filling its cavities, [W.K^{-1}]
	Clause 8: heat of conversion from normal to para Hydrogen, [J.kg^{-1}]
h_k	Kapitza conductance, [W.m^{-2}.K^{-1}]
h_{fg}	heat of vaporization or sublimation, [J.kg^{-1}]
h_l	thermal conductance of the liquid within a porous medium, [W.K^{-1}]
h_q	heat of combustion, [J.kg^{-1}]
h_s	thermal conductance of the porous medium, [W.m^{-1}]
$\vec{j}$	mass flux density (Vector), [kg.m^{-2}.s^{-2}]
k	Clauses 5 and 8: Boltzmann's constant, k = 1,38054 x 10^{-23} J.K^{-1}
	Clauses 7 and 8: thermal conductivity, [W.m^{-1}.K^{-1}]
k_j	coefficient in the approximate expression, $k = k_j T$. [W.m^{-1}.K$^{-(j+1)}$]
k_x	thermal conductivity across the insulation, [W.m^{-1}.K^{-1}]
k_y	thermal conductivity along the insulation, [W.m^{-1}.K^{-1}]
$\bar{k}$	temperature-averaged effective thermal conductivity of the insulation, [W.m^{-1}.K^{-1}] $\bar{k} = \int_0^1 k(\theta) d\theta$
l	length, [m] height in the gravitational field above a reference level, [m]
m	Clause 6: Cryogen bol-off rate, [kg.s^{-1}]
	Clause 7: fluid mass flow rate, [kg.s^{-1}]
m_{He}	atomic mass of helium, m_{He} = 6,6435 x 10^{-27} kg
m_o	Cryogen boil-off rate because of the heat leaks

	through a conventional MLI system. [kg.s^{-1}] $m_o = \frac{\bar{k}A(T_H - T_C)}{h_{fg}t}$.
n	Clause 6: number of vapor cooled shields Clause 9: exponent in fatigue crack growth rate equation (Paris equation)
n_B	background photon number flux, [s^{-1}.m^{-2}]
p	Clause 6: number of supports Clauses 5, 7, 8 and 9: pressure, [Pa]
p_b	boiling pressure at 300 K, [Pa]
p_r	reduced pressure, $p_r = p/p_c$
q	tortuosity of a porous medium, it is defined in Table 7-46.
$\vec{q}$	heat flux (vector), [W.m^{-2}]
q_m	heat flux through a guard shroud used in the thermal test of a support, [W.m^{-2}]
r	Clause 6: dimensionless convective heat transfer coefficient, it is defined in Eq. [6-37] Clause 7: roughness factor, defined as the ratio of rough to macroscopic surface area
s	specific entropy, [J.kg^{-1}.K^{-1}]
t	thickness, [m]
t	time, [s], [d] or [yr]
t_l	liner wall thickness, [m]
t_o	overwrap thickness, [m]
$\vec{u}$	fluid velocity (vector), [m.s^{-1}]
v	Clause 7: cross-sectional average of the local velocity u. [m.s^{-1}] Clause 8: molar volume, [m^3.kg^{-1}]
$\vec{v}_d$	diffusion velocity (Vector), [m.s^{-1}]
v_{nc2}	second normal critical velocity, [m.s^{-1}]

v_{sc1}	first superfluid critical velocity, [m.s^{-1}]
v_t	relative velocity between normal fluid and vortex line, [m.s^{-1}]
x	Clause 6: distance to the cold face of the insulation, [m] it is measured across the insulation Clause 7: axial distance to the entry in a tube or porous plug, [m]
y	distance between a point in the insulation and the venting duct axis, [m] it is measured along the insulation
z	vertical distance, [m]
Δ	difference
ΔK	Clause 6: curvature difference, [m^{-1}] Clause 9: stress intensity factor range during fatigue cycling, [Pa.m$^{1/2}$]
Δp	pressure drop [Pa]
Θ_j	j-th term in the power series development of the "inner" expression of θ near the insulation cold face.
Λ	aspect ratio
Ξ	stretched dimensionless distance from the insulation cold face, $\Xi = \xi(k_y/k_x)^{1/2}(t/R)$
Φ	Clauses 6 and 7: volume porosity, it is defined in Table 7-46. Clause 7: Rayleigh viscous dissipation function, [W.m^{-3}]
α	Clause 6: outer radius of the venting duct made dimensionless with the radius, R, of the insulation surface Clause 7: wall interaction dimensionless constant in Vinen's theory Clause 7: wall interaction Van der Waals constant, [kg.m^{-2}.s^{-2}] thermal accommodation coefficient, dimensionless temperature, $\alpha = T_H/T_C$, particle shape factor Table 7-47. Clause 9: thermal diffusivity, [m^2.s^{-1}] $\alpha = k/\rho c$, where c is the specific heat

β	fluid isobaric compressibility, [K^{-1}] also known as coefficient of volumetric thermal expansion
δ	Clause 7: superfluid film thickness, [m] Clause 9: tensile elongation
δ_c	crack opening displacement at the cract tip corresponding to the onset fracture, [m]
ε	Clauses 4: emittance Clause 5: parameter in intermolecular potential function, [J] Clause 6: normal to lateral heat conduction parameter, $\varepsilon = (k_x/k_y)(R/t)^2$
ζ	dimensionless distance across the insulation $\zeta = \frac{\bar{k}}{k(T_H)}\frac{m_{Nu}}{m_o}\xi$
η	Clause 5: efficiency Clause 6: dimensionless distance along the insulation, $\eta = y/R$
η_c	Carnot efficiency, $\eta_c = 1 - T_C/T_H$
θ	Clause 6: dimensionless temperature, $\theta = (T-T_C)/(T-T_H)$ liquid-solid contact angle [angular degrees] polar angle, [angular degrees]
$\dot{\theta}$	angular velocity, [$rad.s^{-1}$]
$\ddot{\theta}$	angular acceleration, [$rad.s^{-2}$]
θ_a	spreading angle of a bubble contacting two concentric spheres, [angular degrees]
θ_D	Debye temperature, [K]
κ	strength of a quantized vortex ring, [$m^2.s^{-1}$]
λ	Clause 4: wavelength, [m] Clause 7: friction factor, it is defined in major clause 11.2.2
λ_c	detector cutoff wavelength, [m]
μ	Clause 5: Joule-Thomson parameter, [$K.m^2.N^{-1}$] $\mu = (\partial T / \partial p)_h$.

	Clauses 6 and 8: fluid dynamic viscosity, [Pa.s] it is also known as viscosity coefficient
	Clause 7: chemical potential, [$m^2.s^{-2}$]
μ_n	Clause 6: n-th root of $Y_1(\mu_n\alpha)J_1(\mu_n)-J_1(\mu_n\alpha)Y_1(\mu_n) = 0$, J_1 and Y_1 being the Bessel functions of order one (first and second kind respectively)
	Clause 7: dynamic viscosity of the normal fluid component, [Pa.s]
ν	Kinematic viscosity, [$m^2.s^{-1}$]
ξ	Clause 6: dimensionless distance across the insulation, $\xi = x/t$
	Clause 7: dimensionless distance along a tube, $\xi = (L-1)/l$
ρ	density, [$kg.m^{-3}$]
ρ_l	liquid density, [$kg.m^{-3}$]
ρ_v	gas density, [$kg.m^{-3}$]
σ	Clause 6: strength, [Pa]
	Clauses 6, 7 and 8 surface tension, [$N.m^{-1}$]
σ_f	fatigue strength, [Pa]
σ_{ult}	ultimate tensile strenght, [Pa]
σ_2	tensile yield strength, [Pa] 2% offset
τ	dimensionless temperature, $\tau = T/T_H$
χ_1	dimensionless vortex generation parameter in Vinen's theory
χ_2	dimensionless vortex decay parameter in Vinen's theory
ψ	Clause 6: dimensionless heat transfer rate, $\psi = Q/(m_o h_{fg})$
	Clause 7: superfluid velocity potential, [$m^2.s^{-2}$]
ψ_1	dimensionless heat load, $\psi_1 = Q_1/(m_o h_{fg})$
ω	frequency, [$rad.s^{-1}$]
ω_{Nu}	factor accounting for the influence of the finite convective heat transfer on boil-off rate

ω_i	factor accounting for the influence of the i-th deviation from the ideal model on the boil-off rate
ω_k	factor accounting for the influence of the temperature-dependent. thermal conductivity on the boil-off rate
ω_n	factor accounting for the influence of the finite number of vapor cooled shields on the boil-off rate
ω_{nk}	factor accounting for the simultaneous influence of the finite number of vapor cooled shields and of the temperature-dependent thermal conductivity on the boil-off rate
ω_y	factor accounting for the influence of the finite thermal conductivity of the vapor cooled shields on the boil-off rate

Subscripts

A	ambient
C	cold
H	hot
Nu	refers to a vapor cooled shield system when finite convective heat transfer in the venting duct is taken into account
b	fluid bulk properties
c	critical conditions
eff	effective
i	Clauses 5 and 7: inlet conditions Clause 6: i-th element in a set of several elements
j	j-th element in a set of several elements
k	refers to a vapor cooled shield system with temperature-dependents thermal conductivity
l	liquid conditions
max	maximum
min	minimum
n	Clause 6: refers to a vapor cooled shield system having n cooled shields

	Clauses 7 and 8: normal component in superfluid helium flow
nk	refers to a vapor cooled shield system having n cooled shields and temperature dependent thermal conductivity
o	Clause 7: outlet conditions
	Clauses 7 and 8: reference state
phon	phonon
r	reduced value
s	Clause 6: refers to supports
	Clauses 7 and 8: superfluid component in superfluid helium flow
sat	conditions along the saturation curve
v	vapor conditions
y	Clause 6: refers to a vapor cooled shield system when heat transfer along the cooled shields is taken into account
	Clause 7: y component
z	z component
λ	helium-4 conditions at the lambda point

Superscripts

o	perfect gas conditions
-	averaged value.
*	Local boiling conditions.

4
General introduction

This Part concerns cooling to temperatures below 100 K.

These low temperature levels are dictated by the use of improved Earth-applications instruments (promising higher resolution in the infrared (IR) region), by a growing interest in infrared, gamma-ray and high-energy astronomy, and by the advent of a large number of opportunities for instrument launches both by use of the Shuttle (7 to 30 days) and of unmanned spacecraft (1 to 5 years).

Table 4-1, from Sherman (1978) [216], lists disciplines which require cryogenic cooling in space, with estimates of temperatures and cooling loads. The table concerns only NASA involvement, but ESA, DOD, DFVLR and CNES, among others, also need cryogenic systems in space. The development, by ESA of a Helium II cryostat for Spacelab payloads is described by Lizon-Tati & Girard (1978) [134]. A similar effort is being undertaken in Germany by DFVLR (Lemke, Klipping & Römisch (1978) [131], Seidel (1978) [212]. On the other hand, CNES in France is developing a solid cryogen cooler for spaceborne IR detectors (Rolfo & Prost (1978) [198].

The cryogenic cooling techniques that are at present either in use or in development state, or that promising for the near future, are listed in Table 4-2, which has been also borrowed from Sherman (1978) [216].

Table 4-1: NASA Mission Categories Requiring Cryogenic Cooling in Space

Discipline	Temp. Range [K]	Coating Load
Applications Missions (Weather, Earth Resources, Pollution Monitoring, etc.)	10 to 100	Milliwatts to 10 W
High-Energy and Gamma-Ray Astronomy	4 to 100	Milliwatts to 10 W
IR Astronomy	0. 3 to 10	Microwatts to 0,1 W
Relativity Missions	0,001 to 1,5	Microwatts to Milliwatts
Superconducting Devices	1 to 15	Wide Range
Basic Research Experiments	1 to 10	Below 0,1 W

NOTE From Sherman (1978) [216]

Table 4-2: Spacecraft Cryogenic Cooling Techniques

Cooling Technique	Temp. Range [K] [a]	Cooling Load for Year Mission [b] [W]
Radiant Coolers	70 to 100	0 to 0,01 to date; higher capacity foreseeable
Stored Solid-Cryogen Coolers	10 to 90	0 to 0,8
Stored Liquid-Helium Coolers	1,5 to 5,2	0 to 0,1
He^3 Coolers	0,3	0 to 10^{-4}
Dilution Refrigerators & Adiabatic Demagnetization Refrigerators	0,001 to 0,3	0 to 10^{-4} Adiabatic
Mechanical Coolers	4 to 100	0 to 300

[a] These values are not theoretical limits but are estimates of temperatures and loads based on the designs as they appear to be evolving.

[b] For missions of shorter duration (7 to 30 day Shuttle sortie) significantly higher cooling loads could be accommodated.

NOTE From Sherman (1978) [216].

4.1 Radiant coolers

Radiant coolers are at present the most widely used system for cooling at cryogenic temperatures aboard spacecraft. These devices are described in ECSS-E-HB-31-01 Part 9, clause 6.

Radiant coolers offer a relatively simple, passive, low weight technique for cooling spaceborne sensors. They present, however, severe limitations with respect to temperature (>70 K), cooling load (milliwatts), placement on spacecraft, and spacecraft orbit.

Studies to advance the design of radiant coolers have been made. For example, Sherman & Brennan (1976) [219] suggested the addition of a cryogenic heat pipe between the detector and the radiant cooler in order to allow for more flexibility in locating the instrument with respect to the cooler. They found that in the 80 K to 100 K temperature range, the parasitic heat loads to the heat pipe require radiant coolers larger than those being developed at present (by NASA). As the cooler temperature level increases, the effect of the heat pipe in system performance becomes less significant because its parasitic losses decrease when the cooler capacity increases.

The use of cryogenic diode heat pipes (see ECSS-E-HB-31-01 Part 8, clause 9.2) has been considered for applications in which the cooler is exposed to a hot environment such as cyclic solar or earth inputs. When the cooler becomes warmer than the heat source, the diode) shuts down to isolate the system from the environment.

In spite of these or similar studies for alleviating some of the limitations of radiant coolers, other spacecraft cryogenic systems are being developed to meet the increasing demands of lower temperatures, higher cooling loads and further flexibility of integration and operation.

4.2 Stored solid-cryogen coolers

Stored solid-cryogen systems for long-term cooling detectors in space have been under development for the last ten years. These cryogenic systems are passive and not limited by orbit, spacecraft orientation, or locations within the spacecraft.

Cooling is performed in these systems through sublimation of a solid or boiling of a liquid. For 10 K to 90 K detector instrument cooling in space, stored solid-cryogen systems offer many advantages over stored liquid systems.

1. Cryogens for this temperature range have heats of sublimation about 10 % to 15 % higher than their heats of vaporization.
2. With a stored-liquid system, liquid phase-gas phase separation under microgravity is difficult, because of the uncertain location of the liquid free surface.
3. For a given volume, the cooling capacity of the stored-solid cryogen is larger than that of the stored liquid cryogen since the solid cryogen will have a density 10 % to 15 % higher than the liquid.

The operating temperature range of a solid cryogen is limited from above by the triple point, and from below by the requirement that pressure around the sublimating solid be large enough to overcome pressure losses in the venting tube, allowing the venting of vapors resulting from solid sublimation. Although the mentioned pressure losses obviously depend on the geometrical configuration of the venting plumbing, the outer pressure and the mass flow rate, a value of the order of 0,1 torr (13,33 Pa) is appropriate in most cases.

Several stored-solid cryogen coolers are described in Clause 6.5 of this Part.

4.3 Stored liquid Helium (He4) coolers

Many applications in the fields of IR astronomy, cosmic rays at the top of the atmosphere, and basic physics will demand cooling in the 1,8 K to 4,2 K temperature range. Superfluid liquid helium (He^4) is well suited to this purpose.

Superfluid liquid helium presents a number of unusual properties which should be taken into account by the designer of the cooler. These properties are discussed in Clause 3 of this Part.

The crucial areas in the design of stored-liquid-helium coolers are:

1. Insulation. Helium has a heat of vaporization in the 1,8 K to 5,2 K temperature range of about 22×10^3 $J.kg^{-1}$, which is an order of magnitude below the heat of sublimation of solid cryogens. This underscores the importance of minimizing the heat leaks to liquid helium. On the other hand, since gaseous helium has a high specific heat, helium vapors can be used very efficiently to cool the insulation before venting to space. This is achieved in the so called Vapor Cooled Shield (VCS) Dewars. VCS Dewars are extensively discussed in Clause 6 of this Part.
2. Containment and liquid/vapor separation. liquid cryogen into the venting tube of the Dewar should be avoided by all means. Otherwise a waste of cryogen will result. Fortunately, there is a peculiar effect in superfluid helium, the thermo-mechanical effect (see clause 7.1.1.1), which allows the venting of the vapors through a porous plug while still retaining the superfluid liquid. The superfluid porous plug is considered in clause 7.4 of this Part.
3. Filling of a superfluid helium container (clause 1.1) is not an easy task, since much care should be exercised to minimize the liquid loss in the container while pumping down.

Two different filling approaches are presently envisaged. 1) Storage of the liquid helium in the normal state at ground, and pumping down in space upon opening the effluent port. 2) Filling of superfluid liquid helium at ground. The first approach looks simpler, in terms of ground support equipment, but would result in about 40 % helium loss.

4. Sloshing of the superfluid liquid helium is a not yet satisfactorily solved problem. Notice that the mass of the liquid is significant and that the cryostat may be required to be highly stable with reference to its own experiments (for instance, when an instrument scans) and with reference to other experiments in the same spacecraft.

The study of the He^4 free surface poses a substantial challenge to both theorists and experimentalists, not to mention the new problems associated to the microgravity environment. According to Sherman (1978) [216] zero-g testing aboard aircraft indicates that the incorporation of a porous material within the Dewar to capture the liquid can solve the sloshing problem, but this is by no means clear because of the superfluid velocity component which may not be impeded by the porous material unless very narrow channels are used.

4.4 Trends toward lower temperatures

The performance of IR bolometers under low-background radiation is greatly enhanced by operation at the lowest possible temperatures. For instance, Sherman (1978) [216] indicates that operating a bolometer at 0,3 K as opposed to the 1,8 K, which can be reached by He^4 Dewars, results in a noise equivalent power reduction of an order of magnitude or more.

The simplest way for reaching temperatures significantly below 1 K is by using a He^3 cooler. He^3, which is an isotope of helium, presents two favorable characteristics which are well suited to this aim. First, the vapor pressure of He^3 is at all temperatures higher than the vapor pressure of He^4. The ratio of He^3 to He^4 vapor pressures is 74 at 1 K, 610 at 0,7 K and 9800 at 0,5 K (Lounasmaa (1974) [138]). Second, there is no He^3 film. A He^3 bath may thus be pumped via a wide tube at the low temperature and, without need for a narrow constriction to impede film flow.

The normal boiling point of the He^3 is 3,19 K, its critical temperature and pressure are 3,32 K and $1{,}16 \times 10^5$ Pa respectively, and its heat of vaporization is less than half that of He^4. In addition to its low heat of vaporization, He^3 presents the drawback of its extreme expensiveness, approximately 250 $/l under normal pressure and temperature conditions (10^{-6} m^3 of liquid correspond to 0,6 l of gas at normal conditions). This high cost of He^3 urges using closed-cycle coolers.

Lounasmaa (1974) [138] presents the basis of He^3 cryostat design and describes several laboratory apparatus. Figure 4-1 shows a ground-based closed-cycle He^3 cryostat, intended to cool three bolometers to 0,3 K, and which is designed, fabricated and being tested by NASA Goddard Space Flight Center. The heat load (60×10^{-6} W) is absorbed by vaporization of the He^3 as it is pumped via charcoal adsorption. Under normal operating conditions the charcoal canister is kept at about 1,8 K by thermal switching to the He^4 Dewar. When all the liquid He^3 (5×10^{-6} m^3) is adsorbed, the cycle is reversed by opening the thermal switch and heating the canister. As the charcoal is warmed to about 40 K the adsorbed He^3 is driven off and is subsequently condensed in an internally finned condenser. The He^3 then flows back into the container. The heat switch in then closed, cooling down the charcoal to 1,8 K, and starting up a new cycle.

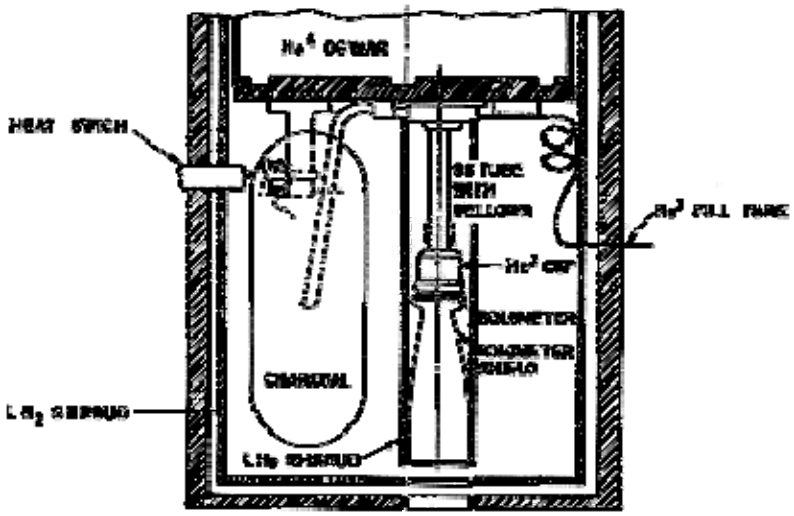

Figure 4-1: He^3 cooler being developed by NASA. From Sherman (1978) [216].

Critical problems in the adaption of the basic He^3 cycle to spacecraft are, according to Sherman (1978) [216], the capillary system sustaining the He^3 in the cup, and the structure capable of surviving launch while limiting heat leaks to extremely low values.

A similar He^3 cryostat, developed for the cooling of bolometers in ballon-borne astronomy and aeronomy experiments has been flight-tested (Torre & Chanin (1978) [240].

There are three methods presently available for cooling to 10^{-2} K and below. These are: the He^3/ He^4 dilution refrigeration, Pomeranchuk cooling, and adiabatic nuclear demagnetization. The principles of all three are presented in Lounasmaa (1974) [138]. The first and last methods are being considered for 10^{-3} K spacecraft coolers. The dilution refrigerator operates continuously, it is quite simple in construction and easy to operate (systems for terrestrial laboratory use are commercially available), but presents many zero-g fluid management problems that do not exits with adiabatic demagnetization. This last technique, however, is basically a single-cycle method of cooling, after demagnetization the system begins to warm up and, thence, can be only used in single shot-type of experiments.

4.5 Mechanical refrigerators

Mechanical refrigerators will be required for providing cooling over lifetimes of the order of years. A great deal of effort has been expended for the last ten years in the development of these devices. An account of the several types, their development problems, and the state of the art (mainly) up to 1982 is given in Clause 5 of this Part. A long-lifetime (2 yr to 5 yr) mechanical cooler with stable and consistent performance is still to be developed.

The spacecraft mechanical coolers that have received the greatest attention, among the many refrigerating cycles available, include reverse Brayton-cycle, Stirling-cycle and Vuilleumier-cycle machines.

The ideal reverse-Brayton thermodynamic cycle is described in Clause 5.2 of this Part. This ideal cycle is not thermodynamically reversible. Further, with this cycle it is difficult for machinery to achieve high efficiency, especially for small coolers.

The reverse-Brayton thermodynamic cycle can be approximated with turbo machinery systems. These cooling systems have a long-lifetime potential because its high rotational speed (above 10^5 rpm)

allows the efficient use of gas bearings. Coyler et al. (quoted by Sherman (1978) [216] describe a detailed design study of a turbo-refrigerator for space application, with nominal cooling loads of 1,5 W at 12 K and 40 W at 60 K, $3x10^4$ h lifetime, and a maximum power consumption of $4x10^3$ W.

Miniature refrigerators based on the reverse-Brayton thermodynamic cycle use the rotary-reciprocating mode of action. In the rotary-reciprocating system (clause 5.2) the pistons used to compress (or to expand) the working fluid are rotated as well as reciprocated. ArthurD. Little's rotary-reciprocating refrigerator (clause 5.2 and clause 5.2.1) employs reciprocating motion for refrigeration action and rotary motion to allow the use of gas bearings for long-lifetime potential. In accord with Sherman (1978) [216], no complete test program for these coolers has been performed up to this moment.

Stirling-cycle refrigerators (clause 5.2) have been employed in aircraft and short to medium duration space missions. Several Stirling-cycle refrigerators under development are listed in clause 5.2.1. In orbit performance of space-qualified Stirling-cycle refrigerator (rhombic drive) is discussed in clause 5.2.1.

Preliminary test results of a magnetically-suspended Stirling-cycle refrigerator, under development by North American Philips (see clause 5.2) have been reported by Daniels et al. (1984) [50].

The Vuilleumier refrigerator presents many features which offer the possibility of long-lifetime operation. These include relatively low bearing loads and a less stringent seal requirement as compared to the Stirling-cycle refrigerators.

The main features of the Vuilleumier refrigerators are described in Clause 5.2 of this Part. These refrigerators incorporate regenerators designed for low pressure drop, thus the cooler requires little compression or expansion of the working fluid and the displacers separate chambers whose pressures are nearly equal at any moment. Consequently, the electric-motor power, bearing loads and vibrations are small.

Several Vuilleumier refrigerators under development are listed in clause 5.2.1.

NASA Goddard's Vuilleumier refrigerator program started in 1969. According to Sherman (1978) [216], a machine built by Garret Ai-Research met thermal performance goals with 299 W required to achieve 7 W of cooling at 75 K. The unit ran $6x10^3$ h without a mechanical fix.

The US Air Force has had an extensive Vuilleumier refrigerator program during the past decade. Much work has been concentrated on the development of three-stage machine with 12 W, 10 W and 0,3 W cooling loads at 75 K, 33 K and 11,5 K respectively. This machine has a lifetime goal of $2x10^4$ h of unattended operation with a maximum of $2{,}7x10^3$ W of input power. To accomplish these goals, parallel development efforts have been carried out by Philips Laboratories and Hughes Aircraft (see clause 5.2.1).

4.6 Low temperature requirements to IR sensors

Available IR sensors are capable of detecting extremely small amounts of incoming radiant energy, provided that extraneous sources of radiant and thermal energy are reduced to levels far below those emanating from the target.

The sources of energy interfering with the detection process are:

1. Sources other than the target existing in the scene.
2. Radiation from the sensor optical system.
3. Excitations of the detector due to its own temperature.

The aim of cryogenic cooling is to reduce the effect of the last two sources of interference. The following discussion is a summary of a paper by Caren & Sklensky (1970) [37].

4.6.2 Radiation from the optical system

The sensor detection capability depends on the ratio of the number of target photons to the RMS of the fluctuation in the number of background photons arriving at the detectors during the dwell time of the optical system (signal to noise ratio).

The sources of background radiation from the optical system are the interior of the optical cavity and the optics itself. Although the optics have generally a low emittance, most of the background energy arriving at the detector comes from the optics, since the radiation from the optical cavity is shielded as sketched in Figure 4-2.

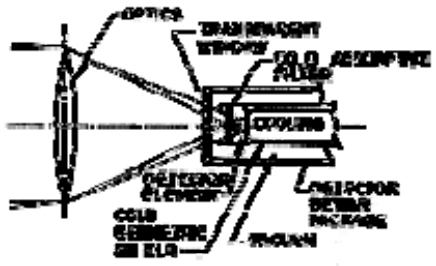

Figure 4-2: Procedure to reduce the background flux from the optics. From Caren & Sklensky (1970) [37].

The monochromatic background power reaching the detector is equal to the power radiated by the optics per unit area, per unit spectral bandwith, multiplied by the optics surface area and by the view factor between optics and detector.

The monochromatic power depends on the wavelength, λ, and its maximum value moves with temperature to shorter wavelengths, as expressed by Wien's law ($\lambda_{max}T$ = 2,8978 x 10^{-3} m.K).

The photon number, corresponding to a given λ, and leaving the unit area of the emitting surface is equal to the monochromatic power divided by the energy carried by one photon, which is $2\pi hc/\lambda$ ($2\pi h$ = 6,6256 x 10^{-34} J.s is the Planck constant, and c = 2,9979 x 10^{8} m.s^{-1} is the speed of light in vacuum).

To calculate the background photon number flux on the detector, the monochromatic contribution is integrated up to the detector cutoff wavelength, λ_c.

In order to reduce the background power reaching the detector, λ_c (which depends on the characteristics of the target) ought to be smaller than λ_{max}. Since $\lambda_{max}T$ is constant, the detector temperature, T, is decreased when the cutoff wavelength, λ_c, is increased. This is illustrated in Figure 4-3, which gives the detectivity, D^*, of the detector as a function of the cutoff wavelength, λ_c, for different values of the optics temperature, T.

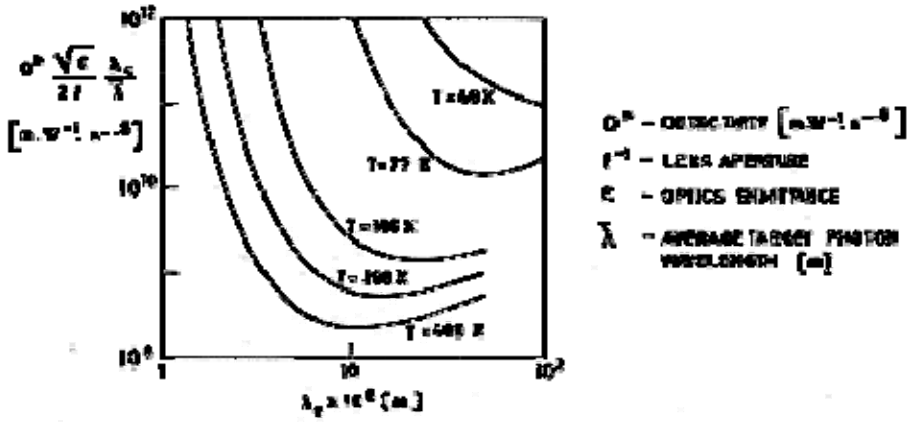

Figure 4-3: Detectivity, D^*, of a photon noise-limited detector as a function of cutoff wavelength, λ_c, for several values of the optics temperature, T. From Caren & Sklensky (1970) [37].

The detectivity, D^*, which is a figure of merit of the detector, is defined as:

$$D^* = \frac{\sqrt{A_d / t}}{NEP} \qquad [4\text{-}1]$$

where A_d is the detector area in m², t is the dwell time of the system in s, and NEP the Noise Equivalent Power in W. NEP is the power that have to reach the detector to provide a noise signal of the magnitude of the noise observed.

4.6.3 Noise from the detector

The detector which are currently used for infrared sensing are semiconductor materials exhibiting photoconductive properties.

When a photon of energy equal to or greater than some given threshold energy (the energy gap) is absorbed by one such material a rise in the conductivity of the material results. This effect, which is due to the generation of a hole-electron pair (free carrier), disappears, and the material experiences a transition to its previous undisturbed state, once a given time is elapsed. This transition is called recombination.

Fluctuations in the arrival of background photons from the optics result in fluctuations in the electrical resistance of the material. This, in turn, is converted into a voltage or current fluctuation which constitutes the noise signal.

There are several alternative sources of noise in the detector itself and in the electronics associated with it. Usually, generation-recombination of free carriers (GR) dominates the noise producing mechanism. The free carriers are constantly generated optically and thermally, and recombined through many possible processes.

When, for a given flux level, the background photon generation rate of free carriers exceeds the thermal generation rate, the detector is said to be BLIP (Background Limited Infrared Photoconductor) at this flux level.

An upper bound of the detector operating temperature for BLIP operation, can be estimated equating the background photon and thermal generation rates.

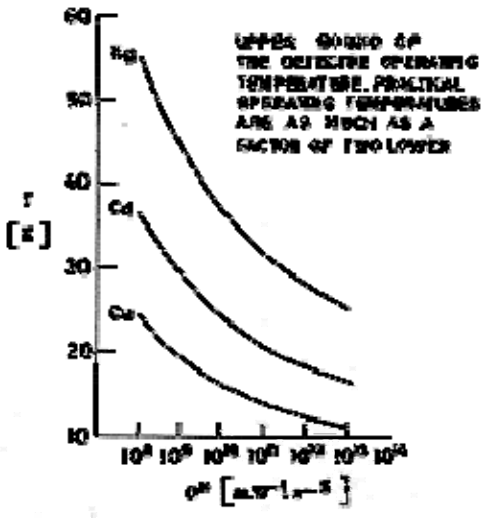

Figure 4-4: Typical detector operating temperature, *T*, vs. detectivity, *D. The detector is germanium doped either with mercury, with cadmium or with copper. From Caren & Sklensky (1970) [37].**

Figure 4-4 gives the upper bounds of the detector operating temperatures, *T*, vs. detectivity, *D**, for germanium doped with three types of dopants. To relate the background photon number flux, n_B, reaching the detector, to the detectivity, *D**, the following expression has been used:

$$D^* = \frac{\overline{\lambda}}{2\pi h\sqrt{n_B}} \qquad [4\text{-}2]$$

Where $\overline{\lambda}$ is the wavelength of the detector peak response.

It can be deduced from Figure 4-4that low detector operating temperatures are required to achieve high sensitivity.

5
Refrigerating systems

5.1 General

The various types of refrigerating systems applicable to spacecraft are described with some detail in this Clause.

Clause 5.2 concerns mechanical refrigerators or closed cycle systems. These systems will be used in the near future for thermal conditioning payloads with high cooling loads (above 5 W), low operating temperatures (below 100 K), and log lifetimes of unattended service (2 to 5 yr). Unfortunately, the state of development of these systems is far from satisfactory and, thus, only a description of the thermodynamic cycles on which they are based, and of the development problems they face, are given here.

Open cycle or expendable refrigerating systems, which are subject of clause 5.3, are much simpler than mechanical refrigerators although their lifetime is obviously smaller (see Table 4-2, in General Introduction of Clause 4). Open cycle systems are basically of two types: those using a high-pressure gas whose cooling effect is produced by a Joule-Thomson adiabatic expansion, and those using a stored solid or liquid cryogen in thermal contact with the heat source. Since stored-cryogen coolers are extensively dealt with in

5.2 Closed cycle

A number of mechanical refrigerators adaptable to spaceborne operation is presented in this Section. The basic thermodynamic cycles and the development problems associated to each type of refrigerator are discussed. The data are arranged in the following order: Brayton (Rotary-Reciprocating Systems), Brayton & Claude (Turbo machinery Systems), Gifford-McMahon/Solvay, Joule-Thomson, Stirling, Vuilleumier.

Spaceborne mechanical refrigerators are characterized by: low mass (which includes masses of refrigerator, power supply, and heat rejection system), low power, low acoustic noise, and extended reliability without opportunity for maintenance and/or repair. To meet these requirements emphasis must be placed on both mechanical and the thermal design.

Much effort has been expended for the last ten years in the development of mechanical refrigerators. Several of the development programs have been general in nature with emphasis in raising the related technology level, while others aimed at developing refrigerator for a particular mission. In spite of this effort, systems with stable and consistent performance are scanty.

Technical data on many mechanical refrigerators for spacecraft application are presented in clause 5.2.1. The heading, "Existing Systems", which is used in this clause for consistency with similar material in the other Parts, is a bit misleading here, since most of the described systems are in the

development phase (even, work on some of them has been interrupted). The mentioned data are included to be used as an aid in the preliminary design of new systems.

5.2.1 Reverse-Brayton cycle

(Rotary-Reciprocating Systems)

5.2.1.1 Description

Figure 5-1 describes the ideal reverse-Brayton cycle for a single-stage system.

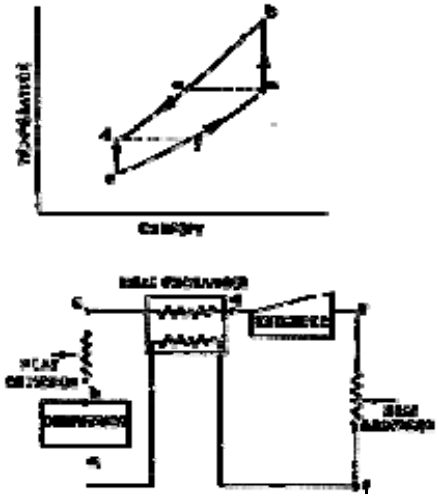

Figure 5-1: Reverse-Brayton Cycle Refrigerator. From Sherman (1978) [216].

The thermodynamic processes associated with this cycle are the following (see Figure 5-1):

a to b. The gas is compressed with some increase in entropy.

b to c. Heat is rejected to the ambient temperature heat sink in an aftercooler.

c to d. The high pressure gas is cooled in the main heat exchanger. In the real cycle the pressure in d is slightly less than that in b because of the pressure losses in the two heat exchangers.

d to e. Expansion with some entropy increase in the expander.

e to f. Heat addition in the heat load exchanger.

f to a. The gas is heated in the main heat exchanger and returns to the compressor inlet.

The ideal cycle is not thermodynamically reversible. Although Brayton cycle refrigeration systems are frequently used in plant installations because of the component simplicity and acceptable efficiency, it is difficult for small coolers to achieve high efficiency.

Miniature refrigerators utilizing rotary-reciprocating machinery are being developed for space applications by Arthur D. Little (Figure 5-2). In these machines the pistons are rotated as well as reciprocated. This permits the use of ports to control the gas flow and clearance seals to limit leakage. Electromagnetic actuators drive the pistons. The machinery has relatively few moving parts, all of which are completely supported on self-acting gas bearings. There are no rubbing or sliding surfaces as in conventional reciprocating equipment. The required refrigeration machinery is contained in two separate units: a compressor assembly and an expander package.

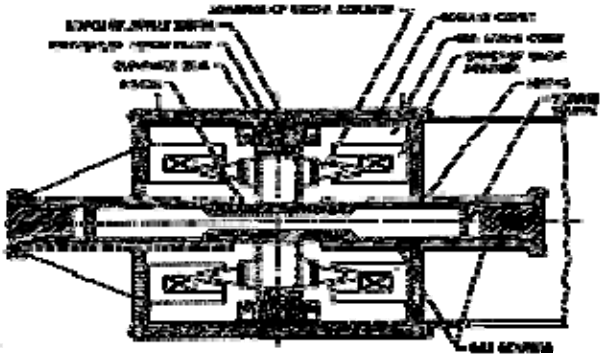

Figure 5-2: Compressor cross section of ADL rotary-reciprocating refrigerator. From Donabedian (1972) [59].

The spaceborne refrigerator system includes radiators for cooling of the compressed gases and for rejecting the heat generated by electrical losses in the housing. Power conditioning equipment is required to convert the output of the basis source of electrical power into an AC of the power frequency, amplitude and phase.

The test program for the ADL rotary-reciprocating cooler is not yet complete (Sherman (1978) [216]).

5.2.1.2 Development problems

The rotary-reciprocating refrigerator holds promise of extended life since most of the problems associated with wear, sealing, and contamination have been essentially eliminated. However, the complexity of this system represents an inherent development risk since it is a relatively novel approach. A summary of potential problem areas is shown in Table 5-1.

Table 5-1: Development Problem Areas of Brayton Cycle Rotary-Reciprocating Refrigerators

Component	Problem
Counterflow Heat Exchanger	Non-metallic spacer material being used in current design to reduce longitudinal heat conduction could be a source of contamination. The use of laminated materials is a potential source of leakage.
Linear Actuators	Out gassing of the coils could contaminate the piston bore assemblies.
Rotary Motors	Assessment of the performance in a submerged environment is needed.
Gas Springs and Bearing	Manufacturing tolerance must be build up.
Linkages (Reed Connectors)	Fatigue due to load reversals and end loading.
Traps/Filters	Filter failure due to improper assembly.

NOTE From Donabedian (1972) [59].

5.2.2 Reverse-Brayton and Claude cycle refrigerators

(Turbo machinery system)

5.2.2.1 Description

The reverse-Brayton cycle, which has been described above, can be approximated by a turbo-refrigerator. This type of cooler has long-lifetime potential because its high rotational speed (above 10^5 rpm) allows the efficient use of gas bearings. Lubrication of the cycle working fluid alleviates contamination and fouling problems in the low temperature regions of the cycle.

In these refrigerators the working gas, initially at ambient temperature, is compressed and then cooled back to the ambient temperature in the aftercooler. The high pressure gas is then passed through a series of counterflow heat exchangers and is expanded in one or more turbines where the mechanical energy is extracted. The gas is then directed through the cooling load heat exchanger.

As the minimum temperature , point e in Figure 5-1, is lowered partial condensation of the working fluid may appear. For such low temperatures Joule-Thomson or throttling expansion (clause 5.3) is used instead of the expansion in a turbine. This is the basic idea of the Claude cycle. It can be seen by comparison of Figure 5-3 and Figure 5-5 that the Claude cycle is effectively a Joule-Thomson cycle in which the effective sink temperature is lowered by a Brayton cycle refrigerator.

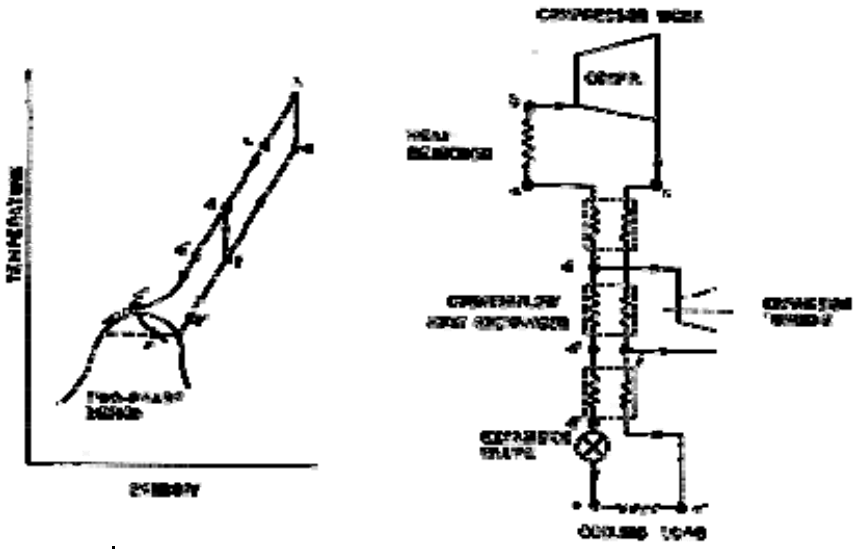

Figure 5-3: Claude Cycle Refrigerator. From Donabedian (1972) [59].

5.2.2.2 Development problems

The turbo machinery refrigerator has a favorable potential for achieving long life spaceborne systems. There are currently no identifiable life limiting components. Potential problem areas identified are shown in Table 5-2.

The present status of turbo machinery development in miniature refrigerators seems to indicate that:

1. It is possible to construct small turbo expanders and compressors suitable for refrigeration application.
2. The reliability and continuous running time for these units can be very good, with maintenance intervals of 10^4 hours or better expected.

3. The heat exchanger and the compressor presently set the limit on size reduction of turborefrigerators.
4. It is not likely that a miniature turbo machinery refrigerator will be commercially available for several years.

Table 5-2: Development Problem Areas of Brayton and Claude Cycle Refrigerators

Component	Problem
Counterflow Heat Exchanger	Non-metallic spacer material being used in current design to reduce longitudinal heat conduction could be a source of contamination. The use of laminated materials is a potential source of leakage.
Compressors	Rigid dimensional accuracy is required to maintain proper clearances between rotating assemblies and thrust bearings.
Turbo-Alternators	Particle contamination of the gimbaled thrust bearing assembly.
Gas Bearing	Manufacturing tolerance must be build up.
Traps/Filters	Manufacturing and improper assembly could cause filter breakthrough.

NOTE From Donabedian (1972) [59].

5.2.3 Gifford-McMahon/Solvay cycle refrigerators

5.2.3.1 Description

The basic refrigeration cycle used in this type of systems was originally conceived by E. Solvay in 1886 as a basic derivative of the Stirling cycle. A number of modifications have been made by various researchers such as K. W. Taconis, W. E. Gifford, and H. O. McMahon. Refrigerator units manufactured are usually marketed using various names, such as Gifford-McMahon and Solvay, with and without the adjective "modified". They are basically the same cycle but with different modifications in the expander.

The basic expansion process is illustrated in Figure 5-4. In position at the inlet valve is open and the exhaust closed. The regenerator and other void volumes are filled to the higher pressure.

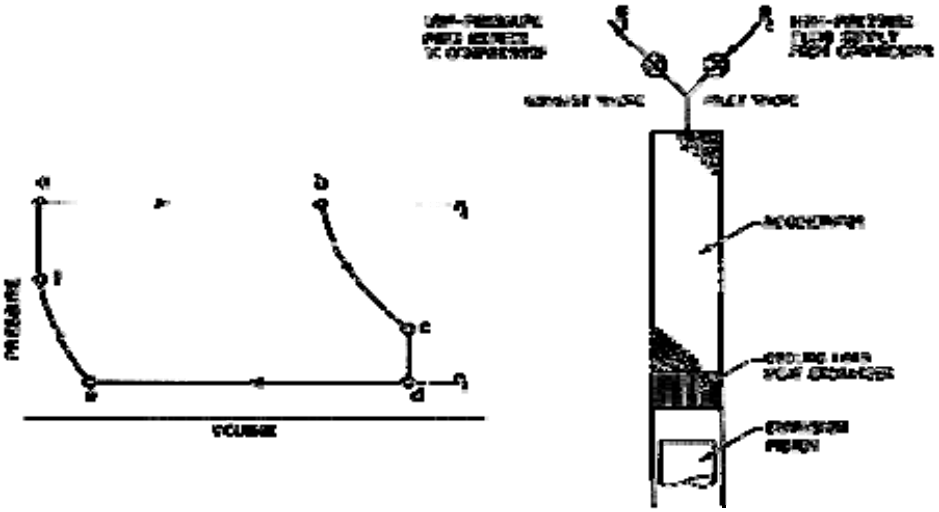

Figure 5-4: Solvay Cycle Refrigerator. From Donabedian (1972) [59].

a to b. This piston moves outward and working fluid enters the cylinder after being cooled in the regenerator.

b to c. The inlet valve is closed and the fluid pressure falls until the piston reaches its outermost position.

c to d. The exhaust valve is opened and the fluid in the system expands to d.

d to e. The piston moves inward, expelling the cold working fluid from the system. This fluid also cools the regenerator.

e to f. The exhaust valve is closed and the piston continues to move until it reaches the innermost position.

f to a. The inlet valve is closed and the fluid in the system is compressed from f to a.

5.2.3.2 Development problems

Because of the commercial attractiveness of the Gifford-McMahon/Solvay cycle units, substantial development effort and production knowledge have been achieved. The primary advantage of this type of cooler is that the cooling head can be separated from the compressor, and thence it can be more easily integrated with the load.

The primary limitation is the lower efficiency of the system, as compared with Vuilleumier or Stirling systems, thence it requires significantly higher power input than systems based on the mentioned two cycles for the same cooling load. Nevertheless, the Gifford-McMahon/Solvay cycle units currently provide the bulk of commercial low temperature cooling and the longest unattended lifetime. Although significant improvements in power requirements, are not likely, substantial mass reduction in the systems may be expected with the use of compressor units which are optimized for minimum mass.

5.2.4 Joule-Thomson Closed Cycle Refrigerator

5.2.4.1 Description

A practical Joule-Thomson refrigerator cycle is shown in Figure 5-5. This cycle is essentially identical to the reversed Brayton cycle except for one fundamental difference: the expansion process, d to e, is accomplished by expansion through a throttling valve rather than through a turbine.

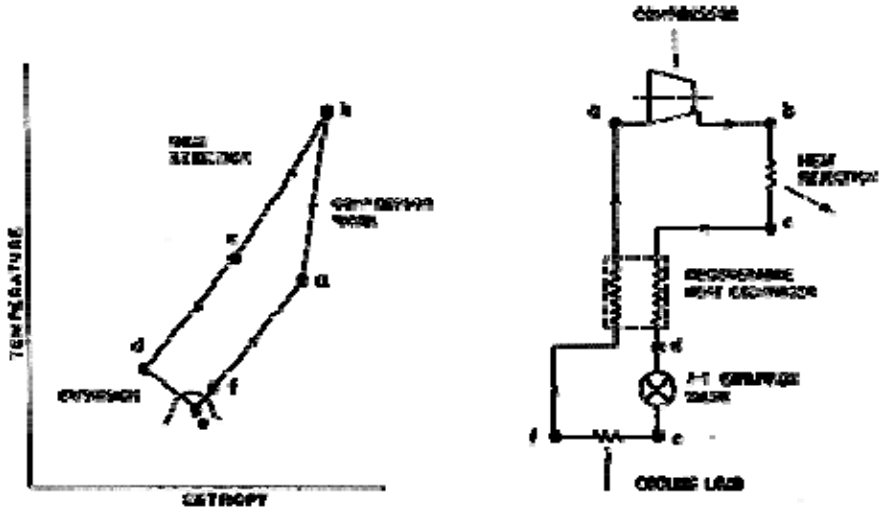

Figure 5-5: Joule-Thomson Closed Cycle Refrigerator. From Donabedian (1972) [59].

In a typical application, the working fluid, gaseous nitrogen, undergoes the following transformations:

a to b. The fluid is compressed to approximately 1,72x10^7 Pa in a multistage oil-lubricated reciprocating compressor.

b to c. Once compressed, the gaseous nitrogen is cooled by ram air or by a fan mounted on the compressor assembly. The gaseous nitrogen then passes through an absorber/filter component in order to remove oil vapor and other trace contaminants, which might solidify at cryogenic temperatures.

c to d. The purified high-pressure nitrogen enters the miniature regenerative heat exchanger where it is cooled by the returning low-pressure gas.

d to e. The high-pressure gaseous nitrogen is expanded at the exit of the heat exchanger. This produces a temperature drop which is sufficient to partially liquefy the gas.

e to f. The latent heat of the liquid nitrogen is used to provide the main cooling.

f to a. The low-pressure gas, after being used for precooling in incoming gas, returns to the first stage of the compressor to begin a new cycle.

5.2.4.2 Development problems

The major advantage of Joule-Thomson closed cycle coolers is that the compressor module can be located far from the heat sink, and thence the entire cooling system can be packaged into varied configurations. Other advantages are that no adjustment is required regardless of ambient

temperatures, and that rapid cool-down can be achieved (approximately in 3 to 5 minutes). Overhaul times from 200 to 500 hours are typical with mean time between failures of 1000 to 2000 hours.

The primary disadvantage of the Joule-Thomson closed cycle system from the stand-point of space application is its high power requirements. For this reason the system has not been extensively developed for spacecraft application. Another disadvantage is that heat rejection is produced isothermally only at the liquid temperature of the refrigerant being used, that limits the flexibility of application.

5.2.5 Stirling cycle refrigerators

5.2.5.1 Description

The Stirling system possesses several of the primary requirements of a spaceborne refrigerator system, such as low power consumption and small size and mass. Its ideal efficiency reaches the Carnot limit (see clause 5.2.1).

Heat evolution takes place in the Stirling cycle by alternately compressing and expanding a given quantity of a gas in a closed cycle. Compression takes place at ambient temperature so as to facilitate heat rejection; the expansion is performed at the required cold temperature.

For the sake of explanation, the Stirling cycle may be split up into four stages, as indicates in Figure 5-6. Ideal cycle diagrams are sketched in Figure 5-7.

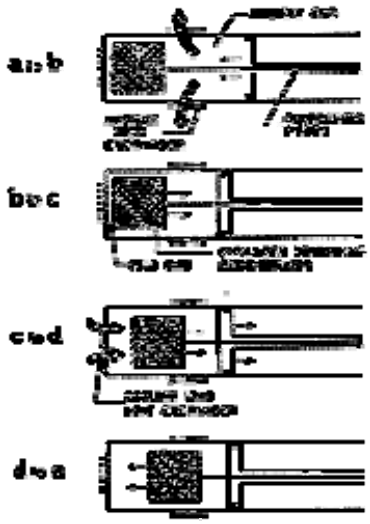

Figure 5-6: Stirling Cycle Refrigerator Operation. From Sherman (1978) [216].

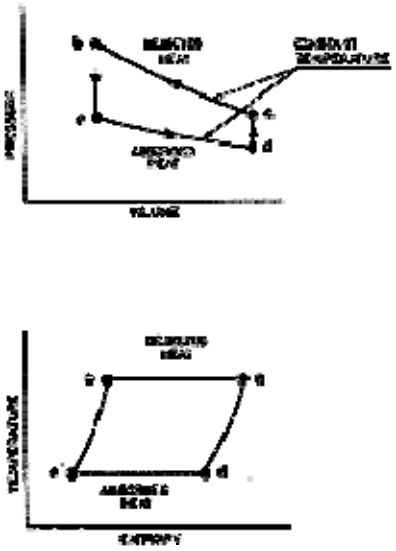

Figure 5-7: Stirling Cycle Refrigerator Ideal Pressure-Volume and Temperature-Entropy Diagrams. From Sherman (1978) [216].

In position a most of the working gas occupies the so called ambient end, at ambient temperature.

a to b. Isothermal compression. The gas is compressed by inward motion of the compressor piston. This compression takes place at room temperature. Heat is rejected through the ambient heat exchanger.

b to c. Constant volume cooling. The gas is transferred, through the regenerator, from the ambient to the cold end, at constant overall volume, by means of the displacer which usually encloses the regenerator. The gas flowing through the regenerator is cooled to nearly the temperature which prevails in the cold end. Heat transferred to the regenerator will be rejected in stage d to a.

c to d. Isothermal cooling. The gas is expanded by moving together both the displacer and the compressor piston. The sensor, or whatever device, is cooled through the cooling load heat exchanger.

d to a. Constant volume heating. The gas is displaced from the cold to the ambient end by the displacer. During this transfer, the flowing gas lowers the temperature of the regenerator.

5.2.5.2 Development problems

Although small Stirling cycle refrigerators have been employed in aircraft and short-duration space missions such as Skylab (Sherman (1978) [216]), the only truly long-duration data presently available are provided by four refrigerators which were launched on Feb. 24, 1979 aboard the DOD P-78-1 Satellite to provide orbital cooling of two gamma-ray spectrometers (Sherman (1982) [217]).

The refrigerator was developed by the North American Philips Corporation, with the John Hopkins Applied Physics Laboratory providing the electronic controls and the space qualification program. Integration with the gamma-ray spectrometers and evaluation of orbital operation data was made by Lockheed, Palo Alto Research Laboratories (Naes & Nast (1980) [160]).

A schematic representation of this refrigerator is shown in Figure 5-8. Performance data are summarized in clause 5.2.1.

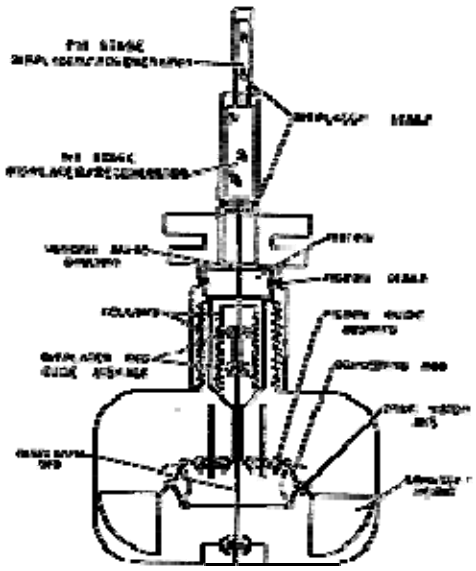

Figure 5-8: Schematic representation of North American Philips refrigerator, showing rhombic drive mechanism. The drive has two counter-rotating crankshafts, each powered by a drive motor. By adjusting the mass of the reciprocating members of the drive and by adding appropriate counterweights to the crankshafts, the center of the gravity of all the moving parts can be kept stationary. From Balas, Leffel & Wingate (1978) [16].

A description of the cooler design, qualification tests, performance and lifetime tests on ground has been made by Balas, Leffel & Wingate (1978) [16]. In orbit performances have been reported by Naes & Nast (1980) [160].

As of July 1980, when the spacecraft has been in orbit for 500 days, the cumulative operating time of each of the four coolers was 2657, 5134, 9542 and 6518 h. The latest data (Sherman (1982) [217]) show that one of the machines has surpassed 15000 h running time. A detailed report of the in-orbit performance of these coolers is given below.

A very recent approach to the long lifetime problem consists in driving reciprocating components directly with linear motors, avoiding contact between moving components and the machine housing or the motor. Non contact operation can be achieved by magnetic or gas bearing and clearance seals.

The North American Philips single stage magnetic bearing refrigerator, Figure 5-9, has been devised with the following requirements in mind:

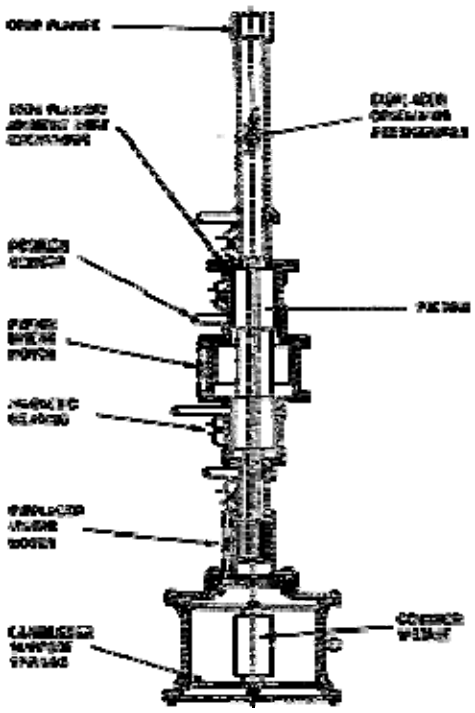

Figure 5-9: Schematic representation of North American Philips Magnetic Bearing refrigerator, showing the linear motors for piston and displacer and the magnetic bearing. The displacer rod passes through the piston. From Sherman, Gasser, Benson & McCormick (1980) [221].

1. No rubbing surfaces
2. Linear drive system without mechanical linkages
3. Electronic control of piston and displacer motions
4. Dynamical balance
5. All metal working-gas chamber

Performance data of this refrigerator are given in clause 5.2.1. For a description of the design, definition studies and component testing see Sherman et al (1980) [221] or the more recent paper by Daniels, Gasser & Sherman (1982) [49].

A linear reciprocating refrigerator based on the above philosophy (no rubbing surfaces, linear driving) but using gas bearing has been studied by Energy Research and Generation, Inc, see clause 5.2.1. Results from the design study have been reported by Sherman et al (1980) [221].

5.2.5.3 In orbit performance

Four Rhombic Drive Stirling Cycle mechanical refrigerators provided orbital cooling of two identical gamma-ray spectrometer detectors, called Gamma003 and 004. Each detector used two refrigerators which will be identified in the following as refrigerators 1 and 2 for Gamma 003, and refrigerators 3 and 4 for Gamma 004.

One single refrigerator is sufficient to cool each detector. However, two units were placed in parallel to increase the overall system reliability. Thus, as the performance of one refrigerator degrades, both are operated together to further reduce the detector temperature.

The entire system is enclosed within a vacuum shell. Vacuum is maintained both on ground and in orbit by a 2 $l.s^{-1}$ vacuum pump.

Figure 5-10 shows a schematic of the system of refrigerators 1 and 2.

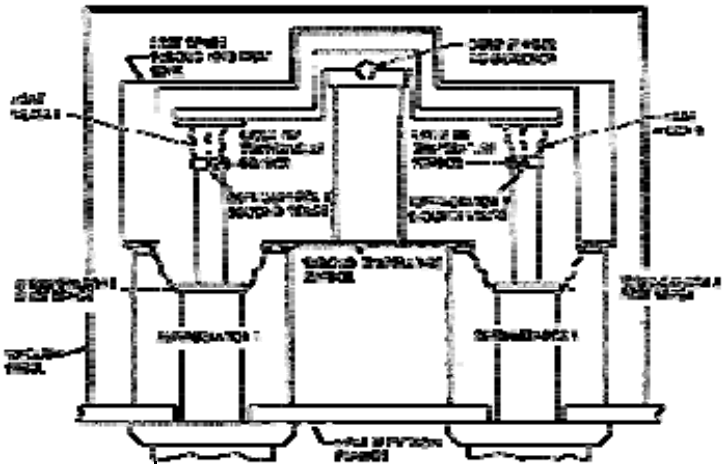

Figure 5-10: Coupling of two refrigerator units to provide cooling of a single detector. The complete refrigerator can be seen in Figure 5-8. Here, on the contrary, only the first and second stages of both refrigerators are shown. From Naes & Nast (1980) [160].

Attached to both first and second stage cold tips are flexible mechanical coupling, the aim of which is reducing the launch structural loads transmitted to the cold tip by the thermal system as well as suppressing microphonics from the refrigerator to the detector. Both flexible couplings to the second stage cold tips were instrumented and calibrated to allow for measurement of the cold tip heat transfer rate.

Cooling of the detector is achieved via a copper cold finger the cross-section of which can be seen in the figure.

A thermal guard shroud surrounds the second stage cold tips of both refrigerators and the detector cold finger attach point. This shroud is thermally coupled to the first stage cold tips, providing an intermediate temperature environment to the second stage.

Enclosed by the shroud is a large thermal capacitor (no details given) designed to retard the detector heating rate to less than 8 $k.h^{-1}$ once the refrigerator is turned off. This large heating time is needed for data collection by the detector with the refrigerators off, to avoid excessive microphonics to the detector.

Performance-related data taken in orbit were: Cold tip temperature and heat transfer rate, crankcase pressure and working gas pressure, motor speed and motor current, all them related to the refrigerator itself. In addition, shroud and base plate temperature, and pressure within the vacuum shell were measured.

Data in Figure 5-11 correspond to refrigerator 2. First and second stage temperatures were measured, in the laboratory, vs. the applied heat transfer rate to each stage.

Figure 5-12 gives the temperatures of shroud and refrigerator cold tip (second stage) in Gamma 004 system.

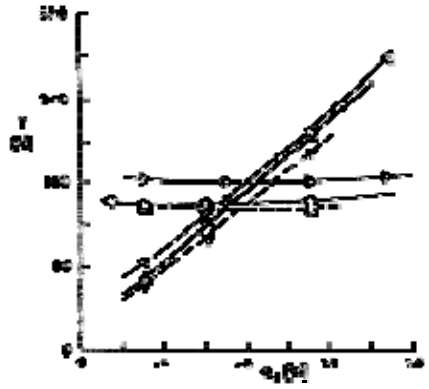

Note: non-si units are used in this figure

Figure 5-11: Ground Test temperatures, of the first and second stage vs. Second stage heat transfer rate, Q_2, for different values of the first stage heat transfer rate, Q_1, and motor rpm. The data correspond to refrigerator 2 but are typical of the four units. From Naes & Nast (1980) [160]. ○ first stage, Q_1 = 1,5 W, 1000 rpm; □ first stage, Q_1 = 1,5 W, 1150 rpm; △ second stage Q_1 = 1,5 W, 1000 rpm; ▽ second stage Q_1 = 1,5 W, 1150 rpm; ▷ first stage, Q_1 = 2 W, 1000 rpm; ◁ Q_1 = 2 W, 1000 rpm.

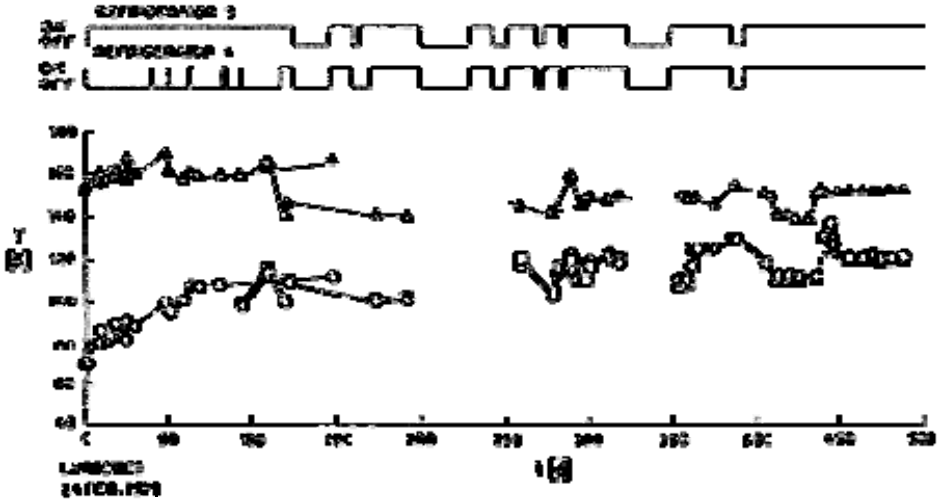

Figure 5-12: In orbit temperature, T, of several components of Gamma 004 systems vs. Orbital time, t . From Naes & Nast (1980) [160]. ○ cold tip of refrigerator 3; □ cold tip of refrigerator 4; △ shroud; ● ground test value of cold tip of refrigerator 3; ▲ ground test value of shroud.

Although initial temperatures agreed with ground test data, a gradual warming trend soon appeared. At approximately 150 days in orbit both refrigerators, 3 and 4, were simultaneously operated. This did not improve the performance of the system because of helium losses in refrigerator 4, as will be discussed below.

The behavior of Gamma 003, Figure 5-13, was somewhat different. The initial cold finger temperature greatly exceeded the ground test value of 68 K. Nevertheless, the same warming trend as for Gamma 004 can be observed. After 125 days, operation with both refrigerators was initiated, which resulted in a substantial temperature reduction. This mode of operation was interrupted, because of power limitations, approximately at 330 days.

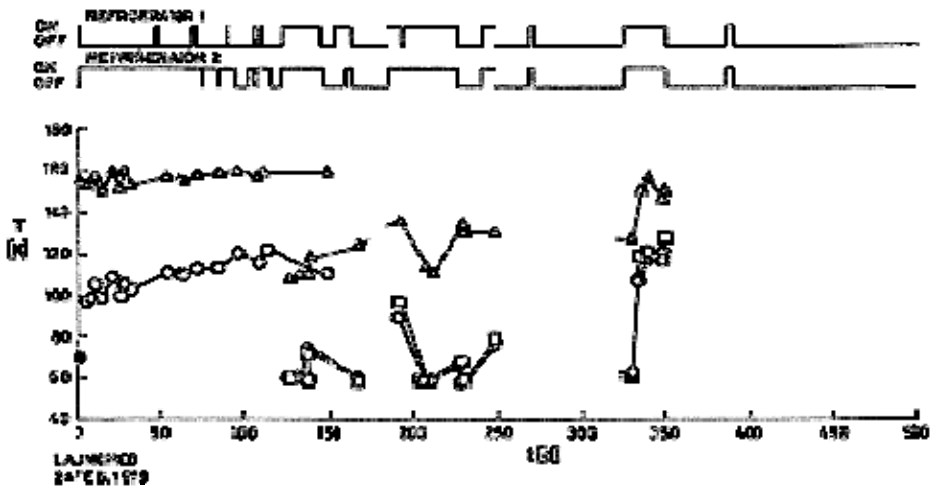

Figure 5-13: In orbit temperature, *T*, of several components of Gamma 003 systems vs. Orbital time, *t* . From Naes & Nast (1980) [160]. ○ cold tip of refrigerator 2; □ cold tip of refrigerator 1; △ shroud; ● ground test value of cold tip of refrigerator 2; ▲ ground test value of shroud.

Finally, Figure 5-14 shows the heat transfer rate from the detector and from the individual refrigerators, for the Gamma 003 system.

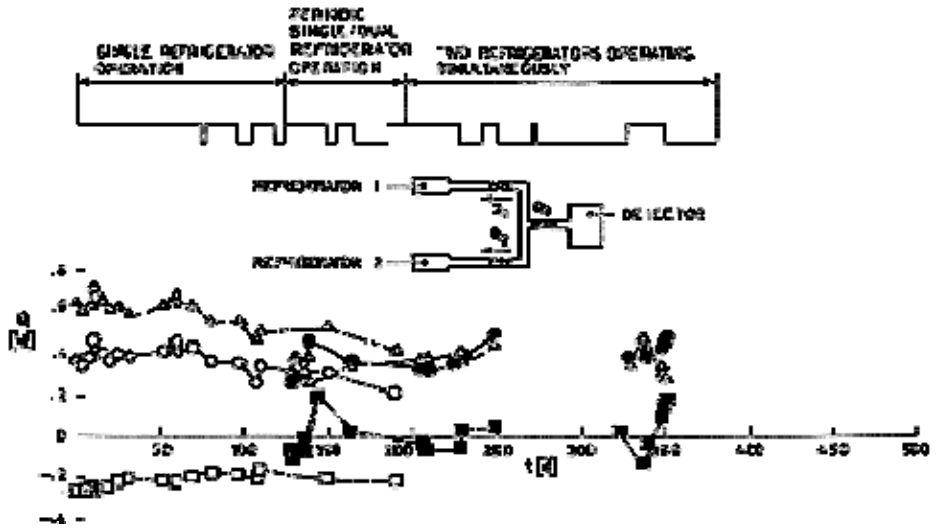

Note: non-si units are used in this figure

Figure 5-14: In orbit heat transfer rates, *Q*, from Gamma 003 detector to refrigerators 1 and 2, vs. orbital time, *t*. From Naes & Nast (1980) [160]. ○ detector heat load. Refrigerator 2 on; □ heat load through meter 1, Q_1 . Refrigerator 1 off; △ heat load through meter 2, Q_2 . Refrigerator 2 on; ● refrigerators 1 and 2 on; ■ refrigerators 1 and 2 on; ▲ refrigerators 1 and 2 on.

The relative cooling load attributable to each refrigerator is measured by the meters placed at the flexible couplings near the second stage cold tip. The heat transfer rate from the detector, Q_3, is presumably deduced from Q_1 and Q_2. The total heat removed by refrigerator 2, Q_2, is initially 0,6 W, which is the sum of the detector plus the parasitic heat transfer rate from the off unit 1. The detector

heat rate is substantially higher than 0,114 W measured in ground testing. This accounts for the higher initial cold tip temperature shown in Figure 5-13.

Causes of system degradation:

1. 1) Helium loss. The four refrigerators were recharged to the design pressure of $4{,}89 \times 10^5$ Pa three months prior to launch.

   At launching time, refrigerators 1, 2 and 3 had lost pressure at a rate of $4{,}5 \times 10^3$ Pa.mo^{-1}, within expectations. On the other hand, the pressure in refrigerator 4 had dropped to approximately 3×10^5 Pa.

   Ground test data show that a reduction in pressure from $4{,}89 \times 10^5$ Pa to $4{,}17 \times 10^5$ Pa will cause an increase in the cold finger temperature from 75 K to 105 K at the design rate of 0,3 W.

   Helium loss could, thus, explain most of the long term temperature increase experienced by both detectors.

   Although refrigerator 4 showed abnormal helium losses, the effect is hardly noticed in Figure 5-12, since this refrigerator started operation after 250 days in orbit. Notice that operation of unit2 produces larger temperature reductions, Figure 5-13, than those due to refrigerator 4 in Figure 5-12.

2. 2) Abnormally high detector heat load in system Gamma 003, Figure 5-13 and Figure 5-14.

   The high heat transfer rates are possibly due to water vapor deposition on the low emittance gold surfaces.

   The high vacuum surrounding the Gamma 003 detector could not be maintained after launch, and the system was open to space. As the detector was launched cold (prechilled with liquid nitrogen), critical surfaces became contaminated. Partial decontamination was achieved, after 75 days and also after 100 days in orbit, by warming up the system above 200 K. This caused a significant reduction in the detector heat load, although ground test results could not be reproduced.

Table 5-3: Potential Problem Areas Associated with the Stirling Refrigerators

Component	Problem	Potential Solutions	Further Problems
Fluid Working Space in General	Contamination	Careful purging and outgassing. All metal working spaces. Dry seals and bearings...	Solid particles obstructing passages.
Regenerator	Aging and contamination. Matrix flexure and rubbing…	As above. External (not in the displacer).	
Counterflow Heat Exchanger	Manufacturing tolerances may shift flow character istics (see ECSS-E-HB-31-01 Part 13 clauses 11.4.3 and 11.5).		
Seals	Wear...	Oil lubrication…	Contamination of fluid

Component	Problem	Potential Solutions	Further Problems
	Working fluid leakage.	Hard on hard spring loaded... Clearance (non contact seals)...	working space. Solid particles obstructing passages. Manufacturing tolerances. Working fluid leakage.
Bearings	Wear.	Oil lubrication… Hard on hard bearing. Non contact operation (gas or magnetic)...	Contamination of fluid working space. Development work required.
Piston	Large axial temperature gradients.	Regenerator incorporated into piston.	Matrix flexure and rubbing.
Driving Mechanism	Vibrations... Phasing piston and displacer....	Counter rotating masses... Rectilinear driving… Electronic control, when rectilinear driving is used…	No perfect balance is achieved. Development work required. Passive or active balancing required. Development work required.
Detector	Degradation due to machine microphonics... Degradation due to EMI. Contamination...	Flexible coupling between cold tip and detector. Brushless DC motors. Outgassing.	

5.2.6 Vuilleumier cycle refrigerator

5.2.6.1 Description

This constant volume cycle was patented by Rudolph Vuilleumier in 1918. The interest in the development of a Vuilleumier-cycle refrigerator for spacecraft application was aroused fairly recently because a refrigerator of this type promises the advantages of long-lifetime operation, compactness, and low weight.

Figure 5-15 gives a schematic of the Vuilleumier refrigerator. It consists of a hot cylinder, cold cylinder, and sump (or ambient section). The working gas is moved from one section of the machine to the other and through the two regenerators by the movement of hot and cold displacers. An electric motor drives the displacers through the crank mechanism.

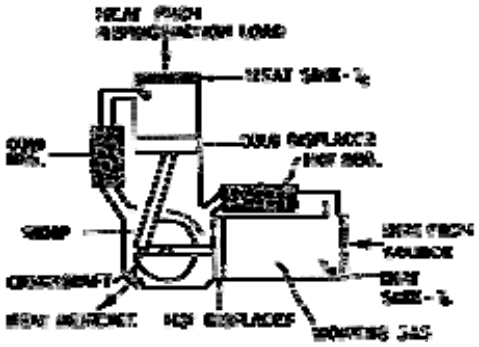

Figure 5-15: Schematic of the Vuilleumier-Cycle Refrigerator. From Sherman (1978) [216].

Because the regenerators are designed for low pressure loss, the Vuilleumier refrigerators have little compression or expansion of the working gas by the motion of the displacers. Consequently, the electric-motor power, bearing loads, and vibrations are small.

The steady state operation of the Vuilleumier refrigeration cycle can be explained by resorting to Figure 5-16 (a schematic of four crank positions encountered during operation) and Figure 5-17 (the pressure volume diagrams for the cold cylinder, hot cylinder and total gas volume). It is assumed in the explanation that the pressure loss across the regenerators is zero, and thence the pressure in the three sections are always the same. It should be noted, in addition, that the following is a simple view of the operation of the Vuilleumier refrigerator, in that only the predominant processes for a given crank position are pointed out. Additional details on the actual operation can be founded in Sherman (1971) [218].

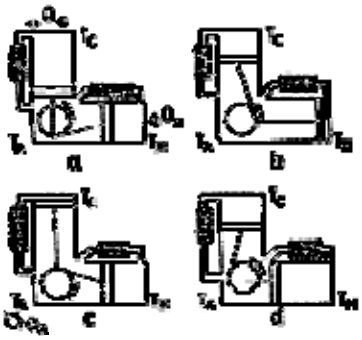

Figure 5-16: Vuilleumier-Cycle Refrigerator. From Sherman (1971) [218].

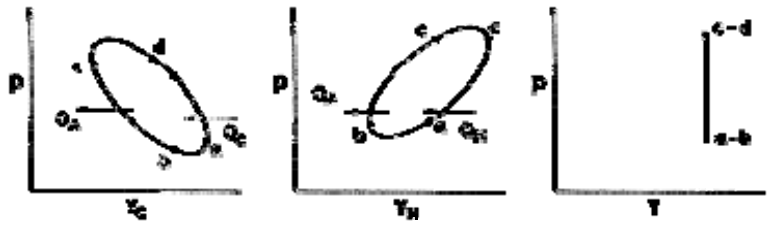

Figure 5-17: Pressure-Volume Diagrams, for the Cold Cylinder, Hot Cylinder and Total Gas, of the Vuilleumier-Cycle Refrigerator. From Sherman (1971) [218].

We begin with the crank in position a. At this point the cold displacer is at its maximum displacement position, and the hot displacer is only at its half-maximum position. The mean gas temperature in the refrigerator is relatively low, and consequently the gas pressure is low.

a to b. Both the hot and the cold cylinder volumes decrease. Part of the cold gas is forced through the cold regenerator where it is heated to nearly T_A before entering the ambient section. Similarly, part of the hot gas is forced through the hot regenerator where it is cooled to nearly T_A before entering the ambient section. The mean gas temperature and the gas pressure change very little during this process. Nevertheless, some gas expansion, with the resulting heat absorption from the load, takes place.

b to c. The hot cylinder volume increases and the cold cylinder volume decreases. The cold gas which is forced through the cold regenerator is heated to nearly T_A, while part of the ambient gas, which flows through the hot regenerator, is heated to nearly T_H before entering the hot cylinder. The net effect of the hot cylinder volumetric increase and the cold cylinder decrease is an increase in the mean gas temperature and the gas pressure (a compression). Thence, heat is rejected at the ambient section.

c to d. Both the hot and cold cylinder volumes increase. Part of the ambient gas moves through the cold regenerator, losses heat and enters the cold volume at nearly T_C. On the hot side, part of the ambient gas moves through the hot regenerator, absorbs heat, and enters the hot volume at nearly T_H. The system pressure does not greatly change during this process. Nevertheless, there is some gas compression with the corresponding heat rejection at the ambient section.

d to a. The hot cylinder volume decreases forcing the gas through the hot regenerator where it is cooled to nearly T_A, whereas the cold cylinder volume increases forcing the gas through the cold regenerator where it is cooled to T_C. The net effect is the decrease of both the mean gas temperature and the gas pressure (an expansion). This expansion results in heat absorption at the cold and hot ends.

5.2.6.2 Development problems

The basic problem areas associated with the development of Vuilleumier refrigerators are listed in Table 5-4 below. The principal degradation mode of the Vuilleumier refrigerator seems to be difficult to maintain the required temperature. This is traced to two causes: Contamination of refrigerant and seal wear.

Table 5-4: Development Problem Areas of Vuillemier Cycle Refrigerators

Component	Problems
Regenerators	Degradation of the characteristics due to aging and contamination.
Counterflow Heat Exchanger	Manufacturing tolerances may shift flow characteristics
Heat Coils	Assembly defects and aging may cause performance anomalies.
Displacer Seals	Wear causes both contamination and leakage.
Crankshaft Seals	Use of rolling seals may cause leakage through the seal material. Either substantial improvement in the seal design or working fluid resupply devices are required.
Displacers	Large temperature gradient along the length of displacers.
Drive Bearing	Require oil lubrication for extensive life.

NOTE From Donabedian (1972) [59].

The present state of several Vuilleumier refrigerator programs has been reviewed by Sherman (1978) [216].

NASA-Goddard' Vuilleumier-cycle refrigerator program started in 1969. The program lead to a nominal 5 W, 75 K machine (built by Garrett AiResearch, see Clause 5.2.1) that has many interesting features, such as solid bearing composed of Boeing compact 6-84-1 running against Inconel 718 (flame-sprayed with tungsten carbide in the sump and chromium carbide at the hot end), and labyrinth seals for both hot and cold displacers. Tests with the Goddard Vuilleumier refrigerator met thermal goals with299 W required to achieve 7 W of cooling at 75 K. The unit ran 6000 h without a mechanical fix.

The Air Force has had an extensive Vuilleumier refrigerator program during the past decade. Work has been concentrated on the development of a three-stage machine with 12 W, 10 W, and 0,3 W cooling loads at 75 K, 33K and 11,5 K, respectively; a lifetime goal of $2x10^4$ h of unattended operation and a maximum of 2700 W of input power were established. Development contracts were awarded to Hughes Aircraft and Philips Laboratories.

The Hughes Aircraft three-stage Vuilleumier refrigerator uses dry-lubricated (MoS_2) ball bearings, with a bearing retainer made of Roulon A (filled Teflon) with 5% MoS_2. This refrigerator has spring-loaded lip seals on both displacers and flexure pivots at the displacer drive-rod interfaces. After several mechanical and test problems, the machine accumulated a total of about 3000 h of operation, but then had to have a crack in the crankcase repaired and, at the same time, many parts upgraded. Testing of the refrigerator has now resumed.

The Philips Vuilleumier refrigerator has unloaded, sleeve type, displacer seals and an oil-lubricated rhombic drive with unequal strokes. This wet lubrication (using a "rolling sock"-a polyurethane rubber seal) is the main feature of the Philips Vuilleumier refrigerator. The rubber seal isolates the oil-filled crankcase from the helium working volume while being subjected to the reciprocating motion of the refrigerator drive shafts. The oil is then supplied to the drive-mechanism bearings by gear-type oil pumps driven by the machine crankshafts.

Unfortunately this basically simple Philips approach presents several drawbacks. First, because of its strength limitations the pressure differential across the rolling seal is limited to a few atmospheres. This necessitates the use of an auxiliary oil pump/regulator system. Second, because the helium gas can penetrate the rolling-seal diaphragm, it is necessary to use a helium-makeup supply for the working volume and a helium separator for the oil supply.

5.2.7 Existing systems

Technical data on closed cycle mechanical refrigerators are collected in this clause. These data are arranged as shown in Table below.

In order to provide a comparative evaluation of the various cycles, the inverse efficiency and the system mass per unit of refrigeration power, of several refrigerator types, have been plotted versus the operating temperature in Figure 5-18 and Figure 5-19 respectively. The inverse efficiency is defined as the required mechanical power per unit of refrigeration power.

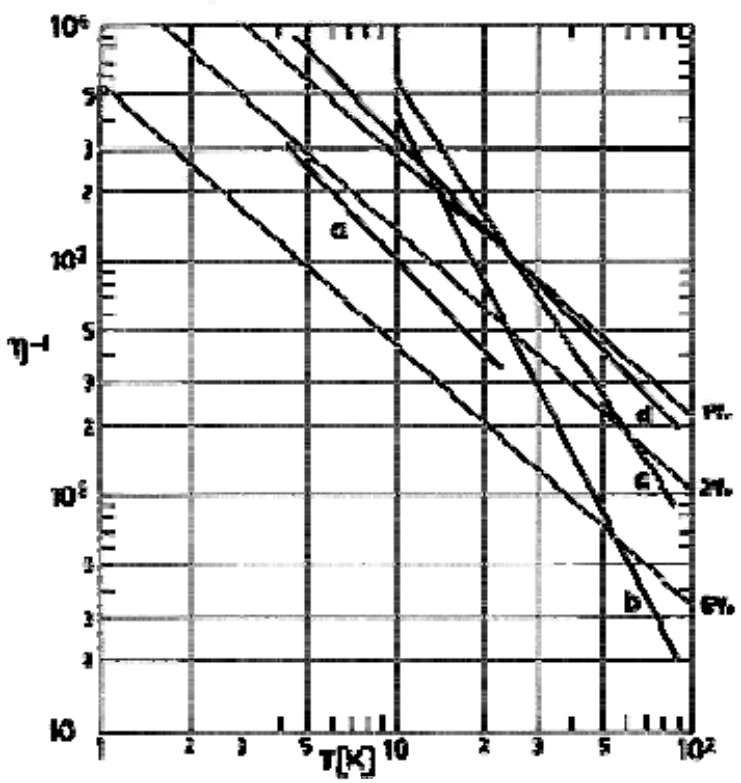

Figure 5-18: Inverse efficiency (required power per unit of refrigeration power) $\eta 1$, vs. operating temperature, T, for several closed cycle refrigerators.
a - Brayton refrigerators (Turbo machinery Systems).
b - Stirling refrigerators.
c - Vuilleumier refrigerators.
d - Gifford-McMahon/Solvay refrigerators.
From Donabedian (1972) [59].
Also shown are curves for closed cycle refrigerators operating with the quoted efficiencies (in percentages of Carnot) through the whole temperature range. From Haskin & Dexter (1979) [83].
The Carnot efficiency for a machine working between T_C and T_H temperatures is given by $\eta_c = 1 - T_C/T_H$. Very low operating temperatures result in a reduced efficiency for a given cooling load and a given cycle.

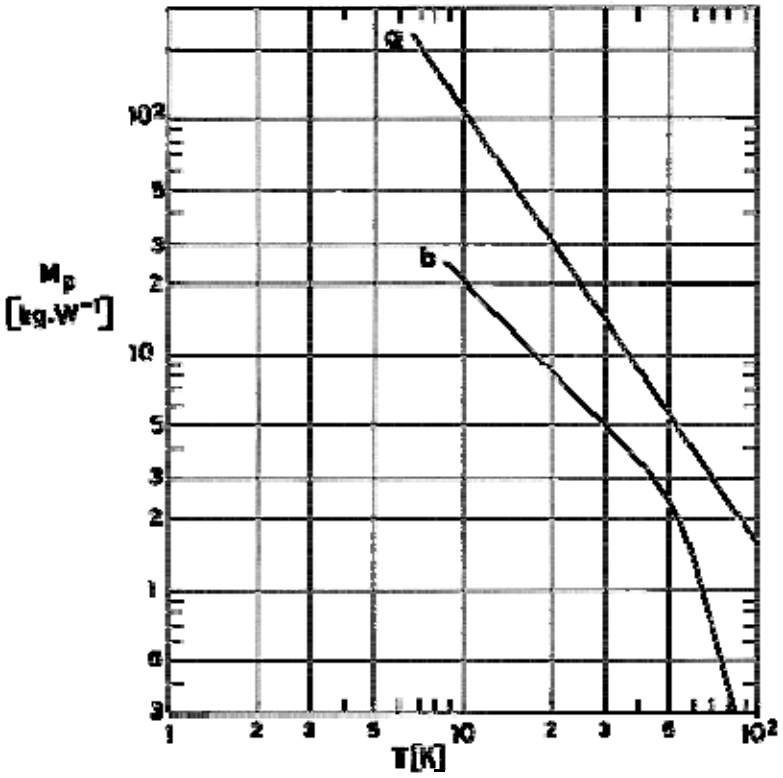

Figure 5-19: System mass per unit of refrigeration power, M_p, vs. operating temperature, T for several closed cycle refrigerators.
a - Gifford-McMahon/Solvay refrigerators.
b - Stirling refrigerators.
From Donabedian (1972) [59].

The plotted curves only represent gross trends since they have been drawn through the cluster of data points from the individual units listed in the data tables. Precise correlations are very difficult to obtain because of the wide scattering and inconsistencies in the data. Furthermore, no curves are shown for several of the closed cycle systems presented in the tables since the available data are insufficient to warrant inclusion of the curves.

Figure 5-20 shows the system mass per unit of refrigeration power, Mp, for representative closed cycle refrigerating systems, and for passive radiant coolers (see ECSS-E-HB-31-01 Part 9, clause 6). Both cooling techniques could compete, when the lifetime must exceed two years, at temperatures between 80 K and 110 K for refrigerating powers or cooling loads below 1 W, and for larger cooling loads at higher temperatures.

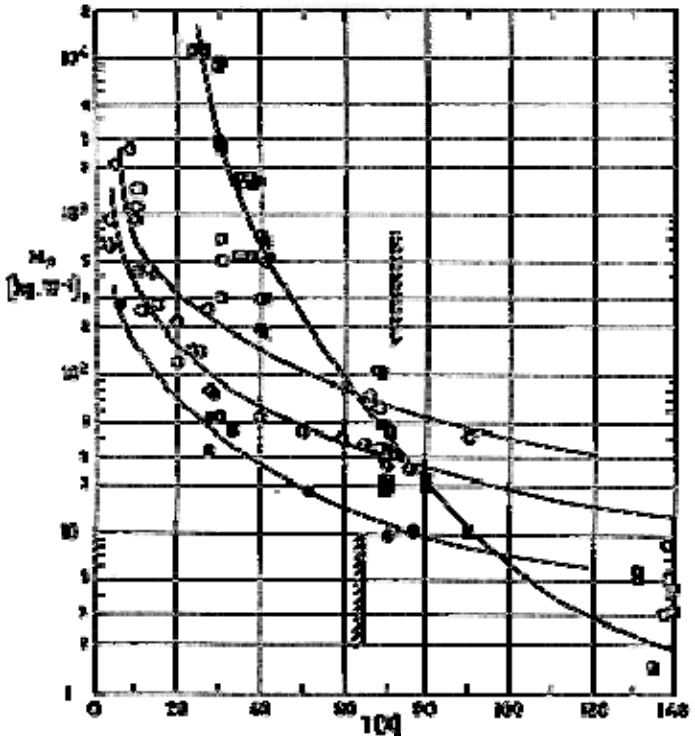

Figure 5-20: System mass per unit of refrigeration power (or cooling load), M_p, for representative closed cycle refrigerating systems and for passive radiant coolers. ○ Closed cycle refrigerators, Q = 0,1 W. ◑ Closed cycle refrigerators, Q = 1 W. ◐ Closed cycle refrigerators, Q = 10 W. □ Passive radiant coolers; Q = 0,1 W. ◨ Passive radiant coolers; Q = 1 W. ◧ Passive radiant coolers; Q = 10 W. From Haskin & Dexter (1979) [83]. ▒ Smallest temperature attained by closed cycle refrigerators in orbit. ▒ Smallest temperature attained by passive radiant coolers in orbit. From Sherman (1982) [217].

Arrangement of the Compiler Data on Closed Cycle Refrigerators		
Cycle	**Manufacturer**	**No.** [a]
Brayton (Rotary-Reciprocating Systems).	A.D. Little	3
Brayton (Turbomachinery Systems)	A.D. Little Garrett-AiResearch Hymatic Engineering Co.	1 1 1
Claude	Air Products & Chemicals, Inc. General Electric Co.	1 3
Gifford-McMahon	Cryogenic Technology, Inc. Cryomech, Inc.	10 4
Joule-Thomson	Air Products & Chemicals, Inc. Garrett-AiResearch Santa Barbara Research Center	2 6 1
Solvay	Air Products & Chemicals, Inc. Kinergetics	6 1
Stirling	Hughes Aircraft Co. Malaker Corp. North American Philips Corp. (USA) Philips with APL Johns Hopkins Philips under NASA Goddard Energy Research and Generation, Inc. Philips Laboratories (Netherlands)	3 7 4 1 1 1 1
Taconis	British Oxygen Co., Ltd.	1
Vuilleuimier	Garrett-AiResearch Hughes Aircraft Co. Kinergetics North American Philips Corp. (USA) RCA Defense Electronics Laboratory	1 10 1 3 1

[a] Number of refrigerators listed.

The mentioned figure is a summary of a trade off performed by Haskin & Dexter (1979) [217] on the following bases:

1. Source of the data. Data were taken from examples found in the literature consisting of flight worthy hardware, test models and design proposals.
2. System mass. The cryogenic refrigerator includes:

   Refrigerator itself, which accounts for 10 % to 40 % of total system mass.

   Heat rejection radiator with associated pumps, valves, piping,...

Power supply which, in most cases, consists of solar cell arrays, electrical storage batteries and regulation equipment.

When data for the heat rejection radiator were unavailable, an average value of 22 $W.kg^{-1}$ heat rejection capability was assumed. A common penalty of 8,8 $W.kg^{-1}$ was applied in any case to account for current solar array and battery power supply capabilities in the orbits considered.

The passive radiant cooler includes:

Radiator fins.

Heat pipes to couple the radiator to the instrument to be cooled.

Supports, shrouds, insulation.

When the actual mass of the radiator was unknown an average value of 17 $kg.m^{-2}$ was used to derive the system mass.

3. Orbit. Favorable orbits for passive radiant coolers have been considered (geosynchronous and sun synchronous orbits above 740 km). Less favorable orbits would require larger radiator areas. The chosen orbits are also well suited for solar array power supplies.

4. Operating temperatures. Values of *Mp* in Figure 5-20 have been plotted vs. the design temperature of the cooling device under consideration.

Closed cycle refrigerating systems are often staged, and the stages used to provide cooling at different temperature levels. The added penalty for secondary cooling at other stages is often a minor consideration since staging is provided for other reasons.

Similarly, when staging of the radiant cooler is used to reduce the heat transfer to the surroundings, the higher temperature stages can be used to cool optical elements or other detectors significant penalty.

Data points for passive radiant coolers in Figure 5-20 are almost independent of the cooling load *Q*, and can be scaled up or down proportionally to *Q*. This is not so for refrigerators whose *Mp* decreases and whose efficiency increases with increased refrigeration power.

Figure 5-20 shows that the closed cycle refrigerator systems exhibit lower weights when cooling at very low temperatures is required, whereas the passive radiant coolers have lower weights at higher temperatures. The crossover points for Q = 0,1 W, 1 W and 10 W can be seen in the figure. It can be inferred that the refrigerators will be competitive at still higher temperatures for cooling loads above 10 W.

Other parameter of interest is the area required per unit refrigerating power.

For closed cycle refrigerators the associated area is the sum of the solar cell array and radiator area. Any other exposed area (refrigerator, pump, etc.) was assumed to be negligible. A solar cell array specific power of 89 $W.m^{-2}$ was taken in any case. When no data on the radiator size were available an appropriate area was derived assuming a heat rejection capability of 150 $W.m^{-2}$.

For passive radiant coolers the projected area refers to total radiator and shield area refers to total radiator and shield areas as projected onto a plane that is parallel to the radiating surface.

Results are shown in Figure 5-21. Although they have been obtained for Q = 1 W, the Q dependence is surely negligible.

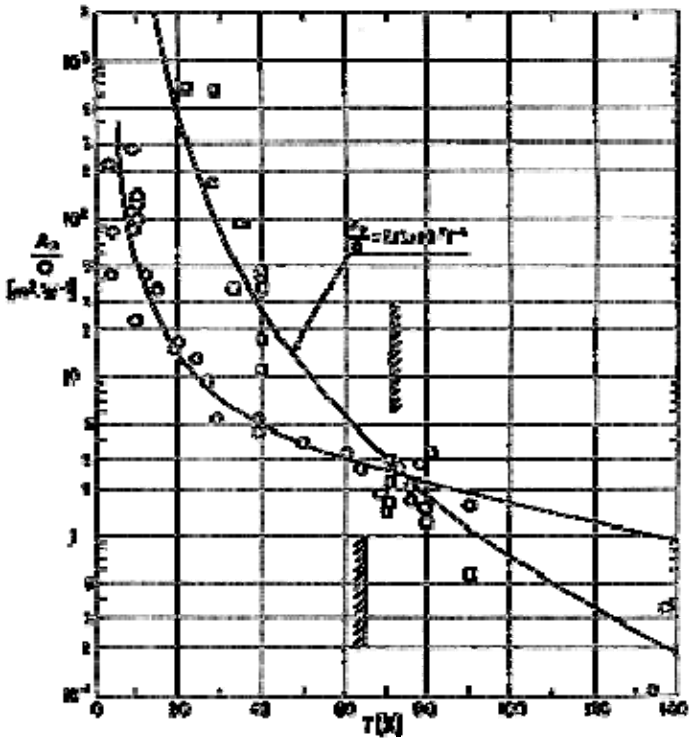

Figure 5-21: System area per unit of refrigeration power (or cooling load), A_p/M_p, for closed cycle refrigerating systems and for passive radiant coolers. ○ Closed cycle refrigerators, Q = 1 W. □ Passive radiant coolers; Q = 1 W. From Haskin & Dexter (1979) [83]. Although the areas, A_p, have been calculated for 1 W cooling, they could be scaled in approximately direct proportion to the cooling load. $A_p/Q = 7{,}13 \times 10^7\ T^{-4}$ is the best fitting, by the least squares method, to the data for passive radiant coolers. ▏Smallest temperature attained by closed cycle refrigerators in orbit. ▏Smallest temperature attained by passive radiant coolers in orbit. From Sherman (1982) [217].

Finally, additional considerations to be taken into account in the section of the cooling method employed are,

1. Factors such as reliability and component availability. Closed cycle refrigerators for greater than one year missions probably will not be available until mid 1980's. On the other hand, large cryogenic radiators are still unproven.
2. Costs for refrigerator systems are probably higher than for passive radiant coolers when associated research and development is considered.
3. The competitive position of the refrigerator systems may improve in coming years. For example, the mere combination of the solar cell array and the heat rejection radiator into one structure could save up to 20 % in mass and 30 % in required area.

CLOSED CYCLE REFRIGERATORS					
CYCLE	**BRAYTON (Rotary-Reciprocating Systems)**			**BRAYTON (Turbomachinery Systems)**	
MANUFACTURER	A.D. Little [a]			A.D. Little [a]	Garrett [b]
TRADE NAME					
MODEL OR PROGRAM	Design Study				Prototype
WORKING FLUID	Helium			Helium	Nitrogen
OPERATING TEMP. RANGE [K]	15 to 50 (two stages)	15 to 30 (two stages)	20 to 60 (two stages)	3,6	80
OPERATING PRESSURE RANGE $px10^{-5}$ [Pa]					0,30 to 0,73
TYPICAL REFRIGERATION	15 W at 50 K 1 W at 15 K	15 W at 30 K 1 W at 15 K	20 W at 60 K 2 W at 20 K	1 W at 3,6 K	2 W at 80 K
SETTING-ON-TIME WITHOUT LOAD [min]					360 approx.
TEMP. STABILITY [K]					
EXPANDER [rpm]					
POWER INPUT [W]	1300	2160	1760	1310	375
VOLTAGE [V]					115
PHASE/FREQUENCY [Hz]					3/60
COOLING MEAN					Water
AMBIENT TEMP. [K]					
CRYOSTAT SIZE [m]	0,305 Diameter 1,219 Length		0,305 Dia. 1,016 Length		
COMPRESSOR SIZE [m]	0,203 Dia. 0,914 Length	0,216 Dia. 0,914 Length	0,203 Dia. 0,914 Length		
REFRIGERATOR	70,75	91,61	83,90	56,23	68,48

MASS [kg]					
MEAN TIME BETWEEN FAILURES [h]					
OVERHAUL TIME [h]					
AVAILABILITY TIME [mo]					
SYSTEM COST [$]					

[a] A.D. Little, Inc., Cambridge, Massachusetts, USA.

[b] Garrett Corp., AiResearch Manufacturing Co., Phoenix, Arizona, USA.

NOTE From Donabedian (1972) [59].

CLOSED CYCLE REFRIGERATORS					
CYCLE	BRAYTON	CLAUDE			
MANUFACTURER	Hymatic [a]	Air Products [b]	General Electric Co. [c]		
TRADE NAME					
MODEL OR PROGRAM	Prototype	E-311	Army ATP	USAF ADP	
WORKING FLUID	Helium or Neon [d]	Helium	Helium		
OPERATING TEMP. RANGE [K]	19 to 28	3,3 to 4,5	4,4	5 to 150 (Three stages)	12 to 60 (Two stages)
OPERATING PRESSURE RANGE $px10^{-5}$ [Pa]	1,01 to 30,4	0,61 to 20,3			
TYPICAL REFRIGERATION	0,3 W at 28 K	1 W at 3,9 K	2 W at 4,4 K	200 W at 150 K 40 W at 50 K 3,5 at 5 K	40 W at 60 K 1,5 W at 12 K
SETTING-ON-TIME WITHOUT LOAD [min]	30	420 for 6,8 kg of Copper			
TEMP. STABILITY [K]		+/- 0,01			
EXPANDER [rpm]	1500	365			
POWER INPUT [W]		7000	9000	16000	4000
VOLTAGE [V]		208-460			
PHASE/FREQUENCY [Hz]		3/60			
COOLING MEAN		Air			
AMBIENT TEMP. [K]		241 to 325			
CRYOSTAT SIZE [m]		0,508 x 0,635 x 1,346		0,610 Dia. [e] 1,219 Length	0,508 Dia. [e] 1,651 Length
COMPRESSOR SIZE [m]		0,686 Dia. 1,067 Length			

CRYOSTAT MASS [kg]		86,17		113,38 [e]	
COMPRESSOR MASS [kg]		104,31			
MEAN TIME BETWEEN FAILURES [h]		33640			
OVERHAUL TIME [h]		3000 to 6000			
AVAILABILITY TIME [mo]		6			
SYSTEM COST [$]		40000 to 100000			

[a] Hymatic Engineering Company, England.

[b] Air Products and Chemicals, Inc., Allentown, Pennsylvania, USA.

[c] General Electric Co., Schenectady, New York, USA.

[d] From Streed, Murphy & Brna (1971) [229].

[e] These values are related to the entire refrigerator.

NOTE Data in this table are from Donabedian (1972) [59] unless otherwise stated.

CLOSED CYCLE REFRIGERATORS					
CYCLE	GIFFORD-McMAHON				
MANUFACTURER	Cryogenic Technology [a]				
TRADE NAME	Cryodyne				
MODEL OR PROGRAM	400	0110	1020	350	0120/RC-30
WORKING FLUID	Helium				
OPERATING TEMP. RANGE [K]	3,8 to 4,5	6,5 to 25	12 to 28	15 to 28	19 to 28
OPERATING PRESSURE RANGE px10^{-5} [Pa]	1 to 19,8	5,1 to 19,2	5,1 to 18,7	4,6 to 12,7	8,6 to 22,3
TYPICAL REFRIGERATION	1,25 W at 4,2 K	1 W at 10 K	2 W at 13 K	2 W at 18,5 K	1 W at 26 K
SETTING-ON-TIME WITHOUT LOAD [min]	180	60	30	45	15
TEMP. STABILITY [K]	+/- 0,12	+/- 1	+/- 1	+/- 1	+/- 1,5
EXPANDER [rpm]	72				150
POWER INPUT [W]	5500	2100	6100	2100	650
VOLTAGE [V]	440	208-230	208-440	208-230	208
PHASE/FREQUENCY [Hz]	3/60	1/50-60	3/50-60	1/50-60	3/400
COOLING MEAN	Air				
AMBIENT TEMP. [K]	268 to 325	241 to 325		241 to 328	219 to 328
CRYOSTAT SIZE [m]	0,457 Diameter 1,219 Length	0,061 x 0,127 x 0,305	0,330 x 0,203 x 0,508	0,457 x 0,127 x 0,203	
COMPRESSOR SIZE [m]	0,762 x 0,813 x 1,372	0,431 x 0,381 x 0,711	0,533 x 0,660 x 1,041	0,432 x 0,381 x 0,711	
CRYOSTAT MASS [kg]	56,69	13,61	14,97	9,98	2,04

COMPRESSOR MASS [kg]	362,8	79,36	192,74	79,36	9,52
MEAN TIME BETWEEN FAILURES [h]	13500				3000
OVERHAUL TIME [h]	3000				1000
AVAILABILITY TIME [mo]	6	4	3	1-2	3
SYSTEM COST [$]	75000	18000	15500	13500	8000

[a] Cryogenic Technology, Inc., Waltham, Massachusetts, USA.

NOTE From Donabedian (1972) [59].

CLOSED CYCLE REFRIGERATORS					
CYCLE	GIFFORD-McMAHON				
MANUFACTURER	Cryogenic Technology [a]				
TRADE NAME	Cryodyne				
MODEL OR PROGRAM	0125	077	0120	0277	1020
WORKING FLUID	Helium				
OPERATING TEMP. RANGE [K]	19 to 28	25 to 150	19 to 30	40 to 120	13 to 20
OPERATING PRESSURE RANGE px10^{-5} [Pa]	9,6 to 18,7	5,1 to 20,3	9,6 to 18,9		5,2 to 19,1
TYPICAL REFRIGERATION	1 W at 26 K	125 W at 77 K	1 W at 26 K	3 W at 77 K	10 W at 20 K
SETTING-ON-TIME WITHOUT LOAD [min]	15	30	15	10	30
TEMP. STABILITY [K]	+/- 1,5	+/- 2			
EXPANDER [rpm]	200	150		333	72

POWER INPUT [W]	750	6100	800	525	5600
VOLTAGE [V]	115	206	208		220
PHASE/FREQUENCY [Hz]	1/50-60	3/400			3/60
COOLING MEAN	Air				
AMBIENT TEMP. [K]	241 to 328	241 to 325	292 to 328	219 to 328	269 to 325
CRYOSTAT SIZE [m]	0,152 x 0,127 x 0,279	0,419 x 0,178 x 0,381	0,038 Dia. 0,263 Length	0,025 Dia. 0,127 Length	
COMPRESSOR SIZE [m]	0,381 x 0,305 x 0,229	0,686 x 0,381 x 0,356	0,267 x 0,267 x 0,203	0,254 x 0,229 x 0,165	
CRYOSTAT MASS [kg]	4,54	12,70	2,27	1,36	14,97
COMPRESSOR MASS [kg]	22,68	52,15	9,07	5,90	192,74
MEAN TIME BETWEEN FAILURES [h]	10000	3000			
OVERHAUL TIME [h]	3000	1000	500		3000
AVAILABILITY TIME [mo]	4	3			
SYSTEM COST [$]	11000	18500			

[a] Cryogenic Technology, Inc., Waltham, Massachusetts, USA.

NOTE From Donabedian (1972) [59].

CLOSED CYCLE REFRIGERATORS					
CYCLE	GIFFORD-McMAHON				JOULE-THOMSON
MANUFACTURER	Cryomech Inc. [a]				Air Products [b]
TRADE NAME					
MODEL OR PROGRAM	GB02	GB12	AL01	AL02	J-80-1000
WORKING FLUID	Helium				Nitrogen
OPERATING TEMP. RANGE [K]	7,5 to 25	9 to 30	23 to 80	23 to 89	77
OPERATING PRESSURE RANGE px10^{-5} [Pa]	10,1 to 24,3				
TYPICAL REFRIGERATION	1 W at 9,5 K	4 W at 13 K	1 W at 25 K	10 W at 30 K	2 W at 77 K
SETTING-ON-TIME WITHOUT LOAD [min]	25	35	12	25	5
TEMP. STABILITY [K]	+/- 0,5				
EXPANDER [rpm]	144				3850 [c]
POWER INPUT [W]	3000		900	3000	600
VOLTAGE [V]	220		110-220	220	
PHASE/FREQUENCY [Hz]	1/50-60				
COOLING MEAN	Air				Air
AMBIENT TEMP. [K]					
CRYOSTAT SIZE [m]	0,127 x 0,127 x 0,533	0,127 x 0,127 x 0,610	0,064 x 0,064 x 0,368	0,127 x 0,127 x 0,457	0,127 x 0,203 x 0,305
COMPRESSOR SIZE [m]	0,737 x 0,483 x 0,686			0,457 x 0,737 x 0,686	

CRYOSTAT MASS [kg]	11,34	2,27	11,34	8,16 [d]
COMPRESSOR MASS [kg]	79,36		79,36	
MEAN TIME BETWEEN FAILURES [h]	5000			
OVERHAUL TIME [h]	3000			500
AVAILABILITY TIME [mo]	1,5-2			
SYSTEM COST [$]	13200	8600	10300	9000

[a] Cryomech Inc., Jamesville, New York, USA.

[b] Air Products and Chemicals, Inc., Allentown, Pennsylvania, USA.

[c] This value is related to the compressor.

[d] Total mass of the refrigerator.

NOTE From Donabedian (1972) [59].

CLOSED CYCLE REFRIGERATORS					
CYCLE	JOULE-THOMSON				
MANUFACTURER	Air products [a]	Garrett-AiResearch [b]			
TRADE NAME					
MODEL OR PROGRAM	J-30-3500	133386	133488	144406	800334
WORKING FLUID	Nitrogen/ Helium	Nitrogen			
OPERATING TEMP. RANGE [K]	23 and 77 (Two stages)	77			
OPERATING PRESSURE RANGE $px10^{-5}$ [Pa]		1 to 157		1 to 178,3	1 to 111,4
TYPICAL REFRIGERATION	2 W at 77 K 0,35 W at 23 K	0,75 W at 77 K 2,25 W at 77 K [c]	5 W at 77 K	3 W at 77 K	1 W at 77 K
SETTING-ON-TIME WITHOUT LOAD [min]		6	12	6,5	8
TEMP. STABILITY [K]		+/- 0,5			
EXPANDER [rpm]	3850 [d]	None			
POWER INPUT [W]	1050	450	650	450	460
VOLTAGE [V]		115-208			
PHASE/FREQUENCY [Hz]		3/400			
COOLING MEAN	Air	Ram Air	Air	Ram Air	Air-Fan [c]
AMBIENT TEMP. [K]		233 to 329			
CRYOSTAT SIZE [m]		$14,16x10^{-3}$ m^3 (Volume)	$42,48x10^{-3}$ m^3 (Volume)	$12,74x10^{-3}$ m^3 (Volume)	$42,48x10^{-3}$ m^3 (Volume)
COMPRESSOR SIZE [m]					
REFRIGERATOR MASS [kg]	8,16	11,34	10,20	8,84	10,20
MEAN TIME BETWEEN FAILURES [h]		1000	1000	2000	

OVERHAUL TIME [h]	500	200	300	400	500
AVAILABILITY TIME [mo]		4	4	6	4
SYSTEM COST [$]		10500	9000	8000	12000

[a] Air products & Chemicals, Inc., Allentown, Pennsylvania, USA.

[b] Garrett Corp. AiResearch Manufacturing Company, Phoenix, Arizona, USA.

[c] From Streed, Murphy & Brna (1971) [229].

[d] This value is related to the compressor.

NOTE Data in this table are from Donabedian (1972) [59] unless otherwise stated.

CLOSED CYCLE REFRIGERATORS					
CYCLE	JOULE-THOMSON			SOLVAY	
MANUFACTURER	Garrett-AiResearch [a]		Santa Barbara [b]	Air Products [c]	
TRADE NAME					Displex
MODEL OR PROGRAM	800398	800656		I-1	
WORKING FLUID	Nitrogen		Nitrogen	Helium	
OPERATING TEMP. RANGE [K]	77		77	30 to 150	5 to 300
OPERATING PRESSURE RANGE $px10^{-5}$ [Pa]	1 to 157	1 to 178,3		10,1 to 23,3	6,1 to 20,3
TYPICAL REFRIGERATION	1 W at 77 K	2,5 W at 77 K	2 W at 77 K	20 W at 77 K	1,5 W at 77 K
SETTING-ON-TIME WITHOUT LOAD [min]	4		5	16	5
TEMP. STABILITY [K]	+/- 0,5			+/- 2	
EXPANDER [rpm]	None			144	385
POWER INPUT [W]	650	530	326	1700	340
VOLTAGE [V]	115-208			208-460	

PHASE/FREQUENCY [Hz]	3/400			3/60	
COOLING MEAN	Air-Fan [d]		Air	Air	Liquid
AMBIENT TEMP. [K]	233 to 329			278 to 316	Up to 338
CRYOSTAT SIZE [m]	42,48 x 10^{-3}m^3 (Volume)	37,66 x 10^{-3}m^3 (Volume)	0,178 Dia. 0,318 Length	0,041 Dia. 0,203 Length	0,038 x 0,025 x 0,025
COMPRESSOR SIZE [m]				0,330 x 0,737 x 0,330	0,127 x 0,140 x 0,184
CRYOSTAT MASS [kg]	10,43 [e]	9,07 [e]	7,26 [e]	4,81	0,23
COMPRESSOR MASS [kg]				59,96	4,76
MEAN TIME BETWEEN FAILURES [h]	1000	2000		5000 to 10000	3086
OVERHAUL TIME [h]	300 1000 [d]	100	500	5000	
AVAILABILITY TIME [mo]	4	3		3	
SYSTEM COST [$]	10000	7000	10000	5000 to 10000	

[a] Garrett Corp., AiResearch Manufacturing Company, Phoenix, Arizona, USA.

[b] Santa Barbara Research Center, Goleta, California, USA.

[c] Air Products & Chemicals, Inc., Allentown, Pennsylvania, USA.

[d] From Streed, Murphy & Brna (1971) [229].

[e] Total mass of the refrigerator.

NOTE Data in this table are from Donabedian (1972) [59] unless otherwise stated.

CLOSED CYCLE REFRIGERATORS					
CYCLE	SOLVAY				
MANUFACTURER	Air Products [a]				Kinergetics [b]
TRADE NAME		Displex			
MODEL OR PROGRAM	CS-102	CS-202	CS-1003	MS-1003	SRC-07
WORKING FLUID	Helium				
OPERATING TEMP. RANGE [K]	30 to 200	30 to 300	50 to 300	30 to 77	50 to 77
OPERATING PRESSURE RANGE px10^{-5} [Pa]				10,1 to 25,3	
TYPICAL REFRIGERATION	17 W at 77 K	1 W at 17 K	1 W at 77 K		1 W at 38 K
SETTING-ON-TIME WITHOUT LOAD [min]	20	45	5		
TEMP. STABILITY [K]					
EXPANDER [rpm]					
POWER INPUT [W]	1700	1735	400	368	400
VOLTAGE [V]	230			115	
PHASE/FREQUENCY [Hz]	1/60	3/60		3/400	
COOLING MEAN	Air				
AMBIENT TEMP. [K]		277 to 317		Up to 330	
CRYOSTAT SIZE [m]	0,381 x 0,432 x 0,559 [c]	0,102 x 0,102 x 0,432	0,013 Dia. 0,127 Length	0,032 Dia. 0,095 Length	
COMPRESSOR SIZE [m]		0,559 x 0,432 x 0,381	0,533 x 0,381 x 0,279	0,184 Dia. 0,216 Length	
CRYOSTAT MASS [kg]			1,50	0,23	5,62

COMPRESSOR MASS [kg]	68,03	68,03	27,21	6,35	
MEAN TIME BETWEEN FAILURES [h]				3100	
OVERHAUL TIME [h]	3000		4500	1200	
AVAILABILITY TIME [mo]		Immediate			
SYSTEM COST [$]					

[a] Air Products & Chemicals, Inc., Allentown, Pennsylvania, USA.

[b] Kinergetics (Formerly the Submarine System Division of Sterling Electronics). Tarzana, California, USA.

[c] Total size of the refrigerator.

NOTE From Donabedian (1972) [59].

CLOSED CYCLE REFRIGERATORS					
CYCLE	STIRLING				
MANUFACTURER	Hughes Aircraft Co. [a]			Malaker Corp. [b]	
TRADE NAME				Cryomite	
MODEL OR PROGRAM				VII-C	VII-R
WORKING FLUID	Helium			Helium	
OPERATING TEMP. RANGE [K]	25	80	80	25 to 77	40 to 125
OPERATING PRESSURE RANGE $px10^{-5}$ [Pa]					
TYPICAL REFRIGERATION	0,8 W at 25 K	1,5 W at 80 K	2 W at 77 K	2 W at 25 K 1 W at 22 K [c]	60 W at 77 K
SETTING-ON-TIME WITHOUT LOAD [min]	15	3	5	8	38
TEMP. STABILITY [K]				+/- 0,02	

EXPANDER [rpm]					
POWER INPUT [W]	620	500	580	480	1220
VOLTAGE [V]	115			208	
PHASE/FREQUENCY [Hz]	3/400			3/400	
COOLING MEAN	Air	Air or Liquid		Air or Liquid	Air
AMBIENT TEMP. [K]	241 to 327	218 to 344		MIL-STD-210B	
CRYOSTAT SIZE [m]	0,216 x 0,127 x 0,254	0,211 x 0,142 x 0,152	0,211 x 0,127 x 0,152	0,122 Dia. 0,292 Length	0,165 Dia. 0,597 Length
COMPRESSOR SIZE [m]	None			None	
CRYOSTAT MASS [kg]	7,26	4,54	5,90	7,03 [d]	18,14 [d]
COMPRESSOR MASS [kg]					
MEAN TIME BETWEEN FAILURES [h]				40000	
OVERHAUL TIME [h]	500			1000	
AVAILABILITY TIME [mo]				Immediate	
SYSTEM COST [$]				5195	17500

[a] Hughes Aircraft Co., Culver City, California, USA.

[b] Malaker Corp., High Bridge, New Jersey, USA. All operations on this firm were terminated in 1972.

[c] From Streed, Murphy & Brna (1971) [229].

[d] Total mass of the refrigerator.

NOTE Data in this table are from Donabedian (1972) [59] unless otherwise stated.

CLOSED CYCLE REFRIGERATORS					
CYCLE	STIRLING				
MANUFACTURER	Malaker Corp. [a]				
TRADE NAME	Cryomite				
MODEL OR PROGRAM	Mark XX	Mark XIV-A	Mark XV	Mark XVI-3	Mark XV-4
WORKING FLUID	Helium				
OPERATING TEMP. RANGE [K]	40 to 120	45 to 100	54 to 100	77 to 110	54 to 100
OPERATING PRESSURE RANGE px10^{-5} [Pa]					
TYPICAL REFRIGERATION	110 W at 77 K	2,8 W at 77 K	1 W at 77 K	8,2 W at 77 K	1 W at 77 K
SETTING-ON-TIME WITHOUT LOAD [min]	7,4	7	8	7	8
TEMP. STABILITY [K]					
EXPANDER [rpm]					
POWER INPUT [W]	1990	108	29,5	208	29,5
VOLTAGE [V]	208		24 DC		
PHASE/FREQUENCY [Hz]	3/400				
COOLING MEAN	Air or Liquid	Air			Free Convection
AMBIENT TEMP. [K]	MIL-STD-210B				
CRYOSTAT SIZE [m]	0,483 x 0,457 x 0,406	0,074 Dia. 0,337 Length	0,074 Dia. 0,311 Length	0,089 Dia. 0,356 Length	0,076 Dia. 0,286 Length
COMPRESSOR SIZE [m]					
REFRIGERATOR	29,48	2,49	2,27	4,54	2,27

MASS [kg]					
MEAN TIME BETWEEN FAILURES [h]	40000				
OVERHAUL TIME [h]	1000				
AVAILABILITY TIME [mo]	Immediate				
SYSTEM COST [$]	24000	9000		8500	9000

[a] Malaker Corp., High Bridge, New jersey, USA. All operations of this firm were terminated by 1972.

NOTE From Donabedian (1972) [59].

CLOSED CYCLE REFRIGERATORS					
CYCLE	STIRLING				
MANUFACTURER	Philips [a]				Philips with APL Johns Hopkins [a]
TRADE NAME		Cryogem	Micro-Cryogem		Rhombic Drive Cooler
MODEL OR PROGRAM		42100		P/N 460600	Nuclear Monitoring Research Office DOD, ARPA
WORKING FLUID	Helium				
OPERATING TEMP. RANGE [K]	7 to 300	20 to 40	40 to 300	40 to 80	64 to 70 and 135 to 150 (Two stages) [b]
OPERATING PRESSURE RANGE $px10^{-5}$ [Pa]	3,7 to 6,1	8,6 to 17,2	4,6 to 8,6		4,8 [c]
TYPICAL REFRIGERATION	0,5 W at 12 K	2 W at 30 K	1,5 W at 77 K	1 W at 50 K	1,5 W at 140 K [b,c] 0,3 W at <75 K
SETTING-ON-TIME WITHOUT LOAD [min]	15	10	3	4	
TEMP. STABILITY [K]					

EXPANDER [rpm]	600	1750	1800		1000 can vary within +/- 200 [b]
POWER INPUT [W]	700	350	90	120	30 [b,c]
VOLTAGE [V]	320	208	24 DC	115	24 to 30 DC
PHASE/FREQUENCY [Hz]	3/60	3/400		3/400	
COOLING MEAN	Water	Air	Air or Liquid	Air	
AMBIENT TEMP. [K]		219 to 316	218 to 348		267 to 322 for storage. [b] 272 to 318 for conduction heat rejection.
CRYOSTAT SIZE [m]	0,152 x 0,305 x 0,610	0,152 x 0,127 x 0,279	0,102 x 0,102 x 0,203	0,038 Dia. 0,267 Length	0,154 x 0,180 x 0,307 [b,c]
COMPRESSOR SIZE [m]					
REFRIGERATOR MASS [kg]	15,88	5,44	1,36	1,81	5,3 without electronics [b] 7,2 with electronics [b,c]
MEAN TIME BETWEEN FAILURES [h]		1500			
OVERHAUL TIME [h]		600	500	1000	15000 [c]
AVAILABILITY TIME [mo]		2-4	Immediate		Immediate. Four refrigerators were launched on Feb. 24, 1979.
SYSTEM COST [$]		8500	6500		

[a] North American Philips Corporation, Briarcliff Manor, New Jersey, USA.

[b] From Balas, Leffel, & Wingate (1978) [16].

[c] From Sherman (1982) [217]. See also Naes & Nast (1980) [160].

NOTE Data in this table are from Donabedian (1972) [59] unless otherwise stated.

CLOSED CYCLE REFRIGERATORS			
CYCLE	STIRLING		
MANUFACTURER	Philips under NASA Goddard [a]	Energy Research and Generation, Inc. [b]	Philips [c]
TRADE NAME	Magnetic Bearing Cooler	Gas Bearing Cooler	
MODEL OR PROGRAM	Prototype	Design Study	N-20 [d]
WORKING FLUID	Helium		
OPERATING TEMP. RANGE [K]	65 to 300 [e,f,g]	65 to 300 [g]	12 [d]
OPERATING PRESSURE RANGE px10^{-5} [Pa]	16 [e]		
TYPICAL REFRIGERATION	5 W at 65 K [e]	11,3 W at 65 K [g]	10 W at 20 K [d]
SETTING-ON-TIME WITHOUT LOAD [min]			15 [d]
TEMP. STABILITY [K]			
EXPANDER [rpm]	1650 [g]		1750 [d]
POWER INPUT [W]	180. [g] Cooler alone, 96	48 [g]	1750 [d]
VOLTAGE [V]			2000 VA [d]
PHASE/FREQUENCY [Hz]	/28 [f]		3/50-60 [d]
COOLING MEAN	Air [g]	Air [g]	Air or Liquid [d]
AMBIENT TEMP. [K]		300	
CRYOSTAT SIZE [m]	0,063 Diameter [h] 0,750 Length	0,032 Diameter [g] 0,063 Length	0,102 Diameter [d] 0,191 Length
COMPRESSOR SIZE [m]	0,370 Diameter [h] 1,050 Length	0,042 Diameter [g] 0,237 Length	0,483 x 0,356 x 0,330 [d]

REFRIGERATOR MASS [kg]	20 without electronics [f]	3 [g]	50,79 [d]
MEAN TIME BETWEEN FAILURES [h]			
OVERHAUL TIME [h]	26000 to 44000 [g]	26000 to 44000 [g]	4000 [d]
AVAILABILITY TIME [mo]			
SYSTEM COST [$]			

[a] North American Philips Corporation, Briarcliff Manor, New Jersey, USA.

[b] Energy Research and Generation Corporation, Oakland, California, USA.

[c] Philips Research Laboratories, Eindhoven, Netherlands.

[d] From Donabedian (1972) [59].

[e] From Sherman (1982) [217]. See also Naes & Nast (1980) [160].

[f] From Daniels, Gasser & Sherman (1982) [49].

[g] From Sherman, Gasser, Goldowsky, Benson & McCormick (1980) [221].

[h] Estimated by the compiler after Fig. 9 of Sherman (1982) [217] and a volume of $5{,}4 \times 10^{-3}$ m^3 quoted by Sherman, Gasser, Goldowsky, Benson & McCormick (1980) [221].

CLOSED CYCLE REFRIGERATORS					
CYCLE	TACONIS	VUILLEUMIER			
MANUFACTURER	British Oxygen [a]	Garrett [b]	Hughes Aircraft Co. [c]		
TRADE NAME					
MODEL OR PROGRAM	IR16-MK II	ICICLE	Flight Test Models		
WORKING FLUID	Helium	Helium	Helium		
OPERATING TEMP. RANGE [K]	12 to 23	75	25 to 75	70 to 90	75 to 90
OPERATING PRESSURE RANGE $p \times 10^{-5}$ [Pa]	10,1 to 20,2	48,1 to 55,3			
TYPICAL REFRIGERATION	2,5 W at 12 K	5 W at 75 K	2 W at 25 K 3 W at 75 K	0,2 W at 85 K	1,5 W at 75 K

SETTING-ON-TIME WITHOUT LOAD [min]	40		25 for 0,1 kg of Copper	15	10
TEMP. STABILITY [K]					
EXPANDER [rpm]	166	400		900	
POWER INPUT [W]	2640	3665 [d]	1200	180	200
VOLTAGE [V]	240		115	28 DC	28 DC
PHASE/FREQUENCY [Hz]	1/50		3/400		
COOLING MEAN	Air and Water	Heat Pipe to Radiator [e]	Liquid	Heat Pipe to Radiator	Air
AMBIENT TEMP. [K]	300 Approx.	255 to 322		394	218 to 344
CRYOSTAT SIZE [m]	0,203 Dia. 0,330 Length	Not specified	0,191 x 0,241 x 0,254		0,165 x 0,145 x 0,127
COMPRESSOR SIZE [m]	0,914 x 0,533 x 0,686	None	None		
CRYOSTAT MASS [kg]	9,07	Refrigerator: 3,2; Isotope & Structure: 11,1, Insulation, active control: 8 [e]	8,84 [f]	3,81 [f]	2,61 [f]
COMPRESSOR MASS [kg]	108,84				
MEAN TIME BETWEEN FAILURES [h]		6000 [g]	3000	1000	Objective: 5000 [h]
OVERHAUL TIME [h]		17000 to 43000	1000	3000	1000 [h]
AVAILABILITY TIME [mo]					
SYSTEM COST [$]	9100				

[a] British Oxygen Co. LTD., London, England.

[b] Garrett Corp., AiResearch Manufacturing Company, Phoenix, Arizona, USA.

[c] Hughes Aircraft Co., Culver City, California, USA.

[d] Power supplies are both thermal (350 W) and electrical (15 W). 200 W are for displacer action, the remaining accounts for insulations losses (mainly isotope housing and hot heat pipe). The isotope source, coupled to the refrigerator via the hot heat pipe, provides the thermal power (Shelpuk, Crouthamel & Cygnarowicz (1970) [215].

[e] From Shelpuk, Crouthamel & Cygnarowicz (1970) [215].

[f] Total mass of the refrigerator.

[g] From Sherman (1978) [216].

[h] From Streed, Murphy & Brna (1971) [229].

NOTE Data in this table are from Donabedian (1972) [59] unless otherwise stated.

CLOSED CYCLE REFRIGERATORS					
CYCLE	VUILLEUMIER				
MANUFACTURER	Hughes Aircraft Co. [a]				
TRADE NAME					
MODEL OR PROGRAM	Prototype			X447550	SESP-712
WORKING FLUID	Helium				
OPERATING TEMP. RANGE [K]	Around 77 [b]	15 to 75	30 to 75	30 and 75 (Two stages)	15 and 60 (Two stages)
OPERATING PRESSURE RANGE $px10^{-5}$ [Pa]				Up to 27,4	33,4 to 41,5
TYPICAL REFRIGERATION	0,6 W at 77 K [b]	0,15 W at 15 K	0,5 W at 30 K	0,5 W at 30 K 6 W at 75 K	0,15 W at 15 K 3,5 W at 55 K
SETTING-ON-TIME WITHOUT LOAD [min]		30			
TEMP. STABILITY [K]					+/- 0,1
EXPANDER [rpm]				240	260
POWER INPUT [W]	60 [b]	370	550	480	540
VOLTAGE [V]		28 DC			24-30 DC

PHASE/FREQUENCY [Hz]					
COOLING MEAN	Air [b]	liquid			
AMBIENT TEMP. [K]					
CRYOSTAT SIZE [m]		0,267 x 0,345 x 0,198			
COMPRESSOR SIZE [m]		None			
REFRIGERATOR MASS [kg]				4,35	27,21
MEAN TIME BETWEEN FAILURES [h]					
OVERHAUL TIME [h]	Objective [b] 3000	Objective [b] 10000			4300
AVAILABILITY TIME [mo]					
SYSTEM COST [$]					

[a] Hughes Aircraft Co., Culver City, California, USA.

[b] From Streed, Murphy & Brna (1971) [229].

NOTE Data in this table are from Donabedian (1972) [59] unless otherwise stated.

CLOSED CYCLE REFRIGERATORS		
CYCLE	VUILLEUMIER	
MANUFACTURER	Hughes Aircraft Co. [a]	
TRADE NAME		
MODEL OR PROGRAM	Prototype [b]	HI CAP [c]
WORKING FLUID	Helium	
OPERATING TEMP. RANGE [K]	50 to 120 [b]	Around 8,5, 11 and 50 (three stages) [c]
OPERATING PRESSURE RANGE px10^{-5} [Pa]		
TYPICAL REFRIGERATION	0,6 W at 77 K [b]	< 1 W at 12 K [c]

		10 W at 33 K 17 W at 75 K
SETTING-ON-TIME WITHOUT LOAD [min]	20 [b]	
TEMP. STABILITY [K]	+/- 5 [b]	
EXPANDER [rpm]		Six values between 100 and 300 [c]
POWER INPUT [W]	105 [b]	200 to 300 for 28 V source. [c,d] 1200 to 1800 for 100 V source.
VOLTAGE [V]		28 DC and 100 DC
PHASE/FREQUENCY [Hz]		
COOLING MEAN		Coolanol 20 [c]
AMBIENT TEMP. [K]		278 to 313 [c]
CRYOSTAT SIZE [m]		0,889 x 0,762 x 0,317 [c]
COMPRESSOR SIZE [m]	None	
REFRIGERATOR MASS [kg]	2,95 [b]	68 plus [c] 14,5 (electronic interface unit)
MEAN TIME BETWEEN FAILURES [h]	3000 [b]	
OVERHAUL TIME [h]	1000 [b]	20000 [c]
AVAILABILITY TIME [mo]		
SYSTEM COST [$]		

[a] Hughes Aircraft Co., Culver City, California, USA.

[b] From Donabedian (1972) [59].

[c] From Doody (1980) [60].

[d] At present electrically powered from resistance heaters (Doody (1980) [60]). Thermal energy storage units are being developed (Richter & Mahefkey (1980) [195]).

CLOSED CYCLE REFRIGERATORS					
CYCLE	VUILLEUMIER				
MANUFACTURER	Kinergetics [a]	Philips [b]			RCA [c]
TRADE NAME					
MODEL OR PROGRAM		Prototype		Prototype	
WORKING FLUID	Helium	Helium			Helium
OPERATING TEMP. RANGE [K]	77	77 to 200	77	60 to 100	77
OPERATING PRESSURE RANGE $px10^{-5}$ [Pa]		28,4 to 38,5	30,4 (High pressure)		
TYPICAL REFRIGERATION	0,4 W at 77 K	0,5 W at 77 K	1 w at 77 K	0,5 W at 77 K	1,6 W at 77 K
SETTING-ON-TIME WITHOUT LOAD [min]		9		20	
TEMP. STABILITY [K]					
EXPANDER [rpm]		750	600		
POWER INPUT [W]	65	70	120	90	Thermal
VOLTAGE [V]					
PHASE/FREQUENCY [Hz]					
COOLING MEAN	Air	Air			Air
AMBIENT TEMP. [K]					
CRYOSTAT SIZE [m]		0,305 x 0,203 x 0,152	1,067 x 0,457 x 0,457		
COMPRESSOR SIZE [m]					
REFRIGERATOR MASS [kg]	2,72	36,73	6,80	4,67	7,26

MEAN TIME BETWEEN FAILURES [h]				3000	
OVERHAUL TIME [h]				1000	
AVAILABILITY TIME [mo]					
SYSTEM COST [$]					

[a] Kinergetics (Formerly the Submarine Systems Division of Sterling Electronics), Tarzana, California, USA.

[b] North American Philips Corporation, Briarcliff Manor, New Jersey, USA.

[c] RCA, defense Electronics Laboratory, Camden, New Jersey, USA.

NOTE From Donabedian (1972) [59].
80 K COOLER ("BAe cooler")
Manufacturer: British Aerospace Space Systems, Ltd. BAe has manufactured 3 batches of 6 coolers.
Description: "Oxford type" cooler. Single stage 80 K split Stirling cycle.

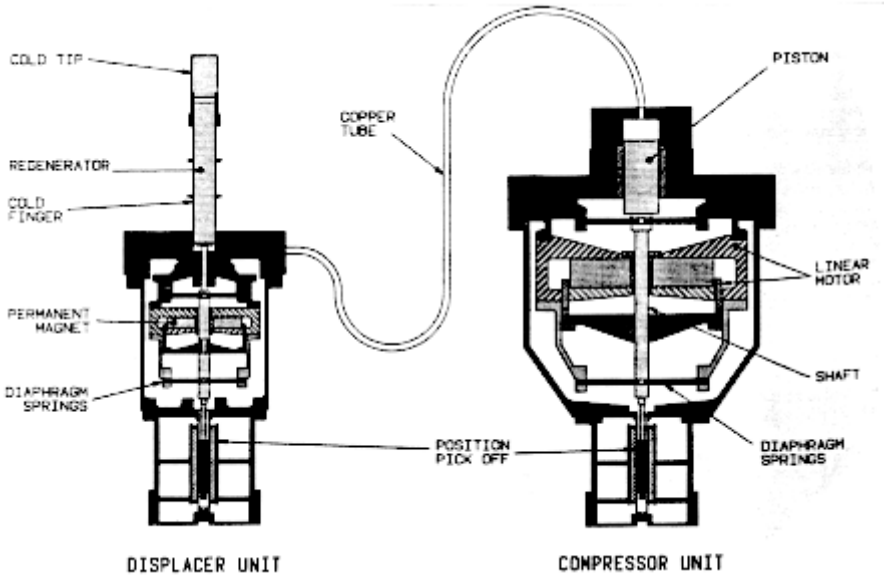

Figure 5-22: 80 K cooler schematic. From Jewell (1991) [103].

Mass

Compressor: 3,0 kg.

Displacer: 0,9 kg.

Electronics: 4,5 kg.

Size

Compressor: length 0,20 m, diameter 0,12 m.

Displacer: length 0,19 m, diameter 0,075 m.

Electronics: 0,225 m x 0,230 m x 0,150 m.

Power consumption (typical): 30 W

Working fluid: Helium.

Performance (typical): 0,8 W cooling at 80 K (for 30 W input power).

Performance testing

Cooler no.6 of 1st batch.

Ambient temperature 293 K.

Input power 15–35 W.

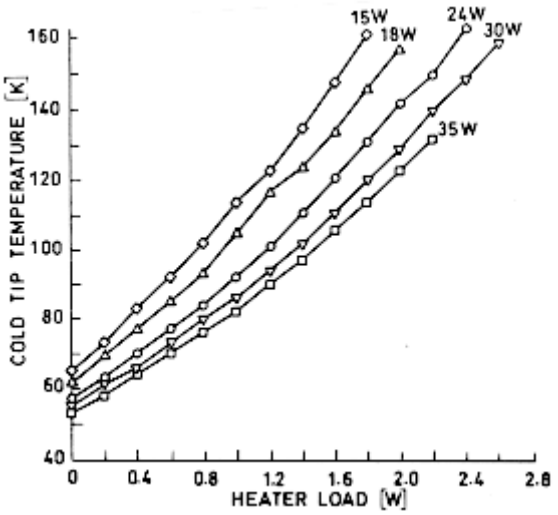

Figure 5-23: Cooler heat lift performance vs. gross compressor input power. From Scull & Jewell (1991) [211].

References: Jewell (1988,1991) [104]& [103], Lewis (1988) [133], Scull & Jewell (1991) [211].

20 K COOLER

Manufacturer/Developer: British Aerospace Space Systems, Ltd. (Engineering model). Rutherford Appleton Laboratory (Development model).

Description: Two stage 20 K split Stirling cycle (based on "Oxford type" technology).

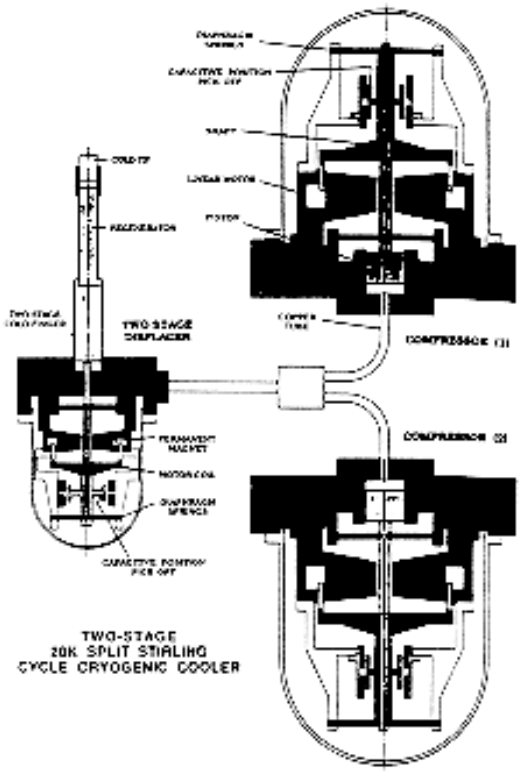

Figure 5-24: 20 K cooler schematic. From Jones et al. (1991) [110].

Mass

Compressor (each): 3,5 kg.

Displacer: 1,3 kg.

Electronics: 4,5 kg.

Size

Compressor (each): 0,13 m x 0,14 m x 0,16 m.

Displacer: 0,075 m x 0,075 m x 0,21 m.

Electronics: 0,251 m x 0,254 m x 0,186 m.

Power consumption

Compressor (each): 35 W.

Displacer: 2 W.

Electronics: 30 W.

Working fluid: Helium.

Performance

60 mW at 20 K.

300 mW at 30 K.

Performance testing

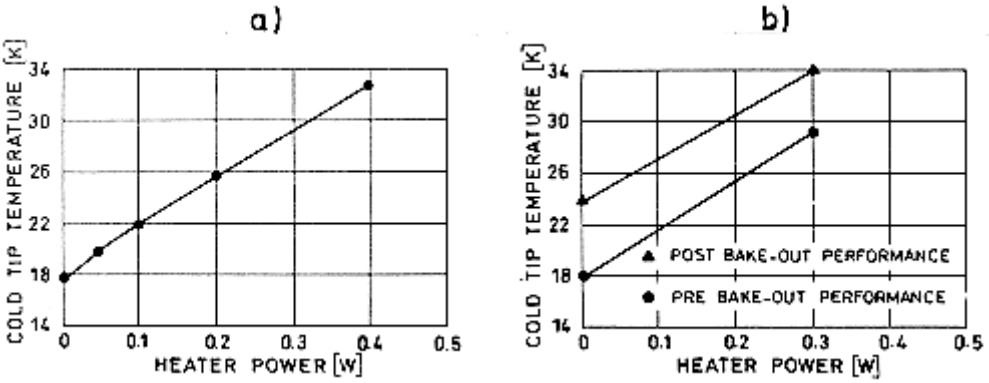

Figure 5-25: Heat lift performance of: a) development model; b) engineering model. From Jones et al. (1991) [110].

References: Jewell (1991) [103], Jones et al. (1991) [110].

4 K COOLER

Developer: Rutherford Appleton Laboratory.

Description: Two stage Stirling cooler (20 K cooler above) and a precooler for a 4 K Joule Thomson stage. Development model.

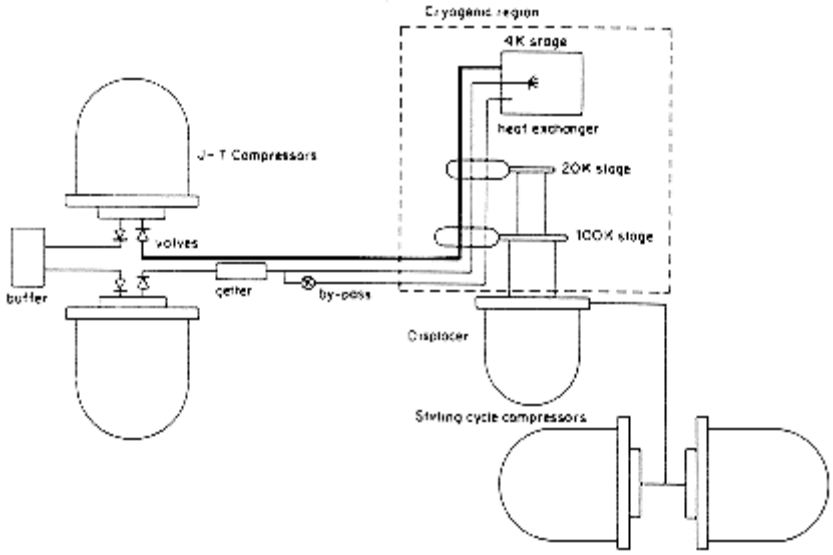

Figure 5-26: 4 K cooler layout. From Bradshaw & Orlowska (1988) [27].

Mass

Size

Working fluid: Helium.

Performance

Precooler: 300 mW of cooling at 30 K for ~80 W input power.

4 K stage: 1,5 mW at 4,17 K for 126 W input power, with a mass flow of 3,9 mg/s. (Goal : 5 mW at 4 K for <150 W)

Performance testing

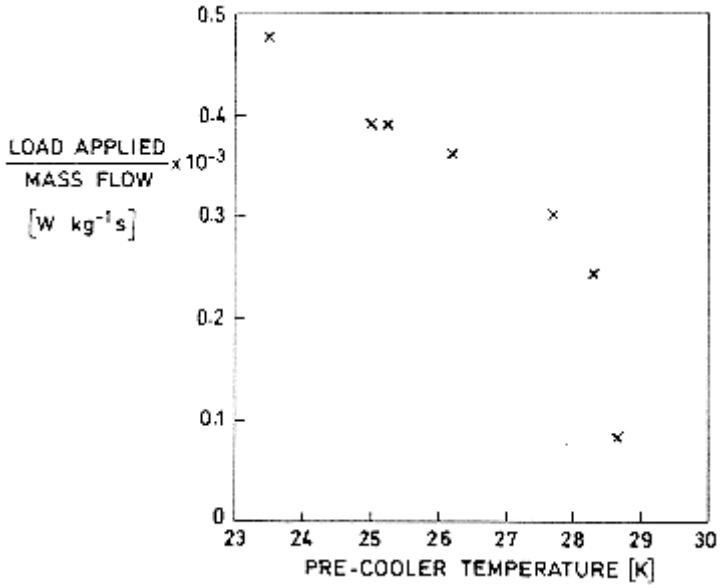

Figure 5-27: Cooling power/mass flow vs. precooler temperature. From Bradshaw & Orlowska (1991) [28].

NOTE: A 2,5 K prototype cooler practically identical to the 4 K cooler (except for the use of He_3 gas) is under development. Performance goal: 50 μW at 2,5 K.

References: Bradshaw & Orlowska (1988,1991) [27] & [28], Jewell (1991) [103].

5.3 Open cycle

Open-cycle or expendable refrigeration systems of interest for space application include the use of high-pressure gas combined with Joule-Thomson expansion valve, cryogenic liquids either in the subcritical or supercritical state, cryogenic solids and, for some special applications, liquids which can be stored at room temperature.

The basic attractiveness of these system is based on: simplicity, reliability, relative economy and negligible power requirements.

The basic disadvantages are the limited life due to heat leakage, and the rapid increase in mass and volume for extended missions.

In the following pages, main emphasis is placed on high-pressure gas Joule-Thomson cryostats. Cryostats for stored solid, liquid or gaseous cryogens are shortly discussed in clause 5.3.1 and more extensively in Clause 6 of this Part.

5.3.1 Joule-Thomson open cycle refrigerators

5.3.1.1 Description

The Joule-Thomson cryogenic cooler is based on the cooling caused by the adiabatic expansion of a gas.

When a real gas is expanded at constant enthalpy (Joule-Thomson or throttling process) the total temperature does not remain constant, opposite to what happens with a perfect gas. Rather, if the temperature of the gas is below a certain inversion temperature (which depends on pressure) the total temperature will decrease when the pressure decreases, which will result in a cooling of the gas.

Let p_0 and T_0 be the pressure and temperature in a gas after throttling from given initial conditions p_i p_0 and T_i. When T_0 is plotted vs. p_0 a curve exhibiting a maximum value of T_0 results. Similar curves will be obtained for different initial conditions, see the isenthalps, thin nearly horizontal lines in Figure 5-28. The local slope, μ, of the curves is the Joule-Thomson (or Joule-Kelvin) coefficient, $\mu = (\partial T/\partial p)_h$, where h indicates that the evolution from i to o takes place at constant enthalpy.

The Joule-Thomson inversion temperature curve, heavy lines in Figure 5-28, is the locus of points where $\mu = 0$. In the region where $\mu > 0$ an isenthalpic expansion will decrease the total temperature of the gas, and conversely where $\mu < 0$.

For perfect gases $\mu = 0$ everywhere (constant enthalpy means constant temperature).

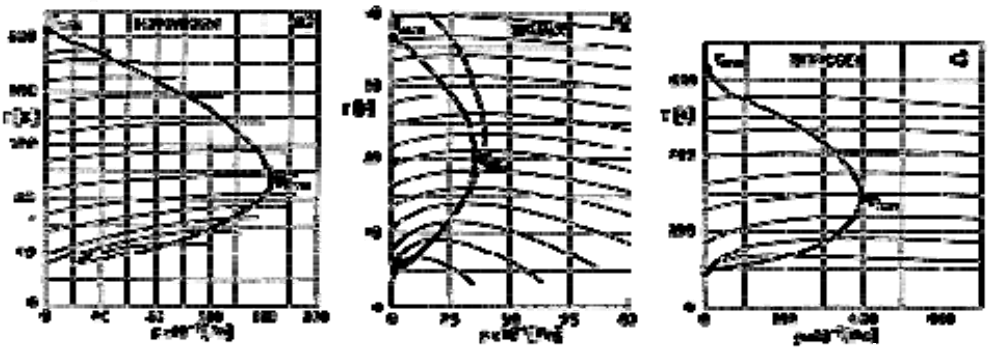

Figure 5-28: Isenthalps and inversion curve for different gasses. a Hydrogen. b Helium. c Nitrogen. From Zemansky (1968) [272]. Data in b, after Hill & Loumasmaa (1960) [89], are no longer valid for above 20 K. Upper isenthalps are instead from Angus & de Reuck (1977) [6], pp. 64-127 . The locus of the maxima has been drawn by the compiler as a dotted line.

Purely thermodynamic considerations indicate that the expansion should start at the inversion temperature curve. For certain gases the maximum inversion temperature (that corresponding to zero pressure) is below room temperature (see for example T_{max} for Hydrogen or Helium in Figure 5-28) and, thence, precooling to the indicated temperature is required before Joule-Thomson expansion. Many other gases (for example Nitrogen in Figure 5-28) have maximum inversion temperatures above room temperature and no precooling is required.

Values of T_{max} and p_{max} for typical gases are given in Table 5-5.

Table 5-5: Maximum Inversion Temperature and Pressure of Selected Cryogens

CRYOGEN	T_{max} [K]			$P_{max}x10^{-7}$ [Pa]	
	Calculated [a]	Calculated [b]	Reported [c]	Calculated [a]	Reported [c]
Ar Argon	1018	775 789	723	4,50	
CO_2 Carbon Dioxide	2053	1223 1326	~ 1500	6,64	
H_2 Hydrogen	224	189 239	202	1,18	1,67
He Helium	35	39 66	~ 40	0,20	0,38
N_2 Nitrogen	852	615 620	621	3,06	4,05

[a] Calculated by the compiler through van der Waal's two-constant equation. $T_{max} = 27\ T_c/4$, $P_{max} = 9\ p_c$. See Loeb (1961) [135]. Critical point conditions have been taken from Table 8-1, Clause 8.1.1.

[b] Calculated by the compiler from the virial equation ofstate and force constants for the Lennard-Jones intermolecular potential. $T_{max} = 6{,}47\ \varepsilon/k$. Helium exhibits quantum deviations from this law. See Hirschfelder, Curtiss & Bird (1954) [91], Fig. 6.6-3, p. 174 and Table I-A, pp. 1110-1112.

[c] From Zemansky (1968) [272].

Joule-Thomson cryostats are used to cool infrared sensors in electro-optical devices. Normally sensor and cryostat are packaged inside a double walled glass dewar. A schematic of the cryostat-dewar system is illustrated in Figure 5-29.

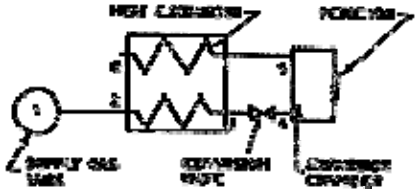

Figure 5-29: Schematic of a typical JT cryostat-dewar system. From Hellwig (1980) [86].

Gas stored in the supply tank flows through the heat exchanger 2-3 where it is cooled by the exit gas 5-6. Between 3 and 4 the gas is expanded at constant enthalpy through the expansion or throttling valve. The gas becomes partially liquefied in the expansion chamber where it is vaporized again by contacting the warm detector. The outgoing vapor flows through the heat exchanger 5-6.

In the simpler design the gas is supplied continuously from a high pressure source. More sophisticated devices use some kind of gas flow regulation. Modern JT cooled cryostats could have either a rapid-starting capability, an external control system to operate on a self-demand basis, or both.

Normal flow control consists, Figure 5-30, in a needle actuated by a pressurized bellows which allows for wide open flow until the liquid build up in the expansion chamber condenses the pressurant and the bellows is drawn into the cryostat restricting flow.

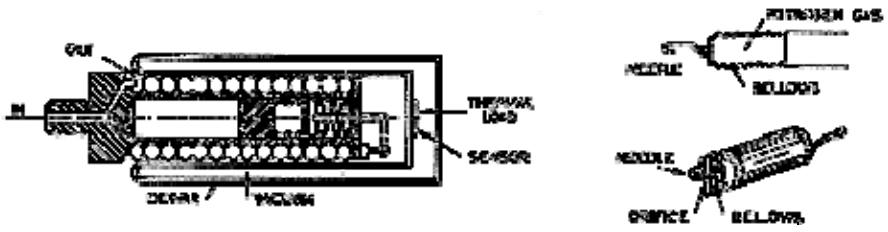

Figure 5-30: Schematic of a self-demand flow JT cryostat-dewar system. From Oren & Gutfinger (1979) [175]. The sketch of the variable-orifice controlling device is from Buller (1970) [35].

In several instances (Buller (1970) [35]) the bellows does not respond to the presence of the liquid at the detector, rather it is thermally attached to the heat exchanger support a small distance away from the cold end. The bellows is pressurized so that when it actuates liquid and vapor coexist inside and, thence, the internal pressure, bellows length and needle position only depend on temperature.

Bimetallic elements or electronic circuits are also used for flow control. For instance, Peterson, Wurtz & Winner (1976) [180] describes an impedance responsive electronic switch circuit which energizes the winding of a normally open solenoid valve when liquid nitrogen wets an absorbing packing.

5.3.1.2 Development problems

Many manufacturers are involved in a number of open-cycle Joule-Thomson cooling units for specific applications.

The most common problem of JT cryostats is clogging of the finned tube which constitutes the heat exchanger. Dust particles and traces of high-freezing point gases should be excluded from the gas entering the tube. To avoid clogging, a chemical dryer containing an absorbent material which removes the excess moisture, and a porous sintered metal filter, to remove any floating particle, can be inserted in the high pressure line ahead of the finned tube.

The stored gas mass and volume are the primary penalty factor in these units.

General considerations for the design and optimization of high-pressure storage vessels are fairly well-known. Basically, these relate to the desirability of minimizing container volume penalties by the use of large storage pressures without incurring excessive pressure shell mass.

Gas compressibility effects are of extreme importance in pressure vessel design. At pressures over 10^6 Pa gases become less and less compressible so that volume saving at high pressures are diminished. It is therefore of extreme importance to investigate in detail the effect of initial pressure, on both container mass and volume, in the optimization of storage vessel design. Although p_{max}, Figure 5-28, could be a good starting point in the estimation of the required initial pressure, reliable data on T_{max} are not easily found. On the other hand, the accuracy of the computed data, based on diluted gas theories, is at high pressures.

5.3.2 Existing systems

Technical data concerning open cycle refrigerators are collected in this clause. These data are arranged as shown in the Table below.

Arrangement of the Compiled Data on Open Cycle Refrigerators

Cycle	Manufacturer	No [a]
Joule-Thomson	Air Products & Chemicals, Inc. Hughes Aircraft Co. Hymatic Engineering Co. Santa Barbara Research Center	6 1 2 4

[a] Number of refrigerators listed.

OPEN CYCLE REFRIGERATORS					
CYCLE	JOULE-THOMSON				
MANUFACTURER	Air Products [a]				
TRADE NAME	Cryo-Tip				
MODEL OR PROGRAM	AC-1	AC-2	AC-2L	AC-3L	AC-1-101-A
WORKING FLUID	Nitrogen	Nitrogen or Hydrogen	Liquid Nitrogen or Hydrogen	Liquid Nitrogen, Hydrogen or Helium	Nitrogen
OPERATING TEMP. RANGE [K]	68 to 300	16 to 300	16 to 300	3,6 to 300	80 to 300
OPERATING PRESSURE RANGE $px10^{-5}$ [Pa]	80 [b]		80 [b] 1 to 152 [c]	80 [b]	
TYPICAL REFRIGERATION	7 W at 80 K	4 W at 23 K	6 W at 22 K	0,5 W at 4,4 K	0,75 W at 80 K
TEMP. STABILITY [K]	+/- 0,10				
COOL-DOWN TIME (NO LOAD) [min]	5	10		40	

GAS FLOW RATE AT TYPICAL REFRIGERATION [kg.h^{-1}]	1,58	1,79 (N_2) 0,113 (H_2)	0,401 (LN_2) 0,142 (H_2)	0,401 (LN_2) 0,127 (H_2) 0,354 (He)	0,345
REQUIRED ATTITUDE	None		30 deg. of vertical		None
COOLING MEAN			None [c]		
AMBIENT TEMP. [K]					
CRYOSTAT SIZE [m]	0,089 x 0,089 x 0,127	0,089 Dia. 0,191 Length	0,152 Dia. 0,432 Length	0,152 Dia. 0,584 Length	
CRYOSTAT MASS [kg]	0,453	0,680	9,98	9,98	0,227
MEAN TIME BETWEEN FAILURES [h]					
OVERHAUL TIME [h]			1000 [c]		
PRIMARY USE	Laboratory				
AVAILABILITY TIME [mo]	Immediate				
SYSTEM COST [d] [$]	1585	2690	3395	4430	2850

[a] Air products and Chemicals, Inc., Allentown, Pennsylvania, USA.

[b] Minimum supply pressure.

[c] From Streed, Murphy & Brna (1971) [229].

[d] Not includes gas storage.

NOTE Data in this table are from Donabedian (1972) [59] unless otherwise stated.

OPEN CYCLE REFRIGERATORS				
CYCLE	JOULE-THOMSON			
MANUFACTURER	Air Products [a]	Hughes [b]	Hymatic Engineering [c]	
TRADE NAME	Cryo-Tip		Minicooler	
MODEL OR PROGRAM	AC-2-209	JTO-001	MAC-215	MC-8
WORKING FLUID	Nitrogen or Hydrogen [d]	Argon	Hydrogen or Air	Argon, Nitrogen or Air
OPERATING TEMP. RANGE [K]		87	21, 27	80 to 90
OPERATING PRESSURE RANGE $px10^{-5}$ [Pa]	187,2 (N_2) [d,e] 118,2 (H_2)	116 [e]	120 [e]	
TYPICAL REFRIGERATION	0,25 at 22 K [d]	40 W at 87 K	2 W at 21 K	10 W at 80 K
TEMP. STABILITY [K]			+/- 0,10	
COOL-DOWN TIME (NO LOAD) [min]	12 from 245 K [d] 23 from 295 K	0,2	3	0,5
GAS FLOW RATE AT TYPICAL REFRIGERATION [$kg.h^{-1}$]	0,320 to 0,355 (N_2) [d] 0,023 to 0,026 (H_2)	0,113	0,055 (H_2) 0,118 (Air)	0,128 (N_2)
REQUIRED ATTITUDE		None	None	
COOLING MEAN				
AMBIENT TEMP. [K]				
CRYOSTAT SIZE [m]	0,006 Diameter [d] 0,130 Length		0,025 Diameter 0,063 Length	0,0076 Diameter 0,051 Length
CRYOSTAT MASS [kg]			0,068	0,0056 [f]

MEAN TIME BETWEEN FAILURES [h]				
OVERHAUL TIME [h]				
PRIMARY USE	Mariner Mars [d]	Falcon Missile		
AVAILABILITY TIME [mo]		Immediate	Immediate	
SYSTEM COST [$]			4300	

[a] Air Products and Chemicals, Inc., Allentown, Pennsylvania, USA.

[b] Hughes Aircraft Co., Culver City, California, USA.

[c] Hymatic Engineering Co. LTD, The, Redditch, Worcs. England.

[d] From Hughes & Herr (1973) [97].

[e] Minimum supply pressure.

[f] From Anon (1966) [7].

NOTE Data in this table are from Donabedian (1972) [59] unless otherwise stated.

OPEN CYCLE REFRIGERATORS				
CYCLE	JOULE-THOMSON			
MANUFACTURER	Santa Barbara [a]			
TRADE NAME				
MODEL OR PROGRAM	9159	41614	42902	
WORKING FLUID	Nitrogen	Argon	Argon or Nitrogen [b]	Argon [c]
OPERATING TEMP. RANGE [K]	77 to 300	87 to 300	77 to 300	87 to 100 [c]
OPERATING PRESSURE RANGE $px10^{-5}$ [Pa]	50 to 550 [d]			
TYPICAL REFRIGERATION	0,2 W			
TEMP. STABILITY [K]			+/- 5 [e]	
COOL-DOWN		0,033 [f]		0,5 [c]

TIME (NO LOAD) [min]				
GAS FLOW RATE AT TYPICAL REFRIGERATION [kg.h^{-1}]	0,294 at 0,69x10^{7} Pa 0,490 at 1,10x10^{7} Pa	0,028 at 5,50x10^{7} Pa	0,022 (Ar) at 4,15x10^{7} Pa 0,026 (N_2) at 3,40x10^{7} Pa	0,032 [c]
REQUIRED ATTITUDE	None			
COOLING MEAN				
AMBIENT TEMP. [K]	300			
CRYOSTAT SIZE [m]	5,28x10^{-3} Dia. [g] 0,051 Length	5,28x10^{-3} Dia. [g] 0,025 Length	5,28x10^{-3} Dia. [g] 0,051 Length	
CRYOSTAT MASS [kg]				
MEAN TIME BETWEEN FAILURES [h]				
OVERHAUL TIME [h]				
PRIMARY USE	IR sensors cooling			
AVAILABILITY TIME [mo]				
SYSTEM COST [$]				

[a] Santa Barbara Research Center, Goleta, California, USA.

[b] Additional data on this refrigerator are given in Oren & Gutfinger (1979) [175].

[c] From Hellwig (1980) [86].

[d] Supply pressure.

[e] 42902 is a demand-flow cryostat which can be adjusted to operate either with constant detector temperature or with some temperature fluctuation (as stated) to obtain maximum gas economy.

[f] At maximum operating pressure, before actuation of a flow-restricting needle.

[g] These values are related to the heat exchanger only.

NOTE Data in this table are from Buller (1970) [35] unless otherwise stated.

5.3.3 Stored liquid or solid cryogen open refrigerators

5.3.3.1 Description

Cryogens may be stored: 1) As liquid in equilibrium with their vapors, subcritical storage, 2) at higher pressures and temperatures, as supercritical, homogeneous fluids, and 3) as solid cryogens.

1. Under normal gravity conditions, the fluid is usually stored in the two-phase form because of the associated mass saving.

   Temperatures available using most common liquefied gases, in the subcritical storage systems, range from approximately 4 to 77 K. By varying the pressure, the temperature of a liquefied gas can be varied to provide cooling from the triple point to the critical point. A constant temperature cooling can be provided, within this range, by pressure control.

   The cooling systems which use this concept could be of two types, namely: the direct-contact, or integral coolers, and the liquid feed coolers.

2. In the spaceborne system, the absence of gravity or acceleration orientation impedes the use of the standard two-phase systems, since random orientation of the liquid vapor interface during weightlessness could result in liquid ejection through the venting duct (see clause 6.4.1).

   Space storage system of cryogenic liquids can also be accomplished by pressurization of the cryogen to supercritical pressures. Now the absence of gravity or acceleration orientation forces does not effect the delivery or venting of fluid since the supply and venting ports are, at all times, in direct communication with a relatively homogeneous fluid. However, the total mass per unit mass of fluid stored is greater with supercritical systems than that encountered with low-pressure two-phase systems.

   When extended storage of cryogens is required to provide cooling at a specified low temperature, new design problems appear. For example: during a constant pressure with-drawal of a supercritical fluid from a tank, the temperature of the fluid continually rises due to he added input energy from the environment to the container. In order to maintain a relatively constant temperature for cooling purposes, a decaying tank pressure must be utilized. Other problems arise when using vapor cooled shields in subcritical systems (see Clause 6), since the vented fluid may not be available for shield cooling before being used for cooling the load. In such cases a secondary or guard cryogen may be used (see Clause 6.4.1).

3. Cryogens can be stored in the solid phase. Cooling system based on the sublimation of a solid coolant show considerable promise since a number of problems associated with either subcritical or supercritical storage are avoided. Solid cryogen refrigerators consist in a solidified gas, an insulated container, a venting path to space, and a conduction path from the coolant to the device being cooled. The operating temperature obtainable with these systems depends upon the choice of coolant, the pressure maintained in the system, and the heat load. The advantages of the use of a solid cryogen over normal liquid cryogens have been mentioned in the General Introduction of Clause 4 of this Part.

6
VCS Dewars

6.1 General

This Clause concerns Dewars holding cryogens used for cooling systems in the temperature range 0-100 K.

These low temperature levels are mainly required by spaceborne electronic systems operating under very low noise conditions.

Cooling by liquid or solid cryogens may be based on either of the following ideas (see also clause 5.3).

1. The cryogen is stored as a source of low temperature gases. The usefulness of these open-cycle cooling systems, based on stored liquid cryogens, appears to be confined to cases where refrigeration is required for relatively short period (Breckenridge (1972) [29]).
2. The cryogen is in direct contact with the component to be cooled. The heat is transferred from the component through boiling or sublimation of the cryogen at the component surface. The resulting vapors are, in most cases, ejected outside. These vapors could be used to cool the insulation surrounding the cryogenic container, as in the case of the Vapor Cooled Shield Dewars (VCS Dewars). Only when the boiling point of the coolant exceeds the environment temperature makes sense to condense the vapors and send them back to the container to repeat the cycle.

For space applications solid cryogens offer the following advantages over (normal) liquid cryogens:

1. Latent heat of sublimation is greater than latent heat of vaporization.
2. Liquid pose problems of phase separation under reduced gravity conditions.
3. Solid density is higher than liquid density.

A solid cryogen cooler for an IR detector is shown in Figure 6-1.

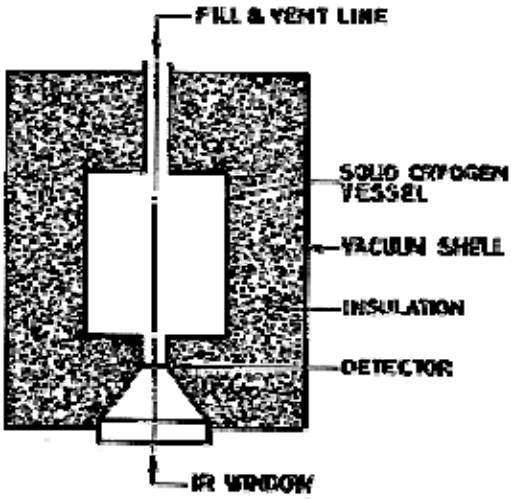

Figure 6-1: Schematic representation of a solid gryogen cooler. From Breckenridge (1972) [29].

Superfluid liquid helium, on the other hand, has a number of unusual properties which make it exceptionally suitable to provide very low temperature environments. It is a superconductor of heat, it forms a thin and highly conductive film in all surfaces, and it has essentially zero viscosity for certain types of flow. Because of these reasons, many VCS Dewars under development will use superfluid helium as the cooling cryogen

The amount of cryogen required to perform a given mission, and thus the mass of the system, depends not only on the detector cooling load and on the lifetime, but also on the parasitic heat leaks. Extremely efficient thermal insulations should be devised to keep low these heat leaks.

The VCS Dewars which are being introduced can be also used for long term storage of cryogenic propellants in space, the main differences between both applications are the temperature level and the geometric scale.

The basic idea of these Dewars consists in using the coldness of the evaporating cryogen to cool the insulation. This is achieved by means of a number of highly conductive metallic shields placed within the insulation -perpendicularly to the temperature gradient- and set in contact with venting ducts conducting the boil-off vapors.

The contact between the metallic shields and the venting ducts could be achieved by either of the following procedures.

1. The shields are soldered around the circumference of metallic discs which have been previously joined to the venting duct or penetration. This procedure will henceforth be called normal attachment since the axis of the penetration is roughly perpendicular to the shield.

2. In the tangential attachment, the vapor-venting duct, in the shape of a cooling coil, is either soldered or cemented to the metallic foil. Normally the entrance and the exit ends of the coil are connected to the neck of the cryostat.

Additional details concerning VCS systems are given in Clause 6.4 of this Part. For the present purposes it is sufficient to envisage a VCS Dewar as it is sketched in Figure 6-2. The highly conductive shields are placed between the layers of a multilayer insulation extending along the entire container. No precise details concerning the thermal contact between shields and venting tube are required at this moment.

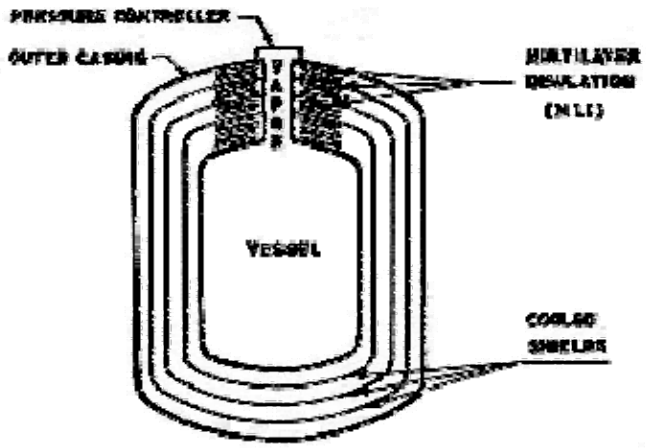

Figure 6-2: Sketch of a typical VCS Dewar. From Niendorf & Choksi (1967) [169].

The advantage of the VCS system can be understood from Figure 6-3, which represents that part of the insulation close to a venting duct in a normal attachment system. The relative amount and the direction of the heat transfer to or from the system is indicated by means of arrows of varying lengths.

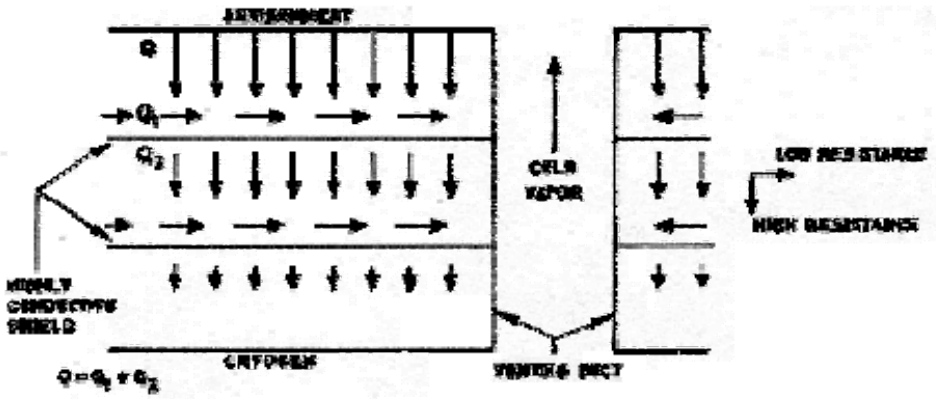

Figure 6-3: Heat transfer mechanism through a normal attachment VCS Dewar. From Niendorf & Choksi (1967) [169].

It can be seen that the heat, Q, to the outer shield is equal to the heat, Q_1, transferred to the vented gas through the shield, plus Q_2 -the heat which continues through the insulation. This mechanism is repeated at each conductive shield, reducing the heat which would be transferred through a conventional multilayer insulation system.

6.2 Theoretical analysis

6.2.1 Introduction

The following analysis is an extension of the work performed by Paivanas, Roberts & Wang (1965) [177], and by Niendorf & Choksi (1967) [169]. Here the effect of penetration on the heat leaks is taken into account in a fairly simplified way.

A theoretical model which is intended to describe the behavior of a VCS should consider the following points:

1. Thermal conductivities of insulation, venting ducts and supports as function of temperature.
2. Finite number of metallic shields attached to the venting duct.
3. Finite thermal conductivity along the metallic shields.
4. Thermal resistance between the metallic shields and venting duct.
5. Convective heat transfer between gas and venting duct, and between gas and cooled supports, if any.
6. degradation of the insulation because of the penetrations.

A theory based on such fine details, however, would greatly hinder the attainment of the insight required to deal easily with VCSs. Thus, a model based on the following simplifying assumptions will be used:

1. Thermal conductivities of insulations, venting ducts and supports are uniform and based on some mean temperature.
2. The number of metallic shields is infinite.
3. Conductivity along the shields is infinite, so that there is no temperature gradient along them. As a consequence, a one-dimensional model of heat transfer through the shield can be applied, in this model the temperature is only function of the coordinate, x, across the insulation.
4. There is no thermal contact resistance between the shields and the venting duct.
5. Thermal conduction through the insulation and through supports occur separately but simultaneously, with no interchange of heat between them. Thence, is no degradation of the insulation because of the penetrations.
6. The heat transfer rate between vented vapors and duct walls is infinite, so that the gas temperature at each cross section of the duct is that corresponding to the duct wall at the same cross section.
7. An area-weighted average of the venting duct and the insulation thermal conductivity is represented by a single function, $k(T)$.
8. The insulation is cooled by the vapors flowing through the venting duct, whereas cooling of the supports -if they are vapor-cooled- is provided by the vapor flowing through each of them.
9. The specific heat of the vapor is constant.

The validity of the most significant of these simplifying assumptions will be discussed in further clauses.

6.2.2 The idealized model

The one-dimensional equation for the heat balance in an infinitely thin layer of the insulation, as that sketched in Figure 6-4, may be written as follow:

$$\frac{d}{dx}\left(kA\frac{dT}{dx}\right) = mc_p\frac{dT}{dx} \qquad [6\text{-}1]$$

with the boundary conditions:

$$x = 0 \quad , \quad T = T_C \quad , \quad x = t \quad , \quad T = T_H \qquad [6\text{-}2]$$

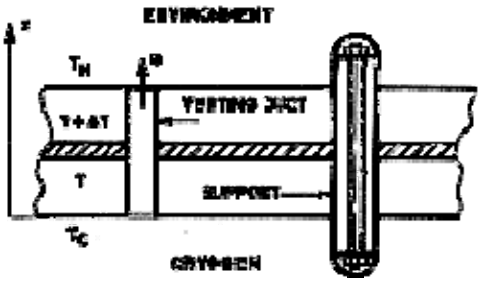

Figure 6-4: Insulation model geometry.

Similar equations and boundary conditions are applicable to each one of the p supports; it is only required to substitute k_{sj}, A_{sj},T_{sj}, m_{sj}, and t_{sj},(j = 1, 2, ...p) for k, A, T, m and t.

In addition, the boil-off rate is related to the heat input to the cryogen by means of the expression:

$$\left(m + \sum_{j=1}^{p} m_{sj} \right) h_{fg} = Q_1 + Q_m + Q_s = \\ = Q_1 + \left(kA \frac{dT}{dx} \right)_{x=0} + \sum_{j=1}^{p} \left(k_{sj} A_{sj} \frac{dT_s}{dx} \right)_{x=0} \qquad [6\text{-}3]$$

Eq. [6-1] with boundary conditions [6-2] can be integrated, when k is uniform, leading to the following equation:

$$kA \left(\frac{dT}{dx} \right)_{x=0} = mc_p \frac{T_H - T_C}{e^{\frac{mc_p}{kA} t} - 1} \qquad [6\text{-}4]$$

Substituting Eq. [6-4], and similar expressions for each support, into Eq. [6-3] one obtains:

$$\psi_1 \frac{m_o}{m} + \frac{S}{e^{mS/m_o} - 1} - 1 + \sum_{j=1}^{p} \frac{m_{sj}}{m} \left[\frac{S}{e^{\frac{m}{m_o} S \frac{m_{sj} t_{sj}}{mt} \frac{kA}{k_{sj} A_{sj}}} - 1} - 1 \right] = 0 \qquad [6\text{-}5]$$

where ψ_1 is the dimensionless detector heat load, m_0 is the characteristic boil-off rate, and S the sensibility of the cryogen. All these magnitudes have been defined in the List of Symbols. In particular, m_0 is the boil-off rate of the same cryogen stored in a vessel having the same size as that being considered, but thermally insulated by means of a conventional MLI with the same k and no penetrations (by stored it is meant here that no electronic device is to be cooled). S is the ratio of the maximum cooling by vapor convection to that by phase change.

Eq. [6-5] would give, through the ratio m/m_0, a measure of the improvement achieved by vapor cooling. For example, $m/m_0 < 1$ for a VCS storage container, Whereas $m/m_0 = 1$ for a conventionally insulated storage container. When additional heat loads are taken into account, either because penetrations or electronic devices, m/m_0 can be larger than unity, as will be shown below. For each value of these additional heat loads, however, m/m_0 will be a monotonic function of S. The largest value of m/m_0 will be always that corresponding to $S = 0$ (no vapor cooling), and the smallest that corresponding to $S \to \infty$.

For slightly cooled supports ($(m_{sj}/m)^2 << 1$) Eq. [6-5] becomes:

$$\psi_1 \frac{m_o}{m} + \frac{S}{e^{mS/m_o} - 1} - 1 + \frac{m_o}{m} \frac{t}{kA} \sum_{j=1}^{p} \frac{k_{sj} A_{sj}}{t_{sj}} - \sum_{j=1}^{p} \frac{m_{sj}}{m} = 0 \qquad [6\text{-}6]$$

For the conventional MLI ($S = 0$) the ratio m/m_0 becomes:

$$\left(\frac{m}{m_o} \right)_{S=0} = \frac{\psi_1 + \frac{t}{kA} \sum_{j=1}^{p} \frac{k_{sj} A_{sj}}{t_{sj}} + 1}{1 + \sum_{j=1}^{p} \frac{m_{sj}}{m}} \qquad [6\text{-}7]$$

For vapor cooling with a cryogen of infinitely large sensibility:

$$\left(\frac{m}{m_o} \right)_{S \to \infty} = \frac{\psi_1 + \frac{t}{kA} \sum_{j=1}^{p} \frac{k_{sj} A_{sj}}{t_{sj}}}{1 + \sum_{j=1}^{p} \frac{m_{sj}}{m}} \qquad [6\text{-}8]$$

Values of the ratio m/m_0 for different heat additions to the cryogen, other than those across the insulation, have been plotted against the sensibility, S, in Figure 6-5. It is shown in this Figure that the largest gain for a given cryogen, i.e., the smallest value of m/m_0, is achieved when the heat transfer across the insulation is dominant, i.e., when the cryostat is exclusively used for storage purposes. In these cases, vapor cooling is clearly advisable for high sensibility cryogens such as hydrogen or helium.

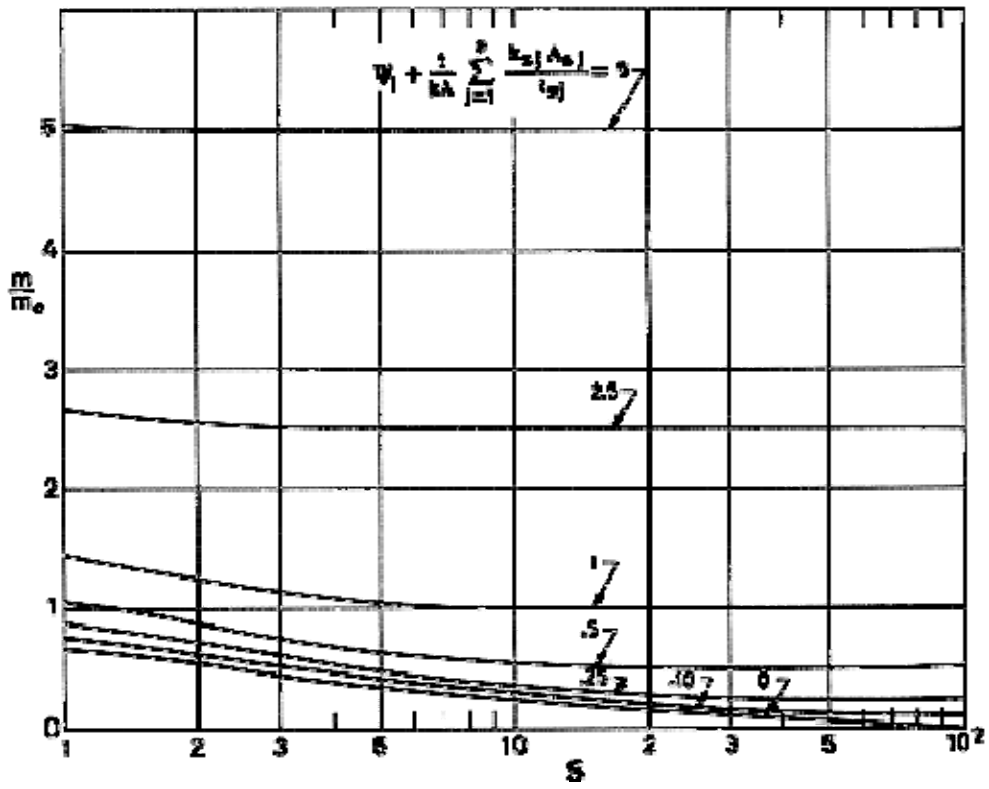

Note: non-si units are used in this figure

Figure 6-5: Ratio m/m_0 against the cryogen sensibility, S, for different values of the heat additions to the cryogen other than those across the insulation. No cooled supports ($m_{sj} = 0$). Calculated by the compiler.

When other paths of heat addition to the cryogen (such as penetrations or electronic heat loads) are present, the improvement because of vapor cooling is not so large. It can be deduced from Eqs. [6-7] and [6-8] that the ratio of the smallest to the largest evaporation rates tends to unity when the heat loads other than those across the insulation increase. The reason for this is clear: when the heat transfer through the insulation is not dominant no substantial gain is achieved by reducing it.

Table 6-1 gives values of the lower bounds of m/m_0 for several typical cryogens. The advantage of the VCS system is noteworthy, at least for storage or shipping cryostats.

Values of the lower bounds of m/m_0 for temperature dependent thermal conductivity, k, of the insulation are also given in Table 6-1. These values have been obtained by the procedure explained in Clause 6.2.3.1.

The thermophysical data which have been used for estimating $S$and m/m_0 are given in the upper part of Table 6-1. A more extensive collection of data can be found in Clause 8.1 of this Part.

Table 6-1: Benefit Obtained from a VCS System in a Storage Container

CRYOGEN		Helium	Hydrogen	Neon	Nitrogen	Argon	Oxygen	Methane
Normal Boiling Point [K]		4,2	20,39	27,2	77,4	87,4	90,1	111,6
Normal Melting Point [K]		[a]	13,98	24,5	63,4	83,6	54,4	90,7
Vapor Specific Heat c_px10^{-3} [J.kg^{-1}.K^{-1}]		5,23	13,88	1,03	1,04	0,52	0,91	2,09
Heat of Vaporization h_{fg}x10^{-3} [J.kg^{-1}]		20,52	448,2	89,09	199,3	161,7	213,1	508,2
Heat of Sublimation h_{fg}x10^{-3} [J.kg^{-1}]			508,2	105,6	224,7	185,6	226,8	568,7
LIQUID	T_H [K]							
Sensibility, S	300	64,148 [b]	8,659	3,154	1,162	0,684	0,896	0,775
	200	42,462 [b]	5,562	1,998	0,640	0,362	0,469	0,364
	150	31,618 [b]	4,014	1,420	0,379	0,201	0,256	0,158
m/m_o ($k = \bar{k}$)	300	0,065	0,262	0,452	0,664	0,762	0,714	0,740
	200	0,089	0,338	0,550	0,773	0,853	0,820	0,853
	150	0,110	0,402	0,622	0,848	0,911	0,890	0,928
m/m_o k depends on T	300	0,030	0,182	0,365	0,614	0,726	0,673	0,708
	200	0,045	0,256	0,475	0,745	0,836	0,800	0,840
	150	0,059	0,322	0,560	0,833	0,904	0,882	0,925
SOLID	T_H [K]							
Sensibility, S	300		7,812	2,687	1,095	0,606	0,985	0,770
	200		5,081	1,712	0,632	0,326	0,584	0,402
	150		3,715	1,224	0,401	0,186	0,384	0,218
m/m_o ($k = \bar{k}$)	300		0,279	0,486	0,675	0,782	0,696	0,742
	200		0,355	0,583	0,775	0,866	0,788	0,841
	150		0,417	0,653	0,841	0,917	0,846	0,905
m/m_o k depends on T	300		0,193	0,398	0,622	0,747	0,641	0,704
	200		0,267	0,508	0,742	0,849	0,753	0,823
	150		0,331	0,591	0,822	0,910	0,825	0,897

[a] Helium remains fluid even at absolute zero, provided that the pressure does not exceed about $2{,}5 \times 10^6$ Pa.

[b] According to Paivanas et al. (1965) [177], Helium sensibility has been lowered by 15% to allow for the significant fraction of vaporized liquid which remains in the tank as saturated vapor.

6.2.3 Evaluation of the restrictions involved in the idealized model

The simplifying assumption listed in Clause 6.2.1 will be critically appraised in the following paragraphs.

In many cases, corrective factors, which enable the calculation of the deviations from the ideal model, have been tabulated and/or graphically plotted. In other cases the problem is more complicated and references to experiments or computerized analysis by others are given.

The corrective factors will be presented as:

$\omega_i = m_i/m$,

where m_i is the value of the evaporation mass flow rate increased by the ith adverse effect, and m the value obtained under the idealized model.

Obviously ω_i is larger than one in any case. The only exception appears in the study of the influence of the temperature dependent thermal conductivity of the insulation.

A method to account for the simultaneous departures of the adverse effects from the ideal level is shown in Clause 6.2.3.5.

The information concerning each individual adverse effect is arranged as follows: First, the analytical background is briefly reviewed, as far as possible, then values of ω_i are given; finally, recommendations are suggested concerning how the system should be designed or installed to hold these adverse affects into a negligible level.

A summary of the several corrective effects is shown in Table 6-2.

Table 6-2: Relaxation of the Restrictions Involved in the Idealized Model

Basic Assumption of the Ideal Model	More Elaborate Model	Corrective Factor	Comments
Temperature-independent thermal conductivity.	One-dimensional purely conducive model. $k = k_1 T$.	$\omega_k > 1$	It is assumed in any case that heat transfer through the insulation is purely conductive. The validity of this assumption is evaluated in Clause 6.2.3.1.1.
The number of vapor cooled shields is infinitely large.	One-dimensional purely conducive model with a finite number of vapor cooled shields.	$\omega_n > 1$	Optimum positioning of the shields, and misplacing effects are also considered. A factor ω_{nk} taking into account both n and k effects is also given.
Conductance along the shield is infinitely large.	Axisymmetrical configuration, centered in a venting duct. Purely conductive model. Finite	$\omega_y > 1$	Three-dimensional effect. Other three-dimensional effects arise, which are common to any MLI applied around small

Basic Assumption of the Ideal Model	More Elaborate Model	Corrective Factor	Comments
	conductance along the shield.		containers.
Other three-dimensional effects.			Values of k_{eff} for MLI wrapped around a tank of a solid cryogen VCS Dewar are 1,3 to 4,1 times larger than those deduced from flat-plate calorimeter techniques. (Bell, Nast & Wedel (1977) [21]).
Thermal conductance between shields and venting duct is infinitely large.			Procedures to increase this contact thermal conductance are widely known.
Convective heat transfer from venting tube walls to flowing vapors is infinitely large.	Realistic values of the Nusselt number for both laminar and turbulent flow through cylindrical tubes.	$\omega_{Nu} > 1$	
Heat transfer processes through the insulation and through penetrations do not interact.			Results from a computerized analysis for a MLI indicate that a very small degree of coupling takes place (Bell, Nast & Wedel (1977) [21]).

The list of simplifying assumptions used in the idealized model is larger than the list of correcting factors accounting for the inaccuracies of these assumptions. Even when we are unable to estimate the correction, we list the simplifying assumption to emphasize the need for further study.

6.2.3.1 Temperature dependence of thermal conductivity

The problem defined by the differential equation [6-1] with boundary conditions [6-2], concerning the heat transfer through the insulation devoided of penetrations, can be solved when the thermal conductivity, *k*, is a known function of temperature. The dimensionless boil-off rate is (Paivanas et al. (1965) [177]):

$$\frac{m}{m_o} = \frac{1}{k}\int_0^1 \frac{k(\theta)d\theta}{1+S\theta} \qquad [6\text{-}9]$$

$$\frac{m}{m_o} = \frac{\ln(1+S)}{S} \qquad [6\text{-}10]$$

could be used to calculate the sensitiveness of the results which have been obtained to the assumption of uniform thermal conductivity throughout the insulation.

6.2.3.1.1 Data on $k(\theta)$

Data on the temperature dependence of k cannot be obtained easily. Although a large amount of tests have been performed to measure the effective thermal conductivity of an MLI as a function of the warm boundary temperature, T_H, or of a characteristic temperature defined somehow, it is stressed that the values from these tests should not be considered as an average thermal conductivity of the materials constituting the insulation, rather they give, in an expeditious way, the heat flux as a function of temperature for a very complex transfer process involving conduction, radiation, and (perhaps) convection.

If the above objection, which is applicable to any Fourier law-type analysis of the heat transfer through an MLI, is skipped, one can estimate $k(\theta)$. Representative examples giving the effective thermal conductivity of several MLIs are shown in Table 6-3.

It can de deduced from these examples that the conduction term dominates the heat transfer at the low temperatures involved.

Table 6-3: (Effective) Thermal Conductivity of Several MLIs vs. Temperature.

SAMPLE DESCRIPTION: Shields of Aluminium foil. Spacers of glass-fiber paper. TYPICAL VALUES: N/t = 2x10³ m⁻¹ to 4x10³ m⁻¹. ρ = 88 kg.m⁻³. k_{eff} = 3,1x10⁻⁵ W.m⁻¹.K⁻¹ for T_H = 294 K, T_C = 20 K. EMPIRICAL CORRELATION: $k_{eff} = 1{,}854\text{x}10^{-7}T + 2{,}775\text{x}10^{-13}T^3$. REFERENCES: Sample description and typical values from Matsch (1962) [143]. Empirical correlation after Paivanas et al. (1965) [177].	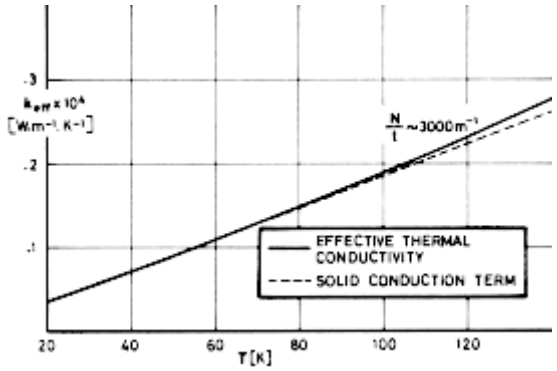
SAMPLE DESCRIPTION: Shields of double-aluminized Mylar. Spacers of silk net. TYPICAL VALUES: N/t = 1,5x10³ m⁻¹. k_{eff} = 6,6x10⁻⁶ W.m⁻¹.K⁻¹ for T_H = 135 K, T_C = 55 K. EMPIRICAL CORRELATION: k_{eff}=6,80x10^{-13}(N/t)^{1,56}(T_H+T_C)/2+ 5,40x10^{-10}ε($T_H^{4,67}$ -$T_C^{4,67}$)/(T_H-T_C)$^{N/t}$ REFERENCES: Sample description and measured data from Keller et al. (1974) [118]. Empirical correlation from Bell et al. (1977) [21].	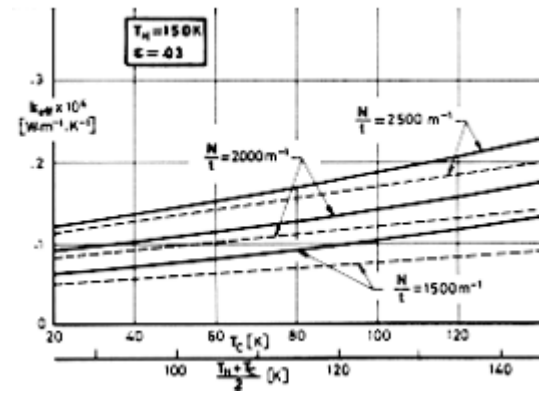
SAMPLE DESCRIPTION: Shields of double-aluminized Mylar. Spacers of Tissuglas. TYPICAL VALUES: N/t = 4,3x10³ m⁻¹. k_{eff} = 1,3x10⁻⁵ W.m⁻¹.K⁻¹ for T_H = 296 K, T_C = 54 K. EMPIRICAL CORRELATION: k_{eff}=4,65x10^{-19}(N/t)^{2,91}(T_H+T_C)- 3,22x10^{-22}(N/t)^{2,91}(T_H^3 -T_C^3)/(T_H-T_C)+ 8,01x10^{-10}ε($T_H^{4,67}$ -$T_C^{4,67}$)/(T_H-T_C)$^{N/t}$ REFERENCES: Sample description and measured data from Keller et al. (1974) [118]. Empirical correlation from Bell et al. (1977) [21].	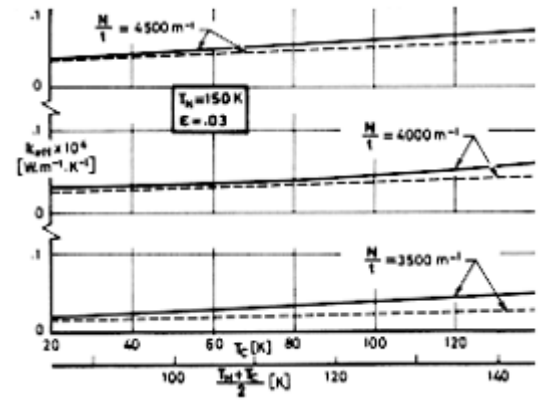

6.2.3.1.2 Analytical background

The three set of data presented in Table 6-3 indicate that a linear k vs. T relationship could represent fairly accurately the effective thermal conductivity of a typical MLI at temperatures below 200 K. In addition, since conduction controls the heat transfer process, it makes sense to introduce the concept of insulation local thermal conductivity.

Under the validity of this assumption, Eq. [6-9] with $\bar{k}$ => $k_1(T_H+T_C)/2$ yields:

$$\frac{m}{m_o}=\frac{2T_C}{T_H+T_C}\frac{\ln(1+S)}{S}+2\frac{T_H-T_C}{T_H+T_C}\frac{1}{S}\left(1-\frac{\ln(1+S)}{S}\right) \qquad [6\text{-}11]$$

Data on Table 6-1 labelled "*k* depends on *T*" have been calculated by means of Eq. [6-11].

Dividing the value of m/m_0 given by Eq. [6-11] by that deduced from Eq. [6-10] one deduces the corrective factor, ω_k,or the influence of the temperature-dependent thermal conductivity.

It is understood that the values of $\bar{k}$ for> both systems under comparison (that with temperature-independent *k*, and that with *k* linearly depending on *T*) should be identical, otherwise the characteristic boil-off rates, m_0, would differ, and their ratio should be taken into account calculate ω_k.

The data given in Table 6-1 indicate that m/m_0 is fairly sensitive to the uniform thermal conductivity assumption, particularly when *S* is large.

The corrective factor, ω_k, is shown in Figure 6-6 as a function of the sensibility, *S*, of the cryogen, for several values of the ratio T_C/T_H.

Notice that ω_k, which is smaller than one in this particular case, does not depend on the specific value of k_1, assuming -of course- that $\bar{k}$ is> the same for both systems under comparison.

In order to magnify the corrective effect, $1-\omega_k$ has been plotted in lieu of ω_k in Figure 6-6. The fact that ω_k is smaller than one indicates that the variable conductivity insulation is more effective than that with uniform conductivity, and this is so because of the effect of the cooler layers of the insulation.

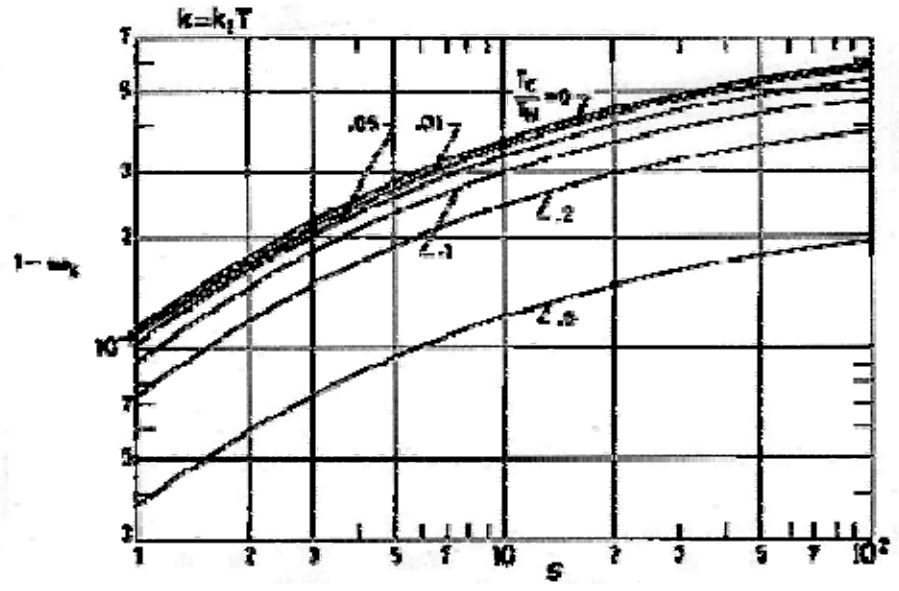

Figure 6-6: Corrective factor, ω_k, for the dependence of insulation thermal conductivity, k, on temperature, T, against the sensibility, S, of the cryogen, for several values of the temperature ratio, T_C/T_H. A linear thermal conductivity vs. temperature dependence has been assumed. Calculated by the compiler.

6.2.3.2 Finite number of cooled shields

Let us consider a system with a finite number, n, of cooled shields, joined to the venting duct, within an otherwise homogeneous insulation. The aim of this clause is threefold: 1) to optimize shield positioning, once n is fixed, in order to minimize the heat transfer through the insulation; 2) to calculate the corrective factor, ω_n, as a function of cryogen properties, boundary temperatures, and number of shields, assuming that the cooled shields are placed in their optimum positions, and 3) to evaluate how sensitive the heat transfer through the insulation is to shield positioning other than the optimum one.

6.2.3.2.1 Analytical background

The heat balance for the ith cooled shield can be written, in terms of the usual dimensionless variables, as follows (see Figure 6-7):

$$\frac{m_n}{m_o} S\left(\theta_i - \theta_{i-1}\right) = \psi_i - \psi_{i-1} \quad , \quad i = 1,2,\ldots,n \qquad [6\text{-}12]$$

In Eq. [6-12] ψ_i is the dimensionless heat transfer rate through the ith insulation layer:

$$\psi_j = \frac{D_j}{\Delta\xi_j} \quad , \quad j = 0,1,2,\ldots,n \qquad [6\text{-}13]$$

where

$$D_j = \int_{\theta_j}^{\theta_{j+1}} \frac{k(\theta)}{\bar{k}} d\theta \qquad [6\text{-}14]$$

and

$$\Delta\xi_j = \xi_{j+1} - \xi_j \quad , \quad \xi_o = 0 \quad , \quad \xi_{n+1} = 1 \qquad [6\text{-}15]$$

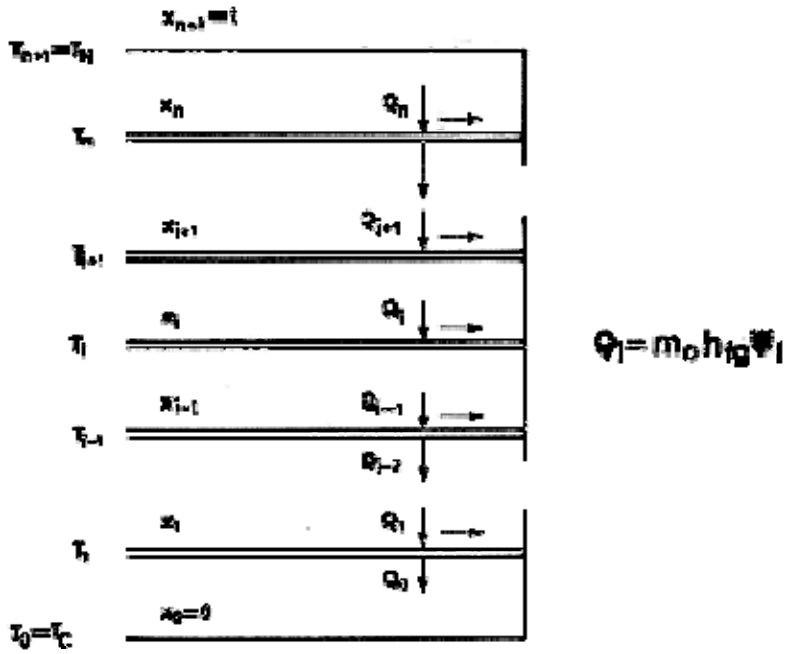

Figure 6-7: Insulation model with finite number of shields.

Obviously the sum of thicknesses between shields plus those between the bounding faces of the insulation and the neighbouring shields will equal the total insulation thickness, *t*.

Thence

$$\sum_{j=0}^{n} \Delta\xi_j = 1 \qquad [6\text{-}16]$$

Note: non-si units are used in this figure

The problem is now to minimize the ratio m_n/m_0, which appears in the *n* equations [6-12], with the *n*+2 auxiliary conditions [6-13] and [6-16]. Following an idea set forth by Bejan (1975), who dealt with a similar problem, the method of Lagrange multipliers will be used. To this end we first introduce 2*n*+2 additional unknowns, α_i, β_j and λ, and then minimize a new function, *F*, defined as follows:

$$F \equiv \sum_{i=1}^{n} \alpha_i \left[\frac{m_n}{m_o} S(\theta_i - \theta_{i-1}) - \psi_i + \psi_{i-1} \right] + \\ + \sum_{j=0}^{n} \beta_j \left[\frac{D_j}{\Delta\xi_j} - \psi_j \right] + \lambda \left[\sum_{j=0}^{n} \Delta\xi_j - 1 \right] \qquad [6\text{-}17]$$

with the auxiliary conditions [6-12], [6-13] and [6-16]. In other words, we are to solve the following $5n+4$ equations: $\partial F/\partial\theta_i = 0$; $\partial F/\partial\psi_j = 0$; $\partial F/\partial\Delta\xi_j = 0$; Eq. [6-12]; Eq. [6-13], and Eq. [6-16] -which are n, $n+1$, $n+1$, n, $n+1$ and 1 equations, respectively- to determine the proper values of: m_n/m_0, θ_i, ψ_j, $\Delta\xi_j$, α_i, β_j and λ. There are $5n+5$ unknowns, but one among α_i, β_j or λ can be assumed to be equal to unity. Elimination of ψ_j, α_i, β_j and λ yields:

$$\frac{\Delta\xi_i}{\Delta\xi_{i-1}} = -\frac{\theta_i - \theta_{i-1}}{D_{i-1}} \frac{\partial D_i}{\partial\theta_i} \qquad [6\text{-}18]$$

Note: non-si units are used in this figure

and

$$\frac{1 + S\theta_{i-1}}{1 + S\theta_i} = -\frac{\theta_i - \theta_{i-1}}{D_i} \frac{\partial D_i}{\partial\theta_i} \qquad [6\text{-}19]$$

Note: non-si units are used in this figure

where, according to Eq. [6-14], $\partial D_i/\partial\theta_i = -k(\theta_i)/\bar{k}$.>

1. When the insulation thermal conductivity is temperature independent, $D_i = \theta_{+1} - q_i$, thence Eq. [6-14] becomes:

   $\Delta\xi_i = \Delta\xi_{i-1}$.

   This equation indicates that the minimum heat flux through the insulation occurs when the distances between shields, and between the bounding faces of the insulation and neighbouring shields, are all equal.

   Combination of Eqs. [6-12], [6-13] and [6-14] yields:

$$\theta_{i+1} - \theta_i = \left(1 + \frac{m_n}{m_o} \frac{S}{n+1} \right) (\theta_i - \theta_{i-1}) \qquad [6\text{-}20]$$

Note: non-si units are used in this figure

whereas the expression relating the boil-off rate with the heat input to the cryogen,

$$\theta_1 = \frac{m_n}{m_o} \frac{1}{n+1} \quad , \quad \theta_o = 0 \qquad [6\text{-}21]$$

Note: non-si units are used in this figure

provides us with the dimensionless temperature for the 1st cooled shield. From Eqs. [6-20] and [6-21], with $\theta_{n+1}= 1$, one can deduce the temperature jump, $\theta_{i+1} - q_i$, in terms of i, m_n/m_0, S and n. Addition of the several temperature jumps gives

$$\frac{m_n}{m_o} = (n+1)\frac{(1+S)^{\frac{1}{n+1}} - 1}{S} \qquad [6\text{-}22]$$

Note: non-si units are used in this figure

The corrective term, ω_n, which gives the influence of the finite number of shields - assuming temperature independent thermal conductivity- becomes, after recalling Eq. [6-10],:

$$\omega_n = \frac{m_n}{m} = (n+1)\frac{(1+S)^{\frac{1}{n+1}} - 1}{\ln(1+S)} \qquad [6\text{-}23]$$

Note: non-si units are used in this figure

2. When the insulation thermal conductivity is a linear function of temperature, $k = k_1 T$, Eqs. [6-24] and [6-25], below, should substitute for Eqs. [6-18] and [6-19].

$$\frac{\Delta\xi_i}{\Delta\xi_{i-1}} = \frac{2T_i}{T_i + T_{i-1}} \qquad [6\text{-}24]$$

and

$$\frac{(T_H - T_C) + S(T_i - T_C)}{(T_H - T_C) + S(T_{i-1} - T_C)} = \frac{T_{i+1}^2 - T_i^2}{2T_i(T_i - T_{i-1})} \qquad [6\text{-}25]$$

These two equations together with Eq. [6-16] furnish the optimum shield spacing and the corresponding temperature field.

The corrective factor, ω_{nk}, for the finite number of shields when k is a linear function of T, can be expressed as:

$$\omega_{nk} = \frac{m_{nk}}{m} = \frac{1}{\xi_1}\frac{T_1^2 - T_C^2}{T_H^2 - T_C^2}\frac{S}{\ln(1+S)} \qquad [6\text{-}26]$$

Note: non-si units are used in this figure

where T_1 and ξ_1, which correspond to the first cooled shield, can be deduced as has been indicated. The resulting expression is complicated, and only the numerical results will be given.

6.2.3.2.2 Some numerical results

The above mathematical background has been applied to the computation of the following data.

1. For uniform insulation thermal conductivity.

   Table 6-4 gives numerical values of the corrective factor, ω_n, as calculated by Eq. [6-23], for typical cryogens, when T_H = 300 K, 200 K or 150 K.

   Figure 6-8 presents similar data. Now ω_n–1 is plotted against the cryogen sensibility, S, for various values of n.

   It can be deduced from both Table 6-4 and Figure 6-8 that when the sensibility, S, of the cryogen is large, as for liquid helium, a very reduced number, n, of cooled shields will decrease substantially the boil-off rate.

Table 6-4: Corrective Factor, ω_n, Giving the Influence of the Number, n, of Conductive Shields on the Boil-off Rate of Several Cryogens. ($k = \bar{k}$).

n	Liquid Helium [a]	Solid Hydrogen	Solid Neon	Solid Nitrogen	Solid Argon	Solid Oxygen
T_H = 300 K						
0	15,370	3,590	2,059	1,481	1,279	1,437
1	3,387	1,809	1,410	1,210	1,128	1,193
2	2,172	1,469	1,253	1,134	1,083	1,124
3	1,763	1,329	1,182	1,098	1,062	1,091
4	1,563	1,253	1,143	1,078	1,049	1,072
5	1,445	1,205	1,117	1,064	1,041	1,059
6	1,368	1,173	1,099	1,055	1,035	1,051
8	1,273	1,131	1,076	1,042	1,027	1,039
10	1,216	1,106	1,062	1,034	1,022	1,032
T_H = 200 K						
0	11,266	2,815	1,716	1,290	1,115	1,270
1	2,967	1,624	1,297	1,133	1,074	1,124
2	2,001	1,371	1,186	1,086	1,049	1,081
3	1,663	1,264	1,136	1,064	1,036	1,060
4	1,493	1,204	1,107	1,051	1,029	1,047
5	1,392	1,167	1,088	1,042	1,024	1,039
6	1,325	1,141	1,075	1,036	1,020	1,034
8	1,242	1,107	1,058	10,28	1,016	1,026
10	1,193	1,087	1,047	1,023	1,013	1,021
T_H = 150 K						
0	9,079	2,396	1,531	1,189	1,090	1,181
1	2,705	1,511	1,229	1,089	1,044	1,086
2	1,890	1,309	1,146	1,058	1,029	1,056
3	1,595	1,222	1,107	1,043	1,022	1,042
4	1,446	1,172	1,084	1,034	1,017	1,033
5	1,356	1,141	1,070	1,029	1,014	1,028
6	1,296	1,119	1,059	1,024	1,012	1,024
8	1,221	1,091	1,046	1,019	1,010	1,018
10	1,177	1,074	1,037	1,015	1,008	1,015

[a] Helium sensibility has been lowered by 15% to allow for the significant fraction of vaporized liquid which remains in the tank as saturated vapor.

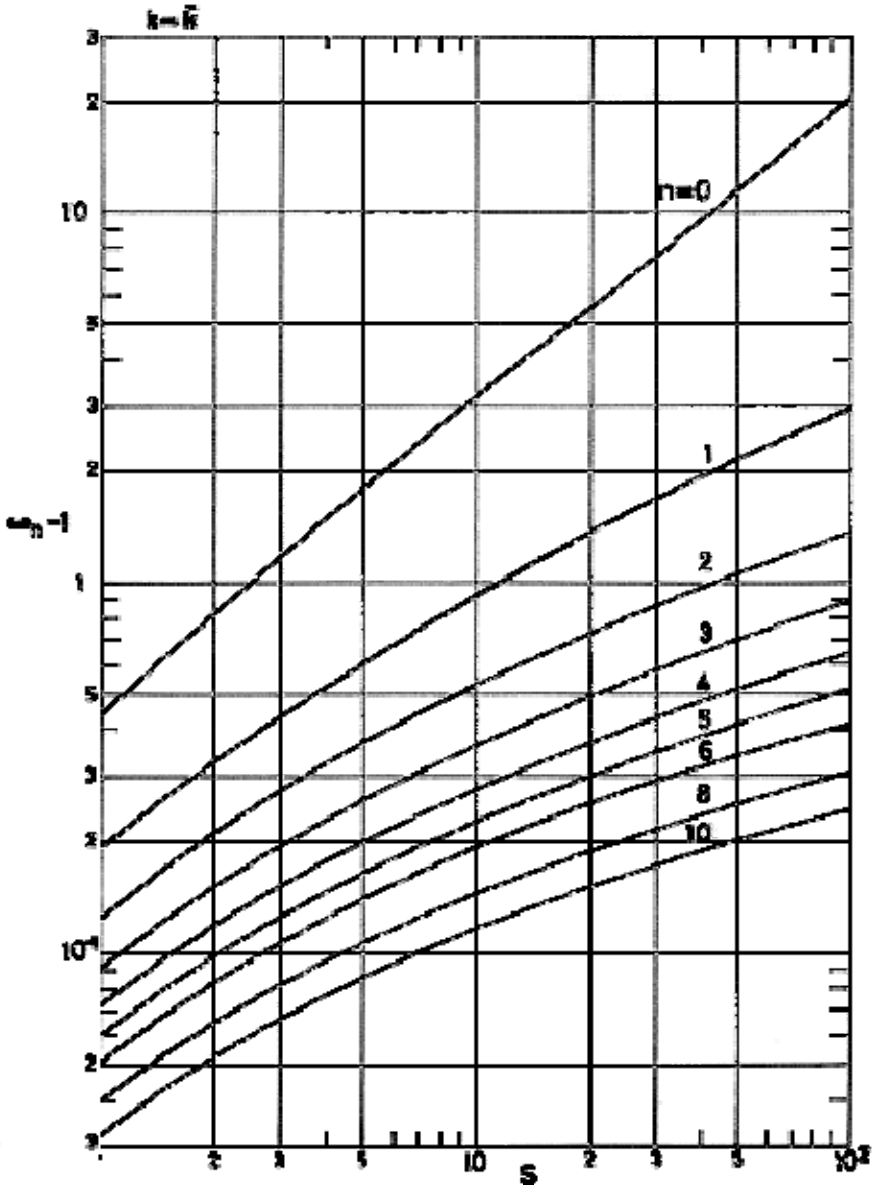

Figure 6-8: Corrective factor, ω_n, accounting for the influence of the finite number, n, of shields, vs. the sensibility S of the cryogen, for several values of n. Calculated by the compiler.

2. Data for systems whose thermal conductivity is a linear function of temperature are shown in Table 6-5 and Table 6-8.

   Table 6-5 gives the cooled shield temperatures, T_i, and dimensionless positions, ξ_i, which minimize the boil-off rate for several cryogens; two to seven cooled shields are considered.

   The factor ω_{nk} appears in Table 6-8 for the same cryogens, boundary temperatures, and number of shields as those in Table 6-4. It is deduced from both tables that the gain achieved by a number, n, of optimally placed cooled shields is larger when the thermal conductivity varies linearly with temperature.

Table 6-5: Cooled Shield Temperatures, T_i, and Dimensionless Shield Positions, ξ_i, Which Minimize the Boil-off Rate for Several Cryogens. ($k = k_1 T$)

LIQUID HELIUM [a]	Table 6-6
SOLID HYDROGEN	
SOLID NEON	
SOLID OXYGEN	
SOLID NITROGEN	Table 6-7
SOLID ARGON	
LIQUID OXYGEN	
SOLID METHANE	

[a] Helium sensibility has been lowered by 15% to allow for the significant fraction of vaporized liquid which remains in the tank as saturated vapor.

Table 6-6: Cooled Shield Temperatures, T_i, and Dimensionless Shield Positions, ξ_i, Which Minimize the Boil-off Rate for Several Cryogens. ($k = k_1 T$)

	LIQUID HELIUM [a]		SOLID HYDROGEN		SOLID NEON		SOLID OXYGEN	
	T_i [K]	ξ_i [b]	T_i [K]	ξ_i	T_i [K]	ξ_i	T_i [K]	ξ_i
H	300	1	300	1	300	1	300	1
2	119,6	0,499	166,9	0,534	192,1	0,553	215,5	0,580
1	32,6	0,180	73	0,199	100,7	0,212	134,4	0,239
C	4,2	0	14	0	24,5	0	54,4	0
H	300	1	300	1	300	1	300	1
3	160,3	0,597	198,9	0,637	219	0,656	237	0,680
2	71,1	0,307	118,3	0,348	146,5	0,369	175,7	0,401
1	23,2	0,114	57,1	0,133	82	0,145	115,4	0,170
C	4,2	0	14	0	24,5	0	54,4	0
H	300	1	300	1	300	1	300	1
4	187,4	0,666	218,9	0,704	235,4	0,721	249,8	0,741
3	105,2	0,405	150,1	0,455	175,8	0,478	200,7	0,509
2	50,3	0,213	93,4	0,252	121,2	0,273	152,3	0,304
1	18,5	0,081	48,2	0,099	71,1	0,109	104	0,131
C	4,2	0	14	0	24,5	0	54,4	0
H	300	1	300	1	300	1	300	1
5	206,2	0,716	232,4	0,751	246,3	0,766	258,3	0,784
4	132,3	0,483	173,1	0,533	196	0,556	217,4	0,584

	LIQUID HELIUM [a]		SOLID HYDROGEN		SOLID NEON		SOLID OXYGEN	
	T_i [K]	ξ_i [b]	T_i [K]	ξ_i	T_i [K]	ξ_i	T_i [K]	ξ_i
3	77,1	0,298	121,8	0,348	148,9	0,372	176,9	0,404
2	39	0,159	78,3	0,196	105	0,214	136,8	0,243
1	15,7	0,062	42,5	0,078	63,8	0,088	96,3	0,107
C	4,2	0	14	0	24,5	0	54,4	0
H	300	0,753	300	1	300	1	300	1
6	219,9	0,544	242,2	0,785	254,1	0,799	264,4	0,814
5	153,6	0,371	190,2	0,593	210,6	0,615	229,3	0,640
4	100,8	0,232	143,9	0,424	169,4	0,449	194,6	0,479
3	60,5	0,126	103,3	0,279	130,5	0,302	160,1	0,333
2	32	0,050	68,2	0,158	93,7	0,175	125,6	0,202
1	13,9	0	38,6	0,064	58,6	0,073	90,7	0,090
C	4,2		14	0	24,5	0	54,4	0
H	300	1	300	1	300	1	300	1
7	230,2	0,782	249,5	0,811	259,9	0,823	268,9	0,838
6	170,5	0,593	203,3	0,639	221,6	0,660	238,2	0,683
5	120,8	0,431	161,4	0,485	185,1	0,510	207,8	0,539
4	80,7	0,296	123,8	0,349	150,3	0,374	177,6	0,405
3	49,8	0,187	90,3	0,231	117,1	0,253	147,5	0,283
2	27,3	0,103	61	0,132	85,3	0,148	117,3	0,173
1	12,6	0,041	35,6	0,054	54,7	0,062	86,5	0,078
C	4,2	0	14	0	24,5	0	54,4	0

[a] Helium sensibility has been lowered by 15% to allow for the significant fraction of vaporized liquid which remains in the tank as saturated vapor.

[b] For the definition of ξ_i see sketch.

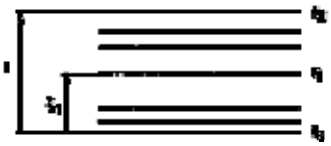

Table 6-7: Cooled Shield Temperatures, T_i, and Dimensionless Shield Positions, ξ_i, Which Minimize the Boil-off Rate for Several Cryogens. ($k = k_1 T$)

	SOLID NITROGEN		SOLID ARGON		LIQUID OXYGEN		SOLID METHANE	
	T_i [K]	ξ_i [b]	T_i [K]	ξ_i	T_i [K]	ξ_i	T_i [K]	ξ_i
H	300	1	300	1	300	1	300	1
2	216,6	0,586	228	0,598	226,2	0,602	227,8	0,602
1	138,2	0,247	156,5	0,260	156,5	0,265	158,4	0,265
C	63,4	0	83,6	0	90,1	0	90,7	0

	SOLID NITROGEN		SOLID ARGON		LIQUID OXYGEN		SOLID METHANE	
	T_i [K]	ξ_i [b]	T_i [K]	ξ_i	T_i [K]	ξ_i	T_i [K]	ξ_i
H	300	1	300	1	300	1	300	1
3	237,6	0,684	246,3	0,694	244,6	0,697	246	0,697
2	177,7	0,408	192,9	0,422	191,4	0,426	193,4	0,426
1	120,1	0,177	139,1	0,188	140,1	0,192	141,9	0,192
C	63,4	0	83,6	0	90,1	0	90,7	0
H	300	1	300	1	300	1	300	1
4	250,2	0,745	257,2	0,754	255,7	0,755	256,9	0,756
3	202	0,514	214,6	0,528	212,8	0,531	214,6	0,532
2	155,1	0,311	171,9	0,324	171,1	0,329	173,1	0,329
1	101,9	0,137	128,6	0,147	130,3	0,151	132	0,151
C	63,4	0	83,6	0	90,1	0	90,7	0
H	300	1	300	1	300	1	300	1
5	258,6	0,786	264,5	0,794	263,1	0,795	264,1	0,795
4	218,2	0,589	229,1	0,601	227,2	0,604	228,8	0,604
3	178,8	0,410	193,6	0,424	192,1	0,428	194	0,428
2	140,2	0,250	157,9	0,263	157,7	0,267	159,6	0,267
1	101,9	0,112	121,5	0,120	123,6	0,124	125,3	0,124
C	63,4	0	83,6	0	90,1	0	90,7	0
H	300	1	300	1	300	1	300	1
6	264,6	0,816	269,6	0,823	268,4	0,823	269,3	0,824
5	229,9	0,644	239,3	0,655	237,5	0,657	239	0,658
4	195,9	0,485	209	0,499	207,2	0,502	209,1	0,502
3	162,5	0,340	178,6	0,353	177,4	0,357	179,4	0,357
2	129,5	0,209	147,8	0,221	148,1	0,225	150	0,225
1	96,7	0,095	116,3	0,102	119,1	0,105	120,5	0,105
C	63,4	0	83,6	0	90,1	0	90,7	0
H	300	1	300	1	300	1	300	1
7	269	0,839	273,5	0,845	272,4	0,845	273,1	0,846
6	238,6	0,686	247	0,697	245,3	0,698	246,6	0,699
5	208,8	0,544	220,5	0,557	218,6	0,559	220,4	0,560
4	179,4	0,411	194	0,425	192,4	0,428	194,4	0,429
3	150,4	0,289	167,2	0,302	166,5	0,306	168,5	0,307
2	121,6	0,179	140,2	0,190	141	0,194	142,8	0,194
1	92,7	0,082	112,4	0,088	115,4	0,091	116,9	0,091
C	63,4	0	83,6	0	90,1	0	90,7	0

[b] For the definition of ξ_i see sketch.

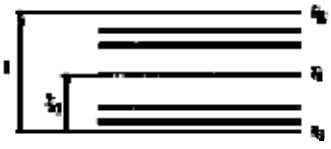

Table 6-8: Corrective Factor, ω_{nk}, Giving the Influence of the Number, n, of Conductive Shields on the Boil-off Rate of Several Cryogens. ($k = k_1 T$).

n	Liquid Helium [a]	Solid Hydrogen	Solid Neon	Solid Nitrogen	Solid Argon	Solid Oxygen
T_H = 300 K						
0	15,370	3,590	2,059	1,481	1,279	1,437
1	1,737	1,335	1,200	1,132	1,089	1,117
2	0,991	1,030	1,038	1,050	1,039	1,041
3	0,781	0,918	0,972	1,013	1,016	1,007
4	0,688	0,862	0,936	0,993	1,003	0,988
5	0,636	0,827	0,914	0,980	0,994	0,976
6	0,603	0,805	0,899	0,971	0,989	0,968
8	0,564	0,776	0,880	0,959	0,981	0,957
10	0,542	0,760	0,868	0,952	0,976	0,950
T_H = 200 K						
0	11,266	2,815	1,716	1,290	1,155	1,270
1	1,651	1,285	1,161	1,095	1,058	1,085
2	1,006	1,043	1,040	1,044	1,030	1,037
3	0,814	0,950	0,982	1,020	1,017	1,015
4	0,726	0,902	0,950	1,007	1,009	1,002
5	0,676	0,872	0,930	0,998	1,004	0,994
6	0,645	0,852	0,916	0,992	1,001	0,988
8	0,607	0,827	0,899	0,984	0,996	0,981
10	0,585	0,812	0,888	0,979	0,993	0,976
T_H = 150 K						
0	9,079	2,396	1,531	1,189	1,090	1,181
1	1,596	1,251	1,135	1,070	1,037	1,064
2	1,018	1,051	1,044	1,036	1,021	1,032
3	0,839	0,971	1,004	1,021	1,014	1,016
4	0,775	0,929	0,982	1,011	1,009	1,008
5	0,707	0,903	0,968	1,006	1,006	1,002
6	0,677	0,885	0,958	1,001	1,004	0,998
8	0,639	0,863	0,946	0,996	1,001	0,993
10	0,618	0,849	0,938	0,992	1,000	0,989

[a] Helium sensibility has been lowered by 15% to allow for the significant fraction of vaporized liquid which remains in the tank as saturated vapor.

6.2.3.2.3 Shield position tolerance

Once the number, n, of shields is fixed, the sensitiveness of the heat transfer to shield misplacing is considered.

1. In the case of uniform thermal conductivity, the expression relating the dimensionless boil-off rate, m_n/m_0, to shield positioning, ξ_i, can be written for $n = 2$, as follows:

$$\xi_2^2 - \xi_2(1-3\xi_1) - \left[\begin{array}{c} \xi_1(1-2\xi_1) + \dfrac{1}{1+\dfrac{m_2}{m_o}S\xi_1} \\ \left(\xi_1(1-\xi_1) - \dfrac{1}{S}\dfrac{m_o}{m_2}\left(\dfrac{m_o}{m_2}-1\right)\right) \end{array}\right] = 0 \qquad [6\text{-}27]$$

Note: non-si units are used in this figure

where subscripts 1 and 2 denote shield positioning, except for m_2/m_0 which is the dimensionless boil-off rate of the system with two cooled shields.

Representative results are given in Figure 6-9. Contours of constant values of the ratio of the flux to the uncooled shield heat flux are plotted as functions of the dimensionless distances of both shields to the cold boundary of the insulation. Different cryogen sensibilities have been considered. The numerical values labelling the various contours indicate the corrective term $\omega_n/\omega_{nopt}-1$. Obviously the resulting configuration is symmetrical about a 45° axis, since the shield positions are interchangeable, nevertheless only contours where $\xi_1 < \xi_2$ have been represented. This mapping procedure has been used by Atherton & Prentiss (1973) [12].

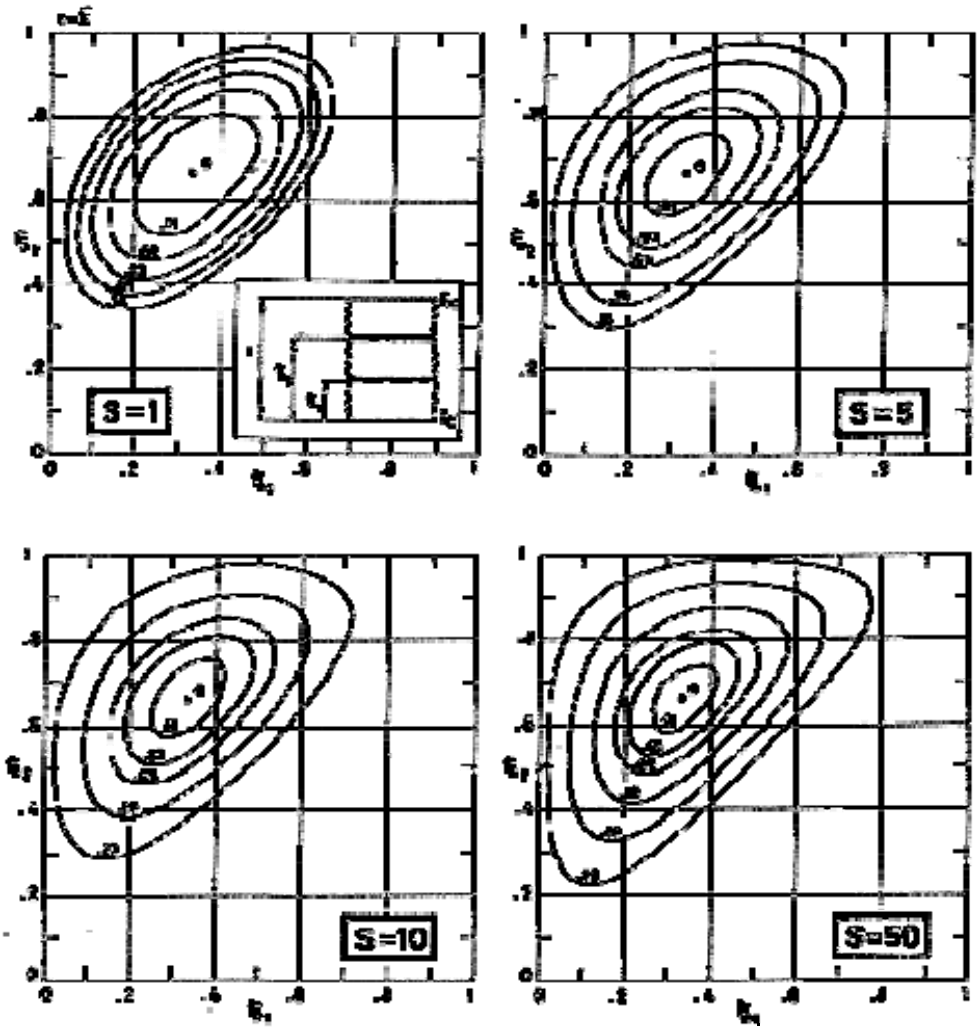

Note: non-si units are used in this figure

Figure 6-9: Contours of constant values of the ratio of the heat flux through the VCS system to the uncooled shield heat flux, mapped as functions of the dimensionless distances, ξ_1 and ξ_2, of the two vapor cooled shields to the cold face of the insulation, for several values of the sensibility, *S*, of the cryogen. Uniform insulation thermal conductivity. The numerical values labelling the contours corresponds to $\omega_n/\omega_{nopt} - 1$. Calculated by the compiler.

It can be deduced, from the distortion which the contour suffer when *S* increases, that the sensitiveness of the heat flux to shield misplacing increases with *S*, but the increased heat flux is, in any case, small.

Although the calculation of the optimum position for any number of cooled shields presents no insurmountable difficulties, the graphical representation of the results becomes increasingly difficult with increasing number of shields. Figure 6-10, borrowed from Atherton & Prentiss (1973) [12], presents data for three vapor-helium cooled shields. The minimum heat flux is obtained with ξ_1 = 0,25, ξ_2 = 0,50, ξ_3 = 0,75. The mapped contours give the displacement of the first shield, from its optimum position, which increases the heat flux by 10 % as functions of the positions, ξ_2 and ξ_3, of the other two shields. Again we note that the heat flux is remarkably insensitive to discrepancies in shield positioning. For example, if the second shield is correctly placed at ξ_2 = 0,5 and the

third shield misplaced at $\xi_3 = 0{,}9$, the first shield can still be placed anywhere within $\xi_1 = 0{,}25 \pm 0{,}10$ without increasing the heat flux more than 10 % from the minimum value.

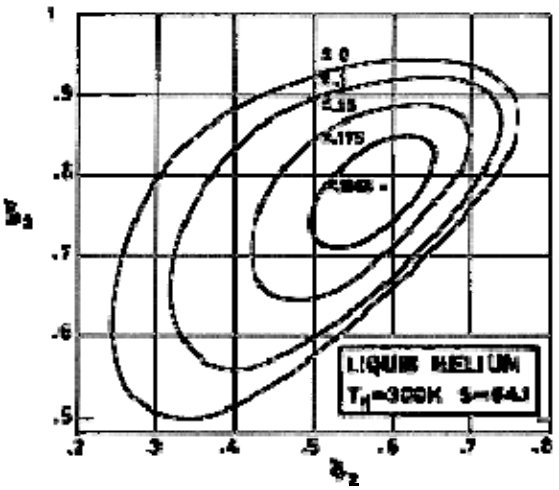

Note: non-si units are used in this figure

Figure 6-10: Contours of dimensionless displacements of a single shield from its optimum position ($\xi_1 = 0{,}25$) which produce a 10% increase in the heat flux through a three shield system. The contours are mapped as functions of the remaining two shields dimensionless positions. Numerical values are for helium between 4 K and 300 K. From Atherton & Prentiss (1973) [12].

2. When the thermal conductivity is a linear function of temperature, the expression relating the dimensionless boil-off rate to shield positioning becomes very involved. It is, nevertheless, feasible to plot Figures equivalent to Figure 6-9. This has been done and the results are presented in Figure 6-11. It can be deduced from this Figure that although the tolerance to shield misplacing is less than in the case of uniform thermal conductivity it is still fair for manufacturing purposes.

6.2.3.3 Finite convective heat transfer in the venting duct

So far it has been assumed that the vapor bulk temperature at each cross section of the venting duct is equal to the duct wall temperature at that cross section. This is tantamount to assume that the convective heat transfer coefficient is infinitely large.

We will consider now the case where the convective heat transfer coefficient is finite, so that the vapor bulk temperature, T_b, will be different from the venting tube wall temperature, T_w.

The adverse effects associated to the finite convective heat transfer in the vapors flowing through the venting duct are particularly critical when the shields are normally attached to the duct. Thence the content of this clause concerns, unless otherwise stated, the normal attachment mode.

It is assumed throughout the clause that the duct temperature, T_w, is equal to the insulation temperature at the corresponding value of x. It is required that: 1) the shield to duct thermal joint conductance be infinitely large, and 2) some procedure be devised to avoid the longitudinal heat transfer along the tube wall. This precaution is not required in the case of tangential attachment.

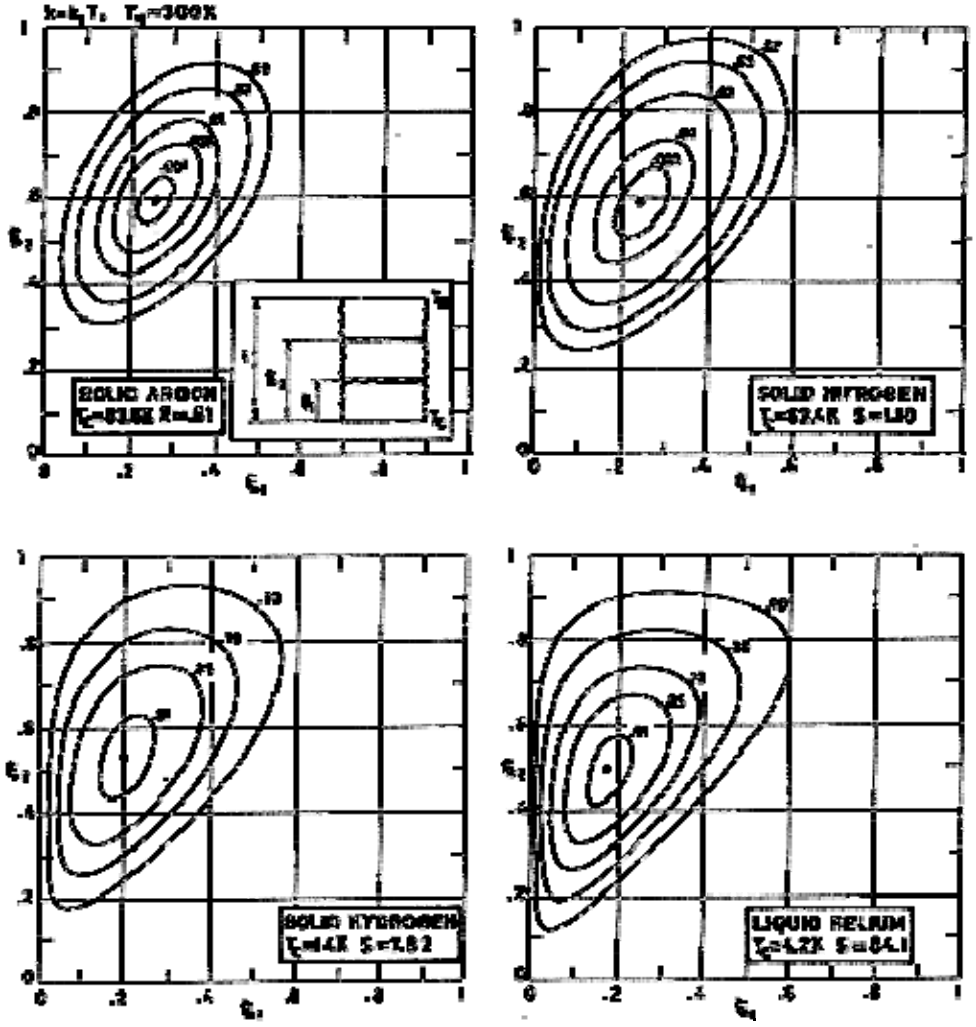

Note: non-si units are used in this figure

Figure 6-11: Contours of constant values of the ratio of the heat flux through the VCS system to the uncooled shield heat flux, mapped as functions of the dimensionless distances, ξ_1 and ξ_2, of the two vapor cooled shields to the cold face of the insulation, for several cryogens in typical cases. Temperature dependent insulation thermal conductivity ($k = k_1 T$). The numerical values labelling the contours corresponds to $\omega_n/\omega_{nopt} - 1$. Calculated by the compiler.

6.2.3.3.1 Analytical background

The heat balance through the insulation can be written, in terms of the usual dimensionless variables and parameters, as follows:

$$\frac{d}{d\xi}\left(\frac{k}{\bar{k}}\frac{dT}{d\xi}\right) = \frac{m_{Nu}}{m_o} S \frac{dT_b}{d\xi} \qquad [6\text{-}28]$$

Note: non-si units are used in this figure

T is used instead of the dimensionless function θ to introduce more easily the temperature dependence of the physical magnitudes involved.

Concerning the vapor flowing through the venting duct:

$$\frac{dT_b}{d\xi} = \frac{m_o}{m_{Nu} S} \frac{\pi t^2}{A} \frac{k_b}{\bar{k}} Nu\left(T - T_b\right) \qquad [6\text{-}29]$$

Nu being the Nusselt number (see ECSS-E-HB-31-01 Part 13 Clause 6.2 and 6.3).

The boundary conditions are:

$$\xi = 0 \quad , \quad T = T_b = T_c \quad , \quad \xi = 1 \quad , \quad T = T_H \qquad [6\text{-}30]$$

the boil-off rate is given by:

$$\frac{m_{Nu}}{m_o}\left(T_H - T_C\right) = \left(\frac{k}{\bar{k}} \frac{dT}{d\xi}\right)_{\xi=0} \qquad [6\text{-}31]$$

Note: non-si units are used in this figure

Before integrating the above system, let us examine the dependence on temperature of the parameters involved.

1. In the case of laminar flow through a circular duct with fully developed velocity and temperature profiles, the Nusselt number, *Nu*, becomes (Figure 6-1, ECSS-E-HB-31-01 Part 13 Clause 6.3.1.1):

   Nu = 4,364 for constant heat flux along the duct [6-32]

   Nu = 3,66 for constant wall temperature along the duct [6-33]

   The first value applies to the normal attachment case, and the second to the tangential attachment.

   For turbulent flow (Dittus-Boelter formula (see ECSS-E-HB-31-01 Part 13 Clause 9.2)):

   $$Nu = 0{,}023\left(Re^2 Pr\right)^{0,4} \qquad [6\text{-}34]$$

   where the fluid properties are evaluated at the arithmetic mean temperature difference (see ECSS-E-HB-31-01 Part 13 Clause 6.2). Eq. [6-34] is valid under the following conditions:

   1) Re > 10^4. For not too high values of the Prandtl number this bound can be lowered down to $4x10^3$ (ESDU 68006 (1968) [65]).

   2) 0,7< *Pr* < 100. 3) *t/d* 60.

It is deduced that Nu depends on temperature at most through the exit temperature difference, and thence can be considered as a constant parameter when interesting the above system of equations.

2. The temperature dependence of the fluid physical properties are, for most vapors, roughly as follows: $k_b \sim \mu_b \sim T^{0,7}$, whereas c_p is practically temperature independent. From this fact it is deduced that S and m_0 are temperature independent. m is also temperature independent because the requirement of mass preservation.

3. 3) The insulation thermal conductivity is assumed to be a linear function of temperature, $k = k_1 T$.

   Introducing the dimensionless temperature, $\tau = T/T_H$, and the new dimensionless independent variable $\zeta = (\bar{k} / k(T_H))(m_{Nu} / m_0)\,\xi$, the above system, after integrating once Eq. [6-28], becomes:

$$\tau \frac{d\tau}{d\zeta} = 1 - \tau_C + S(\tau_b - \tau_C) \qquad [6\text{-}35]$$

$$\frac{d\tau_b}{d\zeta} = \left(\frac{m_o}{m_{Nu}}\right)^2 \frac{1}{S} r \tau_b^{0,7} (\tau - \tau_b) \qquad [6\text{-}36]$$

where r is the dimensionless heat transfer coefficient, which is defined as:

$$r = \frac{\pi t^2}{A} \frac{k(T_H) k_b(T_H)}{\bar{k}^2} Nu \qquad [6\text{-}37]$$

The boundary conditions are:

$$\begin{aligned} &\zeta = 0 \quad , \quad \tau = \tau_b = \tau_C \\ &\zeta = \frac{1+\tau_C}{2} \frac{m_{Nu}}{m_o} \quad , \quad \tau = 1 \end{aligned} \qquad [6\text{-}38]$$

Eqs. [6-35] and [6-36] with boundary conditions [6-38] define an eigenvalue problem. The third boundary condition can be only met when m_{Nu}/m takes a definite value which depends on S, r and τ_C.

6.2.3.3.2 Some numerical results

The above mentioned problem has been solved numerically by a "shooting" method (Nachtsheim & Swigert (1965) [159]).

Numerical values of the corrective factor $\omega_{Nu} = m_{Nu}/m$ have been plotted versus r, for different cryogens in Figure 6-12 to Figure 6-14. The sole parameter which distinguishes these Figures from each other is the warm temperature, T_H. It can be deduced from this Figures that, unless r is sufficiently large, ω_{Nu} is somewhat larger than unity, which indicates that substantial additional boil-off is caused by inadequate convective heat transfer in the venting duct.

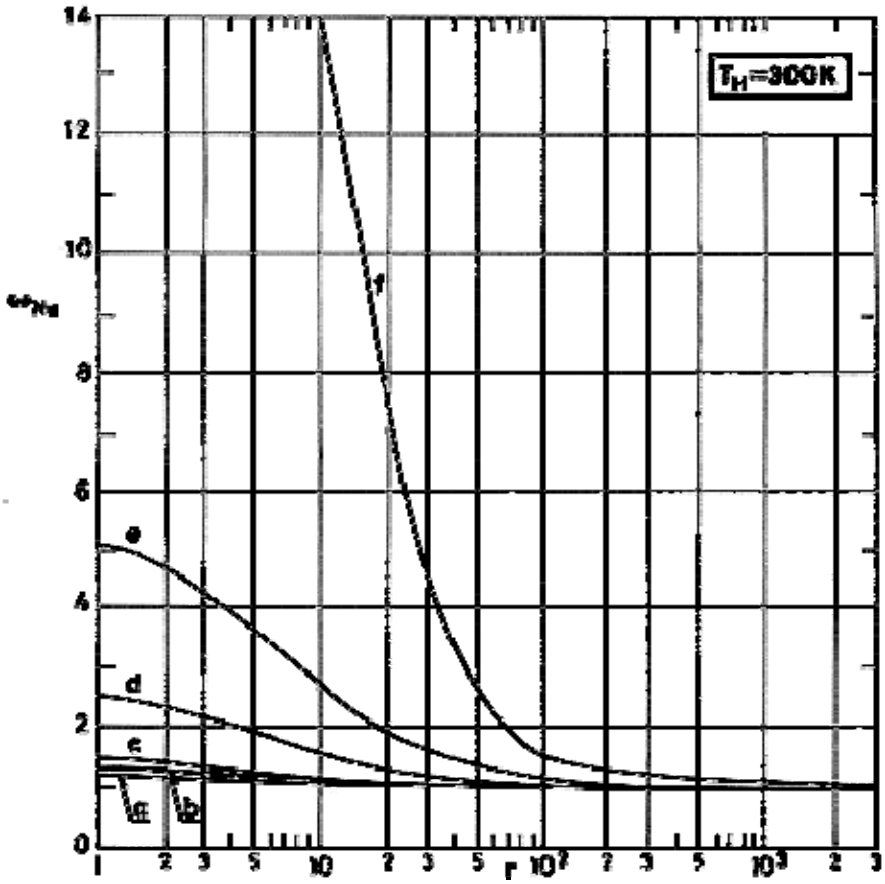

Figure 6-12: Factor ω_{Nu}, accounting for finite convective heat transfer in the venting duct, vs. coefficient r, for several cryogens. T_H = 300 K. Calculated by the compiler.

EXPLANATION

Key	Cryogen (liquid)	S	ω_{Nu} for r = 0
a	Argon	0,684	1,38
b	Oxygen	0,896	1,49
c	Nitrogen	1,162	1,64
d	Neon	3,154	2,77
e	Hydrogen	8,659	5,59
f	Helium	64,148	33,3

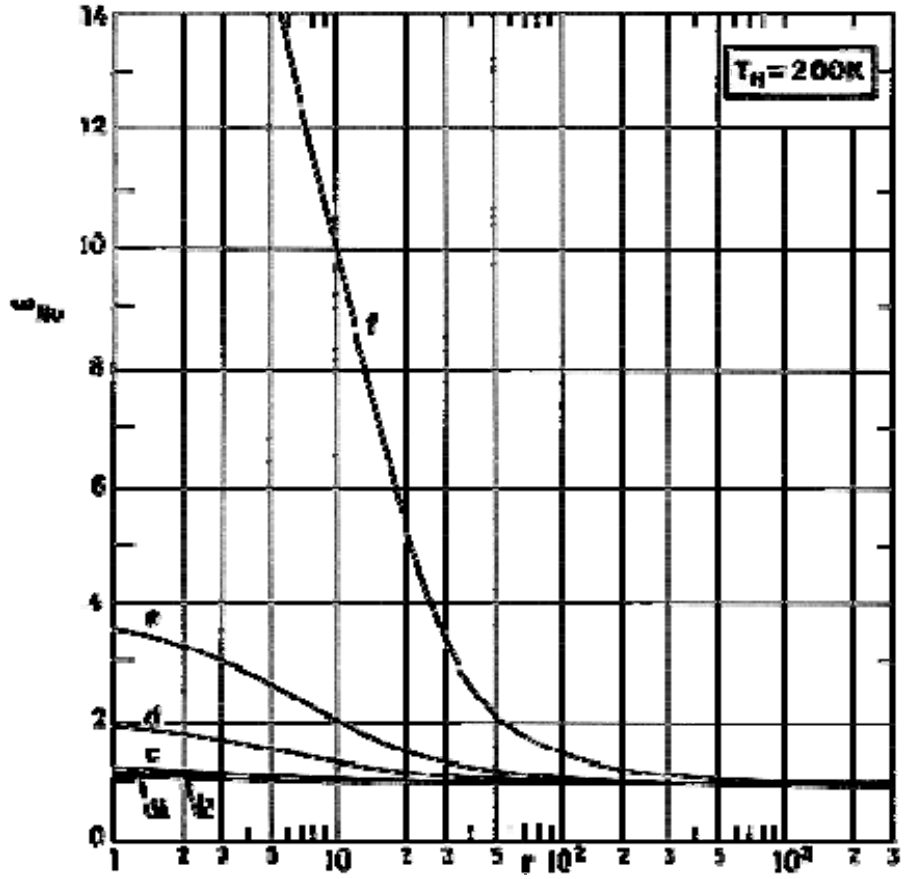

Figure 6-13: Factor ω_{Nu}, accounting for finite convective heat transfer in the venting duct, vs. coefficient *r*, for several cryogens. T_H = 200 K. Calculated by the compiler.

EXPLANATION

Key	Cryogen (liquid)	*S*	ω_{Nu} for *r* = 0
a	Argon	0,362	1,20
b	Oxygen	0,469	1,25
c	Nitrogen	0,640	1,34
d	Neon	1,998	2,11
e	Hydrogen	5,562	3,92
f	Helium	42,462	22,7

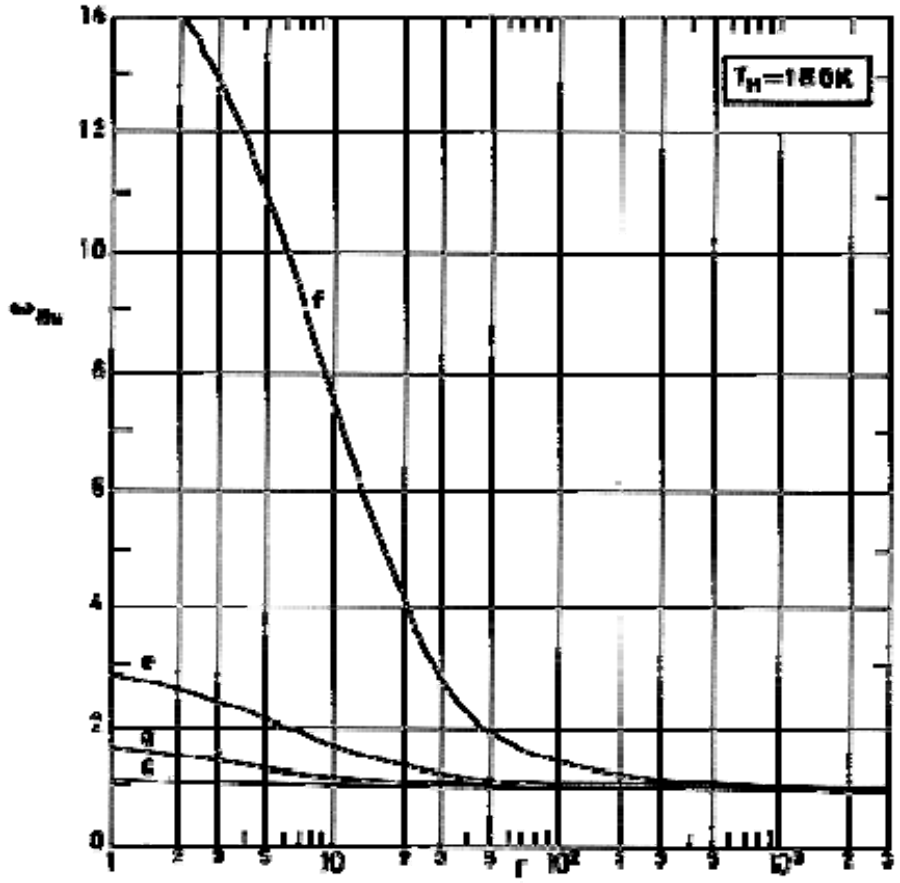

Figure 6-14: Factor ω_{Nu}, accounting for finite convective heat transfer in the venting duct, vs. coefficient *r*, for several cryogens. T_H = 150 K. Calculated by the compiler.

EXPLANATION

Key	Cryogen (liquid)	*S*	ω_{Nu} for *r* = 0
c	Nitrogen	0,379	1,20
d	Neon	1,420	1,79
e	Hydrogen	4,014	3,11
f	Helium	31,618	16,9

To look more closely at the influence of *r* on the temperature of the vapors emerging from the venting duct, Figure 6-15 gives $T_b = \tau_b T_H$ against $T_b = \tau T_H$, for several values of the dimensionless heat transfer coefficient, *r*. The fluid is vapor helium and the warm face temperature, T_H = 300 K. It can be seen that the vapor exit temperature -value of T_b corresponding to T = 300K- decreases sharply when *r* is decreased.

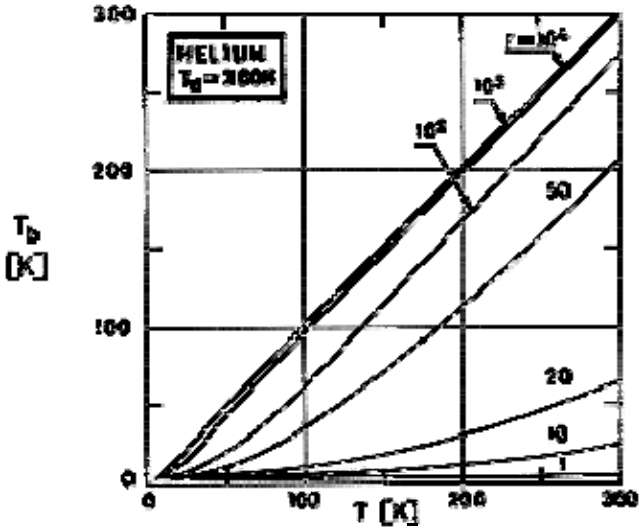

Figure 6-15: Helium vapor bulk temperature, T_b, vs. insulation temperature, T, for different values of the dimensionless heat transfer coefficient, r. T_H = 300 K. Calculated by the compiler.

Figure 6-16 gives the distribution of temperature across the insulation in the same cases as in the previous Figure. The intricate nature of the influence of r on $T(\xi)$, which has been noted by Tsao (1974) [242], can be explained as follows: When r is small, the helium flowing through the duct has a low and practically constant temperature, as shown in Figure 6-15. Hence the thermal conductivity, k_b, of helium is relatively low. This small value of k_b prevents sufficient heat from being transferred from the insulation to the gas and keeps the insulation hot and, thus, its thermal conductivity large. The high k and the low k_b condition induces a large heat flux across the insulation and a small heat flux across the duct wall. This effect starts at the cold end and extends to the warm end. As r increases the insulation temperature decreases first and then increases again. For large values of r the vapor temperature and the insulation temperature are almost equal and increase uniformly across the insulation.

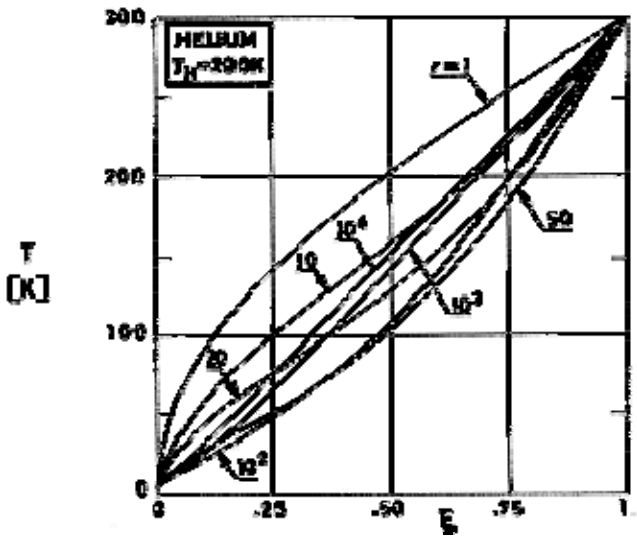

Note: non-si units are used in this figure

Figure 6-16: Temperature, *T*, across the insulation for different values of the dimensionless heat transfer coefficient *r*. Helium vapor cooling. T_H = 300 K. Calculated by the compiler.

6.2.3.3.3 Reduction of the adverse effects

To achieve larger values of *r* the designer has the following choices:

1. Increasing *Nu* by convective heat transfer enhancement in the duct. Augmentative convection heat transfer devices are extensively discussed in ECSS-E-HB-31-01 Part 13 Clause 5. The application of these techniques here does not look very promising.
2. Increasing the local value of the insulation thickness, *t*, as sketched in Figure 6-17. This local increase can be very effective, since *t* appears squared in Eq. [6-40]. It is also convenient from the manufacturing point of view.

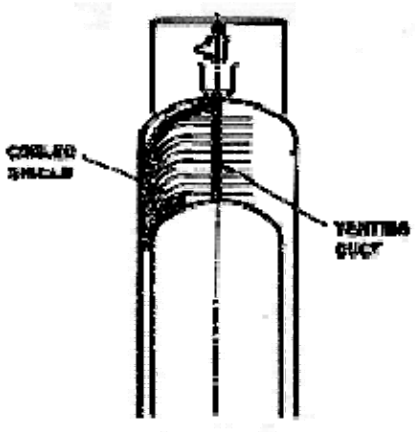

Figure 6-17: Sketch of a VCS insulation in the nearness of the venting duct. Normal attachment. After Paivanas et al. (1965) [177].

3. Joining the venting duct, in the shape of a spiral, to the inner surface of a tube, filled with insulating powder to which the conductive shields are attached. To minimize heat

conduction along the enclosing tube the thread of the spiralling venting duct should be much larger than its diameter.

4. Attaching the venting duct tangentially to the shield. This solution allows a drastic increase in the duct length.

In the tangential attachment system the venting duct is joined to several metallic shields. After spiralling around one shield, the duct is attached, for another spiral, to the next shield, and so on.

To estimate the length of venting duct which is attached to each metallic shield, one assumes that the thermal joint conductance between the shield and the duct is very large, and that the longitudinal heat conduction along the duct is negligible. Thence, the wall temperature of a portion of the duct will be that of the shield to which this portion is attached.

The length of the part of the duct attached to a shield should afford the fluid bulk temperature to increase from some initial value, T_i (the temperature of the nearest inner shield) to a value close to the duct wall temperature, T_w.

The required duct length, for the laminar flow case, can be found in Jacob (1958) [101], Vol. 1, p. 461. Fig. 25-6.

The turbulent case is considered in Kays (1966) [117]. The temperature field is extressed as an infinite series expansion in Eigen functions. The five leading terms in the series are tabulated in Table 12-7 of the mentioned source. The Reynolds numbers (and, thence, the mass flow rates) required for fully developed turbulent flow rates, however, much too large for the present application.

6.2.3.4 Finite thermal conductivity of the cooled shields

The assumption of infinitely large thermal conductivity of the conductive shields is justified when thick shields of highly conductive metals are used. The thickness of the shields. And thus their thermal conductivity is, however, weight limited so that the assumption could be no longer valid in many instances.

The above mentioned assumption will be evaluated in terms of a small parameter, ε, defined as:

$\varepsilon = (k_x/k_y)(R^2/t^2)$.

k_x and k_y, which are assumed to be constant, are the thermal conductivities across and along the insulation, respectively, whereas t and R are the characteristic lengths.

To keep the analysis simple enough we will consider the axisymmetrical configuration which is sketched in Figure 6-18 (b).

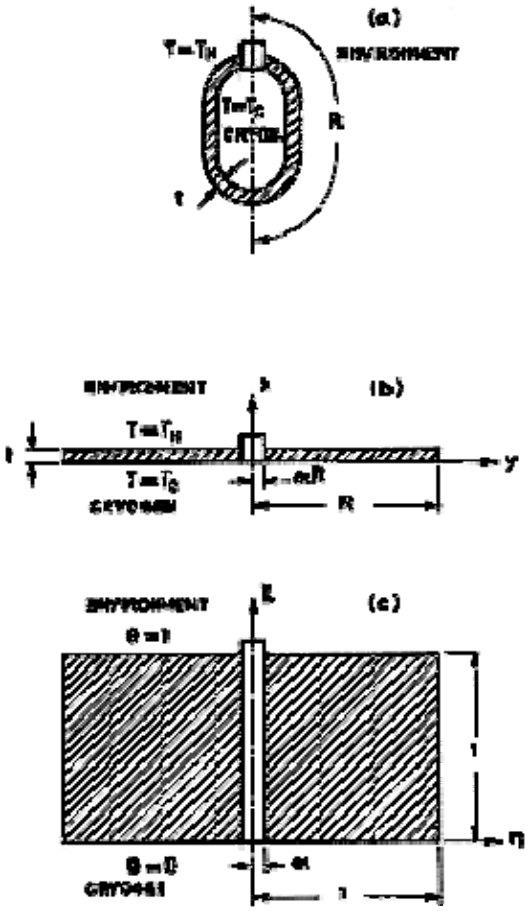

Figure 6-18: Sketch of the insulation and of the simplified configurations used to analyze the influence of the finite thermal conductivity of the shields. (a) Insulation. (b) Simplified configuration in the physical coordinates *x*, *y*. (c) Simplified configuration in the stretched coordinates, *ξ*, *η*.

6.2.3.4.1 Analytical background

The problem is mathematically defined, in terms of the dimensionless function, θ, and the dimensionless variables, $\xi = x/t$; $\eta = y/R$, as follows:

Differential equation:

$$\varepsilon \frac{\partial^2 \theta}{\partial \xi^2} + \frac{1}{\eta} \frac{\partial}{\partial \eta} \left(\eta \frac{\partial \theta}{\partial \eta} \right) = 0 \qquad [6\text{-}39]$$

Boundary conditions:

$$\xi = 0 \quad , \quad \theta(0, \eta) = 0 \qquad [6\text{-}40]$$

$$\xi = 1 \quad , \quad \theta(1, \eta) = 1 \qquad [6\text{-}41]$$

$$\eta = \alpha \quad , \quad \alpha \frac{\partial \theta(\xi,\eta)}{\partial \eta_{\eta=\alpha}} = \varepsilon \frac{1-\alpha^2}{2} S \frac{m_y}{m_o} \frac{\partial \theta(\xi,\alpha)}{\partial \xi} \qquad [6\text{-}42]$$

$$\eta = 1 \quad , \quad \frac{\partial \theta(\xi,\eta)}{\partial \eta_{\eta=1}} = 0 \qquad [6\text{-}43]$$

where m_y, m_0 and S are defined as before. In particular, m_0 is given by:

$$m_o = \frac{k_x \pi R^2 \left(1-\alpha^2\right)\left(T_H - T_C\right)}{h_{fg} t} \qquad [6\text{-}44]$$

The expression relating the heat addition to the cryogen boil-off rate becomes:

$$\frac{m_y}{m_o} = \frac{2}{1-\alpha^2} \int_{\alpha}^{1} \frac{\partial \theta}{\partial \xi_{\xi=0}} \eta d\eta \qquad [6\text{-}45]$$

The right hand side in Eq. [6-45] is the dimensionless heat transfer rate across the cold face of the insulation ($\xi = 0$).

6.2.3.4.2 Orders of magnitude of α and ε

The Dewar sketched in Figure 6-19 is similar to that flown on the Nimbus F weather satellite containing solid methane. This Dewar has been quoted repeatedly and is described with detail in Clause 6.4.3.1.

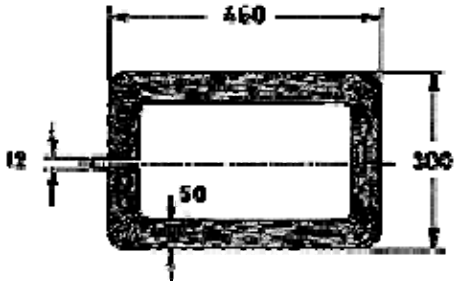

Figure 6-19: Sketch of a typical spaceborne Dewar. All the dimensions are in mm.

The MLI is doubled-aluminized Mylar-Tissuglas t = 0,025 m thick. According to Nast, Barnes & Wedel (1976) [161] there are two blankets with a single cooled shield sandwiched between them. The fact that in the Nimbus F Dewar this cooled shield is grounded to a second tank containing solid ammonia and does not completely surround the methane tank will be disregarded here.

The effective thermal conductivity of the MLI, deduced from Bell, Nast & Wedel (1977) [21], Fig. 2, is:

k_x = 3,3 x 10^{-5} W.m^{-1}.K^{-1} ; T_H =296 K and T_C = 50 K.

Neither of the above mentioned references gives the characteristics of the cooled shield, thence we will assume that this shield is copper, $3{,}8 \times 10^{-5}$ m thick. For copper at 150 K, which is the ammonia tank temperature, k = 400 $W.m^{-1}.K^{-1}$ (see Figure 8-55 in this Part). Assuming that the lateral thermal conductance is exclusively due to the copper shield,

$k_y = (0{,}4 \times 10^{3})(3{,}8 \times 10^{-5})/(5 \times 10^{-2}) = 0{,}3\ W.m^{-1}.K^{-1}$.

On the other hand, R, measured as indicated in Figure 6-18(a), takes a value R = 0,76 m. Thus,

$\varepsilon = (k_x/k_y)(R/t)^2 = 2{,}5 \times 10^{-2}$.

This value of ε justifies a small perturbation approach to the problem of lateral heat transfer, ε being the small parameter.

Notice that α is also small; according to Figure 6-19 a typical value is α = 0,08, and this simplifies the numerical computations on which the results presented in Clause 6.2.3.4.4 are based.

6.2.3.4.3 Singular perturbation approach

Since the parameter ε is small, we seek straightforward expansion of the solution in the form:

$$\theta(\xi,\eta) = \sum_{i=0}^{\infty} \varepsilon^i \theta_i(\xi,\eta) \qquad [6\text{-}46]$$

Substituting the expansion [6-46] into Eq. [6-39] with boundary conditions [6-40], and equating coefficients of equal powers of ε leads to the following set of differential equations and boundary conditions (i = 0, 1, 2,...):

$$\frac{\partial}{\partial\eta}\left(\eta\frac{\partial\theta_o}{\partial\eta}\right) = 0$$
$$\frac{\partial^2\theta_{i-1}}{\partial\xi^2} + \frac{1}{\eta}\frac{\partial}{\partial\eta}\left(\eta\frac{\partial\theta_i}{\partial\eta}\right) = 0 \quad for\ i \geq 1 \qquad [6\text{-}47]$$

$$\xi = 0 \quad , \quad \theta_i(0,\eta) = 0 \qquad [6\text{-}48]$$

$$\xi = 1 \quad , \quad \theta_o(1,\eta) = 1 \quad , \quad \theta_i(1,\eta) = 0 \quad for\ i \geq 1 \qquad [6\text{-}49]$$

$$\eta = \alpha \quad , \quad \alpha\frac{\partial\theta_i(\xi,\eta)}{\partial\eta_{\eta=\alpha}} = \frac{1-\alpha^2}{2} S \frac{m_y}{m_o}\frac{\partial\theta_{i-1}(\xi,\alpha)}{\partial\xi} \qquad [6\text{-}50]$$

$$\eta = 1 \quad , \quad \frac{\partial\theta_i(\xi,\eta)}{\partial\eta_{\eta=1}} = 0 \qquad [6\text{-}51]$$

The differential equations [6-47] with boundary conditions [6-51] suggest seeking for solutions of the form:

$$\theta_o(\xi,\eta) = A_o(\xi) \qquad [6\text{-}52]$$

$$\theta_1(\xi,\eta) = A_1(\xi) + \frac{1}{2}\frac{d^2 A_o}{d\xi^2} f_1(\eta) \qquad [6\text{-}53]$$

$$\theta_2(\xi,\eta) = A_2(\xi) + \frac{1}{2}\frac{d^2 A_1}{d\xi^2} f_1(\eta) + \frac{1}{4}\frac{d^4 A_o}{d\xi^4} f_2(\eta) \qquad [6\text{-}54]$$

where $f_i(\eta)$ is the solution of the ordinary differential equation

$$\frac{d}{d\eta}\left(\eta\frac{df_1}{d\eta}\right) = -2\eta \quad , \quad \frac{d}{d\eta}\left(\eta\frac{df_{i+1}}{d\eta}\right) = -2\eta f_i \quad for\ i \geq 1 \qquad [6\text{-}55]$$

with the boundary conditions

$$\eta = \alpha \quad , \quad f_i(\alpha) = 0 \qquad [6\text{-}56]$$

$$\eta = 1 \quad , \quad \frac{df_i}{d\eta_{\eta=1}} = 0 \qquad [6\text{-}57]$$

In order to calculate $A_i(\xi)$ we enforce the fulfillment of the boundary conditions [6-50]. this yields the following set of ordinary differential equations (notice that $\alpha(df_i/d\alpha) = 1-\alpha^2$):

$$\frac{d^2 A_o}{d\xi^2} - S\frac{m_y}{m_o}\frac{dA_o}{d\xi} = 0 \qquad [6\text{-}58]$$

$$\frac{d^2 A_1}{d\xi^2} - S\frac{m_y}{m_o}\frac{dA_1}{d\xi} = \frac{1}{2}\left(S\frac{m_y}{m_o}\right)^3 F_1(\alpha)\frac{dA_o}{d\xi} \qquad [6\text{-}59]$$

where

$$F_1(\alpha) = -\frac{\alpha\dfrac{df_2}{d\alpha}}{1-\alpha^2} \qquad [6\text{-}60]$$

The general solutions of the differential equation [6-58] are

$$A_o(\xi) = M_o + N_o e^{S\frac{m_y}{m_o}\xi} \qquad [6\text{-}61]$$

$$A_1(\xi) = M_1 + N_1 e^{S\frac{m_y}{m_o}\xi} + \frac{1}{2}\left(S\frac{m_y}{m_o}\right)^3 F_1(\alpha)\xi\left[A_o(\varepsilon) - M_o\right] \qquad [6\text{-}62]$$

where M_i and N_i are yet unknown integration constants. In order to calculate these integration constants, we take into account the boundary conditions [6-48] and [6-49]. The zero order solution results to be that corresponding to an infinitely large thermal conductivity along the shields. The boundary conditions [6-48] and [6-49] cannot be satisfied for any η when $i \geq 1$ because of the η functions which appear in the right hand side of Eqs. [6-53], [6-54],... . Thence, we will enforce the fulfillment of these boundary conditions for $\eta = \alpha$ exclusively. This gives:

$$N_o = \frac{1}{e^{S\frac{m_y}{m_o}} - 1} \qquad [6\text{-}63]$$

$$N_1 = -\frac{1}{2}\left(S\frac{m_y}{m_o}\right)^3 F_1(\alpha) N_o(1 + N_o) \qquad [6\text{-}64]$$

and similar expressions for M_i that we do not reproduce here since the overall heat flux through $\xi = 0$ is of concern whereas the temperature distribution is not.

The mathematical problem defined by means of Eqs. [6-47] and [6-48] presents two noteworthy characteristics:

1. One must proceed to first order to find the zero order solution, to second order to find the first order, and so on. This greatly complicates the algebra involved. The backward influence of the successive differential equations [6-47] is typical of elliptical problems as the one under consideration.

2. The functions $\theta_i(\xi,\eta)$, $i \geq 1$, which are usually called "outer" functions (Nayfeh (1973) [162]), do not fulfil the boundary conditions at both end faces ($\xi = 0$; $\xi = 1$) except for $\eta = \alpha$. Therefore the resulting outer solution for θ, although it approximates (up to the order considered) the exact solution as $\varepsilon \to 0$ away from both end faces, breaks down in regions of non uniformity close to these faces. These regions are called boundary layers or "inner" regions. Within them exact solution changes sharply with ξ in order to retrieve the boundary conditions.

To determine an inner expansion valid in the boundary layer close to $\xi = 0$, the layer is stretched by a factor $\varepsilon^{-\lambda}$. The exponent λ is determined so that both terms in Eq. [6-39] become of the same order when both $\varepsilon^{-\lambda}\xi$ and η are of order unity. It is seen that this is achieved when $\lambda = 1/2$. The same stretching is applicable to the boundary layer close to $\xi = 1$. The thickness of the either layer being of order $\varepsilon^{1/2}$.

In order to solve the inner problem near the cold end face, $\xi = 0$, we introduce the inner variable $\Xi = \xi\varepsilon^{-1/2}$ (which is of order unity throughout the inner layer) and we try a composite expansion of the form:

$$\theta(\Xi,\eta) = \underbrace{Outer\ solution + \sum_{j=0}^{\infty} \varepsilon^{\frac{j+1}{2}} \Theta j(\Xi,\eta)}_{inner\ solution} \qquad [6\text{-}65]$$

Note: non-si units are used in this figure

The "Inner Solution" will ensure the fulfillment of the boundary conditions at $\Xi = 0$ and will, in addition, fade out for distances from the cold end face of order $\varepsilon^{1/2}$. The reason for the existence of terms $\varepsilon^{1/2}$, $\varepsilon^{3/2}$, ..., can be made apparent when the boundary condition [6-42] is expressed in terms of the inner variables Ξ , η. Finally, no zero order terms appear in the solution, since the boundary condition at $\Xi = 0$ is satisfied, to zero order, by the outer solution.

The inner functions $\Theta j(\Xi , \eta)$ will be defined by the following sequence of differential equations and boundary conditions ($j = 0, 1, 2,...$):

$$\frac{\partial^2 \Theta_j}{\partial \Xi^2} + \frac{1}{\eta}\frac{\partial}{\partial \eta}\left(\eta \frac{\partial \Theta_j}{\partial \eta}\right) = 0 \qquad [6\text{-}66]$$

$$\begin{aligned} &\Xi = 0 \quad , \quad \Theta_j(0,\eta) = -\Theta_i(0,\eta) \quad for\ j = 2i-1 \\ &\Theta_j(0,\eta) = 0 \quad for\ j = 2i-2 \quad , \quad i \geq 1 \end{aligned} \qquad [6\text{-}67]$$

$$\Xi \to \infty \quad , \quad \Theta_i(\infty,\eta) = 0 \qquad [6\text{-}68]$$

$$\eta = \alpha \quad , \quad \alpha \frac{\partial \Theta_j(\Xi,\eta)}{\partial \eta_{\eta=\alpha}} = \frac{1-\alpha^2}{2} S \frac{m_y}{m_o} \frac{\partial \Theta_{j-1}(\Xi,\eta)}{\partial \Xi} \qquad [6\text{-}69]$$

$$\eta = 1 \quad , \quad \frac{\partial \Theta_j(\Xi,\eta)}{\partial \eta_{\eta=1}} = 0 \qquad [6\text{-}70]$$

$\Theta 0(\Xi,)$, which satisfies homogeneous boundary conditions, vanish identically. The problem for $\Theta 1(\Xi,)$ then becomes:

$$\frac{\partial^2 \Theta_1}{\partial \Xi^2} + \frac{1}{\eta}\frac{\partial}{\partial \eta}\left(\eta \frac{\partial \Theta_1}{\partial \eta}\right) = 0 \qquad [6\text{-}71]$$

Note: non-si units are used in this figure

$$\Xi = 0 \quad , \quad \Theta_1(0,\eta) = -\Theta_1(0,\eta) \qquad [6\text{-}72]$$

$$\Xi \to \infty \quad , \quad \Theta_1(\infty,\eta) = 0 \qquad [6\text{-}73]$$

$$\eta = \alpha \quad , \quad \frac{\partial \Theta_1(\Xi,\eta)}{\partial \eta_{\eta=\alpha}} = 0 \qquad [6\text{-}74]$$

$$\eta = 1 \quad , \quad \frac{\partial \Theta_1(\Xi,\eta)}{\partial \eta_{\eta=1}} = 0 \qquad [6\text{-}75]$$

Notice that $\Theta_1(\Xi,)$ does not contribute to the overall heat flux through $\Xi = 0$, it merely readjusts the temperature field. This is so since, according to the boundary conditions [6-73] to [6-75], no heat is transferred through three of the boundaries, thence the overall heat flow through the fourth boundary will be zero. Nevertheless, Θ_1 is calculated in order to proceed to higher order terms.

Solutions to problems of heat flow in semi-infinite hollow circular cylinders, which are very similar to that defined by means of Eq. [6-71] with boundary conditions [6-72], are widely known (see f.e., Carslaw (1921) [38] pp. 127-129 or Budak et al. (1964) [33] pp. 468-469). Following the usual practice, we reach the expression of $\Theta_1(\Xi, \eta)$:

$$\Theta_1(\Xi,\eta) = -2\sum_{n=1}^{\infty} e^{-\mu_n \Xi} \frac{\int_{\alpha}^{1} \eta \theta_1(0,\eta) C_o(\mu_n \eta) d\eta}{C_o^2(\mu_n) - \alpha^2 C_o^2(\mu_n \eta)} C_o(\mu_n \eta) \qquad [6\text{-}76]$$

Note: non-si units are used in this figure

where $C_0(\mu_n \eta) = Y_1(\mu_n \alpha) J_0(\mu_n \eta) - J_1(\mu_n \alpha) Y_0(\mu_n \eta)$, $J_\nu(\mu_n \eta)$ and $Y_\nu(\mu_n \eta)$ are the Bessel functions of first and second kind respectively (Abramowitz & Stegun (1965) [1]), and μ_n are the roots of the equation $Y_1(\mu_n \alpha) J_1(\mu_n) - J_1(\mu_n \alpha) Y_1(\mu_n) = 0$.

The above expression for $\Theta_1(\Xi,\eta)$ becomes, after some algebra:

$$\Theta_1(\Xi,\eta) = \frac{2(1-\alpha^2)}{\pi\alpha} \frac{d^2 A_o}{d\xi^2_{\xi=0}} \sum_{n=1}^{\infty} e^{-\mu_n \Xi} \frac{1}{\mu_n^3 C_o^2(\mu_n) - \frac{4\mu_n}{\pi^2}} C_o(\mu_n \eta) \qquad [6\text{-}77]$$

Note: non-si units are used in this figure

Once $\Theta_1(\Xi,\eta)$ has been calculated, the problem for $\Theta_2(\Xi,\eta)$ becomes:

$$\frac{\partial^2 \Theta_2}{\partial \Xi^2} + \frac{1}{\eta} \frac{\partial}{\partial \eta} \left(\eta \frac{\partial \Theta_2}{\partial \eta} \right) = 0 \qquad [6\text{-}78]$$

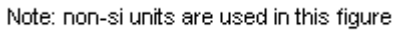

$$\Xi = 0 \quad , \quad \Theta_2(0,\eta) = 0 \qquad [6\text{-}79]$$

$$\Xi \to \infty \quad , \quad \Theta_2(\infty,\eta) = 0 \qquad [6\text{-}80]$$

$$\eta = \alpha \quad , \quad \alpha \frac{\partial \Theta_2(\Xi,\eta)}{\partial \eta_{\eta=\alpha}} = -\frac{2\left(1-\alpha^2\right)^2}{\pi^2\alpha^2} S \frac{m_y}{m_o} \frac{d^2 A_o}{d\xi^2{}_{\xi=0}} \sum_{n=1}^{\infty} \frac{e^{-\mu_n \Xi}}{\mu_n^3 C_o^2(\mu_n) - \frac{4\mu_n}{\pi^2}} \qquad [6\text{-}81]$$

$$\eta = 1 \quad , \quad \frac{\partial \Theta_2(\Xi,\eta)}{\partial \eta_{\eta=1}} = 0 \qquad [6\text{-}82]$$

Notice again that we do not need the full solution of this problem to calculate the heat transfer rate across the cold face of the insulation ($\Xi = 0$), since the overall heat transfer rate through this cold face must balance that through the cylinder $\eta = \alpha$.

$$\int_{\alpha}^{1} \frac{\partial \Theta_2}{\partial \Xi_{\Xi=0}} \eta d\eta = -\alpha \int_{0}^{\infty} \frac{\partial \Theta_2}{\partial \eta_{\eta=\alpha}} d\Xi \qquad [6\text{-}83]$$

where the right hand side will be evaluated by resorting to boundary conditions [6-81].

Using Eqs. [6-61] and [6-63] for calculating $d^2A_0/d\xi^2$ results in:

$$\int_{\alpha}^{1} \frac{\partial \Theta_2}{\partial \Xi_{\Xi=0}} \eta d\eta = \frac{2\left(1-\alpha^2\right)^2}{\pi^2\alpha^2} \frac{\left(S\frac{m_y}{m_o}\right)^3}{e^{S\frac{m_y}{m_o}} - 1} \sum_{n=1}^{\infty} \frac{1}{\mu_n^4 C_o^2(\mu_n) - \frac{4\mu_n^2}{\pi^2}} \qquad [6\text{-}84]$$

Bringing θ_0 and θ_1 of the outer solution plus term Θ_2 of the inner solution in the right hand side of Eq. [6-45],

$$\frac{m_y}{m_o}=\frac{2}{1-\alpha^2}\left[\begin{array}{l}\underbrace{\int_\alpha^1 \frac{\partial\theta_o}{\partial\xi}_{\xi=0}\eta d\eta+\varepsilon\int_\alpha^1 \frac{\partial\theta_1}{\partial\xi}_{\xi=0}\eta d\eta+}_{\text{Outer Solution}} \\ \underbrace{+\varepsilon^{3/2}\int_\alpha^1 \frac{\partial\theta_2}{\partial\xi}_{\xi=0}\eta d\eta+}_{\substack{\text{Inner Solution}\\ \text{in Outer variables}}}\ \textit{Higher order terms}\end{array}\right] \qquad [6\text{-}85]$$

Curiously enough the correction to the cryogen boil-off rate because of the first inner term, θ_2, is of order ε. This can be seen by recalling that $\xi = \varepsilon^{1/2}\Xi$ and, thence

$$\varepsilon^{3/2}\int_\alpha^1 \frac{\partial\theta_2}{\partial\xi}_{\xi=0}\eta d\eta=\varepsilon\int_\alpha^1 \frac{\partial\Theta_2}{\partial\xi}_{\xi=0}\eta d\eta \qquad [6\text{-}86]$$

Note: non-si units are used in this figure

Coming back to Eq. [6-85], we deduce from Eqs. [6-52], [6-55] and [6-61],

$$\frac{2}{1-\alpha^2}\int_\alpha^1 \frac{\partial\theta_o}{\partial\xi}_{\xi=0}\eta d\eta=S\frac{m_y}{m_o}N_o \qquad [6\text{-}87]$$

$$\frac{2}{1-\alpha^2}\int_\alpha^1 \frac{\partial\theta_1}{\partial\xi}_{\xi=0}\eta d\eta=S\frac{m_y}{m_o}N_1 \qquad [6\text{-}88]$$

where N_0 is given in Eq. [6-63] and N_1 in Eq. [6-64].

Substitution of Eqs. [6-84], [6-86], and [6-87] with [6-63], into Eq. [6-85] yields:

$$\frac{e^{S\frac{m_y}{m_o}}-1}{S}=1+\varepsilon\left[\begin{array}{l}-\frac{F_1(\alpha)}{2}\left(S\frac{m_y}{m_o}\right)^3\frac{e^{S\frac{m_y}{m_o}}}{e^{S\frac{m_y}{m_o}}-1}+\frac{4\left(1-\alpha^2\right)}{\pi^2\alpha^2} \\ \sum_{n=1}^{\infty}\frac{1}{\mu_n^4C_o^2(\mu_n)-\frac{4\mu_n^2}{\pi^2}}\left(S\frac{m_y}{m_o}\right)^2\end{array}\right]+0\left(\varepsilon^{3/2}\right) \qquad [6\text{-}89]$$

We can further assume that in the right hand side of Eq. [6-89] Sm_y/m_0 is equivalent to $ln(1+S)$. This is the zero order approximation and its substitution into first order terms will result in an error of order ε^2. Then, neglecting other terms of order ε^2, we finally arrive to (recall Eq. [6-10]:

$$\omega_y = \frac{m_y}{m} = 1 + \varepsilon \left[\begin{array}{l} -\dfrac{F_1(\alpha)}{2}\ln(1+S) + \dfrac{4(1-\alpha^2)}{\pi^2\alpha^2} \\ \displaystyle\sum_{n=1}^{\infty} \dfrac{1}{\mu_n^4 C_o^2(\mu_n) - \dfrac{4\mu_n^2}{\pi^2}} \dfrac{S}{1+S}\ln(1+S) \end{array} \right] + 0\left(\varepsilon^{3/2}\right) \qquad [6\text{-}90]$$

6.2.3.4.4 Some numerical results

Eq. [6-90] has been used for calculating the corrective factor ω_y as a function of the small parameter ε, for representative values of the sensibility S and the dimensionless outer radius, α, of the venting tube to which the shields are supposed to be attached.

The coefficient of the first order term in the expansion of ω_y in power series of ε has been plotted vs. S, for two different values of α, in Figure 6-20.

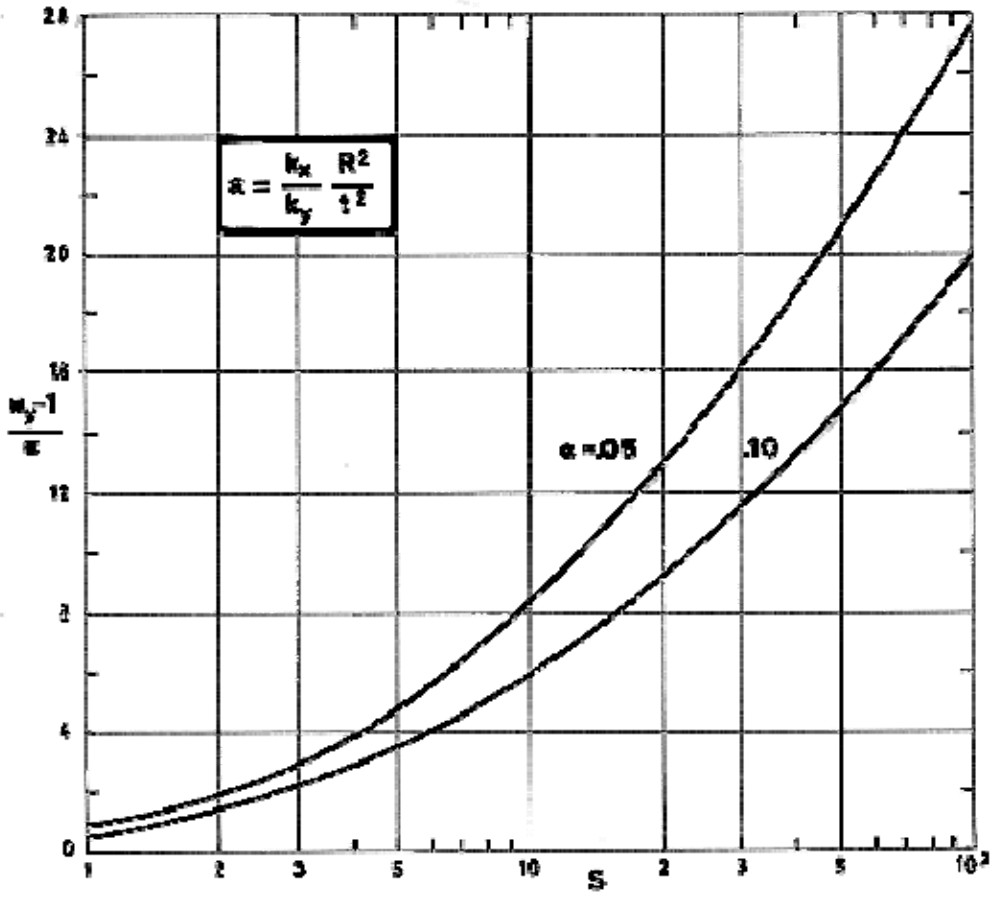

Note: non-si units are used in this figure

Figure 6-20: Coefficient, $(\omega_y - 1)/\varepsilon$, of the first order correction accounting for the influence of the finite thermal conductivity of the VCSs on the cryogen boil-off rate, as a function of the cryogen sensibility, S, for two values of the dimensionless outer radius of the venting duct, α. The results have been obtained by means of a perturbation scheme in the small parameter, ε, which measured the ratio of normal

to lateral heat flux, and are valid provided that terms of order $\varepsilon^{3/2}$ can be neglected. Calculated by the compiler.

The correction is larger than that from Paivanas et al. (1965) [177], Fig. 5, by a factor of the order of 3, but this factor decreases when α increases. The axial symmetry of the configuration sketched in Figure 6-18 allowed us to show forth the influence of the radius αwhich does not appear in the two-dimensional model of the above authors.

6.2.3.4.5 Reduction of the adverse effects

It should be said that the designer has not a fair chance to reduce ε in a system of given size. Notice that it is more effective to reduce the size (R) than to increase the number of conductive shields, or the thickness of each shield (k_y). This seems to indicate that normal attachment of the shields (see Clause 6.1) is best suited to small systems.

When the system size id fixed, two possibilities are open:

1. To increase the insulation thickness, t, keeping constant the number N/t, or radiation shields per unit thickness in order not to increase k_x which, loosely speaking, is inversely proportional to N/t.
2. To attach the venting duct tangentially to the shields. In this case the characteristic length along the insulation, R, is not of the order of the perimeter of the system, it is, on the contrary, of the order of the pitch of the spiral-shaped venting duct.

6.2.3.5 Superposition of adverse effects

The preceding sections dealt with the individual corrections to a simplified model of heat transfer through a VCS insulation. Now a prediction method is required to account for the simultaneous departure of several of the degrading effects from the ideal level.

Lacking of a rigorous theory, the assumption will be introduced that there is no interaction between the several non-ideal phenomena. Thus, the boil-off rate could be obtained simply by multiplying the ideal boil-off rate by the corrective factors ω_i.

Logically the designer would try to keep the adverse effects as reduced as possible. In that case all the corrective factors accounting for these adverse affects would be close to unity. Under these conditions a linear theory -which is equivalent to the assumption of the interaction- would be justified.

There is one case in which the above assumption can be evaluated. Table 6-4 gives the corrective factor, ω_n, which accounts for the influence of the number, n, of shields for temperature independent thermal conductivity, whereas Table 6-8 presents similar data when the thermal conductivity depends linearly on temperature. the ratio, ω_{nk}/ω_n, between both corrective factors should be close to ω_k, which takes into account the influence of temperature dependent thermal conductivity on the boil-off rate.

To check this conjecture, let us consider the values in the following table, which have been deduced from Table 6-4 and Table 6-8. The data correspond to helium with T_H = 300 K.

n	0	1	2	3	4	5	6	8	10
ω_{nk}/ω_n	1,0	0,5128	0,4563	0,4430	0,4402	0,4401	0,4408	0,4431	0,4457

In Table 6-1 two values of m/m_0, are given for helium with T_H = 300 K. The first one correspond to k = $\bar{k}$ and> the second one to k depending on temperature. The ratio of the second value to the first one is ω_k = 0,46.

It is seen that the error incurred in assuming no interactive adverse effects is close to 4% except for situations corresponding to large deviations from the ideal case, as in the case n = 0 of the above table.

6.3 Supports

6.3.1 Introduction

Supports are basic components of cryogenic tankage whose aim is transferring inertial loads, due to the masses of cryogen and inner vessel, to the outer shell.

In the absence of supports, these inertial loads would act directly on the insulation, compressing it and degrading its characteristics, not to mention the problems which could arise as a result of breakage of vent tubes and filling lines.

From the thermal control point of view the supports pose severe problems because:

1. their thermal conductivity is larger than that of the insulation and,
2. the performance of an MLI is highly sensitive to penetrations through the layers.

These penetrations locally degrade the insulation, and its negative effects can extend over significant areas.

Since the heat leaks from the cryogen could be greatly affected by the supports, considerable care and ingenuity should be exercised to design supports being both strong, to withstand the stresses to which the tank is likely to be subjected, and good insulators, to contribute little to heat inleaks.

The configuration chosen to support an insulated vessel depends on the designer ability to tackle the specific problems of a particular design. Its manufacture will involve craftmanship and technology.

Some commonly used supports are:

1. Tension rods of high-strength material,
2. tensile ties,
3. saddle bands of metal or plastic,
4. plastic compression blocks,
5. multiple-contact supports (stacked discs) and
6. compression tubes.

In the case of spaceborne VCS Dewars the most commonly used are:

1. Tubes under tensional-flexural loads, and
2. low thermal conductance tensile ties.

The use of plastic compression blocks has found limited application (see JPL-Caltech VCS Dewar, Clause 6.4.3.2).

Stacked discs use the thermal joint conductance between two solids tore duce heat leaks through them. This idea, which was first suggested by Mikesell & Scott (1956) [151] and extensively developed by Probert (1967) [186], has been considered for supporting spaceborne cryogenic-propellant

containers (Glaser et al. (1967) [75]). Its use for small containers, however, seems to be ruled out because of the bulky framework required to hold the discs in place.

Vapor cooling of the supports has been analyzed by Tsao (1974) [242], and Bejan (1975) [20]. In Tsao's analysis helium vapors cool the entire length of the support, whereas in the system considered by Bejan cooling is concentrated at some points along the support (cooling stations) leaving the in-between stretches free of coolant. The idea of combining support and venting tube has been often suggested (see, for example, Bennet et al. (1974) [23].

A helpful concept in the first choice of the support material is the "Material Figure of Merit" or strength-thermal conductivity ratio. Composite design allows the combination of several materials in the most favorable way.

This Clause concerning supports is arranged in a general-to-specific order. Figures of merit for several materials at cryogenic temperatures are given in Clause 6.3.2. Then, data on low thermal flux tubing are presented in Clause 6.3.3. Finally, several representative supports are described in full detail. Tensile and flexural supports are dealt with in Clause 6.3.4 and compressive supports in Clause 6.3.5.

The information presented here could be complemented with that in Clause 6.5 (Existing Systems). Duplicity in presentation is avoided in any case.

6.3.2 Support materials

Support materials have a high structural strength as well as low thermal conductivity.

Leaving aside the cooled supports, the heat transfer through the support is expressed as (Fourier's law):

$Q_s = -k_s A_s(\Delta T_s/\Delta x)$,

where k_s is a mean value for the support material thermal conductivity in the temperature range T_C to T_H.

The support cross-sectional area depends on the maximum load, P, to be supported. Thus:

$A_s = P/\sigma$,

σ being the design stress at the given temperature.

Combination of the above equations yields,

$Q_s = -(k_s/\sigma)P(\Delta T_s/\Delta x)$.

P and $\Delta T_s/\Delta x$ do not depend on the material properties, thence the chosen material should have a strength-conductivity ratio, σ/k_s, as large as possible in order to minimize the heat leaks through the support.

Table 6-9 gives the ratio σ/k_s for several materials used in tensile supports, at cryogenic temperatures. It should be emphasized that σ/k_s is not the only parameter which defines the merit of a given support material. The material heat capacity and the thermal inertia of the selected design ought to be as low as possible to minimize cryogen boil-off during the cool-down.

Table 6-9: Figure of Merit, σ/k, of Several Tensile Support Materials at Cryogenic Temperatures [a]

Material	Ultimate Tensile Strength, $\sigma_{ult}x10^{-6}$ [Pa]	Yield Stress, $\sigma_{0,2}x10^{-6}$ [Pa]	Thermal Conductivity, k [$W.m^{-1}.K^{-1}$]	Figure of Merit, $(\sigma/k)x10^{-6}$ [$Pa.m.K.W^{-1}$]
METALLIC				
Copper Annealed		82,7	475,0	0,104
Brass	412,0		100,0	1,65
Aluminium 2024		379,0	81,3	2,80
Aluminium 7075		482,0	86,5	3,34
Stainless Steel (annealed)		251,0	10,2	14,8
Titanium		586,0	15,8	22,2
35 Ni - 50 - Fe - 14 Cr Alloy	702,0		12,6	22,2
K Monel		689,0	17,1	24,2
Hastelloy B		448,0	9,35	28,7
Stainless Steel Drawn Wire		1030,0	8,8	70,2
Titanium Alloy (4% Al - 4% Mn)		1000,0	5,87	102,0
INORGANIC				
68% Fiber-glass 32% Resin	378,0		0,36	420,0
Fiber-glass	1720,0		0,92	748,0
ORGANIC				
Nylon High Tenacity	606,0		0,245	247,0
Terylene (high tenacity Polyester)	730,0		0,15	487,0

Material	Ultimate Tensile Strength, σ_{ult}x10^{-6} [Pa]	Yield Stress, $\sigma_{0,2}$x10^{-6} [Pa]	Thermal Conductivity, k [W.m^{-1}.K^{-1}]	Figure of Merit, (σ/k)x10^{-6} [Pa.m.K.W^{-1}]
Araldite 6060	830,0		0,17	488,0
Fortisan 36	1070,0		0,20	535,0

[a] Data in this Table correspond to temperature close to 100 K.

NOTE Design stress is taken as 60% of yield stress or 40% of ultimate tensile strength for metallic and inorganic materials, and 10% of ultimate tensile strength for organic materials.

From : Molnar (1971) [154].

6.3.3 Low thermal conductance tubing

Fiber-glass tubing design have been developed to reduce both the heat leaks through penetrations and supports, and the system mass.

Data on the thermal conductivity of fiber-glass-epoxy structural tubes in the temperature range 4 K-320 K have been reported by Foster, Naes & Barnes (1975) [70]. Some of these data are collected in Clause 8.4.

Composite tubing incorporates a thin metal tubing liner overwrapped with fibrous material using a suitable matrix.

These tubes were first developed for cryogenic transfer systems (Hall et al. (1971) [80]). The metallic liners were intended to provide leak-free service, whereas the fiber-glass composite provided strength and protection from handling damage. Because the overwrap is a good thermal insulator and the liner has a very small wall cross-sectional area, longitudinal thermal conductance is considerably reduced when compared to an all-metal support.

A composite support strut with titanium end fittings and a conventional all-metal support are shown in Figure 6-21. According to Hall & Spond (1977) [81], thermal conductivity tests performed with S-glass and boron-epoxy composites indicate that composite tank supports result in a reduction in heat leak of 60% over the conventional all-metal configuration.

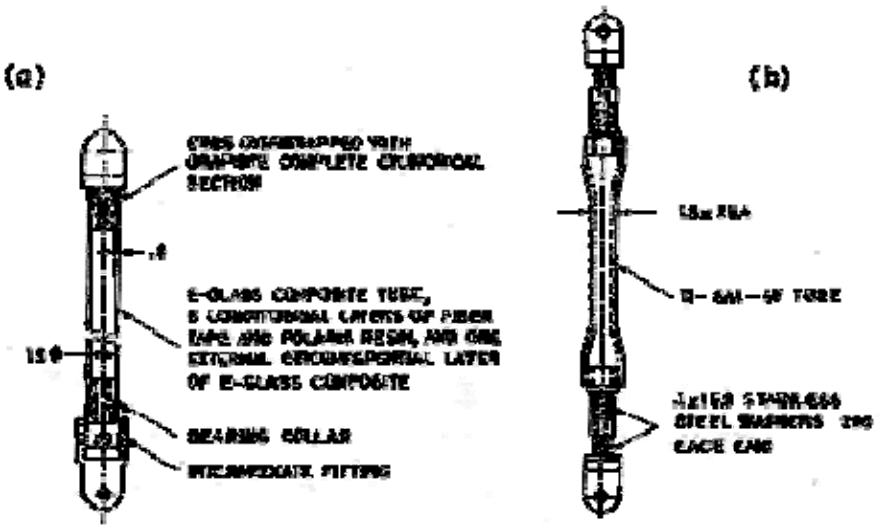

Figure 6-21: Cryogenic supports tubes. a) Composite. b) All-metal. All dimensions are in mm. From Hall & Spond (1977) [81].

A thorough information on the manufacture and testing of these tubes is given by Hall et al. (1971) [80]. A less complete but more accessible reference is that by Hall & Spond (1977) [81]. Unfortunately no tensile and/or flexural tests of complete tube assemblies are reported, probably because of the fact that the main emphasis was placed on the development of cryogenic transfer lines, nevertheless the manufacturing details and heat transfer data may be of interest.

Twelve styles of tubing with diameters $12{,}7 \times 10^{-3}$ m, $50{,}8 \times 10^{-3}$ m and 127×10^{-3} m were fabricated, and tested at temperatures from 20 K to 294 K pressure up to $20{,}7 \times 10^{6}$ Pa.

Metal liners were fabricated by resistance welding, fusion welding or chemically milling a thicker stock material.

End fittings were joined to the liners by fusion or resistance welding. Explosive forming techniques provide capability for joining aluminium end fittings directly to thin stainless steel liners.

Stainless-steel is recommended for liners. 321 CRES (321 Stainless Steel: 0,18 Cr, 0,10 Ni, 0,04 Ti, ≤ 0,08 C, Fe Balance. CRES: Crucible Electric Steel Co., Homestead, Pa.) exhibits excellent welding properties, although, after fusion welding, a relatively large heat affected zone appears in the weld area and, thence, the structural properties are reduced. 347 CRES (347 Stainless Steel: 0,18 Cr, 0,10 Ni, 0,08 Nb, ≤ 0,08 C, Fe Balance. CRES: Crucible Electric Steel Co., Homestead, Pa.) has been selected because of its excellent welding and forming characteristics.

Overwrapping was performed by either machine-wrapped filament winding, overwrap by braiding, or hand tape-wrapping.

The recommended reinforcement is 20 end S/HTS glass roving with an epoxy-compatible finish.

Resin matrix is selected on the basis of good mechanical properties at room temperatures, reasonably good performance at cryogenic temperatures, shelf life in prepreg form (in excess of 2 weeks), and adequate curing temperature. The resin 58-68R fulfils these requirements, it cures at 422 K.

Some results from the thermal tests are summarized in Figure 6-22 to Figure 6-25. An outer thermal guard shroud was placed to minimize the radical heat flux, q_m, during the performance of the tests. On the contrary, no insulation was placed internally and the tubes were evacuated. Data, not given here, indicate that the effect of changes in the internal tube emittance, ε, is negligible. Only data for tubes with diameters $12{,}7 \times 10^{-3}$ m and $50{,}8 \times 10^{-3}$ m have been reproduced here.

Although the tubes are too slender for supporting purposes some of the trends in Figure 6-22 to Figure 6-25 are worth being mentioned. It can be seen, for example, that there is a limit in the reduction of heat flux to be gained by using the fiber-glass overwrap technique, and that the reduction in liner thickness decreases the heat flux ten times more effectively than the reduction in the overwrap thickness.

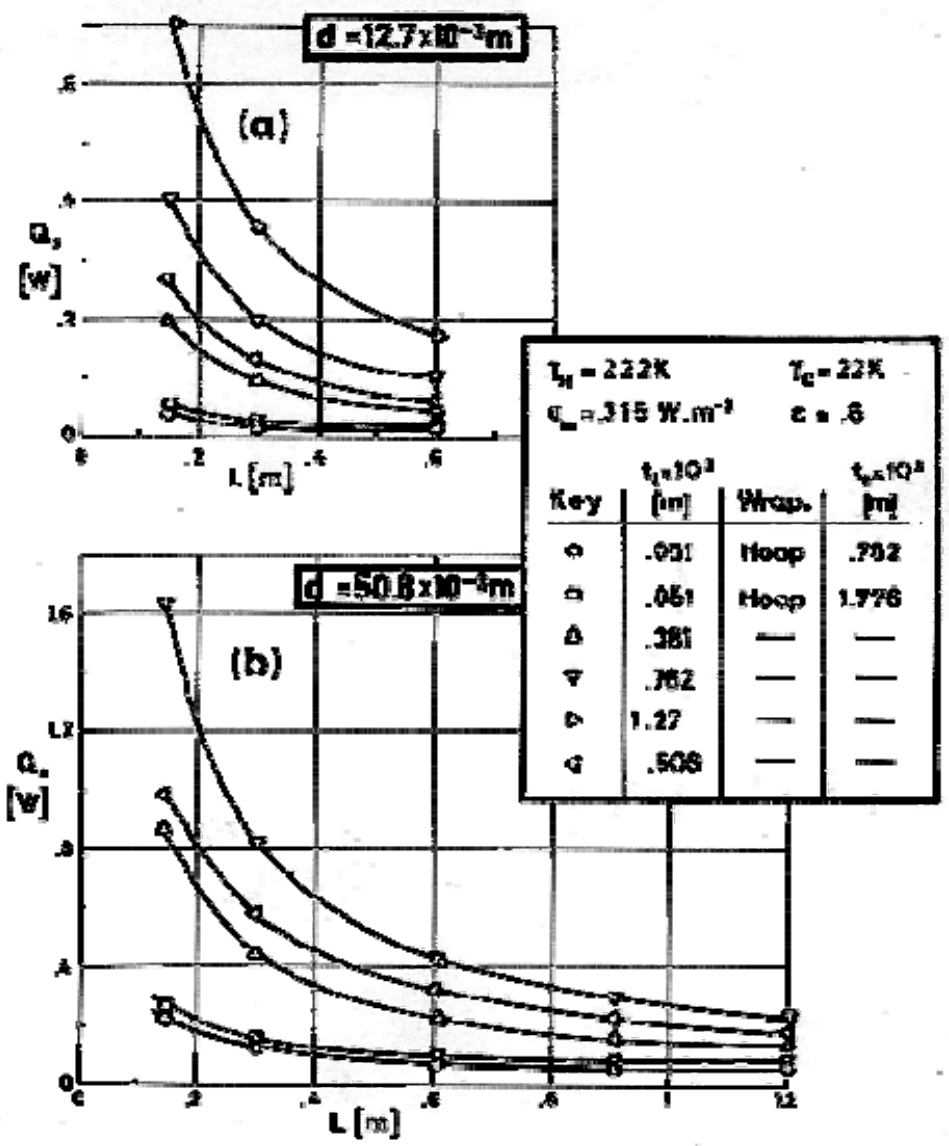

Figure 6-22: Heat transfer rate, Q_s, through fiber-glass overwrapped and through all-stainless-steel supports vs. support length, L, for several values of liner wall thickness, t_l, and overwrap thickness, t_o. (a) Inner diameter of the tube, d = 12,7x10^{-3} m. (b) d = 50,8x10^{-3} m. From Hall et al. (1971) [80].

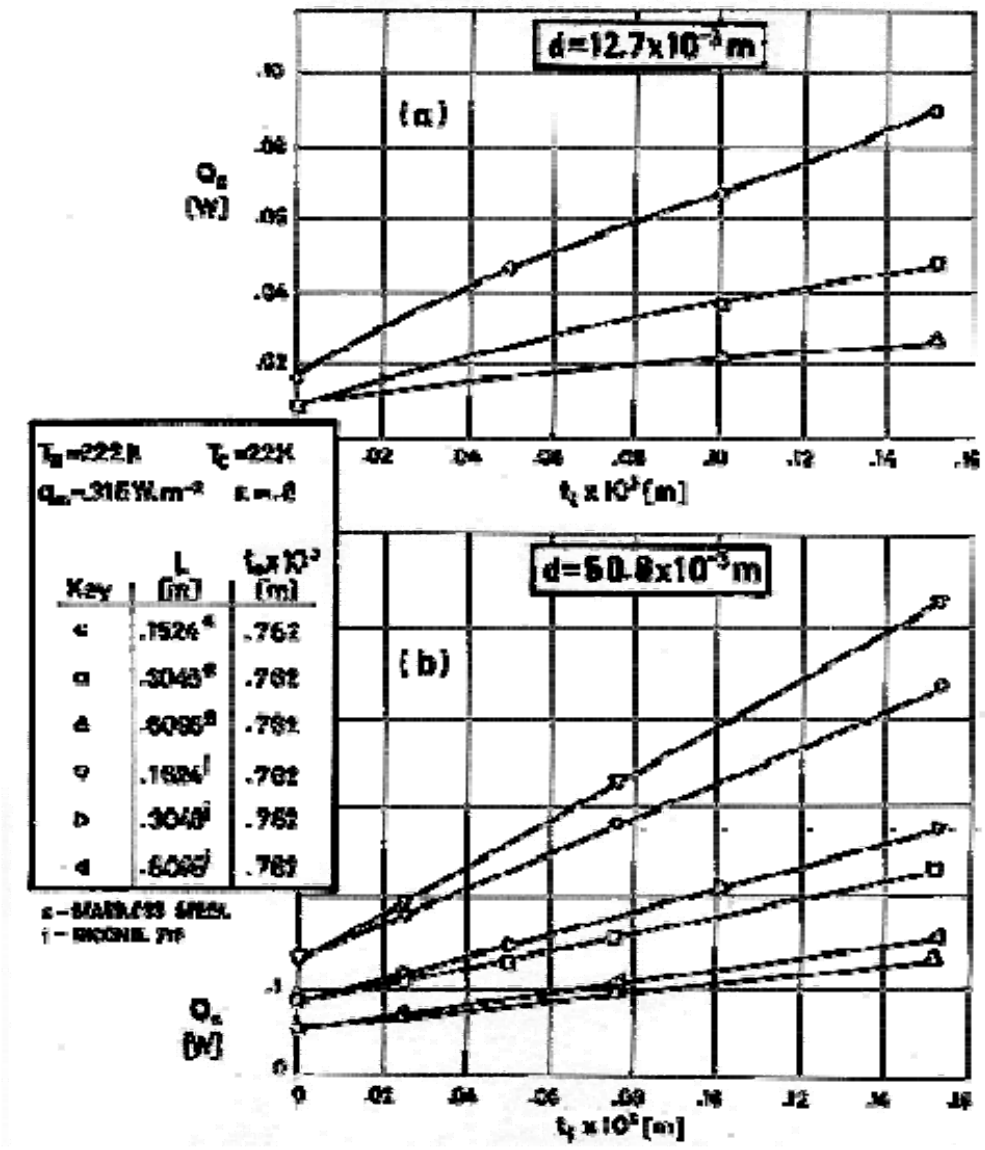

Note: non-si units are used in this figure

Figure 6-23: Heat transfer rate, Q_s, through fiber-glass overwrapped supports vs. liner wall thickness, t_l, for several support lengths, L and overwrap thickness, t_o = 0,762x10^{-3} m. Hoop wrapping. (a) Inner diameter of the tube, d = 12,7x10^{-3} m. (b) d = 50,8x10^{-3} m. From Hall et al. (1971) [80].

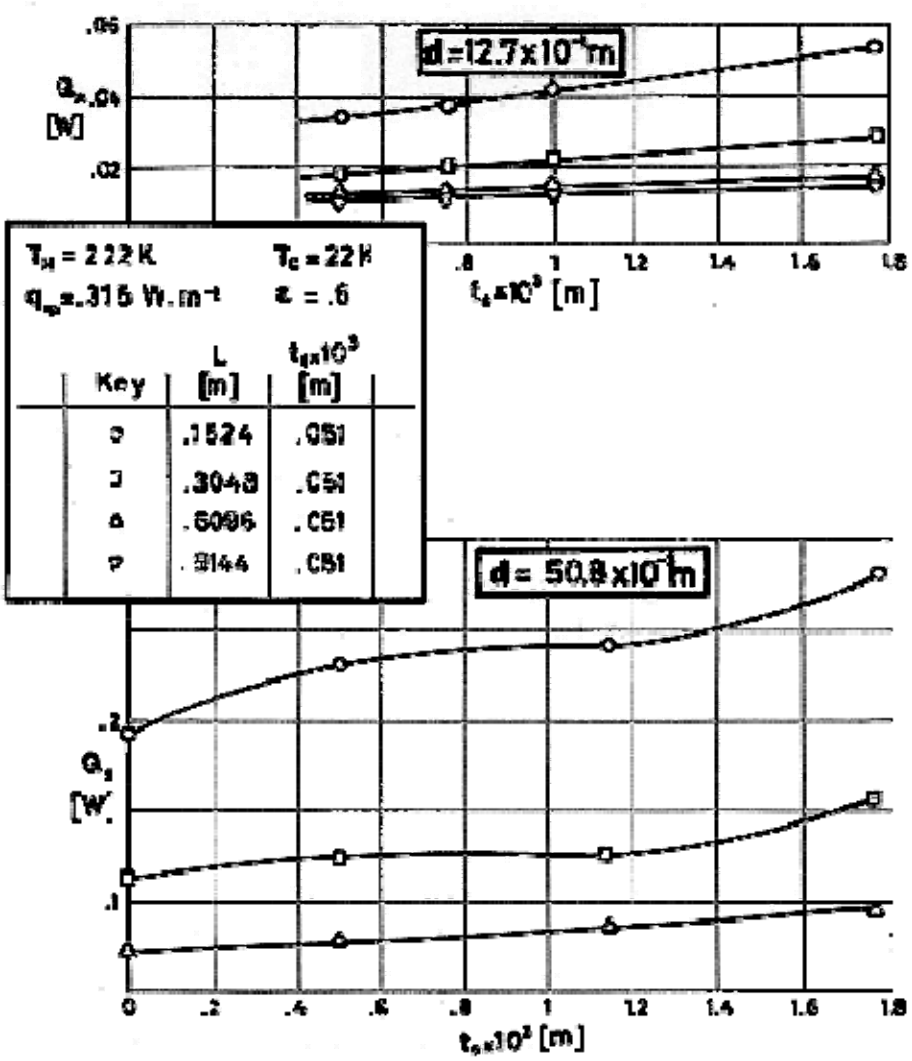

Note: non-si units are used in this figure

Figure 6-24: Heat transfer rate, Q_s, through fiber-glass overwrapped stainless-steel supports vs. overwrap thickness, t_o, for several supports lengths, L, and liner wall thickness t_l = 0,51x10^{-3} m. Hoop wrapping. (a) Inner diameter of the tube, d = 12,7x10^{-3} m. (b) d = 50,8x10^{-3} m. From Hall et al. (1971) [80].

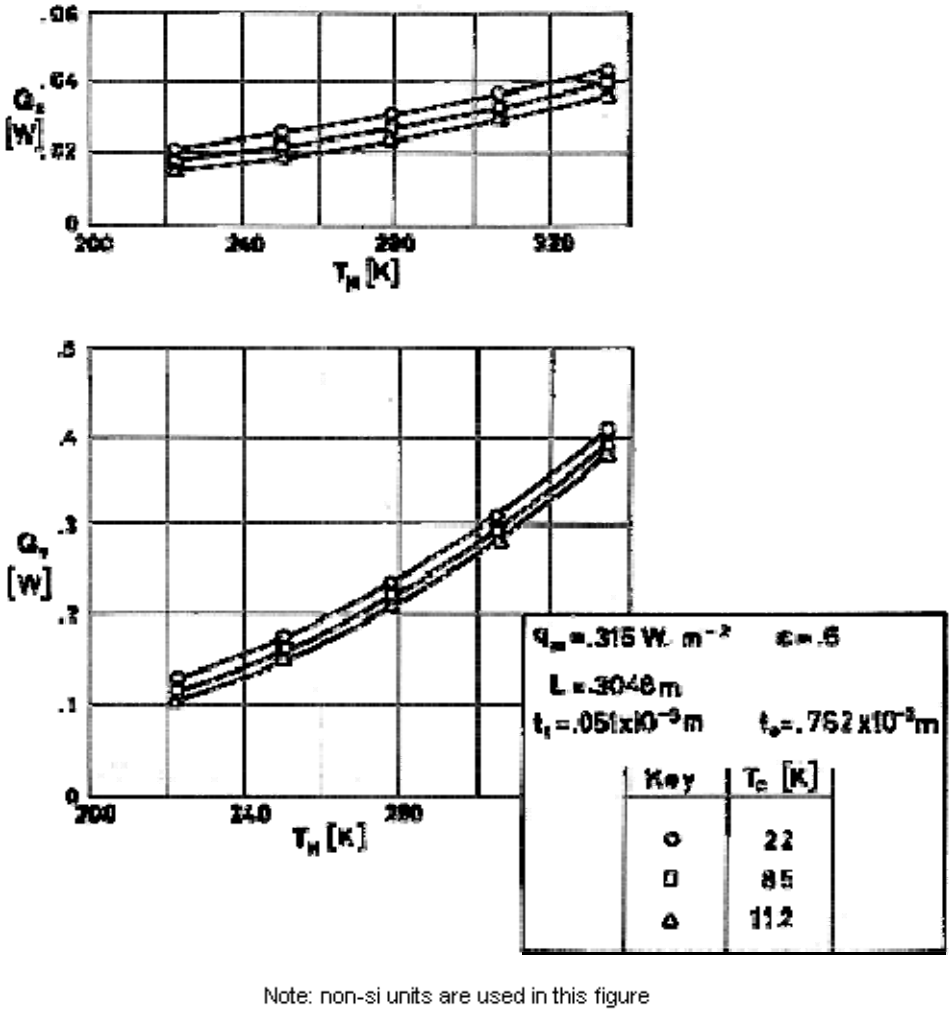

Note: non-si units are used in this figure

Figure 6-25: Heat transfer rate, Q_s, through fiber-glass overwrapped stainless-steel supports vs. warm boundary temperature, T_H, for several values of the cold boundary temperature, T_C. Tube length, L, liner wall thickness, t_l, and overwrap thickness, t_o, as indicated in the insert. Hoop wrapping. (a) Inner diameter of the tube, d = 12,7x10^{-3} m. (b) d = 50,8x10^{-3} m. From Hall et al. (1971) [80].

6.3.4 Tensile and flexural supports

Tensile flexural supports could be of the following types:

1. Tubes, made mainly from plastic composites and/or aluminium or titanium.
2. Low thermal conductance ties.

Metallic or plastic saddle bands, wire cables or chains are also used for tensile applications.

Support length should be as large as possible in order to minimize the heat flux through it. If the available space between the inner and outer vessel is not large enough to accommodate a long suspension member, standoffs are added to the outer and/or inner vessels as shown in Figure 6-26(b). Further resistance to heat transfer can be achieved by using springs or washers at either end or at both ends of the supports.

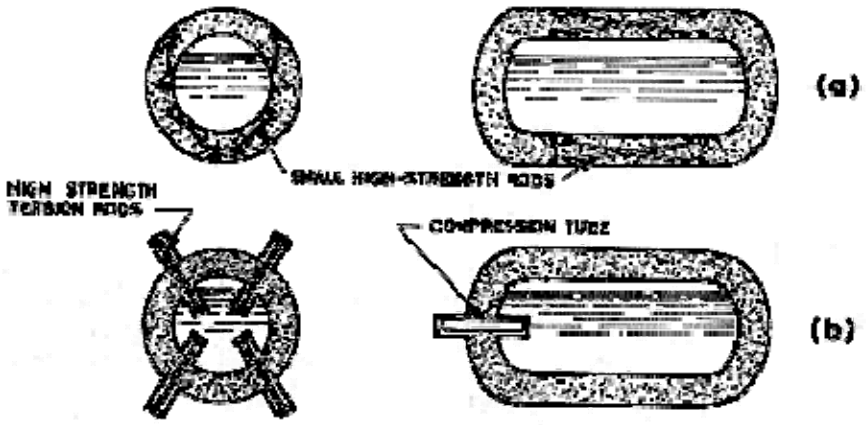

Figure 6-26: Typical supporting methods. Notice how the rods shown in (a) are crossed to minimize the effect of thermal contraction and to increase the length of the heat flow path. In (b), long suspension rods are accommodated in standoffs. From Barron (1966) [18].

Figure 6-27 shows a close-up of a support for a Dewar of the liquid helium-cooled IR telescope being developed by German Space Agency (DFVLR) for use onboard the Shuttle/Spacelab. These supports are constructed of fiber-glass-reinforced composite with cross sections of $0{,}87 \times 10^{-4}$ m² (those supports in the bottom of the container) and $0{,}33 \times 10^{-4}$ m² (those in the top), and are designed to withstand the launch vibration of the vehicle, the minimum frequency being 30 Hz. The heat leaks through all supports would be 150 mW, but can be considerably reduced by contacting the supports to the VCS.

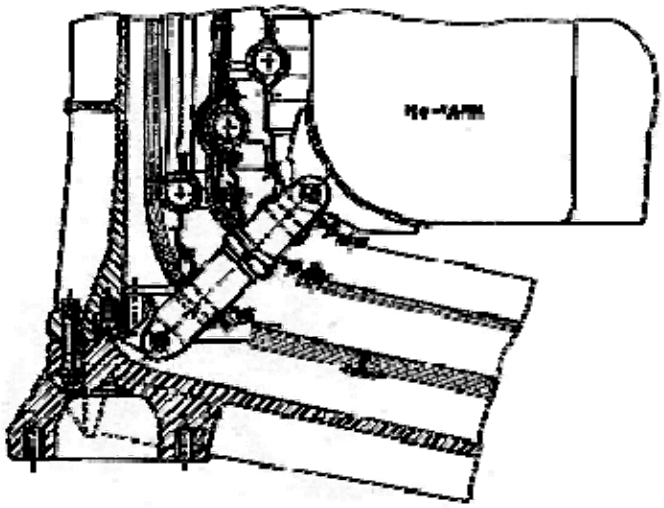

Figure 6-27: Tensile support of a liquid helium tank. From Lemke, Klipping & Römisch (1978) [131].

In addition to supporting the inner vessel and other items, the support ca be also used to restrain the cooled shields of the VCS system so that they do not contact each other bringing forth a "thermal bridge". This can be achieved by spacing discs locked on the support as sketched in Figure 6-28. These discs provide spacing between the shields without imposing axial loads which would tend to buckle the shields.

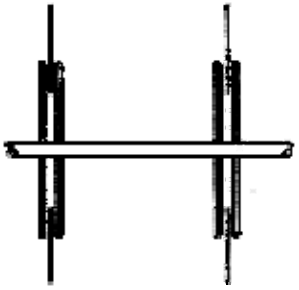

Figure 6-28: Spacing discs. From Bennett et al. (1974) [23].

The use of variable geometry supporting systems has been set forth recently. Urbach & Herring (1976) [243] depict a liquid helium Dewar, developed by Ball Brothers Research Corp. (see Clause 6.4.3.2), whose supporting system consists of six titanium supports which are retractable, plus six fiber-glass supports o which the VCSs are attached. The titanium supports are used during the high acceleration phase of launching. Once in orbit these supports are retracted into the cryogen container which rests on the fiber-glass supports.

6.3.4.2 Support tubes

The inner vessel of a VCS Dewar can be supported by a hollow cantilever beam. This configuration could present several advantages, in addition to its structural appropriateness.

1. The beam can be fashioned as an extension of the inner vessel neck tube, providing direct access to the container for cryogen filling.
2. Vapor cooling of the support can be easily achieved.
3. If a single beam can withstand the design loads, it penetrates through the insulation only once, whereas a system of multiple rods would penetrate repeatedly.
4. Finally, the beam could serve as a heat exchanger between the highly conductive metallic shields and the boil-off vapors. It is, however not always easy to profit from this advantage without increasing the heat transfer along the beam walls.

Figure 6-29, which has been borrowed from Bennett et al. (1974) [23], shows a hollow beam devised to support a liquid helium Dewar which has been studied by International Research & Development Co. Ltd. Newcastle upon Tyne.

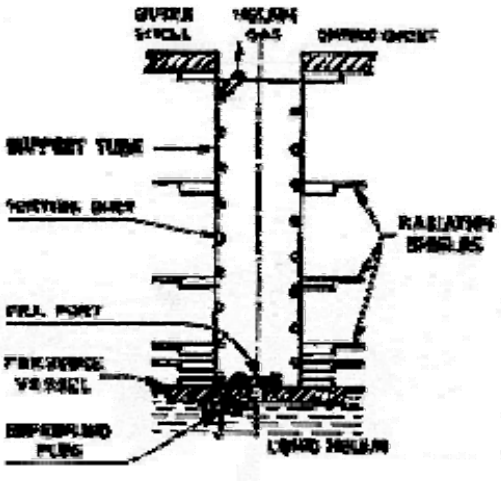

Figure 6-29: Support tube for a liquid helium Dewar. From Bennett et al. (1974) [23].

The support is made from 304 Stainless Steel. It is 0,3 m long. Its cross-sectional area is 2,09x10^{-4} m^2 at the warm end, and 0,88x10^{-4} m^2 at the cold end.

The supported mass is 390 kg. The support can withstand a steady acceleration of 10 g and ± 5 g vibration, both in the axial direction.

The venting duct is thermally connected to the inner surface of the support by either soft soldering or brazing. Thus the support serves as a heat transfer medium between cooled shields and venting duct. To insure that the venting duct does not contribute significantly to the thermal conduction along the support tube the thread of the spiralling venting duct should be several times its diameter.

After the cryostat is filled with helium, the support tube is packed with metallized hollow microspheres to provide insulation for both the prelaunch condition and the mission.

The inner vessel is restrained from lateral movement by three radial fiber-glass ties, each 0,5 m long and 0,165x10^{-4} m^2 in cross-sectional area. Spacing discs as those sketched in Figure 6-28 are provided.

The cryogen temperature is 2 K. The estimated heat leak through the support is not given.

6.3.4.3 Low thermal conductance ties

Two ways of supporting cryogenic containers by tensile ties are sketched in Figure 6-30. Six tension members are required in both cases. In the system depicted in Figure 6-30(a) each set of three structural members connects to a cantilever that penetrates through the insulation. In the Figure 6-30(b) each structural member reaches the inner vessel at a different location and, therefore, penetrates the insulation separately.

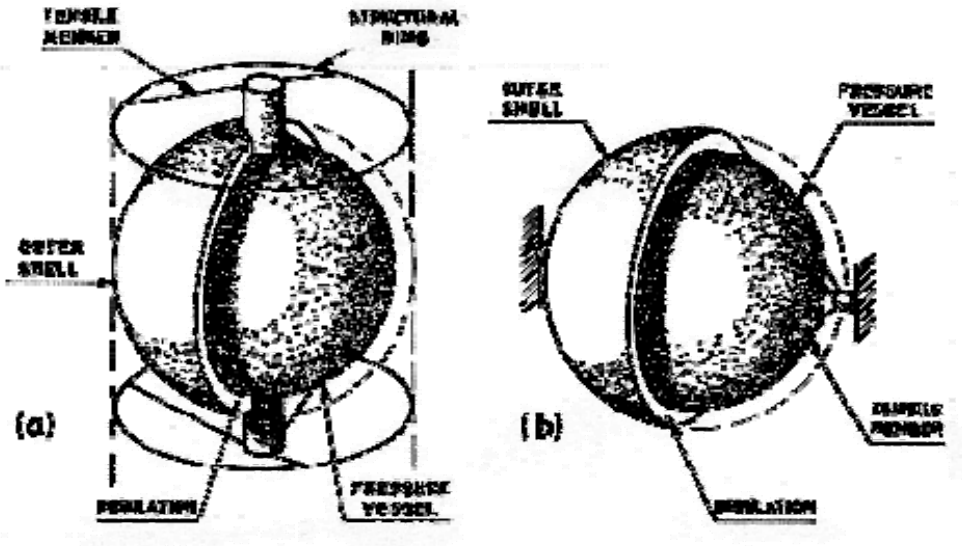

Figure 6-30: Two ways of supporting cryogenic containers by means of tensile ties. After Glaser et al. (1967) [75].

The liquid helium cryostat shown in Figure 6-31, being developed by ESA for use on board Spacelab, has a tank supported by 24 fiber-glass struts. Each strut is composed of three parts connected together at the level of each shield in order to facilitate the integration and to achieve a good thermal contact.

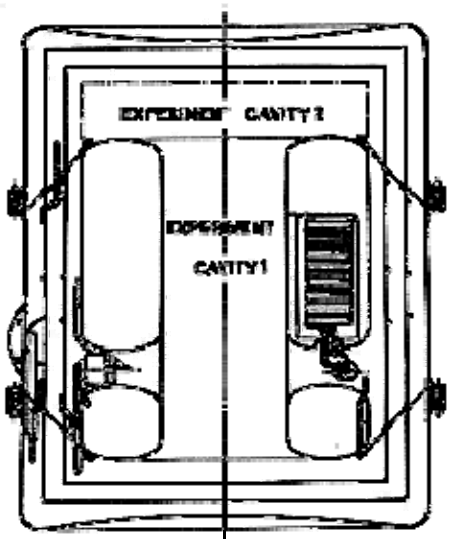

Figure 6-31: Sketch of the Superfluid Helium Cryostat for Space Use (CRHESUS) showing the tensile ties used for supporting the helium tank. From Lizon-Tati & Girard (1978) [134].

The heat flow between the main elements of the cryostat is shown in Figure 6-32.

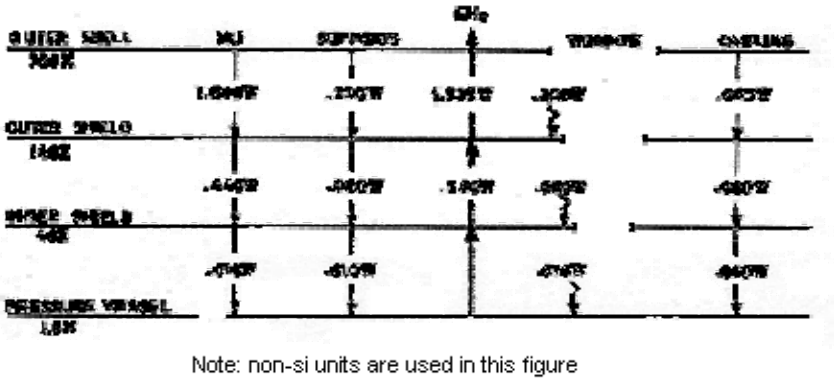

Figure 6-32: CRHESUS heat flow diagram. From Lizon-Tati & Girard (1978) [134].

6.3.5 Compressive supports

There are two main philosophies for the design of compressive supports, namely: supports manufactured using low thermal conductance materials, and supports based on the high thermal contact resistance which can be achieved between contacting materials in vacuum. Only the first type of support will be described here.

6.3.5.1 Low thermal conductance compressive supports

Mason (1972) [142] briefly describes two configurations that were considered for supporting liquid helium cryostats. The first design is a titanium strut, and the second a fiber-glass pad. The last one turns out to be more efficient. Each one of the supports (titanium rod or fiber-glass pad) is thermally connected to each cooled shields, passing through it, so that the inward-flowing heat would be largely intercepted and carried off by the outflowing helium gas (see JPL-Caltech VCS Dewar, Clause 6.4.3.2).

Another low-temperature structural support, which is not particularly designed for spacecraft although it purports interesting features, is described by Heim & Fast (1973) [85]. This support is constructed using three tubes and four flanges as it is shown in Figure 6-33. Notice that a decrease in the length of the intermediate tube because of thermal contraction will increase the overall column length. Selecting tube materials such that the thermal contraction of the intermediate tube be equal to the sum of the contraction of the inner and the outer tubes, the overall column height will not change when the column is cooled down to operating conditions.

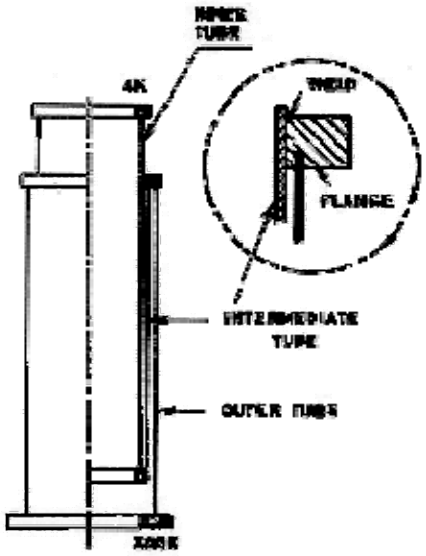

Figure 6-33: Composite column compressive support. From Heim & Fast (1973) [85].

The supports were constructed using aluminium for the intermediate tube and fiber-glass-epoxy for the inner and outer tubes. Both fiber-glass-epoxy tubes have a $1{,}6 \times 10^{-3}$ m wall thickness since this was the thinnest tube wall manufactured using normal shop practice. A wall $3{,}2 \times 10^{-3}$ m thick was chosen for the aluminium tube to assure good tube-to-flange welds. Four aluminium flanges were machined with 6×10^{-3} m deep groves, to accept the epoxy fiber-glass tubes, and two of these flanges were welded to the aluminium tube as shown in Figure 6-33. Prior to bonding with epoxy, all aluminium bonding surfaces were chemically etched with a sodium dichromate sulphuric acid solution, whereas the inner and outer bonding surfaces were lightly sanded and wiped with cleaning agent. All flange joints were bonded together with a low-temperature epoxy and cured at room temperature.

After curing, the top and bottom flanges were machined normally to the column center line. Several layers of superinsulation were inserted between the tubes to minimize heat transfer.

The specimen which has been described was tested with the following results:

Collapse load.....$8{,}53 \times 10^{4}$ N

Heat leak.....$13{,}53 \times 10^{-3}$ W

Height change.....0

These composite columns are being used at the US National Accelerator Laboratory, Batavia, Illinois, to superconducting magnet coils. The VCS Dewar flown on the Nimbus *F* weather satellite had similar supports.

6.4 Phase separators

6.4.1 Introduction

This Clause deals with phase separators for dewars holding cryogens other than superfluid helium. This means that separation between liquid and vapor cannot be based on the "thermo-mechanical effect" (see Clause 7.1.1.1). The superfluid porous plug, based on this effect, will be introduced in Clause 7.4.

The ultimate aim of any phase separator is to allow venting of vapor-only for relieving the pressure increases which result from the heat input to the stored cryogen. Venting of liquid would result in a loss of coolant and a decrease of the cooling effectiveness of the system.

Venting of vapor-only, to relieve the container, can be achieved efficiently under steady conditions, in the terrestrial laboratory, when the neck-support of the dewar is placed vertically upwards or only slightly tilted. Under reduced-gravity conditions, on the contrary, the liquid-vapor interface can shift easily by the action of small disturbing forces and seepage of refrigerant liquid would result.

Phase separation is also a problem in liquid propellant tankage, but there the aim is two-fold: 1) Venting of vapor-only, as above, and 2) Feeding the engines with liquid only. Problems associated with liquid retention devices are occasionally considered in this Clause inasmuch as liquid retention ensures venting of vapors, but the mass (below 100 kg), size (below 1 m) and other characteristics of the tanks indicate that they are used for cryogenic-cooling purposes.

Several (mostly desirable) features of separating systems for cryogenic-cooling dewars are summarized in Table 6-10.

Table 6-10: Main Features of Separating Systems for VCS Dewars

Aim	Venting of vapors-only
Background Requirements	1. Work at cryogenic temperatures. 2. work under reduced gravity. 3. Sturdy. can withstand structural effects of accelerations. 4. Satisfactory performance can be promptly recuperated after accelerations. 5. No moving parts. 6. Passive. No extra energy required. 7. Based on available design data.
Criticallity	Small ullages.
Alternative Starting Fluid Configuration	1. Single bubble. 2. Many bubbles (Low-quality-fluid). 3. Many droplets (High-quality-fluid).
Suitable Devices	1. Bubble positioner. 2. Low-quality-fluid separator. 3. High-quality-fluid separator.

Various devices, with their advantages and limitations, are introduced in Table 6-11. Most of them do not completely fulfil the background requirements in Table 6-10.

Table 6-11: Phase Separating Systems

Basic Principle	Concept	Description	Advantages	Drawbacks	References
Vehicle acceleration	Settling rocket	Rocket and a vent valve.	Simple, widely used.	Single-restart, short missions only.	
Centrifugal active	Mechanical stirrers	Moving blades. Drive unit inside tank.	Highly efficient separation for high quality fluids (nearly vapors).	Motor power dissipating into the bath. Gyroscopic effect on the spacecraft.	Mitchell et al. (1967) [152], Seidel (1982) [213]
		Drive unit outside tank. Rotation transferred through a magnetic clutch.	As above. Motor power not dissipating into the bath.	Gyroscopic effect. EMI.	Seidel (1982) [213]
	Peripheral fan	Outer fluid layer set into motion by a centrifugal fan.	Minimizes the mass of moving parts.	Motor power dissipating into the bath. Gyroscopic effect.	
	Rotating tank	Whole tank driven by an outer unit.	Motor power not dissipating into the tank. In steady-state, fluid rotates without friction.	Increased gyroscopic effect. Rotating sealing and bearing lubrication problems.	
Centrifugal passive	Separator nozzle.	Fluid is forced to move in highly curved paths, through a multistage nozzle. Liquid is drained out.	Separation itself is passive.	A pump is required to drain the liquid	Seidel (1982) [213]
	Cyclon	Fluid enters tangentially a	As above. Low	As above. Only effective with	

		vortex cavity. Resulting gas glows via a heat exchanger. Liquid is drained out.	complexity.	high quality fluids.	
	Local vortex	A local vortex is mechanically generated at the tank center. Gas in the vortex core enters a heat exchanger through a throttling valve.	Favourable liquid-stirring effect on the temperature field	Motor inside the bath. Liquid motion could affect satellite stabilization.	
Ultrasonic	Droplet arrester	Ultrasonic standing waves in a resonator tube prevent liquid droplets from entering the tube.	Simple design, low weight.	Input power dissipates into the bath. Droplet-size dependent performance. Lifetime problems.	
	Atomizer	Droplet vaporization ultrasonically enhanced.	As above.	Input power dissipates into the bath. Lifetime problems.	
Capillary	Total	Liquid-vapor interface is controlled by suitable baffles or bundle of tubes. See Clauses 6.4.3 to 6.4.7	Completely passive.	Small tanks only. Require much development work. Recovery after accelerations above design values is unknown.	Mitchell et al. (1967) [152], Seidel (1982) [213]
	Partial	A passage with porous walls draws the liquid in contact with the wall by capillary action. This liquid is pumped back into the tank. The vapor enters a small heat exchanger.	Heat exchanger operates under constant and defined conditions, provided that the system operation is not interrupted.	Operation is interrupted when the pressure difference (inside to outside passage) exceed the capillary pressure. Considerable development work.	
Dielectro-phoretic	Total	A non-uniform electric field is produced by an array of electrodes. Liquid moves	No moving parts.	Requires high voltages (~10^6 V). Electrical insulation problems. Electrodes do not	

		toward regions of high field strength. Vent valve is placed into the low field region.		withstand accelerations. Recovery after accelerations above design values is unknown.	
	Partial	Fluid is introduced into the separator. Liquid held between electrodes as above. Vapor is vented.	As above. Phases are separated in a partial compartment.	As above. Efficiency is unknown.	
Diffusion	Separating membrane	A membrane, permeable to gas, closes the tank outset.	No moving parts. Low complexity. Separating membranes are used in the industry.	Membranes are fluid-specific. Lifetime problems.	Seidel (1982) [213], Henis & Tripody (1983) [87]

Thermo-dynamic	Forced convection	The fluid drawn from the tank is throttled to a lower pressure and temperature and passed through a heat exchanger where it completely vaporizes cooling the bulk fluid which is forced by a fan unit through the other side of the exchanger. Operation is intermittent.	Operation does not depend on liquid-vapor distribution in the tank. Proven concept.	If an electrically driven fan is used, heat is dissipating into the bath.	Mitchell et al. (1967) [152], Seidel (1982) [213]
	Pulsed constant volume	Fluid is admitted, by throttling, to a control volume. There it is completely vaporized while it refrigerates the bulk.	Low complexity.	Vaporization time is too large to accommodate transients. Fluid-specific.	
	Pulsed constant pressure	As above, but the heat exchanger is a tube spirally would around the tank wall.	Applicable to any fluid. Enhances insulation	Lifetime, reliability and wearing of the valves are unknown. Valves dissipate	Seidel (1982) [213], Müller et al. (1983) [157]

		The tube inlet will be placed near a support of the tank. A tank exit valve is open for a preset time interval when the lower specified tank pressure is exceeded, and then kept closed for a preset time. The valve is permanently open if the upper pressure limit is reached. Pressure within the tube is maintained by a relief valve (the phase separator exit valve (see Figure 6-34b)).	effectiveness. The concept has been tested.	heat into the bath.	
	Pulsating (Flip Flop)	A hot wire analyzes the fluid which enters the separator, activating a valve with two exit ports, so that either liquid or gas is throttled in a throttling cascade. After throttling the fluid enters a heat exchanger.	Low complexity and system mass. Safe operation of the hot were has been demonstrated.	Lifetime, reliability and wearing of the valve are unknown. Valve and hotwire dissipate heat into the bath.	Seidel (1982) [213]

6.4.2 Thermodynamic vent system

This system, also known as Heat Exchange or Thermal Conditioning System is the simplest and most reliable among those being considered at present. Two different versions are sketched in Figure 6-34.

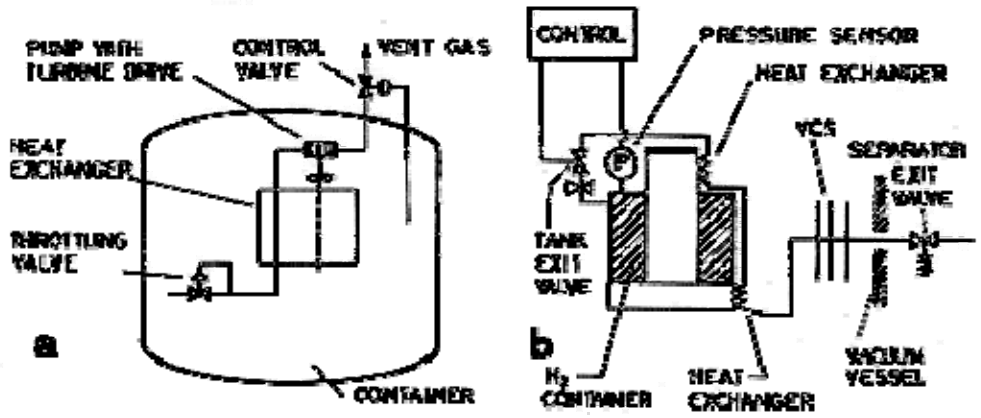

Figure 6-34: Schematic of thermodynamic vent system. a) Forced convection. From Mitchell et al. (1967). b) Pulsed constant pressure. From Müller et al. (1983) [157].

The two-phase fluid drawn from the container is throttled and passed through a heat exchanger to vaporize any liquid still remaining in the vent stream, and to cool the bulk tank fluid circulating through the other side of the exchanger.

After leaving the heat exchanger, the vent fluid can be either vented directly or further expanded through a turbine to supply power to a tank mixer.

Since the quality of the inlet stream could vary, a modulating valve is used for controlling the throttling process. Flow control downstream of the heat exchanger is maintained by a valve sensing container pressure.

The main advantage of the system is that its operation is independent of the liquid-vapor distribution in the container or disturbing accelerations on the vehicle.

Bulk mixing is used for temperature uniformization. If the mixer is electrically driven there is an increase in the external heat input to the container. This could be eliminated by use of a turbine drive.

The heat exchanger can be a coiled tube, plate and fin, or a porous plug close to a heat source. In the so-called internal configuration, the heat exchanger is placed within the container, as in Figure 6-34a. The cryogenic fluid and vapor are the heat-exchanger hot-sidefluid. Operation of the system then reduces the pressure within the container. Other locations of the heat exchanger, such as on the insulation (Figure 6-34b), or on the container wall, will result in larger system masses but do not require recirculation of the fluid for effective cooling. Nevertheless, recirculation is still useful in containers holding cryogenic liquids for long times, to avoid temperature stratification (Moses & Gluck (1973) [156]) and to provide a more uniform fluid. Capillary pumping has been considered for these purposes (Blatt & Aydelott (1978) [25]).

The performance of an internal heat exchanger should not vary significantly with gravity level. The mixing process, on the contrary, strongly depends on this level. Aydelott (1976, 1979) [14] & [15] considered jet stirring in partially filled containers under reduced gravity. The interaction of the jet with the liquid-vapor interface and the resulting bubbles, unsteadiness of the interface, etc... are

complicated phenomena deserving careful watching. The non-steady effects of superimposed accelerations have not been considered yet.

A very simple thermodynamic phase separator which has been utilized in Dewars onboard the "Cosmos" series is shown in Figure 6-35. It consists of a tube twisted into a spiral (the heat exchanger) with a throttling device at the input end.

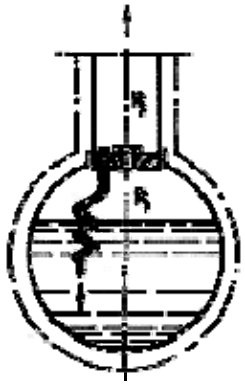

Figure 6-35: Thermodynamic phase separator. From Fradkov & Troitskii (1975) [71].

The inner pressure of the container is p_1. The exit pressure p_2 ($p_2 < p_1$) is kept constant during the flight by controlling the gas exhaust into space.

Under the action of the pressure difference, p_1-p_2, throttling of a small part of the cryogen from the container takes place in the throttling device and the fluid temperature within the spiral tube is lowered. As a result of the heat transfer from the bulk liquid, the liquid within the heat exchanger evaporates and only vapor reaches the exit.

6.4.3 Capillary barriers

A capillary barrier is a perforated plate which inhibits fluid motion through capillary action and provides a mechanism for viscous energy dissipation.

6.4.3.1 Capillary barriers under static conditions

Let us consider a capillary barrier initially placed on a liquid-vapor interface.

When gas begins to pass through any small opening which is initially wet, the interface anchored to the edges of the opening becomes curved and a pressure differential (the capillary or bubble pressure) prevents the passage of the gas into the liquid.

Figure 6-36 illustrates the behavior of a capillary barrier in the presence of a wetting liquid.

Figure 6-36: A capillary barrier in static equilibrium. From McCarthy (1968) [144].

The pressure at level A in the liquid is

$p_l = p_v - \rho g l$,

whereas the pressure in the vapor, the density of which is negligible, is p_v at any level.

The shape of the interface in the level A opening must result in a capillary pressure balancing the difference $p_v - p_l$

$\sigma(1/R_1+1/R_2) = \rho g l$,

where σ is the liquid-vapor surface tension and R_1, R_2 the two principal radii of curvature of the interface.

For a circular opening, diameter d, an a wetting liquid, the largest pressure difference appears when the interface becomes hemispherical, $R_1 = R_2 = d/2$. Thus,

$4\sigma/d \geq \rho g l$

and the curvature of the interface decreases as l decreases, as sketched in Figure 6-36.

Static equilibrium, in terms of the static Bond number (see Clause 6.4.7.1), requires

$Bo = \rho g l d/\sigma \leq 4$.

It is assumed that the liquid wets the barrier (i.e., the liquid-solid contact angle, θ, is close to zero). Thus, the barrier offers resistance to vapor only. Conversely, when θ approaches 180° there is no resistance to passage of vapor.

Fluids such as those used for cryogenic cooling and cryogenic propellants have, in general, zero contact angles on steel, aluminium, titanium, and all other metals that have been investigated, and on ceramic or organic glassy solids (Neu & Good (1963) [166]).

6.4.3.2 Capillary barriers under dynamic conditions

Let a container with a capillary-barrier partition which suddenly suffers an angular disturbance around an axis normal to the plane of the Figure 6-37.

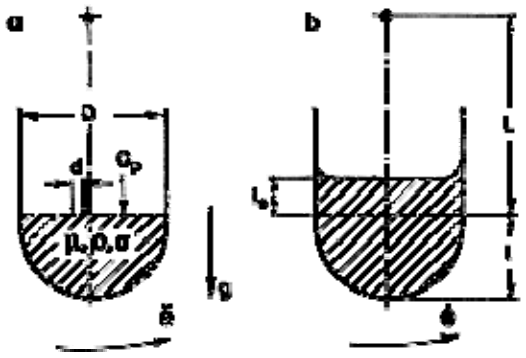

Figure 6-37: Container with a capillary-barrier partition. From McCarthy (1968) [144]. (a) An angular acceleration appears when the interface is formed at the barrier. (b) The configuration reaches a steady angular velocity before interaction of the interface with the barrier. See Table 6-12 for the definition of the experimental conditions.

Table 6-12: Experimental Conditions for Capillary Barrier Stability Studies (Figure 6-37).

Parameters	(a) Bond Number-Controlled Mode	(b) Weber-Number Controlled Mode	Comments
Geometrical Ratios	$0{,}40 < l/D < 0{,}85$	h/D	No effect of l/D and L/D found in case (a). For case (b), see Figure 6-40 and Figure 6-41.
	$1 < L/D < 2$	L/D	
	d/D		No d effect found in case (b) even though d varied by a factor of 3.
		l_o/D	l_o/D small enough for small dissipation but large enough to reach the $\ddot{\theta}$ => 0 state.
	$0{,}1 < O_p < 0{,}46$	O_p	O_p is the ratio of open to total area of the barrier. Akin to Φ porosity, see Clause 7.4.3.
Static Bond Number	$\rho g d D/\sigma = 0$	$\rho g D^2/\sigma = 0$	Tests were conducted in a drop-tower and in a KC-135 parabolic flight aircraft.
Rotational Bond Number	$\rho \ddot{\theta}\ LdD / \sigma$		
Rotational Weber	$\rho \dot{\theta}^{\,2} L^{\,2} D / \sigma$	$\rho \dot{\theta}^{\,2} D^{\,3} / \sigma$	The choice of the second form of the Weber number is based on Figure

Parameters	(a) Bond Number-Controlled Mode	(b) Weber-Number Controlled Mode	Comments
Number			6-41.
Reynolds Number	$\rho\dot{\theta}\ LD/\mu > 1$	$\rho\dot{\theta}\ LD/\mu > 1$	Reynolds number kept large in the tests.

NOTE From McCarthy (1968) [144].

In the case of Figure 6-37a the critical disturbance corresponds to an acceleration parallel to the barrier. This is the counterpart of Figure 6-36 with $\ddot{\theta}L$ instead of g. The results of the tests are shown in Figure 6-38. It is seen that the barrier is less stable under dynamic than under static conditions,> the critical Bond numbers being, respectively, less than 1 and 4. See also Figure 6-39, where a Reynolds number influence appears.

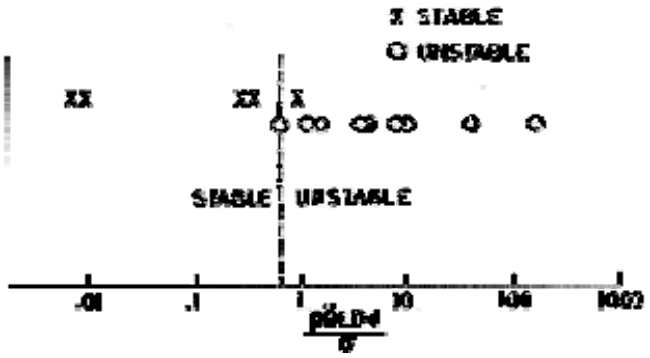

Note: non-si units are used in this figure

Figure 6-38: Results of barrier dynamic stability tests. Bond number-controlled mode. Tests were insufficient for determining the effect on barrier stability of the various dimensionless parameters. From McCarthy (1968) [144].

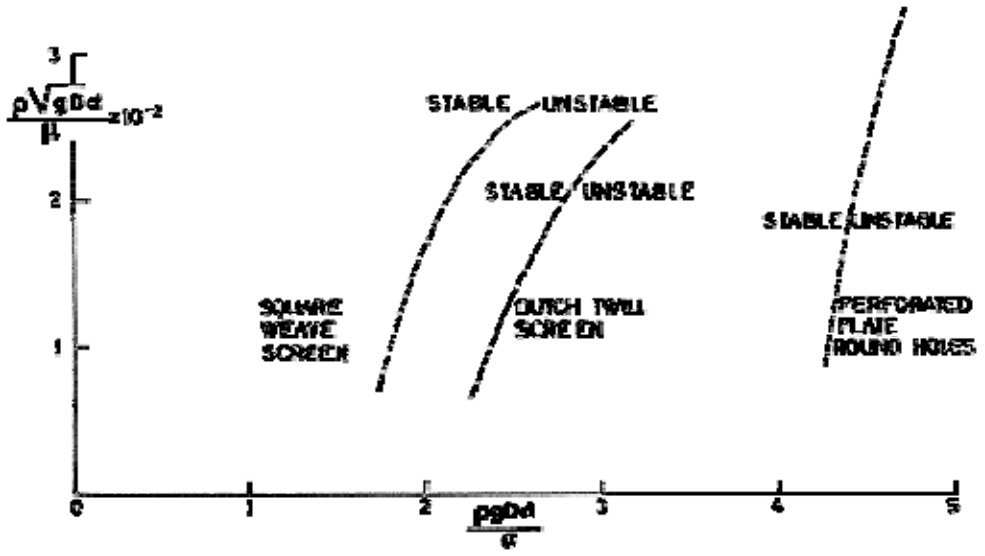

Figure 6-39: Results of dynamic stability tests with different barriers. Bond number-controlled mode. The acceleration, *g*, is parallel to the barrier. From Fester (1973) [67]. A Reynolds number through the hole has been plotted vs. the critical Bond number.

Normal (to barrier) accelerations, which produce the instability of the interface, are usually not critical. When the pores of the capillary barrier are circular of diameter *d*, the critical Bond number happens to be

$Bo = \rho g d^2/\sigma = 3{,}36$

when the contact angle is zero (Fester (1973) [67]). This has been verified by drop tower tests of capillary barriers which also shown that the critical *Bo* for a square weave screen is slightly less than that given above.

Figure 6-37b corresponds to a container which could reach a steady angular velocity before the liquid-vapor interface approaches the barrier, thence the phenomena of interest occur while there is no acceleration of the reference frame (other than gravitational). The controlling parameter is not the Bond number (ratio of hydrostatic to surface tension forces) but the Weber number which is the ratio of dynamic forces in the fluid to surface tension forces (see Clause 6.4.7.1).

Results of several tests are given in Figure 6-40 where We_c is an analytically obtained critical Weber number (Figure 6-41).

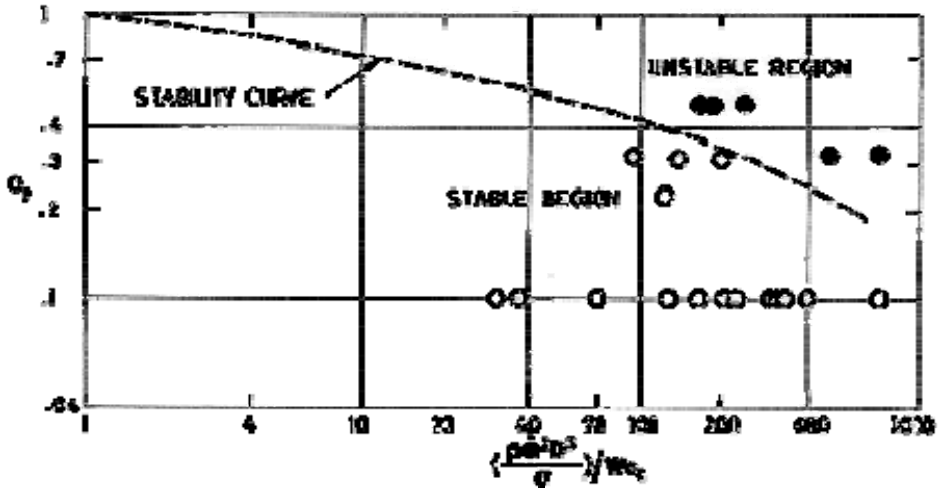

Note: non-si units are used in this figure

Figure 6-40: Results of barrier dynamic stability tests. Weber number-controlled mode. From McCarthy (1968) [144]. The Weber number in abscissae is normalized with an analytical critical Weber number We_c, which is given in Figure 6-41 below.

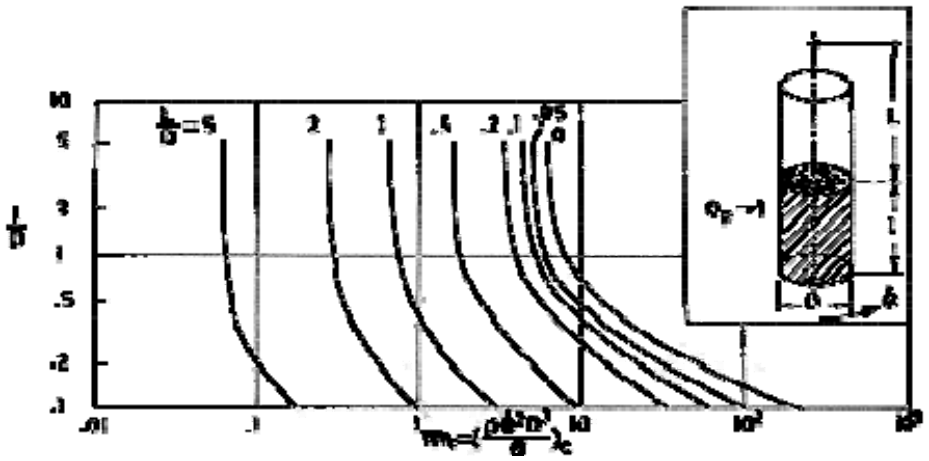

Note: non-si units are used in this figure

Figure 6-41: Critical Weber number, We_c, as a function of geometry, l/D, and position of the axis of rotation, L/D. These results have been obtained by use of a potential (incompressible, inviscid, irrotational flow) theory with $O_p \rightarrow 1$, although assuming that the barrier induces a capillary pressure difference. From Gluck (1970) [76].

The damping effect of perforated barriers can be assessed in terms of a Weber number defined as,

$We = \rho V^2 d/\sigma$,

where V is the liquid impingement velocity. The relative merits of different types of barriers are given in Figure 6-42.

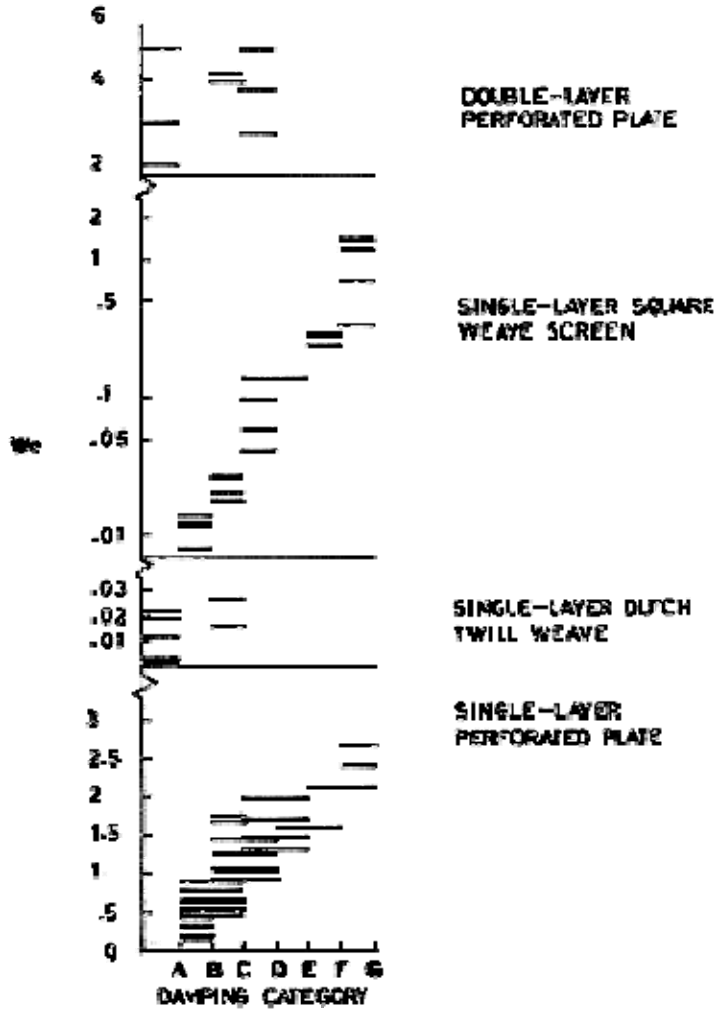

Note: non-si units are used in this figure

Figure 6-42: Damping performance of selected barriers. From Fester (1973) [67]. The damping categories A to G are associated to the flow patterns resulting after impingement of the liquid with the barrier, from orderly (A) to irregular (G).

Capillary barriers are hardly used alone as separating devices. They can, however, enhance the performance of other devices as in the case of the compartmented tank in Figure 6-43.

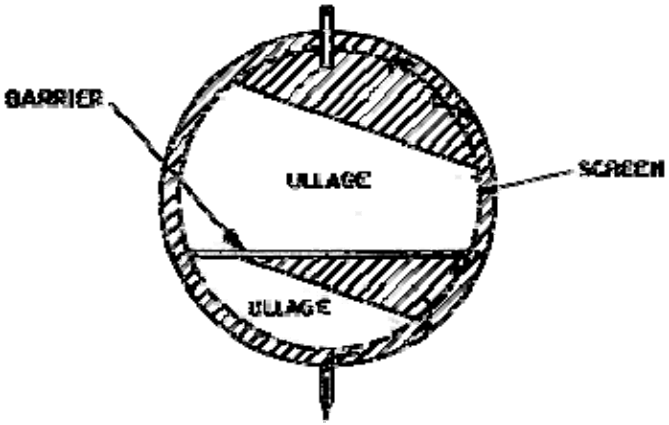

Figure 6-43: Compartmented tank device. From Fester, Eberhardt & Tegart (1975) [68].

In this system a screen liner concentric with the tank wall holds the liquid (or part of it). This liquid can be used either for wall cooling or for feeding the thrusters. Retention of the liquid within the liner depends on the balance of pressure forces (static and dynamic) and surface tension forces. The addition of barriers, as shown in Figure 6-43, reduces the hydrostatic head making it easier to retain liquid in a high-g environment. Obviously, the venting compartment should be depleted prior to the other compartments.

6.4.4 Porous media

Concepts where the liquid is confined to a porous medium can be applied to very small tanks, such as for microthrusters. Systems based on these concepts have been successfully tested in orbit, for example: in the American satellite ATS IV (De Brock et al. (1971)) and Japanese satellite MS-T4 (Enya et al. (1981) [64]).

Points of concern in the design of such systems are:

6.4.4.1 Sustained liquid height

In a capillary tube, the axis of which is parallel to the direction of acceleration, the maximum liquid height sustained under no motion is (Figure 6-44),

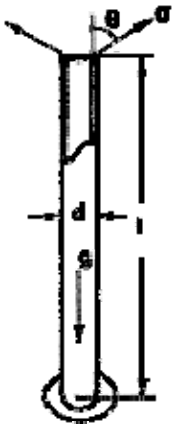

Figure 6-44: Sustained liquid height in a capillary tube.

$$l = 4(L_b)^2 \cos\theta / d \qquad [6\text{-}91]$$

where θ is the solid-liquid-vapor contact angle and L_b the so-called Bond length

$L_b = [\sigma/(\rho_l - \rho_v)g]^{1/2}$

which, for a given g, is a material property (see Clause 6.4.6.2). Usually $\rho_l > \rho_v$ and the later is neglected. The Bond length appears whenever hydrostatic and capillary forces balance each other.

If the liquid wets the surface of the capillary Θ becomes close to zero and l reaches its maximum value for given L_b and d.

Equation [6-91], above, can be used in ordinary fibrous layers, when channel geometry is not uniform, provided that an equivalent diameter, D_E, is used for d.

$D_E = [\Phi/(1-\Phi)]d_o$,

Φ being the volume porosity (see Table 7-46, Clause 7.4.3), and d_o the diameter of the fiber.

Experimental results for several fibers (Φ close to 0,94) are shown in Figure 6-45. Liquid was ethanol. A capsule containing the liquid and packed fibers was centrifuged. Sustained liquid height is deduced from liquid mass inside the capsule before and after centrifugation. Gravity level was around $40g_o$. A small amount of liquid was lost because evaporation into the atmosphere.

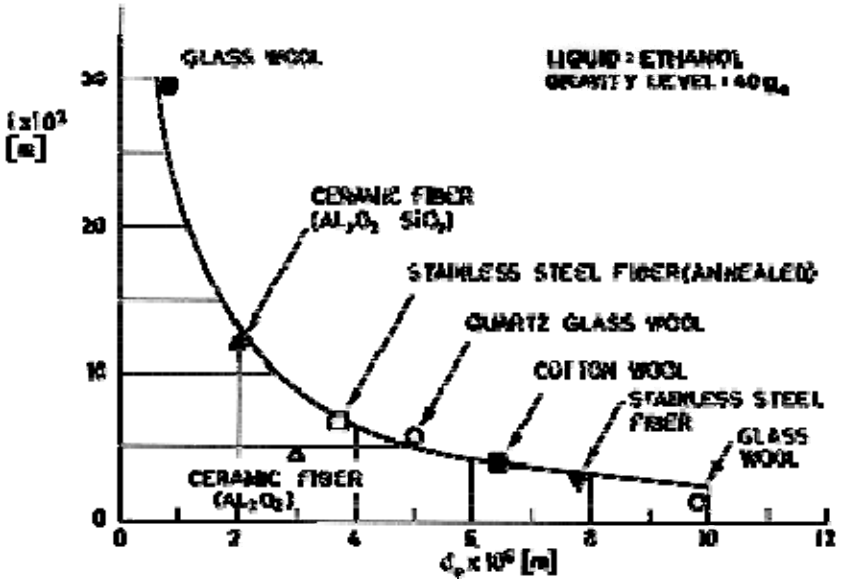

Figure 6-45: Sustained ethanol height, l, vs. diameter of fiber, d_o. Gravity level $40g_o$. From Enya, Kisaragi, Ochiai, Sasao & Kuriki (1981) [64].

The solid line in Figure 6-45 has been deduced from Eq. [6-91] with $\Theta = 0$ and $D_E = 10{,}2d_o$. The correct expression of D_E with $\Theta = 0{,}94$ should be $D_E = 15{,}7d_o$. Thence, experimental heights are 1,5 times higher than those predicted. Reasons for the deviation could be the highly distorted configuration of the channels and uncertainties in the values of Φ and d_o.

Withstanding of the acceleration by the fibers is also important. Ceramic fiber Kaowool (see ECSS-E-HB-31-01 Part 7, clause 5) exhibits good characteristics but small pieces of fiber are entrained intothe vapor.

Figure 6-46 gives similar results for ammonia. The porous medium was packing glass wool, $d_o = 10^{-6}$ m and $\Phi \approx 0{,}95$. Packing length was 20 mm except for point labelled "underfilled NH_3" which was 10 mm.

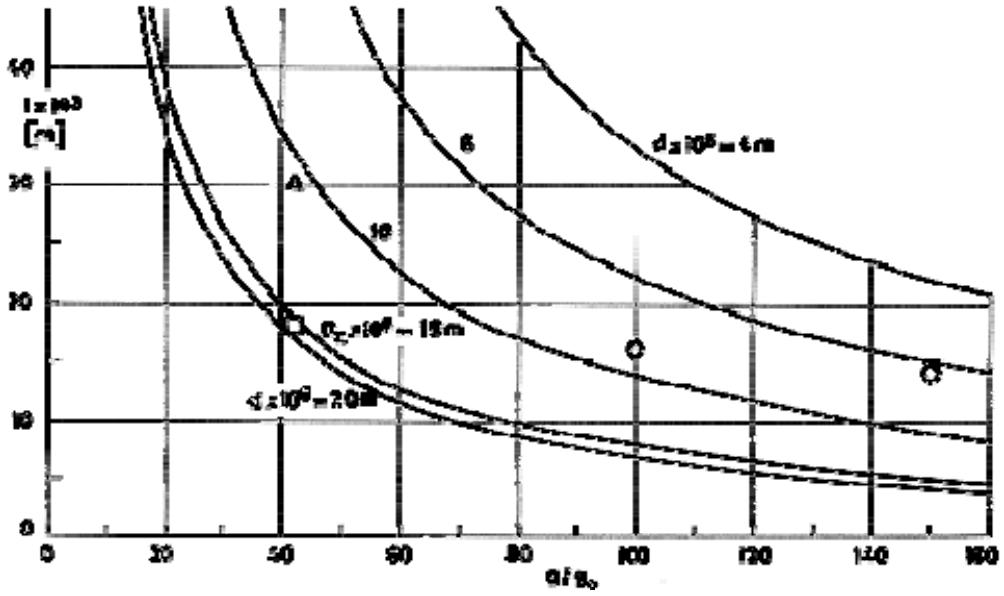

Figure 6-46: Sustained liquid height, l, vs. gravity level, g/g_o. Liquids are: Ammonia (circle), underfilled Ammonia (square), and ethanol (triangle). Matrix is glass wool, $d_o = 10^{-6}$ m. Solid lines have been deduced from Eq. [6-91] with $\theta = 0$ and the quoted values of d. From Enya, Kisaragi, Ochiai, Sasao and Kuriki (1981) [64].

Acceleration was changed from $10g_o$ to $150g_o$.

The capsule was hermetically sealed and the volume of the spread liquid was measured through a scale in the glass container.

Solid lines, which are drawn merely for reference, have been deduced from Eq. [6-91] with $\theta = 0$ and the quoted values of d.

Sustained liquid height was twice as high as the theoretical value. This could be attributed to glass wool geometry or to a perforated Teflon plate placed to prevent ammonia spillage.

6.4.4.2 Boiling within the voids

Boiling within the voids of a porous medium is unlikely, but should not be ruled out completely in practical instances. For a review of boiling in tubes see Collier (1981) [46].

Boiling cannot occur until the wall temperature exceeds the liquid saturation temperature. The difference between both temperatures is the degree of superheat. Obviously the local fluid bulk temperature can be smaller than the saturation temperature, the difference between both is called degree of supercooling.

As the heat flux is increased the first bubbles appear on cavities of the heated wall. If the lowest temperature on the bubble surface is greater than the bubble equilibrium temperature, the bubbles will grow. This criterion is due to Hsu (1962) and is sketched in Figure 6-47. The bubble equilibrium temperature depends on the saturation temperature, T_{sat}, saturation pressure, p_{sat}, heat of vaporization, h_{fg}, gas constant of the vapor, R, and capillary pressure, σ/r.

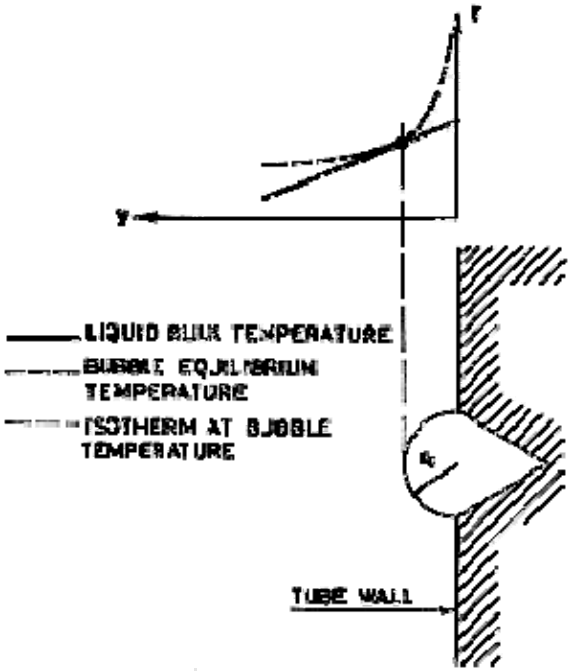

Figure 6-47: Criterion for the onset of nucleation in subcooled boiling. After Collier (1981) [46].

The incipience of nucleate boiling in tubes has been considered by Davis & Anderson (1966) [52]. They give the critical radius, r_c, of an "active" cavity for nucleate boiling as,

$$r_c = \left(Bk_l / q\right)^{1/2} \qquad [6\text{-}92]$$

with

$B = [2\sigma T_{sat}(1/\rho_v - 1/\rho_l)]/h_{fg}$

In these equations the symbols have the usual meanings.

At low values of q and of the pressure (which appears implicitly in B) the critical radii are much larger than the radii of the voids and it is difficult to reach boiling (Enya et al. (1981) [64]). Nevertheless, Eq. [6-92] is based, among others, on the following two hypotheses:

1. Buble radius is much smaller than that of the tube, and
2. There is a sufficiently wide (continuous) range of active cavity sizes available.

When *rc* result to be too large an estimate of the largest "active" cavity on the heating surface should be made. In the case of water reasonable agreement with experimental data was found when a maximum active size of 10^{-6} m radius was used.

6.4.5 Baffled tanks

Several types of internal baffles can be used for ullage bubble positioning, liquid acquisition and center-of-mass control of stored liquids under reduced gravity conditions. The main emphasis is here placed in bubble positioning for liquid-free vapor venting, particularly when the ullage volume is small, in spherical tanks of radius R.

6.4.5.1 Post

A central post, see insert in Figure 6-48, can be used to position a bubble between the top of the post and the top of a tank. The post height, *l*, required to position a given ullage, *U*, is deduced from Figure 6-48 (curve labelled d/R = 0). In this particular instance gravity is nil (spherical bubble), the tank is spherical, and the diameter of the post zero. *U* is given by

$$U = \left(1 - 1/2R\right)^3 \qquad [6\text{-}93]$$

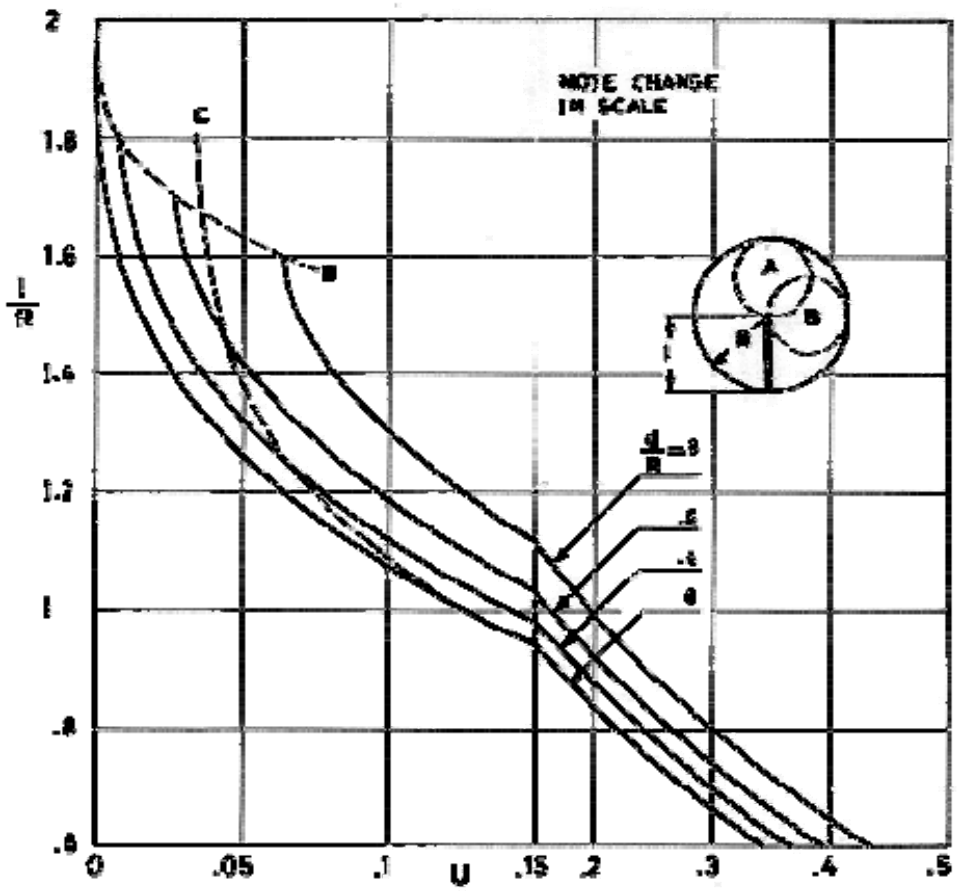

Note: non-si units are used in this figure

Figure 6-48: Post height, *l*, required to position a given ullage, *U*, under reduced gravity. See Clause 6.4.5.2 for explanation of curves *d*/*R* =/ 0, B and C.

An ullage of 0,125 (or 12,5%) corresponds to a spherical bubble of diameter *R*. When the post is very slender ($d \approx 0$) the location of the bubble is indeterminate if the ullage is smaller than 0,125 (notice sphere B in the insert of Figure 6-48). Thus, the post length is usually smaller than the tank radius.

According to a mathematical analysis quoted by Tegart & Fester (1975) [232]:

1. The axial stability of the configuration increases when the post diameter and the taper to the root increases.
2. The interface contacting the top edge of the post is less stable than one intersecting the post elsewhere.

3. The configuration has little lateral stability. Any lateral disturbance produces an offset ullage although recentering occurs when the perturbation disappears.

The posts are simple, easy to design, manufacture and install, but provide poor ullage control.

6.4.5.2 Standpipe

The standpipe is essentially a large diameter, hollow post. Openings are provided around the base so it can fill with liquid. Figure 6-49, from Petrash et al. (1963) [184], shows a configuration the behavior of which under large ullage conditions has been tested in MA-7 spacecraft. Height of standpipe is determined in a manner similar to that used for the post, although the results are slightly modified by the larger values of d. For instance, considering a thin-walled standpipe of diameter d, the ullage fraction, U, sphere A in Figure 6-50, is:

$$U = \left[1 - 1/2R + \left(d/4R\right)^2 / \left(1 - 1/2R\right)\right]^3 \qquad [6\text{-}94]$$

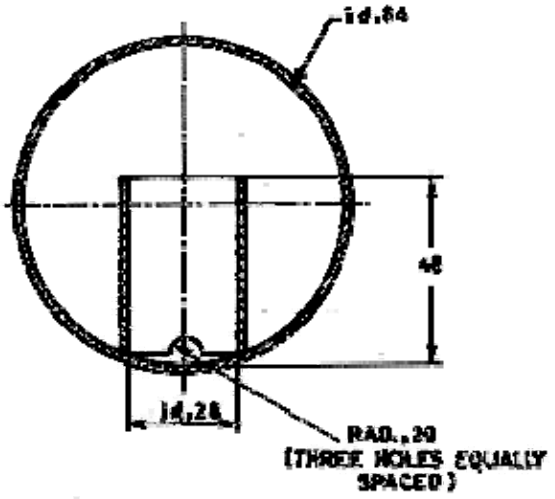

Note: non-si units are used in this figure

Figure 6-49: Experimental glass tank with a standpipe. From Petrash, Nussle & Otto (1963) [184]. All the dimensions are in mm.

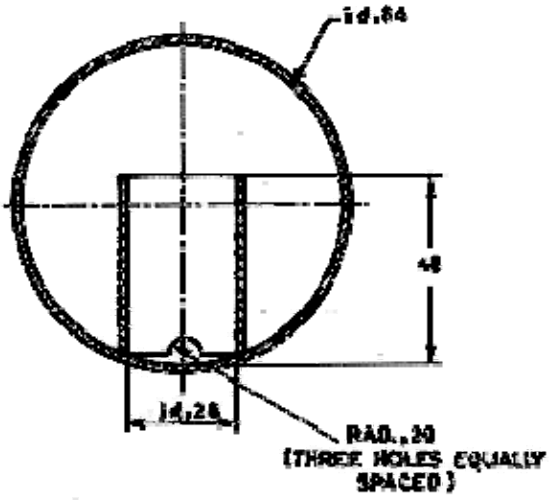

Note: non-si units are used in this figure

Figure 6-50: Minimum ullage centering capability of the standpipe.

which reduces to Eq. [6-93] above when $d << R$. Curves of U for different values of d/R have been shown in Figure 6-48.

The standpipe swallows the bubble, sphere B in Figure 6-50, when

$U \leq d^3/8R^3$.

The corresponding limiting curve has been labelled curve B in Figure 6-48.

Centering of the bubble can not be accomplished for ullage fractions either less than $d^3/8R^3$ (sphere B in Figure 6-50) or less than $(1/2 - d/4R)^3$ (sphere C in Figure 6-50). The last mentioned limitation has been labelled C in Figure 6-48.

Analysis of the ullage centering capability of the standpipe showed that (Tegart & Fester (1975) [232]):

1. At low ullage volumes the lateral stability of the standpipe is much like that of the post.
2. At larges ullages most of the liquid becomes oriented inside the standpipe, Figure 6-51.

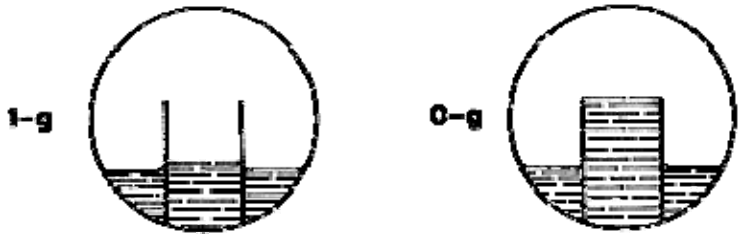

Figure 6-51: Liquid acquisition by the standpipe for large ullages. From Petrash, Nussle & Otto (1983) [184].

The standpipes are simple, easy to design, manufacture and install. Nevertheless, their ullage control is still poor.

6.4.5.3 Post with fingers

A post with fingers, Figure 6-52, is slightly better than the post alone. Smaller bubbles (up to 0,05 ullage volumes) can be stabilized when the ullage is initially centered, but other stable bubble locations are possible. Stability in the axial direction is the same as for the post.

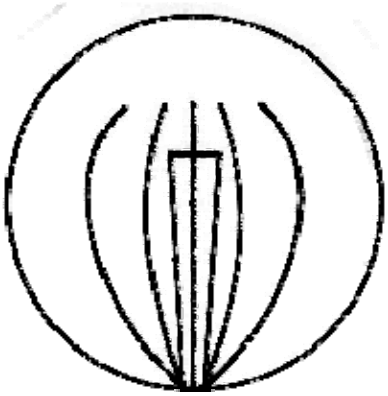

Figure 6-52: Central post with thin, off axis, posts (fingers). From Tegart et al. (1972) [233].

The post with fingers device presents minimum loading and handling problems, and slightly improved ullage control.

6.4.5.4 Vanes

This device consists of several vanes radiating outward from a small supporting post.

The height of the device depends on the ullage volume as in Figure 6-48, other variables being the number and profile of the vanes.

The vane profile is so designed that the sole ullage equilibrium configuration is the centered one, capillary forces push the offset bubble to its equilibrium position.

An inner limit in the vane profile allows the undistorted bubble to be tangent to the tank wall and just touch the vanes. In order to stabilize the bubble in the centered position the vane profile is kept outside the inner limit except for the centered position.

The relationship between the vane profile, ullage volume and number of vanes is deduced from Figure 6-53b

$R_{min}(\theta) = (R\text{-}r)\cos(\alpha/2) - [r^2 - (R\text{-}r)^2\sin^2(\alpha/2)]^{1/2}$

where: $\alpha = (2\pi/n)\sin\theta$, n number of vanes, and $r = RU^{1/3}$.

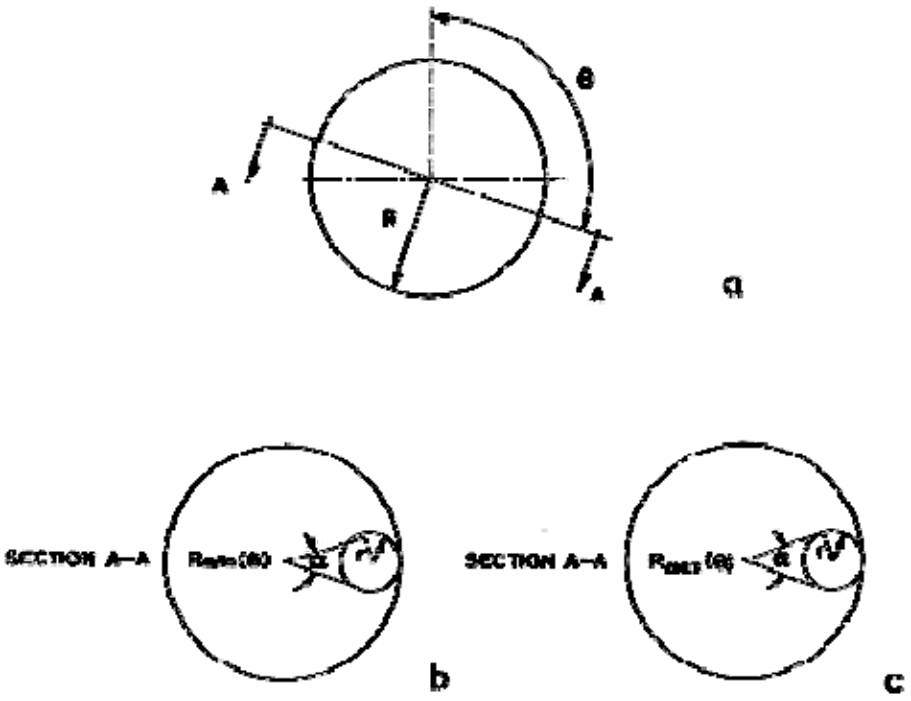

Figure 6-53: Criteria to deduce vane profile limits. From Tegart et al. (1972) [233].

The outer limit is controlled by a phenomenon called "bubble breakup", made apparent in drop tower tests. As a consequence of this breakup the ullage splits into a number of bubbles which fit within the vanes with no capillary forces acting on them. The experiments indicate that the maximum local length of the vane is given by the tangency condition, Figure 6-53c

$R_{max}(\theta) = R\cos(\alpha/2)/[1+\sin(\alpha/2)]$,

which results to be ullage independent since $r = R_{max}\tan(\alpha/2)$.

Inner and outer limits calculated in typical cases are shown in Figure 6-54.

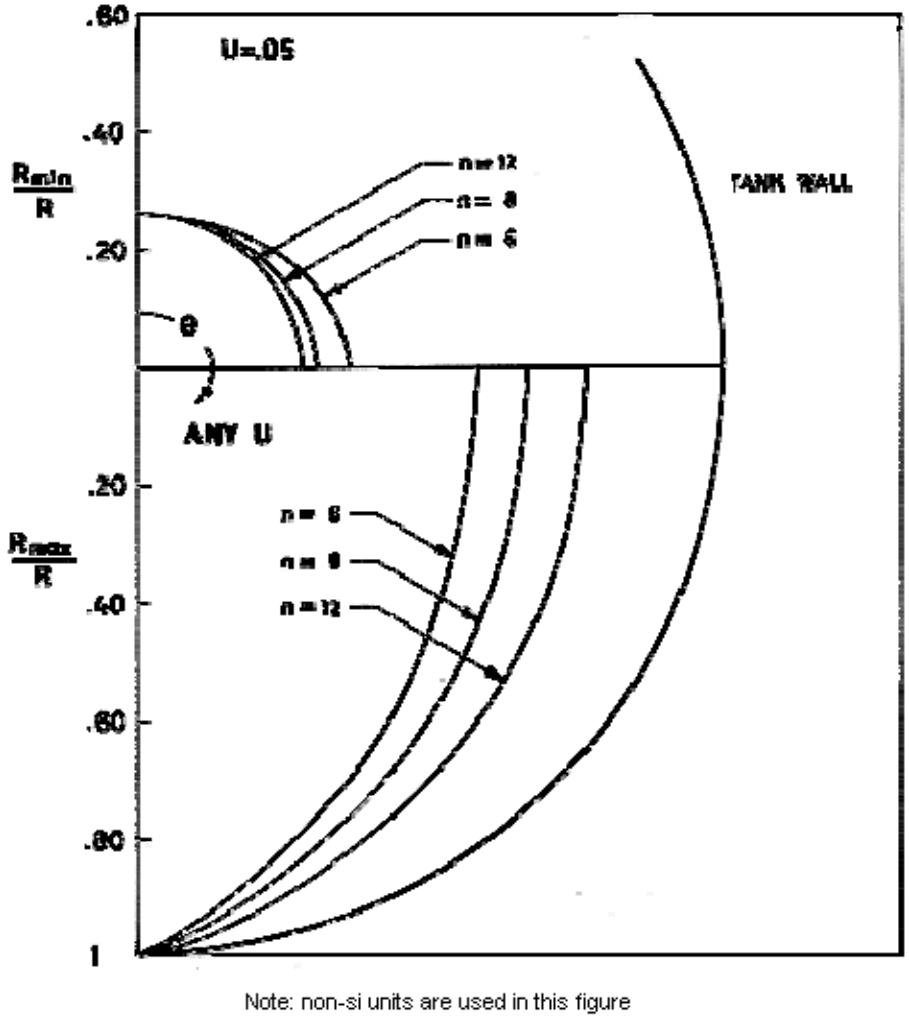

Note: non-si units are used in this figure

Figure 6-54: Limiting vane profiles, R_{min}/R and R_{max}/R for n = 6, 8 and 12 vanes. R_{min}/R has been calculated for an ullage U = 0,05. R_{max}/R is ullage-independent. After Tegart et al. (1972) [233].

In most cases the profile of the vane goes between these two limits. Nevertheless, in some instances the outer limit is exceeded near the root of the central post, for example when operation at larger ullages is required or when the pumping capability of the vane must be enhanced.

The restoring force of an "effective" vane profile can be estimated as follows:

1st. The finite number of vanes (6, 8, 12, ...) is substituted by an infinite number (central axisymmetric body) the radius R_o of which, measured from the tank center, increases with displacement angle, θ.

2nd. The geometry of the displaced and distorted bubble and the capillary forces acting on it are simplified so that the force becomes proportional to the difference in curvature between opposite ends of the bubble, as shown in Figure 6-55.

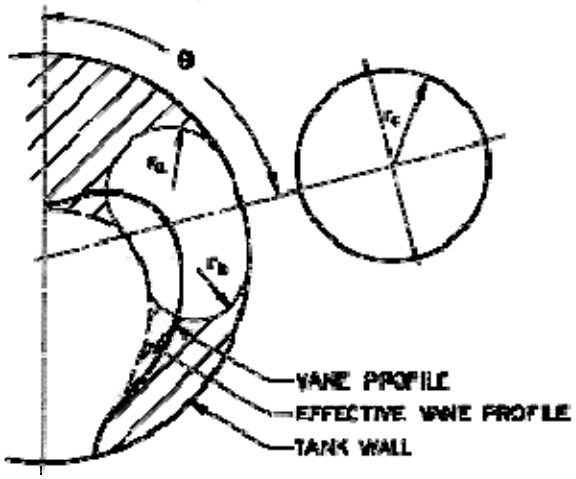

Figure 6-55: Simplified bubble geometry. The bubble is held by two contiguous vanes and shapes up as if it were held by the "effective" vane. From Tegart et al. (1972) [233].

The capillary pressure difference across the bubble is:

$$p_b - p_a = \sigma\left(\frac{1}{r_b}+\frac{1}{r_c}\right)-\sigma\left(\frac{1}{r_a}+\frac{1}{r_c}\right) \qquad [6\text{-}95]$$

Note: non-si units are used in this figure

thence,

$$\Delta K = \frac{1}{r_b}-\frac{1}{r_a} \qquad [6\text{-}96]$$

Note: non-si units are used in this figure

results to be proportional to the restoring force.

The definition of bubble shape is crucial. Unfortunately this is not discussed in the report by Tegart et al. (1975) [233].

When the ullage is not too large and R - $R_o(\theta)$ no too small, it can be assumed that the bubble is stabilized between two concentric spheres with radii R_o and R respectively. Thus, the bubble becomes axisymmetric, Figure 6-56, and its volume can be easily computed. The relationship between the ullage, U, and the angle, θ_a, which characterizes the bubble shape, becomes:

$$U = \frac{1}{2}\left[1-\left(\frac{R_o}{R}\right)^3\right]\left(1-\cos\frac{\theta_a}{2}\right)+\frac{1}{8}\left(1-\frac{R_o}{R}\right)^3 \left(\cos\frac{\theta_a}{2}+\frac{3}{4}\pi\frac{1+R_o/R}{1-R_o/R}\sin\frac{\theta_a}{2}\right) \qquad [6\text{-}97]$$

Note: non-si units are used in this figure

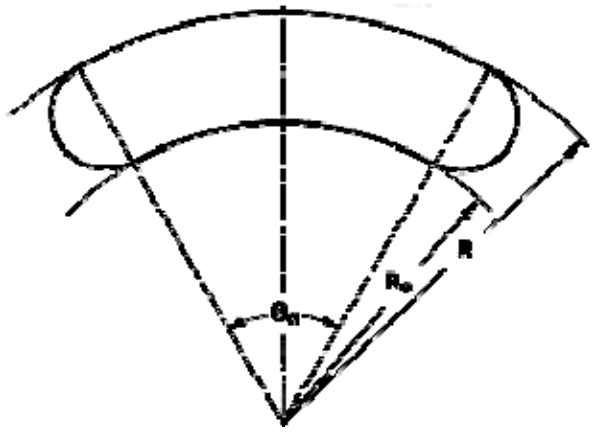

Figure 6-56: The ideal distorted axisymmetrical bubble.

Curves of θ_a vs. R_o/R for several values of the ullage, U, are shown in Figure 6-57.

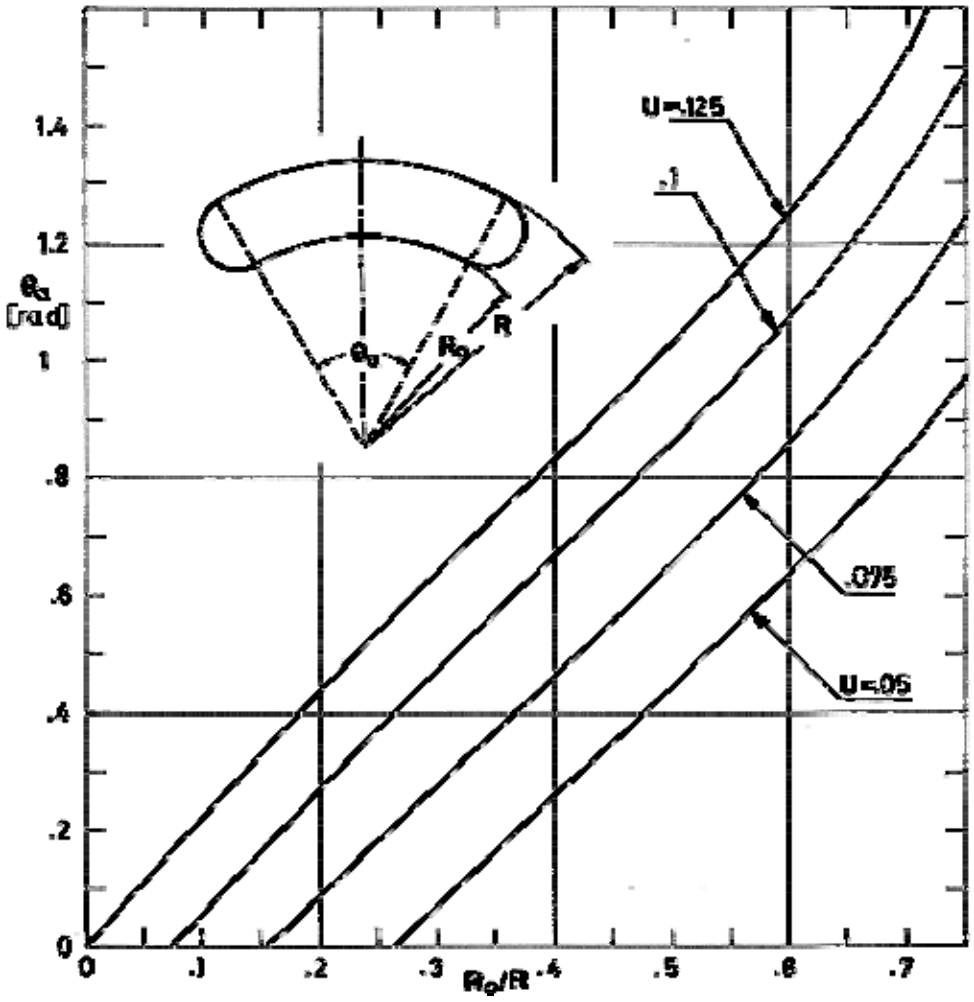

Note: non-si units are used in this figure

Figure 6-57: Angle θ_a which measures the distortion of the bubble vs. ratio, R_o/R, of inner body radius to tank radius. Calculated by the compiler.

Once $R_o(\theta)$ is defined, and θ_a calculated, the curvatures at both ends of the bubble (Figure 6-55) are given by (omitting the contribution of r_c)

$$\frac{1}{r_a} = \frac{2}{R - R_o\left(\theta - \frac{\theta_a}{2}\right)} \quad , \quad \frac{1}{r_b} = \frac{2}{R - R_o\left(\theta + \frac{\theta_a}{2}\right)} \qquad [6\text{-}98]$$

Note: non-si units are used in this figure

and ΔK can be calculated by means of Eq. [6-96] above.

Three vane profiles from Tegart et al. (1972) [233] are shown in Figure 6-58. The dimensionless restoring force $R\Delta K$ corresponding to each profile is also shown.

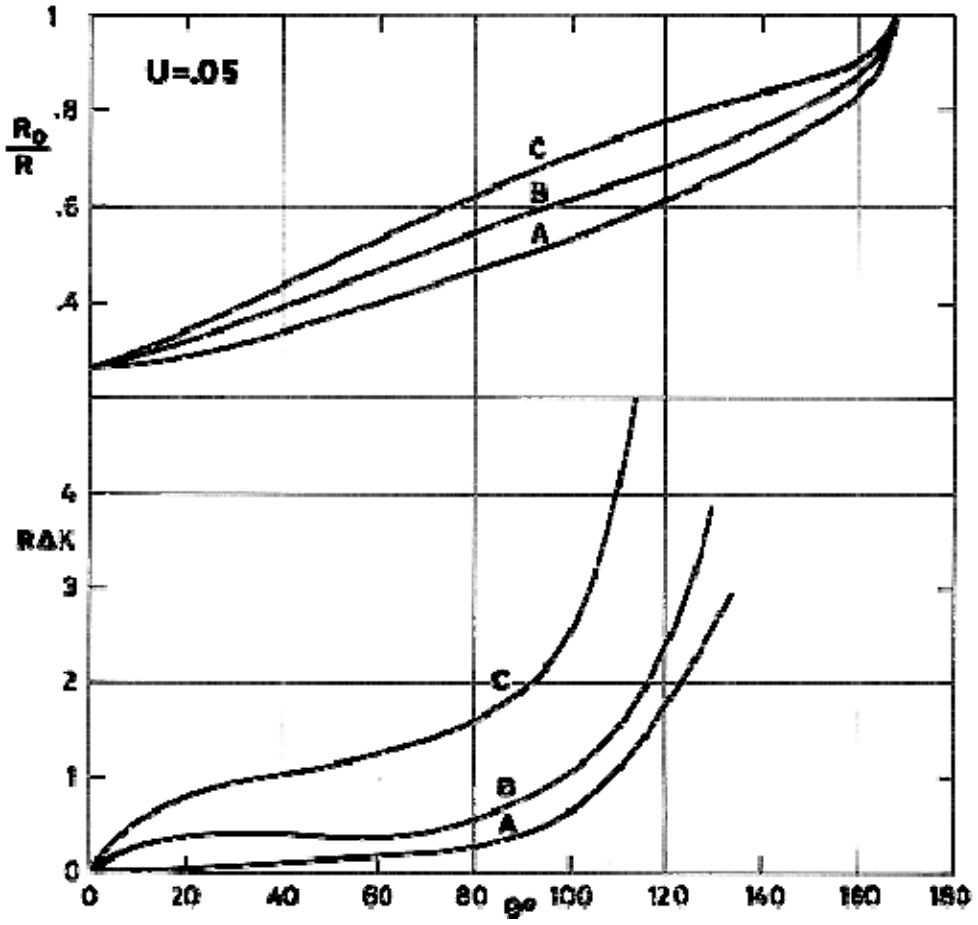

Note: non-si units are used in this figure

Figure 6-58: Typical effective vane profiles, *Ro*/*R*, and dimensionless restoring force, *RΔK*, vs. displacement angle, *θ*. The Figure has been replotted by the compiler after a representation in polar coordinates by Tegart et al. (1972) [233].

The results in Figure 6-59 have been calculated by use of the very simple theory which has been just presented. The profiles are given by the equation,

$$\frac{R_o}{R} = 1 - 2\sqrt[3]{U}\left[1 - \left(\frac{\theta}{k\pi}\right)^m\right] \qquad [6\text{-}99]$$

Note: non-si units are used in this figure

where k and m are two parameters, both close to unity, which individualize the members of the family. Other profiles could be considered. The forces $R\Delta K$ shown in the Figure seem to exhibit the same trends and orders of magnitude as those in Tegart et al. (1972) [233].

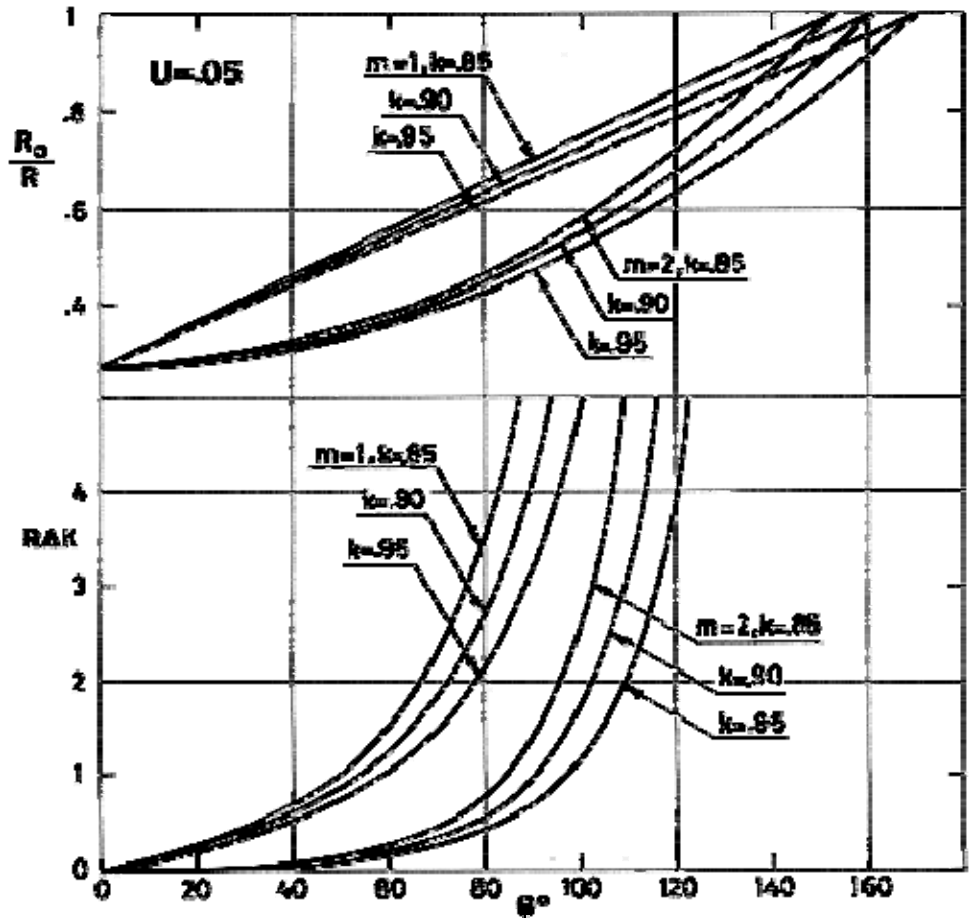

Note: non-si units are used in this figure

Figure 6-59: Typical effective vane profiles, R_o/R, and dimensionless restoring force, $R\Delta K$, vs. displacement angle, θ. The vane profiles have been calculated by Eq. [6-99] with the shown values of k and m. Forces have been deduced from Eqs. [6-96] to [6-98].

3rd. Given the number, n, of vanes, the "actual" vane profile is deduced by intersection of the envelope of the bubbles with couples of planes containing the vertical axis of the tank, forming an angle $2\pi/n$, and contacting symmetrically either end of the bubble.

Vanes are complex to design and difficult to manufacture and install, they are, however, highly reliable and provide a good ullage control.

6.4.5.5 Standpipe with vanes

This combined device is better than each alone. Vane number and profile are the same as for the vane and the performance is similar.

6.4.6 Empirical data for design

6.4.6.1 Surface tension

6.4.6.2 Bond length

Bond number, *Bo*, measures the relative importance of gravitational and surface tension forces (see Clause 6.4.7.1).

$Bo = \delta\rho g l/(\sigma/R)$

where $\delta\rho$ is the density difference, l the extension of the interface in the direction of gravity action (or its distance from the equipotential surface on which the two fluids have the same pressure), σ is the surface tension and R the smallest radius of curvature of the interface.

Usually, the Bond number is written as

$Bo = R_l/(L_b)^2$

with $L_b = [\sigma/(\delta\rho g)]^{1/2}$ the so called Bond length. When R and l are both smaller than the Bond length, gravity effects can be neglected and the configuration at rest is controlled by surface tension forces.

The term bond length appears, with a completely different meaning, concerning interatomic distances (Pauling & Pauling (1975)). Any confusion is avoided if capital *B* is used in Bond when referring to L_b.

Figure 6-60 to Figure 6-62 give the Bond lengths vs. temperature for the cryogens listed in Table 8-1, Clause 8.1.1, at saturation and under normal gravity conditions. Sources of data for drawing the Figures are indicated in Table 6-13. The Parachor approximation (Quayle (1953)) has been used when available data are incomplete (dotted lines in the Figures).

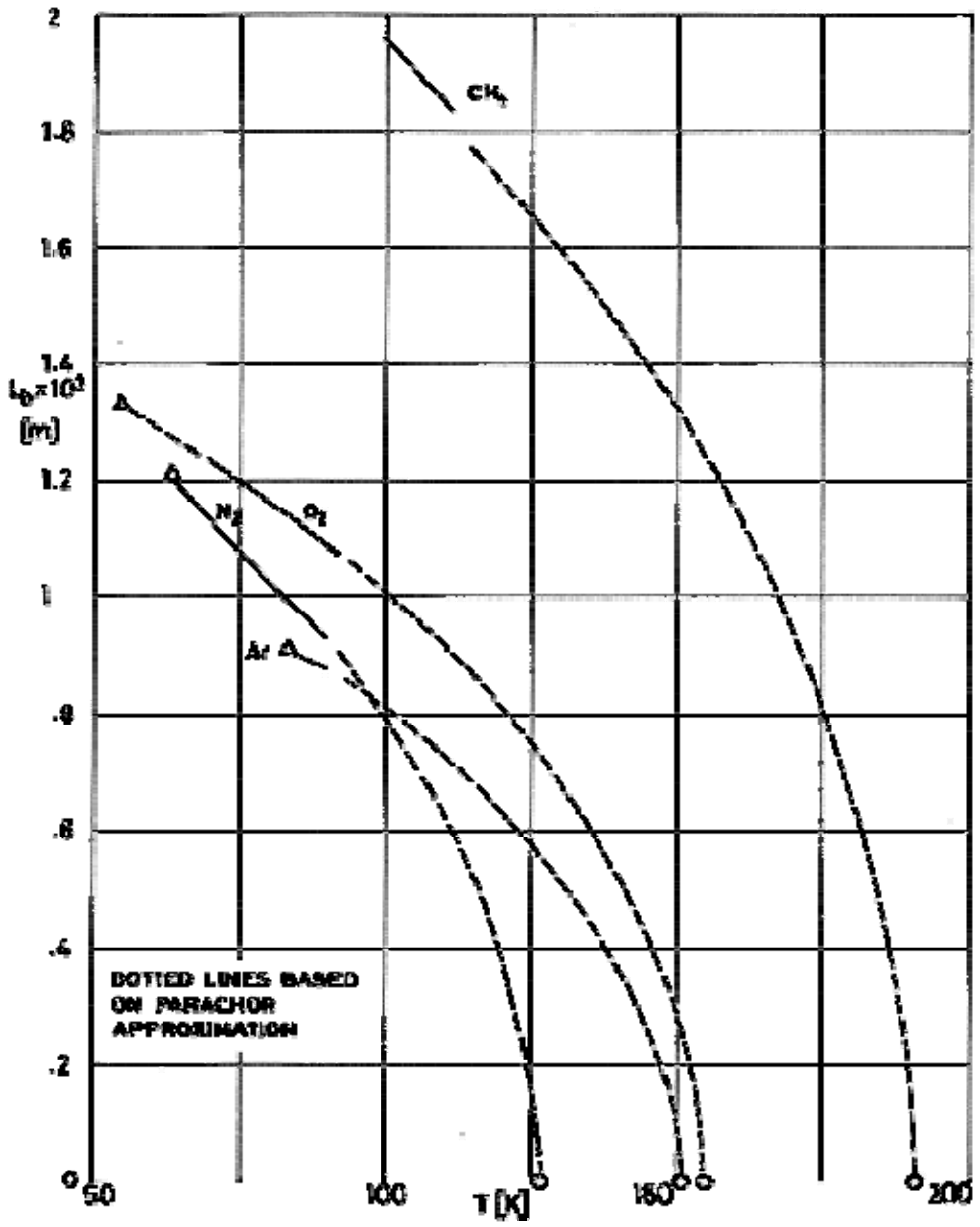

Note: non-si units are used in this figure

Figure 6-60: Bond length, L_b, as a function of T, for saturated Argon, Methane, Nitrogen and Oxygen.

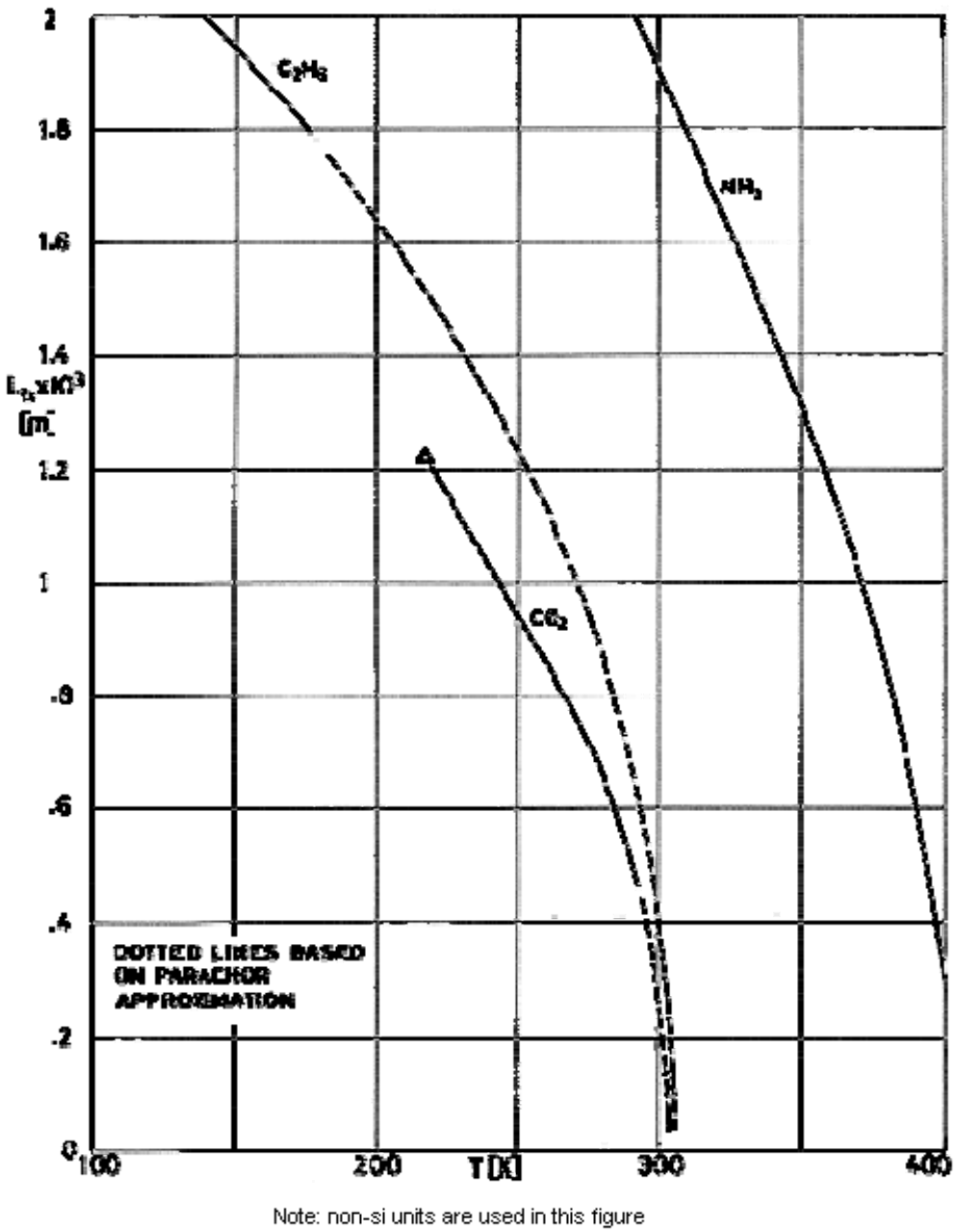

Note: non-si units are used in this figure

Figure 6-61: Bond length, L_b, as a function of T, for saturated Ethane, Carbon Dioxide and Ammonia.

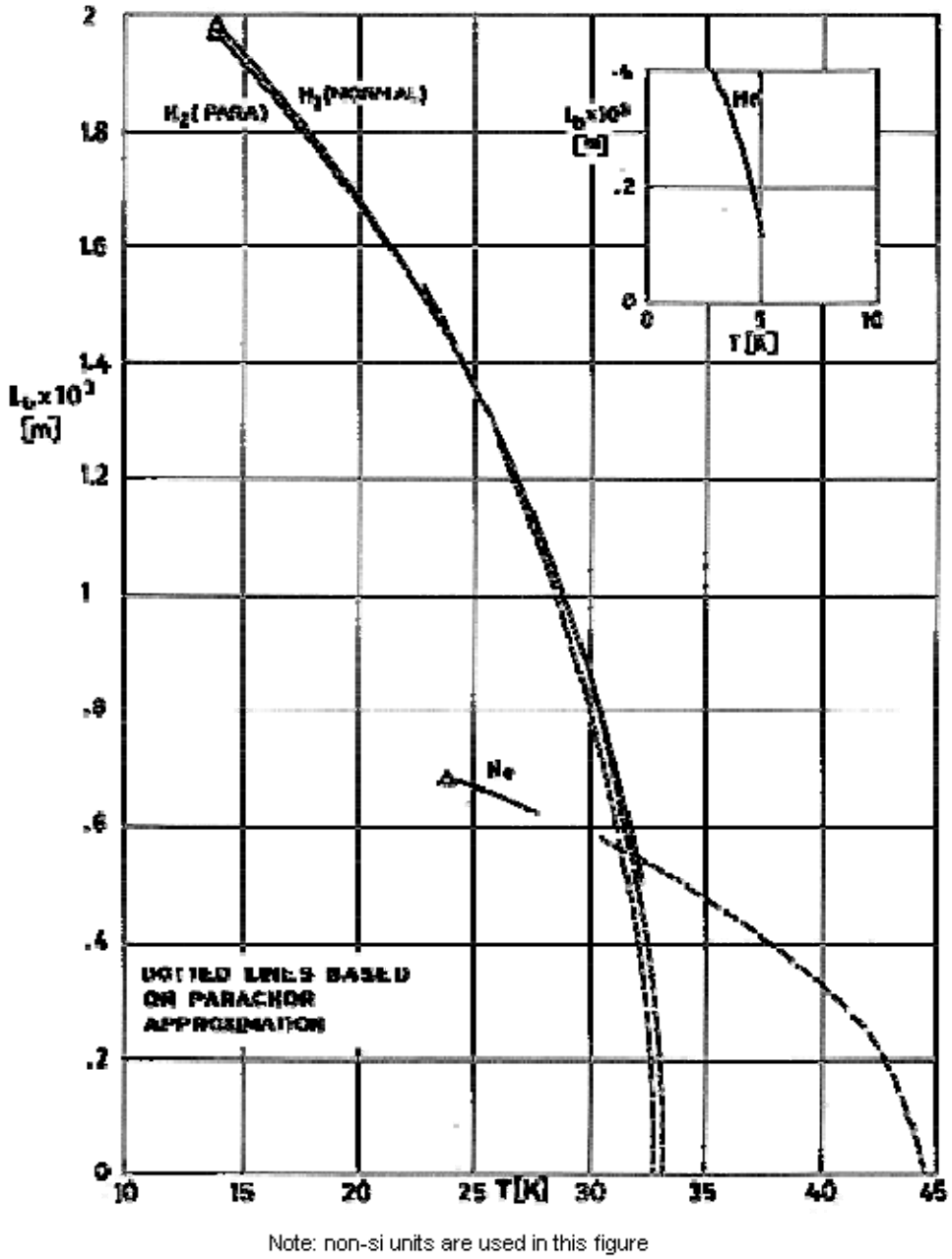

Note: non-si units are used in this figure

Figure 6-62: Bond length, L_b, as a function of T, for saturated Hydrogen, Helium and Neon.

Table 6-13: Sources of Data for Calculating Bond Lengths

	σ Reference Temp. Range [K]	$\rho_l - \rho_v$ Reference Temp. Range [K]	Parachor Reference
Ar Argon	Vargaftik (1975) [253] 84 K - 90 K	Vargaftik (1975) [253] 84 K - 150 K	From σ and $\rho_l - \rho_v$ data in the range 84 K - 90 K
CH_4 Methane	Vargaftik (1975) [253] 93 K - 113 K	Vargaftik (1975) [253] 91 K - 190,55 K	Quayle (1953) [188]
C_2H_6 Ethane	Vargaftik (1975) [253] 113 K - 183 K	Vargaftik (1975) [253] 150 K - 305,5 K	Quayle (1953) [188]
CO2 Carbon Dioxide	Kutateladze et al. (1966) [127] 223 K - 293 K	Kutateladze et al. (1966) [127] Vargaftik (1975) [253] 216,55 K - 304,19 K	Quayle (1953) [188]
H_2 Hydrogen Normal	Vargaftik (1975) [253] 15 K - 32,77 K	Vargaftik (1975) [253] 14 K - 33,23 K	From σ and $\rho_l - \rho_v$ data in the range 15 K - 25 K
H_2 Hydrogen Para	Vargaftik (1975) [253] 14 K - 32,98 K	Vargaftik (1975) [253] 14 K - 32,98 K	From σ and $\rho_l - \rho_v$ data in the range 19 K - 25 K
He Helium	Johnson (1961) [109] 2,5 K - 5,2 K	Vargaftik (1975) [253] 2,2 K - 5,18 K	Values of ρ_v not available above 5,18 K
N_2 Nitrogen	Vargaftik (1975) [253] 68 K - 90 K	Vargaftik (1975) [253] 63,15 K - 126,25 K	From σ and $\rho_l - \rho_v$ data in the range 70 K - 90 K
NH_3 Ammonia	ECSS-E-HB-31-01 Part 9 Clause 6.3 195,3 K -404 K	ECSS-E-HB-31-01 Part 9 Clause 6.3 195,3 - 404 K	N.A.
Ne Neon	Vargaftik (1975) [253] 24 K - 28 K	Vargaftik (1975) [253] 25 K - 44,4 K	From σ and $\rho_l - \rho_v$ data in the range 25 K - 28 K
O_2 Oxygen	Weast (1976) [260] 70 K - 90 K	Vargaftik (1975) [253] 54,35 K - 154,77 K	From σ and $\rho_l - \rho_v$ data in the range 70 K - 90 K

6.4.6.3 Wetting

Wetting of the solid by the liquid is crucial to the performance of any liquid retention system.

Wettability is measured by the liquid-solid contact angle. When the contact angle, θ, is close to zero, it is said that the liquid wets the solid. Unfortunately measurements of the apparent contact angle hardly yield reproducible values due to macroscopic disturbing effects.

The contact angle depends on the liquid-vapor surface tension, and on the characteristics and cleanliness of the surface.

Figure 6-63 indicates that an almost linear relationship exists between $\cos\theta$ and σ for homologous series of liquids on the same solid. The critical surface tension is that corresponding to $\cos\theta = 1$. If the surface tension is less than critical, the liquid spreads on the solid surface.

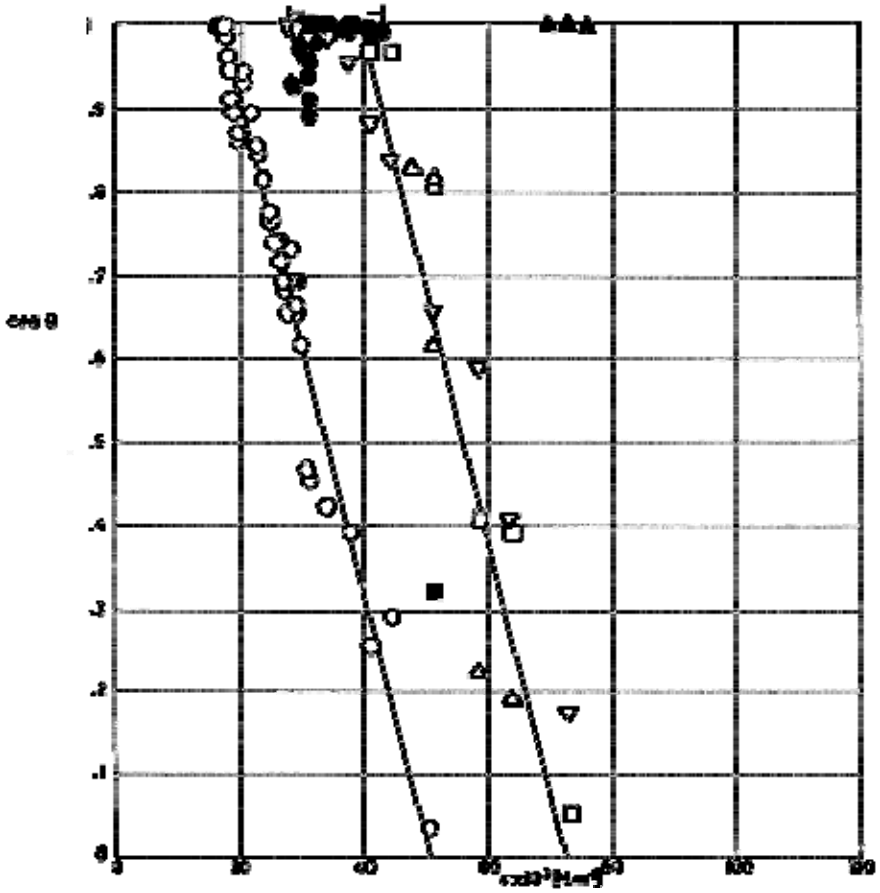

Note: non-si units are used in this figure

Figure 6-63: Relation between contact angle, θ, and surface tension, σ, for several liquids on the quoted surfaces.

Explanation

Key	Surface	Comments	References
○	Polytetrafluorethylene (TFE)	Wide Variety of liquids. T = 293 K	Fox & Zisman (1950), Ellison & Zisman (1954)

Key	Surface	Comments	References
□	Polyvinylchloride (PVC)	T = 293 K	Ellison & Zisman (1954)
△	Polyethylene (PE)		
▽	Polyvinylfluoride (PVF, Tedlar)		
●	Sapphire	T = 293 K	Fox, Hare & Zisman (1955)
Marked line	SS (■ SS with fatty acid monolayer) Brass		
▲	Quartz, Gold, Silver		Enya et al. (1982) [64]

Low-free-energy surfaces have small critical surface tensions, whereas high-free-energy surfaces (like most metals) have large critical surface tensions, but since they have large adsorption forces, they are prone to contamination. The resulting film-coated surface is a low-free-energy surface.

Normally, surface tension decreases with increasing temperature so that liquids which do not spread at lower temperatures could spread on the same surface at higher temperatures.

6.4.6.4 Compatibility

Compatibility of cryogens with their containers should be carefully considered. Many cryogens, particularly propellants, are extremely reactive.

The resistance of many alloys to these liquids depends on the formation of an inert corrosion-resistant barrier coating. In several cases the metals could decompose the liquid. Finally, several metal-oxidizer combinations may ignite under impact, not to mention that there are cryogens which are hazardous materials and require careful handling.

Hydrogen embrittlement is considered in Clause 9.3.1 and material compatibility with Oxygen in Clause 1.1.1 and 9.2.2. Compatibility data of materials with Ammonia (NH_3) are summarized in Table 6-14, below.

Table 6-14: Compatibility of Materials with Ammonia. Non-metals.

Material	Temperature, [K] [a]							
	Gas				Liquid			
	Class 1	Class 2	Class 3	Class 4	Class 1	Class 2	Class 3	Class 4
Organic Materials Rubber, Hard Linings				297			297	
Rubber, Soft Linings				297				297
Rubber, Natural		297		HOT				
GRS *		297		HOT				
Neoprene		297		HOT				
Butyl Rubber		297		HOT				
Thiokol			COLD					
Glass Fabric and Silicone Elastomer		HOT						
Silicone Greases		HOT						
Haveg 41 Epon	373							
Silicone Elastomer		297						
Silicone Resins			297					
Teflon	HOT							
Cork				297				
Vinyl Copolymers		HOT				HOT		
Phenolics		HOT				HOT		
Furans		HOT				HOT		
Polyethylene		HOT				HOT		

Material	Temperature, [K] [a]							
	Gas				Liquid			
	Class 1	Class 2	Class 3	Class 4	Class 1	Class 2	Class 3	Class 4
Kel-F		HOT				HOT		
Vinylidene Chloride			COLD				COLD	
Sulfur Cement			COLD				COLD	
Bitominous Composition			COLD				COLD	
Polystyrene				297				
Polyesters				297				
Phenol Formaldehyde				297				
Nonmetals Glass	373							
Stoneware	373							
Karbate	1366							
Carbon	1366							
Graphite	1366							

NOTE * Glass Fabric and Silicone Rubber.

[a] Maximum temperature permissible for a given material in classes 1 to 3. Minimum temperature at which a give material becomes class 4.

Compatibility Classification for Non-Metals

	Class			
	1	2	3	4
Volume Change Percent	0 to +25	-10 to +25	-10 to +25	< -10 or > +25
Durometer Reading Change	± 3	± 10	± 10	<-10 or > +10

Effect on Cryogen	None	Slight Change	Moderate Change	Severe
Visual Examination	No Change	Slight Change	Moderate Change	Severely blistered or cracked, dissolved
General Usage	Satisfactory	Satisfactory for repeated short term usage	Satisfactory for short time usage	Unsatisfactory

Table 6-14 (Cont.) Compatibility of Materials with Ammonia. Metals

Material	**Temperature, [K]** [a]							
	Gas				**Liquid**			
	Class 1	**Class 2**	**Class 3**	**Class 4**	**Class 1**	**Class 2**	**Class 3**	**Class 4**
Aluminium	373	311	353	353			353	353
302 Stainless Steel	297			<755				
304 Stainless Steel	589			<755				
316 Stainless Steel	589			<755				
347 Stainless Steel			297					
410 Stainless Steel	589			728				
430 Stainless Steel	589			<755				
Worthwite	297			<755				
Durimet 20	297			<755				
Carpenter 20	589							
Mild Steel	589			<755		297		
Cast Iron	589			<755		297		
Si - Iron	373	297					297	

Ni - Cast Irons, Low Cu	297					344		
Ni - Cast Irons, High Cu	297							ALL
Nickel	533		533	<866				297
Inconel	644		866	866		297		
Monel	533		533	<866				297
Hastelloy B	589	589		811				
Hastelloy C	589	589		811				
Hastelloy D	589	589		811				
Hastelloy F		589		811				
Chlorimet 2-3	297							
Nickle-Copper	297							
Copper		297		HIGH				LOW
Yellow Brass		297		HIGH				LOW
Red Brass		297		HIGH				LOW
Tin Bronze		297		HIGH				LOW
Al Bronze		297		HIGH				LOW
Si Bronze		297		HIGH				LOW
Cu-Nickel		297		HIGH				LOW
Gold	373				HIGH			
Lead		297		400		297		
Dow Metal C		LOW						
Dow Metal F-1		LOW						
Dow Metal H		LOW						
Dow Metal J-1		LOW						
Dow Metal M		LOW						

Platinum	373				HIGH			
Ir - Platinum	HIGH				HIGH			
Rh - Platinum	HIGH				HIGH			
Silver	297							HOT
Ag - Cu				ALL				ALL
Titanium	353							
Tantalum	373			HIGH	373		HIGH	
Zinc	297							
Zirconium	353							

[a] Maximum temperature permissible for a given material in classes 1 to 3. Minimum temperature at which a give material becomes class 4.

Compatibility Classification for Metals

Class	Rating	Penetration Rate [mils/yr] [b]	Decomposition of Cryogen	Shock Sensitivity
1	Excellent	< 1	No	No
2	Good	< 5	No	No
3	Fair	5 to 500	Some	No
4	Poor	50	Extensive	Yes

[b] 1 mil = 25,4 x 10^{-6} m.

NOTE From Runck (1965) [203].

6.4.7 Testing

Test of phase separation devices to be used onboard spacecraft seems at first glance to depend on the ability to reproduce the low gravity levels which prevail in orbital flight. This is a hard task particularly for times exceeding a few seconds. Nevertheless, engineering judgement and dimensional analysis can be profitably used to simulate in orbit behavior through 1-g tests.

1. When fluid motion is forced so that the imposed pressure differences are larger than hydrostatic pressure differences at 1-*g*, the effect of the gravity level is irrelevant. System behavior can be understood in terms of laboratory observations.
2. Systems which exhibit similar performances working in their normal and in up-side down position are not very sensitive to the gravity level.

3. Matters are quite different when imposed pressure differences are low and non-planar interfaces exist, as in the case of capillary-dominated configurations. In particular, interfaces are larger under reduced gravity since the weight of the fluid contained by surface tension forces is smaller. Even in this case useful results can be obtained on Earth by reproducing the dominant dimensionless parameters.

6.4.7.1 Dimensionless parameters

For purely mechanical problems (no gradients of temperature and/or concentration), and when interfaces are present, the relevant dimensionless parameters are:

Bond number: ratio of gravity to surface tension forces,

$Bo = \delta\rho g l/(\sigma/R)$.

Capillary number: ratio of viscous to surface tension forces,

$Ca = \mu V/\sigma$.

Weber number: ratio of inertia to surface tension forces,

$We = \rho V^2 l/\sigma$.

where V is a characteristic velocity, l and R are characteristic length (usually l is measured in the direction of gravity action and R the smallest radius of curvature of the interface), ρ is the density of the denser liquid, $\delta\rho$ the density difference, μ the surface tension and σ the dynamic viscosity of one of the liquids (normally the denser one).

To exactly reproduce all three parameters is usually not easy nor required. In hydrostatics the controlling parameter is the Bond number, Bo.

Reduced Bond number operation can be achieved on Earth by reducing l (which is often impractical) or $\delta\rho$ (Plateau simulation). Another technique consists in using a colloidal suspension of magnetic particles in the test fluid which is suported by an electromagnetic field, the strength of which is adjusted to simulate low-g body forces on the fluid.

In the case of bulk flow, when no interfaces appear, the relevant parameters for purely mechanical problems are:

Froude number: ratio of inertia to gravity forces,

$Fr = V^2/gl$.

Reynolds number: ratio of inertia to viscous forces,

$Re = \rho V l/\mu$.

Eckert number: ratio of pressure to inertia forces,

$Ec = p/\rho V^2$,

where l is a characteristic length, p a reference pressure and the other variables are defined as above.

Sometimes a Grashof number, Gr, is used, $Gr = Re/Fr$.

The reproduction of these numbers does not present a great difficulty via an appropriate choice of the characteristic length, l, the working fluid, μ and ρ, the forced flow velocity, V, and the pressure level, p.

6.5 Existing systems

6.5.1 Introduction

There are a vast variety of cryogenic systems, for terrestrial and space applications, whose insulation is cooled by an evaporating cryogen. Stored cryogens in space have long been used for several purposes: rocket propulsion, environmental control systems, and fuel cells. Liquid neon was used for Gemini flights 6 and 7 to provide 32 K cooling for interferometer spectrometers. Nevertheless, only in recent years has development proceed on VCS Dewars for long-term cooling of detectors and optical components.

Stored solid-cryogen systems offer distinct advantages over stored liquid systems for 10 K to 90 K cooling in space (see Clause 6.1 in this Clause). Liquid helium (He^4) is used to cover the 1,8 K -4,2 K temperature range.

In many instances the VCSs are cooled by the vapors from the cryogen stored in the inner container. Some other systems, however, use a guard cryogen in addition to the primary cryogen. Figure 6-64 shows a schematic of a dual stage solid-cryogen cooler. The primary cryogen maintains the desired sensor temperature, while the secondary cryogen, which has a substantially higher heat of sublimation than the primary cryogen, intercepts heat from the outer shell and provides a low temperature environment around the primary stage.

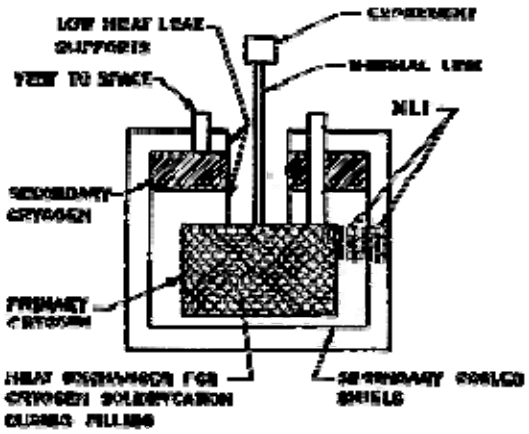

Figure 6-64: Sketch of a dual stage solid cooler. From Nast et al. (1976) [161].

Figure 6-65 depicts two configurations of He^4 coolers for instruments. That in Figure 6-65(a) is a single-stage cooler whose toroidal shape allows the IR telescope to be surrounded by the cooler. Figure 6-65(b) shows a cooler employing a solid cryogen secondary stage.

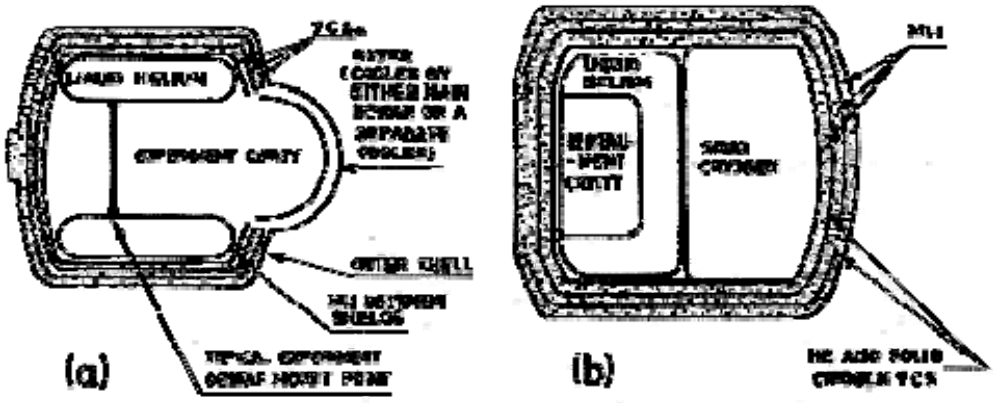

Figure 6-65: Liquid helium (He^4) coolers. a) Single stage. b) Dual stage. From Sherman (1978) [216].

A critical problem in the performance of the VCS insulation systems is the attachment of the cooled shields to the cooling duct. This attachment can be achieved either normally or tangentially.

1. In the normal attachment mode the cooled shields reach the cooling duct perpendicularly to it. The thermal contact can be achieved either joining the shields to the venting duct, by soft soldering or brazing, as in Figure 6-17, or through heat stations across the piping penetrations which are thermally bonded to both a support tube and the cooling duct, Figure 6-66.

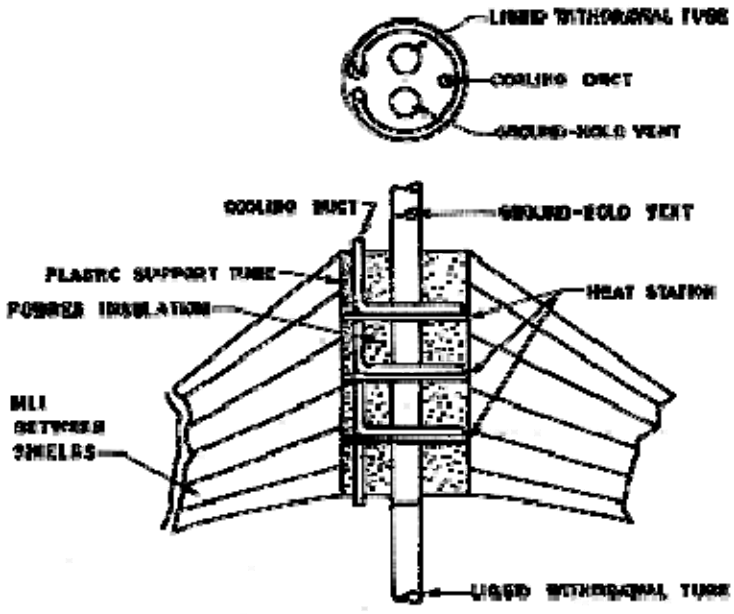

Figure 6-66: Normal attachment of the VCSs to the cooling duct through heat stationis. From Glaser et al. (1967) [75].

Normal attachment is used in small systems having several VCSs.

2. In the tangential attachment mode the venting duct, usually in the shape of a cooling coil, is soldered or cemented to the metallic shields. The venting duct, which originates

somewhere in the neck support, spirals around the innermost shield. After this spiral, the duct is attached for the next one around the nearest shield. It makes another spiral before reaching the next shield, and so on, Figure 6-67.

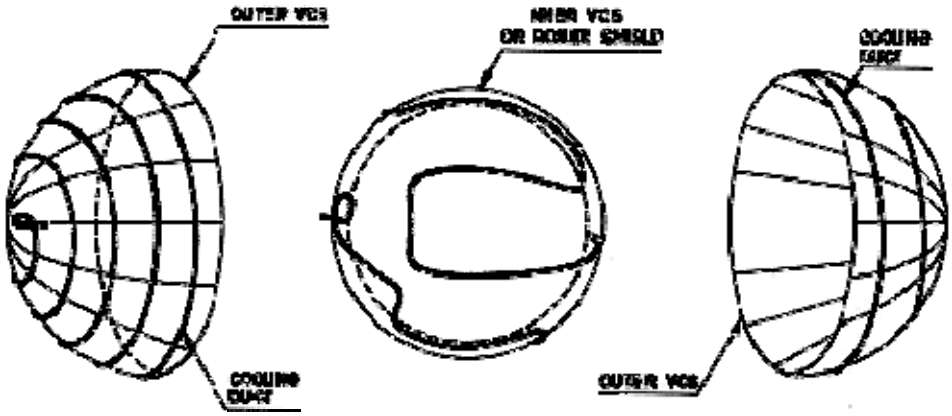

Figure 6-67: Tangential attachment of the cooling duct to the shields. Sketched by the compiler after Hopkins & Chronic (1973) [94].

Several ideas have been set forth in order to increase both the availability and the performance of solid cryogen coolers. The multi-mission cooler (Sherman (1978) [216]) would be reusable and compatible with a variety of cryogens to cover a 10 K to 90 K temperature range with a one to three years lifetime. Another idea, which would increase the lifetime of solid-cryogen coolers has been considered by Sherman & Brennan (1976) [219]. It consists in using a heat pipe-radiator module to cool either the outer shell of the cooler or an intermediate shield.

6.5.2 Data on existing systems

Data on several spaceborne stored-cryogen systems (two dual stage solid-cryogen coolers and three liquid helium coolers) are presented in the following pages.

The information on each cooler is arranged as follows: the left hand side page presents a brief description and comments concerning the system involved, whereas the right hand side page contains a summary table and a sketch of the system.

The most extensively documented among the systems presented was flown on Nimbus F (LOCKHEED VCS DEWAR 1975). In addition to a complete description of the system and its performance, due to Nast et al. (1976) [161], a theoretical study of the gasdynamic behavior of the methane venting has been published by Rae & Dunn (1976) [189]. The aim of this study was to estimate the torques applied to the spacecraft as a result of the vented gases impinging on several surfaces near the exit point.

6.5.2.1 Lockheed VCS Dewar 1968

DESCRIPTION AND COMMENTS. This IR Detector Cooler, developed by Lockheed Missiles and Space Co., Palo Alto. Calif., is designed to operate at 50 K for 1 year, providing a cooling rate of 0,025 W.

The cooler consists of three main parts:

1. A container with solid argon, for cooling the IR detector via a cooper thermal link.

2. Another container with solid carbon dioxide, which is the source of the vapors which cool the insulation surrounding the solid argon container.

3. A liquid nitrogen heat exchanger for the solidification of both cryogens during the filling process.

The usefulness of solid carbon dioxide as a source of cooling vapors arises from the fact that the latent heat of sublimation of carbon dioxide is approximately three times that of argon, whereas their densities are very similar.

The solid argon and solid carbon dioxide containers are from stainless steel sheets $0{,}61 \times 10^{-3}$ m thick (cylindrical surfaces) and $0{,}91 \times 10^{-3}$ m thick (top and bottom). Both containers were designed to withstand internal and external pressure differences up to 10^5 Pa. The solid carbon dioxide container is placed above the solid argon container, and is thermally connected to a $3{,}81 \times 10^{-5}$ m thick copper shield which surrounds the solid argon container. Thence, this solid argon container, which is gold plated, is subjected to solid carbon dioxide radiation temperature. A $5{,}08 \times 10^{-2}$ m thick MLI thermally insulates both the cooled copper shield and the solid carbon dioxide container. This MLI consists in 150 layers of double-aluminized Mylar with Tissuglas spacers. A cage of stainless steel tubing ($1{,}59 \times 10^{-3}$ m outer diameter and $0{,}254 \times 10^{-3}$ m wall thickness), structurally joined to the solid carbon dioxide container, supports the cooled copper shield and the MLI in the area surrounding the solid argon container. A second radiation shield, with a construction similar to that of the abovementioned outer shield, is placed amidst the solid argon container and the outer shield. The inner shield is supported by a system of Nylon threads.

The solid carbon dioxide container is supported by a cantilever beam with a fixed end support and concentrated load at full span. The beam is made from fiber-glass filament wound structure impregnated with an epoxy resin. Its internal diameter is uniform, $4{,}37 \times 10^{-2}$ m, whereas its thickness varies from $1{,}14 \times 10^{-3}$ m at its clamped end to $0{,}305 \times 10^{-3}$ m at its free end. Aluminium flanges are fastened to each end of the beam with epoxy adhesive. The beam is bolted to the cooler support flange and to the carbon dioxide container through these flanges.

The solid argon container is supported from the bottom of the solid carbon dioxide container by three fiber-glass-epoxy laminate columns, $12{,}7 \times 10^{-3}$ m diameter and $0{,}51 \times 10^{-3}$ m wall thickness. In order to increase the thermal path length as far as possible, these columns extend from the bottom of the carbon dioxide container to the bottom of the argon container.

The beam supporting the carbon dioxide container is also used to route the four fill and venting lines (two for the liquid nitrogen heat exchanger, one for the solid carbon dioxide container, and the last one for the solid argon container). Tubing is stainless steel, except for several straight portions, which are Mylar aiming at reducing heat leaks.

The containers, whose filling is made with the cryogens in the gaseous phase, are cooled -during the filling process- with liquid nitrogen flowing through a heat exchanger fashioned from $0{,}653 \times 10^{-3}$ m diameter stainless steel tubing soldered to the outer walls of the container. To provide good thermal contact between the liquid nitrogen heat exchanger and both cryogens -during the cool down process- the containers are partially filled with cooper expanded foam. The same copper foam provides good thermal contact during the mission between solid argon and copper thermal link with the IR detector. The argon gas is liquified and subsequently solidified during cool down. Argon must be continuously supplied in order to maintain a gas pressure in excess of $0{,}685 \times 10^5$ Pa (Argon triple point pressure). In this manner, voids occurring because of solidification contraction are being continuously filled. Solid carbon dioxide is grown directly from the vapor phase. To prevent the growing solid carbon dioxide from blocking the feeding line, the inlet manifold is located near the innermost section of the container, as distant as possible from the liquid nitrogen heat exchanger.

The system has been tested. Table 6-15 below compares predicted to measured characteristics.

Table 6-15: Characteristics of the Lockheed VCS Dewar

	Design Value	Measured Value
Detector Operating Temperature [K]	50	52
Allowable Detector Cooling Load [W]	0,025	0,0176
Heat Leak to Solid Argon [W]	0,015	0,0286
Heat Leak to Solid Carbon Dioxide [W]	0,076	0,074
Total Mass (Outer Vacuum Jacket Excluded) [kg]	13,57	15,47

NOTE Reference: Caren & Coston (1968) [36].

MANUFACTURER AND/OR DEVELOPER	Lockhedd Missiles and Space Company [a]
PRIMARY USE	IR Detector Cooler
CRYOGEN	Solid Argon and Solid CO_2
NATURE OF PROGRAM	Construction of a Prototype
CURRENT STATUS OF PROGRAM	Prototype Tested by March 1967

OUTER TEMPERATURE [K]	300	NUMBER OF VCS	1
OPERATING TEMPERATURE [K]	50 [b]	DETECTOR COOLING LOAD [W]	0,025
OPERATING PRESSURE [Pa]	20 [b]	TOTAL HEAT LEAKS [W]	0,015 [b] 0,076 [c]
LIFETIME [h]	8760 (1 yr)	SYSTEM CONFIGURATION	Cylindrical
TOTAL SYSTEM MASS [kg]	13,57	SYSTEM DIMENSIONS [m] Length/Diameter	0,235/0,235
MASS OF CRYOGEN [kg]	6,22 [b] 3,99 [c]		

[a] Palo Alto. California. USA.

[b] Corresponds to Solid Argon.

[c] Corresponds to Solid CO_2.

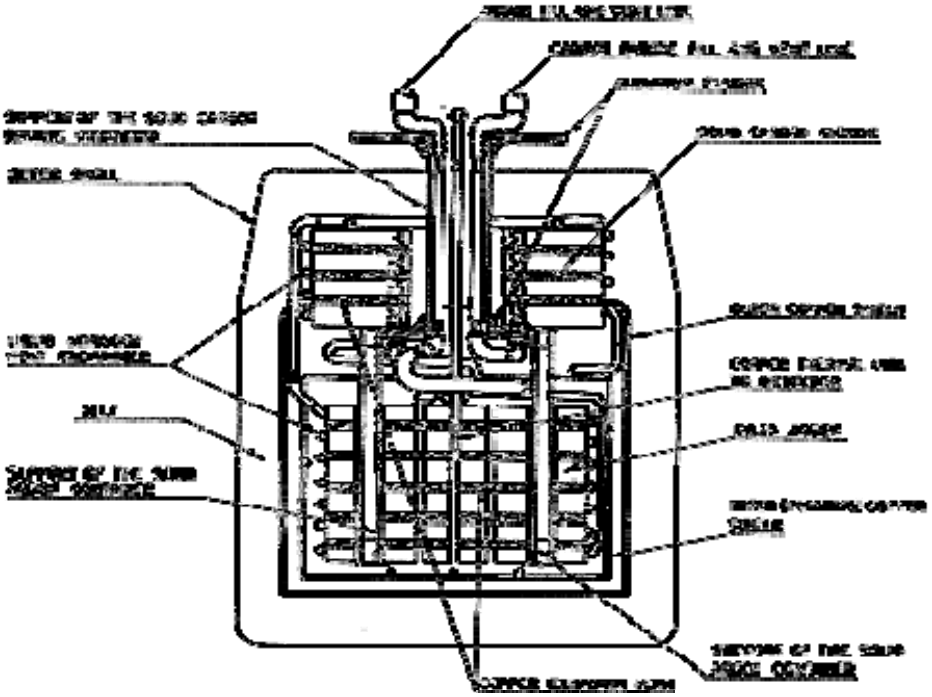

6.5.2.2 LOCKHEED VCS DEWAR 1975

DESCRIPTION AND COMMENTS. This dual stage IR detector cooler, developed by Lockheed Missiles & Space Company, Inc. Palo Alto. Calif., has been employed to cool to 63-67 K a tri-metal detector array and the associated focusing optics and filters, and also to cool at 152 K other optical elements. The cooling rate provided to the detector was 0,043 W. The system was placed into orbit on the Nimbus F Spacecraft.

The cooler consists of a primary cryogen (solid methane) and a secondary or guard cryogen (solid ammonia) whose pressure is maintained below the triple point in order to prevent liquid formation and coolant loss in the microgravity environment. The primary cryogen maintains the sensor temperature at 65 ± 2 K. The secondary cryogen provides a low temperature environment around the primary stage and cools the optics of the detector.

An open cycle liquid nitrogen coolant loop for ground operation is used for cooling purposes during filling, and for maintaining the cryogens in a non-vented condition during vehicle integration and checkout.

The final configuration of the cooler is shown in the next page. The main components are: the detector capsule assembly (DCA), the fiber-glass tube supporting structure, the tanks containing the primary and the secondary coolants, a VCS grounded to the ammonia tank, multilayer insulations (MLI) around the tanks and fiber-glass support tubes, plumbing lines, outer-shell and mounting plate. Fiber-glass tube 1 connects the main support flange to tube 2 which is connected to the ammonia tank. Fiber-glass tube 3 connects the ammonia tank to the tube 4, which is connected to the methane tank. An aluminium tube, thermally grounded to the ammonia tank, is used to decrease the heat transfer between tubes 2 and 3 and to cool the optics of the detector. Slitted MLI is used between tubes: slitting aims at reducing the lateral heat transfer in the MLI. MLI also insulates the methane tank from the ammonia tank and its grounded shields, and insulates the ammonia tank and shield from the outer shell.

The total mass is 24 kg, including 5,4 kg of solid ammonia and 6,4 kg of solid methane (the launched mass of solid methane was, however, 5,8 kg). The diameter of the cooler is 0,356 m and its length 0,654 m.

The DCA interfaces with the cooler through two shrink-fit connections. The first one connects the detector focal plane to the methane tank, and the second connects the DCA thermal guard and optics to a thermal path toward ammonia tank. The DCA can be removed easily at room temperature, while at operational temperatures the differential contraction on the shrink-fit members provides thermal contact and structural integrity.

Support tubes were made of 1543/E787 fiber-glass. The tanks were made of 6061 aluminium. Vent lines are of convoluted Teflon, which minimizes heat leaks and retains a high degree of flexibility at cryogenic temperatures. The methane fill/vent Teflon tube goes from the methane tank through the MLI, then to the ammonia tank, where it is thermally grounded, and through the ammonia MLI to space. The ammonia fill/vent Teflon tube goes from the ammonia tank through the ammonia MLI to space. The sensible heat of the vent gas is used to remove heat from the ammonia tank. Effective vapor cooling of both vent lines and of the MLI also occurred.

The MLI of the tanks consists of double aluminized Mylar-Tissuglas. Layer density was 4300 m^{-1} and layer thickness 25,4x10^{-3} m. The insulation was applied to the tanks by spirally wrapping the layers, goring the ends, and then forming butt joints using aluminized Mylar tape. This process was repeated ten layers at a time (up to 110 layers) with the gore joints staggered to minimize radiation heat transfer through the gaps.

The vacuum shell consists of a 6061 aluminium cylinder with a spun elliptical dome bonded to the cylinder, and a flange which contains an 0 ring and provides the main vacuum seal.

The mounting plate is a 6061 aluminium web stiffened structure to which the exterior plumbing, outer shell, and cooler are attached.

The cooler was launched aboard the Nimbus F vehicle on June 12, 1975. At the time of launch the methane and ammonia were 73 K and 137 K respectively. On the fourth orbit the explosive valve venting the methane to space was fired, and the initial high methane flow rate temporally upset the spacecraft in the roll axis, but control was re-established after a short period of time.

Table 6-16 shows the predicted heat loads through the different components. The temperature history of the infrared detectors and the optics is presented in Figure 6-68. The detector remained within the specific temperature for over six months. The temperature rise near the end of life is believed to be due to the increasing temperature gradient between the small remaining volume of solid cryogen and the container walls. The temperature rise occurred after approximately seven months, when the methane was completely depleted. The ammonia lifetime exceeded the methane by a large value, as shown in Figure 6-68. The ammonia temperature was constant within the data resolution (0,8 K) until methane was exhausted, at which time tha ammonia reached a new equilibrium temperature.

Table 6-16: Predicted Heat Loads

	Q x 10^3 [W]	
	Ammonia Gross *	**Methane Net**
MLI	214	29
Fiber-glass Supports	36	31
Radiation	41	13
Vent Gas	–27	--
Dexiglas Intermediary	12	--
Slitted MLI	13	12
LN_2 and Vent Lines	16	4
Total	305	89

NOTE * The net balance on the ammonia, which includes heat losses to the methane, is calculated to be 0,226 W.

Reference: Nast, Barnes & Wedel (1976) [161].

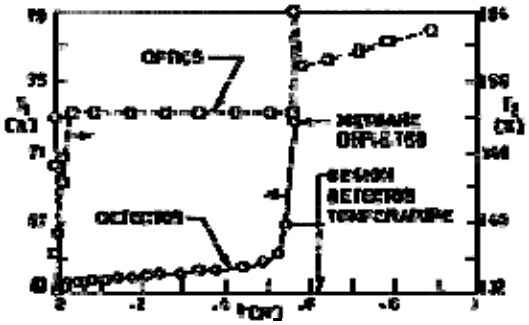

Note: non-si units are used in this figure

Figure 6-68: Detector, T_1, and optics, T_2, temperature vs. orbital time.

MANUFACTURER AND/OR DEVELOPER	Lockheed Missiles and Space Company [a]
PRIMARY USE	IR Detector Cooler
CRYOGEN	Solid Methane and Solid Ammonia
NATURE OF PROGRAM	Development of a Flight Model
CURRENT STATUS OF PROGRAM	Flown in June 1975 on Nimbus P

OUTER TEMPERATURE [K]	300	NUMBER OF VCS	1
OPERATING	63,5-64,5 [b]	DETECTOR COOLING	0,043

TEMPERATURE [K]	152,4 [c]	LOAD [W]	
OPERATING PRESSURE [Pa]		TOTAL HEAT LEAKS [W]	0,089 [b] 0,226 [c]
LIFETIME [h]	5040 [b] (7 mo)	SYSTEM CONFIGURATION	Cylindrical
TOTAL SYSTEM MASS [kg]	24	SYSTEM DIMENSIONS [m] Length/Diameter	0,654/0,356
MASS OF CRYOGEN [kg]	5,76 [b] 5,35 [c]		

[a] Palo Alto Research Laboratory, Palo Alto, California. USA.

[b] Corresponds to Solid Methane.

[c] Corresponds to Solid Ammonia.

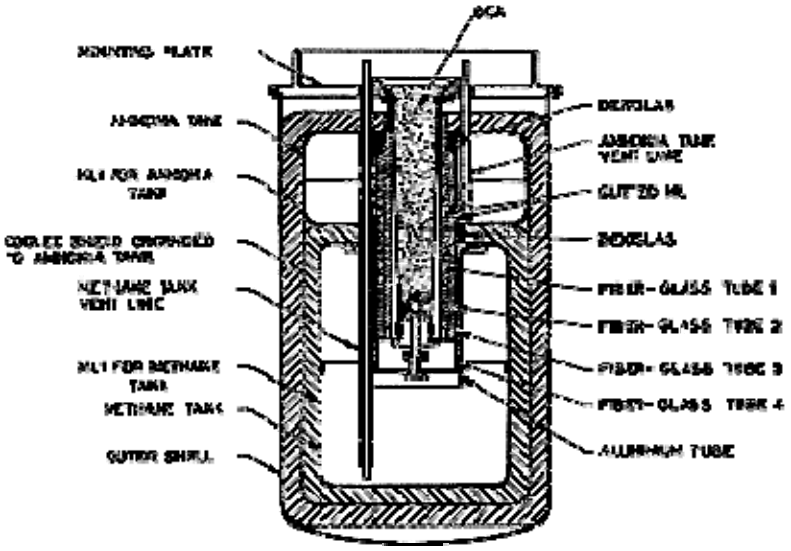

6.5.2.3 JPL & Caltech VCS Dewar

DESCRIPTION AND COMMENTS. This IR Detector Cooler is the result of a cooperative effort by JPL and Caltech aiming at the development of a system for cooling to 2 K a bolometer sensor.

The detector is incorporated into the inner container, in good thermal contact with the superfluid helium, and well within the vapor cooled shields. In this way the heat input to the detector is greatly reduced, the additional heat input through the opening in the VCS insulation system being negligible.

The heat addition to the cryogen is reduced further since the outer container comes only in contact with three main areas (Figure 6-69): the deep space, the bus, from which it is insulated and shielded, and the telescope whose temperature is close to 100 K. Consequently, the outer container temperature is close to 100 K.

Thermal insulation is provided by a system having three equally spaced vapor cooled shields. The distance between shields, and between the bounding faces of the insulation and neighbouring shields

are all equal to 25,4x10^{-3} m. The shields provide both radiation shielding and cooling of the insulation and supports. No padding between shields is used except for supporting purposes.

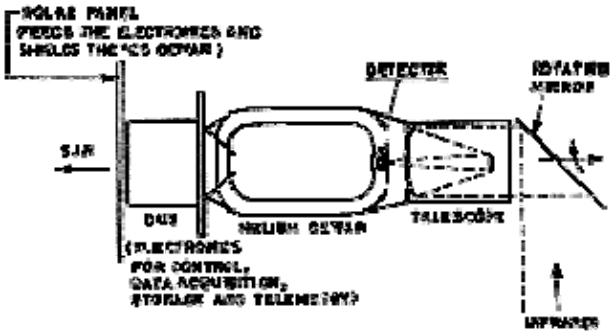

Figure 6-69: JPL-Caltech IR detector cooler arrangement.

The venting duct, which is made from stainless steel tubing, is thermally connected to each shield in turn. Venting duct length is 1,53 m, and its wall surface area is 0,72x10^{-4} m^2.

Two support designs have been considered. Both are sketched in the following page, although only one will be used in the future developments. The titanium strut provides a more rigid linking between detector and telescope, but a fiber-glass pad looks more efficient and, thence, it is only one analyzed. Each support (titanium rod or fiber-glass pad) is thermally connected to the various cooled shields and passes through them so that the heat leak through the supports is largely intercepted and carried off by the out-flowing helium gas. The total cross-sectional area of the eight fiber-glass support pads, four at each end of the container, is 0,15 m^2.

The heat transfer process within the cryostat is controlled by the following remarkable properties of superfluid helium II (see Clause 7 in this Part): 1) a film with thickness of the order 10^{-7}m spreads over all the inner surfaces, 2) the superfluid component flows readily through this film toward the heat sources, whereas the normal fluid flows away from the source carrying the heat either through convectionor through evaporation.

A set of capillary tubes, 5x10^{-3} m in diameter, running parallel to the axis of the cryostat, have been incorporated into the design. Its aim is twofold: 1) to avoid liquid sloshing during launch and insertion operations, and 2) to assure that the liquid helium is in thermal contact with the detector mounting. This thermal contact is achieved through surface tension which, in order to minimize the liquid free surface area, increases the area of the helium-capillary tube interface, which results in the thickening of the helium layer in contact with the detector.

Liquid-vapor phase-separation in the venting duct is presumably achieved by a superfluid plug (see Clause 7.4 in this Part and, in particular, the information from Schotte (1984) [209]).

The flow of boil-off helium is restricted at its exit by a variable orifice valve, controlled so as to maintain the internal pressure at 1,63x10^3 Pa. (helium vapor pressure at 1,8 K).

Reference: Mason (1972) [142].

MANUFACTURER AND/OR DEVELOPER	JPL and Caltech [a]
PRIMARY USE	IR Detector Cooler
CRYOGEN	Liquid Helium
NATURE OF PROGRAM	Design Study [b]
CURRENT STATUS OF PROGRAM	Completed

OUTER TEMPERATURE [K]	100	NUMBER OF VCS	3
OPERATING TEMPERATURE [K]	2	DETECTOR COOLING LOAD [W]	0,035
OPERATING PRESSURE [Pa]	$1,67x10^{3}$	TOTAL HEAT LEAKS [W]	
LIFETIME [h]	4380 (6 mo)	SYSTEM CONFIGURATION	Cylindrical
TOTAL SYSTEM MASS [kg]	116	SYSTEM DIMENSIONS [m] Length/Diameter	0,80/0,65
MASS OF CRYOGEN [kg]	27,3		

[a] Jet Propulsion Laboratory and California Institute of Technology. Pasadena. California. USA.

[b] Preliminary phase of the IRAS Dewar development. IRAS, a joint Dutch-UK-US survey satellite, was launched in 1981 (Neugebauer (1978) [167]).

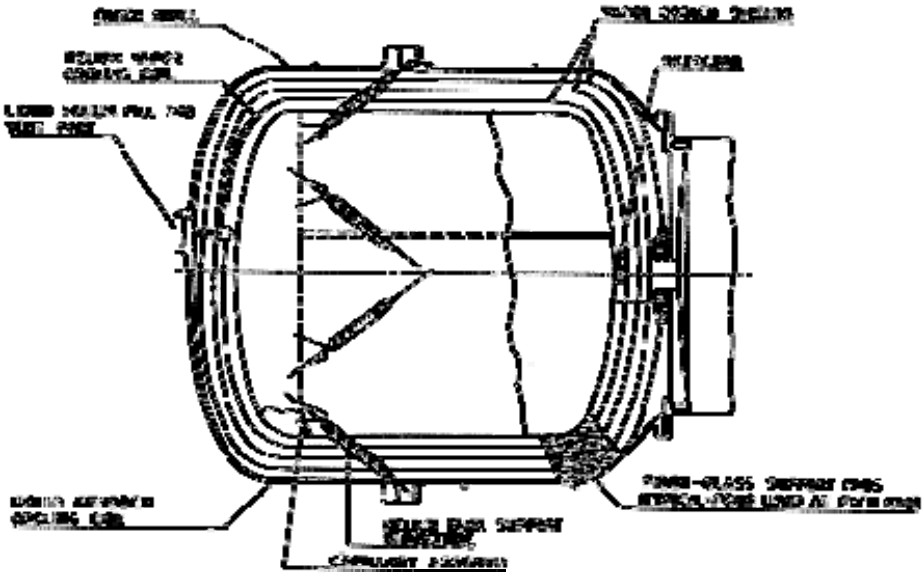

6.5.2.4 Garrett VCS Dewar 1975

DESCRIPTION AND COMMENTS: This Dewar was developed for an orbiting high-field superconducting magnetic spectrometer, with a one year mission, which was planned as a part of the NASA-High Energy Astronomical Observatory (HEAO) series of scientific flights. These flights were initially scheduled for 1975-1977.

The cryogenic cooling system was based on a feasibility study performed by Ball Brothers Research Corp. A contract for designing and building an engineering model of the system was awarded in May 1972 to AiResearch division of the Garrett Corporation in Torrance, California. In January 1973 the HEAO satellite program was redirected and the superconducting magnet experiment postponed (a Dewar, developed by Ball Brothers Research Corp., which will be used on the (HEAO) B and C is described by Sherman (1978) [216]. This Dewar will contain methane as the primary cryogen and ammonia as the secondary. The dimensions are 0,76 m long and 0,56 m in diameter. The loaded mass will be 75 kg. Cooling load: $2x10^{-2}$ W).

The Garrett VCS Dewar has a length of 2,38 m and an outer diameter of 1,83 m. It contains about 430 kg of liquid helium with approximately a 5% ullage.

The support system consists of a relative stiff array of sixteen fiber-glass-epoxy bands between eight equally spaced attach points on a central outer shell girth ring, and four attachment points at each end of the pressure vessel. The band supports are roughly 0,68 m long with a total cross-sectional area of about $8,77x10^{-4}$ m^2. The band supports are preloaded in tension to about $0,483x10^9$ Pa to ensure a relatively high stress after cooldown. With the flight pressure vessel and two magnetic coils the Dewar minimum axial natural frequency would be about 20 to 30 Hz, which would keep maximum load factor below 10 g on a Titan III B launch. The supports are mechanically and thermally connected to the vapor cooled shields to intercept some of the conduction heat which would otherwise flow toward the pressure vessel.

The insulation system consists of MLIs and to aluminium VCSs 10^{-3} m thick. The pressure vessel is insulated with one layer of low emittance foil, whereas the inner and outer VCSs are wrapped with 40 and 120 layers respectively of $6x10^{-6}$ m double-aluminized Mylar with a 10^{-4} m thick Dacron net spacer at a layer density of about 2600 layer.m–1 maximum (see ECCS-E-30-09 Part 7 clause 6.11 , Double-Aluminized Mylar, Silk Netting, for further details regarding similar MLI systems).The insulation thickness is 0,114 m everywhere except at the spatial detector end where the coil is

mounted. There the minimum thickness is 0,076 m on the axis between the two torispherical heads, which approximate 2/1 ellipsoids.

The Dewar has a 2,5 m long stainless steel fill line, a 3,6 m long fill-vent line, and a 46 m long shield heat exchanger line. The innermost vapor-cooled shield functions as a boiler, or external thermodynamic phase separator, in a liquid expulsion mode (see Clause 1.1.1). The shield line starts at a tee, approximately 1,5 m from the pressure vessel,in the fill vent line o the boiler shield, it is spirally wrapped over the shield, and terminates at the tank pressure regulator outside the outer shell.

Phase separation is achieved by using the diamagnetism of superfluid liquid helium (helium is repelled by magnetic fields, but the force per unit volume on the liquid is much larger than the force per unit volume on the vapor). To this aim the mouth of the vent is placed near the magnet, where the product of magnetic field and field gradient is maximum, this results in phase separation which increases the operational lifetime of the Dewar by about 25% (as compared with liquid expulsion).

All instrumentation to the cryostat pressure vessel is contained in either the fill line or the vent line, thus eliminating the need for cold vacuum-tight electrical feed throughs.

Reference: Pope, Smoot, Smith & Taylor (1975) [186].

MANUFACTURER AND/OR DEVELOPER	Garrett AiResearch [a]
PRIMARY USE	Supercooling Magnet Cooling
CRYOGEN	Liquid Helium
NATURE OF PROGRAM	Development of an Engineering Model
CURRENT STATUS OF PROGRAM	Completed

OUTER TEMPERATURE [K]		NUMBER OF VCS	2
OPERATING TEMPERATURE [K]	4	DETECTOR COOLING LOAD [W]	
OPERATING PRESSURE [Pa]		TOTAL HEAT LEAKS [W]	
LIFETIME [h]	8760 (1 yr)	SYSTEM CONFIGURATION	Cylindrical
TOTAL SYSTEM MASS [kg]	1320 [b]	SYSTEM DIMENSIONS [m] Length/Diameter	
MASS OF CRYOGEN [kg]	430		2,38/1,83

[a] Division of Garrett Corp., Torrance, California, USA.

[b] Magnet system mass is also included.

6.5.2.5 Ball Brothers VCS Dewar 1976

DESCRIPTION AND COMMENTS. Over the years 1974 to 1976 Ball Brothers Research Corporation has designed and fabricated a long-life liquid helium Dewar. This development program was initiated to provide a refrigeration system for future scientific experiments in space such as IR telescope, superconducting magnets, and precision gyroscopes. The Dewar can contain 86 kg of superfluid helium in space for a mission of 1 year.

Analytical simulation of the structural performance proved difficult, so a structural model was built prior to completion of the engineering model by mid-1975. Testing with normal liquid helium at ambient conditions successfully concluded the program. Additional testing with superfluid helium was conducted in early 1976.

the pressure vessel (inner container) is 1,02 m long and is made with 5083 aluminium. Two torispherical heads, one at each end, are joined by a cylindrical center section. An instrument cavity, 0,457 m in diameter, is place in the center of the container. Five valves and two superfluid plugs (see Clause 7.2) are placed on the cavity. The valves are used to direct and control flow filling, venting, and/orporous plug operation. After filling, a crossover valve may be opened and the cryostat vented through both (filling and venting) lines, if required. One of the superfluid plugs is ceramic and has an average pore size of $0{,}5 \times 10^{-6}$ m; the other plug is nickel, with a nominal pore size of 2×10^{-6} m. Both plugs have been tested in the laboratory and were set-up in the cryostat for comparison testing.

The insulation system consists of four MLI blankets ($6{,}35 \times 10^{-6}$ m thick Mylar sheets aluminized on both sides and spaced by Dracon net (see ECSS-E-HB-31-01 Part 7 clause 6.1.1, Double-Aluminized Mylar, Silk Netting, for further details regarding similar systems)) whichare separated by three aluminium vapor cooled shields. Stainless steel filling and venting ducts are attached to the vapor cooled shields by metal) clips and aluminium filled polyurethane resin.

The inner container, the VCS and the outer shell are structurally linked by a support system. Six titanium supports are provided for ground and launch operations. These supports are retracted into the inner container for orbital flight. In orbit, the system consists exclusively of six fiber-glass supports which are cooled through the VCS.

The outer container is constructed of 5083 aluminium, and consists of two torispherical heads, of 1,37 m outer diameter, joined by 0,856 m long cylinder. A cover plate, 0,61 m diameter, in the top head is provided for access to the inner cavity. External plumbing is attached to the outer container.

The first lifetime test of the thermal model involved approximately two months of testing, of which the last three weeks were the formal stabilization time. During the last week, the VCS Dewar insulation system was stabilized to within ± 1 K, and the flow rate was stable to less than ±3%. Vacuum pressure was 5×10^{-4} Pa and the tank pressure was $10^5 \pm 10$ Pa. The environmental temperature was 293 ± 2 K. The helium mass boil-off rate was $2{,}5 \times 10^{-6}$ kg.s^{-1} for the last week of the test. This correspond to an overall heat leak of 0,059 W and secures a storage time of 8110 h. The calculated lifetime, based on a heat leak of 0,041 W was 11600 h. A helium leak located in the internal plumbing could account for the below-predicted experimental performance.

A chart of the various thermal element heat leaks, temperatures, and cooling provided by the effluent gaseous helium is presented in Figure 6-70.

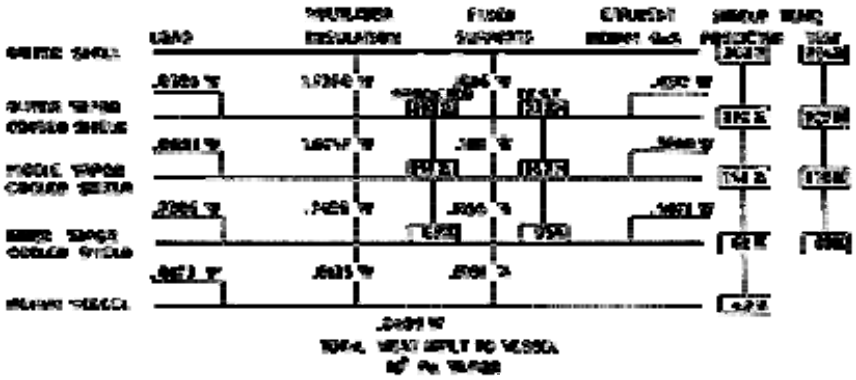

Note: non-si units are used in this figure

Figure 6-70: Heat Flow diagram of the Ball Brothers Liquid helium Dewar.

Reference: Urbach & Herring (1976) [243].

MANUFACTURER AND/OR DEVELOPER	Ball Brother Research Corporation [a]
PRIMARY USE	Long Term Storage
CRYOGEN	Liquid Helium
NATURE OF PROGRAM	Experimental
CURRENT STATUS OF PROGRAM	Completed

OUTER TEMPERATURE [K]	300	NUMBER OF VCS	3
OPERATING TEMPERATURE [K]	4,2	DETECTOR COOLING LOAD [W]	
OPERATING PRESSURE [Pa]	105	TOTAL HEAT LEAKS [W]	0,041
LIFETIME [h]	8760 (1 yr)	SYSTEM CONFIGURATION	Cylindrical
TOTAL SYSTEM MASS [kg]		SYSTEM DIMENSIONS [m]	
MASS OF CRYOGEN [kg]	86	Length/Diameter	1,02/1,37

[a] Boulder. Colorado. USA.

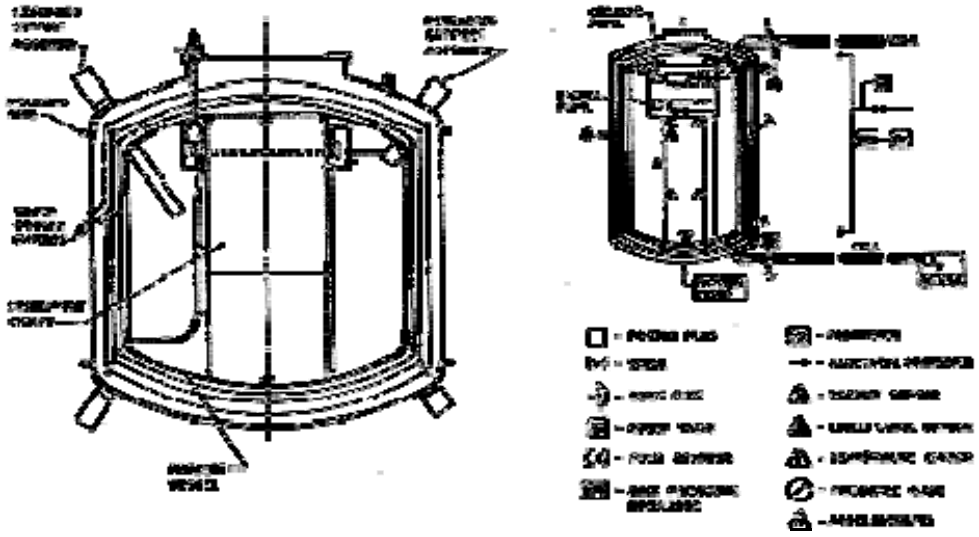

7
Superfluid Helium

7.1 Dynamics of superfluids

At tempertures close to absolute zero, quantum effects would control the properties of a fluid.

Helium remains fluid at absolute zero, provided that the pressure does not exceed about 2,5 x 10^6 Pa (25 atm).

The phase diagram for He^4 is shown in Figure 7-1. The regime considered in this Clause is labelled He II in the diagram.

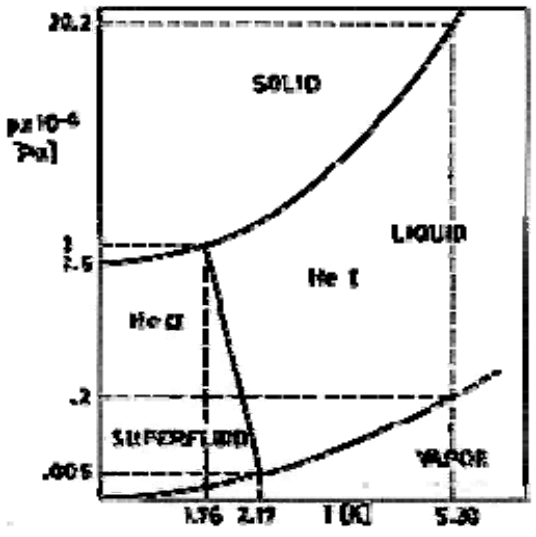

Note: non-si units are used in this figure

Figure 7-1: Phase diagram for He^4 (not to scale). From Arp (1970) [10].

Liquid helium undergoes a phase transition at a temperature of about 2,2 K, at the vapor pressure. This transition is detected by the λ-shaped peak of the specific heat vs. temperature curve.

At temperatures above the lambda point, helium behaves like a normal viscous fluid. This phase is called Helium I.

Below the lambda point, liquid helium -Helium II has a number of remarkable properties, the most important of which is superfluidity. Strictly speaking only one isotope of helium, He^4, becomes superfluid below 2,2 K. In 1971, however, a phase transition was found in the light isotope of Helium, He^3 (see clause 8.3) at a temperature of 2,7 x 10^{-3} K. Only after 1974 it has been widely accepted that this new phase is superfluid (Mermin & Lee (1976) [149]).

Macroscopic superfluid dynamics is based on the following fundamental result of the microscopic theory: At temperatures other than zero He II behaves as if it were a mixture of two different liquids. One of these is a superfluid, which is characterized by a density ρ_s, zero entropy, zero viscosity, and, where motion is involved, a velocity $\vec{u}_s$. The other is a normal viscous fluid, which is characterized by a density ρ_n, and, where appropriate, a velocity $\vec{u}_n$. No friction occurs between these two parts of the liquid in their relative motion, at least provided that both $\vec{u}_n$ and $\vec{u}_s$ are small (see Figure 7-4 in clause 7.1.2 and discussion thereof).

To depict the He II motion as a mixture of normal and superfluid flows allows a simple analysis of the phenomena which occur when quantum effects are important but, like any description of quantum phenomena in classicalterms, it should be viewed with caution.

7.1.1 Relevant equations of superfluid dynamics

It is not intended to derive here the complete system of differential equations and boundary conditions which describe macroscopically the flow of He II, rather the relevant results, which will be used in the last part of this Clause, are outlined.

Because of the existence of critical velocities (clause 7.1.2) the equations of superfluid dynamics for helium II are physicallymeaningful only when the velocities $\vec{u}_s$ and $\vec{u}_n$ are not too large. Unfortunately the relevant equations cannot be consistently derived from the conservation laws when higher powers of the velocities are neglected, therefore our approach will be as follows:

1. The general outline of the calculations leading to the general equations, without making any assumption concerning the velocities $\vec{u}_s$ and $\vec{u}_n$, will be given in this paragraph.
2. The resulting equations will be particularized to the steady, slow flow case (clause 7.1.1.1).
3. Critical velocities will appear through an heuristic introduction of the frictional effects (clause 7.1.2).

Details concerning the basic equations can be found in Landau & Lifshitz (1959) [129], Khalatnikow (1965) [122], and Roberts & Donnelly (1974) [196], among others.

As has been said, He II may be thought of as a mixture of two components: the superfluid component (subscript s) and the normal component (n).

1. The conservation of total mass can be expressed as:

$$\frac{\partial \rho}{\partial t} + \nabla \cdot \vec{j} = 0 \qquad [7\text{-}1]$$

where $\rho = \rho_s + \rho_n$ is the actual density of He II, while the mass flux density vector, $\vec{j}$, is given by

$$\vec{j} = \rho_s \vec{u}_s + \rho_n \vec{u}_n \qquad [7\text{-}2]$$

For one-dimensional steady flow, the mass conservation equation may be written as:

$$m = jA_{FL} \qquad [7\text{-}3]$$

m being the mass flow rate and A_{FL} the duct cross-sectional area.

2. The equations governing the momentum balance for superfluid and normal fluid are, respectively:

$$\frac{\partial \vec{u}_s}{\partial t} + (\vec{u}_s \nabla)\vec{u}_s = -\frac{1}{\rho}\nabla p + s\nabla T - \nabla U \qquad [7\text{-}4]$$

$$\frac{\partial \vec{u}_n}{\partial t} + (\vec{u}_n \nabla)\vec{u}_n + \frac{m_s}{\rho_n}\vec{u}_s + \frac{m_n}{\rho_n}\vec{u}_n = \\ = -\frac{1}{\rho}\nabla p - \frac{\rho_s}{\rho_n} s\nabla T - \nabla U + \frac{\mu_n}{\rho_n}\nabla \vec{u}_n \qquad [7\text{-}5]$$

where p, s and μ_n are respectively the pressure, entropy per unit mass, and normal fluid viscosity, while U is the potential of any conservative body force per unit volume (e.g., gravity) to which the system could be subjected. m_s and m_n are defined, respectively as:

$$m_s = \frac{\partial \rho_s}{\partial t} + \nabla \cdot \rho_s \vec{u}_s \qquad [7\text{-}6]$$

$$m_n = \frac{\partial \rho_n}{\partial t} + \nabla \cdot \rho_n \vec{u}_n \qquad [7\text{-}7]$$

Equation [7-5] results by substraction of Eq. [7-4] to the equation governing the overall momentum balance (see Roberts & Donnelly (1974) [196]).

It is found experimentally (persistence of circulation experiments) that the circulation of the superfluid component of velocity around any superfluid material path remains constant. This is a consequence of the Kelvin-Helmholtz theorem of inviscid fluids in a potential body force field, the only difference being that now the fluid needs not to be incompressible or barotropic.

Constancy of circulation suggests that the total derivative of $\vec{u}_s$ (left hand side of Eq. [7-4]) must be equal to the gradient of a scalar,-(μ+U), where μ will be identified with the chemical potential per unit mass. This chemical potential is a function of p, T and the velocity difference, $\vec{u}_n - \vec{u}_s$.

Neglecting higher order terms in this velocity difference, μ is defined as:

$$\nabla \mu = \frac{1}{\rho}\nabla \rho - s\nabla T - \frac{\rho_n}{2\rho}\nabla(\vec{u}_n - \vec{u}_s)^2 \qquad [7\text{-}8]$$

Strictly speaking, ρ_n and ρ_s are also functions of the velocity difference, but this can be disregarded within the present approximation.

In addition, when the superfluid motion starts from the rest, and both $\vec{u}_s$ and $\vec{u}_n$ are so small that no quantized vortices appear in the superfluid (see clause 7.1.2), the superfluid flow is irrotational, thence $\vec{u}_s$ is equal to the gradient of a scalar, ψ. In that case, Eq. [7-4] becomes,

$$\nabla\left[\frac{\partial\psi}{\partial t}+\frac{1}{2}(\nabla\psi)^2+\mu+U\right]=0 \qquad [7\text{-}9]$$

The non-linear momentum terms $m_s\vec{u}_s$ and $m_n\vec{u}_n$ should appear in Eq. [7-5] instead of being equally divided between Eqs. [7-4] and [7-5], as noted by Landau, who recognized that constancy of circulation of the superfluid component overrules misleading symmetry arguments.

3. An additional equation is needed for the still undefined T. This equation, which comes from the law of conserva tion of energy, is very complicated and, in its complete form, of very limited use.

   For convenience, we will write down the entropy balance equation; to this aim we start with the general expression for a non-reacting binary mixture (von Kármán (1955))

$$\rho\frac{Ds}{Dt}=\nabla\left(k\frac{\nabla T}{T}-\sum_{i=1}^{2}\rho_i s_i\vec{v}_{d_i}\right)+$$
$$+\frac{1}{T}\left[\Phi+k\frac{(\nabla T)^2}{T}-\frac{\nabla T}{T}\cdot\sum_{1}^{2}\rho_i s_i\vec{v}_{d_i}-\sum_{1}^{2}\rho_i\vec{v}_{d_i}\cdot\nabla\mu_i\right] \qquad [7\text{-}10]$$

Note: non-si units are used in this figure

where $\vec{v}_{d_i}$ is the diffusion velocity of species i and Φ the viscous dissipation function (Rayleigh).

The left hand side of Eq. [7-10] gives the entropy variation per unit volume (D/Dt indicates local plus convective derivative). The first term in the right hand side is the reversible entropy flux through the boundary of the unit volume element. This flux comes from: 1) the conductive heat transfer, 2) the diffusion of species. The second term gives the entropy generated in the unit volume element per unit time. The terms involved come from: 1) viscous dissipation, 2) thermal conduction, 3) diffusion.

Fluxes due to coupled effects (Onsager) have been neglected.

Equation [7-10] is now applied to the binary mixture of the normal fluid (1 with $\rho_{1s_1}=\rho_s$!) and the superfluid (2 with $\rho_{2s_2}=0$). $\mu_1-\mu_2=-sT$. The diffusion velocities are,

$$\vec{v}_{d_1}=\vec{u}_n-\left(\frac{\rho_s}{\rho}\vec{u}_s+\frac{\rho_n}{\rho}\vec{u}_n\right)=\frac{\rho_s}{\rho}(\vec{u}_n-\vec{u}_s) \qquad [7\text{-}11]$$

Note: non-si units are used in this figure

$$\vec{v}_{d_2} = \vec{u}_s - \left(\frac{\rho_s}{\rho}\vec{u}_s + \frac{\rho_n}{\rho}\vec{u}_n \right) = -\frac{\rho_n}{\rho}\left(\vec{u}_n - \vec{u}_s\right) \qquad [7\text{-}12]$$

Note: non-si units are used in this figure

The following equation results

$$\rho\frac{\partial s}{\partial t} + \left(\vec{j}\nabla\right)s = \nabla\left[k\frac{\nabla T}{T} - \rho_s s\left(\vec{u}_n - \vec{u}_s\right)\right] + \\ + \frac{1}{T}\left[\Phi + k\frac{(\nabla T)^2}{T} - \frac{\nabla T}{T}\rho_s s\left(\vec{u}_n - \vec{u}_s\right) + \frac{\rho_n\rho_s}{\rho}\left(\vec{u}_n - \vec{u}_s\right)\cdot\nabla sT\right] \qquad [7\text{-}13]$$

Note: non-si units are used in this figure

Usually the heat flux vector is given by

$$\vec{q} = \rho_s sT\left(\vec{u}_n - \vec{u}_s\right) \qquad [7\text{-}14]$$

Note: non-si units are used in this figure

where thermal conduction terms are neglected.

For a static counterflow, in which there is no net mass flow ($\vec{j} = \rho_s\vec{u}_s + \rho_n\vec{u}_n = 0$),

$$\vec{q} = \rho sT\vec{u}_n \qquad [7\text{-}15]$$

Note: non-si units are used in this figure

In the case of one-dimensional steady flow of He II ($j = m/A_{FL}$), the following equation results

$$q = \rho sTv_n\left(1 - \frac{m}{\rho v_n A_{FL}}\right) \qquad [7\text{-}16]$$

Note: non-si units are used in this figure

m is positive when He II flows from the heat source to the heat sink. In the following, v, v_n, v_s will be used to identify cross-sectional averages of the local velocities u, u_n and u_s, respectively.

7.1.1.1 Steady slow flow

Equations [7-4] and [7-5] can be simplified when $\partial / \partial t = 0$ and both the superfluid and normal velocities are so small that it is justified to neglect quadratic terms.

In that case Eq. [7-4] reduces to London's equation,

$$\frac{1}{\rho}\nabla p - s\nabla T + \nabla U = 0 \qquad [7\text{-}17]$$

Note: non-si units are used in this figure

Equation [7-5] for the normal component of velocity can be written down as,

$$\frac{1}{\rho}\nabla p - \frac{\rho_s}{\rho_n} s\nabla T + \nabla U = \frac{\mu_n}{\rho_n}\Delta\vec{u}_n \qquad [7\text{-}18]$$

Note: non-si units are used in this figure

Combination of Eqs. [7-17] and [7-18] yields

$$\frac{1}{\rho}\nabla p + \nabla U = \frac{\mu_n}{\rho}\Delta\vec{u}_n \qquad [7\text{-}19]$$

Note: non-si units are used in this figure

which describes the creeping laminar motion (Stokes flow) of a viscous liquid (density ρ, dynamic viscosity μ_n) due to an applied pressure gradient and to a potential body force field.

Equations [7-17] to [7-18] in terms of μ, and Eq. [7-8] become, respectively

$$\nabla(u + U) = 0 \qquad [7\text{-}20]$$

$$\nabla\mu + \frac{\rho}{\rho_n} s\nabla T + \nabla U = \frac{\mu_n}{\rho_n}\Delta\vec{u}_n \qquad [7\text{-}21]$$

Note: non-si units are used in this figure

and

$$s\nabla T = \frac{\mu_n}{\rho}\Delta\vec{u}_n \qquad [7\text{-}22]$$

Note: non-si units are used in this figure

7.1.1.2 Several thermal effects

The most significant physical results which can be deduced from the last paragraphs (clause 7.1.1 and clause 7.1.1.1) are:

1. The heat transport through He II is accomplished by motion of the normal fluid. Eq. [7-14] shows that the vector $\vec{u}_n - \vec{u}_s$ points away from the heat source. When there is no netmass flow of He II (j = 0), the "warm" normal fluid goes away from the heat source, and the "cold" superfluid toward the heat source. This mechanism of heat transfer in He II, called counterflow heat exchange, is far more effective than is heat transfer by conduction.
2. According to Eq. [7-17], leaving aside the body forces ($\nabla U = 0$), a pressure gradient would result in an equal sign temperature gradient, and conversely.
   (a) Let us consider a pressure gradient through a superleak from a vessel. A superleak is a capillary containing jeweler's rouge or some porous material for preventing the passage of the normal fluid.

   The temperature gradient appears because the superfluid leaving the vessel transfers no heat and, thence, the thermal energy remaining in the vessel becomes distributed over a smaller quantity of He II (the specific thermal energy and, thus, the temperature that increases). This is the so called "Mechano-caloric effect".

   (b) If a temperature gradient is established by heating the fluid in the vessel, the normal fluid, impeded by viscosity, will remain motionless whereas the superfluid will flow up the temperature gradient toward the heated vessel. This will give rise to a pressure gradient ("Thermo-mechanical effect").

   The "helium fountain" vividly illustrates the thermomechanical effect. When a superleak containing a heater and submerged in a helium II bath, is connected to a capillary (not a superleak) extending above the bath, a jet of helium emerges from the capillary once the heater is switched on.

7.1.2 Frictional effects

Frictional effects other than that for the normal fluid have been observed in experiments where superfluid helium flows along narrow capillaries.

Terms corresponding to these frictional effects can be added to Eqs. [7-17] and [7-19], integrated along the tube, neglecting potential body forces, much in the same way as Bernoulli equation for ideal fluids is generalized to real fluids by adding the pressure drop due to friction (see ECSS-E-HB-31-01 Part 13 clause 7.2). The resulting expressions are strictly valid only for steady flow.

Usually two types of frictional forces are introduced. They are defined as forces per unit volume ([Pa.m^{-1}]).

1. F_n represents the exchange of momentum between the normal fluid and the wall.
2. F_{sn} the mutual exchange between normal and superfluid. Several authors (van der Heijden, van der Boog & Kramers (1974) [247]) postulate the existence of a third frictional force, F'_s, which describes (apart from a capillary-exit correction, which will be introduced below) the loss of momentum of the superfluid not transferred, through mutual friction, to the normal fluid. The existence of this non-zero F'_s is not widely accepted however (de Haas & van Beelen (1976) [55], p. 143).

Since only two independent equations are available, no experimental confirmation of the existence of F'_s can be obtained. Thence, different interpretations of similar experimental data can be found in the literature.

Friction forces are related to vortex generation, motion and decay. Vortices are created in the bulk fluid by thermal fluctuations. Wall roughness is probably unimportant, at least results obtained with different metal and glass capillaries are sufficiently similar to support this statement.

The motion of the vortex line is governed by the velocity at its axis. The superfluid velocity results from the superposition of the transport flow and of the velocity induced by all vortices and images.

Equation [7-20] with $\nabla U = 0$, integrated along the cylindrical tube of length L with mutual and superfluid friction effects included, becomes,

$$\rho_s \frac{\Delta\mu}{L} + F_{sn} + F'_s = 0 \qquad [7\text{-}23]$$

Similarly, from Eq. [7-19],

$$\frac{\Delta p}{L} + F_n + F'_s = 0 \qquad [7\text{-}24]$$

In these equations Δ indicates difference between two sections of the tube separated by a distance L, F_{sn} is the mutual friction force, F'_s the superfluid friction force and F_n the normal friction force, per unit volume in any case.

Equations [7-23] and [7-24] with experimentally determined values of $\Delta\mu$ ($\Delta\mu = (1/\rho)\Delta p - s\Delta T$) and Δp allow the determination of two relations between the three forces.

A systematic set of experiments with superfluid helium flow through capillaries, where v_s and v_n were independently controlled, was performed by a group of the Kamerlingh Onnes Laboratory, Leiden University, the Netherlands. The experimental layout basically consists of a closed circuit partially filled with liquid helium, the capillary being a part of the circuit (Figure 7-2).

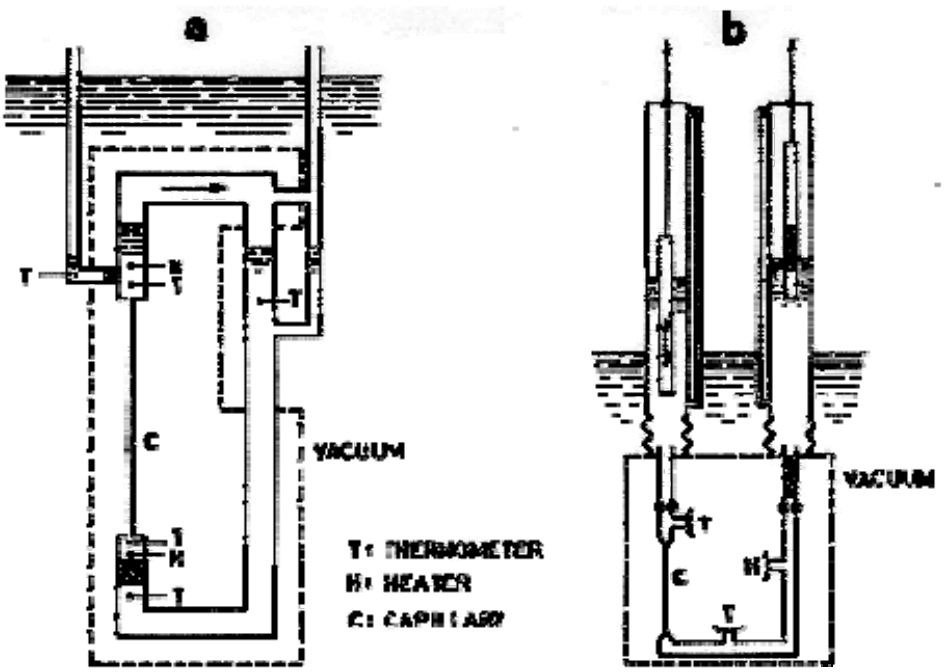

Figure 7-2: Schematic of the apparatus used by the Leiden group to produce helium flow through capillaries with independent variation of superfluid and normal velocities. a) From Van der Heijden, Van der Boog & Kramers (1974) [247]. b) From De Haas & Van Beelen (1976) [55].

A heater placed upstream the capillary produces a normal transport velocity, v_n, through it. The mass flux, $\rho_s v_s + \rho_n v_n$, can be independently controlled in two alternative ways. Van der Heijden, van der Boog & Kramers (1974) [247], and IJsselstein, de Goeje & Kramers (1979) [98] used a second heater which evaporates the liquid helium in the tube downstream the capillary, and a heat exchanger where helium gas condenses restarting the circuit, Figure 7-2a De Haas & van Beelen (1976) [55], and Slegtenhorst & van Beelen (1981) [224] used two plungers which move in opposite directions at the same speed within either reservoir of the circuit, Figure 7-2b.

The following combinations of velocities can be obtained, by appropriate inputs to the heaters or displacement of the plungers.

(a) Constant normal velocity, v_n, and varying superfluid velocity, v_s.

(b) Constant velocity ratio, v_n/v_s.

(c) Constant mass flux, $\rho_s v_s + \rho_n v_n$.

ΔT (as well as the mean temperature) is measured. $\Delta\mu$ is related to the hydrostatic pressure difference between the helium in both reservoirs at known temperatures Eq. [7-20]. Δp is deduced from these values by use of Eq. [7-8], neglecting the velocity difference term.

Couples of v_s,v_n values corresponding to iso chemical-po tential ($\Delta\mu$=0), isothermal (ΔT=0) and isobaric (Δp=0) flows can be obtained. In addition, flows with $\Delta\mu$ = 0 are produced in a circuit containing a heater, to control v_n, and a porous plug (Staas, Taconis & van Alphen (1961) [227], de Haas & van Beelen (1976) [55]). This type of flow will be interesting in connection with the superfluid porous plug (see Clause 7.4).

The results of experiments performed by van der Heijden et al. (1974) [247],will be summarized in the following. These authors postulate an $F'_s \neq 0$.

In these experiments, capillaries with D_E = 294 x10^{-6} m (or 95 x 10^{-6} m), L = 0,146 m were used (T = 1,2 K). Similar experiments have been reported by de Haas et al. (1976) [55], IJsselstein et al. (1979) [98] and Slegtenhorst et al. (1981) [224].

The scarcity of results from other sources, or under widely different geometrical conditions, impedes the formulation of comparisons based on dimensionless parameters.

The flow is called supercritical when $\rho\Delta\mu \neq 0$, otherwise it is called subcritical. This could be misleading when an $F'_s \neq 0$ is postulated since (Eq. [7-23]) $\Delta\mu$ could be zero when F_{sn} and F'_s, although large, balance each other (see Figure 7-6, below).

a. The normal contribution to the friction forces always deceleratesthe normal flow. The pressure drop due to this contribution, Δp_n, is determined by Poiseuille's law (see ECSS-E-HB-31-01 Part 13 clause 7.2.2) when the flow of normal fluid is laminar

$$\Delta p_n = -LF_n = -32\frac{\mu_n L}{D_E^2}v_n \qquad [7\text{-}25]$$

Note: non-si units are used in this figure

A kinetic energy correction originating from the exit of the capillary should be taken into account when relating measured pressure drops to friction forces. In the presently discussed experiments this correction is negligible.

Normal fluid flow results to be laminar in subcritical flow as well as in supercritical flow when either $v_s \approx 0$ or $v_s - v_n = 0$.

Van der Heijden et al. (1974) [247] assume that Eq. [7-25] is valid even in supercritical flow. This assumption allows them to calculate LF_{sn} and LF'_s from Eqs. [7-23] and [7-24].

b. The superfluid contribution to the friction forces always decelerates the superfluid flow. Isobaric flow results, according to Eq. [7-24], when the effects of normal and superfluid friction balance each other. For example, in the present experiments this happens when the superfluid and normal velocities are, respectively, v_s = -0,044 m.s^{-1} and v_n = 0,038 m.s^{-1}.

The pressure drop due to superfluid contribution, Δp_s, can be expressed as:

$$\Delta p_s = -LF'_s = -LF_s - \rho_s v_s^2 ,$$

where LF_s accounts for the superfluid friction in the capillary and $\alpha\rho_s v_s^2$, with $\alpha \approx 1$, is the kinetic energy correction.

Experiments performed under constant mass flux conditions ($\rho_s v_s + \rho_n v_n$ = Const.) indicates the tendencies sketched in Figure 7-3. In particular, although F_s increases with $v_n - v_s$ in the vicinity of $v_n - v_s = 0$, this trend ceases near $v_n - v_s$ = 0,02 m.s^{-1}, where $\Delta\mu$ happens to be zero.

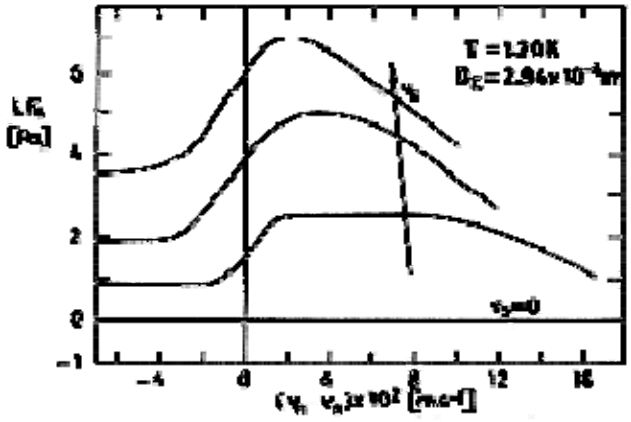

Figure 7-3: The superfluid friction, LF_s, vs. relative velocity, v_n-v_s, for various runs with $\rho_s v_s + \rho_n v_n$ = Const. From van der Hejden, van der Boog & Kramers (1974) [247].

Let v_{so} be the value of v_s corresponding to $v_n = 0$.

1. For $v_{so} < 0{,}05$ m.s^{-1} and $Re_s = \rho_s v_s D_E/\mu_n < 1100$, the following "modified" Poiseuille's law holds,

$$LF_s = -32\frac{\mu_n L}{D_E^2}v_s \qquad [7\text{-}26]$$

2. For v_{so} 0,05 m.s^{-1}, the Blasius formula applies (see ECSS-E-HB-31-01 Part 13 clause 7.2.2.1),

$$LF_s = -158L\left(\frac{\rho^3 \mu_n v_s^7}{D_E^5}\right)^{1/4} \qquad [7\text{-}27]$$

Recall the transitional flow in classical hydrodynamics (ECSS-E-HB-31-01 Part 13 clause 7.2). Here the normal fluid remains laminar, whereas thesuperfluid becomes turbulent. De Haas & van Beelen (1976) [55], however, suggest that in the Blasius branch the whole fluid should behave as an) ordinary viscous liquid (see also Olijhoek et al. (1967)).

c. The mutual friction contribution to the friction forces decelerates the superfluid as long as $v_s < v_n$ and conversely.

The mutual friction term appears in Figure 7-4 as a function of vn-vs. According to Gorter & Mellink (1949) [77], Fsn should be have as |vs-vn|n, with n ◎ 3, but the figure indicates that the exponent n is certainly different from 3 except for large values of the relative velocity |vs-vn| (where F's, if existent, would be negligible compared to Fsn, see Figure 7-5. We will come back to this point very soon). Near vn-vs = 0 the relationship appears to be linear and exhibits a slope depending on vso. Notice the circles in the abscissae axis (zero mutual friction) which correspond to subcritical strict counterflow. Other circles correspond to high-velocity (supercritical) strict counterflow, where Gorter & Mellink formula approximately holds.

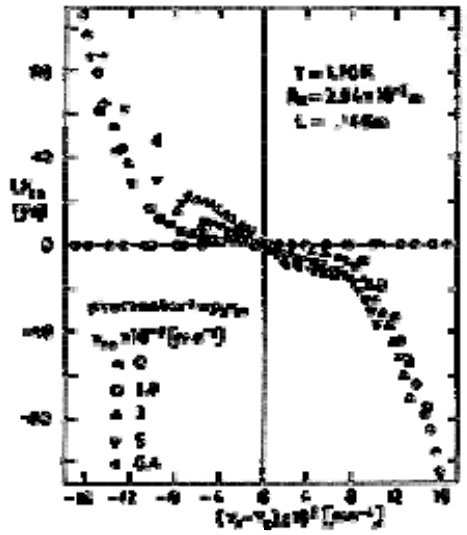

Note: non-si units are used in this figure

Figure 7-4: The mutual friction, LF_{sn}, vs. relative velocity, v_n-v_s, from various constant mass flux runs. From van der Hejden, van der Boog & Kramers (1974) [247].

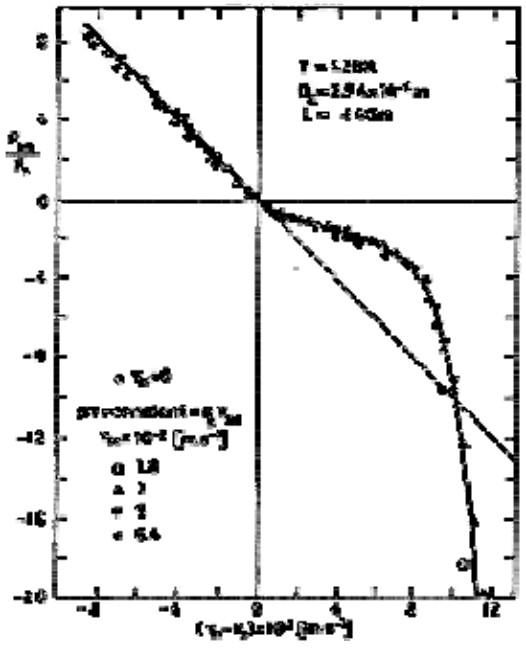

Note: non-si units are used in this figure

Figure 7-5: Mutual friction to superfluid friction ratio, F_{sn}/F_s, vs. relative velocity, v_n-v_s, from various runs with $v_s \geq 0$ and $v_n \geq 0$. From van der Heijden, van der Boog & Kramers (1974) [247].

Figure 7-5 indicates that a surprisingly simple dependency between F_{sn}/F_s and v_s-v_n exists for the results deduced from many different runs. Similar results, with T = 1,35 K, have been obtained. The significance of these results, based on a superfluid friction force, F'_s, the mere existence of which is open to question, is by no means clear.

It has been already indicated that the part of Figure 7-4 which corresponds to sufficiently large values of $|v_n-v_s|$ is fairly insensitive to the assumption on F'_s (be it zero or not). As an example, the circles in Figure 7-4 and Figure 7-5 (corresponding to $v_n = 0$) allow us to estimate LF_{sn} and LF_s, respectively, versus v_s. The kinetic energy correction can be also estimated by use of Table 8-13, clause 8.2, since the temperature is given. At v_s= 0,16 m.s^{-1}, F'_s/F_{sn} is less than 0,1 although this ratio increases for smaller values of v_s.Then, the value of $\rho_s\Delta\mu$ in Eq. [7-23] is, in the region of large $|v_n-v_s|$, fairly insensitive to F'_s. The departure of F_{sn} from the Gorter & Mellink formula with $n = 3$, mentioned in connection with Figure 7-4, could then be due to the assumed existence of F'_s.

d. Isothermal and iso chemical-potential curves. Figure 7-6 is a summary plot drawn with the values of v_s and v_n at which either ΔT or $\Delta\mu$ become zero. Shaded area, with its ill defined boundary, corresponds to truly subcritical flow ($\Delta\mu$=0).

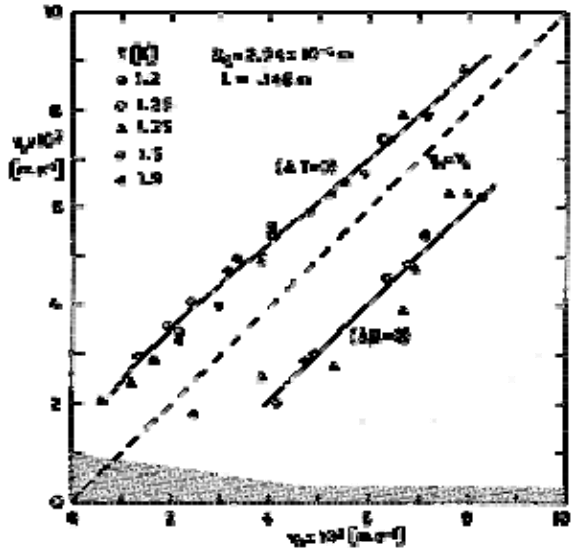

Note: non-si units are used in this figure

Figure 7-6: Isothermal and iso chemical-potential flows in the v_n,v_s plane. The shaded region corresponds to subcritical flow ($\Delta\mu$=0). From van der Heijden, van der Boog & Kramers (1974) [247].

The curves are for the wide capillary experiments and seem to be temperature independent. Results for the narrow capillary are slightly diferent.

An extrapolation of the data for $\Delta T = 0$ suggests that the isotherm intersects the $v_n = 0$ axis at a critical velocity v_{sc} = 0,01 m.s^{-1}. For the narrow capillary, v_{sc} = 0,03 m.s^{-1}.

7.1.3 Counterflow heat transfer

We will consider in the following the counterflow heat transfer through He II filling long cylindrical tubes of circular cross section. The data could be applied to other channels of simple geometry by assuming that the "D_E" in these equations represents the hydraulic diameter (four times cross-sectional area divided by cross-sectional perimeter). Nevertheless, serious errors in the estimation of the critical velocities could appear for complex, multiply connected channels (Chase (1963) [43]).

Gravitational or other body forces are neglected throughout this paragraph.

Physically, counterflow corresponds to motion of warm normal fluid away from the heat source and counter-motion of cold superfluid toward the heat source. Although both components can be independently controlled, as said in clause 7.1.2, we will restrict the discussion here to the case in which the net mass flux is zero ($\rho_s v_s + \rho_n v_n = 0$).

Three different steady-state flow regimes appear sequentially in counterflow as the velocities v_s and $|v_s - v_n|$ increase (see the review by Arp (1970) [10] and the more recent papers by Childers& Tough (1976) [44] and Ladner & Tough (1979) [128]). Transitions between these regimes seem to be associated to the onset of superfluid vorticity (first critical velocity) and to the onset of turbulence in both components of the He II flow (second critical velocity).

1. Regime of low velocities. As long as the velocities v_s and v_n are small, the equations given in clause 7.1.1 and 7.1.1.1 (with $\nabla U = 0$) are valid. In the case of slow flow through long cylindrical tubesof equivalent diameter D_E, Poiseuille's law Eq. [7-25] holds.

   Assuming counterflow heat exchange, combination of Eqs. [7-16] with$m = 0$, and [7-25] yields

$$\frac{dp}{dx} = -32\frac{\mu_n q}{\rho s T D_E^2} \qquad [7\text{-}28]$$

   if, in addition, Eq. [7-17] with $\nabla U = 0$ is taken into account,

$$\frac{dT}{dx} = -32\frac{\mu_n q}{\rho^2 s^2 T D_E^2} \qquad [7\text{-}29]$$

   It can be deduced from Eq. [7-29], and from the dependence of μ_n, ρ and s on T, that $q/(dT/dx)$ varies approximately as $T^{12} D_E^2$.

2. Intermediate flow regimes. As v_s or $|v_s - v_n|$ increase, quantized vortices appear in the superfluid because the irrotational superfluid flow pattern becomes energetically unfavorable.

   The definition of the superfluid critical velocity, v_{sc1}, has been the subject of controversies in the past. Even its determination on the basis of experimental data has not been without ambiguities (see Keller (1969) [119], p. 289 and ff).

   (a) Early calculations (Feynman (1955) [69]) equated the kinetic energy of the flow to the energy of a quantized vortex formed in a flow passage of diameter D_E, obtaining the following expression for the superfluid critical velocity, v_{sc1}:

$$v_{sc1} = \frac{h}{m_{He}}\frac{1}{D_E}\ln\frac{D_E}{2a_o} \qquad [7\text{-}30]$$

   h is the Planck's constant ($2\pi h = (6{,}62517 \pm 0{,}00023)\times10^{-24}$ J.s), m_{He} the atomic mass of helium ($m_{He} = 4{,}0026 \times (1{,}65979 \pm 0{,}00004)\times10^{-27}$ kg), and a_o an empirical vortex core radius ($a_o \approx 10^{-10}$ m).

   (b) Van Alphen et al. (1969) [246], summarizing data from different sources, which cover seven orders of magnitude in D_E, and which were obtained by use of

different experimental techniques, arrived at the following empirical expression (Leiden critical velocity):

$$v_{sc1} = 3{,}162 \times 10^{-3} D_E^{-1/4} \qquad [7\text{-}31]$$

where v_{sc1} is measured in m.s^{-1} and D_E in m. Although the data supporting Eq. [7-31] were all taken in the neighbourhood of T = 1,4 K, Van Alphen et al. pointed out that this critical velocity is temperature independent in the temperature region lower than 5 x 10^{-2} K below the λ-point.

The differences between the values predicted by Eqs. [7-30] and [7-31] are enormous, especially for large tubes (Figure 7-7). The reader interested in further details concerning this point could consult Keller (1969) [119] or Arp (1970) [10]. In any case, it should be said that much work needs to be done before predicting with confidence the onset of superfluid vorticity.

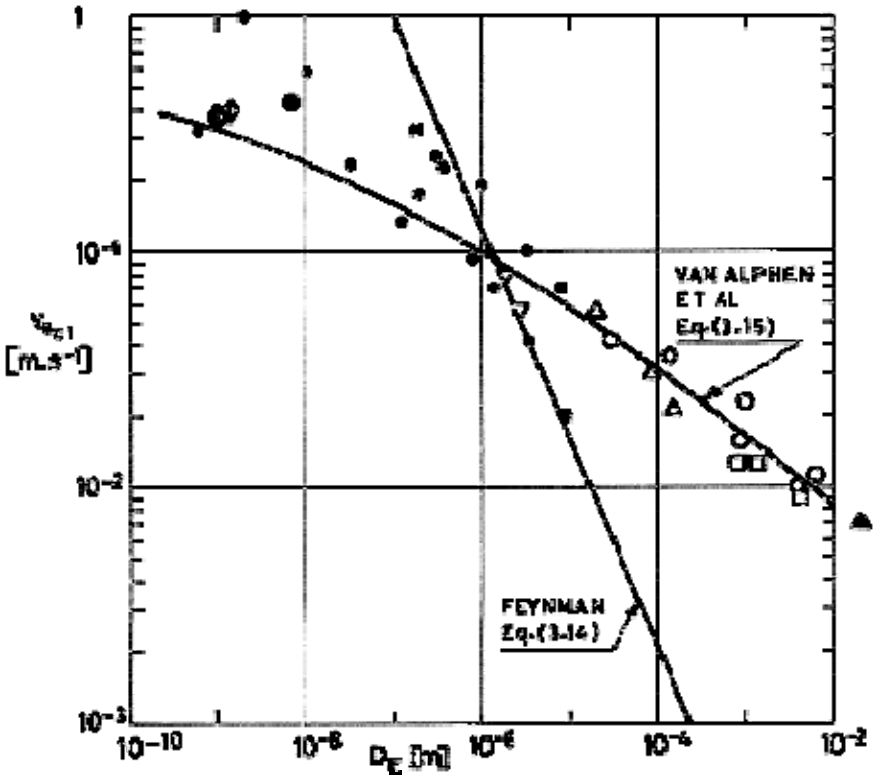

Figure 7-7: Correlations between the critical superfluid velocity, v_{sc1}, and the tube diameter, D_E. The experimental data have been re-plotted by the compiler after van Alphen et al. (1969) [246]. They correspond to widely different flow conditions. * Clow and Reppy, T_λ-T 50 x 10^{-3} K. ✪ Fokkens, film flow. ▲ Pellman, "superfluid wind tunnel". ☐ Chase, heat conduction $T \rightarrow T_\lambda$; $v_n \rightarrow 0$. △ Van Alphen, adiabatic flow rate. ○ Van Alphen, energy dissipation technique. ▼ Kramers, second sound attenuation in puresuperfluid flow. ● Van Alphen, critical flow through jeweller's rouge. ▽ Keller and Hammel, isothermal flow. • Data from reviews of Atkins, and Hammel and Keller.

Although it should be emphasized that v_{sc1} is not that value of v_s at which departures from the linear behavior appear (Keller (1969) [119], p. 289), the validity of the slow flow assumption (clause 7.1.1.1) in the regime of low velocities can be assessed at this stage -once the upper bound of v_s,and thus of v_n, are known- by means of an order of magnitude analysis of Eqs. [7-4] and [7-5]. The momentum terms in these equationsare negligible compared to the pressure gradient terms provided that

$$\rho v_s^2 \approx \rho v_n^2 / L << 32 \mu_n v_n / D_E^2 ,$$

where L is the total length of the tube, and Eq. [7-25] has been used to estimate dp/dx. The above inequalities yield the following two conditions:

1. $$\frac{\rho v_n D_E}{\mu_n} \frac{D_E}{L} << 32$$

2. ρ_s not too small compared to ρ_n.

   $\rho v_n D_E/\mu_n$ is in this regime, at most, of order 50, whereas D_E/L could be of the order of 10^{-3} or even smaller; thence, the first condition is fulfilled through the whole region of low velocities. The second condition ceases to be true in the proximity of the λ point.

   No simple analysis of the flow structure in the intermediate range is available. Childers & Tough (1976) [44] and Ladner & Tough (1979) [128] experimentally investigated the pressure and temperature drops associated with the thermal counterflow of He II in long capillaries. They monitored continuously the pressure and temperature differences along the tube as the heat flow increased from zero. For low values of q straigth lines corresponding to Eqs. [7-28] and [7-29], respectively, are generated (Figure 7-8).

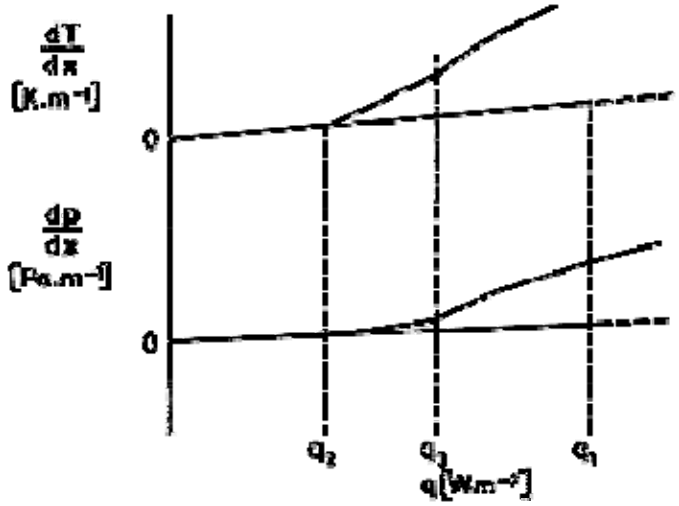

Figure 7-8: Schematic of pressure and temperature drop data as a function of heat flux.

At a given q_1 (which will correspond to v_{sc1}) dp/dx jumps to a slightly larger value, while dT/dx jumps more markedly. The jumps can be triggered by mechanical vibration of the cryostat or by small but abrupt changes in q. If at this time q is decreased, a hysteresis loop through points q_2 and q_3 appears as in Figure 7-8. The region between q_2 and q_3 (but not that past q_3) can be described in terms of a mutual friction force (Vinen (1957) [255]).

According to Vinen, mutual friction affects the heat flow through the scattering of the normal fluid thermal excitation by a tangled mass of quantized vortex lines in the

counterflowing superfluid. The basic variable in the theory is the length per unit volume, L_v, of vortex line. L_v [m^{-2}] depends on $|v_n - v_s|$, T and D_E.

The mutual friction force per unit volume, F_{sn}, is re lated to the force per unit length, f, on a single vortex line by

$$F_{sn} = \frac{2}{3} f L_v ,$$

where the factor 2/3 takes into account that only the axial component of f contributes to F_{sn}. For the normal fluid at rest, the force per unit length, f, on a vortex line moving at velocity v_t will be

$$f = \frac{1}{2} B \frac{\rho_s \rho_n}{\rho} \kappa v_t ,$$

directed opposite to v_t. B is a dimensionless parameter of order one related to the vortex line-roton scattering crosssection. κ is the strength of a quantized vortex ring ($\kappa = h/m_{He}$, Eq. (7.14)), v_t is the relative velocity between the normal fluid and the vortex lines. For counterflow Vinen assumed $v_t \approx v_s$.

Once F_{sn} is known, combination of Eqs. [7-23] and [7-24], the last with $F'_s = 0$, yields ($\Delta/L = d/dx$)

$$\frac{dT}{dx} = \frac{F_{sn}}{\rho_s s} + \frac{1}{\rho s}\frac{dp}{dx} \qquad [7\text{-}32]$$

Note: non-si units are used in this figure

When $F_{sn} = 0$ the relationship between dT/dx and dp/dx for the regime of low velocities (Eqs. [7-28] and [7-29]) is restored. In the regime of our present concern the normal fluid still flows laminarly, thus the second term in the right hand side of Eq. [7-32] is the part of the temperature drop which corresponds to the irrotational superfluid flow, and the rest gives the additional drop which we will call dT'/dx.

The evolution of the length per unit volume, L_v, of vortex line is controlled by two mutually competing although independent mechanisms: vortex generation and decay. Both concern an infinite medium with no restricting boundaries, but the effect of the wall can be taken into account by assuming that it interferes with the generation mechanism within a distance $\delta = \alpha/L_v^{1/2}$, α being a dimensionless constant, of order one, on which rests the existence of a critical velocity.

Figure 7-9 shows a typical sketch of L_v for steady state (generation balancing decay). In addition to $L_v = 0$ a nose-shaped curve appears in the figure, indicating that L_v is a double-valued function of v_s provided that $v_s D_E$ exceeds some critical value, which is given by

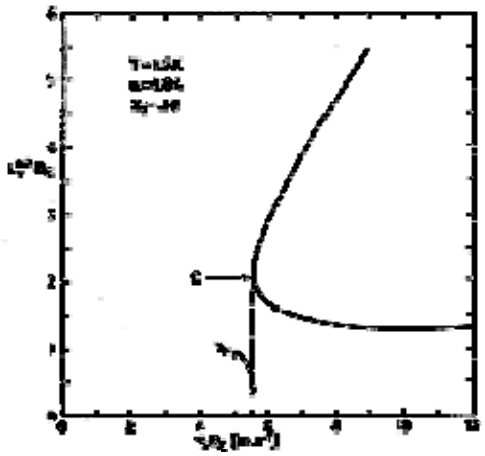

Note: non-si units are used in this figure

Figure 7-9: Schematic of $L_v^{1/2}D_E$ vs. v_sD_E under steady-state conditions. From Childers & Tough (1976) [44].

$$v_{s_c} D_E = \frac{4}{\pi} \frac{\rho}{\rho_n} \frac{\alpha\chi_2}{\chi_1} \frac{\kappa}{B}$$

Note: non-si units are used in this figure

where χ_1 and χ_2 are two more dimensionless, temperature-dependent, parameters of order one which account for the geometrical structure of the vorticity. χ_1 is a generation and χ_2 a decay parameter.

Only in the upper part of the curve in Figure 7-9 L_v increases with v_s, consequently the only stable allowed values of L_v are $L_v = 0$ and those defined by the upper part.

Figure 7-8 can now be understood in terms of Vinen's theory. Increasing the heat flux from zero, the regime in whichthe normal fluid is laminar and the superfluid irrotational is crossed over. When q is increased slowly beyond q_2, curve$L_v = 0$ would correspond to a metastable equilibrium and a sudden jump to the configuration defined by the upper part of the curve would result. Once vorticity has been generated, the only way to regain the condition $L_v = 0$ is to reduce the heat flux below q_2.

A theory based on so many experimental parameters (χ_1, χ_2,α,B) will inevitably agree with the experimental data. Nevertheless, as shown by Childers & Tough (1976) [44], and Ladner & Tough (1979) [128], once two combinations of these parameters are deduced from experimentally determined v_{sc} and dT'/dx for a given tube at a single temperature, the functional form of the mutual friction region is given at all temperatures. Furthermore, the temperature dependence of χ_1/χ_2, which in Vinen's model is de termined from experiments, can be calculated by use of a theory due to Schwarz (1978) [210]. The agreement of this theory with values of χ_1/χ_2 obtained by Ladner & Tough in long glass tubes of rectangular cross-section is fair.

Vinen's model does not provide a picture of the onset of vorticity, since the generation term results to be zero when $L_v = 0$. According to Schwarz (1978) [210], two types of onset behavior are possible. In narrow channels, the rate at which the microscopic vortex fluctuations of a critical size are thermally nucleated in the fluid seems to be controlling. In wide channels one observes an intermittent behavior similar to that in classical fluids.

3. Regime of large velocities. Mutual friction between both components controls the flow structure in this regime where the Gorter & Mellink expression holds (see clause 7.1.2)

$$F_{sn} = -A\rho_s\rho_n\left|v_n - v_s\right|^n \qquad [7\text{-}33]$$

with $n \approx 3$. In this equation A [$m^{4-n}.s^{n-2}.kg^{-1}$] is the Gorter & Mellink constant, a slowly varying function of temperature and (perhaps) of geometry.

Assuming that equation [7-33] is valid in this regime, combination of Eqs. [7-14] (with cross-sectional average values), [7-32] and [7-33] yields

$$\frac{dT'}{dx} = \frac{dT}{dx} - \frac{1}{\rho s}\frac{dp}{dx} = -A\frac{\rho_n}{s}\left(\frac{q}{\rho_s sT}\right)^n \qquad [7\text{-}34]$$

Note: non-si units are used in this figure

where dT'/dx concerns the temperature gradient resulting from mutual friction. Notice that the diameter, D_E, does not appear in Eq. [7-34].

The phenomenological equation [7-33] also applies when v_s and v_n, although pointing in opposite directions are not related to each other through $\rho_s v_s + \rho_n v_n = 0$. Other mechanisms seem to be responsible for the non-linear mutual friction in tubes with v_n v_s or v_s v_n.

The second critical velocity, bounding from below this regime of large velocities can be estimated from experimental results. A critical Reynolds number, Re_c, based on the normal flow velocity, has been experimentally verified in some experiments although it does not appear clearly in others (Ladner & Tough (1979) [128]). The range of Re_c (10^3 to 3 x 10^3) is similar to that corresponding to transition to turbulence in classical fluid flow, although a clear dependence on temperature can be observed in the present case.

Figure 7-10, from Arp (1970) [10], gives the critical Reynolds number vs. temperature for counterflow heat exchange, as deduced from

$$Re = \frac{\rho v_{nc2} D_E}{\mu_n} = \frac{D_E}{\mu_n sT} q \qquad [7\text{-}35]$$

Note: non-si units are used in this figure

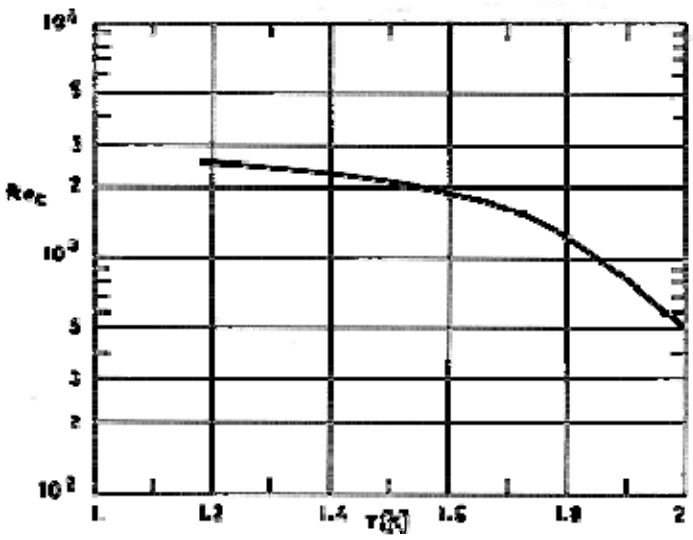

Note: non-si units are used in this figure

Figure 7-10: Critical Reynolds number for counterflow heat exchange, Re_c, as a function of temperature, T. From Arp (1970) [10].

The values of v_{nc2} in the above expression are those found experimentally by Staas, Taconis & van Alphen (1961) [227].

The same authors also observed that the relationship between the pressure gradient and the normal flow velocity is, in this regime, that corresponding to a classical turbulent flow (see clause 7.1.2 and also ECSS-E-HB-31-01 Part 13 clause 7.2).

The validity of Figure 7-10 has been disputed by Slegtenhorst (1981a),who argues that since the flow mesurements of Staas et al. correspond to flow with $\Delta\mu = 0$, they cannot be automatically applied to counterflow.

In sum, the existence of two critical fluxes is by no means clear. In some cases q_{c1} and q_{c2} are fairly sharply defined, while in other cases they apparently tend to merge, or one of them tends to smear out. It appears that the experimental resolution in most of the early experiments on thermal counterflow was such that the entire upper portion of the hysteresis loop in Figure 7-8 appeared as a single continuous curve where $dT/dx \approx q^n$ with $n \approx 3$.

4. Summary of the results concerning conterflow heat exchange in He II. Plots of dT/dx vs. q for temperatures in the range 1,5 K - 2 K are given in Figure 7-11. The figures are similar to those by Arp (1970) [10], although they cover a slightly different range of tube diameters.

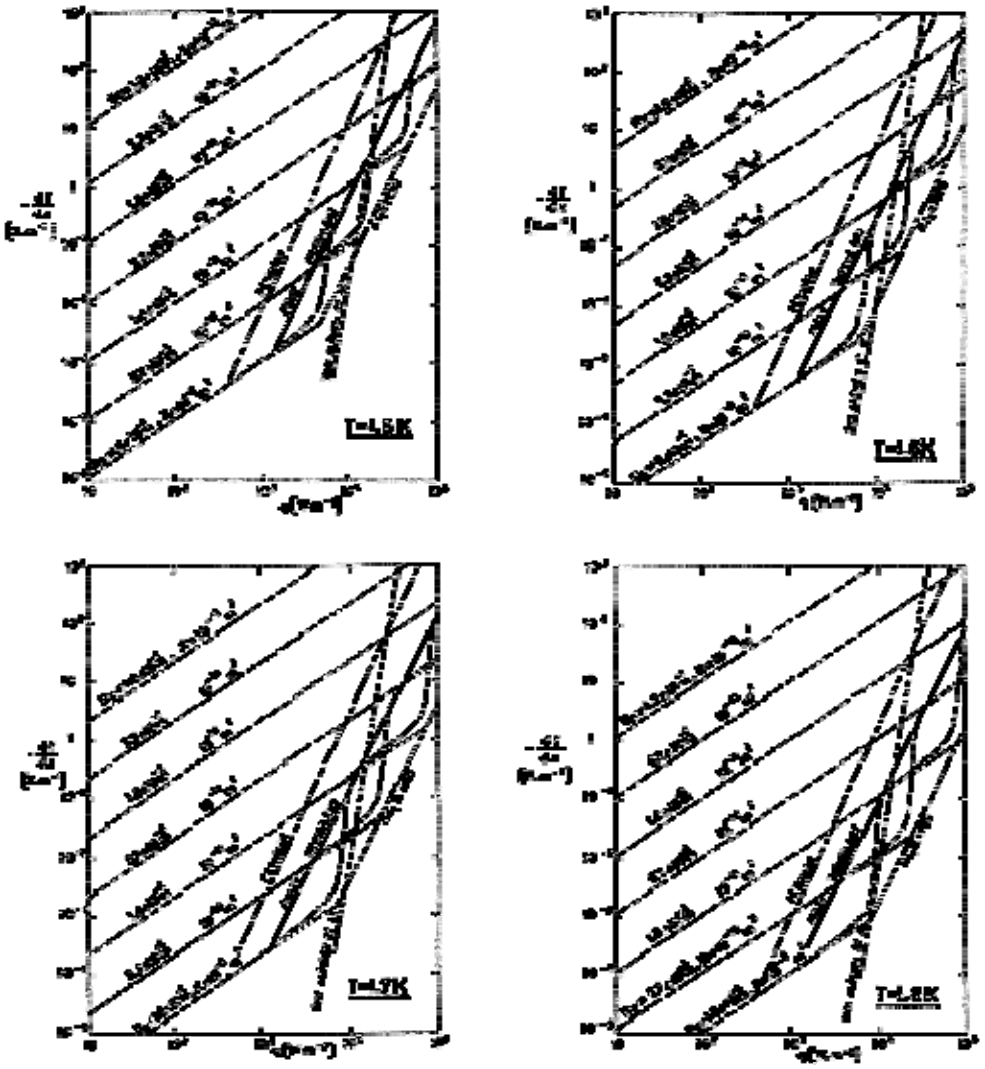

Note: non-si units are used in this figure

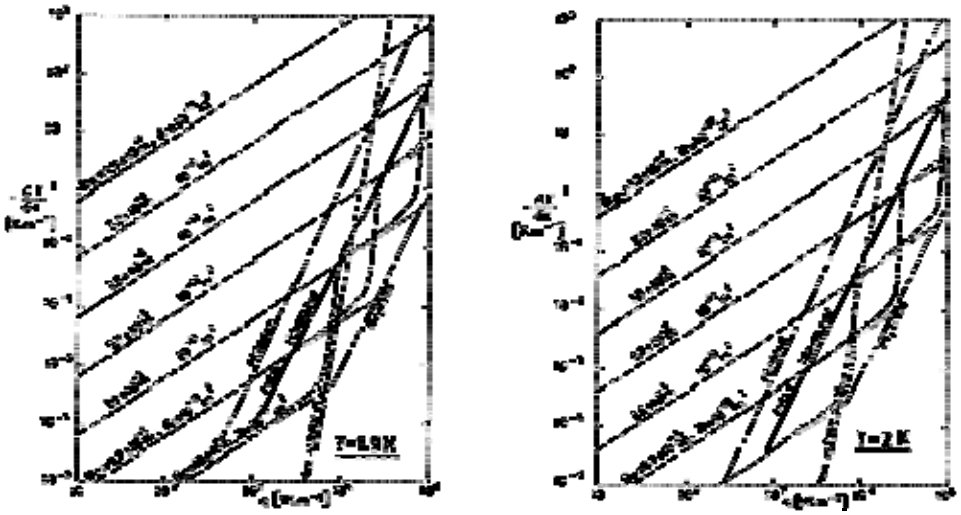

Note: non-si units are used in this figure

Figure 7-11: Diagrams which relate the thermal gradient, dT/dx, to the heat flux, q, in counterflow heat exchange. T=1,5 K to 2 K. Calculated by the compiler after Arp (1970) [10].

The curves labelled with tube diameters, D_E, correspond to the regime of low velocities and have been deduced from Eq. [7-29]. The "K", which is also used to identify these lines, is the permeability or geometric factor of an equivalent porous medium (see clause 7.4.2.4).

The critical values of q have been deduced from Eq. [7-15] with $\vec{u}_n$ calculated as follows:

▬•▬ $v_{sc\,1}$ from Eq. [7-30] with $a_o = 10^{-10}$ m and v_{nc1} related to v_{sc1} through the condition $j = 0$

▬••▬ $v_{sc\,1}$ from Eq. [7-31] and v_{nc1} as above;

▬▬•▬▬ $v_{nc\,2}$ from Eq. [7-35] and Figure 7-10.

The last curve will be used to estimate the heat transfer rate in the intermediate region. Finally, the solid line has been deduced from Eq. [7-34].

The behavior of dT/dx vs. q in the intermediate regime has been conjectured by Arp (1970) [10] as follows.

1. The temperature gradient required to transfer a given rate, once v_{sc1} has been just exceeded, will be slightly larger than that predicted by means of Eq. [7-29].
2. When the normal flow velocity increases up to v_{nc2}, dT/dx vs. q predicted by Eq. [7-29] is one to two orders of magnitude less than predicted by Eq. [7-34]. The real curve should be somewhere between these two, and not too close to the upper one.
3. Once Re_c has been exceeded, turbulence becomes fully developed as velocities further increase by a factor of two or less, then Eq. [7-34] applies.

Dotted lines in Figure 7-11 have been sketched with these arguments in mind.

Equation [7-16], with $m = 0$, indicates that large values of q can be obtained, without v_n exceeding v_{nc},when p and, thence, ρ is large enough. That is why pressurized superfluid helium constitutes a very appropriate coolant.

Experimental data for counterflow heat exchange in He II at atmospheric pressure have been reported by Bon Mardion, Claudet & Seyfert (1979) [26]. Their results are summarized in Figure 7-12, where

$$X(T) = L(T)q^{3,4} \qquad [7\text{-}36]$$

$L(T)$ [m] being the distance between the channel section at temperature T and the warm end at T_λ. q [W.m^{-2}] is the wall mean heat flux between both sections.The curve in Figure 7-12 could be used in several ways.

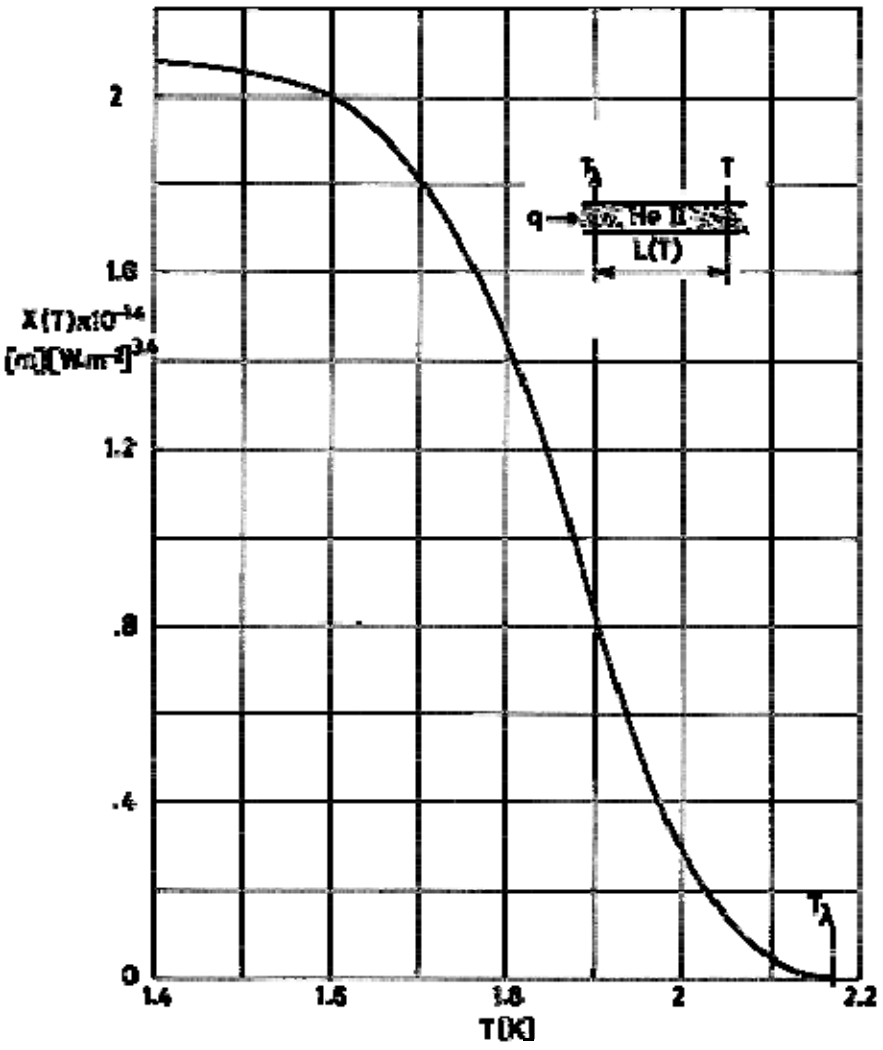

Note: non-si units are used in this figure

Figure 7-12: Temperature profile along a channel filled with He II at atmospheric pressure in conterflow heat exchange. From Bon Mardion, Claudet & Seyfert (1979) [26].

1. When q = 1 W.m^{-2}, $X(T)$ is the length L giving the position of the cross section of the tube at which the temperature is T, measured from that where $T = T_\lambda$. In this sense the Figure 7-12 represents the temperature profile along the tube.

2. For given q and end temperatures, T_i and T_o, the required channel length will be

$$L = \left[X\left(T_i\right) - X\left(T_o\right)\right] q^{-3,4} \qquad [7\text{-}37]$$

Equation [7-37] together with Figure 7-12 will also:

3. Provide q when L, T_i and T_o are given.

4. Provide $X(T_o)$ when L, q and $X(T_i)$ are known.

The range of parameters explored experimentally was

1,4 K ≤ $T \leq T_\lambda$

$2 \leq 10^3 D_E \leq 5$

$1 \leq 10^2 L \leq 100$

The uncertainty inherent in the curve of Figure 7-12 is of the order of 3%.

7.1.4 Heat transfer at arbitrary combinations of vn and vs

Among the many experiments performed in wide channels those done on the simple counterflow configuration have been the most extensive and, to some extent, those giving the least ambiguous results.

Counterflow could not be representative of the general behavior of He II when both transport velocities are independently controlled. This type of experiments are not easily found in the literature however. Olijhoek et al. (1973, 1974) [173] & [174] reported results of tests which can be analyzed in terms of the Gorter & Mellink friction (Eq. [7-33]) although v_n and v_s are independent from each other.

Strict counterflow seems to appear even in complicated geometries where v_n and v_s should vary in an independent fashion. In an experimental configuration (Slegtenhorst (1981b) [223]) a closed circuit is formed by two identical glass capillaries (1 and 2) connected in series via a superleak (through which $\Delta\mu = 0$) The remaining part of the circuit is a He bath the temperature of which is kept constant. Two independently controlled heaters at either side of the superleak are used to adjust the normal velocities through either capillary.

The results from this experiment can be predicted from the flow characteristic of the individual capillaries. A linear in crease of dT_2/dx is observed when v_{n2} is slowly increased from zero, for constant v_{n1}. The value of dT_1/dx, on its turn, remains totally unaffected by the increasing of v_{n2}. At higher values of v_{n2} this linear flow state appears to become metastable (recall the discussion in clause 7.1.3, in connection with Figure 7-8). At an unpredictable high value ofv_{n2} a sudden jump in T_2 occurs, accompained by a similar change in T_1. The transition can be iniciated at smaller values of $v_{n2}$by the application of a mechanical shock, but once it has occurred, a return to the linear flow state through variation of v_{n2} is not possible.

Experimental evidence indicates that in the laminar region independent strict counterflows are established in both capillaries at least for high values of v_n. This contradicts the principle of constancy of the circulation in the superfluid (see clause 7.1.1), as we will see. Mutual friction, after starting, creates the circulation which is present in the loop during the experiment.

If the superfluid motion starts from rest (and no mutual friction exists), the circulation in the superfluid should be zero at any instant. That is,

$v_{s1} - v_{s2} = 0$,

where contributions to circulation other than through the capillaries (which are very slender) have been neglected. The sign of the circulation is different in both capillaries. On the other hand, mass conservation in the loop requires

$$\rho_n v_{n1} + \rho_s v_{s1} + \rho_n v_{n2} + \rho_s v_{s2} = 2\rho_s v_{s1} + \rho_n \left(v_{n1} + v_{n2}\right) = 0 .$$

Then, conservation of circulation would yield

$$v_{s1} = v_{s2} = -\frac{\rho_n}{2\rho_s}\left(v_{n1} + v_{n2}\right)$$

Note: non-si units are used in this figure

,

which does not correspond to strict counterflow in both capillaries ($v_{s1} = -\rho_n v_{n1}/\rho_s$, $v_{s2} = -\rho_n v_{n2}/\rho_s$).

7.1.5 Vapor formation

Vapor formation within the He II bulk could be of concern when the pressure and temperature within the liquid are close to the saturated liquid line in the absence of thermal flux. This situation could occur, under normal gravity conditions, in an open system where the liquid helium is in equilibrium with its vapor at the liquid surface.

Local boiling in counterflow heat exchange of He II in a nozzle has been analyzed by Broadwell & Liepmann (1969) [30]. Their nozzle geometry insured that $|v_n\text{-}v_s|$ was only large near the throat where Gorter & Mellink regime prevailed. The case of a cylindrical channel under turbulent conditions has been considered by Arp (1970) [10]. A somewhat different situation, in volving low heat fluxes, which could be suitable to superfluid porous plugs (see Clause 7.4), is considered here.

In Figure 7-13 He II is in equilibrium with its vapor at a liquid surface placed above the top end of a slender cylindrical vertical tube. It is assumed that heat is added only to the liquid within the tube either from the top or from the bottom.

Figure 7-13: Tube and He II bath arrangement.

Assuming counterflow heat exchange at low velocities (clause 7.1.3) the distribution of pressure and temperature within the tubecan be expressed, after Eqs. [7-15], [7-28] and [7-29], as follows:

$$p(x) - p_1 = \rho g(1+x) \pm \frac{32q}{D_E^2} \int_0^x \frac{\mu_n}{\rho s T} dx \qquad [7\text{-}38]$$

Note: non-si units are used in this figure

$$T(x) - T_1 = \pm \frac{32q}{D_E^2} \int_0^x \frac{\mu_n}{\rho^2 s^2 T} dx \qquad [7\text{-}39]$$

The sign - before the integral will be used when the heat source is top placed in the cylindrical tube.

If $(dp/dT)_{sat}$ is the slope of the vapor-liquid equilibrium line, the power input, q^*, necessary for local boiling at level x^* can be deduced from

$$\left(\frac{dp}{dT}\right)_{sat} = \frac{\frac{32q^*}{D_E^2} \int_0^{x^*} \frac{\mu_n}{\rho s T} dx \pm \rho g(1+x^*)}{\frac{32q^*}{D_E^2} \int_0^{x^*} \frac{\mu_n}{\rho^2 s^2 T} dx} \qquad [7\text{-}40]$$

This equation is only valid when boiling occurs within the tube ($x^* \geq 0$).

When the heat source is top-placed and the temperature differences are so small that the introduction of a mean value of T to evaluate the integrals in Eq. [7-40] is justified, the following simplified expression results.

$$q^* = \frac{\rho s T D_E^2}{32\mu_n} \frac{1}{1 - \frac{(dp/dT)_{sat}}{\rho s}} \rho g \frac{1 + \frac{x^*}{l}}{\frac{x^*}{l}} \qquad [7\text{-}41]$$

Note: non-si units are used in this figure

Usually $(dp/dT)_{sat}/\rho s \approx 0{,}1$ and $x^*/l \ll 1$, thus the above expression can be further simplified.

Equation [7-41] furnishes an estimate of the fraction x^*/l, of tube length which is filled with liquid He II for a given value of the heat flux, q^*, under the assumption of onedimensional flow (planar vapor-liquid interface). In real practice matters concerning boiling in very slender tubes are not so simple, as we will see in the next paragraph. See also clause 7.4.2.4.

7.1.6 Superfluid Helium film

Solid surfaces in contact with He II are covered by a thin film of liquid.

It is presumed that this thin film will be the critical thermal link between the heat source, which is the device to be cooled, and the heat sink, which is the boil-off vapor. This will be particularly so during the latter stages of the depletion of the stored Helium II. Thus, the calculation of the heat transfer through this film, as a function of film thickness, would be crucial to a proper design.

Various determinations of the film thickness for saturated layers (layers in equilibrium with the bulk liquid), at rest under normal gravity conditions have been performed. For example, in a tube partially filled with He II the thickness at 10^{-2} m height above the meniscus is between 3 and 3,5 x 10^{-8} m, and decreases as the power (-0,4) of the height (Mendelssohn (1960) [148]).

Kontorovich (1956) [125] showed that when a superfluid film undergoes potential flow its thickness should decrease. Let us consider the configuration shown in Figure 7-14, where a film steadily flows down a vertical wall toward a reservoir.

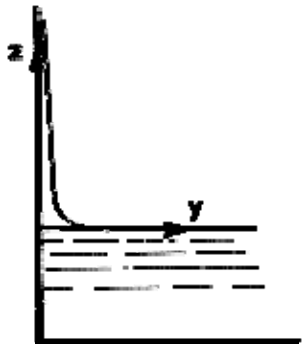

Figure 7-14: Film and bulk liquid configuration

Combination of Eqs. [7-5], with $\partial/\partial t = 0$, and [7-8] yields:

$$\nabla\left(\frac{1}{2}u_s^2 + U + \mu(p,T) - \frac{1}{2}\frac{\rho_n}{\rho}(\vec{u}_n - \vec{u}_s)^2\right) = 0 \qquad [7\text{-}42]$$

Note: non-si units are used in this figure

$$U = gz - \frac{\alpha}{y^3}$$

Note: non-si units are used in this figure

α being a constant which specifies the Van der Waals interaction with the wall, and $\mu(p,T)$ the chemical potential, per unit mass of stationary fluid.

Since the film is extremely thin (see below):

1. We can neglect the motion of the normal component ($\vec{u}_n = 0$).
2. According to the local continuity equation, $u_{sy}/\delta \approx u_{sz}/L$, δ and L being the characteristic lengths parallel to the axes y and z respectively (in particular, δ is the film thickness), and u_{sy}, u_{sz} are the corresponding components of the vector $\vec{u}_s$. Thus, $u_{sy} \approx (\delta/L)u_{sz} << u_{sz}$.
3. Since the motion of the superfluid component is irrotational throughout the fluid region, which includes a part at rest (see clause 7.1.1),

   $$\frac{\partial u_{sz}}{\partial y} = \frac{\partial u_{sy}}{\partial z}$$

   Note: non-si units are used in this figure

   and then the change with y of u_{sz} is negligible compared to u_{sz} itself,
   $\Delta_y u_{sz} \approx (\delta/L)u_{sy} \approx (\delta/L)^2 u_{sz} << u_{sz}$,
   thence we infer that $u_{sz} = v_s(z)$ depends only on z.

Integrating Eq. [7-42], with $\vec{u}_n = 0$, over the film surface

$$\frac{\rho_S}{2\rho}v_s^2 + gz - \frac{\alpha}{\delta^3} + \mu(p_o,T_o) \qquad [7\text{-}43]$$

Note: non-si units are used in this figure

where p_o and T_o are the pressure and temperature of the reservoir. When the flow is isothermal, according to Eq. [7-8],

$$\mu(p,T) - \mu(p_o,T_o) = \frac{p - p_o}{\rho}$$

Note: non-si units are used in this figure

Neglecting changes in hydrostatic pressure of the helium vapor, p-p_o results to be the pressure jump through the film surface at height z. If, in addition, the capillary pressure is negligible (curvature of the film surface small enough), p-$p_o = 0$ and, thence, Eq. [7-43] becomes:

$$\frac{\rho_s}{2\rho} v_s^2 + g - \frac{\alpha}{\delta^3} = 0 \qquad [7\text{-}44]$$

This equation differs from the classical Bernoulli equation for normal liquids in the ρ_s/ρ factor, which is due to the fact that in this case only the superfluid moves. On the other hand, Eq. [7-44] indicates that δ should decrease when v_s increases (Bernoulli thinning).

Now, let m be the mass of fluid transported by the film in unit time across a section of unit width.

$$m = \rho_s v_s \delta \qquad [7\text{-}45]$$

Combination of Eqs. [7-44] and [7-45] yields the following expression to calculate δ:

$$\tilde{z}\tilde{\delta}^3 + \tilde{\delta} - 1 = 0 \qquad [7\text{-}46]$$

where

$\tilde{z} = z / z_c$, $\tilde{\delta} = \delta / \delta_c$, and

Note: non-si units are used in this figure

$$z_c = \frac{m^6}{8\alpha^2 \rho^3 \rho_s^3 g}$$

Note: non-si units are used in this figure and $\delta_c = \frac{2\alpha\rho\rho_s}{m^2}$

are characteristic lengths in the vertical and horizontal direction, respectively.

$\tilde{z}$ *vs.* $\tilde{\delta}$

Note: non-si units are used in this figure

, as given by Eq. [7-46], is represented in Figure 7-15 as a full line.

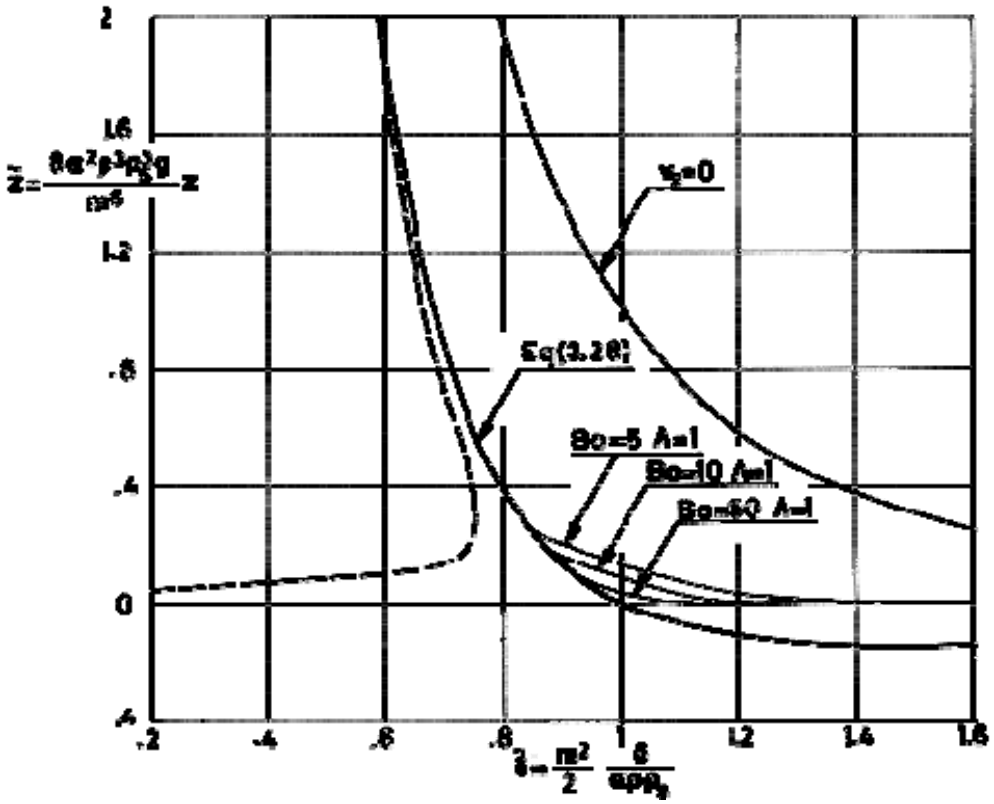

Note: non-si units are used in this figure

Figure 7-15: Bernoulli thinning. The full line corresponds to Eq. [7-46]. The dotted line is the Kontorovich (1956) [125] solution. Neither solution gives the correct transition of the film interface to the horizontal free surface in the reservoir, because capillary pressure has been neglected. Curves labelled with the values of *Bo* correspond to Eq. [7-49].

Kontorovich (1956) [125] gives for δ vs. m the expression

$$\delta = \left(\frac{\alpha}{gz}\right)^{1/3}\left[1-\frac{m^2}{6\alpha\rho\rho_s}\left(\frac{\alpha}{gz}\right)^{1/3}\right] \qquad [7\text{-}47]$$

which can be deduced by approximate solution of Eq. [7-46] when

$\tilde{\delta}$

Note: non-si units are used in this figure

is small enough. In dimensionless coordinates Eq. [7-47] becomes

$$\tilde{\delta} = \frac{1}{\tilde{z}^{1/3}}\left(1-\frac{1}{3\tilde{z}^{1/3}}\right) \qquad [7\text{-}48]$$

Equation [7-48] has been represented in Figure 7-15 by means of a dotted line. It deviates from the exact solution of Eq. [7-46] near $z = 0$, and apparently deviates in the wrong direction (the free surface of the film should vary continuously with z).

Although the corner near the free surface of the reservoir requires a more complete treatment than above, since most of the already introduced simplifying assumptions become invalid in that region, the mere consideration of the capillary pressure yields a realistic shape of the free surface throughout.

When capillary pressure is taken into account, Eq. [7-46] becomes

$$\tilde{z}\tilde{\delta}^3 + \tilde{\delta} - 1 = \frac{\tilde{\delta}^3}{Bo} \frac{d^2\tilde{\delta}/d\tilde{z}^2}{\left[\Lambda^2 + \left(\frac{d\tilde{\delta}}{d\tilde{z}}\right)^2\right]^{3/2}} \qquad [7\text{-}49]$$

where $Bo = \rho g \delta^2/\sigma$ is a Bond number (see clause 6.4.7.1), which depends on the temperature, the mass flow rate and the gravity level. $\Lambda = z_c/\delta$ is an aspect ratio which, in addition to temperature, strongly depends on the mass flow rate. This differential equation is integrated with the following boundary conditions:

1. Far from the reservoir,

   $\tilde{z} \to \infty \quad , \quad \tilde{z}\tilde{\delta}^3 + \tilde{\delta} - 1 \to 0$

   Note: non-si units are used in this figure

2. At the reservoir free surface,

   $\tilde{z} \to 0 \quad , \quad d\tilde{\delta}/d\tilde{z} \to \infty$

   Note: non-si units are used in this figure

Assuming that Bo is large enough, the right hand side of Eq. [7-49] is negligible except near $\tilde{z} \approx \tilde{\delta} - \tilde{1} \approx 0$

Note: non-si units are used in this figure

where the curvature of the free surface becomes very large. An approximate solution of Eq. [7-49], valid when Bo is large, can be obtained by use of the method of "matched asymptotic expansions" (see Van Dyke (1975) [248]).

Let us assume $\Lambda \approx 1$. Introducing "inner variables", which are of order unity in the region under study

$$X = \sqrt{\Lambda Bo}\,\tilde{z}$$

Note: non-si units are used in this figure

$$Y = \sqrt{Bo}\left(\tilde{\delta} - 1\right)$$

Note: non-si units are used in this figure

Eq. [7-49] becomes, after neglecting higher order terms,

$$X + \sqrt{\Lambda} Y = \frac{d^2 Y / dX^2}{\left[1 + \left(dY / dX\right)^2\right]^{3/2}} \qquad [7\text{-}50]$$

Note: non-si units are used in this figure

with the boundary conditions:

$X \to \infty \quad , \quad X + \sqrt{\Lambda} Y \to 0$

Note: non-si units are used in this figure

,

$X \to 0 \quad , \quad dY / dX \to \infty$

Note: non-si units are used in this figure

.

This is the well-known problem of finding a curve the curvature of which is proportional to the distance to a straight line,

$X + \sqrt{\Lambda} Y = 0$

Note: non-si units are used in this figure

.

The solution, with our particular boundary conditions, is too complicated (and useless) to be given here, but it is represented by the curves labelled with the values of *Bo* in Figure 7-15.

Summing up, Kontorovich theory seems to correctly predict the thinning of a superfluid film flowing stationary, but Eq. [7-47] cannot be used for a quantitative assessment of the effect.

Saturated films of helium are typically 100 atomic layers thick (1 atomic layer = 3,6 A = 3,6 x 10^{-10} m) and can flow with velocities up to 0,5 m.s^{-1}. The expected change in thickness for such a film could be about 20 atomic layers in some cases.

The first attempt to experimentally detect the Bernoulli thinning was made by Keller (1970) [120]. In his experiments the saturated film of He II was caused to flow, sub critically, between the plates of a capacitor. Measured capacitance should vary proportionally to the thickness of the film. No change in film thickness was observed within ± 5 A for all flow velocities up to about 0,5 m.s^{-1}.

Many authors followed Keller in the confirmation or disproving of Bernoulli thinning. A list of attempts is given in Table 7-1. The list is by no means complete and should not be considered as a poll to discover the most widely accepted opinion. See also a review by De Bruyn Ouboter (1973) [53] of the work performed up to 1972.

Up to the moment no thinning has been observed in experiments performed under truly steady conditions. Recall that Eq. [7-42] has been obtained by assuming $\partial / \partial t = 0$.

Van Spronsen et al. (1973, 1974) argue that condensation of the vapor tends to restore the original film thickness. In their set of experiments, where helium film covers the inside of a very long and narrow capillary wound into a spiral, condensation is avoided because the film, which oscillates between both end-reservoirs of the tube, drains away the condensates which cannot be accumulated.

Experiments under non-steady conditions have been performed also by Wang & Petrac (1975) [258]. These authors, however recognize that, since the characteristic length of their experimental cell (L = 0,025 m) is much smaller than the wavelength of surface waves (third sound, 2,4 m), non-steady effects introduced by any surface disturbance should be taken into account. Table 7-1.

Table 7-1: Several Attempts to Experimentally Verify the Bernoulli Thinning (BT)

Author	Keller (1970)	Van Spronsen et al. (1973) [251]	Telschow et al. (1975) [234]	Wang & Petrac (1975) [258]
Aim of the experiment	BT detection in steady flow.	Avoidance of condensation by oscillating flow.	Use of more sensitive techniques.	Non-steady and liquid-vapor instability effects.
Temp. [K]	1,1-1,9	1,2-1,8	1,5-1,8	1,1-2,0
Driving force	Hydrostatic pressure.	Hydrostatic pressure.	Thermal.	Thermal.
Type of flow	Subcritical.	Critical.	Subcritical.	Subcritical.
Max. Velocity [$m.s^{-1}$]	0,5	0,3	1.	0,16
Typical layer thickness [A]	400.	150.	40.	1 400.
Characteristic length of the cell [m]	0,08	200.	0,15	0,025
Characteristic length of the flow [m]		2×10^{-5} (see text)		
Frequency [Hz]	0	0,002	0	0,025
Measurement technique	Capacitive	Liquid level in the end reservoirs.	Doppler shift of surface waves.	Capacitive.
Accuracy [A]	5.	0,1	0,07	1.
Thinning detected	No	Yes	No	Independent of BT.

Integrating Eq. [7-4] along each streamline, without neglecting non-steady effects, and pursuing the same reasoning as above to arrive at Eq. [7-44], the following equation results:

$$\frac{\partial}{\partial t}\int_0^x \vec{u}\cdot\vec{dl} + \frac{\rho_s}{2\rho}v_s^2 + gz - \frac{\alpha}{\delta^3} = 0 \qquad [7\text{-}51]$$

Note: non-si units are used in this figure

where

$\vec{dl}$

Note: non-si units are used in this figure

is the vector element of streamline.

Quasi-steady experiments will be performed under conditions such that non-steady terms be negligible compared to the kinetic energy term, i.e.:

$$\frac{L_{eff}}{t} << \frac{\rho_s}{2\rho} v_s$$

Note: non-si units are used in this figure

,

L_{eff} and t being, respectively, a characteristic length and a characteristic time of the fluid flow.

Although in the case of Van Spronsen et al. (1974) the characteristic time can be deduced from a typical frequency of the oscillation, which they quote, the characteristic length is not so clearly defined.

The oscillation of the film (Atkins oscillation), the aim of which is to avoid the accumulation of condensates, is induced by moving up and down, opposite to each other, both end reservoirs. In addition to the characteristic frequency of the oscillation, a characteristic length appears in the definition of the inertial mass of the oscillating system.

$$L_{eff} = \int_0^x \frac{\rho A}{\rho_s A_s} dx$$

Note: non-si units are used in this figure

,

where L is the length of the capillary, A the cross-sectional area of the end reservoirs and A_s the cross-sectional area of the liquid within the tube (the shape of the cross-sections is annular because the film is attached to the wall).

Since A_s is small, L_{eff} is large, $L_{eff} \approx 2 \times 10^5$ m, rendering L_{eff}/t thousand times larger than $\rho_s v_s/2\rho$.

Even assuming that the characteristic length is L, the time derivative term becomes of the same order as the kinetic energy term.

Thence, the thinning observed in this experiment could be, partially or totally, due to other than Bernoulli effect.

Experiments to measure, inter alia, the film thickness under reduced gravity conditions have been performed (Mason et al. (1976) [141], Yang & Mason (1980) [268]).

These experiments were undertaken to check Eq. [7-44] which indicates that the thickness of stationary films ($v_s = 0$) should vary as $(gz)^{-1/3}$.

The first experiments (March 1976) were performed using an aircraft which provided 45 periods of 20 s reduced gravity.

After 1976 a Black Brant sounding rocket was used. It provided a free fall period of about 5 min of 10^{-6} g level. The experiments, together with preparatory laboratory tests on Earth, have been reported by Yang & Mason (1980) [268].

The apparatus used to measure the film thickness was a quartz crystal microbalance (QCM). If a properly cut crystal oscillating in a shear mode is loaded with a liquid film on its surface, its fundamental resonance frequency shifts according to the layer thickness. In this way thicknesses of films several hundreds Angstrom thick can be measured with less than ± 2% error.

The supporting surfaces were oriented one parallel to the thrust axis and two perpendicularly, within a cell maintained at slightly below saturation pressure (Figure 7-16).

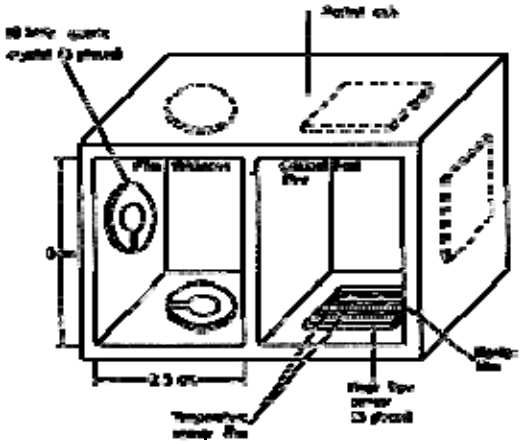

Figure 7-16: Cell used to perform reduced-gravity test. The film thickness experiments were performed in the left hand side compartment. From Yang & Mason (1980) [268].

A crucial, and only partially solved problem was keeping the film thickness in the chamber against temperature variations in the range 1,5 K to 2 K. To this aim, an helium reservoir packed with aluminium powder was connected to the film experiment chamber. The powder package provides an additional large surface area and acts as a capillary retention device which supplies helium to the cell when the temperature rises, absorbing helium when it decreases. This device, although successful, greatly complicated the interpretation of the experiment results.

The main conclusions were the following:

1. The reduced gravity behavior of the helium can be understood in terms of laboratory observations.
2. Film thicknesses are independent of the position in the chamber and are thicker than those in the same chamber under normal gravity by a factor of the order of 2. Thickening of the film, nevertheless, could be partly due to the release of liquid by the powder package.

As a consequence of film thickening under reduced gravity, the critical velocities and van der Waals forces are reduced and, thence, the films became more sensitive to heating.

Another set of experiments on the properties of superfluid helium in zero g (SHFE) has been selected by NASA for performance on board Spacelab 2. The experimental set includes: measurement of the fluid thermal and dynamic behavior properties of quantized surface waves in the superfluid film, and performance of a Dewar in space. A fairly detailed description of the system being developed for this set of experiments is made by Urban et al. (1978) [244].

7.2 Kapitza conductance

Experiments measuring the thermal conductivity of liquid helium at low temperatures should take into account the thermal boundary conductance, h_k, first noticed in experiments with He^4 by Kapitza in 1941.

Formally, h_k is defined as:

$$h_k = \lim_{\Delta T \to 0} \frac{Q/A}{\Delta T}$$

Note: non-si units are used in this figure

where Q/A is the heat flow per unit area across the liquid-solid interface of area A.

h_k ranges between 1 W.m^{-2}.K^{-1} and 50 x 10^3 W.m^{-2}.K^{-1} at 1,9 K for the various solids investigated (1,9 K is an optimum temperature for heat transfer through the bulk fluid, it is, for example, the operating temperature of several superconducting particle accelerators). At 1,9 K, using the highest observed h_k of 50 x 10^3 W.m^{-2}.K^{-1} one finds that the length of helium II which would present an equivalent thermal barrier to a small heat flux is about 3000 km (Snyder (1970) [225]). Thus Kapitza conductance controls the heat transfer from a solid body to helium II at temperatures near the λ point. At lower temperatures of about 0,5 K, where helium is a poor thermal conductor, the reverse may be true.

Kapitza conductance is not associated with the peculiarities of superfluid helium as was shown experimentally with He^3 above the transition temperature (see, f.e., Keller (1969) [119] pp. 192 ff).

The heat transfer between liquid helium and a solid is poorly understood. From the experimental side, Kapitza conductance has been measured for only about two-dozens solids (no data on structural materials such as stainless steels or titanium have been found), and order of magnitude differences have been reported for samples of the same solid. The most apparent explanation is difference in sample preparation, which can be due to one or more parameters of the following list (Mittag (1973) [153]): material impurity density, dislocation density, surface damage, stress, grain size of crystals, surface roughness, impurity and oxide layers on the surface.

The theoretical picture is not better (see the review article by Snyder (1970) [225]). Heat transfer across the interface is described in terms of the transmission and reflection of acoustic waves (phonons) at the interface. The Phonon Radiation Limit appears to furnish an upper limit for the Kapitza conductance but the actual mechanisms of energy exchange at the interface, which determine the lower limits for the conductances, are poorly understood.

Most theoretical work is based in the phonon transmission mechanism put forth by Khalatnikov (Acoustic Mismatch Theory) who suggested that because of the mismatch of the acoustic impedance between a solid and a liquid, only a small fraction of the available phonons should be transmitted. Theoretical expressions predict conductances 2 or 3 orders of magnitude below the phonon radiation limit, and about 1 to 2 orders of magnitude below the values observed experimentally (the figures are not so bad for non-metals). The acoustic mismatch, however, predicts a T^3 temperature dependence for the Kapitza conductance which is approximately obeyed for a variety of solids, although the actual exponent of T ranges from n = 2,3, to n = 4,2 (smaller values have been reported, see Table 7-2 to Table 7-41 below).

Many authors tried to improve upon Khalatnikov theory. For example, Challis et al. (1961) [39] took into account the fact that the layer of heliumclose to the solid has a much higher density than the bulk liquid. They obtained a temperature exponent n = 4,2, and results closer to those observed experimentally in the temperature range 1,4 K to 2,2 K.

A third theoretical approach in terms of a thermal accommodation coefficient, α, has been known long before Kapitza conductance was discovered (see Estermann (1955) [66] for an application to rarefied gas flow problems). Insufficient data are available to profitably use this theory in the present instance.

Summarizing, useful values of Kapitza conductance for design purposes cannot be obtained from the theoretical formulae existing in the literature.

In the following a summary of reported data is given.

Sample characteristics have been specified as far as possible. Nevertheless, the relevance of any given surface parameter is uncertain because of the lack of theoretical understanding of the interface conductance problem.

Materials in Table 7-2 to Table 7-41 have been arranged by ascending Debye temperatures, θ_D.The Debye characteristic temperature is defined as:

$$\theta_D = \frac{h\omega_m}{k}$$

Note: non-si units are used in this figure

where h is the Planck's constant, k is the Boltzmann's constant. k = 1,380 x 10^{-23} J.K^{-1} and ω_m is 2π times the upper frequency of the crystal.

Tables of θ_D for both non-metals and metals can be found in Zemansky (1968) [272] pp. 318 and 327 respectively.

The reason for introducing the Debye temperature is that, according to Challis (1962) [39], h_k varies as θ_D^{-1} when only the highest h_k values reported for each solid are considered.

An attempt has been made to enclose in the tables information regarding the measurement techniques used to get the data.

Basically, the techniques consist in producing a (small) heat flow across the sample-to-liquid interface. The resulting temperature difference between the sample and the liquid is measured when the system reaches thermal equilibrium. It is crucial to avoid heat transfer paths other than through the interface. In order to achieve this a hard vacuum is maintained inside the can which encloses the experimental cell.

The main distinctive features of the several techniques are: the shape and size of the solid, the helium bath in direct contact with the solid, the geometry of the interface with a sharp outline of its boundaries, attachment of the sample, the vacuum environment, heating procedures and temperature measurement in both solid and liquid.

The set of sketches shown below will be referred later in the table. Main advantages and drawbacks of the different techniques are briefly indicated.

7.2.1 Measuring methods

A. Long Sample

The sample is machined to the shape of a top-headed cylinder. The disc heading the cylinder is soft-soldered into a thin sheet forming the base of a small helium cryostat.

Sample and cryostat are in a vacuum and surrounded by a low temperature vessel.

Heat is applied to the lower end of the sample through spool heaters.

Temperatures are measured at two points along the sample and at a single point in the helium bath.

The temperature field in the solid near the interface is certainly not one-dimensional and in several instances appropriate corrections should be introduced.

A1. It is quite similar to A although the interface area is better defined.

A2. The sample supported between two brass flanges by four stainless steel screws. Stainless steel springs keep the pressure on an indium 0-ring seal between the sample and the top brass flange. Sample and flanges are hung from a thin-walled stainless steel tube the top end of which is open to the liquid helium bath.

Temperature is measured in four locations, two in the sample and two in the liquid helium within the tube.

Heat is applied through a strip heater epoxied to the lower end of the sample.

Heat conduction in parallel with the sample is negligible.

A3. The tube containing the liquid helium is fastened to the vacuum chamber whereas the sample is pressed against the tube by means of a spring.

A4. The metal is cast onto the top of a pre-coated sapphire rod resulting in a binary sample of high/low acoustic impedance materials. The top of the sample forms the lower base of the He II bath.

Temperatures are measured at six points in the sample plus one additional point in the helium bath.

Heat is applied to the lower part of the sample.

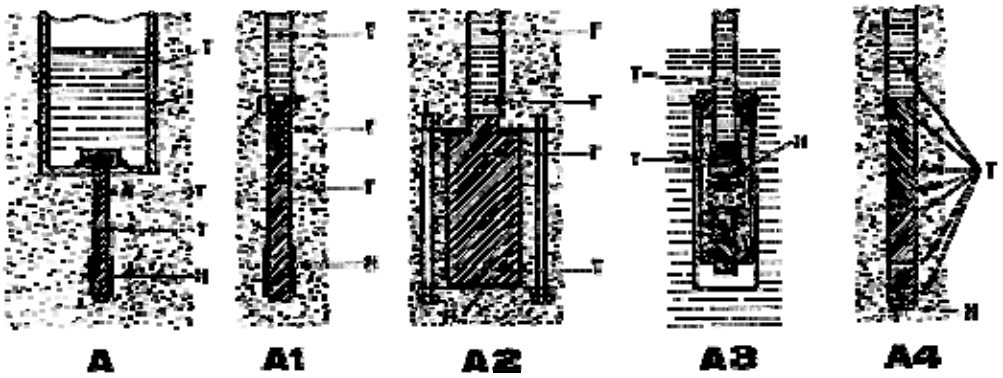

B. Short Sample and Tube

A thin-walled stainless steel tube is soldered (or glued) to the sample and attached to the bottom of a copper container which is evacuated later on. Several such containers are submerged in a helium II bath.

Temperatures are measured with thermometers wound on the sample surface. Bath temperature is closely regulated and measured by a thermometer.

Vacuum face of the specimen is locally heated.

B1. The sample is sealed to a glass tube. Sample and tube are surrounded by a glass vacuum jacket.

Stresses in the glass are relieved by annealing.

B2. The mercury, liquid at room temperature, fills a nylon tube, the lower end of which is forced onto a cupronickel sleeve. A brass plunger, tipped with a Teflon cap, forms a seal impervious to liquid mercury which is removed after the mercury is frozen.

Temperatures are measured in four points along the mercury column by use the thermometers connected to the mercury by platinum wires through holes in the nylon tube.

A heater is placed on the top of the tube. The heater ensures that the sample would freeze from the bottom during cool down, and provides the required heat flux during test.

Heat transfer through the cupronickel sleeve should be accounted for in the normal state tests, although it is quite negligible in the superconducting state.

C. Long Cylinder

A thin-walled stainless steel tube, which contains the He II, is terminated at one end by the sample and at the other end by a surface held at the bath temperature and by the helium feeding line. The sample is sealed to the tube with an indium wire.

A coil former, bolted to the stainless steel tube fulfils the twofold role of fixing the sample and of supporting a heater coil mounted on the top of the sample.

The assembly is enclosed in an evacuated copper can within the He^4 bath (for temperatures above 1 K).

Temperatures are measured at two points along the stainless steel tube and a single point in the sample. A cavity is machined in the sample to place a thermometer as close to the interface as possible.

Differential stresses, partially taken up by the indium seal, could result from cooling to low temperatures.

This method has been used above 0,3 K (with an appropriate He^3 refrigerator).

C1. Differs from C in the sample mounting. Here the coil former and the sample are made of the same material, so that no stresses arise through cooling to low temperatures.

The interface area is nor clearly defined.

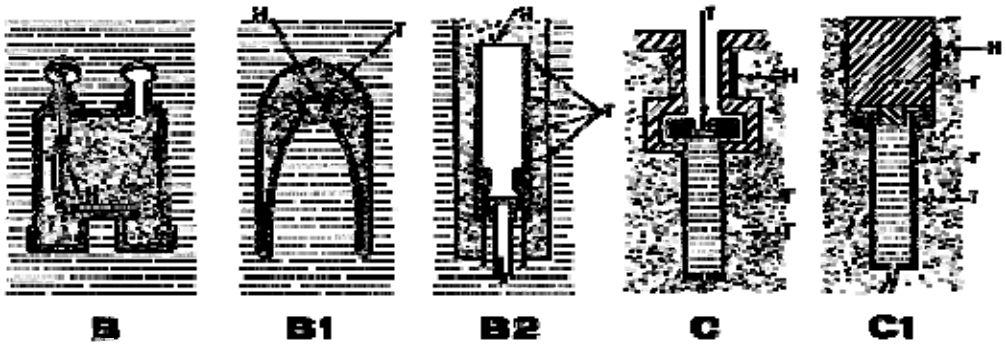

D. Sandwich (Parallel Plate Cell)

The low acoustic impedance medium is cast between two metallic plates furnished with appropriate insulating spacers.

One of the plates is heated, whereas the opposite remains in thermal contact with a helium bath.

Temperatures are measured at the end plates.

D1. When the low acoustic impedance medium freezes at low temperatures, two access ports are provided to the lower plate. Once the space between plates has been filled through one port, the second is sealed off.

Both plates can be independently heated.

The cell is screwed to a copper flange in thermal contact with the helium bath.

E. Hollow Rod

The sample is machined to the shape of a thick-walled cylinder.

Two channels are drilled out in the wall to accommodate the thermometers. The heater is placed in the central cavity.

The aspect ratio of the configuration is less than 10.

Cavities are filled with helium gas at atmospheric pressure.

The assembly is lowered into a helium bath the temperature of which is closely monitored.

F. Resistance Thermometer

A varnish-coated constantan strip (the heater) is fastened to a phenolic substrate.

The constantan strip is coated in its turn by a graphite layer (the sample and resistive component of the thermometer). Potential taps are connected to the graphite layer by means of a silver paint. The assembly is mounted in a He II cryostat.

The thermal conductivity of the graphite should be accounted for in the heat balance.

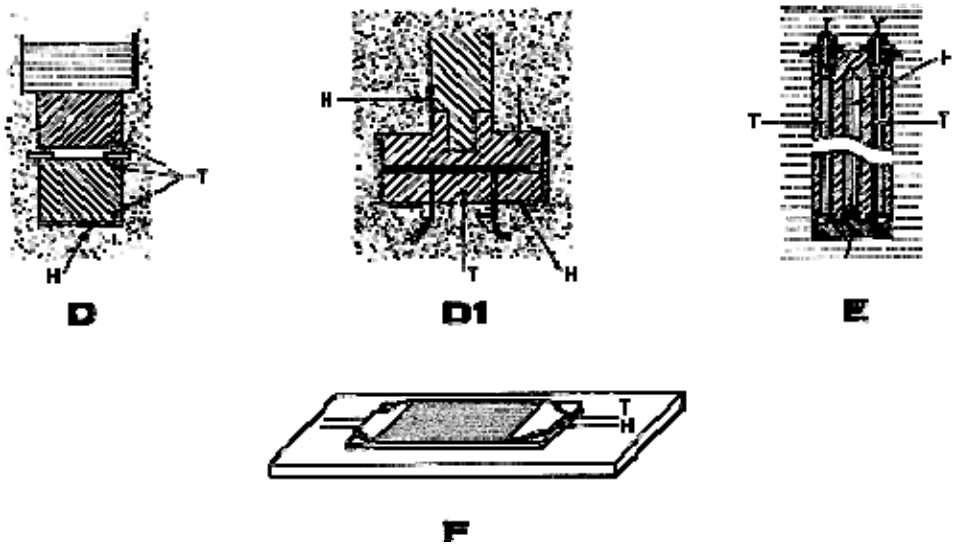

7.2.2 Experimental data

Figures of Kapitza conductance, h_K, vs. temperature, T, summarizing the data, are shown in the following. Figure 7-17 concerns low Debye temperature metals contacting liquid helium. Figure 7-18 corresponds to copper contacting low acoustic impedance materials (acoustic impedance is density times sound velocity). Figure 7-19 is for structural metals and Figure 7-20 for nonmetals, in both cases contacting liquid helium.

More detailed data are given in the subsequent tables. They are arranged as follows: Metallic materials in contact with liquid helium (Table 7-2), Nonmetals in contact with liquid helium (Table 7-32) and Metals in contact with low acoustic impedance media (Table 7-41).

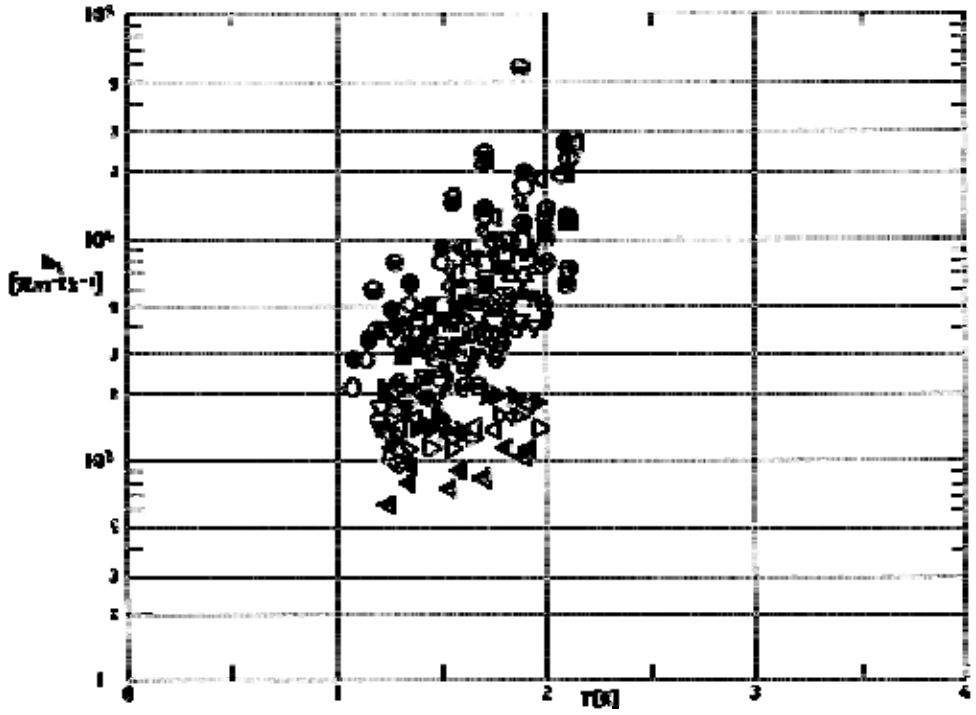

Figure 7-17: Kapitza conductance, h_K, of low Debye temperature metals, Mercury, Lead, Gold and Silver in contact with Liquid Helium, vs. temperature, *T*. See Table 7-2 below.

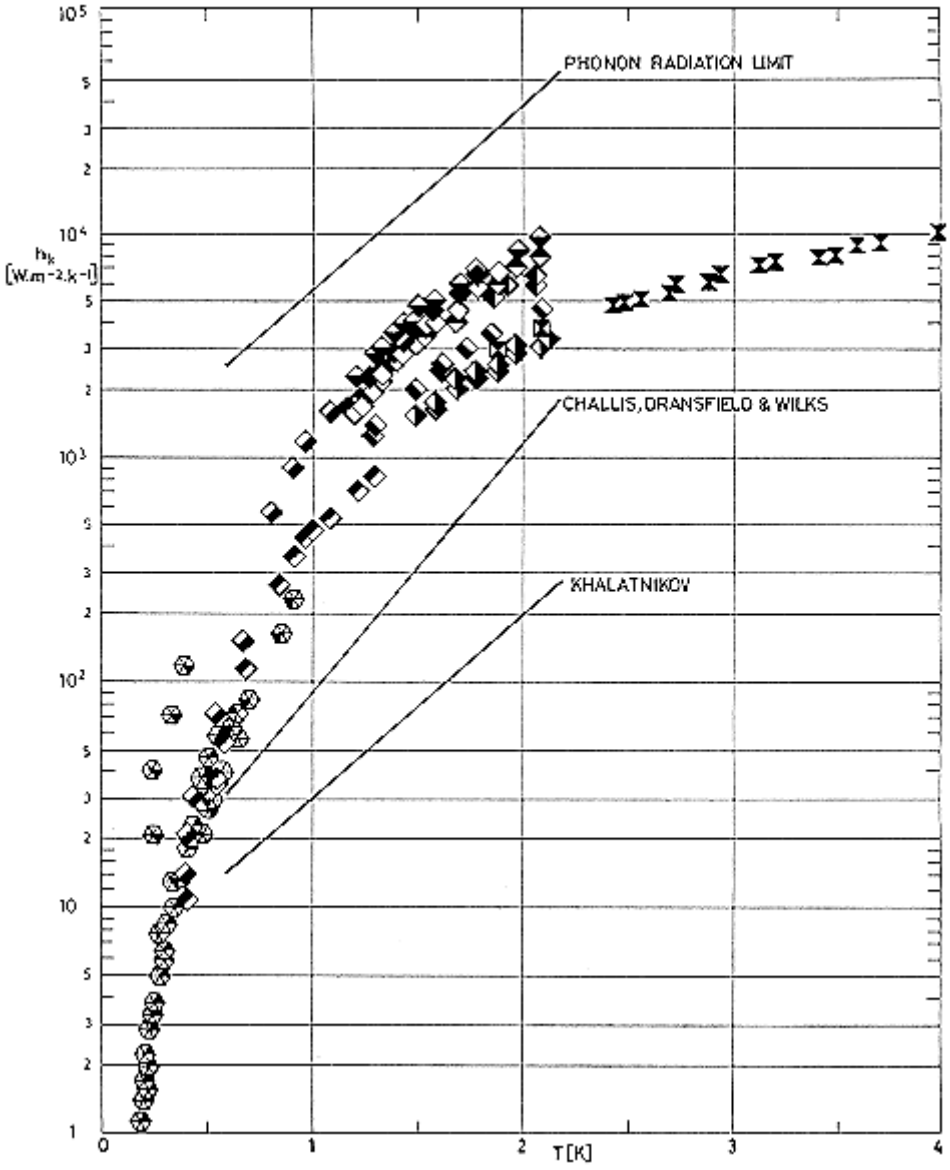

Figure 7-18: Kapitza conductance, h_K, of Copper in contact with various low acoustic impedance materials vs. temperature, *T*. See Table 7-2 and Table 7-41 below. Theoretical results are also shown in this figure.

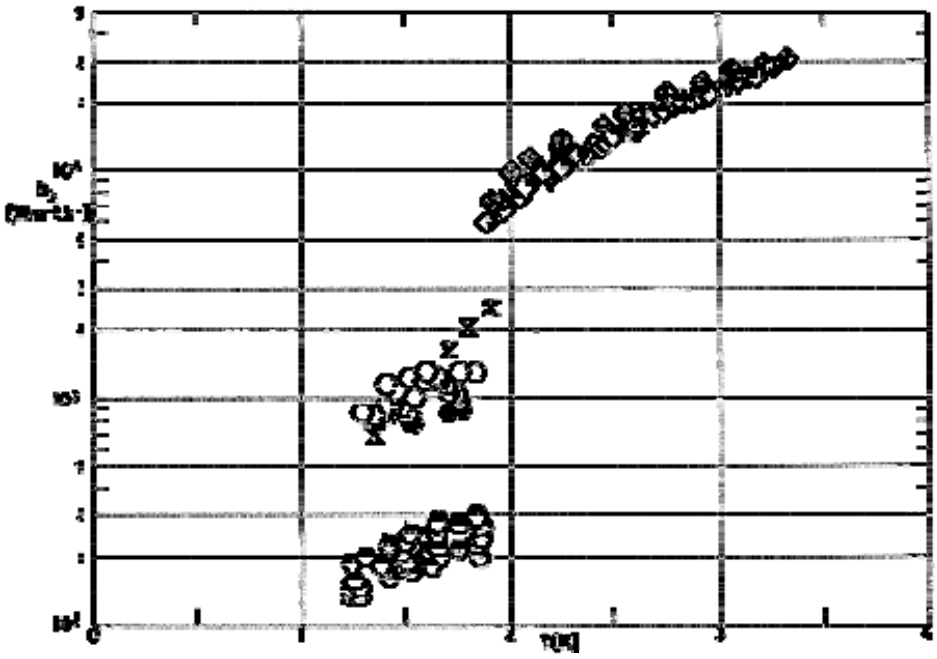

Figure 7-19: Kapitza conductance, h_K, of Tungsten, Aluminium, Molybdenum and Beryllium, in contact with Liquid Helium, vs. temperature, *T*. See Table 7-2 below.

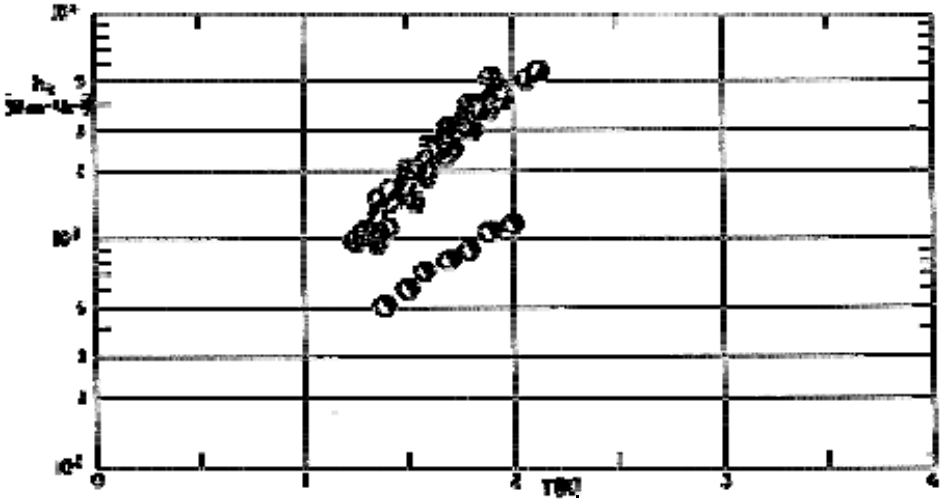

Figure 7-20: Kapitza conductance, h_K, of Nonmetals in contact with Liquid helium vs. temperature *T*. See Table 7-32 below.

Table 7-2: Kapitza Conductance, h_K, of Metals in Contact with Liquid Helium (He II)

Solid θ_D [K]		References
Mercury 72, see Table 7-3		Neeper, Pearce & Wasilik (1967) [164]
Lead 105, see Table 7-5	< 99,995 % pure	Challis (1962) [39]
	99,995 % pure	
	< 99,9995 % pure	
	No details given.	Challis, Dransfeld & Wilks (1961) [40]
	99,9997 % pure	Wey-Yeng (1962) [263]
Indium 108, see Table 7-7		Neeper & Dillinger (1964)
Gold 164, see Table 7-9		Johnson & Little (1963) [108]
Tin 199, see Table 7-11		Wey-Yeng (1962) [263]
Platinum 240, see Table 7-13		
Silver 225, see Table 7-15		Alnaimi & van der Sluijs (1974) [4]
Palladium 274, see Table 7-17		Reivari (1969) [192]
Niobium 275, see Table 7-18		Mittag (1973) [153]
Copper 343, see Table 7-20	99,999 % pure	Jones & van der Sluijs (1973) [111]
	99,9 % pure	Wey-Yeng (1962) [263]
	OFHC (oxygen free high conductivity)	Johnson & Little (1963) [108] Mittag (1973) [153]
	High purity (no further details given)	Challis, Dransfeld & Wilks (1961) [40]
	99,999 % pure	Challis (1962) [39] Patullo & van der Sluijs (1983) [178]
Tungsten 400, see Table 7-22		Johnson & Little (1963) [108]
Aluminium 428, see Table 7-24		Van Sciver (1978) [249] Mittag (1973) [153]
Nickel 450, see Table 7-26		Wey-Yeng (1962) [263]
Molybdenum 450, see Table 7-28		Alnaimi & van der Sluijs (1975) [3]
Beryllium 1440, see Table 7-30		

Table 7-3: Kapitza Conductance, h_k, of Mercury 72 in Contact with Liquid Helium (He II)

Sample	Key	h_k at 1,9 K [W.m^{-2}.K^{-1}]	Temp. Exponent n	Others	Sample Description
99,999 % pure	○	17000	3,6	Surface Ax10^4 [m^2]: 0,4 Measur. Method: A4 Temp. Range [K]: 1,1-2,1	Table 7-4
	●	20000	3,5		

Table 7-4: Sample Description of Mercury 72 in Table 7-3

h_k at 1,9 K [W.m^{-2}.K^{-1}]	Sample Conditions	Storage, Environment before Cool-down	Sample Dimensions [m]	Comments
17000	Mercury was held by a thin-walled nylon tube, the lower end of which was forced on a cupronickel sleeve capped with a seal impervious to liquid mercury. The sleeve was wet with mercury using nitric acid as a flux. The lower base of the assembly was soft-soldered into the bottom of a stainless steel cannister.	The cannister was placed into the Dewar and pressure reduced to 2,7x10^{-4} Pa. Mercury solidified from the bottom upward. Once the cap was removed the mercury contacted the liquid helium. Copper contaminates the lower part of the mercury column.	75x10^{-4} dia. 5x10^{-2} height	C[a]. Superconducting state
20000				C[a]. Normal state

[a] C indicates that the values of h_k and n have been calculated by the compiler through best fitting of $h_k = AT^n$ to data points. These data points have been re-plotted in Figure 7-17, Figure 7-18 and Figure 7-19 and can be identified by the key given in the previous entry of the Table.

Table 7-5: Kapitza Conductance, h_K, of Lead 105 in Contact with Liquid Helium (He II)

Sample	Key	h_K at 1,9 K [W.m^{-2}.K^{-1}]	Temp. Exponent n	Others	Sample Description
< 99,995 % pure		6600	2,9	Measur. Method: A Temp. Range [K]: 1,1-2,1	Table 7-6
99,995 % pure		11000	2,6		
		4200	4,1		
		11000	3,1		
< 99,9995 % pure		46000	4,7		
		32000	3,8		
		9300	2,0		
		6500	2,9		
					
		4900	2,8		
		5700	3,0		
		4500	3,2		
		4400	3,4		
No details given.		15000	3,7	Temp. Range [K]: 1-2,17	
99,9997 % pure		2900	3 ± 0,1	Measur. Method: B Temp. Range [K]: 1,15-2,16	
		1900	3,2 ± 0,1		
		7300	3 ± 0,1		
		5600	3 ± 0,1		
		7100	2,9 ± 0,1		

Table 7-6: Sample Description of Lead 105 in Table 7-5

h_k at 1,9 K [W.m^{-2}.K^{-1}]	Sample Conditions	Storage, Environment before Cool-down	Sample Dimensions [m]	Comments
6600	Machined to size. Annealed in a vacuum for 16 h at 543 K. Normal state (longitudinal field of 6,4x10^4 A.m^{-1}).	During test, surfaces of the sample not contacting He II were in a vacuum surrounded by a vessel at either helium or hydrogen temperatures.		C[a].
11000	Same as above.			C[a].
4200	Same as above. Superconducting state.			C[a]. Uncorrected for the temperature drop near the interface.
11000	Same as above. Normal state (longitudinal field of 6,4x10^4 A.m^{-1})			C[a].
46000	Same as above.			C[a].
32000	Same as above. Test made just after preparation.			C[a]. Extrapolated from $T \leq 1,7$ K.
9300	Same as above. Test made 2,3 months after preparation.	During test, surfaces of the sample not contacting He II were in a vacuum surrounded by a vessel at either helium or hydrogen temperatures. Storage open to laboratory atmosphere.		C[a]. Extrapolated from $T \leq 1,8$ K.
6500	Same as above. Superconducting state. 2,3 months after preparation.			C[a].
	Same as above. 2,4 months after preparation.			One single value.
4900	Same as above. Normal state (6,4x10^4 A.m^{-1}) 18 months after preparation.			C[a].
5700	Same as above. 21 months after preparation.			C[a].
4500	Same as above. Superconducting state. 18 months after preparation.			C[a].
4400	Same as above. 21 moths after preparation.			C[a].

h_k at 1,9 K [W.m^{-2}.K^{-1}]	Sample Conditions	Storage, Environment before Cool-down	Sample Dimensions [m]	Comments
15000	Etched for 3 min with dilute nitric acid.	Exposed to air for a few minutes after etching. Space above the surface was evacuated at room temperature and flushed with clean helium gas.		C[a].
2900	Machined to size. Cleaned with alcohol tetrachloride. Mounted. 1st test. After two months surface cleaned in the liquid helium bath. 2nd test. Seven days at room temperature, cleaned in the helium bath so that further cleaning no longer changed h_k. 3rd test. After four months, 4th test.	The cell containing the sample was evacuated and placed into a helium bath (together with several other cells). No details given on storage between tests.	14x10^{-3} dia. 2,8x10^{-3} thick	1st Test
				2nd Test
1900				3rd Test
7300				4th Test
5600	Machined and cleaned as above. Mounted. 1st test. Electropolished removing a layer of 34x10^{-6} m. Washed, dried and mounted. 2nd test. Electropolished removing 10^{2}x10^{-6} m. Seven days at room temperature. 3rd test.	The cell containing the sample was evacuated and placed into a helium bath (together with several other cells). No details given on storage between tests.	9,2x10^{-3} dia. 5,5x10^{-3} height	1st Test
7100				2nd Test
				3rd Test

[a] C indicates that the values of h_k and n have been calculated by the compiler through best fitting of $h_k = AT^n$ to data points. These data points have been re-plotted in Figure 7-17, Figure 7-18 and Figure 7-19 and can be identified by the key given in the previous entry of the Table.

Table 7-7: Kapitza Conductance, h_k, of Indium 108 in Contact with Liquid Helium (He II)

Sample	Key	h_k at 1,9 K [W.m^{-2}.K^{-1}]	Temp. Exponent n	Others	Sample Description
Spectroscopically pure (99,999 %)		11000 (2800)	3 (2.7)	Surface Ax10^4 [m^2]: 0,32 Measur. Method: B Temp. Range [K]: 1,0-2,1	Table 7-8

Table 7-8: Sample Description of Indium 108 in Table 7-7

h_k at 1,9 K [W.m^{-2}.K^{-1}]	Sample Conditions	Storage, Environment before Cool-down	Sample Dimensions [m]	Comments
11000 (2800)	Polished face of a sapphire substrate was indium coated in a helium atmosphere. Assembly placed in a close-fitting mold and backed in a vacuum of 1,3x10^{-3} Pa. Additional indium was cast and zone-refined in the mold. Free end face of indium was machined.	Assembly with mold returned to vacuum and annealed for two hours at 420 K. Mold cut away.	Indium: 6,35x10^{-3} dia. 38x10^{-3} height Sapphire: 6,35x10^{-3} dia. 32x10^{-3} height	Second value obtained after a few weeks, in either (n) or (s) states.

Table 7-9: Kapitza Conductance, h_k, of Gold 164 in Contact with Liquid Helium (He II)

Sample	Key	h_k at 1,9 K [W.m^{-2}.K^{-1}]	Temp. Exponent n	Others	Sample Description
99,99 % pure	☐	8800	3	Surface Ax10^4 [m^2]: 1,5 Measur. Method: A3 Heat Flux Q/A [W.m^{-2}]: 20-490 Temp. Range [K]: 1,25-2,10	Table 7-10
	■	8300			

Table 7-10: Sample Description of Gold 164 in Table 7-9

h_k at 1,9 K [W.m^{-2}.K^{-1}]	Sample Conditions	Storage, Environment before Cool-down	Sample Dimensions [m]	Comments
8800			2x10^{-2} dia. 1,27x10^{-4} thick	Data points correspond to two similar samples. Gold is quite inert and forms no stable oxides.
8300				

Table 7-11: Kapitza Conductance, h_K, of Tin 199 in Contact with Liquid Helium (He II)

Sample	Key	h_K at 1,9 K [W.m^{-2}.K^{-1}]	Temp. Exponent *n*	Others	Sample Description
99,997 % pure		5200	2,9± 0,1	Measur. Method: B Temp. Range [K]: 1,15-2,16	Table 7-12
		5200	2,9± 0,1		

Table 7-12: Sample Description of Tin 199 in Table 7-11

h_K at 1,9 K [W.m^{-2}.K^{-1}]	Sample Conditions	Storage, Environment before Cool-down	Sample Dimensions [m]	Comments
5200	Machined to size. Cleaned with alcohol and carbon tetrachloride. Mounted. 1st test. Electropolished removing a layer of 2,5x10^{-6} m thick. 2nd test.	The cell containing the sample was evacuated and placed into a helium bath (together with several other cells). No details on storage between tests.	10,2x10^{-3} dia. 12,5x10^{-3} height	Both tests furnished the same results. Transition into the normal state (2,4x10^{4} A.m^{-1} field) had no effect on h_K. The same with rotating helium up to 400 rpm.
5200				

Table 7-13: Kapitza Conductance, h_K, of Platinum 240 in Contact with Liquid Helium (He II)

Sample	Key	h_K at 1,9 K [W.m^{-2}.K^{-1}]	Temp. Exponent *n*	Others	Sample Description
99,9 % pure		2000	2,3± 0,1	Measur. Method: B1 Temp. Range [K]: 1,15-2,16	Table 7-14

Table 7-14: Sample Description of Platinum 240 in Table 7-13

h_k at 1,9 K [W.m^{-2}.K^{-1}]	Sample Conditions	Storage, Environment before Cool-down	Sample Dimensions [m]	Comments
2000	From a foil. Cleaned with alcohol and carbon tetrachloride. Sealed to a glass tube.	Sample and tube were surrounded by a glass vacuum jet. Annealed in an oven at 773 K for 3 h. Mounting.	$7{,}3 \times 10^{-3}$ dia. 10^{-4} thick	

Table 7-15: Kapitza Conductance, h_k, of Silver 225 in Contact with Liquid Helium (He II)

Sample	Key	h_k at 1,9 K [W.m^{-2}.K^{-1}]	Temp. Exponent n	Others	Sample Description
99,992 % pure	△	6100	3,4	Measur. Method: C Temp. Range [K]: 1-2	Table 7-16
	▲	6500	3,3		
	▽	4300	2,1		
	▼	4900	3,2		
	▷	1500	0,80		
	▶	1900	1,2		
	◁	1500	0,30		
	◀	1100	0,70		
	◁	1000	1,2		

Table 7-16: Sample Description of Silver 225 in Table 7-15

h_k at 1,9 K [$W.m^{-2}.K^{-1}$]	Sample Conditions	Storage, Environment before Cool-down	Sample Dimensions [m]	Comments
6100	Annealed for 8 h at 900 K and cooled down slowly. Electropolished using the following electrolytic solution: 35 g of silver cyanide, 37 g of potasium cyanide and 39 g of potasium carbonate in 1 l of water. Current density was 140 $A.m^{-2}$. A layer 10^{-4} m thick was removed	Under vacuum of $1,3x10^{-5}$ Pa from first mounting to end of last test. An exception was made between tests 4 and 5 of sample 1, where the valve to the atmosphere was opened for a short time before vacuum was restored.		Sample 1. Test 1. C[a]
6500				Sample 1. Test 2. C[a]
4300				Sample 1. Test 3. C[a]
4900				Sample 1. Test 4. C[a]
1500				Sample 1. Test 5. C[a]. H_k decreases when the sample is exposed to air.
1900				Sample 1. Test 6. C[a]
1500				Sample 1. Test 7. C[a]
1100				Sample 2. Test 1. C[a]
1000				Sample 2. Test 2. C[a]

[a] C indicates that the values of h_k and n have been calculated by the compiler through best fitting of $h_k = AT^n$ to data points. These data points have been re-plotted in Figure 7-17, Figure 7-18 and Figure 7-19 and can be identified by the key given in the previous entry of the Table.

Table 7-17: Kapitza Conductance, h_k, of Palladium 274 in Contact with Liquid Helium (He II)

h_k at 1,9 K [$W.m^{-2}.K^{-1}$]	Temp. Exponent n	Others	Comments
100 at 1 K	3 (assumed)	Measur. Method: C Temp. Range [K]: 0,1-1	Estimated in the course of an experiment to measure Mössbauer spectra of Fe^{57} with Co^{56} source in a palladium matrix

Table 7-18: Kapitza Conductance, h_k, of Niobium 275 in Contact with Liquid Helium (He II)

Sample	Key	h_k at 1,9 K [W.m^{-2}.K^{-1}]	Temp. Exponent n	Others	Sample Description
99,9 % pure. Less than 500 ppm Ta		1800± 300	3,62± 0,32	Measur. Method: A3 Heat Flux Q/A [W.m^{-2}]: 10-400 Temp. Range [K]: 1,3-2,1	Table 7-19
100 ppm Ta		4000± 500	4,65± 0,28		

Table 7-19: Sample Description of Niobium 275 in Table 7-18

h_k at 1,9 K [W.m^{-2}.K^{-1}]	Sample Conditions	Storage, Environment before Cool-down	Sample Dimensions [m]	Comments
1800± 300	Machined with 0,3x10^{-3} m cut depth. Five months in air. Rinsed with toluene, acetone and ethanol. r = 1,003± 0,0022.		2,5x10^{-2} dia. 2,5x10^{-2} height	Superconducting state (0 Am^{-1} field).
4000± 500	Chemically polished 3 min in a solution of 60x10^{-3} l nitric acid (70%) and 40x10^{-3} l hydrofluoric acid (40%), 273 K - 293 K. High vacuum and high temperature annealed. After vacuum treatment, soft solder deposits were removed. Chemically polished for 6 min, rinsed with ethanol. r = 1,0007± 0,0004.	Vacuum treatment consisted of heating for 18 h in a container at 463 K with an end vacuum 10^{-5} Pa. Remained in the container, under vacuum, for 6 d at 293 K. In air 15 min.		

Table 7-20: Kapitza Conductance, h_k, of Copper 343 in Contact with Liquid Helium (He II)

Sample	Key	h_k at 1,9 K [W.m^{-2}.K^{-1}]	Temp. Exponent n	Others	Sample Description
99,999 % pure		8400	6,4	Measur. Method: C, C1 Heat Flux Q/A [W.m^{-2}]: 16, 23, 32, 50, 92 Temp. Range [K]: 1,2-2,0	Table 7-21
		3800	4,3		
		22000	4,5		
		3900	1,6		
		12500	3,9		
		7500	3,2		
		17000	3,5		
		15000	3,7		
		22000	4,3		
		22000	4,3		
		1100	2,4		
		1400	3,8		
		590	1,6		
		500	1,6		
		1200	4,2		
		890	3,0		
		960	3,0		
		13000	3,1		
		7000	6,1		
		5100	6,6		
		6100	6,0		
		2300	2,0		
		2800	4,2		
		19000	3,0		
		5300	5,9		

Sample	Key	h_k at 1,9 K [W.m^{-2}.K^{-1}]	Temp. Exponent n	Others	Sample Description
		29000	3,7		
		2700	3,2		
		16000	2,5		
		9000	2,2		
		3100	3,2		
99,9 % pure		25500	2,6± 0,1	Measur. Method: E Temp. Range [K]: 0,570-2,075	
OFHC (oxygen free high conductivity)		6600	3,1	Surface $Ax10^4$ [m^2]: 1,5 Measur. Method: A3 Temp. Range [K]: 1,25-2,10	
		6600	3,1		
		6200	3		
		7600	2,6		
		7300± 700	3,34± 0,27	Measur. Method: A3 Heat Flux Q/A [W.m^{-2}]: 10 to 400 Temp. Range [K]: 1,3-2,1	
		6700± 600	4,11± 0,27		
High purity (no further details given)		2700	2,4	Measur. Method: A Temp. Range [K]: 1,4-2,17	
		5500	2,8		
99,999 % pure		4100	2,6	Measur. Method: A Temp. Range [K]: 1,1-2,1	
		3600	2,6		
		380 at 1 K	3,9	Surface $Ax10^4$ [m^2]: 0,159 Measur. Method: C Heat Flux Q/A [W.m^{-2}]: 0,03 to 0,2 at 0,35 K 2 to 25 at 1,3 K Temp. Range [K]: 0,3-1,3	
		1000 at 1 K	4,3		

Table 7-21: Sample Description of Copper 343 in Table 7-20

h_k at 1,9 K [$W.m^{-2}.K^{-1}$]	Sample Conditions	Storage, Environment before Cool-down	Sample Dimensions [m]	Comments
8400	Machined to size. Remachined using the same tools, positioned in the same way at 2150 revolutions per minute, making 4 cuts of $50,8x10^{-6}$ m depth each.	Preserved under a vacuum of about $1,3x10^{-3}$ Pa and exposed to the atmosphere during about 20 min for mounting.	$6x10^{-3}$ dia. $2x10^{-3}$ height	0º tool angle
3800				0º tool angle
22000				0º tool angle
3900				0º tool angle
12500				12º tool angle
7500	Machined as above. Hand polished with increasingly fine polishing paper up to the highest grade available. Electropolished in 30% orthophosporic acid solutions for times varying between 2 min and 53 h. Washed with deionized water and dried under vacuum.			
17000				
15000				
22000				
22000				
1100				$1,5x10^{-6}$ m electropolishing depth
1400				$1,5x10^{-6}$ m electropolishing depth
590				$40x10^{-6}$ m electropolishing depth
500				$80x10^{-6}$ m electropolishing depth
1200				$120x10^{-6}$ m electropolishing depth
890				$120x10^{-6}$ m electropolishing depth
960	Electropolished as above with 10^{-5} m thick layer removed, then silver coated under a vacuum of $1,3x10^{-5}$			$120x10^{-6}$ m e.d. + etched
13000				$3,5x10^{-9}$ m silver coating thickness.

h_K at 1,9 K [W.m^{-2}.K^{-1}]	Sample Conditions	Storage, Environment before Cool-down	Sample Dimensions [m]	Comments
	Pa up to 60 s.			Batch 2
7000				4,0x10^{-9} m silver coating thickness. Batch 2
5100				5,0x10^{-9} m silver coating thickness. Batch 2
6100				7,0x10^{-9} m silver coating thickness. Batch 1
2300				7,0x10^{-9} m silver coating thickness. Batch 1
2800				8,0x10^{-9} m silver coating thickness. Batch 1
19000				11,0x10^{-9} m silver coating thickness. Batch 2
5300				11,5x10^{-9} m silver coating thickness. Batch 1
29000				15x10^{-9} m silver coating thickness. Batch 2
2700				18x10^{-9} m silver coating thickness. Batch 1
16000				35x10^{-9} m silver coating thickness. Batch 2
9000				78x10^{-9} m silver coating thickness. Batch 2
3100				90x10^{-9} m silver coating thickness. Batch 1

h_k at 1,9 K [W.m^{-2}.K^{-1}]	Sample Conditions	Storage, Environment before Cool-down	Sample Dimensions [m]	Comments
25500	Machined to size.	Surface not in contact with He II were in a helium gas atmosphere at normal pressure.	Thick-walled vessel, 5x10^{-3} m i.d., 50x10^{-3} m long	Additional experiments indicated that the pressure dependence of h_k is negligible.
6600	Machined, chemically cleaned and rinsed in water and ethanol. Mounted. 0,47x10^{-4} m^2 of 1,64x10^{-4} m^2 interface cleaned while immersed in He II. Pieces resulting from cutting remained in the interface.		3,17x10^{-2} dia. 1,46x10^{-2} height	C[a].
6600	Above sample once exposed to atmosphere for a week. The 2nd test was carried out with the chips still lying on the interface.	The system was not disturbed during exposure to atmosphere.		C[a].
6200	Machined, cleaned and rinsed as above. 0,85x10^{-4} m^2 interface cleaned while immersed.			C[a].
7600	Above sample once exposed to atmosphere for a week.	The system was not disturbed during exposure to atmosphere.		C[a].
7300± 700	Machined to size, vapor degreased, rinsed with ethanol. R = 1,27± 0,1.	In contact with air after preparation for several hours before pumping down.	2,5x10^{-2} dia. 2,5 x10^{-2} height	
6700± 600	Same as above. Chemically polished 1 min at 343 K. Electropolished 6 min at 293 K. Rinsed in ethanol. R = 1,0004± 0,0003.	In contact with air after preparation for 1 hour before pumping down.		
2700	Polished with jeweller s rouge.	Exposed to air for a few minutes after preparation while being mounted. Subsequently space above the surface was evacuated at room		C[a]. The ratio of h_k under the saturated vapor pressure to that under 20x10^5 Pa is almost
5500	Etched for 3 min with dilute nitric acid.			

h_k at 1,9 K [W.m^{-2}.K^{-1}]	Sample Conditions	Storage, Environment before Cool-down	Sample Dimensions [m]	Comments
		temperature and flushed with clean helium gas before cooling down.		independent of pressure above 1,3 K.
4100	Deformed by hammering and then machined. Mechanically polished.	Surfaces of the sample not contacting He II were in a vacuum and surrounded by a vessel at either helium or hydrogen temperatures during test.		C[a]. Influence of plastic deformation.
3600	Above sample once removed from the experimental cell. Annealed in vacuum at 898 K for 4 h and then lightly polished.			
380 at 1 K	Machined. Annealed under vacuum at 1223 K for 11 h. Cooled over 13 h. Handpolished. Electropolished removing 152x10^{-6} m. Washed.	Mounting took 15-30 min. Pumped on for a total of 29 d up to 4x10^{-5} Pa. Contamination carefully prevented.	5,6x10^{-3} dia. 3x10^{-3} height Hole drilled, 2x10^{-3} dia. 2x10^{-3} height	C[a]. h_k/T^3 shows a maximum at about 1 K. This behavior seems to be characteristic of clean surfaces.
1000 at 1 K	Machined, annealed and handpolished as above. Electropolished removing 61x10^{-6} m. Washed.	Mounting as above. Pumped on for a total of 15 d up to 8x10^{-2} Pa. Contamination carefully prevented.		

[a] C indicates that the values of h_k and n have been calculated by the compiler through best fitting of $h_k = AT^n$ to data points. These data points have been re-plotted in Figure 7-17, Figure 7-18 and Figure 7-19 and can be identified by the key given in the previous entry of the Table.

Table 7-22: Kapitza Conductance, h_k, of Tungsten 400 in Contact with Liquid Helium (He II)

Sample	Key	h_k at 1,9 K [W.m^{-2}.K^{-1}]	Temp. Exponent n	Others	Sample Description
99,95 % pure	⧗	2420	3,5	Surface Ax10^4 [m^2]: 1,5 Measur. Method: A3 Heat Flux Q/A [W.m^{-2}]: 20 to 490 Temp. Range [K]: 1,25-2,10	Table 7-23

Table 7-23: Sample Description of Tungsten 400 in Table 7-22

h_k at 1,9 K [W.m^{-2}.K^{-1}]	Sample Conditions	Storage, Environment before Cool-down	Sample Dimensions [m]	Comments
2420			2x10^{-2} dia. 1,27x10^{-4} thick	C[a].

[a] C indicates that the values of h_k and n have been calculated by the compiler through best fitting of $h_k = AT^n$ to data points. These data points have been re-plotted in Figure 7-17, Figure 7-18 and Figure 7-19 and can be identified by the key given in the previous entry of the Table.

Table 7-24: Kapitza Conductance, h_k, of Aluminium 428 in Contact with Liquid Helium (He II)

Sample	Key	h_k at 1,9 K [W.m^{-2}.K^{-1}]	Temp. Exponent n	Others	Sample Description
99,99% pure RRR = 500± 80	◈	7400± 300	2,8	Surface Ax10^4 [m^2]: 1,48 Measur. Method: A2 Heat Flux Q/A [W.m^{-2}]: 10^4 to 2x10^4 Temp. Range [K]: 1,5-2,1	Table 7-25
99,999% pure RRR = 1500 (RRR is the residual resistance ratio, $\rho_{4,2}/\rho_{300)}$	◈	6700	2,7	Surface Ax10^4 [m^2]: 1,48 Measur. Method: A2 Heat Flux Q/A [W.m^{-2}]: 10^4 to 2x10^4 Temp. Range [K]: 1,7-2,1	
	◈	6400	2,8		
	#	6200	2,9		
	#	6400	2,8		
	◆	6700	2,8		
	◆	6600	2,8		
6061 Al alloy		4000-8000	3± 0,4	Measur. Method: A3 Heat Flux Q/A [W.m^{-2}]: 10 to 400 Temp. Range [K]: 1,3-2,1	
Ultra pure RRR = 13000		5200± 300	4,21± 0,28		

Table 7-25: Sample Description of Aluminium 428 in Table 7-24

h_k at 1,9 K [$W.m^{-2}.K^{-1}$]	Sample Conditions	Storage, Environment before Cool-down	Sample Dimensions [m]	Comments
7400± 300	Machined to size and washed with methyl alcohol. Spacing between machining grooves was typically 10^{-5} m. Groove depth was an order of magnitude smaller.	The entire Dewar containing the experimental cell was evacuated with a liquid nitrogen trapped diffusion pump to less than $1,3x10^{-2}$ Pa at room temperature before cool down. During the test a vacuum of $1,3x10^{-3}$ Pa was maintained in the vacuum, container.	$3x10^{-2}$ dia. $11x10^{-2}$ height	[a]. Near saturated vapor pressure. Bath temperature, T = 1,85 K
6700				[a]. Near saturated vapor pressure. Bath temperature, T = 2,01 K
6400				[a]. Near saturated vapor pressure. Bath temperature, T = 1,89 K
6200				[a]. Near saturated vapor pressure. Bath temperature, T = 1,79 K
6400				[a] at $2,43x10^3$ Pa pressure (saturation). Bath temperature, T = 1,89 K
6700				[a] at $33,4x10^3$ Pa pressure. Bath temperature, T = 1,89 K
6600				[a] at $84,1x10^3$ Pa pressure. Bath temperature, T = 1,89 K
4000-8000	T6 temper. Machined to size. Vapor degreased, then rinsed with ethanol. r = 1,004± 0,002.	In contact with air after preparation for 1 h before pumping down.	$2,5x10^{-2}$ dia. $2,5x10^{-2}$ height	
5200± 300	Vacuum melted, annealed for 1 h in air, cooled down	In contact with air for 1 h before pumping down.		

h_k at 1,9 K [W.m^{-2}.K^{-1}]	Sample Conditions	Storage, Environment before Cool-down	Sample Dimensions [m]	Comments
	to 293 K in 24 h. Machined. Surface ground with No 500 emery paper, vapor degreased, chemically polished for 3,5 min then rinsed with ethanol. r = 1,0004± 0,0004			

[a] C indicates that the values of h_k and n have been calculated by the compiler through best fitting of $h_k = AT^n$ to data points. These data points have been re-plotted in Figure 7-17, Figure 7-18 and Figure 7-19 and can be identified by the key given in the previous entry of the Table.

Table 7-26: Kapitza Conductance, h_k, of Nickel 450 in Contact with Liquid Helium (He II)

Sample	Key	h_k at 1,9 K [W.m^{-2}.K^{-1}]	Temp. Exponent n	Others	Sample Description
99,99% pure		4000	2,9± 0,1	Measur. Method: B Temp. Range [K]: 1,15-2,16	Table 7-27

Table 7-27: Sample Description of Nickel 450 in Table 7-26

h_k at 1,9 K [W.m^{-2}.K^{-1}]	Sample Conditions	Storage, Environment before Cool-down	Sample Dimensions [m]	Comments
4000	Machined to size. Cleaned with alcohol and carbon tetrachloride. Mounted.	Before filling with liquid helium, the Dewar was filled with gaseous helium. No details are given on storage between tests.	1,4x10^{-3} dia. 2,6x10^{-3} thick	
370	Machined and cleaned as above. Electropolished removing 14x10^{-6} m. 1st test. Electropolished removing 56x10^{-6} m. 2nd test. Electropolished removing 140x10^{-6} m. 3rd test.		10,2x10^{-3} dia. 2,8x10^{-3} thick	No changes were observed in the 2nd and 3rd tests. Some capillary effect could arise since pores were observed.

[a] C indicates that the values of h_k and n have been calculated by the compiler through best fitting of $h_k = AT^n$ to data points. These data points have been re-plotted in Figure 7-17, Figure 7-18 and Figure 7-19 and can be identified by the key given in the previous entry of the Table.

Table 7-28: Kapitza Conductance, h_k, of Molybdenum 450 in Contact with Liquid Helium (He II)

Sample	Key	h_k at 1,9 K [W.m^{-2}.K^{-1}]	Temp. Exponent n	Others	Sample Description
99,9% pure	⬡	1400± 100	1,5± 0,1	Surface Ax10^4 [m^2]: 0,126 Measur. Method: C Heat Flux Q/A [W.m^{-2}]: 12, 24 Temp. Range [K]: 1,2-1,9	Table 7-29
	⬢	970± 80	0,8± 0,2		

Table 7-29: Sample Description of Molybdenum 450 in Table 7-28

h_k at 1,9 K [W.m^{-2}.K^{-1}]	Sample Conditions	Storage, Environment before Cool-down	Sample Dimensions [m]	Comments
1400± 100	Annealed under vacuum 1500 K for 14 h. Electropolished to remove 10^{-4} m using a solution of one part sulfuric acid and seven parts methanol. Stainless steel cathode. Current density: 10^3 A.m^{-2}. Washed with methanol.	Stored under a vacuum of 1,3x10^{-3} Pa. Exposed to air for about 20 min during mounting. Pumped down. Different pumping times.		C[a]. Electropolished by error using a mild steel electrode.
970± 80				C[a]. Low temperature exponent. h_k/T^3 vs. T seems to exhibit a maximum near T = 1 K. Stainless steel electrode.

[a] C indicates that the values of h_k and n have been calculated by the compiler through best fitting of $h_k = AT^n$ to data points. These data points have been re-plotted in Figure 7-17, Figure 7-18 and Figure 7-19 and can be identified by the key given in the previous entry of the Table.

Table 7-30: Kapitza Conductance, h_k, of Beryllium 1440 in Contact with Liquid Helium (He II)

Sample	Key	h_k at 1,9 K [W.m^{-2}.K^{-1}]	Temp. Exponent n	Others	Sample Description
99 % pure		260± 40	1,1± 0,5	Surface $Ax10^4$ [m^2]: 0,126 Measur. Method: C Heat Flux Q/A [W.m^{-2}]: 12, 24 Temp. Range [K]: 1,2-1,9	Table 7-31

Table 7-31: Sample Description of Beryllium 1440 in Table 7-30

h_k at 1,9 K [W.m^{-2}.K^{-1}]	Sample Conditions	Storage, Environment before Cool-down	Sample Dimensions [m]	Comments
260± 40	Annealed under vacuum. Electropolished to remove 10^{-4} m using a solution of 100 parts orthophosphoric acid, 3 parts sulfuric acid, 3 parts glycerol, 3 parts ethanol. Stainless steel cathode. 1,2x10^3 A.m^{-2}. Washed with methanol.			C[a]. Low temperature exponent. No pressure dependence of h_k/T^3 has been founded between 10^5 Pa and 3x10^5 Pa.

[a] C indicates that the values of h_k and n have been calculated by the compiler through best fitting of $h_k = AT^n$ to data points. These data points have been re-plotted in Figure 7-17, Figure 7-18 and Figure 7-19 and can be identified by the key given in the previous entry of the Table.

Table 7-32: Kapitza Conductance, h_k, of Nonmetals in Contact with Liquid Helium (He II)

Solid θ_D [K]	References
Graphite 420, see Table 7-33	Haben & Frederking (1975) [79]
Quartz (SiO_2) 470, see Table 7-35	Wey-Yeng (1962) [263] Challis, Dransfeld & Wilks (1961) [40]
Silicon 636, see Table 7-37	Johnson & Little (1963) [108]
Lithium Fluoride 730, see Table 7-39	

Table 7-33: Kapitza Conductance, h_k, of Graphite 420 in Contact with Liquid Helium (He II)

Sample	Key	h_k at 1,9 K [W.m^{-2}.K^{-1}]	Temp. Exponent n	Others	Sample Description
Aquadag coating [b]		1000	2,2	Surface Ax10^4 [m^2]: 0,05 Heat Flux Q/A [W.m^{-2}]: 5,5 to 350 Temp. Range [K]: 1,4-2,0	Table 7-34

[b] Aquadag is a colloidal dispersion of graphite in water produced by Acheson Colloids Company, Port Huron, Michigan, USA.

Table 7-34: Sample Description of Graphite 420 in Table 7-33

h_k at 1,9 K [W.m^{-2}.K^{-1}]	Sample Conditions	Storage, Environment before Cool-down	Sample Dimensions [m]	Comments
1000	A varnish-coated (GE varnish 7031) constantan strip, fastened to the groove of a phenolic substrate, is overcoated with Aquadag. Potential taps are connected to the graphite layer by means of a silver paint.	Dried in ambient air and mounted in the Dewar. After a set of tests the sample was warmed up and exposed to ambient conditions. 2nd test.	Constantan: 3,05x10^{-2} long 3,84x10^{-4} wide 1,8x10^{-5} thick Varnish: 5x10^{-6} to 10^{-5} thick. Graphite: 20x10^{-6} thick.	C[a]. There is a single value from the second test. h_k = 1100 at T = 1,87 K. Applications to thermometry in liquid helium.

[a] C indicates that the values of h_k and n have been calculated by the compiler through best fitting of $h_k = AT^n$ to data points. These data points have been re-plotted in Figure 7-20 and can be identified by the key given in the previous entry of the Table.

Table 7-35: Kapitza Conductance, h_k, of Quartz (SiO_2) 470 in Contact with Liquid Helium (He II)

Sample	Key	h_k at 1,9 K [W.m^{-2}.K^{-1}]	Temp. Exponent n	Others	Sample Description
Single Crystal		5700	3,6± 0,2	Measur. Method: B Temp. Range [K]: 1,151-2,157	Table 7-36
		3800	3	Surface $Ax10^4$ [m^2]: 0,19 Measur. Method: A1 Temp. Range [K]: 1,4-2,17	

Table 7-36: Sample Description of Quartz (SiO2) 470 in Table 7-35

h_k at 1,9 K [W.m^{-2}.K^{-1}]	Sample Conditions	Storage, Environment before Cool-down	Sample Dimensions [m]	Comments
5700	Surface normal to the principal axis of the crystal was ground and polished.	Before filling with liquid helium, the Dewar was filled with gaseous helium.	12,5x10^{-3} dia. 10,9x10^{-3} height	
3800	Surface was ground	Once mounted in the experimental cell, the space above the surface was evacuated at room	0,5x10^{-2} dia. 4,75x10^{-2} height	C[a]. Quartz exhibits a relatively high thermal

h_k at 1,9 K [W.m^{-2}.K^{-1}]	Sample Conditions	Storage, Environment before Cool-down	Sample Dimensions [m]	Comments
		temperature and flushed several times with clean helium gas before cooling down.		conductivity at low temperatures.

[a] C indicates that the values of h_k and n have been calculated by the compiler through best fitting of $h_k = AT^n$ to data points. These data points have been re-plotted in Figure 7-20 and can be identified by the key given in the previous entry of the Table.

Table 7-37: Kapitza Conductance, h_k, of Silicon 636 in Contact with Liquid Helium (He II)

Sample	Key	h_k at 1,9 K [W.m^{-2}.K^{-1}]	Temp. Exponent n	Others	Sample Description
Single crystal grown in the [1,1,1] direction. p type resistivity >10 Ωm, impurities <1,3x10^9 atom.m^{-3}, dislocation: 8x10^4 m^{-2}		3700	3,2	Surface Ax10^4 [m^2]: 1,5 Measur. Method: A3 Heat Flux Q/A [W.m^{-2}]: 20 to 490 Temp. Range [K]: 1,25-2,10	Table 7-38
		4000	4,2		
Same as above except dislocation density: 8x10^6 m^{-2}		4200	4,2		

Table 7-38: Sample Description of Silicon 636 in Table 7-37

h_k at 1,9 K [W.m^{-2}.K^{-1}]	Sample Conditions	Storage, Environment before Cool-down	Sample Dimensions [m]	Comments
3700	Interfacial plane normal to the growth axis, ground and polished.		3,17x10^{-2} dia. 1,46x10^{-2} height	C[a]. Study of the influence of dislocation density on h_k.
4000	Same as above and etched.			
4200	Interfacial plane normal to the growth axis, ground, polished and etched.			

[a] C indicates that the values of h_k and n have been calculated by the compiler through best fitting of $h_k = AT^n$ to data points. These data points have been re-plotted in Figure 7-20 and can be identified by the key given in the previous entry of the Table.

Table 7-39: Kapitza Conductance, h_k, of Lithium Fluoride 730 in Contact with Liquid Helium (He II)

Sample	Key	h_k at 1,9 K [W.m^{-2}.K^{-1}]	Temp. Exponent n	Others	Sample Description
99,99% pure single crystal		4800	3,8	Surface Ax10^4 [m^2]: 1,5 Measur. Method: A3 Heat Flux Q/A [W.m^{-2}]: 20 to 490 Temp. Range [K]: 1,25-2,10	Table 7-40

Table 7-40: Sample Description of Lithium Fluoride 730 in Table 7-39

h_k at 1,9 K [W.m^{-2}.K^{-1}]	Sample Conditions	Storage, Environment before Cool-down	Sample Dimensions [m]	Comments
4800	The interface is an [1,0,0] surface.		2x10^{-2} dia. 1,27x10^{-2} height	C[a]. Basic interest. No heat transfer by charge carriers at liquid helium temperature.

[a] C indicates that the values of h_k and n have been calculated by the compiler through best fitting of $h_k = AT^n$ to data points. These data points have been re-plotted in Figure 7-20 and can be identified by the key given in the previous entry of the Table.

Table 7-41: Kapitza Conductance, h_k, of Metals in Contact with Low Acoustiv Impedance Media (LAIM)

Solid θ_D [K]	References
Indium 108, see Table 7-42	Neeper & Dilliger (1964) [163]
Copper 343, see Table 7-44	Reynolds & Anderson (1976, 1977) [193] & [194] Schmidt (1975) [207]

Table 7-42: Kapitza Conductance, h_k, of Indium 108 in Contact with Low Acoustic Impedance Media (LAIM)

Sample	Key	h_k at 1,9 K [W.m^{-2}.K^{-1}]	Temp. Exponent n	Others	Sample Description
99,99% pure Indium		2280 (2280)	2,88 (2.84)	Surface $Ax10^4$ [m^2]: 0,32 Measur. Method: A4 Heat Flux Q/A [W.m^{-2}]: 6-200 Temp. Range [K]: 1,0-2,1	Table 7-43
		2230 (2240)	2,88 (2.86)		
		2280 (2310)	2,81 (2.80)		
		2070 (2080)	2,81 (2.78)		

Table 7-43: Sample Description of Indium 108 in Table 7-42

h_k at 1,9 K [W.m^{-2}.K^{-1}]	LAIM	Sample Conditions	Storage, Environment before Cool-down	Sample Dimensions [m]	Comments
2280 (2280)	Sapphire	Polished face of a cylindrical sapphire crystal was indium coated in a helium atmosphere. Assembly was placed in a close-fitting mold and backed in a vacuum of 1,3x10^{-3} Pa. Additional indium was cast and refined by the molten zone technique within the mold. Two nominally equal samples (1 and 2) were prepared.	Assembly with mold returned to vacuum and annealed in vacuum for two hours at 420 K. Mold cut away.	Indium: 6,35x10^{-3} dia. 38x10^{-3} height Sapphire: 6,35x10^{-3} dia. 32,10^{-3} height	Sample 1. Test A. Superconducting state or (normal state, up to 0,6x10^6 A.m^{-1})
2230 (2240)					Sample 1. Test B. Superconducting state or (normal state, up to 0,6x10^6 A.m^{-1})
2280 (2310)					Sample 2. Test A. Superconducting state or (normal state, up to 0,6x10^6 A.m^{-1})
2070 (2080)					Sample 2. Test B. Superconducting state or (normal state, up to 0,6x10^6 A.m^{-1})

Table 7-44: Kapitza Conductance, h_k, of Copper 343 in Contact with Low Acoustic Impedance Media (LAIM)

Sample	Key	h_k at 1,9 K [W.m^{-2}.K^{-1}]	Temp. Exponent n	Others	Sample Description
Copper (no details are given)		400 (at 1 K)	3,5	Surface $Ax10^4$ [m^2]: 5,13 (each end plate) Measur. Method: D1 Temp. Range [K]: 0,7-1	Table 7-45
		340 (at 1 K)	3,6		
		300 (at 1 K)	3,4		
		310 (at 1 K)	3,5		
		300 (at 1 K)	3,6		
Commercial Copper		3000	1,9	Measur. Method: D Temp. Range [K]: 1-4	

Table 7-45: Sample Description of Copper 343 in Table 7-44

h_k at 1,9 K [W.m^{-2}.K^{-1}]	LAIM	Sample Conditions	Comments
400 (at 1 K)	Solid He[4]	Both end plates mechanically polished.	C[a]. 33x10^5 Pa pressure
340 (at 1 K)		Both end plates mechanically polished. Then vacuum annealed at 873 K.	
300 (at 1 K)		One end plate mechanically polished and sandblasted. The second mechanically polished and electropolished.	C[a]. 37x10^5 Pa pressure
310 (at 1 K)		Both mechanically polished and electropolished.	
300 (at 1 K)		Same as above.	
3000	Epoxy Resin	Epoxy Resin: CY 221 with hardener HY979 (CIBA Co.) in 10:3 ratio.	Because of h_k the thermal conductivity of filled epoxies strongly depends on the grain size of the metallic filler.

[a] C indicates that the values of h_k and n have been calculated by the compiler through best fitting of $h_k = AT^n$ to data points. These data points have been re-plotted in Figure 7-18 and can be identified by the key given in the previous entry of the Table.

7.3 Thermo-acoustic oscillations

Thermo-acoustic (Taconis) oscillations, which can reach considerable amplitudes, appear in tubes which are hot at their closed end and cold (liquid helium temperature) at their open end. These oscillations are accompained by considerable heat flux along the tube into the helium reservoir increasing the evaporation rate of liquid helium to a value of the order of 10^3 larger than that which would occur without oscillation.

Damping of acoustic waves in long tubes due to friction is an old problem in Gas Dynamics (see Rott (1969) [200] and references therein). Early attempts to use these waves in pulsating combustion are described in Thring (1961) [235].

Oscillations appear and persist because the periodic heat flux to the gas is such that the heat addition coincides with the phase of high pressure, that is to say: the gas shifted toward the hot closed end is both compressed and heated through the walls, whereas in the motion away from the hot closed end both effects reverse their signs.

First attempts to qualitatively calculate thermally driven acoustic oscillations in a tube with a strong axial temperature gradient were based on linearized flow equations, accounting for the wall friction through an oscillating boundary layer (the Stokes layer), the thickness, $(\nu/\omega)^{1/2}$, of which was assumed to be small compared with the tube radius. ν and ω being the kinematic viscosity of the oscillating gas and the angular frequency, respectively.

Comparison with experimental results was disappointing. Calculations only provided the asymptote of a certain branch of the stability curve and, in the particular case of helium, the material constants are such that the asymptote lies at practically infinite hot to cold temperature ratios.

Rott (1969) [200] showed that a second order boundary layer theory is required to obtain the asymptotic value of the stability curve for low viscosity and investigated the stability limits in general (Rott (1973) [201]), calculating in another paper (Rott (1975) [202]) the second order heat flux.

With the aim of simplifying the analysis, Rott assumes that the temperature distribution along the tube axis is a step function with a change at position *l* of the axis. The length of the tube is *L*, and that of the warm part *L*-l. This assumption could be fairly realistic when the tube is supported by a flange attached to the top of the helium bath.

Neutral stability curves for helium are presented by Rott (1973) [201] as α vs. Y_C with ξ as a parameter, where

$$\alpha = \frac{T_H}{T_C} \quad , \quad Y_C = \frac{D_E/2}{(\nu_C/\omega)^{1/2}} \quad , \quad \xi = \frac{L-l}{l}$$

Note: non-si units are used in this figure

.

Subscript C indicates properties of the low temperature gas. In the case of ν the distinction is essential since in Rott's analysis the viscous region reaches the core of the tube in the hot part, but it is very thin compared to the tube radius in the cold part.

Results deduced from Rott's analysis have been experimentally confirmed by Yazaki, Tominaga & Narahara (1979) [269] as can be seen in Figure 7-21. These authors used two U tubes of different internal diameters, and two different warm temperatures. Density (and then ν) was changed by pressurization of the gas, and pressure was measured with transducers placed at the end of the U tubes.

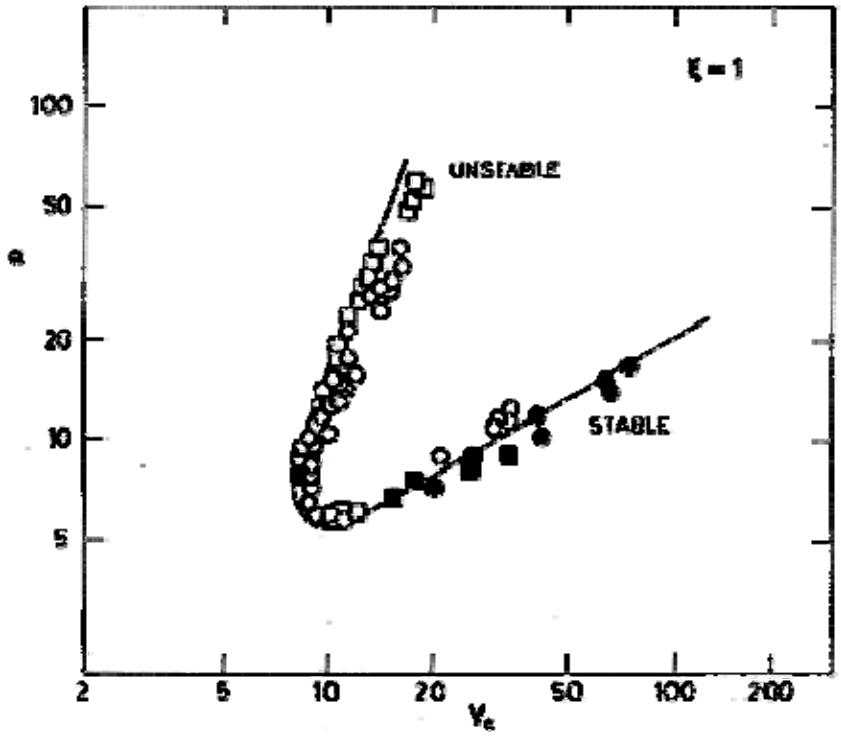

Figure 7-21: The neutral stability curve for Taconis oscillations when $\xi = 1$. ○ D_E = 2,4 x 10^{-3} m, T_H = 288 K; ● D_E = 2,4 x 10^{-3} m, T_H = 77,3 K; □ D_E = 4,4 x 10^{-3} m, T_H = 288 K; ■ D_E = 4,4 x 10^{-3} m, T_H = 77,3 K From Yazaki, Tominaga & Narahara (1979) [269].

A method for preventing pressure oscillations in tubes connecting liquid helium reservoirs to room temperature consists in drilling holes in the tube wall about mid distance between cold and warm ends. Figure 7-22 shows a tube with an enlarged warm end sealed with a thin rubber membrane. When the perforated tube is inserted into a cryostat no oscillations are observed. A second tube simulating the neck of the cryostat is also shown in the figure.

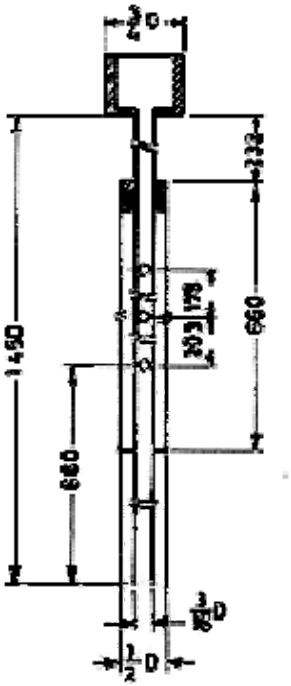

Figure 7-22: Device for preventing Taconis oscillations. All the dimensions are in mm. From Hilal & McIntosh (1976) [88].

With independence of its detrimental effects on the life of the helium contained in the reservoir, Taconis oscillation is used for locating the liquid-vapor interface in helium (Gaffney & Clement (1955) [73]).

7.4 The superfluid plug

7.4.1 Phase separation in superfluid helium

Liquid He II (He^4) can be used for cooling research equipment, such as superconducting magnets, linear accelerators, spaceborne sensors, etc.

A system to maintain cryogenic equipment at temperatures below 2,5 K by immersion in liquid He II was proposed by Selzer, Fairbank & Everitt (1971) [214]. Under zero-g conditions the contact of He II with the equipment to be cooled is achieved in this system by means of the superfluid film which coats all the inner surfaces of the cryostat (see clause 7.1.6).

Among the different problems which this system would pose, that of liquid-vapor phase separation is the subject of this clause.

The aim of phase separators is to avoid the seepage of the liquid refrigerantinto the neck support of the cryostat, whose exit is at ambient temperature, with the consequent rapid evaporation of the liquid and decrease in the cooling effectiveness of the system.

A review of phase separators not based on superfluid effects and which can be applied to any normal (non superfluid) liquid has been made in Clause 6.4.

When the cryogen is He II phase separation may take place within a porous plug.

Even assuming that the total amount of helium entering the plug is liquidHe II, only vapor will emerge from the exit face of the plug if conditions are arranged so that the thermo mechanical forces overcome the mechanical pressure, i.e.: provided that the chemical potential (Eq. [7-8]) at the exit of the plug equals that at the entrance. Under such conditions the liquid evaporates inside the plug, cooling it.

The superfluid porous plug is then a thermal phase separator for He II which is based on the fact that, under the two fluid model, the normal component is driven through the plug by the joint effect of mechanical and thermo-mechanical pressure and is contained by viscous forces (Eq. [7-18]), whereas the superfluid component is contained by the thermo-mechanical pressure. If a given mass flow rate of liquid He II enters the plug, the same mass flow rate of fluid will leave it, but this fluid would be only vapor if thermo-mechanical forces are large enough to contain the superfluid component.

7.4.2 Simplified theory of the superfluid plug

The theory presented in this paragraph is that by Selzer, Fairbank & Everitt (1971) [214], with refinements by Urban, Katz & Karr (1975) [245].

The configuration used to substantiate the discussion is sketched in Figure 7-23. p_1 and p_2 are the vapor pressures of liquid helium at temperatures T_1 and T_2 respectively. In most experiments concerning superfluid plugs liquid is absent from chamber 2, hence p_2 does not depend on T_2.

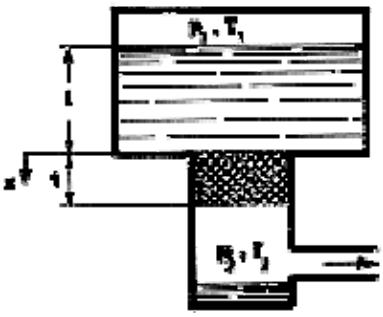

Figure 7-23: Superfluid plug arrangement. The intake face of the plug is located at $x = 0$.

Liquid helium is in direct contact with the upper face of the plug.

Hydrostatic pressure is included since it should be taken into account when performing experiments in the terrestrial laboratory.

The upper chamber is assimilated to the bath of a Dewar containing He II. The lower chamber is vented to absolute vacuum through a line of known impedance. The impedance, F, is the ratio of the mass flow rate to the pressure drop along the line.

7.4.2.1 Simplifying assumptions

1. The flow through the plug is stationary and one-dimensional.
2. The slow flow assumption (clause 7.1.1.1) holds.
3. Differences of temperature between upper and lower chamber are small compared with the prevailing temperature, thus pressure, density and entropy gradients would also be small.

7.4.2.2 Basic equations

1. Under simplifying assumptions 1 and 2 above, the linearized momentum equations for superfluid and normal fluid (Eqs. [7-4] and [7-5]) become respectively the London's equation for the thermo-mechanical pressure (Eq. [7-17], p. 3-9) and Stokes equation for creeping flow of a viscous liquid (Eq. [7-19]).

   The first of the lastly mentioned equations can be integrated between both end faces of the porous plug, under the assumption of constant ρ and s, yielding

$$p_1 + \rho g l - p_2 = \rho s (T_1 - T_2) \qquad [7\text{-}52]$$

   gravity forces within the plug, the thickness, t, of which is of the order of a few millimeters, have been neglected.

2. The heat transfer rate, Q, required to evaporate the mass flow rate, m, through the plug is given by $Q = m(h_{fg} + c_p(T_2\text{-}T_1))$, h_{fg} being the heat of vaporization of the liquid and $mc_p(T_2\text{-}T_1)$ the sensible heat, which in the present case is negligible.

   A heat exchange balance between the fluid in the plug and the plug itself yields,

$$m h_{fg} = h(T_1 - T_2) \qquad [7\text{-}53]$$

   where h is the "thermal conductance of the plug plus fluid".

   The combination of Eqs. [7-52] and [7-53] leads to

$$m = (h / \rho s h_{fg})(p_1 + \rho g l + p_2) \qquad [7\text{-}54]$$

   A similar equation has been obtained by Karr & Urban (1978, 1980) [113] & [114]. Eq. [7-54] relates the mass flow rate to the pressure drop, through the impedance $h/\rho s h_{fg}$.

   When the pressure drop in the venting line is negligible, the factor into parenthesis in the right hand side of Eq. [7-54] is simply the vapor pressure of the upper chamber, $p_{sat}(T_1)$, plus the hydrostatic pressure, $\rho g l$, otherwise the impedance, $F = m/p_2$, of the venting line should be taken into account. In that case, Eq. [7-54] becomes

$$m = \frac{p_1 + \rho g l}{\frac{\rho s h_{fg}}{h} + \frac{1}{F}} \qquad [7\text{-}55]$$

Note: non-si units are used in this figure

   given by Urban et al. (1975) [245]. In most cases F is a function of m, and of the outlet to inlet pressure ratio, p_0/p_2, of the venting line (see clause 7.4.2.5).

   The hydrostatic pressure term can be neglected, compared with p_1,except at very low temperatures. For example, when l = 0,3 m and under normal gravity conditions, $\rho g l$ is equal to the He II saturation pressure for T = 1,455 K and smaller than the saturation

pressure for larger values of T. Nevertheless, ρgl is very seldom negligible compared with p_1-p_2.

7.4.2.3 Thermal conductance of the plug plus fluid

The prediction of the thermal conductance of any liquid-filled porous medium is not an easy task. A discussion of the available models of thermal conduction through porous media may be found in Bear (1972) [19].

It is generally agreed that the upper and lower limits of the thermal conductance, h, are given by the following two expressions:

1. Upper limit. Parallel conduction model,

$$h = (1-\Phi)h_s + \Phi h_l \qquad [7\text{-}56]$$

2. Lower limit. Series conduction model,

$$h = \frac{1}{\frac{1-\Phi}{h_s} + \frac{\Phi}{h_l}} \qquad [7\text{-}57]$$

In these expressions Φ is the plug porosity (volume of pores to bulk volume ratio), h_s is the thermal conductance of a "plug" (of the same size and material) with no voids, and h_l the thermal conductance of the He II filling another fictious plug (same size) with $\Phi = 1$, although with the right value of the permeability (see clause 7.4.2.4). It is indicated again that heat transfer through He II is controlled by motion of the normal fluid.

Early developments of the superfluid plug (Selzer et al. (1971) [214]), which were based on the parallel thermal conduction model, used porous plugs of high thermal conductance. Even more, the plug was embedded in a large metallic block with the aim of further enhancing its thermal conductance.

More recent experimental evidence (Elsner (1973) [63], Petrac (1975) [181], Urban et al. (1975) [245], Karr & Urban (1978) [113]) indicates that ceramic plugs of fairly low thermal conductance are also efficient phase separators. Thence, in the following we will restrict ourselves to the assumption that the heat transfer through the liquid is dominant.

In addition, we will assume that the overall heat conduction takes place according to the parallel model. Notice that, taken for granted that the heat transfer through the liquid is dominant, the thermal conductance, h, according to either model differ in a factor Φ^2. Furthermore, data on porous plugs are scarce and incomplete. Even assuming that the linear theory is appropriate, which is not always the case, as we shall see, the resulting expressions are plagued with uncertainties mainly related to the poorly known characteristics of the porous media. It is, thus, difficult to obtain from the available experimental knowledge a detailed information regarding the thermal conduction model.

7.4.2.4 Thermal conductance of the liquid helium

An effective thermal conductivity (or a thermal conductance) of the liquid helium within the plug, much larger than that resulting from the purely molecular heat transport process, can be deduced from the expression of the heat flow, Eq. [7-16].

Darcy's law for flow through porous media will be used instead of Poiseuille's equation (Eq. [7-25]) to relate the pressure gradient, dp/dx, to the normal velocity component, v_n

$$\frac{dp}{dx} = -\frac{\mu_n}{K} v_n \qquad [7\text{-}58]$$

Note: non-si units are used in this figure

where K [m^2] is the permeability, or geometric factor of the porous medium. This parameter characterizes the ease with which a fluid may be made to flow through the medium by an applied pressure gradient. For a circular tube of diameter D_E, $K = D_E^2/32$ and Poiseuille's equation is restored. For an annular slit of width d, $K = d^2/12$.

To calculate the thermal conductance of the liquid helium we combine Eq. [7-16] ($q = mh_{fg}/A_{FL}$ and $A_{FL} = \Phi A_{FR}$) with Eqs. [7-54] and [7-58].

$$h = \Phi K \frac{A_{FR}}{t} \frac{\rho^2 s^2 T}{\mu_n} \frac{1}{1+\frac{sT}{h_{fg}}} \qquad [7\text{-}59]$$

Note: non-si units are used in this figure

Very usually the last factor in the right hand side of Eq. [7-59] is omitted since $sT << h_{fg}$ ($sT/h_{fg} = 3 \times 10^{-3}$ at T = 1,2 K, $sT/h_{fg} = 10^{-1}$ at T = 2,1 K). A similar equation, with $K = d^2/12$, has been used by Karr & Urban (1978, 1980) following Roberts & Donnelly (1974) [196]. Notice that the expression which results once the last factor of the right hand side in Eq. [7-59] has been omitted, follows from Eq. [7-14] under the counterflow assumption (no net mass flow) although, strictly speaking, this assumption is not required here.

Once h has been obtained, the mass flow rate through the plug can be related to the pressure drop by use of Eq. [7-54]

$$m = \Phi K \frac{A_{FR}}{t} \frac{\rho s T}{\mu_n \left(h_{fg} + sT\right)} \left(p_1 + \rho g l - p_2\right) \qquad [7\text{-}60]$$

Note: non-si units are used in this figure

This is the so-called Allen-Reekie Rule which holds for any value of $p_1+\rho gl-p_2$ provided that the normal fluid flow remains laminar.

The experimental validation of Eq. [7-60] will be attempted in clause 7.4.2.6.

Whether or not liquid and vapor coexist within the plug is a matter of discussion (Schotte (1982) [209]).

Boiling within a bundle of fine capillaries or a porous medium is a very unlikely phenomenon since the bubbles are so small that the superheat of boiling would be exceedingly large (Enya et al. (1981) [64]). Nevertheless, situations occur where, due to the liquid cooling by the plug, an additional fountain pressure appears which pushes upstream the liquid-vapor interface until a balance of

fountain pressure, capillary pressure and van der Waals forces is reached. This effect has been called choking (Schotte (1982,1984) [208] & [209]) see also clause 7.4.2.7.

The calculation of an effective liquid conductivity when liquid and vapor coexist within the plug is very complicated because of the following reasons:

1. The volumetric liquid content cannot be easily estimated, as pointed out in clause 7.1.6.
2. The permeability, K, of the porous medium is a function of that liquid content (Philip (1970) [185]).
3. Vapor inclusions will affect the heat transfer mechanism.

No much attention to this situation has been paid in the literature, hence further analysis will pend on future experimental evidence.

7.4.2.5 The venting line

Although the flow of helium vapor through the venting line is a well known process of classical fluid dynamics it is considered here because in real practice porous plug and venting line are mounted in series and influence each other. Even more, in many instances the pressure drop through the plug is a small fraction of that through the venting line, the precise characterization of which becomes paramount.

When the venting line is assumed to be a straight cylindrical tube of circular cross-section having length L and diameter D, and the flow conditions are isothermal (a situation which very approximately holds for low-speed compressible flows in the absence of deliberate attempts to transfer heat to or from the flow) the intake pressure, p_2, is related to the outlet pressure, p_0, by (Ward-Smith (1980) [259])

$$\frac{p_2^2}{m^2}\left(1-\frac{p_0^2}{p_2^2}\right)-\frac{RT}{\left(\pi D^2/4\right)^2}\ln\left(\frac{p_2}{p_0}\right)^2=\frac{RT}{\left(\pi D^2/4\right)^2}\lambda\frac{L}{D} \qquad [7\text{-}61]$$

Note: non-si units are used in this figure

where the second term in the left hand side stands for the axial momentum flux due to changes in density with pressure at constant temperature (which are significant when D is small). T is the fluid temperature (not necessarily equal to T_2) and λ the friction factor.

The outlet pressure, p_0, could be either a constant or a function of the mass flow rate, m. When the venting line directly discharges into a chamber at pressure p_0, the outlet pressure will be constant no matter the value of m (outlet losses are assumed to be negligible). When the venting line ends in a valve through which the pressure loss is Reynolds number independent (as it usually happens) then the outlet pressure will be $p_0 + m/F_0$, F_0 being the impedance of the valve. More complicated functions of m are also possible when the pressure loss through the valve depends on the Reynolds number.

Expressions for λ, or $f = \lambda/4$, in the case of incompressible flow are given in clause 7.2.2. These expressions can be extended to the case of isothermal compressible flow in smooth pipes of circular cross-section.

In the particular case of gaseous Helium (at low temperatures), $R = \boldsymbol{R}/M$, with $\boldsymbol{R}$ = 8,31432 J.mol^{-1}.K^{-1} and M = 4,0026 x 10^{-3} kg.mol^{-1}. $\mu = \mu(1)T$; $\mu(1)$ = 2 x 10^{-7} Pa.s.K^{-1} (Figure 8-65, clause 8.1.1). and the following expressions result:

1. In the fully-developed laminar flow case, $\lambda = 64/Re$, $Re = 4m/\pi D\mu$ (see ECSS-E-HB-31-01 Part 14, clause 7.2.2)

$$\frac{RT}{\left(\pi D^2/4\right)^2}\lambda\frac{L}{D} = 2{,}808\times10^3\left(\frac{T}{T_r}\right)^2\frac{L}{D^4}\frac{1}{m} \qquad [7\text{-}62]$$

Note: non-si units are used in this figure

where T_r = 288 K is a reference temperature. $p$is measured in Pa, m in kg.s^{-1}, and L and D in m.

If a bunch of n cylindrical tubes of circular cross-section, diameter $D/\sqrt{n}$, placed in parallel, is used to accommodate the same total mass flow rate m, the pressure drop will be controlled by the mass flow rate m/n through every individual tube. This will multiply by a factor n^2 the second term in the left hand side of Eq. [7-62] and will reduce, by a factor $1/n$, the length, L, required to achieve a given pressure drop. The Reynolds number, on the other hand, will be reduced by a factor

$1/\sqrt{n}$.

Note: non-si units are used in this figure

2. In the intermediate region under the validity of the Blasius formula, $\lambda = 0{,}316\ Re^{-0{,}25}$ (see ECSS-E-HB-31-01 Part 14, clause 7.2.2)

$$\frac{RT}{\left(\pi D^2/4\right)^2}\lambda\frac{L}{D} = 2{,}513\times10^4\left(\frac{T}{T_r}\right)^{1{,}25}\frac{L}{D^{4{,}75}}\frac{1}{m^{0{,}25}} \qquad [7\text{-}63]$$

3. In the high Reynolds number range for rough pipes λ is independent of the Reynolds number (see ECSS-E-HB-31-01 Part 14, clause 7.2.2).

$$\frac{RT}{\left(\pi D^2/4\right)^2}\lambda\frac{L}{D} = 9{,}698\times10^5\lambda\frac{T}{T_r}\frac{L}{D^5} \qquad [7\text{-}64]$$

A pressure drop which is independent of the Reynolds number also results when a constriction is mounted in the venting line to control the mass flow rate (see ECSS-E-HB-31-01 Part 13, Figs. 7-16 and 7-26, ECSS-E-HB-31-01 Part 13 clause 7.3.1).

Laminar flow occurs up to Reynolds numbers of about 2 x 10^3.For Reynolds numbers above 4 x 10^3 the flow is fully turbulent. Blasius formula holds for $Re < 10^5$.

A typical example is shown in Figure 7-24, where experiment al data of backward pressure, p_2 vs. mass flow rate, m, through a porous plug have been approximated by means of Eq. [7-62].

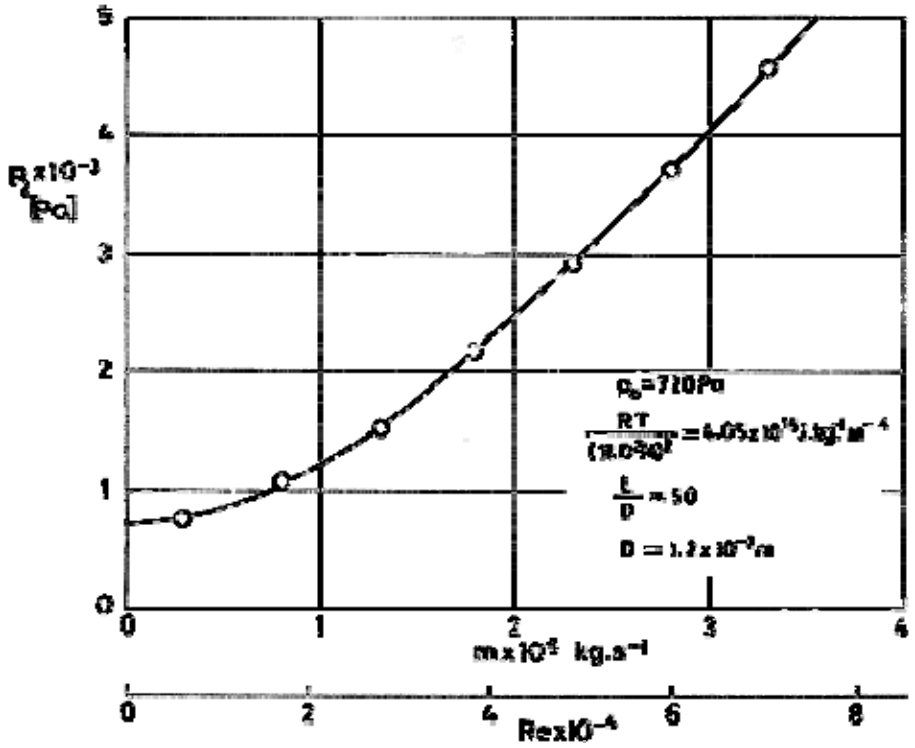

Note: non-si units are used in this figure

Figure 7-24: Backward pressure, p_2, as a function of mass flow rate, m, through the plug. Experimental points are from smooth curves by Karr & Urban (1978, 1980) [113] & [114]. The curve shown in the figure and the Reynolds number in the abscissae axis correspond to turbulent flow (neglecting entrance effects, see ECSS-E-HB-31-01 Part 13 clause 7.2.5) in a straight tube of circular cross-section, under the validity of Blasius formula, for the data shown in the insert. Calculated by the compiler.

7.4.2.6 Experimental test of the steady-linear theory

Equation [7-60] will be checked versus experimental results. To this aim an impedance (per unit volume) of the porous plug is introduced as follows:

$$\frac{m/\Phi K \dfrac{A_{FR}}{t}}{p_1 + \rho g l - p_2} = \frac{\rho s T}{\mu_n \left(h_{fg} + sT\right)} \qquad [7\text{-}65]$$

Note: non-si units are used in this figure

where the right-hand side (the dimensions of which are [$s.m^{-2}$]) only depends on temperature no matter the porous plug involved.

The check is difficult because many data on superfluid plugs have been reported very incompletely. Most of the investigations aim at probing that the device separates liquid from vapor (with no vapor appearing in the exit face), and at defining the operating limits of a separator consisting of a plug in series with a venting line the characteristics of which are not reported at all. In many cases the

pressure loss through the plug happens to be a small fraction of that through the venting line. In these cases any guess on the characteristics of that line drastically influences the evaluation of the data.

The information which ought to be reported in order to arrive to an unambiguous probe of the validity of Eq. [7-65] is summarized in Figure 7-25.

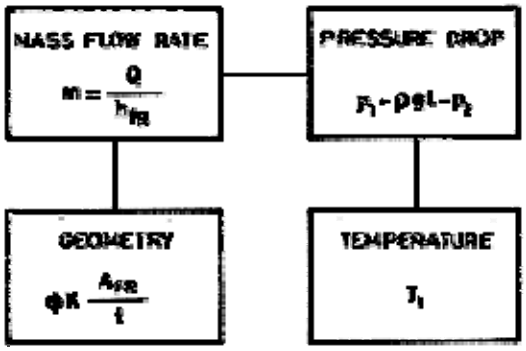

Figure 7-25: Quadrangle of data required in porous plug performance evaluation.

A judicious guess has been made to estimate the outstanding data, when needed. In several instances the result is fairly satisfactory.

The available information has been summarized in the following pages. Eisner, A. (1973) [63].

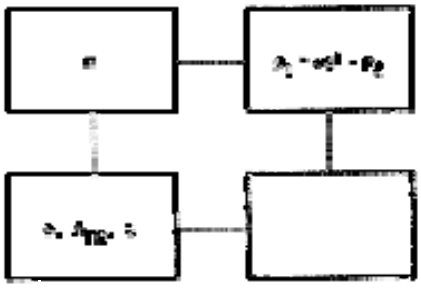

Characteristic of the plug:

Material	Aluminium Silicate
d_{vnom} [m]	10^{-7}
A_{FR} [m^2]	1,26 x 10^{-3}
t [m]	5 x 10^{-3}
Φ	0,4
K [m^2]	

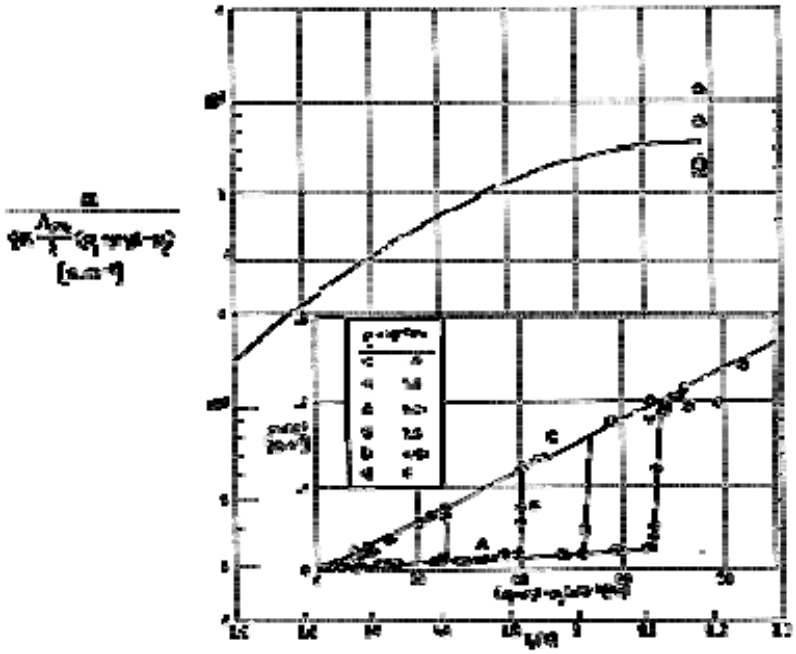

Note: non-si units are used in this figure

Comments:

The aim of this work was assessing the feasibility of plug valves in refilling He II devices. Pressure differences and plug thickness are larger than usual.

The insert shows that the mass flow rate is small (curve A) provided that the pressure difference is less than some critical value. Once this value is exceeded, the mass flow rate increases (curve B). Liquid helium starts leaking through the plug as soon as A turns into B (see clause 7.4.2.7).

Neither T_1 nor K are given. Points labelled as triangle in the insert also appear in Figure 7-29, from which we deduce T_1 = 2,18 K. A value $K = 0{,}6 \times 10^{-6}$ m² has been assumed to replot points triangles from curve A.

Petrac, D. (1975) [181].

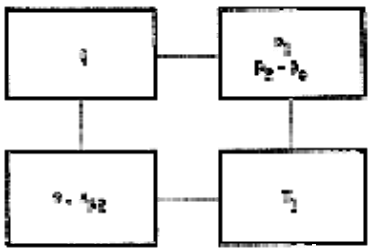

Characteristic of the plug:

Material	Ceramic
d_{vnom} [m]	10^{-5}
A_{FR} [m²]	2×10^{-3}
Φ	0,610

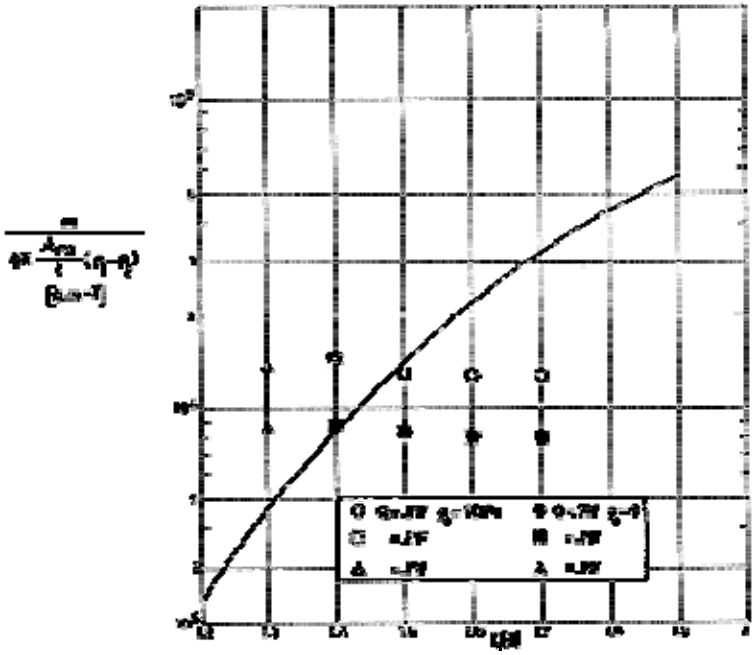

Note: non-si units are used in this figure

Comments:

The analysis of the results is difficult since the data given are incomplete.

Assuming that the porous plug is similar to that used by Urban, Katz & Karr (1975) [245], see below, $\Phi K A_{FR}/t = 4{,}14 \times 10^{-14}\ m^3$.

The second difficulty concerns the exit pressure, p_o. No reasonable trend of p_o vs. m has been found and thence data points have been plotted assuming $p_o = 0$ Pa or $p_o = 50$ Pa.

Urban, E.W., Katz, L., Karr, G.R. (1975) [245].

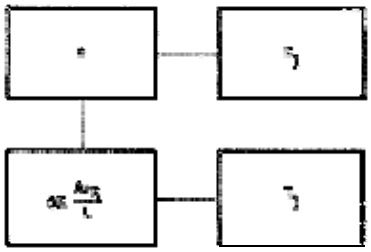

Characteristic of the plug:

Material	Ceramic Al_2O_3
d_{vnom} [m]	$0{,}5 \times 10^{-6}$
A_{FR} [m^2]	$1{,}51 \times 10^{-3}$

t [m]	6,5 x 10^{-3}
Φ	0,548
K [m^2]	5,37 x 10^{-15}

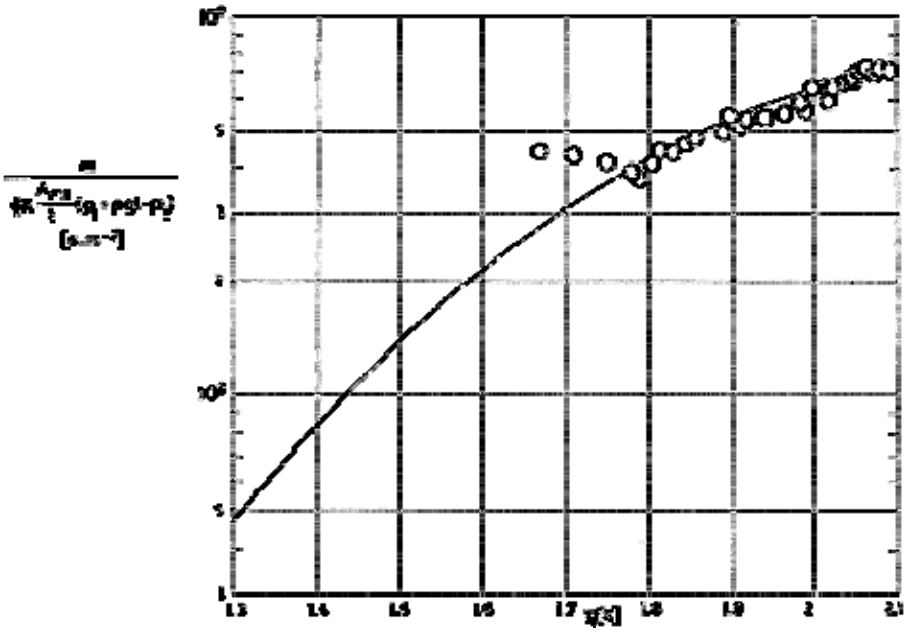

Note: non-si units are used in this figure

Comments:

Neither l nor p_2 are given and no checking of the theory is possible. Nevertheless, when Eq. [7-65] is assumed to hold, p_2 as a function of m can be calculated. The following additional data appear as reasonable: l = 0,2 m, p_2^2-p_o^2 = (7,472 ± 0,176)m^2 x 10^{11} (laminar flow through the venting line), and $p_o \approx$ 80 Pa much smaller than p_2 in any case.

The experimental points have been replotted with these additional data in mind.

The impedance of the plug, F_p, results to be comparable to that of the venting line, F. $F_p/F \approx 1,5$

Urban, E.W., Katz, L., Karr, G.R. (1975) [245].

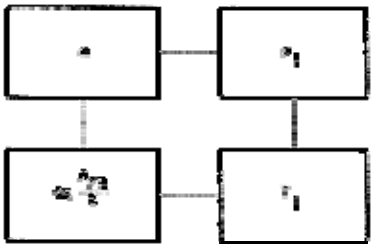

Characteristic of the plug:

Material	Ceramic Al_2O_3
d_{vnom} [m]	10^{-5}
A_{FR} [m^2]	1,51 x 10^{-3}
t [m]	6,6 x 10^{-3}
Φ	0,677
K [m^2]	0,224 x 10^{-12}

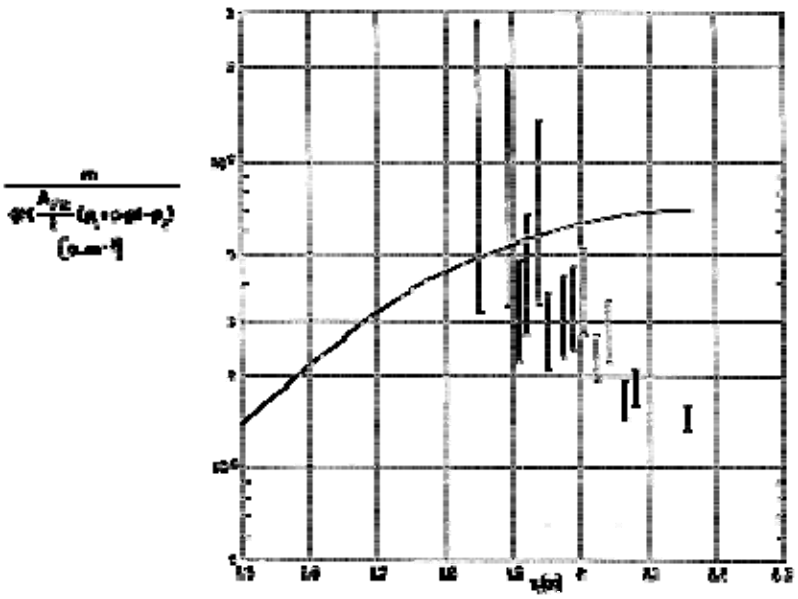

Note: non-si units are used in this figure

Comments:

Neither l nor p_2 are given and no checking of the theory is possible. Proceeding as in the previous case, we arrive at: l = 0,2 m, p_2^2-p_o^2 = (1,425 ± 0,018)m^2 x 10^{12} (laminar flow through the venting line), and $p_o \approx$ 80 Pa.

The ends of the bars in the figure correspond to extreme values of p_2 (+ and - signs in the above expression). The wide scatter is in part due to the very large impedance ratio, $F_p/F \approx 20$ to 10^3. Other experimental points fell beyond the limits of the figure.

Urban, E.W., Katz, L., Karr, G.R. (1975) [245].

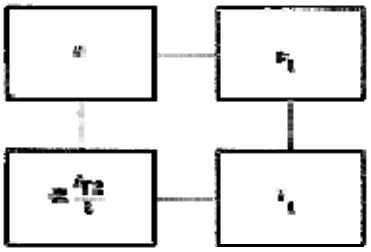

Characteristic of the plug:

Material	Nickel
d_{vnom} [m]	10^{-5}
A_{FR} [m²]	1,51 x 10^{-3}
t [m]	6,3 x 10^{-3}
Φ	0,384
K [m²]	0,377 x 10^{-12}

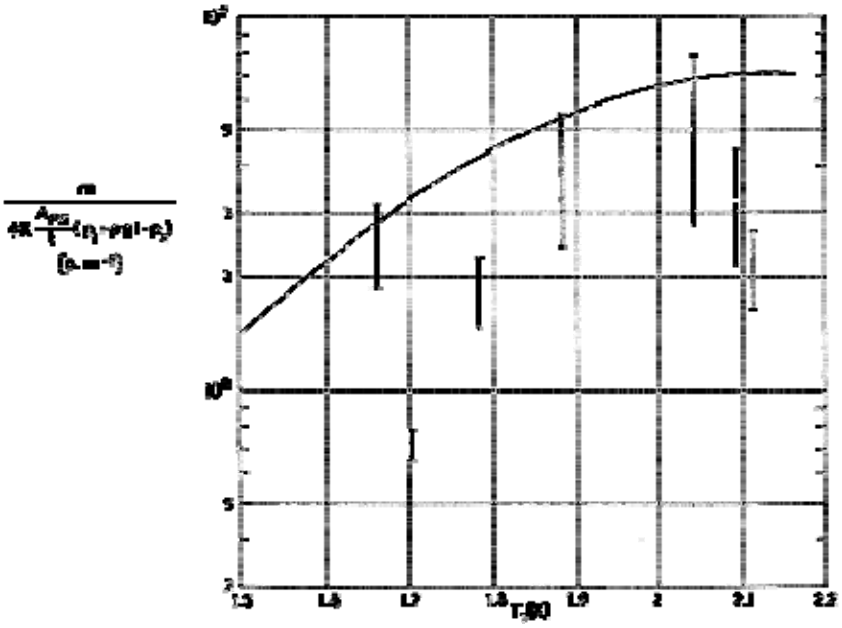

Note: non-si units are used in this figure

Comments:

Neither l nor p_2 are given and no checking of the theory is possible. Proceeding as in the previous case, we arrive at: l = 0,2 m, p_2^2-p_o^2 = (1,344 ± 0,008)m^2 x 10^{18} (laminar flow through the venting line), and $p_o \approx$ 80 Pa.

The ends of the bars in the figure correspond to extreme values of p_2 (+ and - signs in the above expression). The wide scatter is in part due to the very large impedance ratio, $F_p/F \approx 10^2$ to 2 x 10^2.

The authors detected differences between heating and cooling. This could be due to vapor within the plug (see clause 7.4.2.4).

Karr, G.R., Urban, E.W. (1978,1980) [113] & [114].

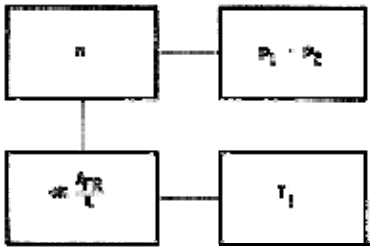

Characteristic of the plug:

Material	Ceramic Al_2O_3
d_{vnom} [m]	0,5 x 10^{-6}
A_{FR} [m^2]	1,51 x 10^{-3}
t [m]	6,5 x 10^{-3}
Φ	0,5177
K [m^2]	5,047 x 10^{-14}

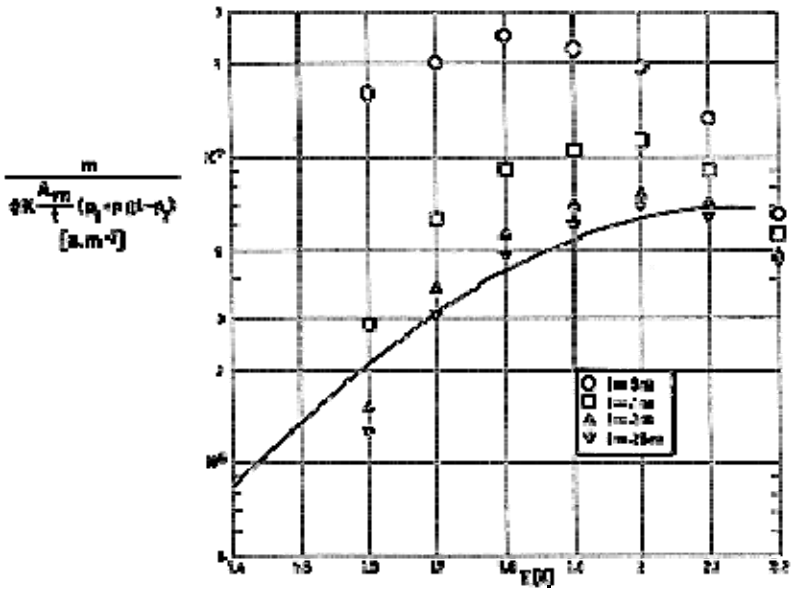

Note: non-si units are used in this figure

Comments:

Data from smooth curves.

l not given, thus data point have been re-plotted for four different values of l.

When l = 0 the curve exhibits a more or less flat plateau, which could indicate that the impedance of the plug, F_p, is constant. This consequence is, however, artificial as it results from neglecting $\rho g l$ compared with p_1 - p_2.

The impedance of the plug is larger than that of the venting line, $F_p/F \approx$ 1,5 to 10. These authors, however, report data on p_2 vs. m.

Petrac, D., Mason, P.V. (1978) [182].

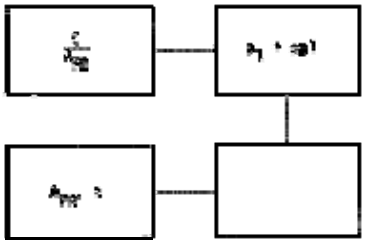

Characteristic of the plug:

Material	Ceramic Al_2O_3
d_{vnom} [m]	7×10^{-6} to 10^{-5}
A_{FR} [m²]	$0{,}36 \times 10^{-3}$ and 2×10^{-3}
t [m]	$6{,}4 \times 10^{-3}$

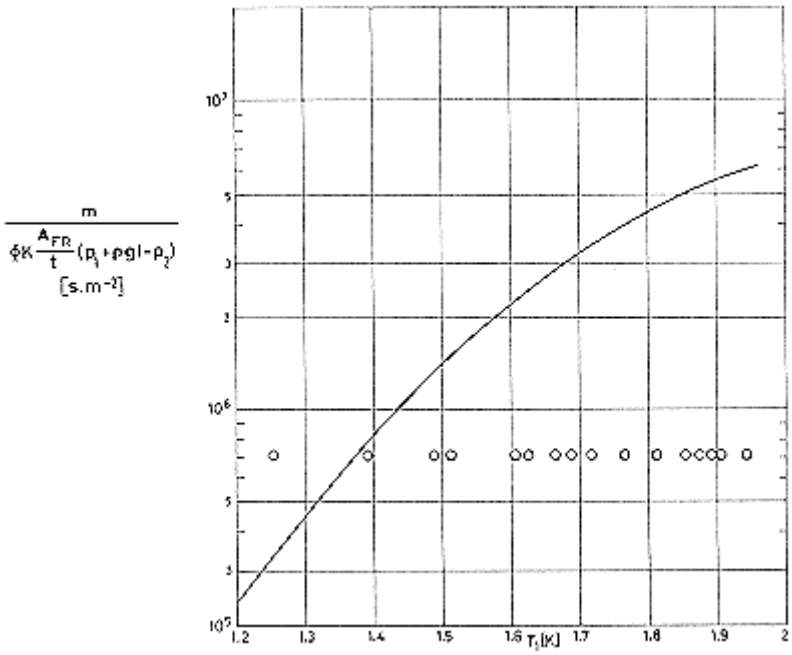

Note: non-si units are used in this figure

Comments:

These authors do not give neither Φ nor K. They indicate that $F_p = m/A_{FR}(p_1+\rho gl-p_2) = 1{,}7 \times 10^{-5}$ m.s^{-1}, "although it decreases above 1,9 K, dropping about 50% when the upstream temperature reaches T_λ". This would indicate that the permeability, K, varies by an order of magnitude in the temperature range of the experiment.

Additional data are required to plot the experimental points in the above figure. T_1 has been deduced from $p_1 + \rho gl$, assuming $\rho gl << p_1$. Φ and K are supposed to be 0,677 and 0,224 x 10^{-12}, respectively, as in one of the previous cases.

Petrac, D., Mason, P.V. (1980) [183].

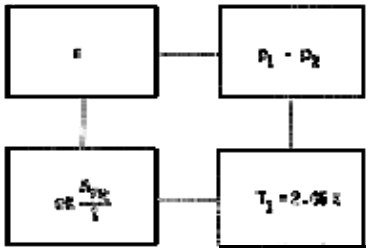

Characteristic of the plug:

Material	Sintered Stainless Steel
d_{vnom} [m]	2 x 10^{-6} to 5 x 10^{-6}
A_{FR} [m^2]	0,47 x 10^{-3}

t [m]	6,7 x 10^{-3}
Φ	0,18
K [m^2]	5,5 x 10^{-14}

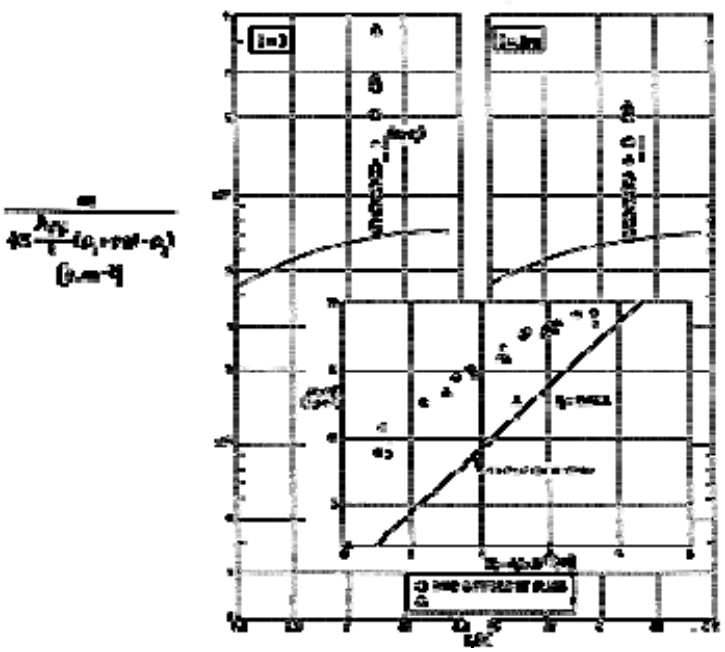

Note: non-si units are used in this figure

Comments:

Since *l* is not given, experimental data points have been replotted for $l = 0$ and $l = 0{,}1$ m.

Schotte (1982) attributes the non-linearity of the *m* vs. p_1-p_2 curve in the insert to choking effect (see clause 7.4.2.7). Notice, however, that points corresponding to the larger values of p_1-p_2 almost fall on the theoretical curve (straight line A in the insert). Should the lower pressure-difference data points correspond to the theory, the required value of the permeability,*K*, would be ten times larger than that given by the authors.

Shotte, U. (1984) [209].

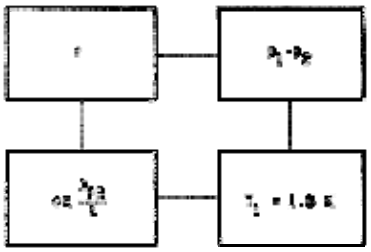

Characteristic of the plug:

Material	Sintered Stainless Steel
d_{vnom} [m]	
A_{FR} [m^2]	0,3 x 10^{-3}
t [m]	6,1 x 10^{-3}
Φ	0,27
K [m^2]	15,45 x 10^{-14}

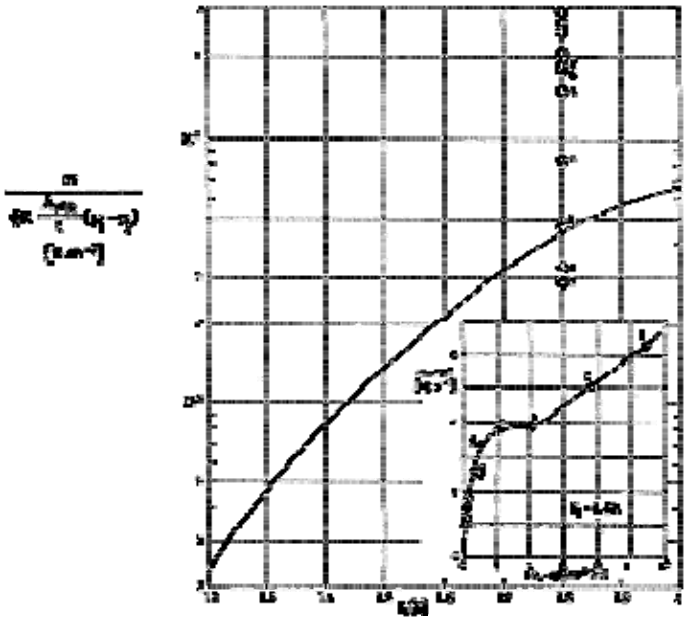

Note: non-si units are used in this figure

Comments:

Laboratory data of the IRAS plug. IRAS was launched on Jan. 25, 1983 from Vandenberg (USA), by a Delta 3910.

For a preliminary phase development of the IRAS Dewar see clause 6.4.3.2.

The permeability, *K*, has been estimated by Schotte from data of the ideal part of the phase separation curve.

The curve in the insert clearly shows the chocking effect (points 3 to 5, see clause 7.4.2.7). Equal numbers in both main figure and insert correspond to the same experimental point.

7.4.2.7 Departures from the simplified theory

The above theory of the superfluid plug is based on the linear version of the Two-Fluid (Landau) Model for steady one-dimensional flow. Needless to say the plug behaves as a classical porous medium when superfluid effects are absent.

Here attention is given to several specific instances where the simplified theory is no longer valid.
Gorter-Mellink Flow

A phase separator could operate under three different regimes: laminar, turbulent (according to Gorter-Mellink model, see clause 7.2.1 and 7.1.3) and vapor flow.

Figure 7-26 clearly indicates that a new flow regime appears when the mass flow rate exceeds some "critical" value. The results of this figure have been obtained by means of a micron-sized flow channel (slit) with adjustable length. This configuration has been used in the Active Phase Separator (APS) for the cooling system of the German Infrared Laboratory (GIRL), (Denner et al. (1982) [57]), see also Figure 7-27.

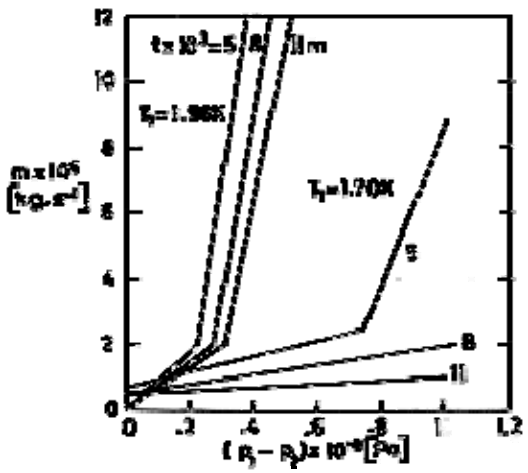

Note: non-si units are used in this figure

Figure 7-26: Mass flow rate, m, vs. pressure drop, p_1-p_2, for slits of various lengths, t, and two different bath temperatures, T_1. From Denner et al. (1980) [56].

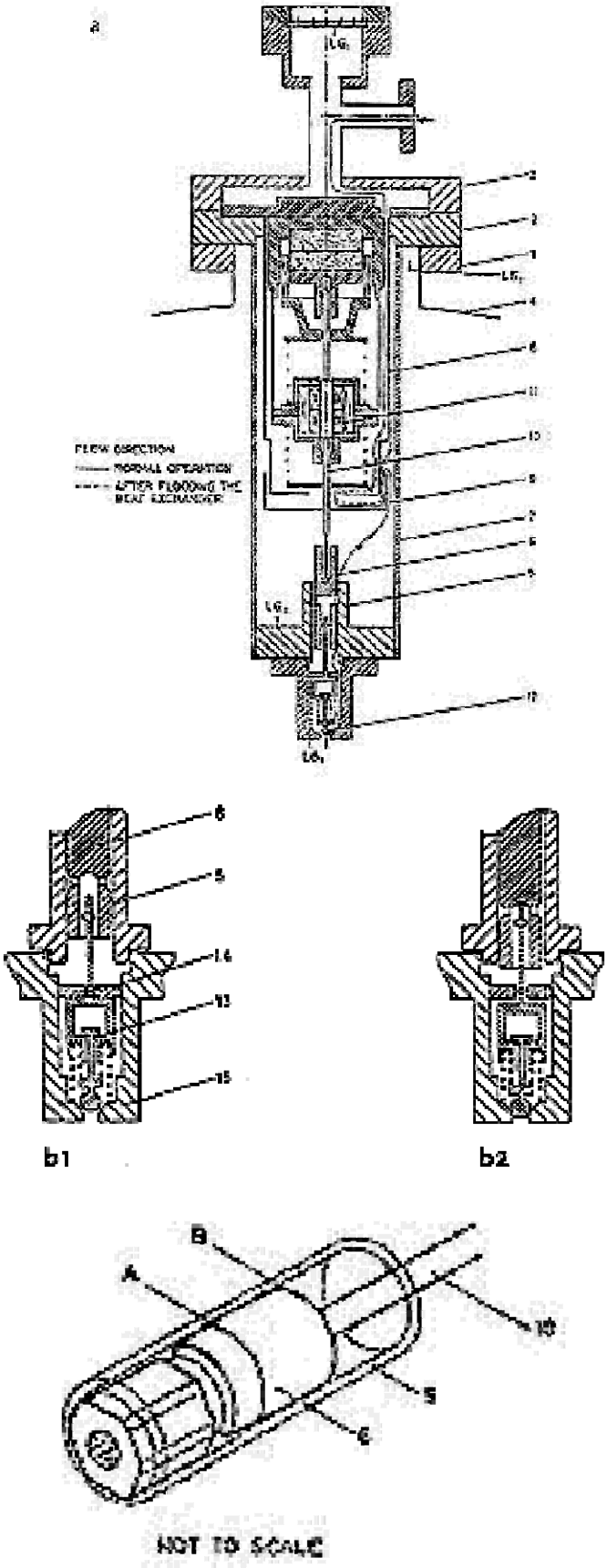

Figure 7-27: Active Phase Separator (APS). From Denner et al. (1982) [57].

In addition to several functional advantages, the slit exhibits a well defined geometry which could be useful in our present discussion. This discussion only concerns configurations with a single-pore width (slits, bundles of equal parallel tubes, ...)

According to Schotte (1982) [208] at the turn-off point the superfluid velocity is given by Eq. [7-31]. Beyond this point bulk helium flows into the venting line, the walls of which are in contact with the bath, where it could be evaporated.

The fact that Gorter-Mellink flow appears when liquid helium starts leaking through the plug has been made clear by Schotte (1984) [209] as follows:

When liquid and vapor coexist in chamber 2 (see clause 7.4.2), p_2 and T_2 are no longer independent from each other since $p_2 = p_{sat}(T_2)$. Thus two different equations are available for the determination of T_2,namely: Eq. [7-52], which describes the iso chemical-potential flow through the plug (we will neglect the hydrostatic pressure for the time being)

$$p_1 - p_2 = \rho s(T_1 - T_2) \qquad [7\text{-}66]$$

and the Clapeyron's formula (see Table 8-13 in clause 8.2) which describes the evolution along the saturation line. For small pressure jumps,

$$p_1 - p_2 = (dp/dT)_{sat}(T_1 - T_2) \qquad [7\text{-}67]$$

In the range of temperatures of interest the temperature drop given by Eq. [7-67] is more than ten times larger than that given by Eq. [7-66]. Thence p_1-p_2-ρs(T_1-T_2) becomes negative (or, in other words, there is a jump in the chemical potential, μ, through the plug).

From Eq. [7-8]; neglecting second order terms, and Eqs. [7-32] and [7-33], the following expression results:

$$\mu_1 - \mu_2 = (p_1 - p_2)/\rho - s(T_1 - T_2) = -tA\rho_n |v_n - v_s|^3 \qquad [7\text{-}68]$$

The slit stops being a phase separator when the flow becomes supercritical. In the particular case of the APS a heat exchanger contacting the bath is added to evaporate all passing liquid. The heat transfer rate provided by the heat exchanger, which results to be much larger than that through the slit, is given by

$$\frac{Q}{A_{FL}} = h_{fg}\left\{\rho v_n - \rho_s\left[\frac{s(T_1 - T_2)}{tA\rho_n}\right]^{1/3}\right\} - \rho_s sT\left[\frac{s(T_1 - T_2)}{tA\rho_n}\right]^{1/3} \qquad [7\text{-}69]$$

Note: non-si units are used in this figure

where the first term in the right hand side is the heat transfer rate through the combined system, and the second term is the heat transfer through the slit.

$(p_1-p_2)/\rho$ has been neglected compared to $s(T_1-T_2)$ in order to reach Eq. [7-69].

Choking

Choking manifests itself by a small flow rate (compared to the predicted one) which appears at low pressure differences and remains up to values very well beyond critical. This effect was first discovered for the smallest slits, and for wider slits at temperatures around 1,6 K. The following explanation of the effect, also from Schotte (1984) [209], is still based on the assumption of a single-pore width.

The one-dimensional theory used up to this moment assumes that liquid bulk and slit wall temperatures are equal at each cross section. Actually there is a difference, which is similar to that discussed in clause 6.2.3.3 with the following two peculiarities. a) The heat transfer in the bulk is very effective (counterflow heat exchange, clause 7.1.1.2). This counterflow should be laminar because of the low flow rates involved, and b) The heat transfer from or to the wall is controlled by the Kapitza effect (clause 7.2) which provides a high resistance to thermal flow.

The problem was considered by Schotte (1982) [208]. If T_1 and T_2 are the wall temperatures at either end of the slit, the following expression for the liquid temperature results

$$T(x)-T_2=\frac{T_1-T_2}{\frac{h_{fg}\rho_{sat}}{\rho s T}+\frac{x}{\Lambda}\coth\frac{x}{\Lambda}} \qquad [7\text{-}70]$$

Note: non-si units are used in this figure

with $\Lambda^2 = D_E^3\rho^2 s^2 T/128\mu_n h_k$, h_k being the Kapitza conductance.

Equation [7-70] indicates that liquid exit temperature is larger than T_2. Cooling by the walls is promoted by low T_1 and small D_E values. Significant effects are to be expected at about $D_E = 10^{-5}$ m down.

Radial cooling does not directly result in axial counterflow. Thence the resulting pressure gradient will be smaller than that predicted from thermo-mechanical effect with the same intake to exit liquid temperature differences. A counter pressure, which could be around 10^4 Pa, results. This pushes backward the liquid-vapor interface until a balance of thermo mechanical pressure, capillary force and van der Waals forces is reached (Figure 7-28b). Notice that although the choking tendency is larger for smaller diameters, capillary forces, which resist to the deformation of the interface, are also larger.

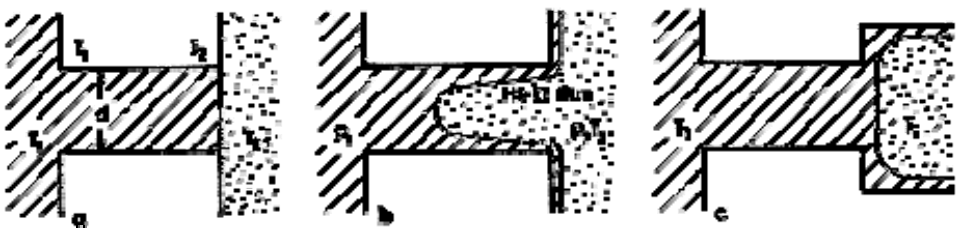

Figure 7-28: Three typical positions of the liquid-vapor interface. a) Ideal flow separation. b) Choking. c) Gorter-Mellink flow. From Schotto (1984) [209].

When the choking effect is strong the mass flow, which is dominated by vapor flow, diminishes.

Choking can be overcome by increasing p_1, either through bath heating or by an extra pressure.

Multiple Pore Widths

The application of Poiseuille's type discussions to saturated porous media is straight-forward regarding Darcy's law (clause 7.4.2.4). The difficulties appear when liquid and vapor coexist within the pores. All three flow types namely: ideal, Gorter-Mellink and choked can coexist in a given plug for any T_1, Δp pair.

Although the Hydrodynamics of classical fluids in unsaturated porous media has reached a high level of complexity (see, f.e., de Gennes (1983)) we are still far from its application to the present instance. Nevertheless, a simple picture could be helpful.

When choking in the smallest pores starts, the larger ones are partially drained. The corresponding outflow delays the transition to supercritical flow in the larger pores. If there are too many wide pores, leakage could occur with $\Delta\mu \neq 0$ for all pores. Schotte (1984) [209] also reports the existence of a supercritical mode with $\Delta\mu = 0$, which he calls "breakthrough" and relates to the conditions $v_n = v_s$ (see curve labelled $\Delta\mu = 0$ in Figure 7-6, clause 7.1.2).

It can be shown that the presence of supercritical flow in the larger pores not necessarily leads to leakage through the plug. To this aim, let us write down the mass flux density through a cylindrical pore, once $v_s$has been related to v_n and $\Delta\mu$ by means of Eq. [7-68], as follows:

$$\frac{m}{A_{FL}} = \rho v_n - \rho_s \left(\frac{\mu_2 - \mu_1}{tA\rho_n} \right)^{1/3} \qquad [7\text{-}71]$$

Note: non-si units are used in this figure

where, for a given pressure gradient, the first term of the right hand side depends on the pore size (Eq. [7-25]), whereas the second does not.

When the flow in the larger voids becomes supercritical, $m > 0$. But for smaller voids in the same cross section of the plug, m in Eq. [7-71] becomes negative (μ, like p, T, ... is a one-dimensional quantity). Therefore the net liquid flow may well be zero.

The conclusion is that the in homogeneity of pore widths extends phase separation into a region where, were the capillaries uniform, liquid leakage could be expected.

Upper Temperature

At least the venting side temperature should be smaller than T_λ if phase separation is to be achieved. Figure 7-29 indicates that the temperature could become smaller than T_λ inside the plug, near the intake face. When the pressure difference increases, the T_λ zone shifts toward the venting side.

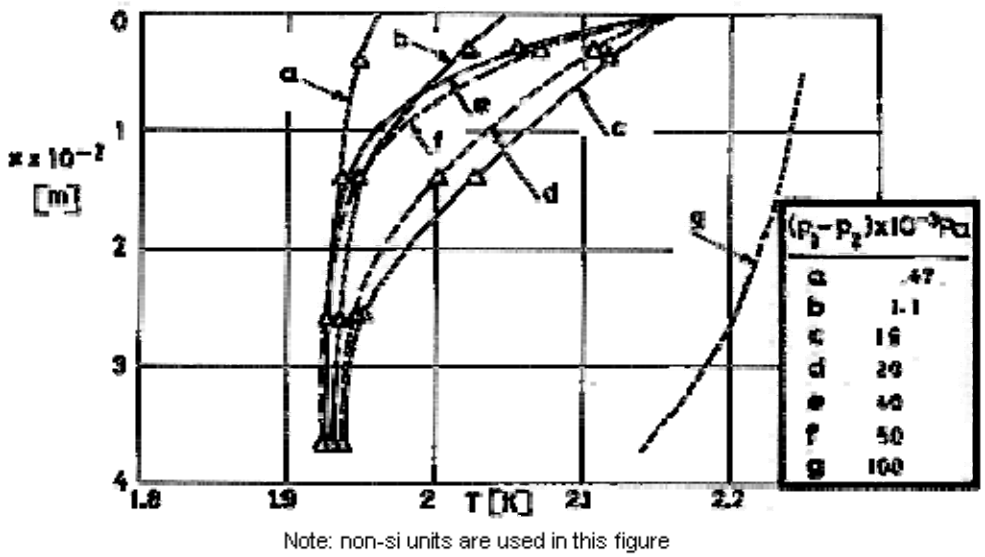

Note: non-si units are used in this figure

Figure 7-29: Temperature distribution within a 4 x 10^{-2} m thick. Ceramic plug for several pressure differences. p_2 = 2,55 x 10^{-3} Pa in any case. From Elsner (1973) [63].

Non-steady Effects

Information on the dynamic behavior of superfluid plugs is very scanty, although several groups seem to be working on downstream flow modulation by use of mechanical or thermal devices (Schotte (1984) [209]).

Limited results have been reported by Karr & Urban (1978, 1980) who used the ceramic plug described previously. These authors give the time constant after power-off or power-on as a function of the heating power (Figure 7-30), and the asymptotic value of p_2 ($p_2(t)$ when $t \rightarrow \infty$). The response is exponential with time, as expected, and faster when the heater is placed at the plug exit (instead of upstream, within the bath). The steady state results are the same no matter the heater is placed upstream or at the plug exit. The response time is of the order of several minutes. The liquid mass within the upstream bath (on which the response should depend) is not given.

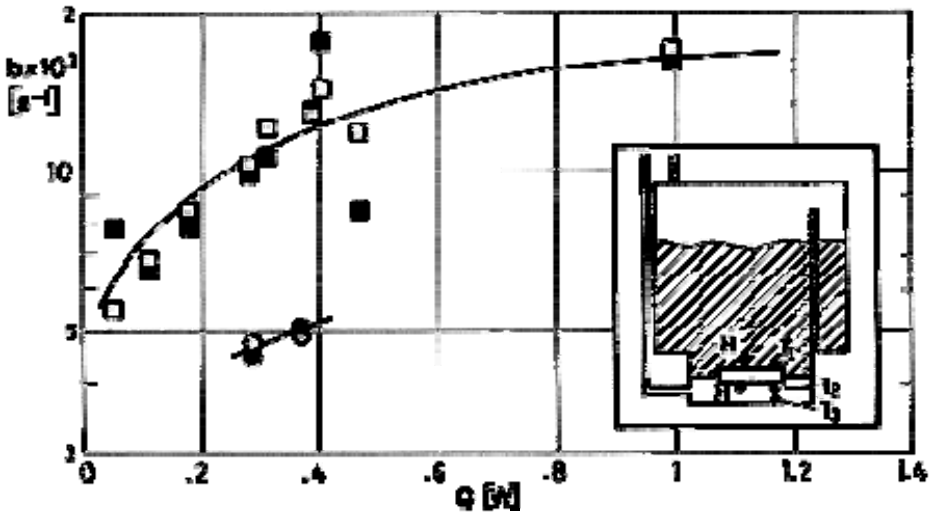

Note: non-si units are used in this figure

Figure 7-30: Time constant, *b*, as a function of heating power, *Q*, for the plug described by Karr & Urban (1978,1980) [113] & [114] in clause 7.4.2.6. Position of

the heaters, *H*, is also shown in the figure. White circle: upstream heater power-on; blackcircle: upstream heater power-off; white square: heater at the plug exit power-on; black square: heater at the plug exit, power-off. From Karr & Urban (1978,1980) [113] & [114]. There is no consistent difference between power-on and power-off.

Flow modulation by downstream heating has been also reported by Murakami et al. (1982) [158], quoted by Schotte (1984) [209].

It is not clear how heating downstream influences the impedance of the system formed by plug and venting line. This heating would decrease the pressure difference across the plug, while keeping constant the kinematic viscosity ($\nu = \mu/\rho$) of the vapors.

7.4.3 Characteristics of porous media

Superfluid plug performance depends on several characteristics of the porous media.

According to the simplified theory (clause 7.4.2) the data required are:

1. The porosity, Φ, for estimating the thermal conductance of both the fluid and the plug.
2. The permeability, K, for relating pressure to mass flow rate, and for calculating the heat transfer through the fluid. (clause 7.4.2.4).
3. The hydraulic diameter, D_E, for estimating the critical value of the mass flow rate (Eq. [7-31]).

No very detailed data concerning these, or similar, characteristics are normally given in the literature. In most cases, only the value of an ambiguously defined "mean pore size" is stated by the manufacturer, and measurements from different sources are widely different. Thence, it is necessary to measure and to correlate the various parameters. Table 7-46 defines several of these parameters.

The details concerning the measurement of the different physical characteristics of the porous medium may be found in Collins (1961) [47], where additional references are given.

Table 7-46: Variables Characterizing the Porous Media

Variable	Symbol	Dimension	Definition	Comments
Specific Surface	M	[m^{-1}]	M = (Total internal area)/(Bulk volume)	A specific area, M_s, is often defined in terms of unit volume of solid, rather than in terms of unit volume of porous medium. $M_s = M/(1-\phi)$, where ϕ is the porosity to be defined below. Bear (1972) [19].
Mean Particle Diameter	d	[m]	$\frac{1}{d} = \sum_{i=1}^{\infty} \frac{f_i}{d_i}$ where f_i is the volume fraction of the particles having diameter d_i.	d is usually known as the harmonic mean diameter. Sometimes d_{10} is used instead of d. d_{10} is a diameter such that 10% (by weight) of the porous matrix consists of grains smaller than it. Bear (1972) [19].
Pore Diameter	d_v	[m]	$d_v = \int_0^{\infty} \delta P_v(\delta) d\delta$ Note: non-si units are used in this figure δ: diameter of the largest sphere constructed around any void point such that the sphere remains within the void. $P_v(\delta)d\delta$: probability that the diameter lies between δ and $\delta + d\delta$	Frequent reference to a characteristic pore diameter is made in the literature, although not many measurements of this variable have been reported. Beran (1968) [24].
Hydraulic Diameter (Equivalent Diameter)	D_E	[m]	$D_E/4$ = (Volume filled with fluid)/(Wetted surface)	$D_E = 4\Phi/M$, *where* Φ is the porosity to be defined below. Bear (1972) [19].
Porosity	Φ		Φ = (Volume of pores)/(Bulk volume)	This is the usual definition (Bear (1972) [19]). Effective porosity is that fraction of the bulk volume constituted by interconnecting pores (Collins (1961)

Variable	Symbol	Dimension	Definition	Comments
				[47]). For a statistically homogeneous media the porosity is the probability of finding a void at any point. This definition can be applied to both area porosity and volume porosity.
Tortuosity	q		q = (Sample thickness/Flow path length)^2	This is the definition by Bear (1972) [19]. Sometimes (Collins (1961) [47]) tortuosity is defined as the ration of flow path length to sample thickness.
Permeability	K	[m^2]	$\vec{u} = -(K/\mu)\nabla p$ (Darcy's law) Note: non-si units are used in this figure $\vec{u}$: mean fluid velocity Note: non-si units are used in this figure ∇p : pressure gradient μ : dynamic viscosity of the fluid	Permeability characterizes the ease with which a fluid may be made to flow through the material by an applied pressure gradient. According to Darcy's law, permeability is a characteristic of the fluid medium which does not depend on fluid properties. Formulae to relate the permeability to other characteristics of the medium are given in Table 7-47.

Statistical information on the structure of porous media may be obtained from a photograph of a planar cross-section (Beran (1968) [24]). The procedure is tedious, but once a satisfactory picture of ample size is obtained, the measurements may be made by relatively untrained people, not to mention that instruments for optical image analysis are presently available. The key for success with these techniques is the specimen preparation. Methods for the preparation of metallic specimens are described by Metzler & Nitsche (1972) [150].

The permeability, *K*, may be either measured or calculated in terms of several geometrical characteristics of the porous medium, see Table 7-47.

Table 7-47: Expressions Relating the Permeability, *K*, to Geometrical Properties of the Porous Medium.
All expressions in this Table are from Bear (1972) [19].

1. Empirical formulae

   (a) Krumbein & Monk formula

$$K = 0{,}617 \times 10^{-3} d^2 \qquad [7\text{-}72]$$

   (b) Fair & Hatch formula

$$K = \frac{\Phi^3}{m(1-\Phi)^2} \frac{1}{\left(\frac{\alpha}{100} \sum \frac{P}{d_m} \right)^2} \qquad [7\text{-}73]$$

   m is the packing factor ($m \sim 5$).

   α is a particle-shape factor varying from 6,0 for spherical particles to 7,7 for angular ones.

   P is the percentage of material held between adjacent sieves.

   d_m is the geometric mean rated sizes of the adjacent sieves.

   This formula has been obtained empirically for unconsolidated material, such as sand. Its main advantage over Eq. [7-77] below, lies on the fact that Eq. [7-72] takes into account more precisely the particle-size distribution of the material constituting the porous medium.

2. Formulae based on Darcy's law

   (a) Kozeny's equation

$$K = c_o \left(\Phi^3 / M^2 \right) \qquad [7\text{-}74]$$

   The porous medium is treated as a bundle of capillary cylindrical tubes of equal length. c_0 is a numerical factor which depends -very slightly- on the geometrical form of these tubes. $c_0 = 0{,}408$ for an ellipse of axis ratio 0,1, $c_0 = 0{,}5$ for a circle, $c_0 = 0{,}562$ for a square, $c_0 = 0{,}597$ for an equilateral triangle, and $c_0 = 0{,}667$ for a strip. A value $c_0 = 0{,}4$ is mentioned as plausible for porous media.

   In terms of M_s, Eq. [7-74] becomes:

$$K = c_0 \frac{\Phi^3}{(1-\Phi)^2} \frac{1}{M_s^2} \qquad [7\text{-}75]$$

   (b) Kozeny-Carman equation

$$K = \frac{1}{5}\frac{\Phi^3}{(1-\Phi)^2}\frac{1}{M_s^2} \qquad [7\text{-}76]$$

Note: non-si units are used in this figure

Introducing a mean particles size, $d_m = 6/M_s$, Eq. [7-76] becomes:

$$K = \frac{d_m^2}{180}\frac{\Phi^3}{(1-\Phi)^2} \qquad [7\text{-}77]$$

Note: non-si units are used in this figure

This equation has been checked for superfluid helium flow through filters by Niinikoski (1971) and by Frederking, Elsner & Klipping (1973) [72]. In both cases the porous medium was totally immersed in the liquid.

(c) Modified Kozeny's equation, in terms of tortuosity,

$$K = c_0 q\frac{\Phi^3}{M^2} = c_0 q\frac{\Phi^3}{(1-\Phi)^2}\frac{1}{M_s^2} \qquad [7\text{-}78]$$

Note: non-si units are used in this figure

when $c_0 = 0{,}4$ and $q = 0{,}5$, Eqs. [7-76] and [7-78] coincide.

Table 7-48 gives information on several porous media. This table shows the disagreement which present the data obtained by different methods. In addition, the table could serve as a guide to the available methods for measuring the characteristics of the porous media.

Table 7-48: Data on Porous Media

Material	Thickness tx10³ [m]	Pore Diameter d_vx10⁶ [m]	Hydraulic Diameter D_Ex10⁶ [m]	Porosity Φ	Tortuos. q	Permeability Kx10¹⁵ [m²]	Manufacturer	Reference
Selas 06 [a]	5,20	0,48 [c] 0,902 [d]		0,29 [e]	0,143 f	0,85 [g]	Selas Flowtronics, Box 300, Spring House, PA 19477.	Hopfinger & Altman (1969) [93]
Selas 04 [a]	6,27	0,89 [c] 1,30 [d]		0,36 [e]	0,236 f	3,63 [g]		
Selas 03 [a]	6,08	1,52 [c] 1,62 [d]		0,55 [e]	0,444 f	15,90 [g]		
Selas 02 [a]	5,99	2,46 [c] 2,80 [d]		0,54 [e]	0,381 f	41,40 [g]		
Selas 01 [a]	5,97	10,3 [c] 16,8 [d]		0,73 [e]	0,186 f	961,0 [g]		
Millipore GS [a]	0,145	0,22 [h] 0,823 [c] 0,864 [d]		0,75 [h] 0,74 [i]	0,444 [f]	6,24 [g]	Millipore Ashby Rd, Bedford, MA 01730.	
Millipore VF [a]	0,135	0,010 [h] 0,142 [c]		0,70 [h] 0,44 [i]		0,111 [g]		
Sintered [a] Aluminium Silicate. Type TZ	40,0	1,0 [h]		0,4 [h]		2,62 [j]	H. Halden-wanger, Berlin	Freder-king et al. (1973) [72]

Material	Thickness tx10³ [m]	Pore Diameter d_vx10⁶ [m]	Hydraulic Diameter D_Ex10⁶ [m]	Porosity Φ	Tortuos. q	Permeability Kx10¹⁵ [m²]	Manufacturer	Reference
Al_2O_3[a]	6,6	7,46 [c]		0,677 [k]		224,0 [g]		Urban et al. (1975) [245]
	6,5	0,18 [c]		0,548 [k]		5,37 [g]		
Copper powder 325 mesh, sintered [b]		18,0 [l]		0,55 [m]		1479,0 [n]	Power from Mackay, A.D. Inc., 198 Broadway, New York, NY.	Niinikoski (1971) [170]
		18,0 [l]		0,60 [m]		2430,0 [n]		
		18,0 [l]		0,65 [m]		4035,0 [n]		
Copper powder, sintered [b]		18,0		0,52		1740		Dunn & Reay (1976) [61]
Stainless Steel [b]	0,79	10,0 [h]	19,4 [o]	0,318 [o]		368,0 [g]	Pall Trinity Micro, Route 281, Cortland, NY 13045	Da Riva et al. (1972) [51]
	1,58	10,0 [h]	32,9 [o]	0,382 [o]		667,0 [g]		
	1,58	35,0 [h]	58,8 [o]	0,422 [o]		6404,0 [g]		
	1,6	3,0 - 8,0 - 10,0 [p]	8,1	0,25		90,0	Mott Metallurgical Corporation, Farmington, CT.	Schotte (1984) [209]
	1,6	8,0 - 18,0 - 21,0 [p]	17,7	0,34		610,0		

Material	Thickness tx10³ [m]	Pore Diameter d_vx10⁶ [m]	Hydraulic Diameter D_Ex10⁶ [m]	Porosity Φ	Tortuos. q	Permeability Kx10¹⁵ [m²]	Manufacturer	Reference
	1,6	19,0 - 20,0 - 26,0 [p]	20,4	0,39		1000,0		
	1,6	29,0 - 33,0 - 42,0 [p]	33,8	0,43		2500,0		
	1,6	38,0 - 43,0 - 58,0 [p]	46,0	0,47		3900,0		
	1,6	72,0 - 79,0 - 114,0 [p]	83,8	0,51		7800,0		
Nickel [b]	6,3	12,58 [c]		0,384 [k]		377,0 [g]		Urban et al. (1975) [245]

[a] Ceramic.

[b] Metallic.

[c] Deduced from K.

[d] From critical capillary pressure experiments, $d_v = 4\sigma/P_c$.

[e] From gas absorption.

[f] Calculated from $K = c_o q \Phi d_v^2/16$; $c_o \approx 0{,}4$.

[g] From isothermal gas flow.

[h] Specified by the manufacturer.

[I] From wet and dry weights.

[j] From liquid He I flow.

[k] From mass of porous medium and density of the material.

[l] Value of d_m in Eq. [7-78], Table 7-47, giving the best fitting to experimental results of K vs. Φ.

[m] Controlled during manufacture.

[n] Deduced from curve fitting of experimental results. Saturated dilute solution of He^3 and He^4.

[o] From statistical analysis of a micrograph.

[p] Minimum-effective-maximum pore sizes, respectively.

7.5 Filling a superfluid helium container

Filling a superfluid helium container can be achieved, in principle, by a series of 4,2 K fills and pump down. 4,21 K is the normal boiling temperature of liquid helium (see Table 8-1, clause 8.1.1).

Even assuming that heat leaks to the cryogen are negligible, there is a loss of liquid mass in the container because of pumping down. This loss will be estimated in clause 7.5.1.

In practical instances it is not difficult to half fill the superfluidhelium Dewar, and a not very long operation to 80% fill it by a series of 4,2 K fills and pump downs but, assuming that the prescribed ullage must be smaller than 20%, liquid He II must be used for filling. Such filling with the liquid He II will generally be applied twice. Firstly during ground preparation several days prior to launch and then, at the last possible moment just prior launch. This last filling may not be required for Dewars whose lifetime is much larger than the ground preparation time, but is certainly necessary for short missions (such as Spacelab) where the mission time may only be twice the time required for ground preparation.

Apparatus for filling a Dewar with liquid He II are available for laboratory purposes. Nicol & Bohm (1960) [168] describe an experimental assembly, operating between 4,2 K and 1 K, which can be used for continuously filling a Dewar whose pressure is kept below atmospheric pressure. A system for a spaceborne He II Dewar has been studied by OXFORD INSTRUMENTS (1976) [176]. Basically these systems consist of a container of He^4 at 4,2 K and atmospheric pressure, which can be filled at a rate equal to that at which liquid helium is being withdrawn. This container is placed at the top of the He II Dewar. The pressure in the He II Dewar is controlled by a vacuum pump. The 4,2 K liquid is expanded by a throttling valve between the normal helium and the He II baths. The throttled liquid is partially vaporized, and the vapors are pumped out whereas the remaining liquid flows down to the He II Dewar. The pumped vapors can be used to cool both containers.

7.5.1 Liquid loss because of pump down

Two alternative approaches can be used to estimate the fraction, *f*, of liquid mass which vaporizes of pump down. According to Nicol & Bohm (1960) [168] these approaches will lead to the most optimistic and the most pessimistic estimates of the liquid mass loss.

1. Reversible-process model. A liquid helium droplet of unit mass and uniform temperature (4,2 K) is surrounded by helium vapors at the same temperature and at atmospheric pressure. When the pressure slightly decreases, a portion of the droplet vaporizes and the temperature decreases, but it is assumed that temperature remains uniform throughout at any time. At a given temperature T (T<4,2 K) a fraction, f, of the droplet mass has been vaporized. Evaporation of a further fraction, df, leads to a change in temperature, dT, as given by:

$$(1-f)c_p(T)dT + h_{fg}(T)df = 0 \qquad [7\text{-}79]$$

Integration of Eq. [7-79] yields,

$$f = 1 - e^{\int_{4,2}^{T_f} \frac{c_p(T)}{h_{fg}(T)} dT} \qquad [7\text{-}80]$$

Note: non-si units are used in this figure

the fraction f of liquid mass loss, as deduced from Eq. [7-80] has been plotted versus final temperature T_f in Figure 7-31 (curve labelled REVERSIBLE).

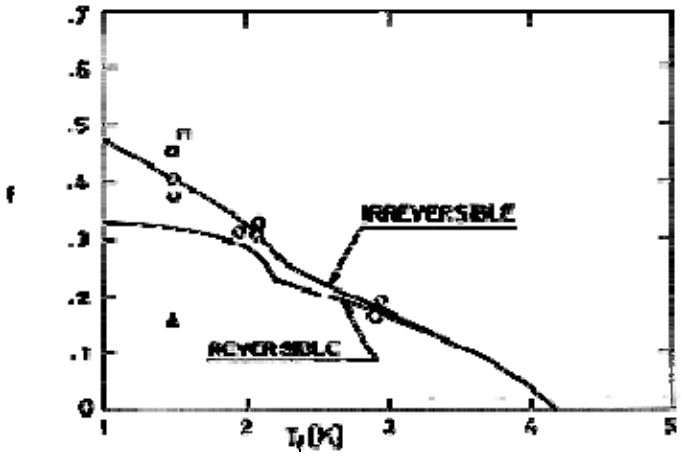

Note: non-si units are used in this figure

Figure 7-31: Fraction, *f*, of liquid mass lost because of pump down vs. final temperature, T_f. Curves labelled REVERSIBLE correspond to Eqs. [7-80] and [7-81] respectively. Experimental results are also shown. From Nicol & Bohm (1960) [168].

2. Irreversible-process model. The unit mass droplet at 4,2 K is suddenly immersed in an atmosphere of helium vapors at the final temperature T_f and the saturation pressure. The outer layer of the droplet is cooled down to T_f in a very short time, whereas the bulk of the droplet remains at higher temperatures for some times. As a consequence of this, vaporization of the liquid takes place at temperature T_f. Energy conservation of the unit mass, which initially was exclusively liquid at 4,2 K, gives:

$$\int_{4,2}^{T_f} c_p(T)dT + fh_{fg}(T_f) = 0 \qquad [7\text{-}81]$$

The fraction f deduced from this equation has been represented in Figure 7-31 (curve labelled IRREVERSIBLE).

Experimental results by Nicol & Bohm (1960) [168] fairly agree with the values deduced from Eq. [7-81]. The exceptionally high losses (squares) were obtained when the liquid flow rate through the throttling valve was abnormally high and warm liquid was sprayed directly onto the walls of the Dewar some distance above the liquid level. Triangles was obtained after cooling the incoming normal liquid helium (and the valve itself) before reaching the valve, by use of the vapors from the He II Dewar.

7.5.2 Pumping down requirements

Pumping down requirements will depend on the helium mass flow rate, on the final temperature, T_f, and on the pressure losses in the venting line. As an illustration, Figure 7-32 gives the volume flow rate, m/ρ, required to produce 10^{-2} W of cooling in a typical laboratory Dewar, as a function of final temperature, T_f, under three different situations.

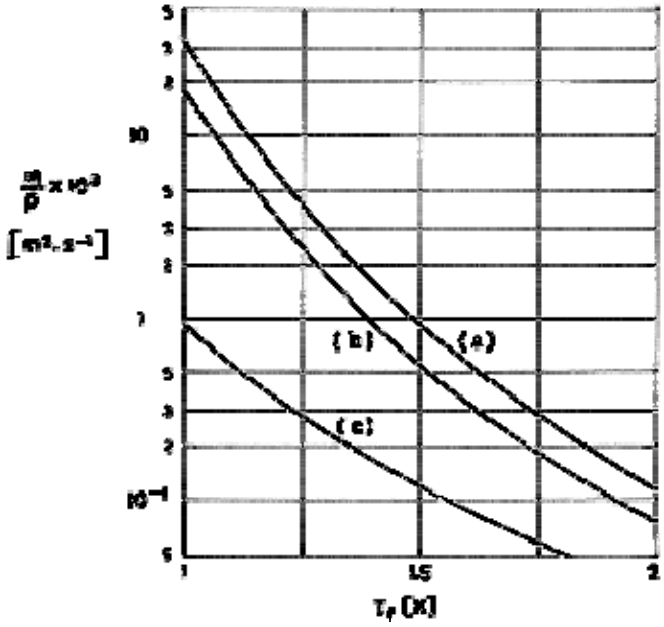

Note: non-si units are used in this figure

Figure 7-32: Mass flow rate, m/ρ, required for a refrigerating load of 10^{-2} W as a function of final temperature, T_f, under three different situations. (a) Liquid He^4 is continuously supplied at 4,2 K for evaporation. (b) No supply of He^4. (c) Liquid He^3 is continuously supplied at 3,2 K for evaporation. From Nicol & Bohm (1960) [168].

Curve (a) gives the pumping requirements assuming that He^4 is being supplied at the required rate, as explained above. In curve (b) no supply of fresh coolant is assumed. Curve (c) corresponds to the case in which He^3 is continuously supplies at 3,2 K for later evaporation.

It can be seen in Figure 7-32 that the pumping problem becomes more acute the lower the final temperature. On the other hand, despite its high initial cost, He^3 is attractive when lower temperatures are required or when, at higher final temperatures, system mass is of concern.

A method for estimating the pumping power requirement given: the mass flow rate into the cryostat, the pressure losses in the venting line, the pressure level at the pump intake, and the required temperature, has been prepared by Kitchens et al. (quoted by Conte (1970) [48]). A detailed example is worked out in Conte (1970) [48] pp. 231-235.

7.5.3 A typical filling sequence

The process of completely filling a Dewar with superfluid helium has been considered in fair detail by OXFORD INSTRUMENTS (1976) [176]. A schematic of the filling assembly is shown in Figure 7-33. The filling sequence is as follows.

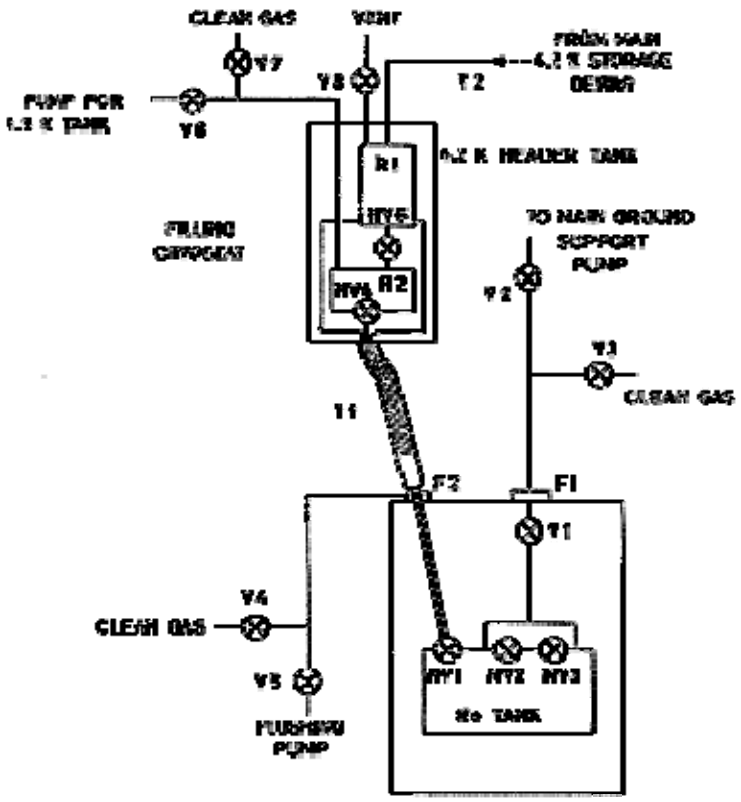

Note: non-si units are used in this figure

Figure 7-33: Superfluid helium filling assembly. Explanation: NV1 to NV4, ruby needle valve; NV5, standard needle valve; V1, remote controlled QSB for flap valve; V2 to V8, standard valves; F1 and F2, external fittings to maintain cleanliness; T1, 120º flexible transfer tube continuous with filling cryostat and having a 4,2 K radiation shield; T2, long flexible transfer tube for filling 4,2 K tank; R1, 4,2 K reservoir and header tank; R2, 1,5 K reservoir. (NV2 is the porous plug seal. NV3 is the gas vent hole seal). From OXFORD INSTRUMENTS (1976) [176].

First Filling Sequence

With a conventional transfer tube transfer normal helium into the He tank. For this purpose F1 & F2 are in position.

1. Extract the filling tube plug and back fill through V4.

2. Insert conventional transfer tube flushing using V4 & V5.

3. Open V1 and flush using V2 & V3.

4. Open NV3 and flush using V2 & V3.

5. Open NV1 and transfer either using an overpressure on the supply vessel or by opening V2 a little rather than V3.

6. Stop the transfer by closing NV1.

7. With a full vessel of normal helium the temperature can now be reduced by closing V3 and opening V2. Monitor the gas flow.

The level of superfluid helium can be further increased by topping up with normal helium into the approximately half-filled vessel.

8. Raise the transfer tube until is exit is only just below F2 and open V5 to ensure the transfer tube is cooled to 4,2 K.

9. Slowly lower the transfer tube, close V5 and open NV1. The vessel will now fill up, the temperature of the bath being less than 4,2 K.

10. Close NV1 and pump down through V2.

An initial fill of the type described above may be quite sufficient for the period prior to launch. Just before launch it will be necessary to completely fill with superfluid and then the supply vessel can be utilized immediately.

Completely Filling with Superfluid Prior to Launch

11. Place the filling cryostat in situ by inserting T1 through F2 flushing using V4 and V5. Have the exit of T1 halfway between F2 and NV1.

12. Create superfluid by first filling R1 and R2 with NV5 open, then closing NV5 while pumping using V6.

13. Pump through V5 and allow a controlled flow through NV4.

14. Once a controlled pressure and flow has been established, lower T1 and open NV1. Temperature sensors may be used to confirm these operations.

15. When full close NV1 and NV4, back fill slowly through V4 and evacuate and plug F2.

16. The porous plug can be operated at any stage, when He II is in the bath, by closing NV3, opening NV2 and continuing to pump through V1 and V2.

To make operations easier, gas flow meters would be inserted at relevant places and flow rates recommended for all stages of the filling sequence.

8
Materials at cryogenic temperatures

8.1 Normal cryogens

8.1.1 General properties

General properties of several normal cryogens are presented.

The cryogens listed in Table 8-1 are those most often quoted as candidate for open cycle cryogenic cooling. They can be stored either in solid or in liquid phase.

Properties of superfluid He II are given in Clause 8.2.

The properties presented can be relevant to one or more aspects of the cryogenic cooling system, such as:

1. The storage (limiting temperatures and pressures).
2. The refrigeration load (Heats of vaporization or sublimation, specific heat).
3. The gas dynamics of the venting process (thermodynamic and transport properties of gases). These properties are given at normal pressure; provided that the gas behaves as a "dilute gas" the influence of pressure is negligible. The values of gas density are for normal conditions, otherwise the perfect gas law gives,

$\rho = (M/R)(p/T)$

where M (kg.mol^{-1}) is the molar mass of the gas, and R the universal gas constant (R = 8,31432 J.K^{-1}.mol^{-1}).

Triple point conditions (triangle) and critical conditions (circle) are indicated in the figures whenever possible and relevant.

Table 8-1: Thermodynamic and Transport Properties of Normal Cryogens

Argon, Ar	Table 8-2
Methane, CH_4	
Ethane, C_2H_6	
Carbon Dioxide, CO_2	
Hydrogen, H_2 [b]	
Helium-4, He_4 [c]	Table 8-3
Helium-3, He_3 [d]	
Nitrogen, N_2	
Ammonia, NH_3	
Neon, Ne	
Oxygen, O_2	

[b] When data in this column are split off, upper values are for Normal Hydrogen and lower values for Parahydrogen.

[c] From Angus & de Reuk (1977) [6].

[d] From Keller (1969) [119].

Table 8-2: Thermodynamic and Transport Properties of Normal Cryogens

CRYOGEN [a]		Ar Argon	CH_4 Methane	C_2H_6 Ethane	CO_2 Carbon Dioxide	H_2 [b] Hydrogen
Molar Mass, Mx10^3 [kg.mol^{-1}]		39,944	16,042	30,068	44,011	2,016
Boiling Temperature, [K] [e]		87,29	111,42	184,52	194,65 [f]	20,38 20,28
Melting Temperature, [K]		83,78	90,66	89,88	216,55	13,95 13,80
Critical Point	T [K]	150,86	190,55	305,5	304,19	33,34 32,98
	px10^{-5} [Pa]	50,00	46,41	49,13	73,82	13,16 12,93
	ρ [kg.m^{-3}]	536	162	212	468	31,6 31,4
Triple Point	T [K]	83,78	88,70 [g]		216,55	13,95 13,80
	px10^{-3} [Pa]	68,75	10,03 [g]		518,00	7,20 7,04
Density, ρ [kg.m^{-3}]	Gas [h]	1,6	0,64	1,22	1,77	0,0808 0,0808
	Liquid	4-1	4-3	4-5	4-6	4-8
	Solid	4-2	4-4		4-7	
Specific Heat, c_p [J.kg^{-1}.K^{-1}]	Gas	4-22				
	Liquid					
	Solid					
Heat of Conversion, h, [J.kg^{-1}]						4-26
Heat of Vaporization, h_{fg}, [J.kg^{-1}]		4-27	4-28	4-29	4-30	4-31
Heat of Sublimation, h_{fg}, [J.kg^{-1}]		4-38				

CRYOGEN [a]		Ar Argon	CH_4 Methane	C_2H_6 Ethane	CO_2 Carbon Dioxide	H_2 [b] Hydrogen
Vapor pressure, p_{sat}, [Pa]	Liquid	4-39	4-41	4-43	4-44	4-46
	Solid	4-40	4-42		4-45	4-47
Thermal Conductivity, k [$W.m^{-1}.K^{-1}$]	Gas	4-57			4-58	4-59
	Liquid					
Dynamic viscosity, μ, [Pa.s]		4-64			4-64	
Prandtl Number, P_r		4-67			4-67	
Thermal Expansion, β, [K^{-1}]	Liquid					
	Solid	4-68				
Surface Tension, σ, [$N.m^{-1}$]		4-73	4-74	4-75	4-76	4-77

[a] All data in this table, unless otherwise stated, are from Vargaftik (1975) [253]. 4-xx indicates that the data are shown in Fig. 8-xx.

[b] When data in this column are split off, upper values are for Normal Hydrogen and lower values for Parahydrogen.

[e] At $1{,}013 \times 10^5$ Pa.

[f] Sublimation temperature at $1{,}013 \times 10^5$ Pa.

[g] From Johnson (1961) [109]

[h] At 105 Pa and 300 K.

Table 8-3: Thermodynamic and Transport Properties of Normal Cryogens

CRYOGEN [a]		He_4 [c] Helium-4	H_3 [d] Helium-3	N_2 Nitrogen	NH_3 Ammonia	Ne Neon	O_2 Oxygen
Molar Mass, Mx10^3 [kg.mol^{-1}]		4,003	3,016	28,016	17,032	20,183	32,000
Boiling Temperature, [K] [e]		4,224	3,191	77,35	239,8	27,09	90,18
Melting Temperature, [K]				63,15	195,5	24,50	54,35
Critical Point	T [K]	5,201	3,324	126,25	405,6	44,40	154,77
	px10^{-5} [Pa]	2,275	1,165	33,96	112,9	26,54	50,90
	ρ [kg.m^{-3}]	69,64	41,3	304	235	483	405
Triple Point	T [K]			63,15	195,42	24,57 [d]	54,35
	px10^{-3} [Pa]			12,53	6,076	43,13 [d]	0,15
Density, ρ [kg.m^{-3}]	Gas [h]	0,1624	0,1208	1,12	0,69	0,81	1,28
	Liquid	4-9	4-11 & 4-12	4-16	4-18	4-19	4-21
	Solid	4-10	4-13 to 4-15	4-17		4-20	
Specific Heat, c_p [J.kg^{-1}.K^{-1}]	Gas	4-22	4-23	4-22			
	Liquid		4-24				
	Solid	4-25	4-25				
Heat of Conversion, h, [J.kg^{-1}]							
Heat of Vaporization, h_{fg}, [J.kg^{-1}]		4-32	4-33	4-34	4-35	4-36	4-37
Heat of Sublimation, h_{fg}, [J.kg^{-1}]				4-38			
Vapor pressure, p_{sat}, [Pa]	Liquid	4-48	4-49	4-50	4-52	4-54	4-56
	Solid			4-51	4-53	4-55	
Thermal	Gas	4-59 & 4-60	4-60	4-57	4-62	4-63	4-57

CRYOGEN [a]		He_4 [c] Helium-4	H_3 [d] Helium-3	N_2 Nitrogen	NH_3 Ammonia	Ne Neon	O_2 Oxygen
Conductivity, k [$W.m^{-1}.K^{-1}$]	Liquid		4-61				
Dynamic viscosity, μ, [Pa.s]		4-64 & 4-65	4-65 & 4-66	4-64			
Prandtl Number, P_r		4-67		4-67			
Thermal Expansion, β, [K^{-1}]	Liquid		4-70 & 4-74	4-69			
	Solid		4-72 & 4-14				
Surface Tension, σ, [$N.m^{-1}$]		4-78	16x10^{-5} [i]	4-79	4-80	4-81	

[a] All data in this table, unless otherwise stated, are from Vargaftik (1975) [253]. 4-xx indicates that the data are shown in Fig. 8-xx.

[c] From Angus & de Reuk (1977) [6].

[d] From Keller (1969) [119].

[e] At 1,013x10^5 Pa.

[h] At 105 Pa and 300 K.

[i] At 0 K (extrapolated).

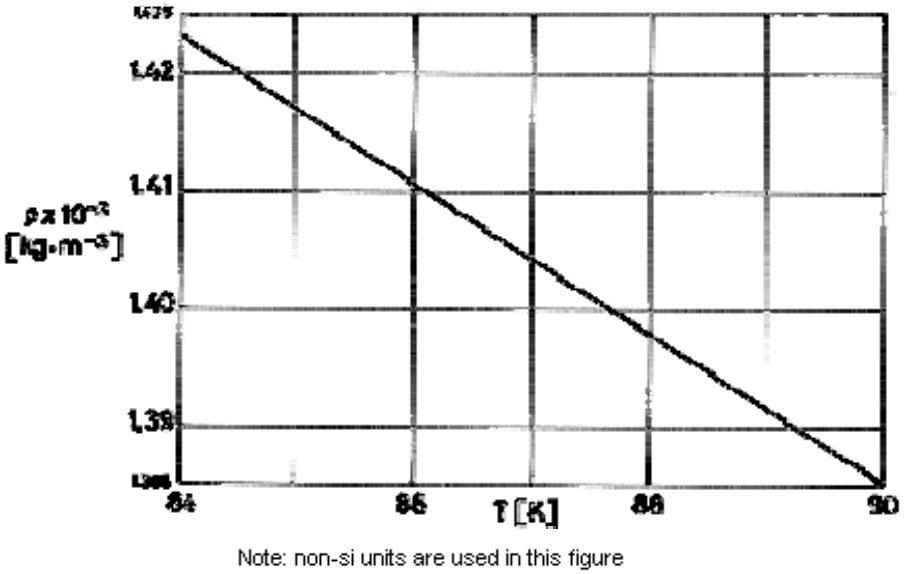

Note: non-si units are used in this figure

Figure 8-1: Density, ρ, of Saturated Liquid Argon vs. temperature, T. From Johnson (1961) [109].

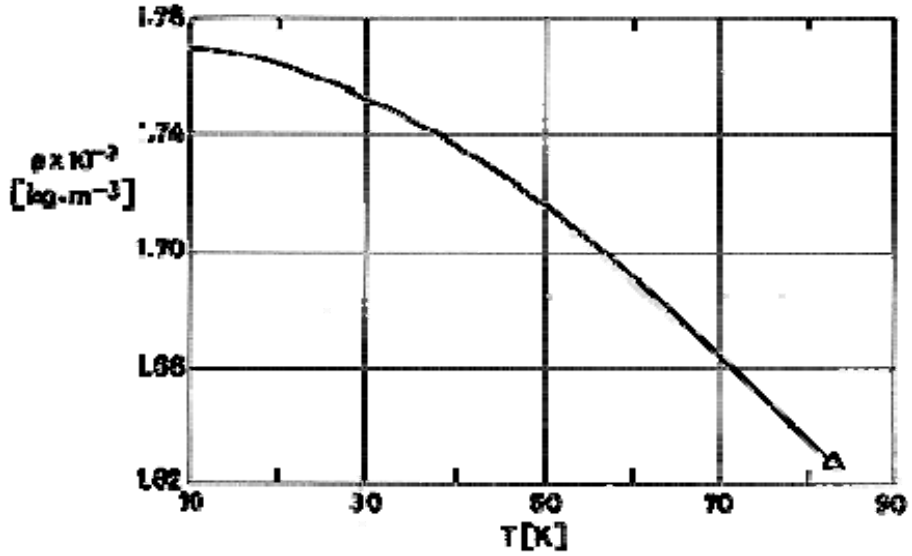

Note: non-si units are used in this figure

Figure 8-2: Density, ρ, of Saturated Solid Argon vs. temperature, T. From Johnson (1961) [109].

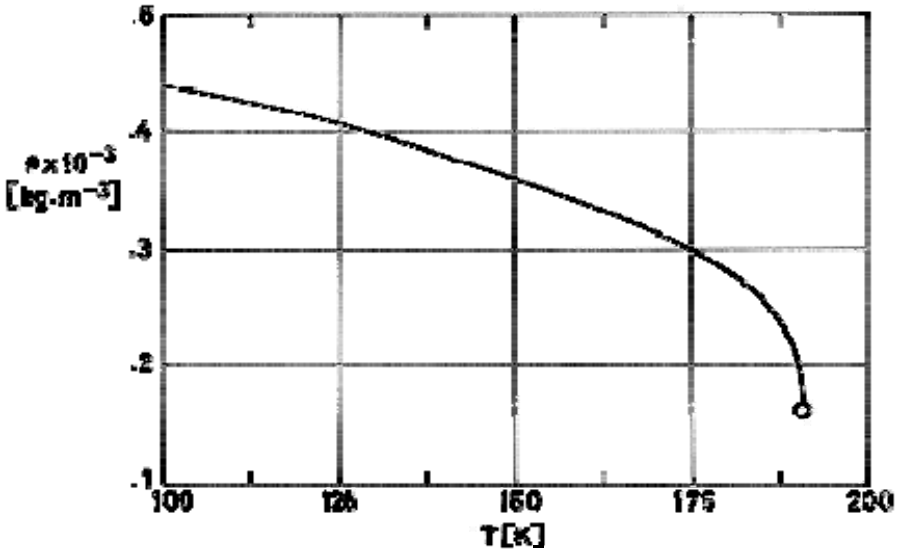

Note: non-si units are used in this figure

Figure 8-3: Density, ρ, of Saturated Liquid Methane vs. temperature, T. From Johnson (1961) [109].

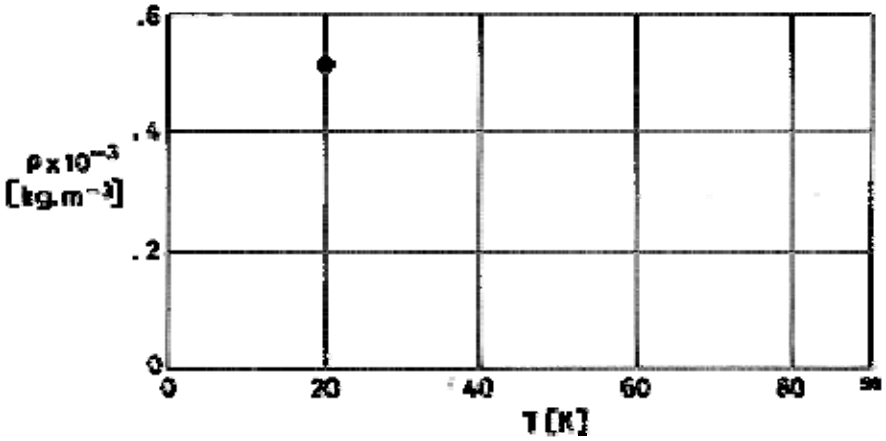

Note: non-si units are used in this figure

Figure 8-4: Density, ρ, of Saturated Solid Methane vs. temperature, T. From Johnson (1961) [109].

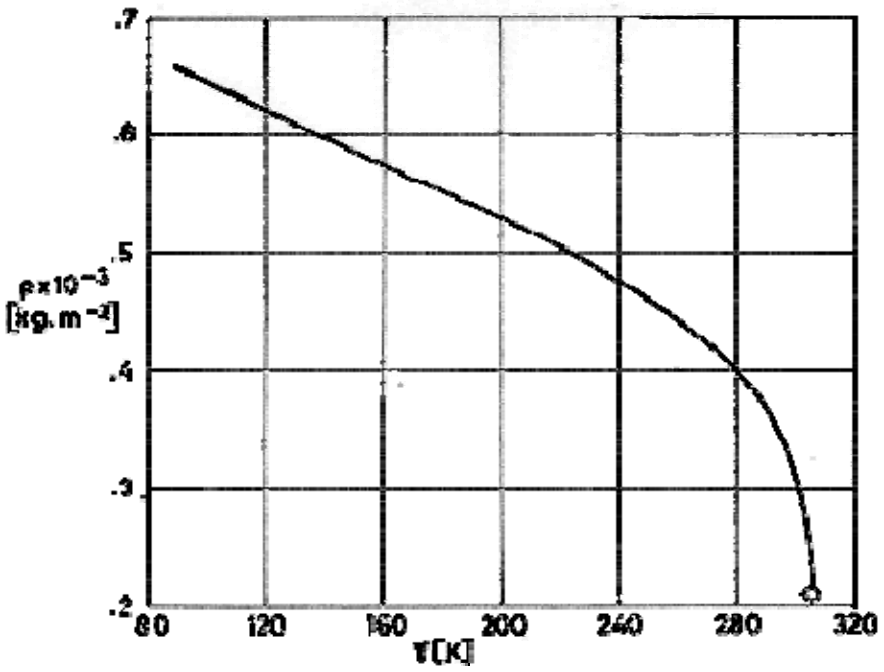

Note: non-si units are used in this figure

Figure 8-5: Density, ρ, of Saturated Liquid Ethane vs. temperature, T. From Johnson (1975) [107].

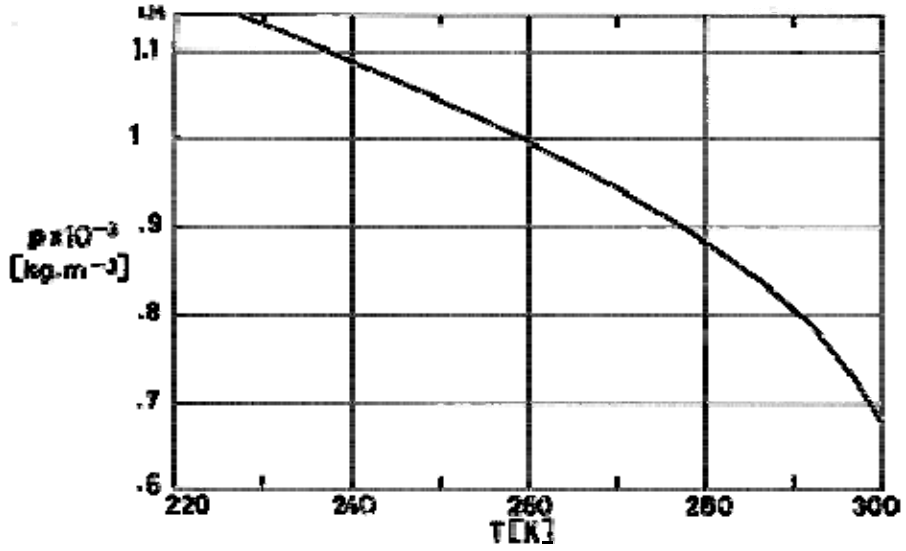

Note: non-si units are used in this figure

Figure 8-6: Density, ρ, of Saturated Liquid Carbon Dioxide vs. temperature, *T*. From LEFAX [130].

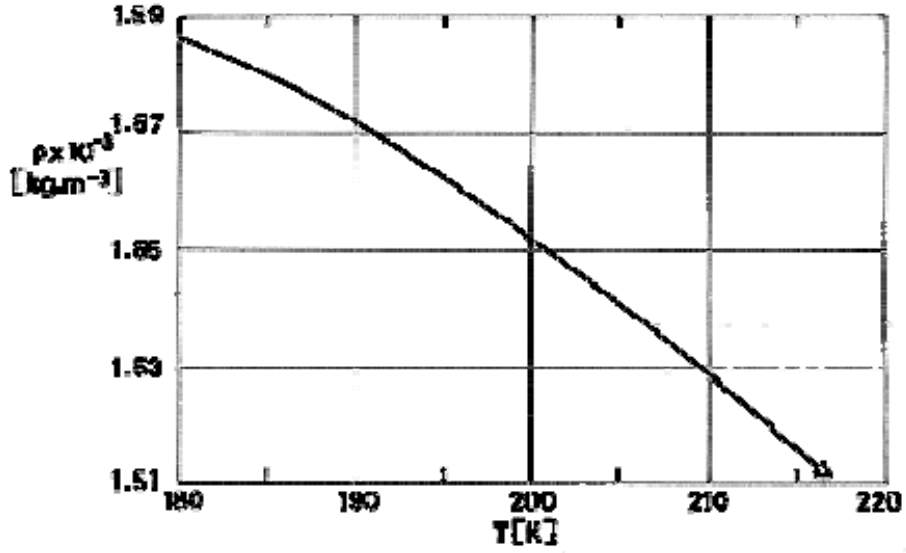

Note: non-si units are used in this figure

Figure 8-7: Density, ρ, of Saturated Solid Carbon Dioxide vs. temperature, *T*. From LEFAX [130].

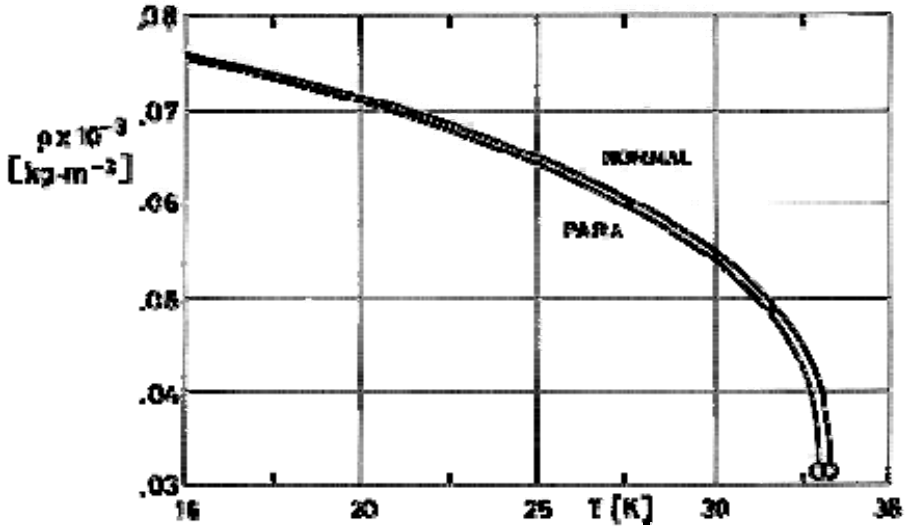

Note: non-si units are used in this figure

Figure 8-8: Density, ρ, of Saturated Liquid Hydrogen vs. temperature, T. From Vargaftik (1975) [253].

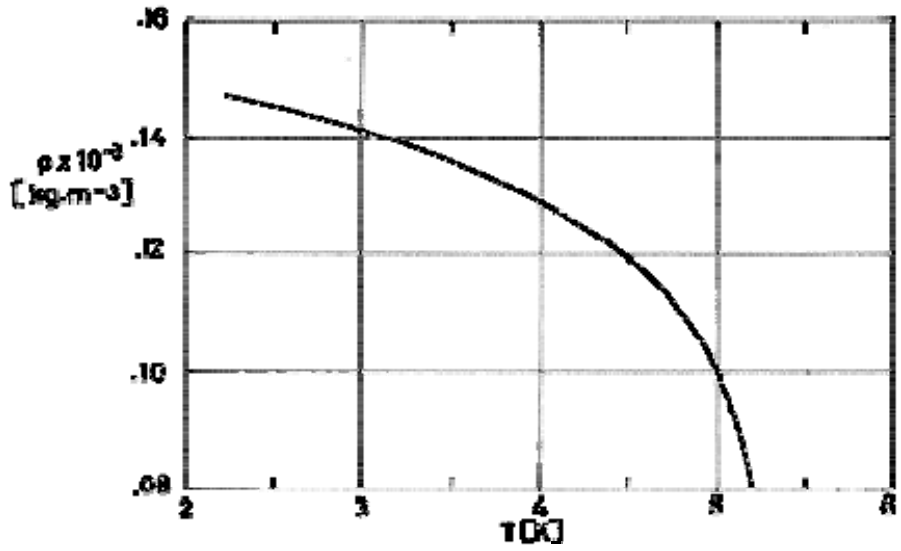

Note: non-si units are used in this figure

Figure 8-9: Density, ρ, of Saturated Liquid Helium-4 vs. temperature, T. From Johnson (1961) [109].

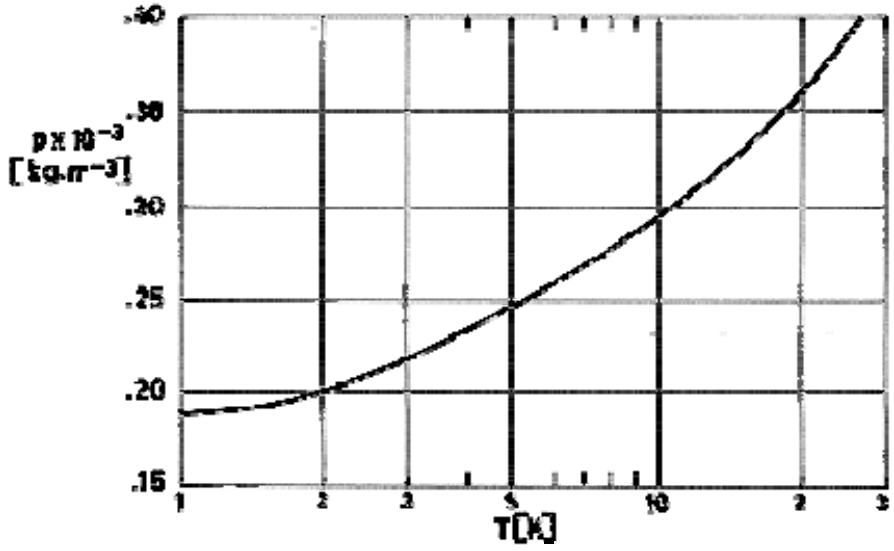

Note: non-si units are used in this figure

Figure 8-10: Density, ρ, of Saturated Solid Helium-4 vs. temperature, *T*. From Johnson (1961) [109].

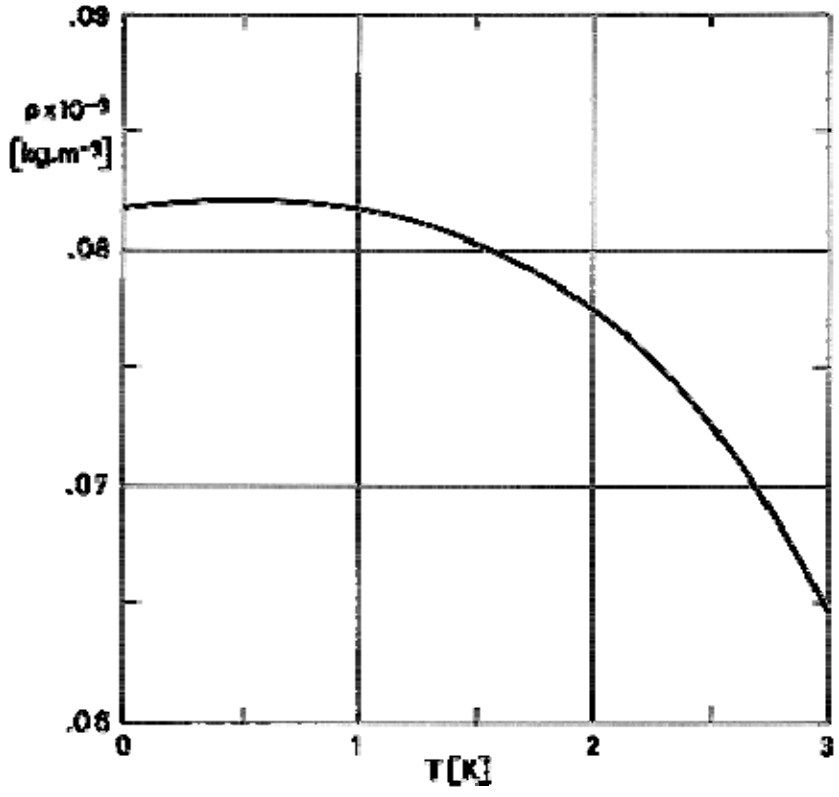

Note: non-si units are used in this figure

Figure 8-11: Density, ρ, of Saturated Liquid Helium-3 vs. temperature, *T*. From Keller (1969) [119].

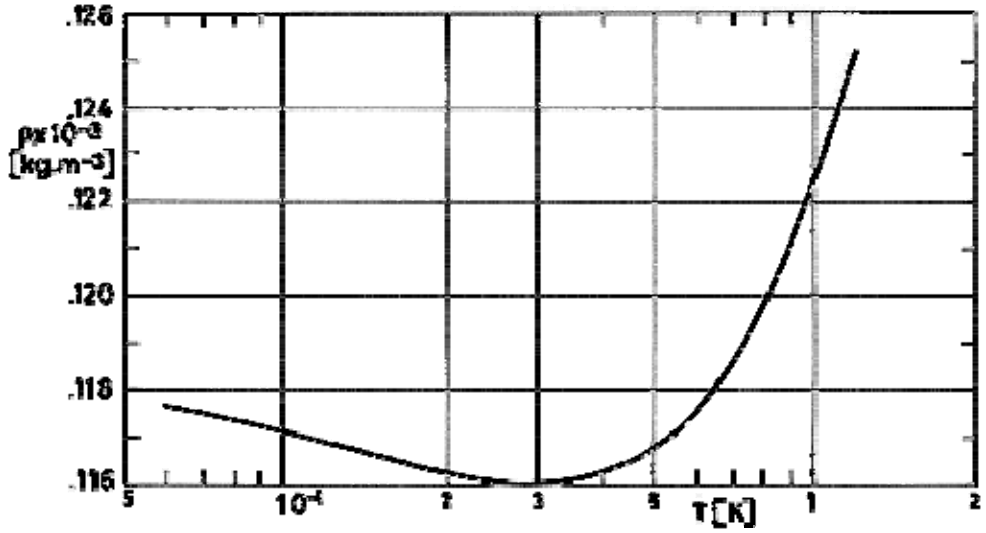

Note: non-si units are used in this figure

Figure 8-12: Density, ρ, of Saturated Liquid Helium-3 -along the freezing curve- vs. temperature, T. From Keller (1969) [119].

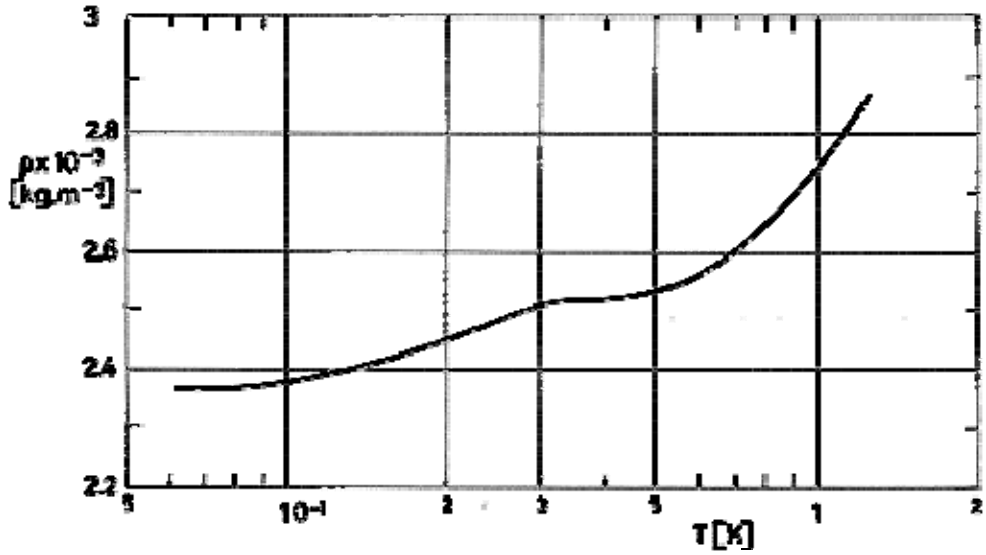

Note: non-si units are used in this figure

Figure 8-13: Density, ρ, of Saturated Solid Helium-3 vs. temperature, T. From Keller (1969) [119].

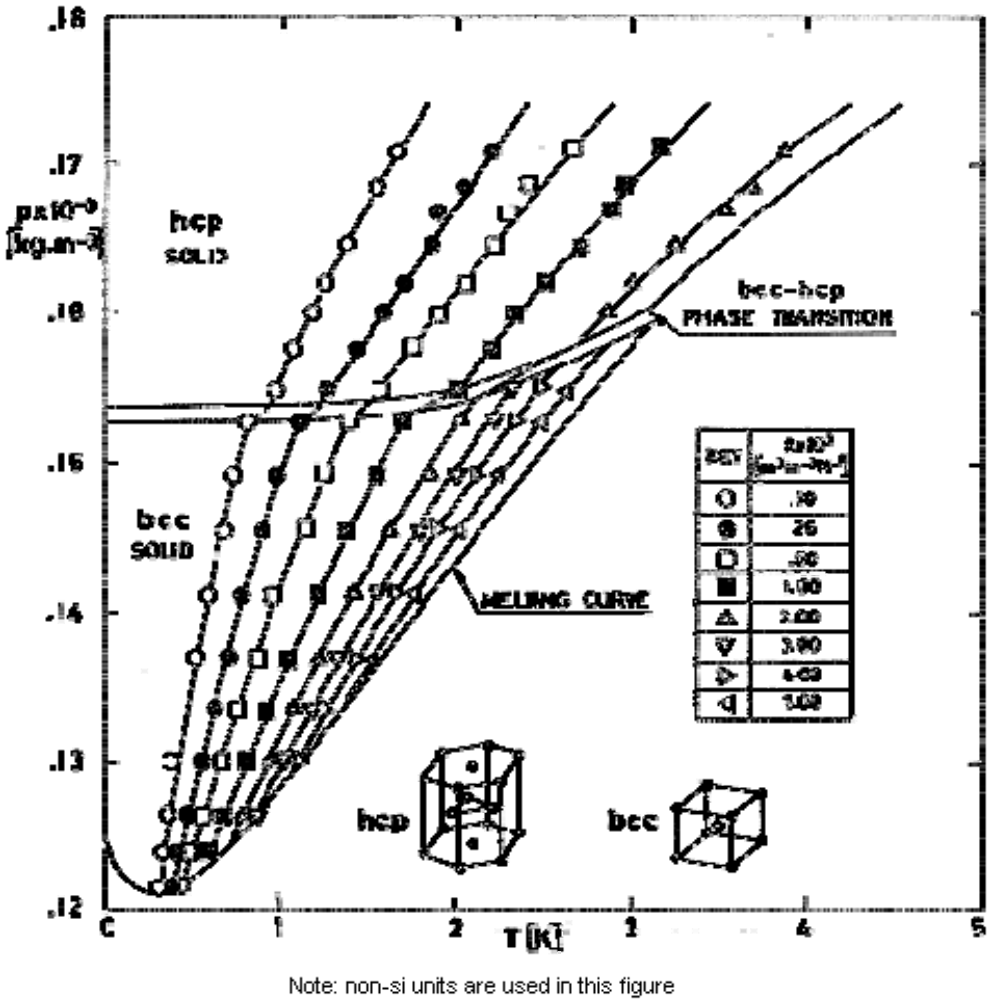

Note: non-si units are used in this figure

Figure 8-14: Density, ρ, of Solid Helium-3 vs. temperature, T. Values of ρ are shown along the melting curve as well as along curves of constant isobaric compressibility. hcp and bcc stand for hexagonal-close-packed and body-centered-cubic phases of Solid Helium-3, respectively. From Straty (1966) [228]. Additional data for a wider temperature range are given in Figure 8-15.

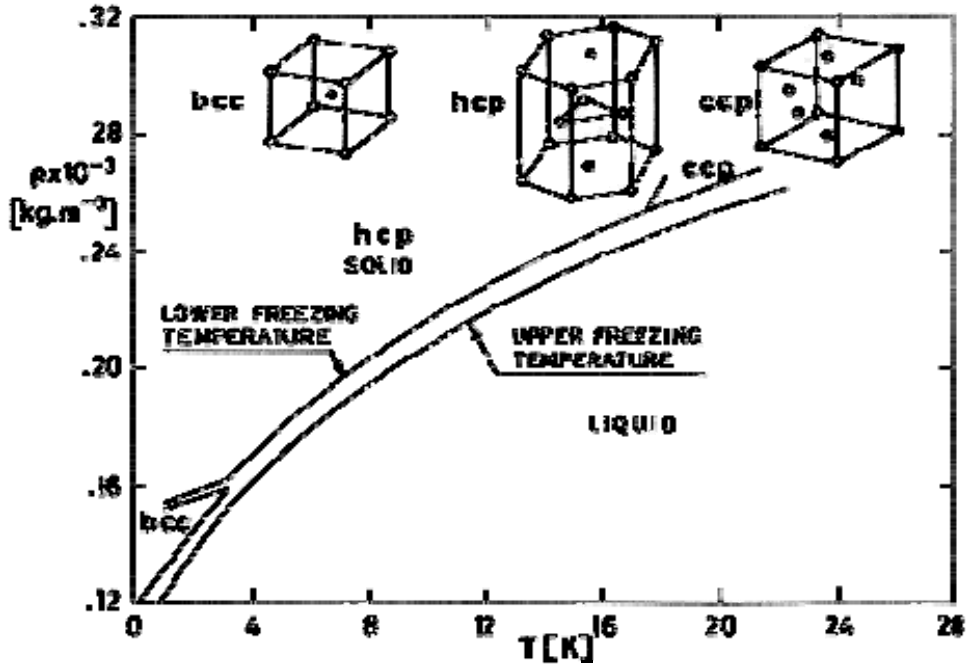

Note: non-si units are used in this figure

Figure 8-15: Density, ρ, of Solid Helium-3 vs. temperature, T, along the melting-freezing curve. Since Helium-3 samples were contaminated with around 0,2 % of Helium-4, two freezing curves appear. The figure also reveals the existence of another solid phase, cubic-close-packed (ccp), at high pressures. From Sample (1966) [205].

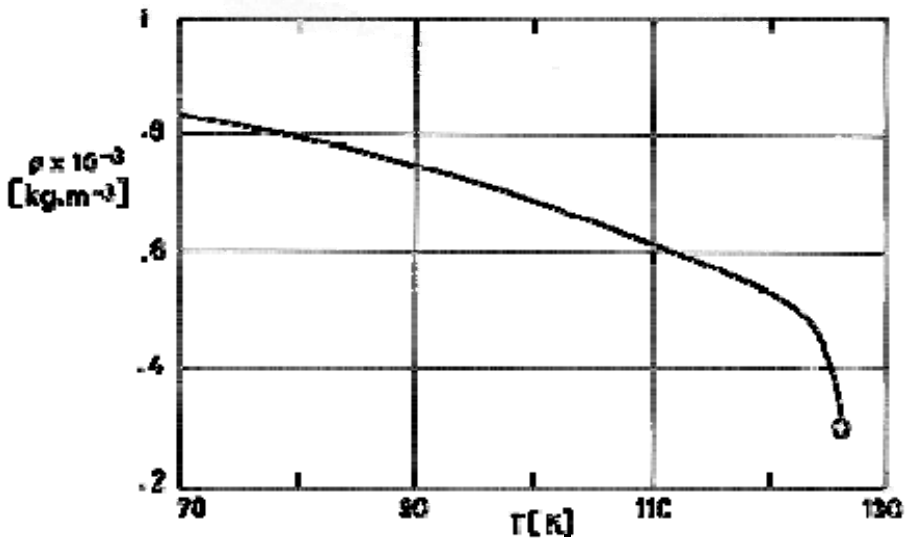

Note: non-si units are used in this figure

Figure 8-16: Density, ρ, of Saturated Liquid Nitrogen vs. temperature, T. From Johnson (1961) [109].

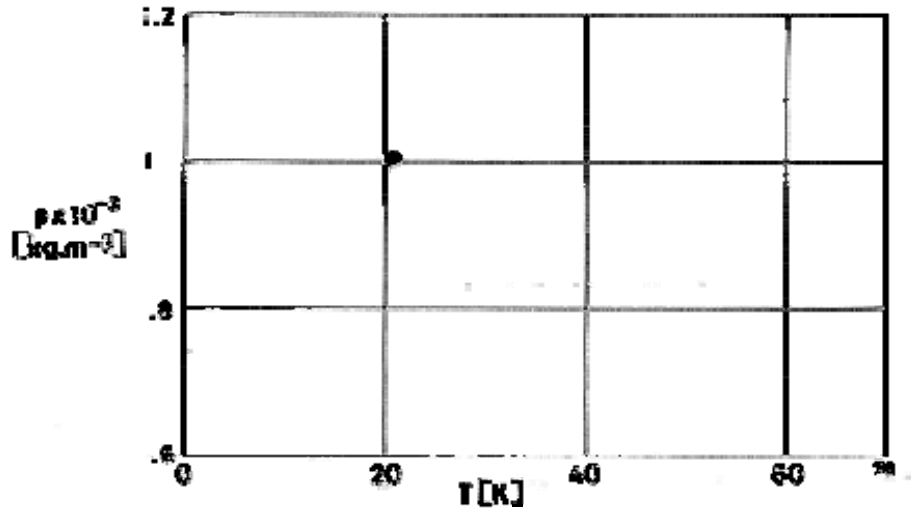

Note: non-si units are used in this figure

Figure 8-17: Density, ρ, of Saturated Solid Nitrogen vs. temperature, T. From Johnson (1961) [109].

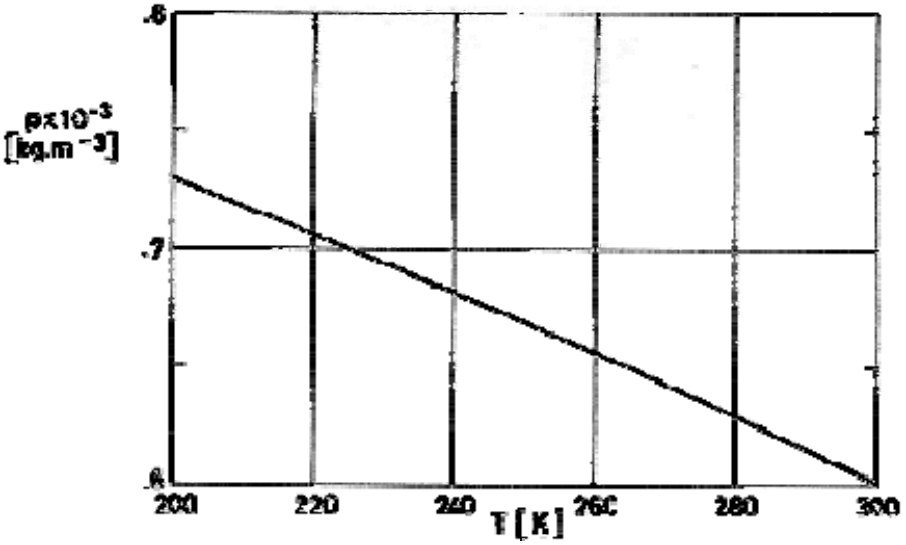

Note: non-si units are used in this figure

Figure 8-18: Density, ρ, of Saturated Liquid Ammonia vs. temperature, T. From Vargaftik (1975) [253].

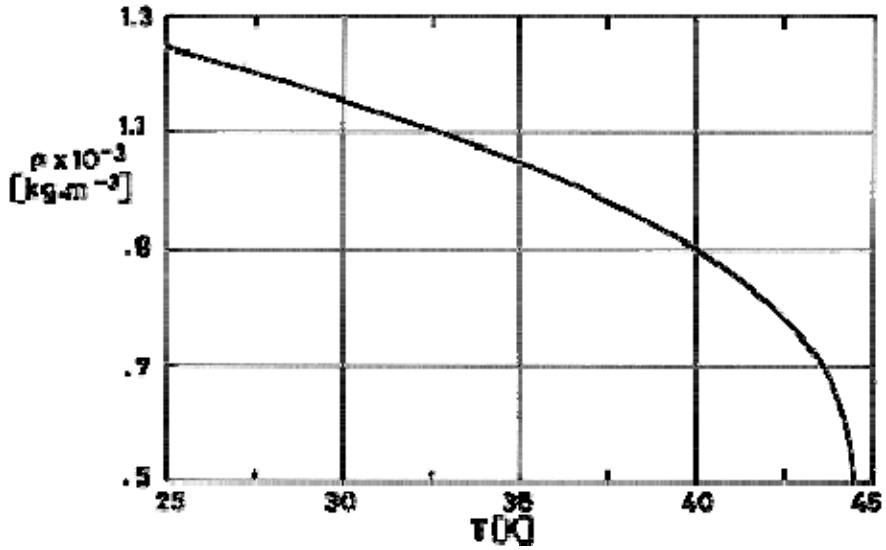

Note: non-si units are used in this figure

Figure 8-19: Density, ρ, of Saturated Liquid Neon vs. temperature, *T*. From Johnson (1961) [109].

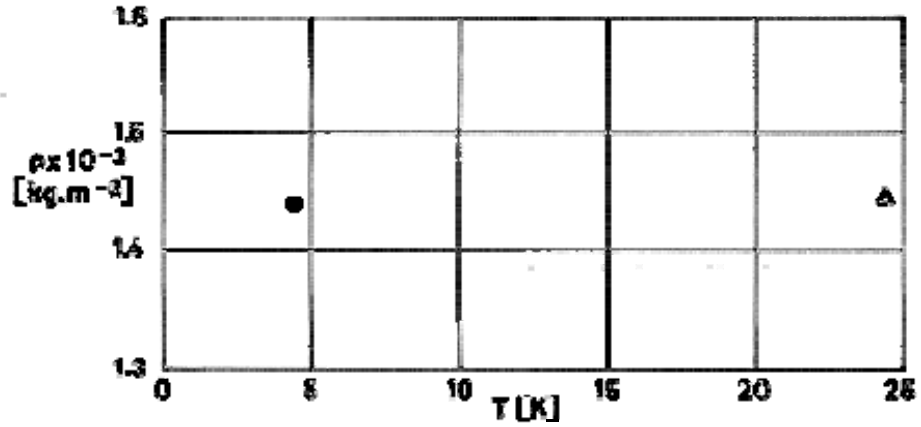

Note: non-si units are used in this figure

Figure 8-20: Density, ρ, of Saturated Solid Neon vs. temperature, *T*. From Johnson (1961) [109].

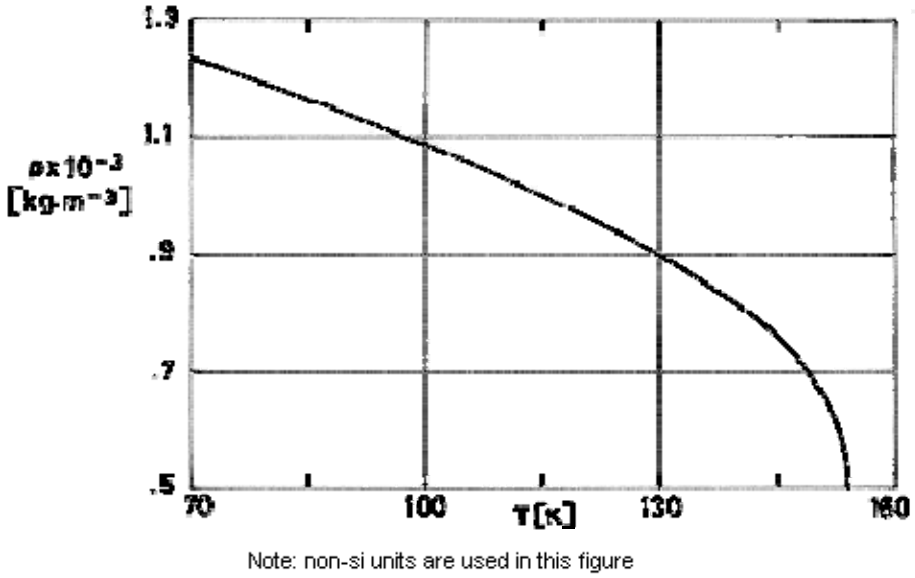

Figure 8-21: Density, ρ, of Saturated Liquid Oxygen vs. temperature, T. From Johnson (1961) [109].

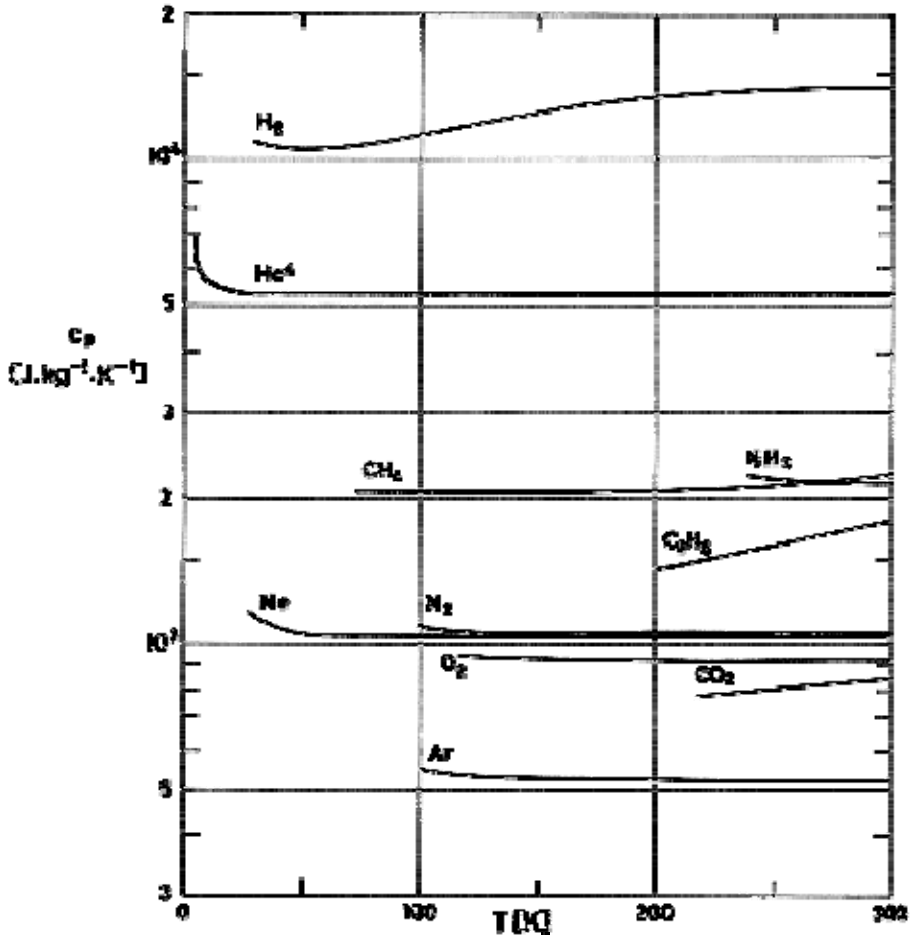

Figure 8-22: Specific heat, c_p, of several gases vs. temperature, T. Sources of data, and pressures are:
Ar, CO_2, H_2, N_2 and O_2, from Hilsenrath et al. (1960) [90], 1 atm.

CH_4 and Ne, from Johnson (1961) [109], 1 atm.
C_2H_6 from Vargaftik (1975) [253], 105 Pa.
He^4 from Angus & de Reuck (1977) [6], 10^5 Pa.
NH_3 from Norris et al. (1967) [171], 1 atm.
1 atm = 1,0135x10^5 Pa.

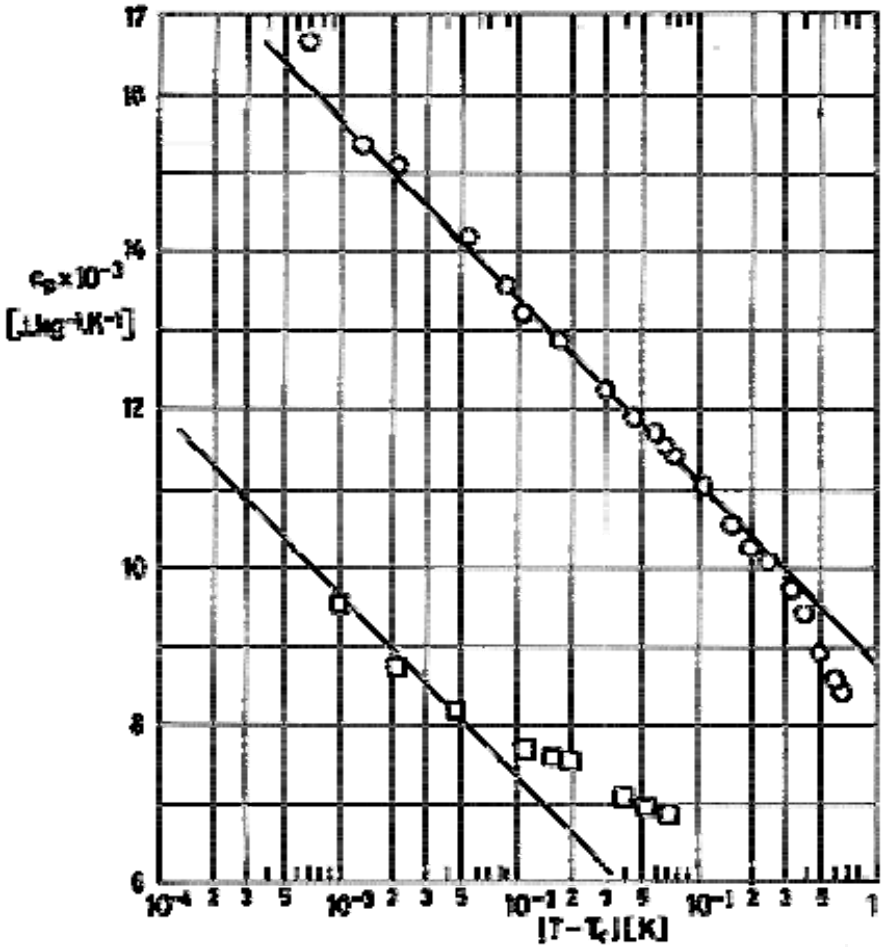

Figure 8-23: Specific heat, c_p, of Gaseous Helium-3 vs. the deviation $|T–T_c|$ from critical temperature, T_c, along nearly critical isochores.
$T < T_c$. ○ Experimental. ▬▬ $c_p = R$[2,7-3,7ln((T_c-T)/T)]
$T > T_c$. □ Experimental. ▁▁ $c_p = R$[0,5-3,7ln((T-T_c)/T_c)]
From Keller (1969) [119].
T_c = 3-324 K, $R = R/M$
R = 8,31432 J.mol^{-1}.K^{-1}
M = 3,01603x10^{-3} kg.mol^{-1}.

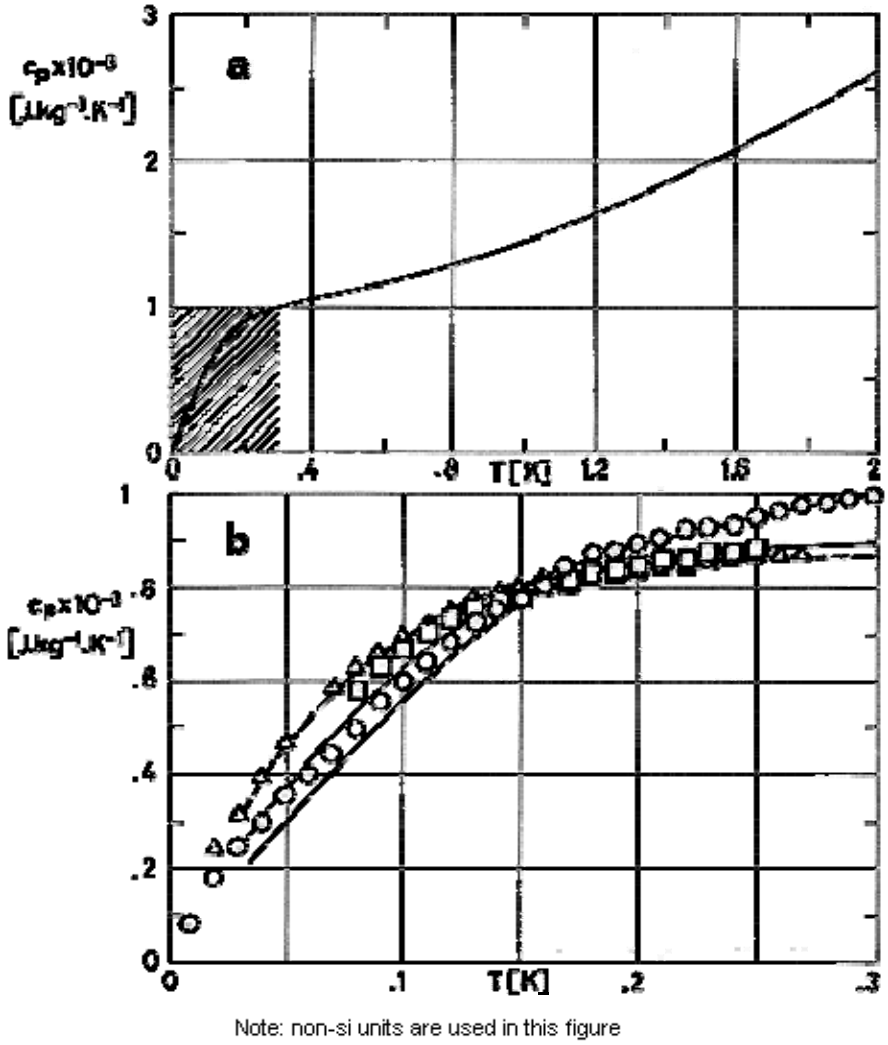

Figure 8-24: Specific heat, c_p, of Liquid Helium-3, vs. temperature, T, at several pressures.

a) is for $p = p_{sat}$, and the shazed zone is enlarged in b).

Data in b) are for the following pressures

○$p = p_{sat}$; ▬▬ $p = p_{sat}$

□p = 14,9x10^5 Pa. ▬▬ p = 11,7x10^5 Pa.

△p = 28,3x10^5 Pa. ▬ ▬ p = 27x10^5 Pa.

Data points are from Strongin et al. (1963) [230] and curves from Keller (1969) [119].

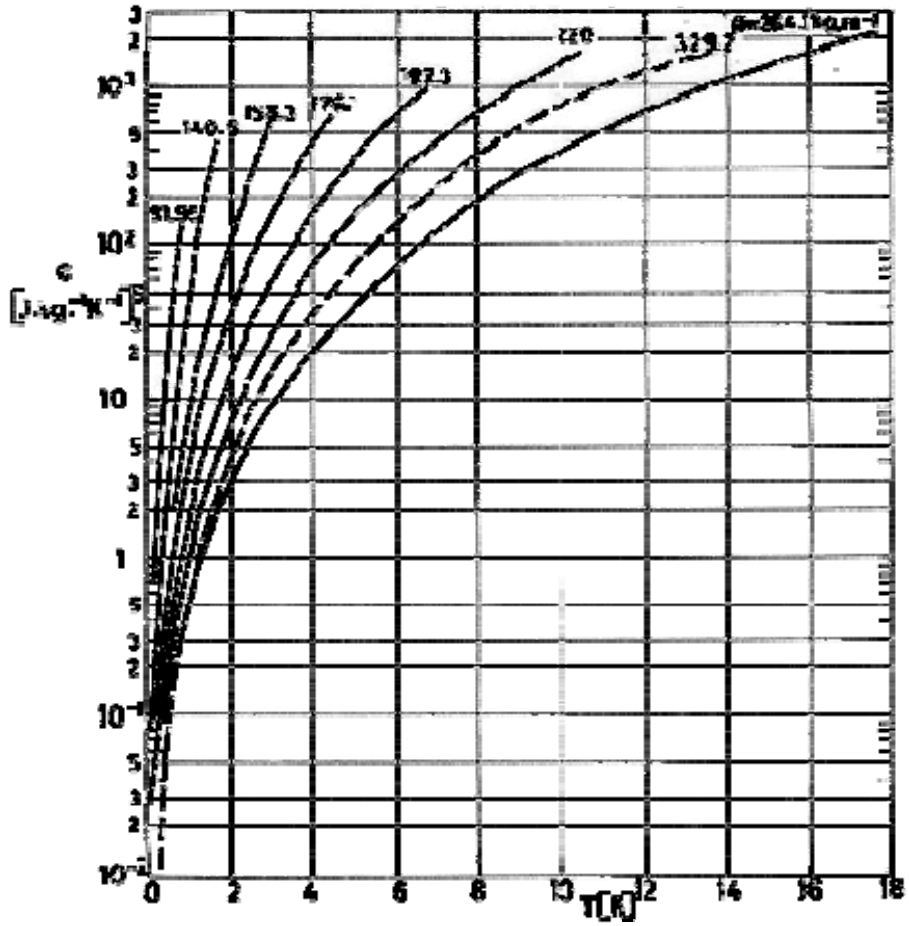

Note: non-si units are used in this figure

Figure 8-25: Specific heat, *c*, of Solid Helium-4 (dashed line) and Solid Helium-3 (full lines), vs. temperature, *T*. Numbers on the curves are densities in kg.m^{-3}. From Sample (1966) [205].

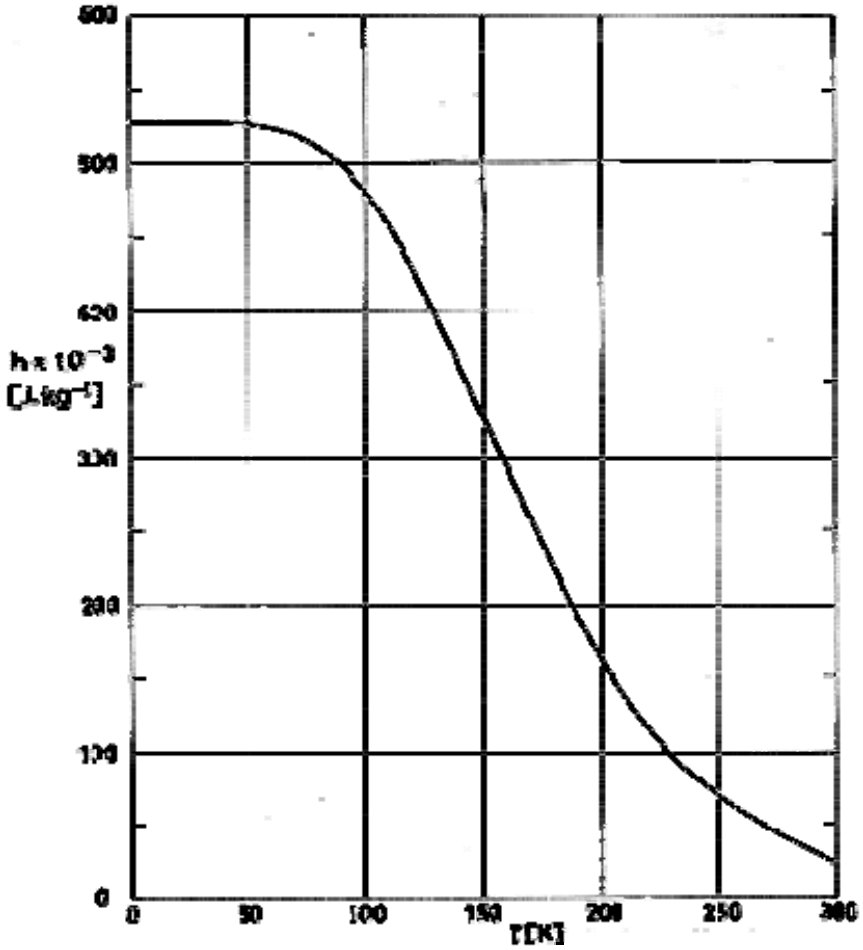

Figure 8-26: Heat of conversion, *h*, from Normal to Para Hydrogen vs. temperature, *T*. From Johnson (1961) [109].

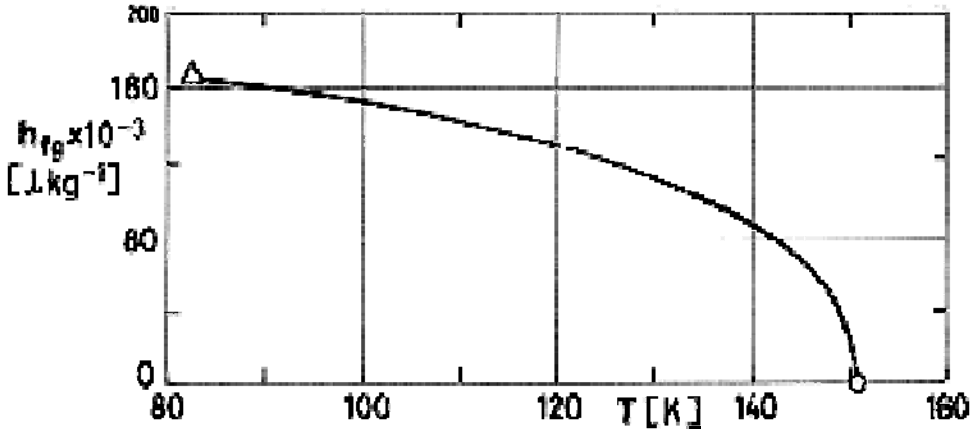

Figure 8-27: Heat of vaporization, h_{fg}, of Saturated Liquid Argon vs. temperature, *T*. From Vargaftik (1975) [253].

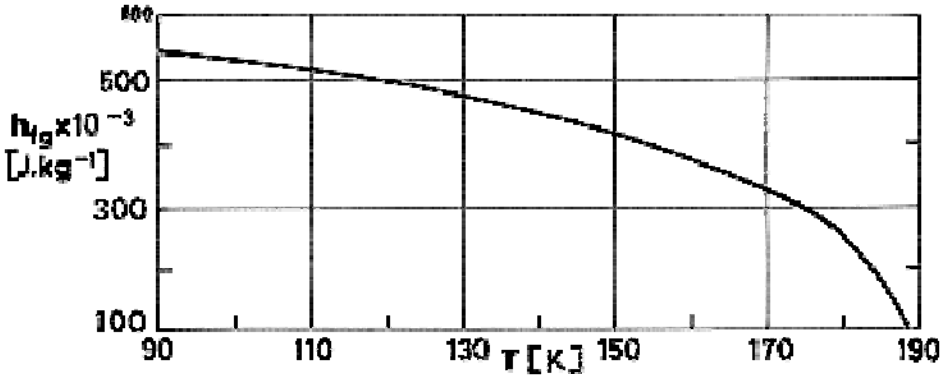

Figure 8-28: Heat of vaporization, h_{fg}, of Saturated Liquid Methane vs. temperature, *T*. From Vargaftik (1975) [253].

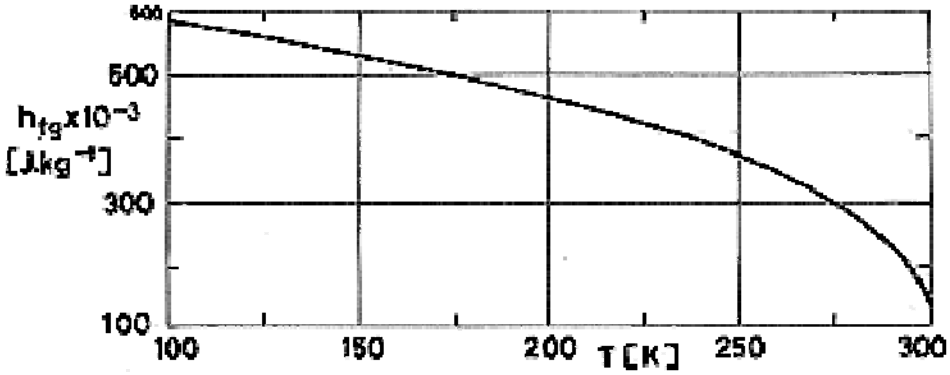

Figure 8-29: Heat of vaporization, h_{fg}, of Saturated Liquid Ethane vs. temperature, *T*. From Vargaftik (1975) [253].

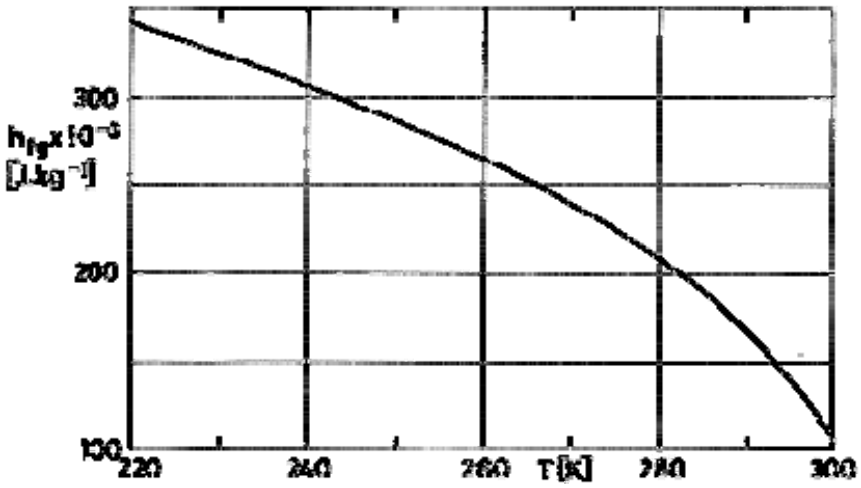

Figure 8-30: Heat of vaporization, h_{fg}, of Saturated Liquid Carbon Dioxide vs. temperature, *T*. From Angus, Armstrong & de Reuck (1976) [5].

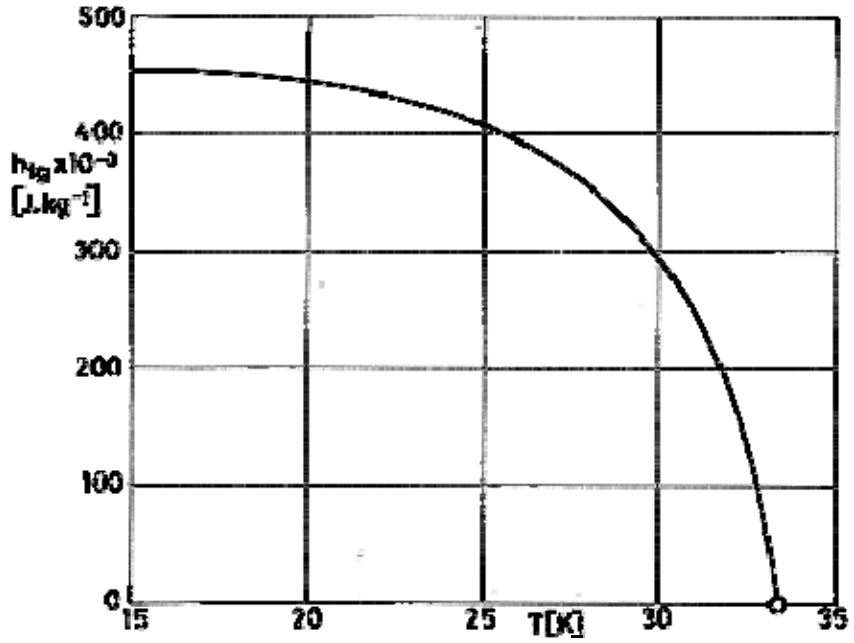

Figure 8-31: Heat of vaporization, h_{fg}, of Saturated Liquid Normal Hydrogen vs. temperature, T. From Johnson (1961) [109].

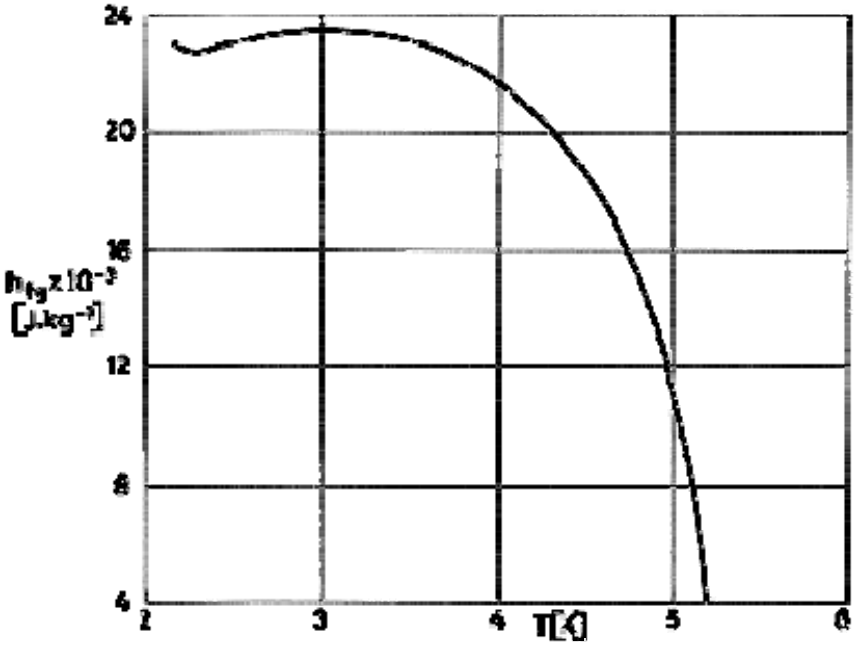

Figure 8-32: Heat of vaporization, h_{fg}, of Saturated Liquid Helium-4 vs. temperature, T. From Angus & de Reuck (1977) [6].

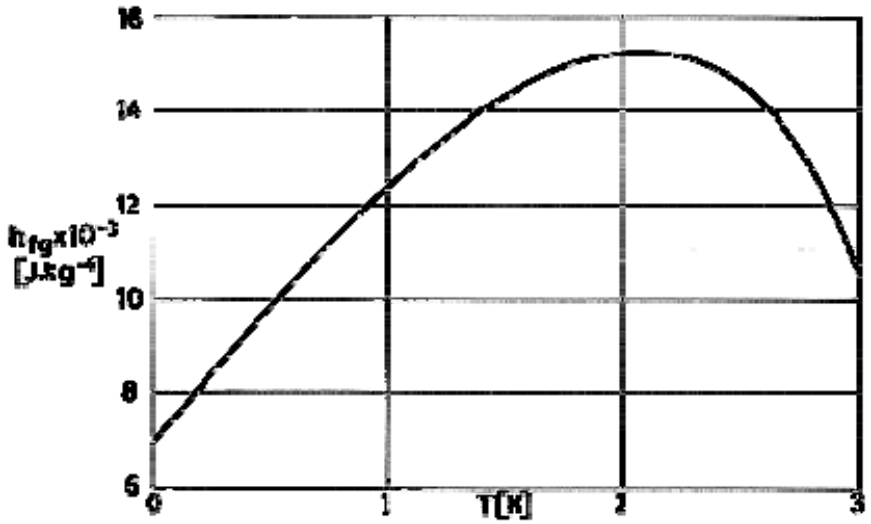

Figure 8-33: Heat of vaporization, h_{fg}, of Saturated Liquid Helium-3 vs. temperature, T. From Keller (1969)[119].

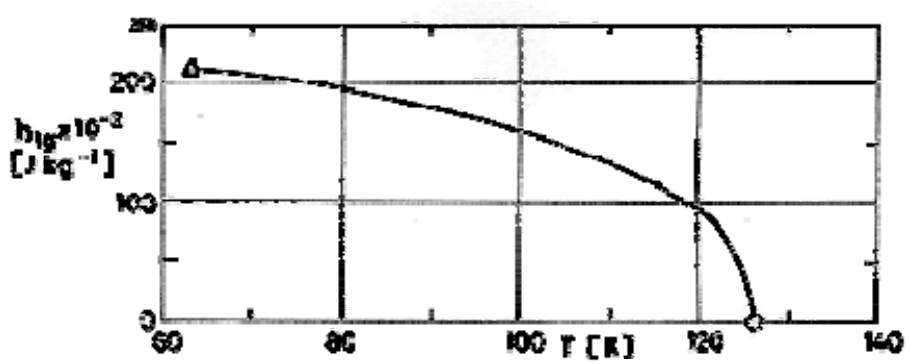

Figure 8-34: Heat of vaporization, h_{fg}, of Saturated Liquid Nitrogen vs. temperature, T. From Johnson (1961) [109].

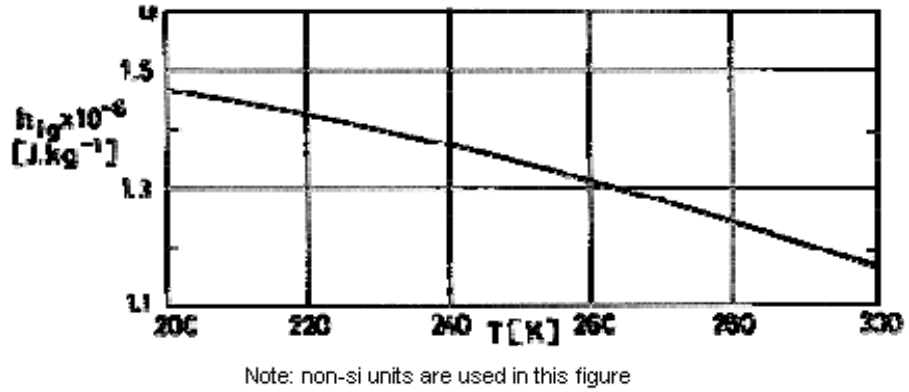

Note: non-si units are used in this figure

Figure 8-35: Heat of vaporization, h_{fg}, of Saturated Liquid Ammonia vs. temperature, T. From Vargaftik (1975) [253].

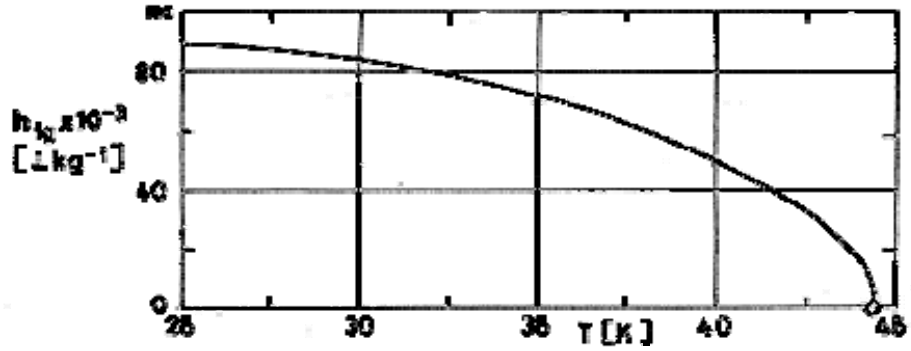

Figure 8-36: Heat of vaporization, h_{fg}, of Saturated Liquid Neon vs. temperature, T. From Johnson (1961) [109].

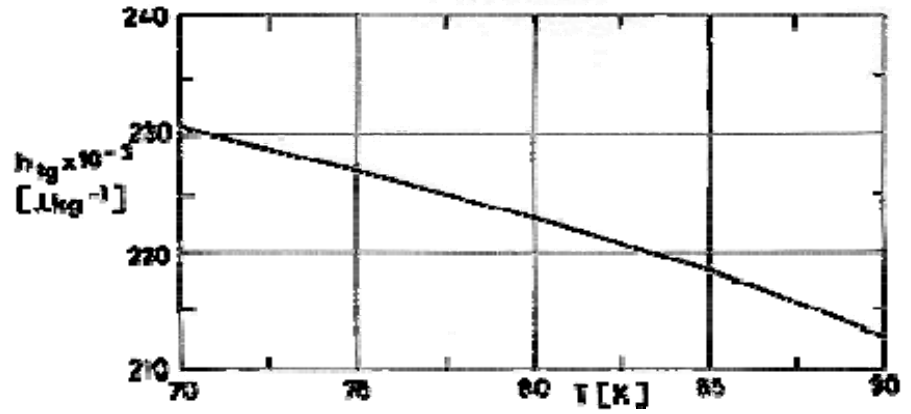

Figure 8-37: Heat of vaporization, h_{fg}, of Saturated Liquid Oxygen vs. temperature, T. From Johnson (1961) [109].

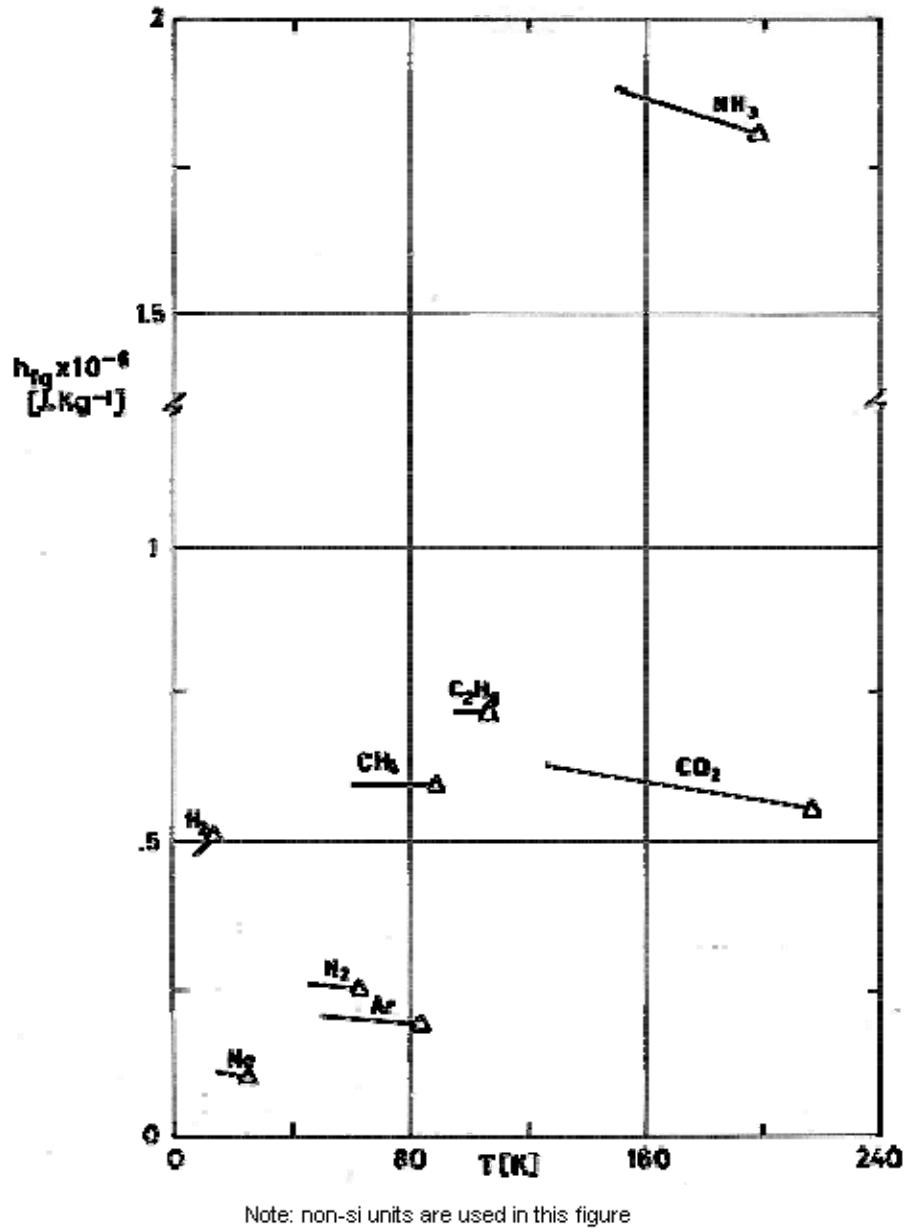

Note: non-si units are used in this figure

Figure 8-38: Heat of sublimation, h_{fg}, of several solid cryogens vs. temperature, *T*. *T* is bounded from above by the triple point and from below by a vapor pressure of 1,33 Pa. From Nast, Barnes & Wedel (1976) [161].

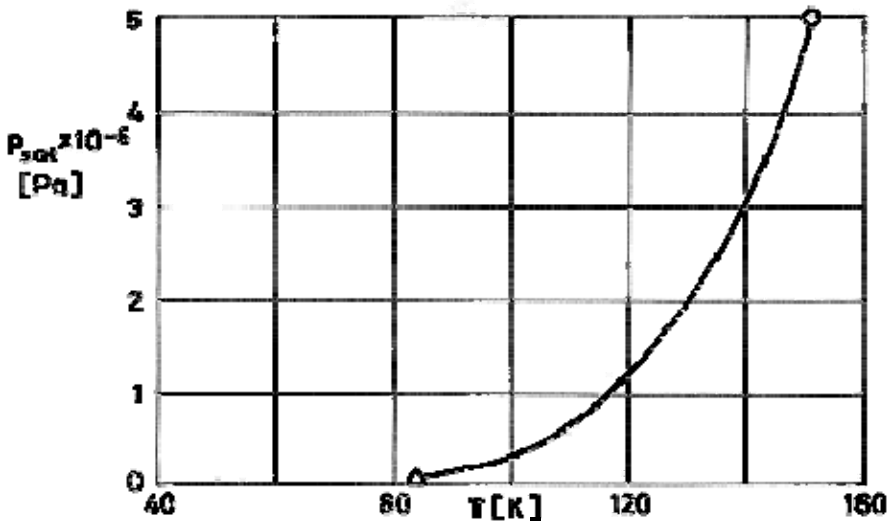

Figure 8-39: Vapor pressure, p_{sat}, of Liquid Argon vs. temperature, T. From Hilsenrath et al. (1960) [90].

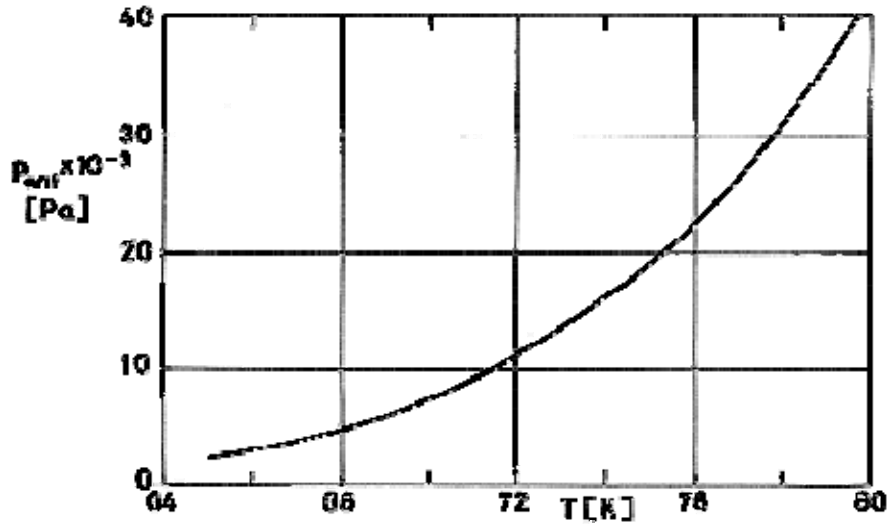

Figure 8-40: Vapor pressure, p_{sat}, of Solid Argon vs. temperature, T. From Hilsenrath et al. (1960) [90].

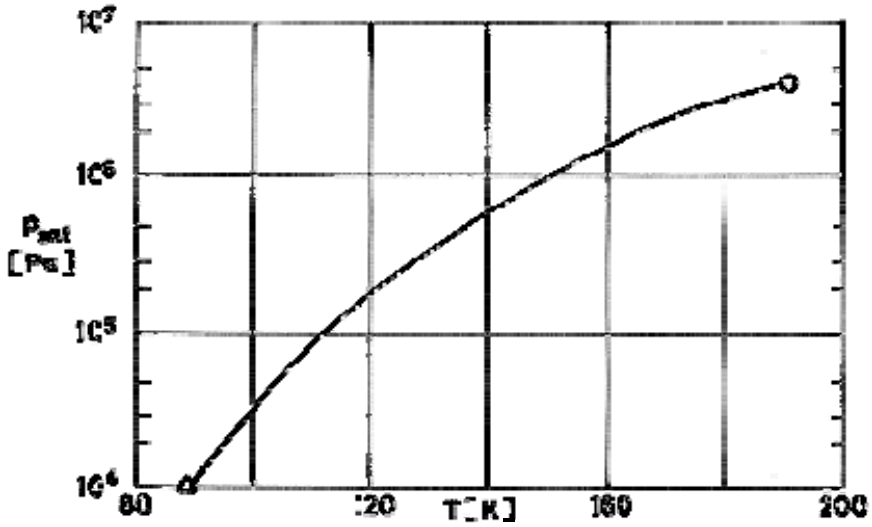

Figure 8-41: Vapor pressure, p_{sat}, of Liquid Methane vs. temperature, T. From Johnson (1961) [109].

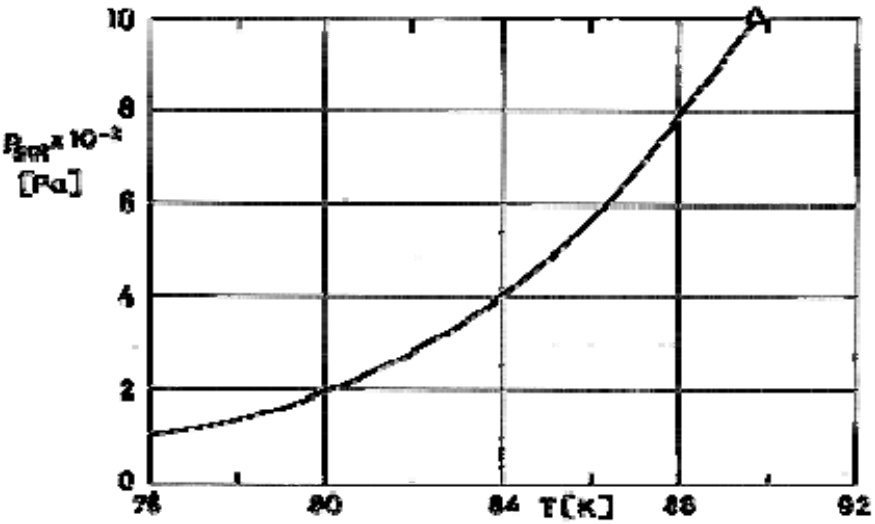

Figure 8-42: Vapor pressure, p_{sat}, of Solid Methane vs. temperature, T. From Johnson (1961) [109].

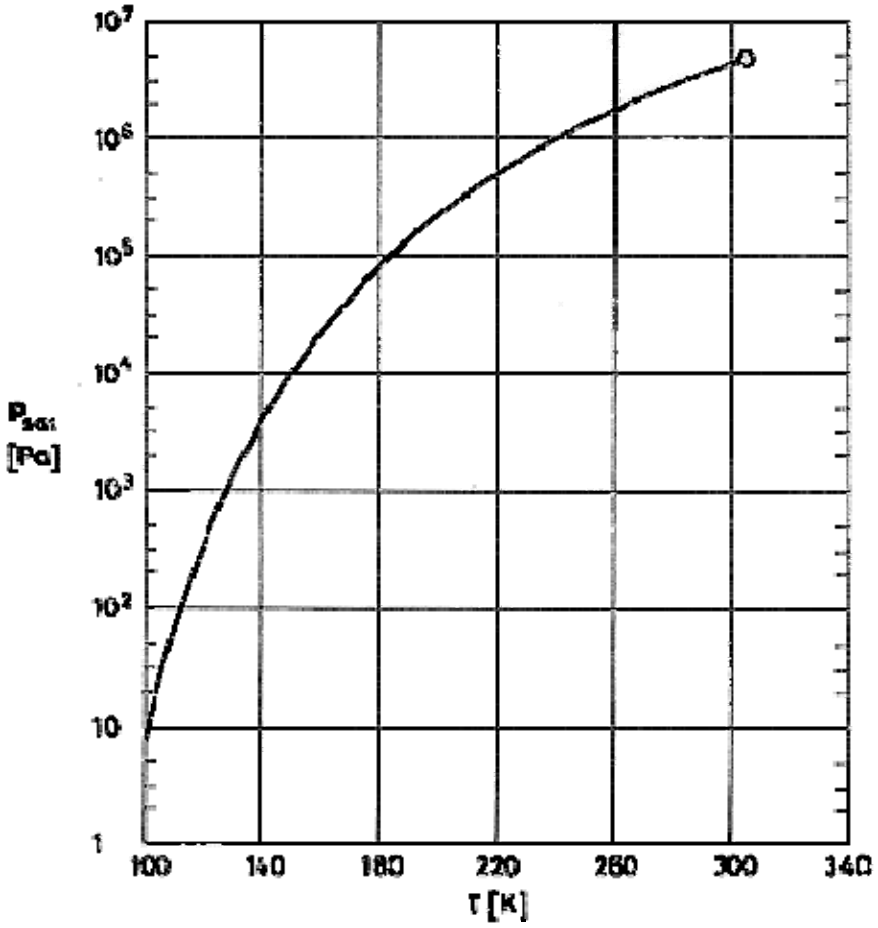

Figure 8-43: Vapor pressure, p_{sat}, of Liquid Ethane vs. temperature, T. From Vargaftik (1975) [253].

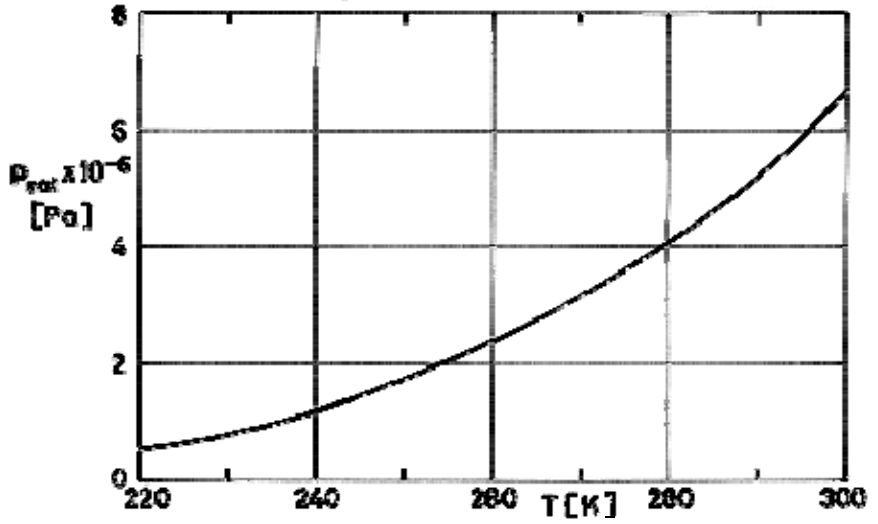

Figure 8-44: Vapor pressure, p_{sat}, of Liquid Carbon Dioxide vs. temperature, T. From Hilsenrath et al. (1960) [90].

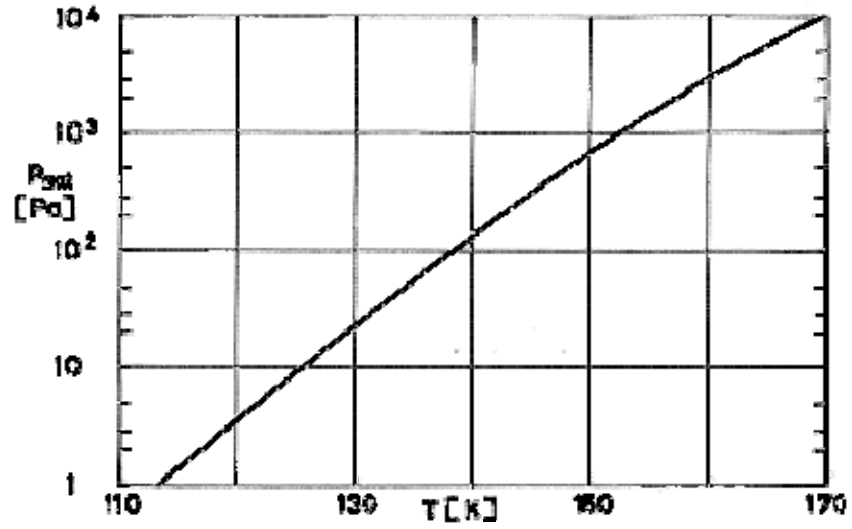

Figure 8-45: Vapor pressure, p_{sat}, of Solid Carbon Dioxide vs. temperature, T. From Caren & Coston (1968) [36].

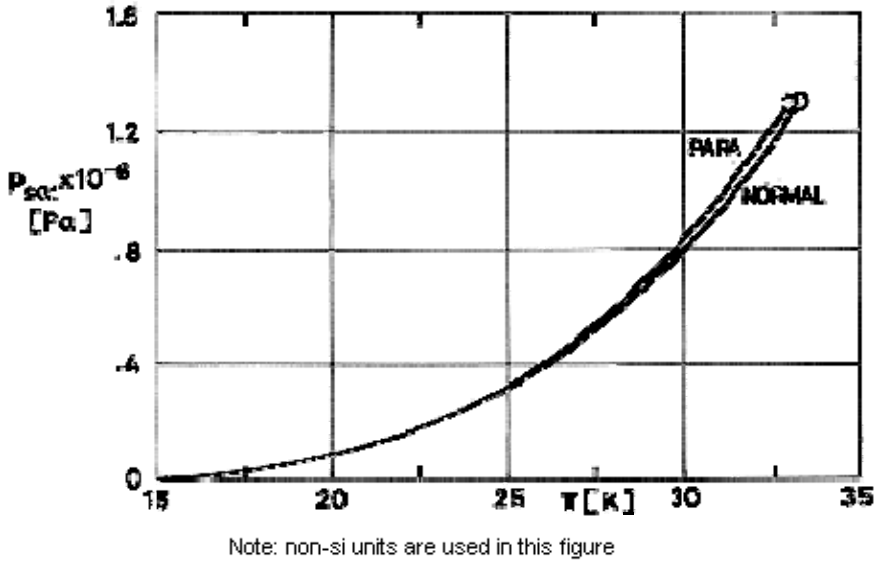

Figure 8-46: Vapor pressure, p_{sat}, of Liquid Hydrogen vs. temperature, T. From Vargaftik (1975) [253].

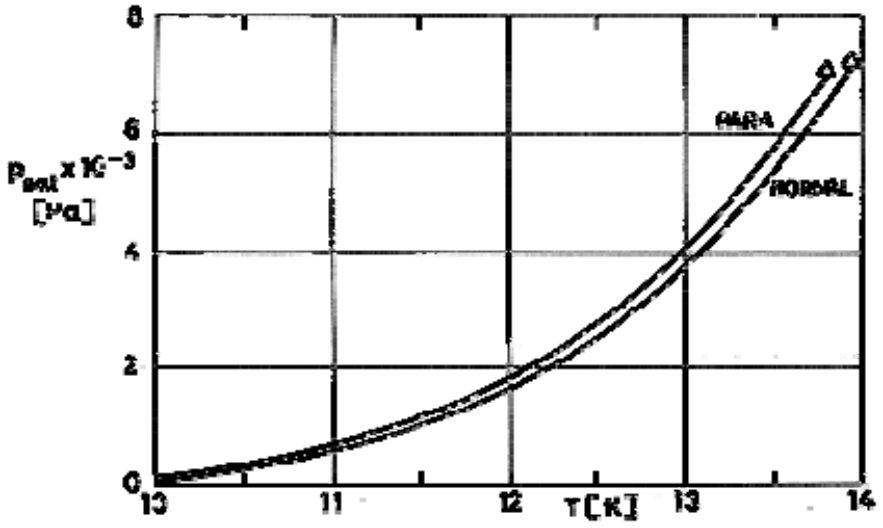

Figure 8-47: Vapor pressure, p_{sat}, of Solid Hydrogen vs. temperature, T. From Johnson (1961) [109].

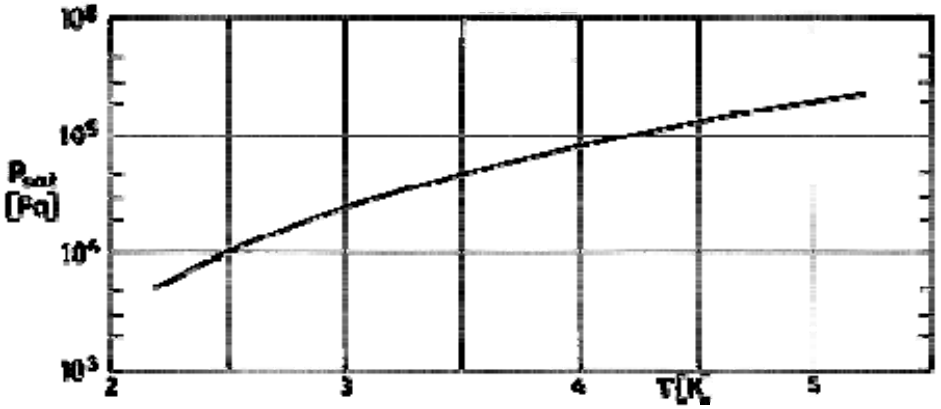

Figure 8-48: Vapor pressure, p_{sat}, of Liquid Helium-4 vs. temperature, T. From Angus & de Reuck (1977) [6].

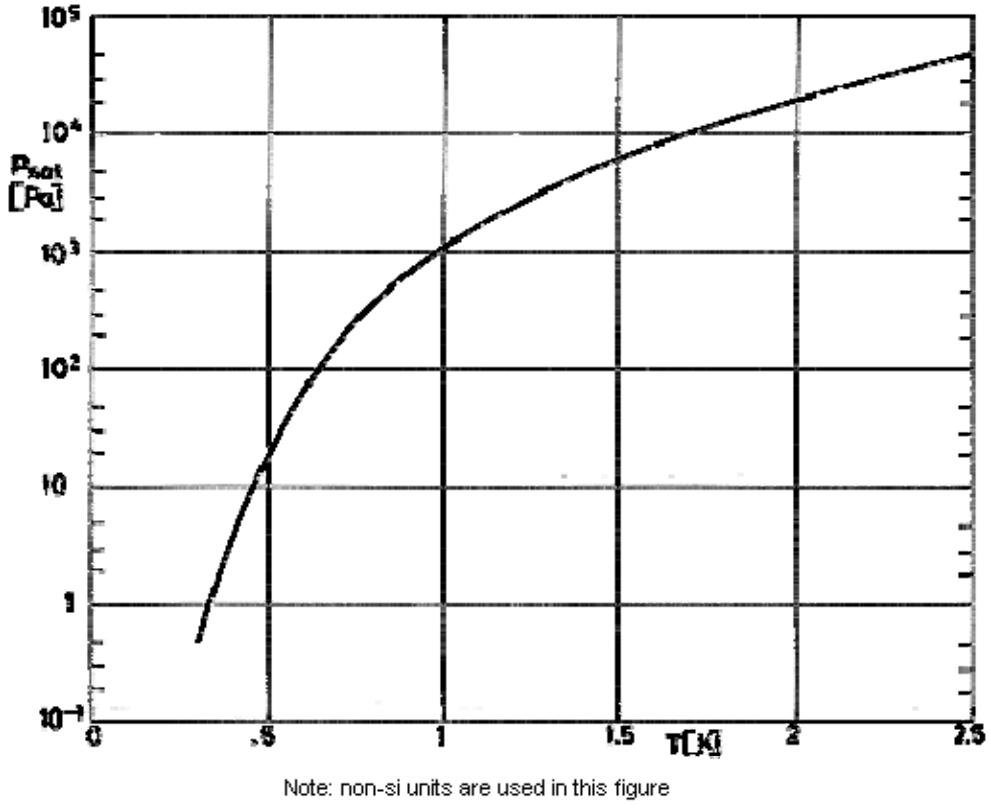

Figure 8-49: Vapor pressure, p_{sat}, of Liquid Helium-3 vs. temperature, T. From Mendelssohn (1960) [148].

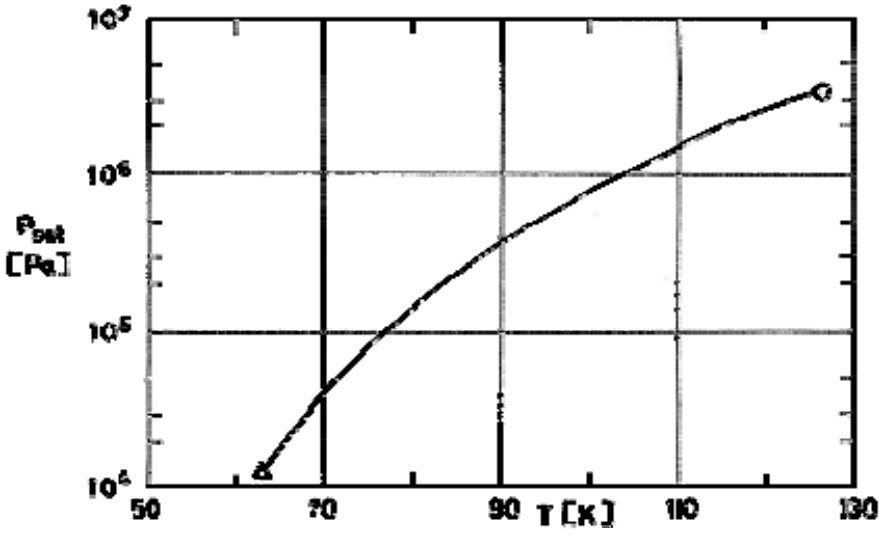

Figure 8-50: Vapor pressure, p_{sat}, of Liquid Nitrogen vs. temperature, T. From Johnson (1961) [109].

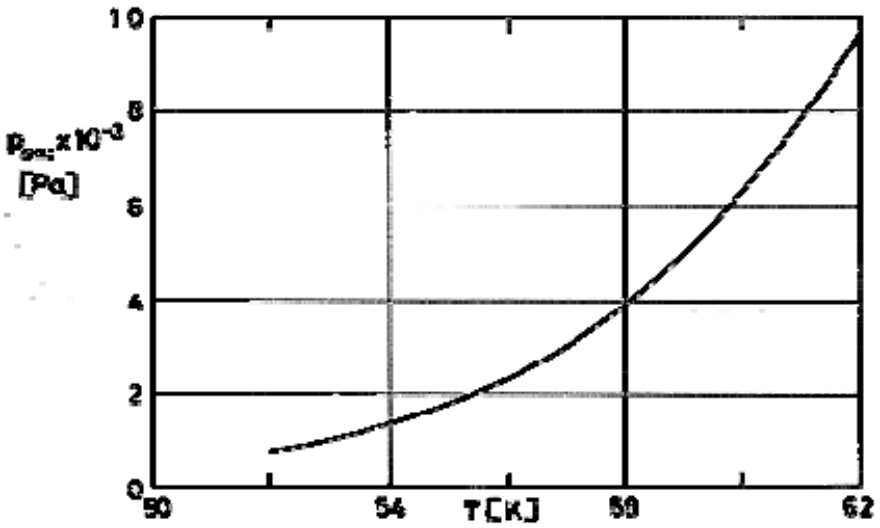

Figure 8-51: Vapor pressure, p_{sat}, of Solid Nitrogen vs. temperature, T. From Johnson (1961) [109].

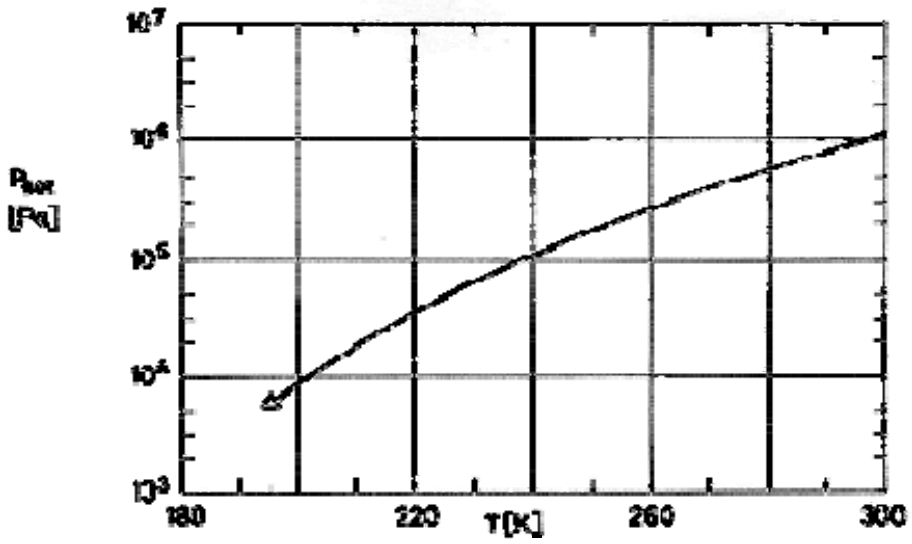

Figure 8-52: Vapor pressure, p_{sat}, of Liquid Ammonia vs. temperature, T. From Vargaftik (1975) [253].

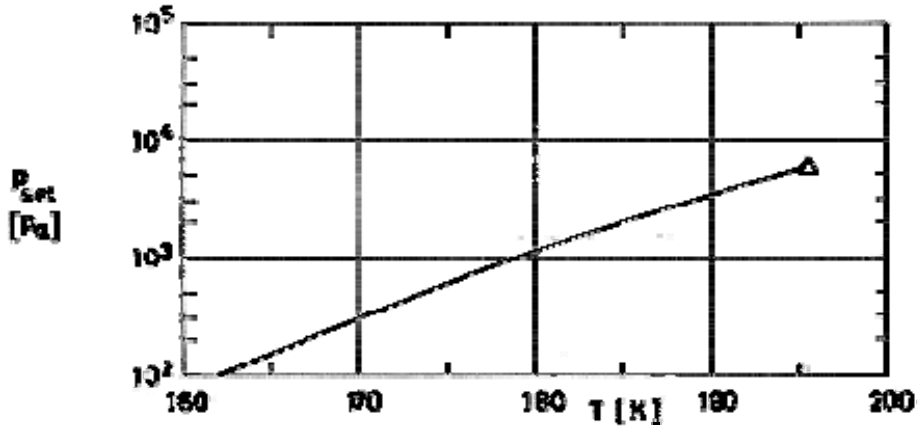

Figure 8-53: Vapor pressure, p_{sat}, of Solid Ammonia vs. temperature, *T*. From Kutateladze & Borishankii (1966) [127].

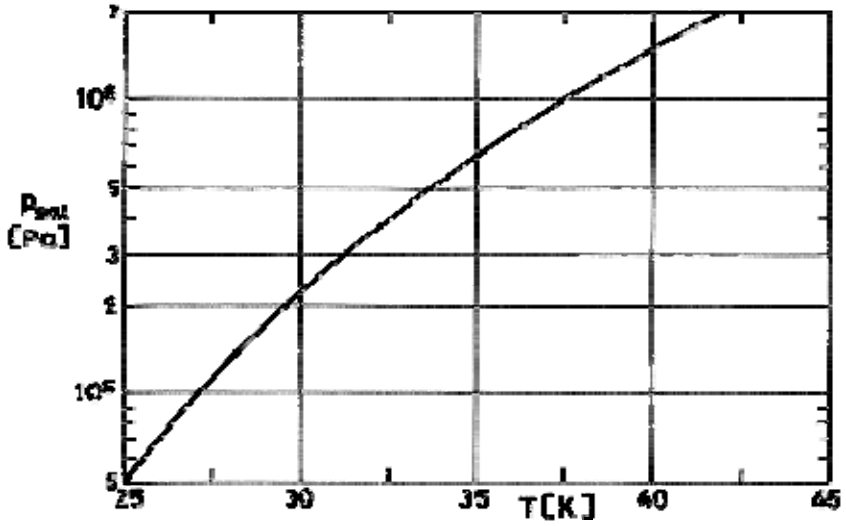

Figure 8-54: Vapor pressure, p_{sat}, of Liquid Neon vs. temperature, *T*. From Johnson (1961) [109].

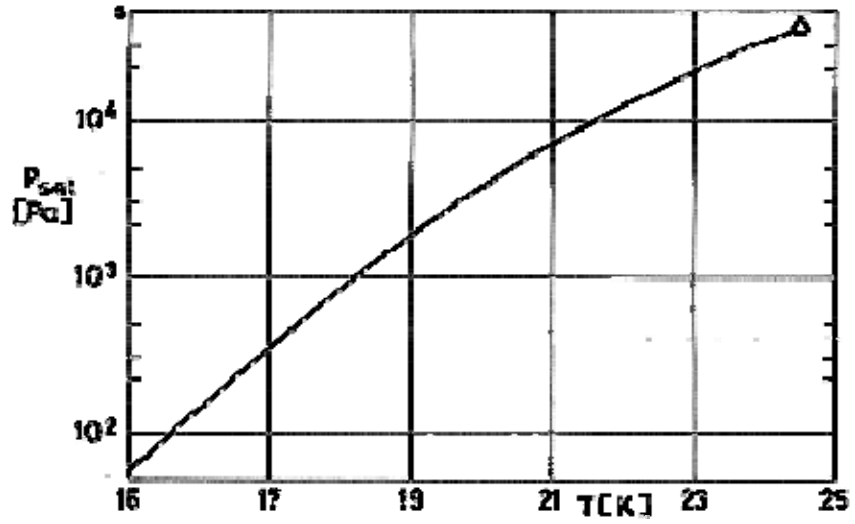

Figure 8-55: Vapor pressure, p_{sat}, of Solid Neon vs. temperature, T. From Johnson (1961) [109].

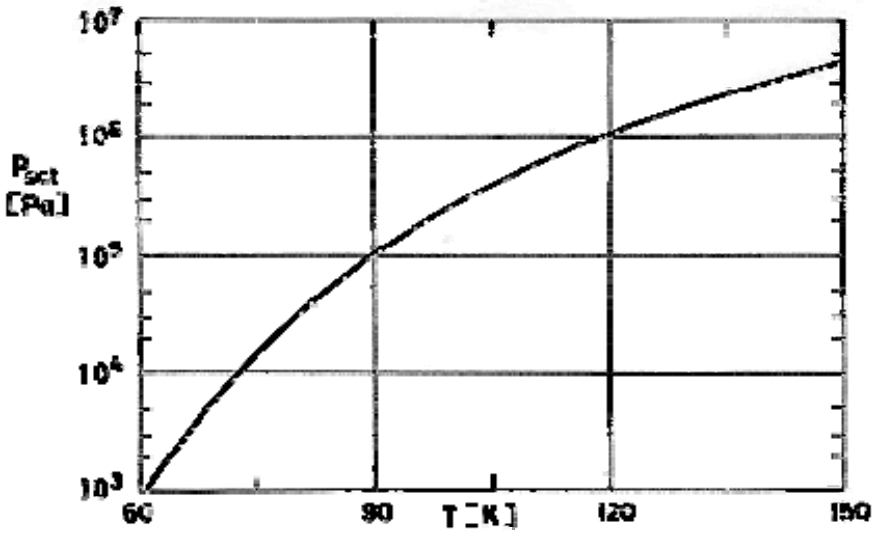

Figure 8-56: Vapor pressure, p_{sat}, of Liquid Oxygen vs. temperature, T. From Johnson (1961) [109].

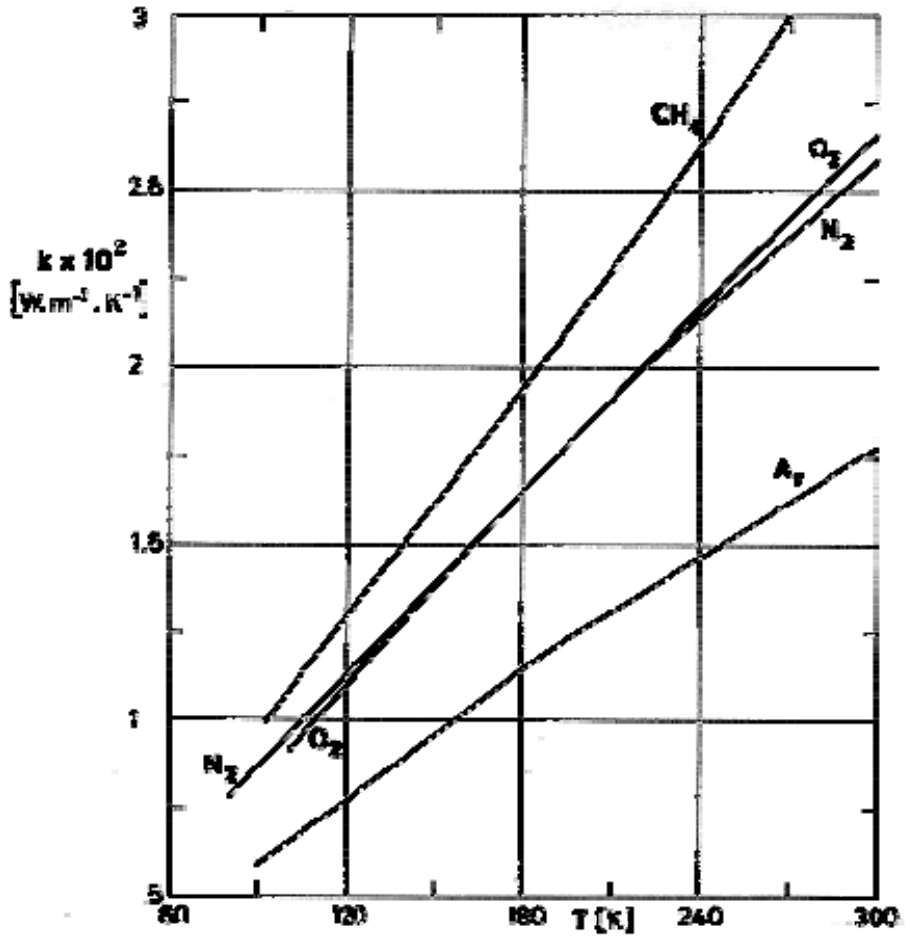

Note: non-si units are used in this figure

Figure 8-57: Thermal conductivity, *k*, of several gases -at a pressure of 10^5 Pa- vs. temperature, *T*. From Vargaftik (1975) [253].

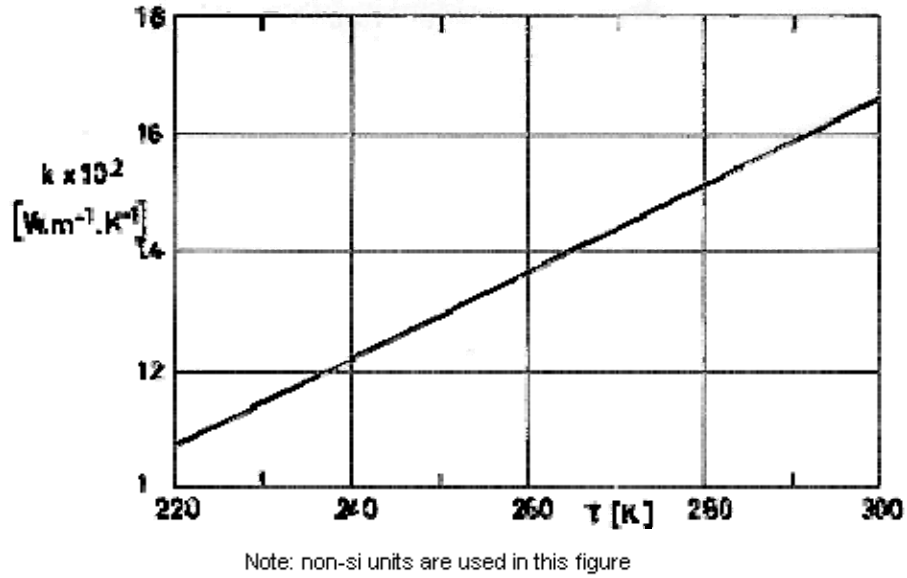

Note: non-si units are used in this figure

Figure 8-58: Thermal conductivity, *k*, of gaseous Carbon Dioxide -at a pressure of 10^5 Pa- vs. temperature, *T*. From Vargaftik (1975) [253].

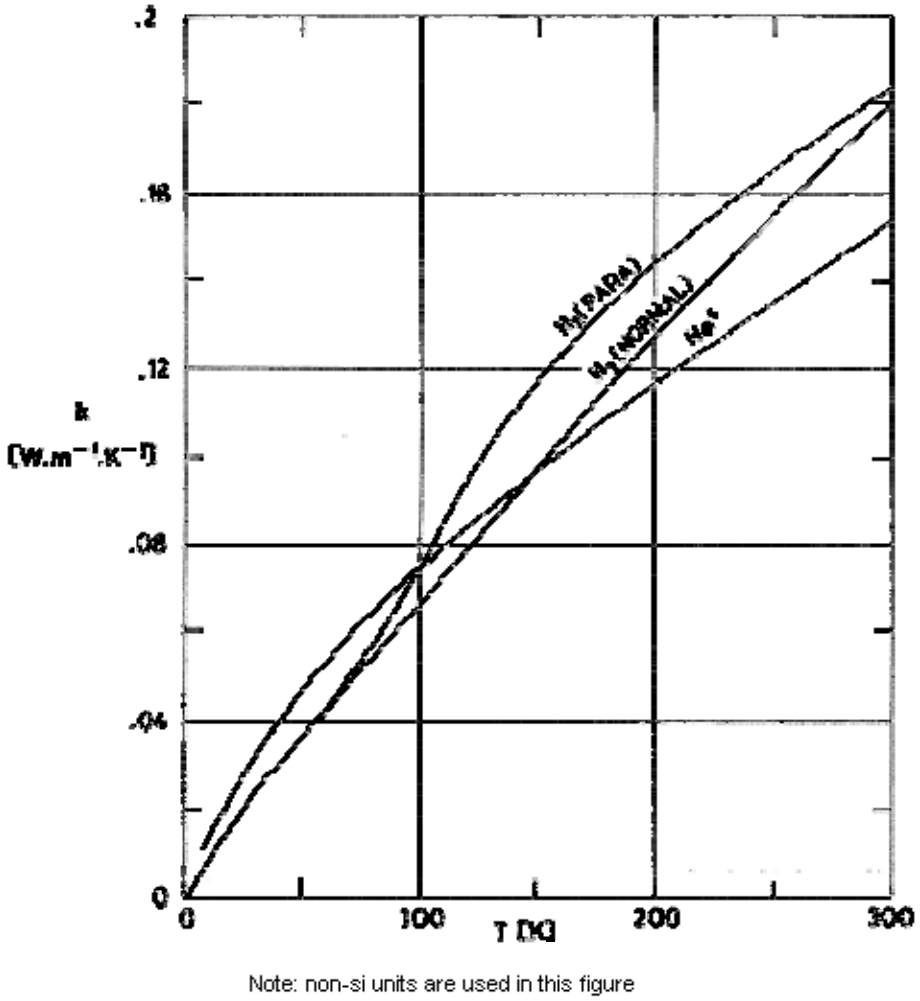

Figure 8-59: Thermal conductivity, *k*, of Gaseous Hydrogen and Helium-4 -at a pressure of one atmosphere (1,013x10^5 Pa) vs. temperature, *T*. From Johnson (1961) [109].

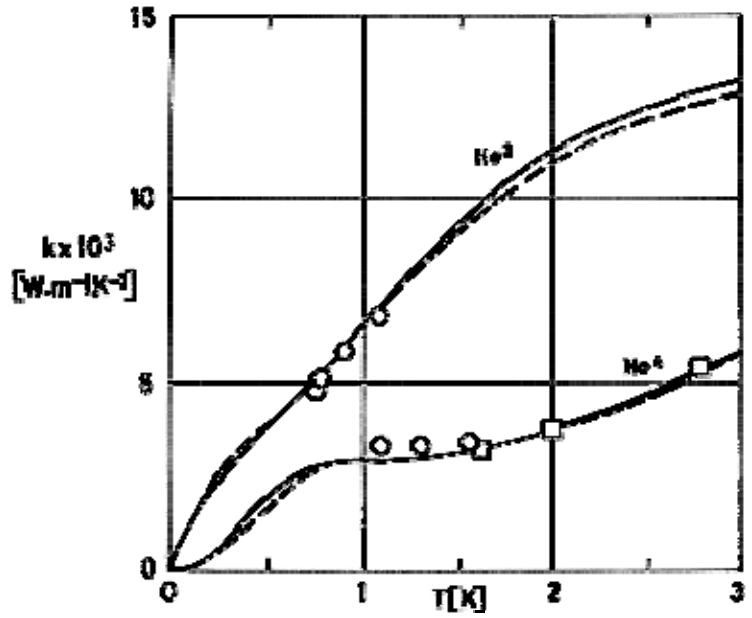

Figure 8-60: Thermal conductivity, *k*, of Gaseous Helium-4 and Helium-3 vs. temperature, *T*. Calculated curves and experimental points are from different sources. From Keller (1969) [119]. The thermal conductivity of Gaseous Helium-4 in a much larger temperature range is given in Figure 8-59.

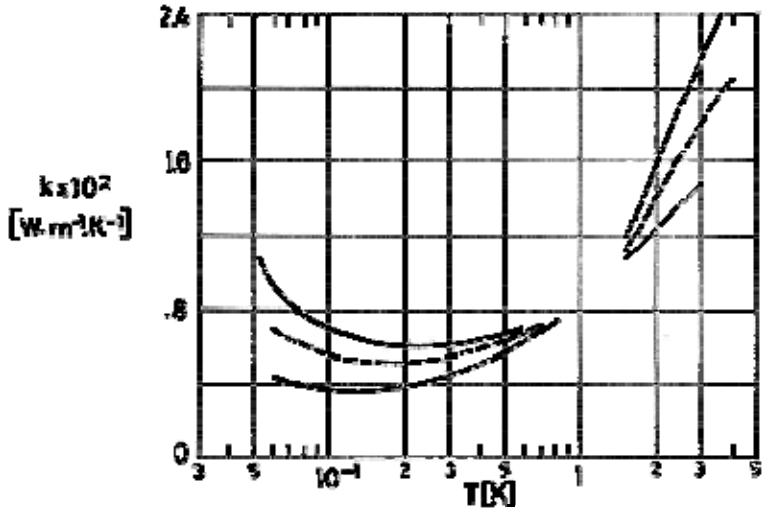

Note: non-si units are used in this figure

Figure 8-61: Thermal conductivity, *k*, of Liquid Helium-3 -at several pressures- vs. temperature, *T*.

——— $p = 10^4$ Pa; ——— $p = 10^5$ Pa

— — $p = 6{,}7 \times 10^5$ Pa; — — $p = 10^6$ Pa

— · — $p = 26{,}9 \times 10^5$ Pa; — · — $p = 34{,}4 \times 10^5$ Pa

From Keller (1969) [119].

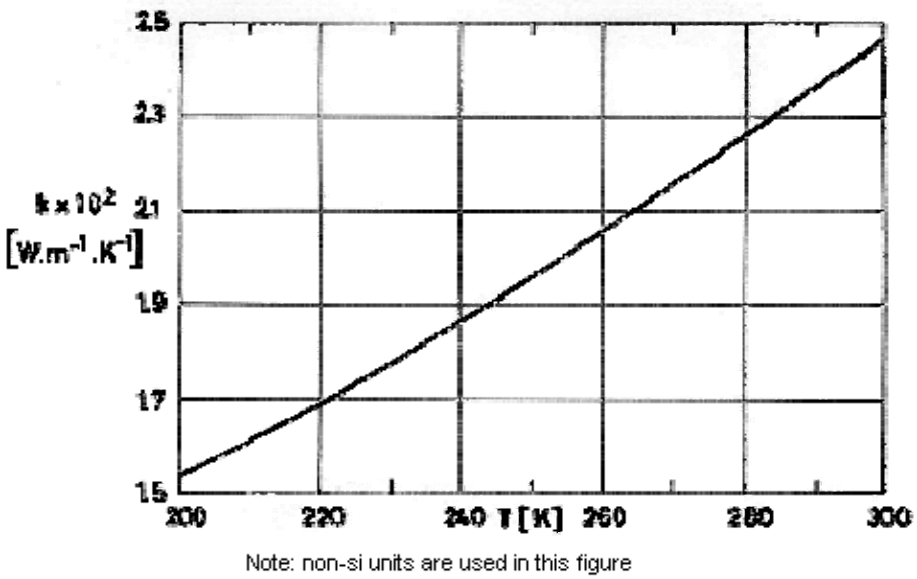

Figure 8-62: Thermal conductivity, *k*, of gaseous Ammonia -at a pressure of 10^5 Pa- vs. temperature, *T*. Calculated curves and experimental points are from different sources. From Vargaftik (1975) [253].

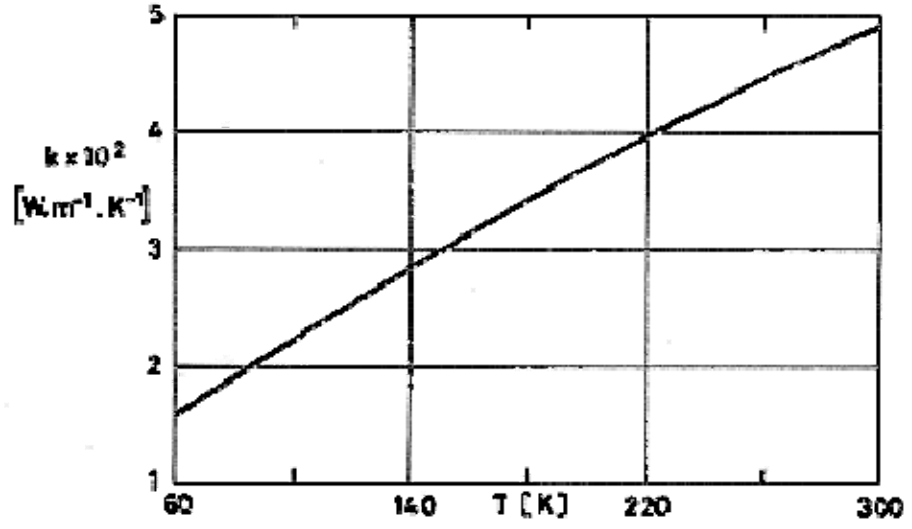

Figure 8-63: Thermal conductivity, *k*, of gaseous Neon -at a pressure of one atmosphere (1,013x10^5 Pa)- vs. temperature, *T*. Calculated curves and experimental points are from different sources. From Johnson (1961) [109].

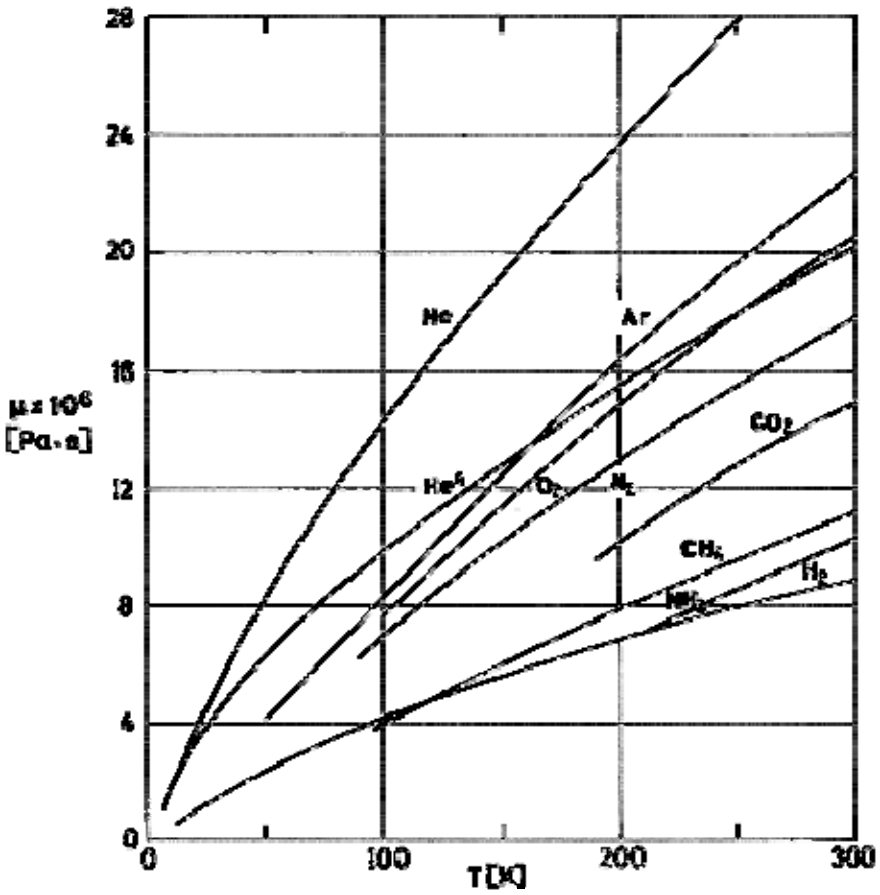

Figure 8-64: Dynamic viscosity, μ, of several gases -at a pressure of one atmosphere (1,013x10^5 Pa)- vs. temperature, *T*. All the data are from Johnson (1961) [109] except those corresponding to Argon and Carbon Dioxide which are from Hilsenrath et al. (1960), and those from Ammonia which are from Raznjevic (1970) [190].

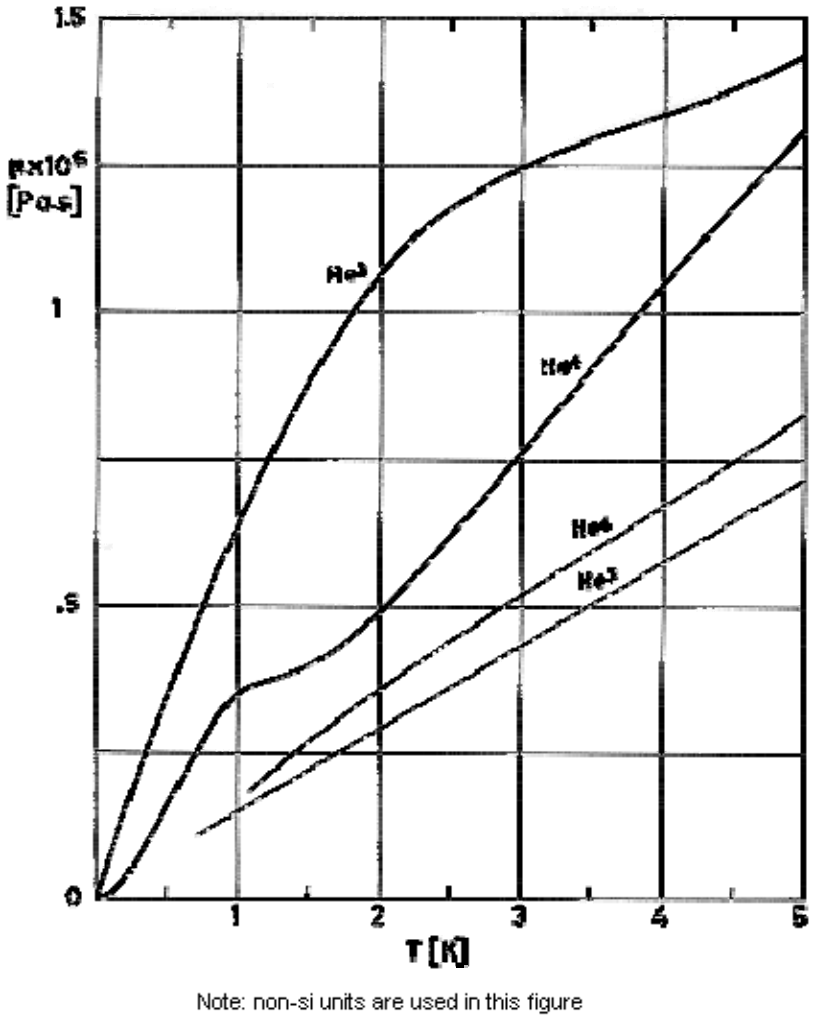

Note: non-si units are used in this figure

Figure 8-65: Dynamic viscosity, μ, of Gaseous Helium-4 and helium-3 vs. temperature, T.
——Calculated accounting for quantum-mechanical effects.
——Classical Mechanics calculations.
From Keller (1969) [119].

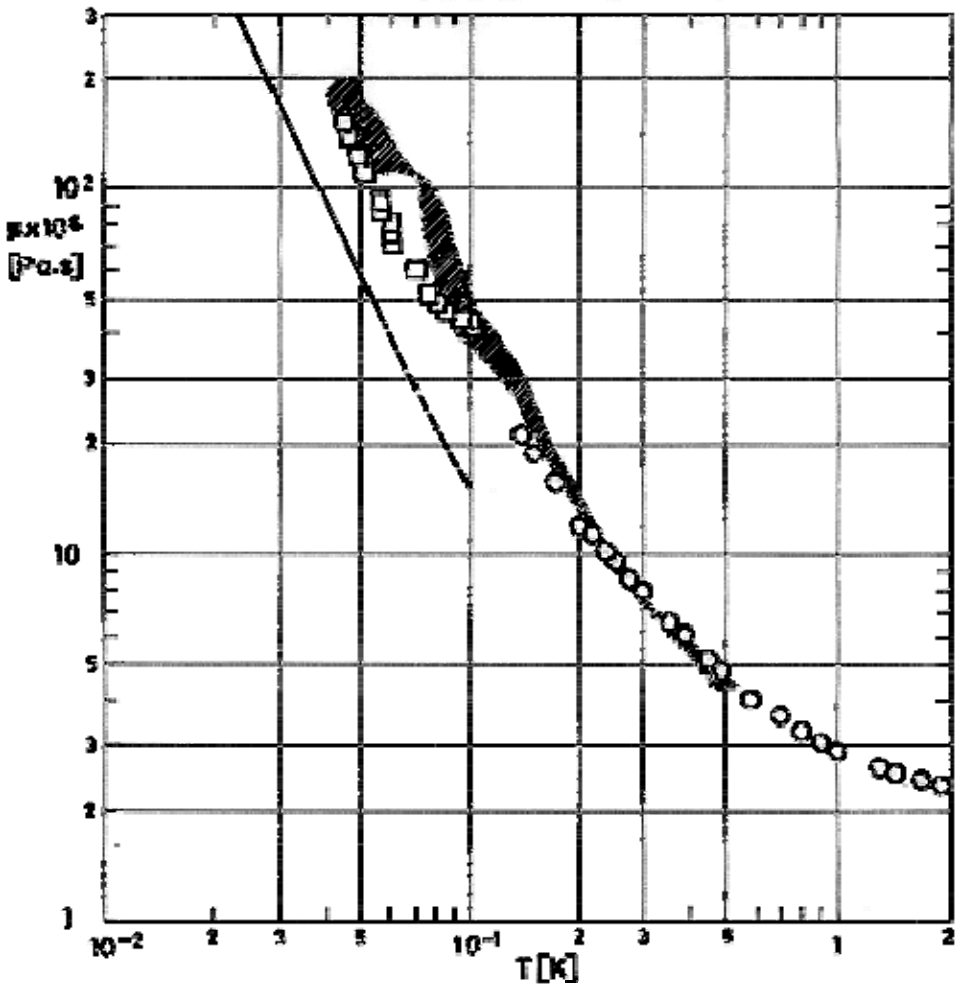

Figure 8-66: Dynamic viscosity, μ, of Liquid Helium-3, at several pressures, vs. temperature, T.
○$p = p_{sat}$, □ p = 0,23x10^5 Pa.
From Conte (1970) [48]
Shaded region enclosed experimental points for $p = p_{sat}$.
From Keller (1969) [119].
The line has been calculated from Hone (1962), p = 0.

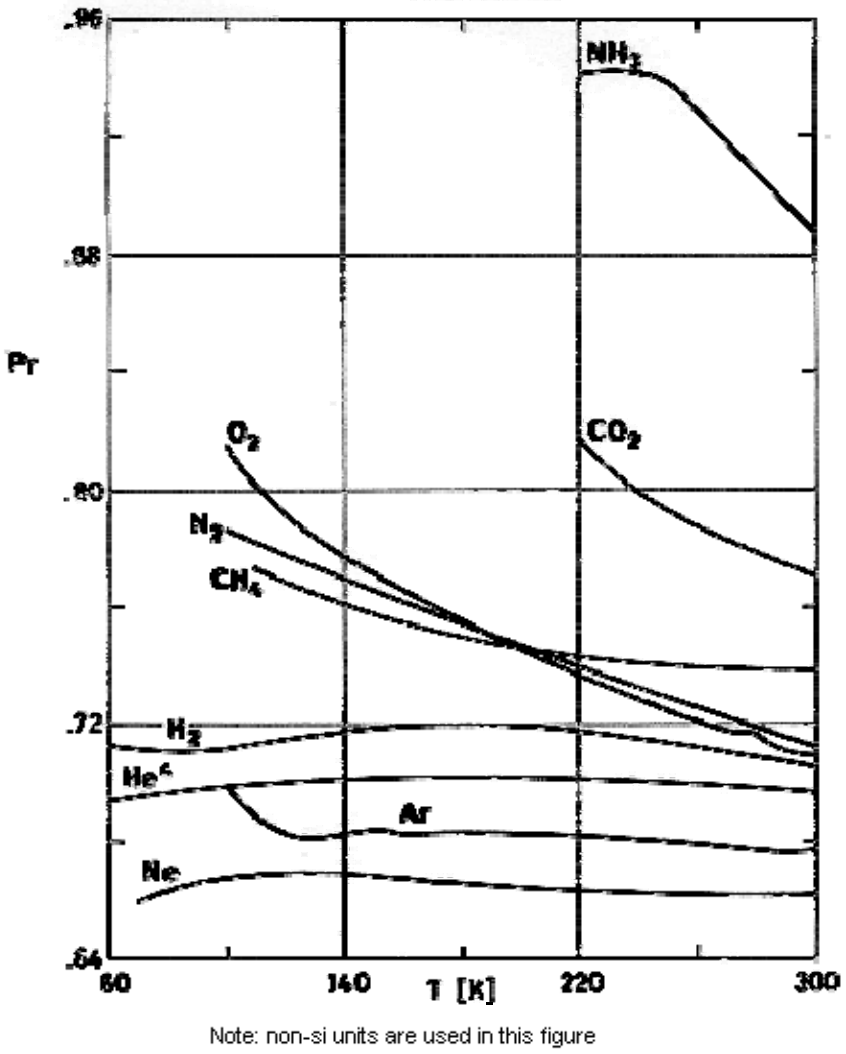

Figure 8-67: Prandtl number, $P_r = \mu c_p/k$, of several gases -at a pressure of one atmosphere (1,0135x10^5 Pa)- vs. temperature, T. All the data are from Hilsenrath et al. (1960) [90] except those corresponding to Methane, Helium-4, Ammonia and Neon which have been calculated by the compiler.

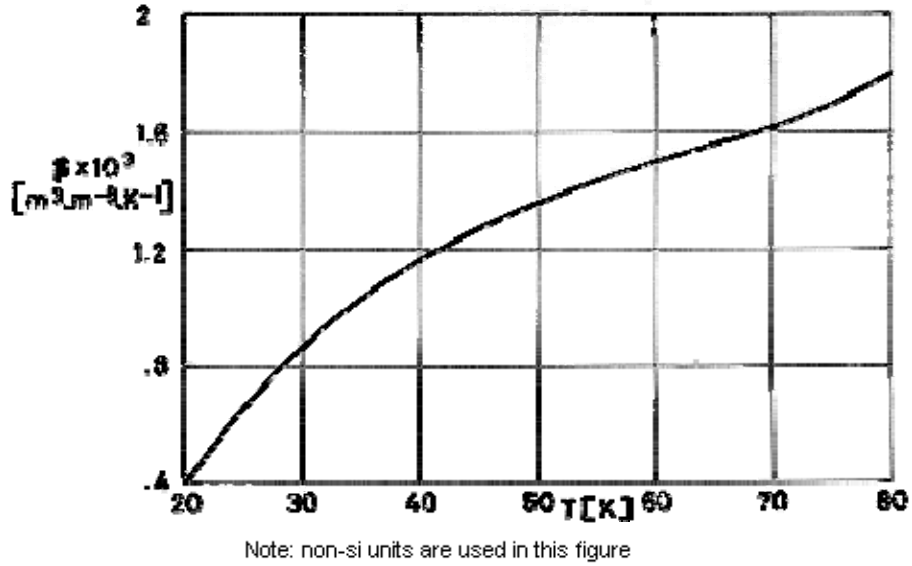

Figure 8-68: Coefficient of linear thermal expansion, β, of Solid Argon vs. temperature, *T*. From Johnson (1961) [109].

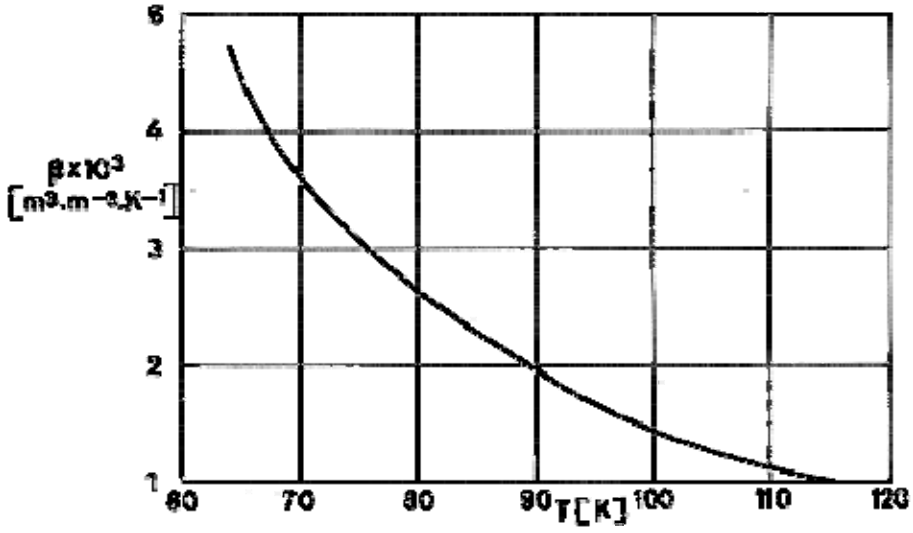

Figure 8-69: Coefficient of volumetric thermal expansion (isobaric compressibility), β, of Liquid Nitrogen vs. temperature, *T*. From Johnson (1961) [109].

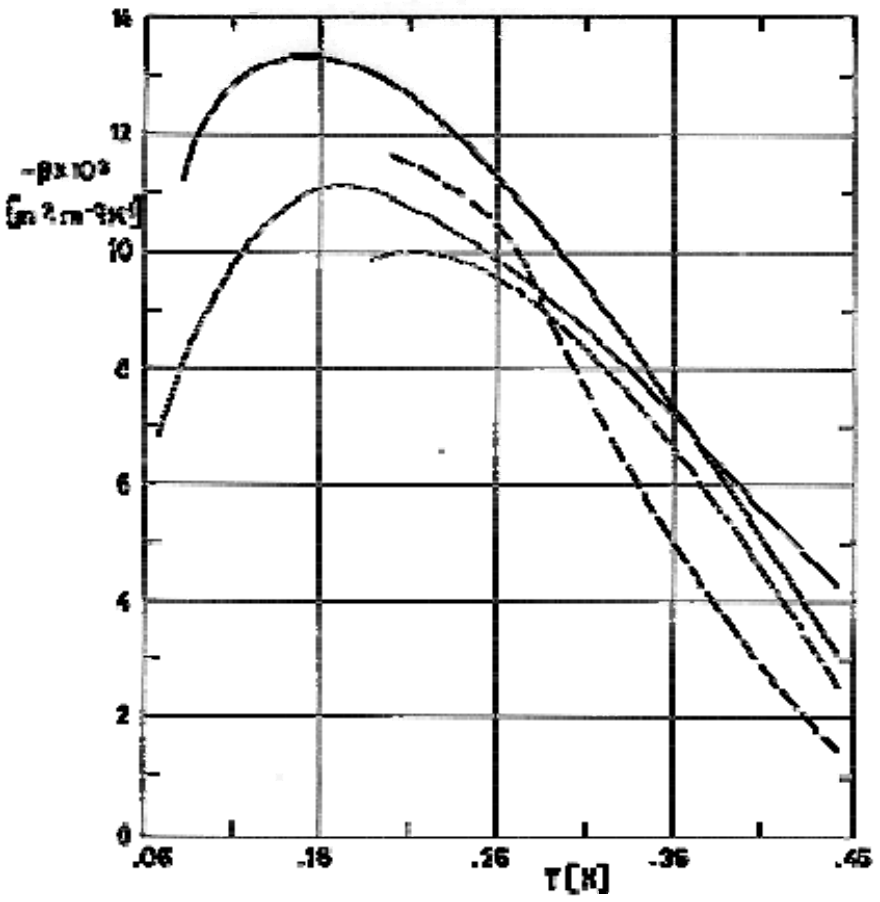

Note: non-si units are used in this figure

Figure 8-70: Coefficient of volumetric thermal expansion (isobaric compressibility), β, of Liquid Helium-3 -at pressures near p_{sat}- vs. temperature, T. Curves come from a wide variety of sources, see Keller (1969) [119]. Notice that β is negative in the pressure and temperature ranges under consideration.
See also Figure 8-71 for values of β vs. T at the melting curve.

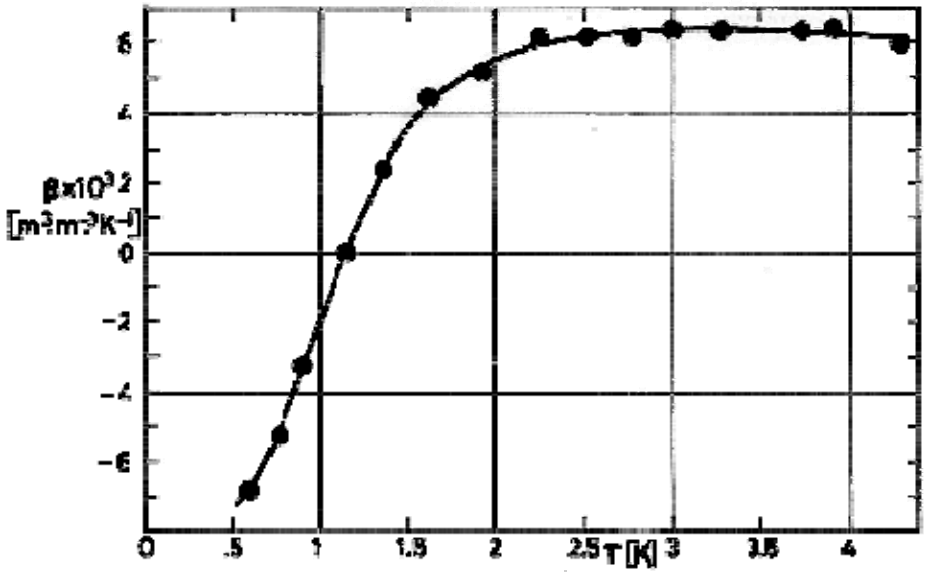

Note: non-si units are used in this figure

Figure 8-71: Coefficient of volumetric thermal expansion (isobaric compressibility), β, of Liquid Helium-3 -at the melting curve- vs. temperature, T. From Straty (1966) [228].

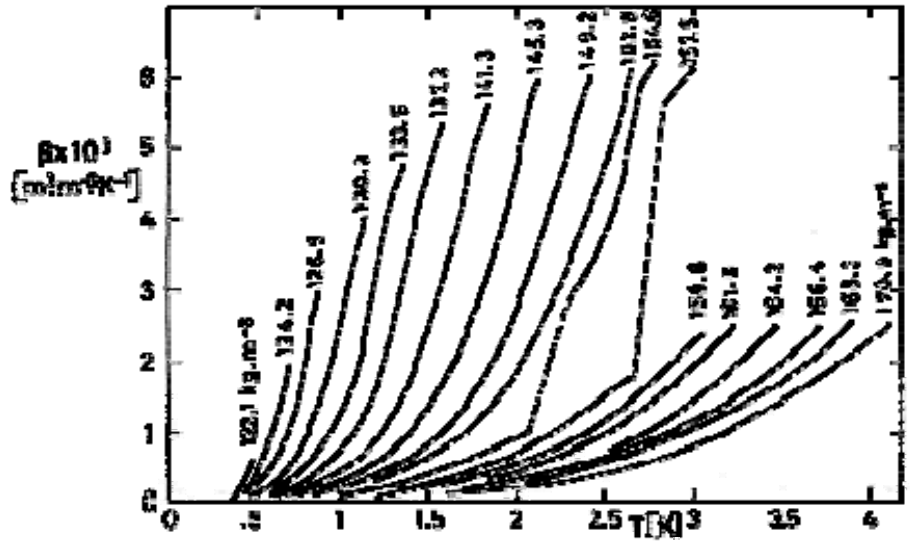

Note: non-si units are used in this figure

Figure 8-72: Coefficient of volumetric thermal expansion (isobaric compressibility), β, of Solid-Helium-3 vs. temperature, T. Numbers on the curves are densities in kg.m^{-3}. From Straty (1966) [228]. See also Figure 8-14.

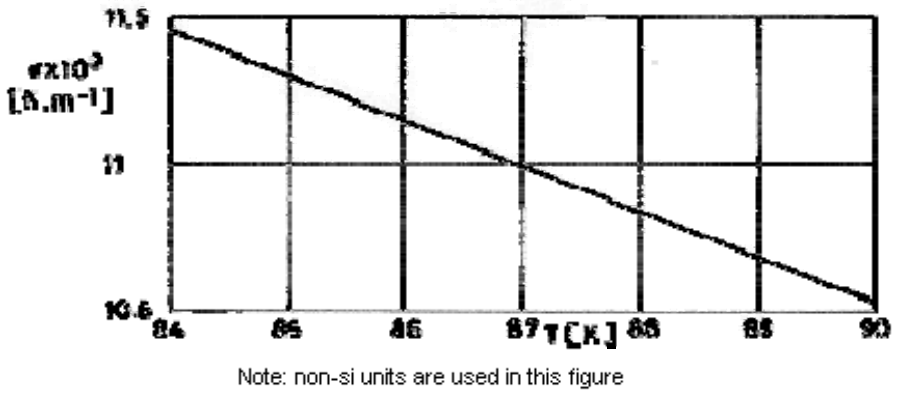

Figure 8-73: Surface tension, σ, of Saturated Liquid Argon vs. temperature, T. From Johnson (1961) [109].

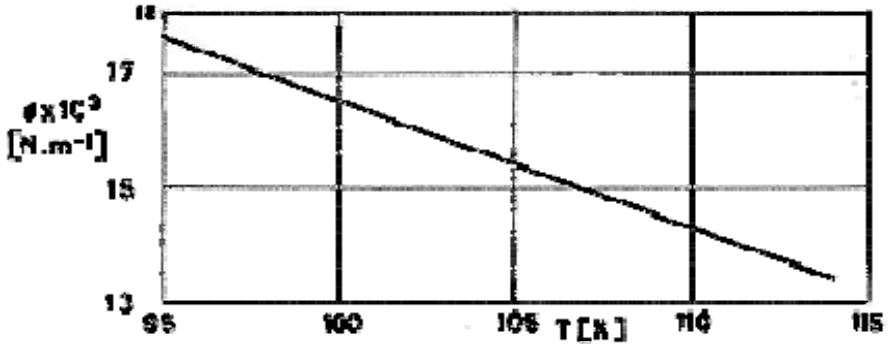

Figure 8-74: Surface tension, σ, of Saturated Liquid Methane vs. temperature, T. From Johnson (1961) [109].

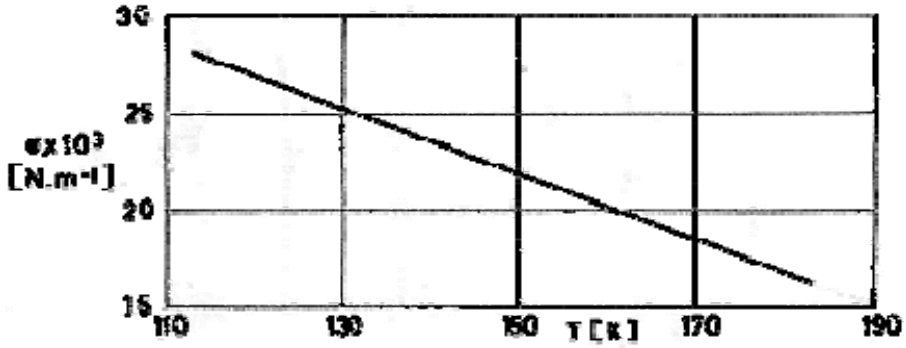

Figure 8-75: Surface tension, σ, of Saturated Liquid Ethane vs. temperature, T. From Vargaftik (1975) [253].

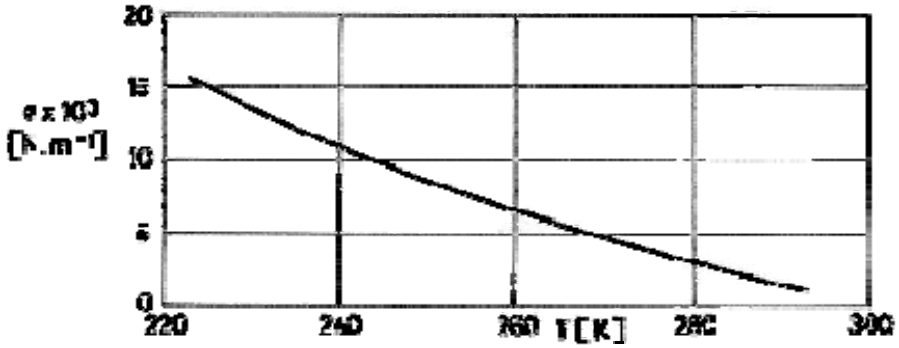

Figure 8-76: Surface tension, σ, of Saturated Liquid Carbon Dioxide vs. temperature, T. From Kutateladze et al. (1966) [127].

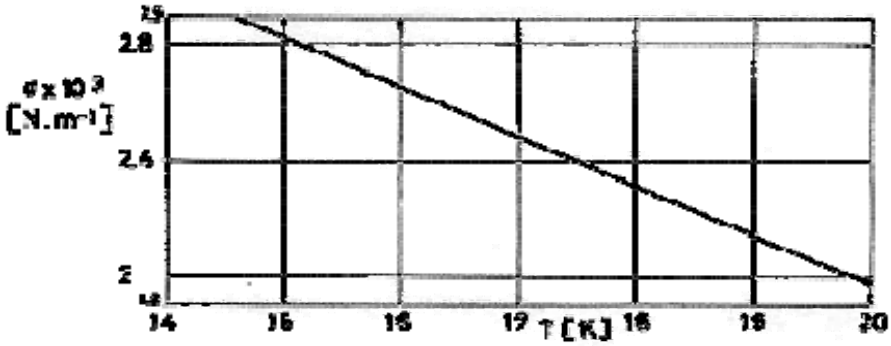

Figure 8-77: Surface tension, σ, of Saturated Liquid Normal Hydrogen vs. temperature, T. From Johnson (1961) [109].

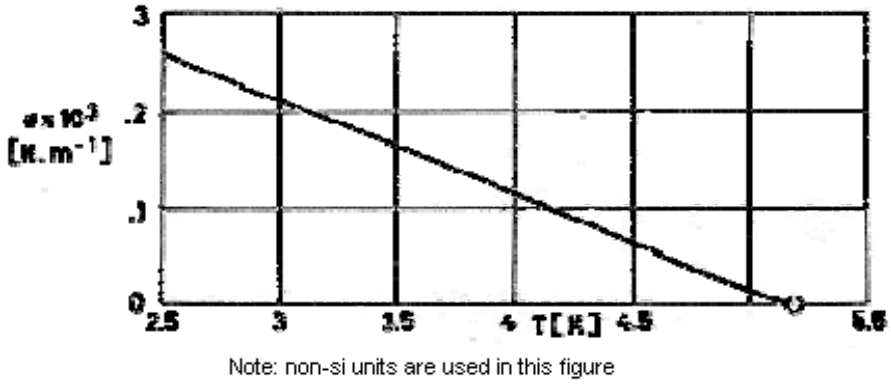

Figure 8-78: Surface tension, σ, of Saturated Liquid Helium-4 vs. temperature, T. From Johnson (1961) [109].

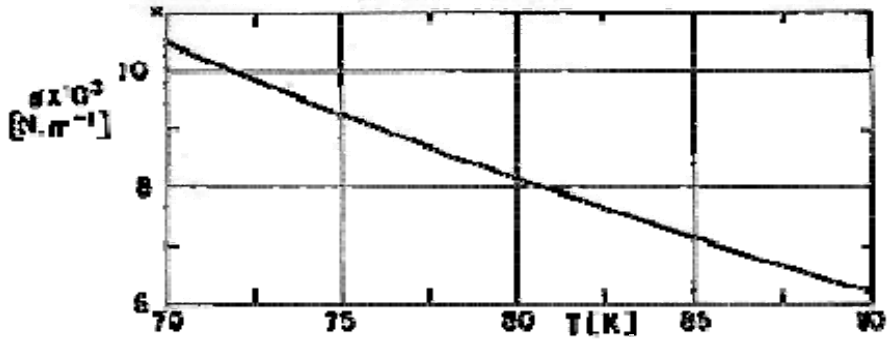

Figure 8-79: Surface tension, σ, of Saturated Liquid Nitrogen vs. temperature, *T*. From Johnson (1961) [109].

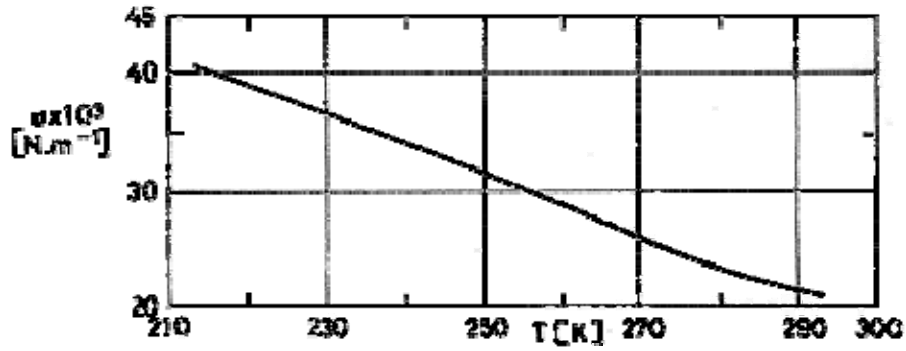

Figure 8-80: Surface tension, σ, of Saturated Liquid Ammonia vs. temperature, *T*. From Dunn & Reay (1976) [61].

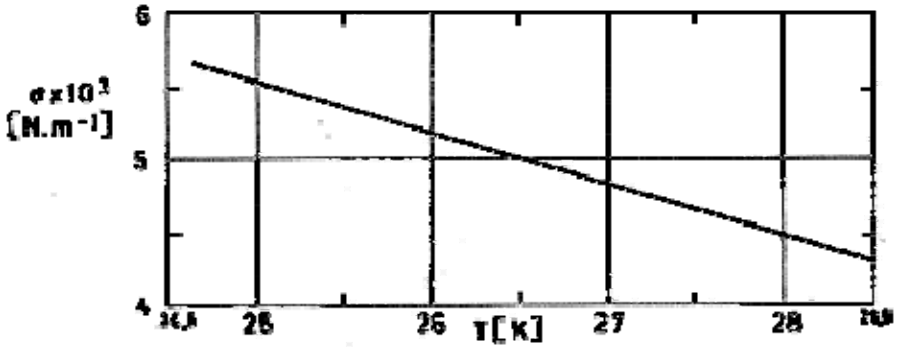

Note: non-si units are used in this figure

Figure 8-81: Surface tension, σ, of Saturated Liquid Neon vs. temperature, *T*. From Johnson (1961) [109].

8.1.2 Entropy diagrams

Entropy diagrams for the normal cryogens listed in Table 8-1, clause 8.1.1, appear in the following pages. The data have been drawn from available tabulated values.

The selection of the pressure and temperature ranges posed problems in planning the diagrams.

A range based on functional criteria for presently available closed cycle refrigerators (clause 5.2.1) would suggest an upper bound of T =300 K for temperature and p= 0,5x10^6 Pa for pressure.

Nevertheless, such uniform diagrams would present in many cases too much irrelevant information, since fluids with low critical pressures and temperatures would exhibit and almost undetectable saturation curve collapsed down the abscissa axis, being most of the plot devoted to curves where perfect gas approximation holds.

Thence a range based on the critical values has been chosen, so that T is bounded from above by 1,2 T_c to 1,5 T_c, and p appears in the 10^5 Pa to near 1,2 p_c range.

Since a quick look at the different diagrams in an uniform temperature and pressure range could be useful, a less detailed mosaic of figures has been prepared, Figure 8-82. In each of these figures T ranges between 0 K and 300 K, while p exceeds the normal value of 10^5 Pa.

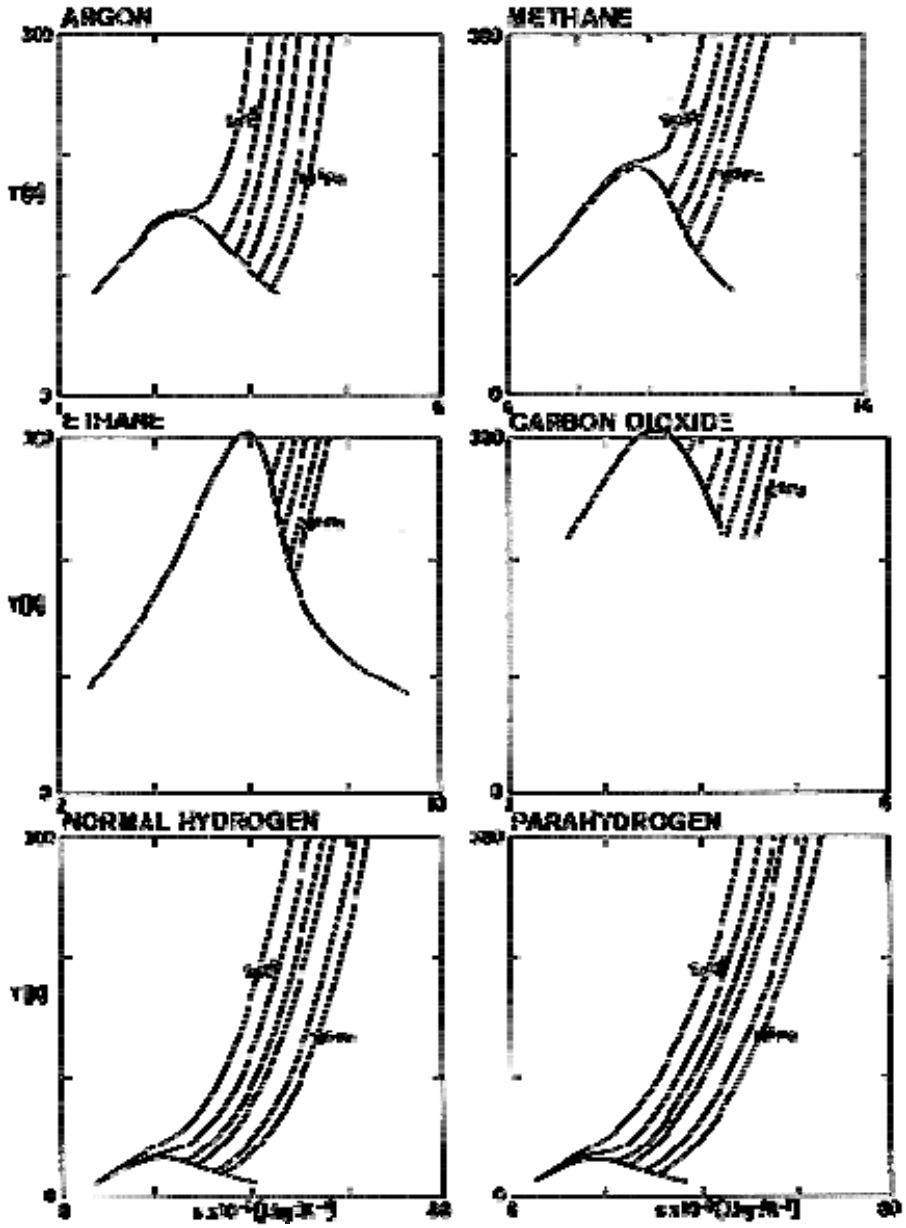
ARGON
METHANE
ETHANE
CARBON DIOXIDE
NORMAL HYDROGEN
PARAHYDROGEN

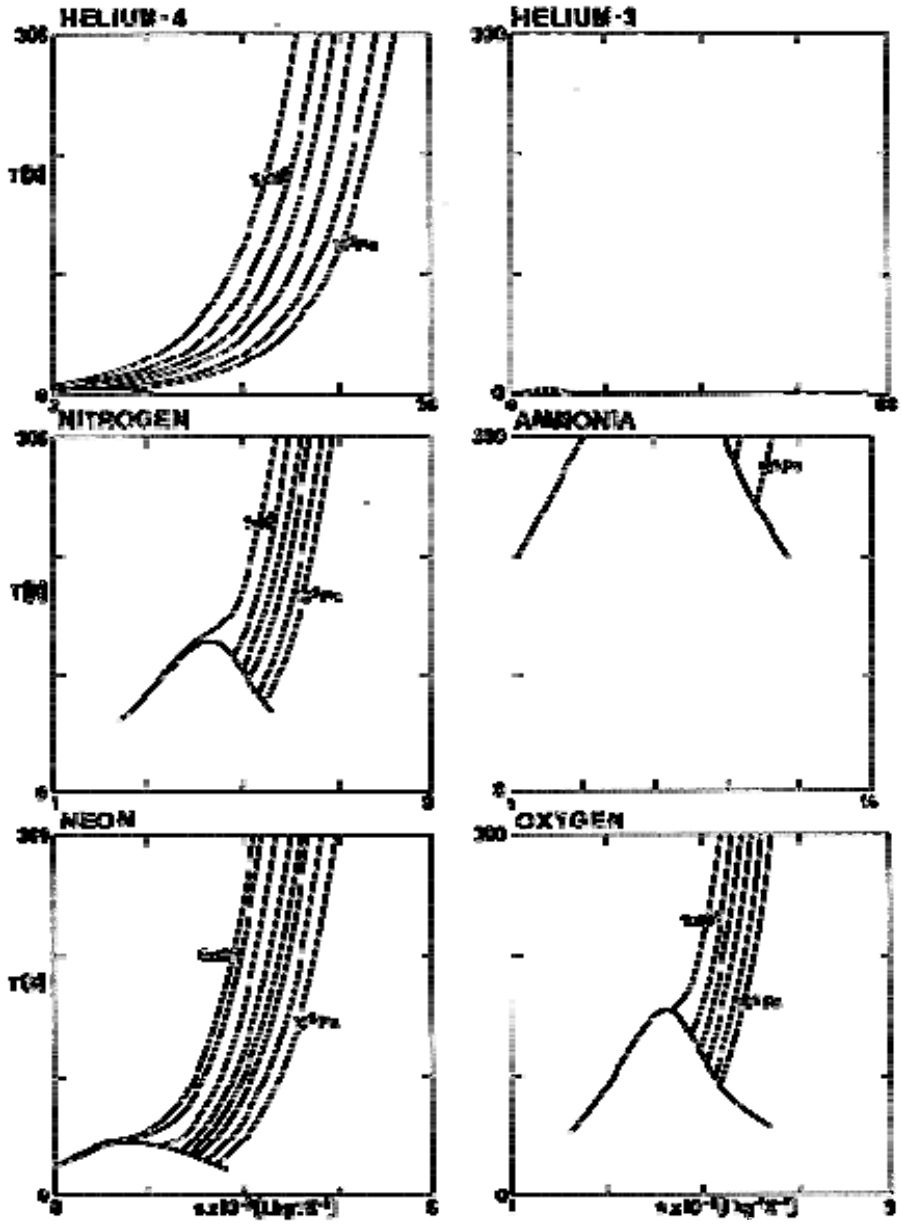

Figure 8-82: Temperature-entropy diagrams for normal cryogens. More details are given in Figure 8-83 to Figure 8-94.

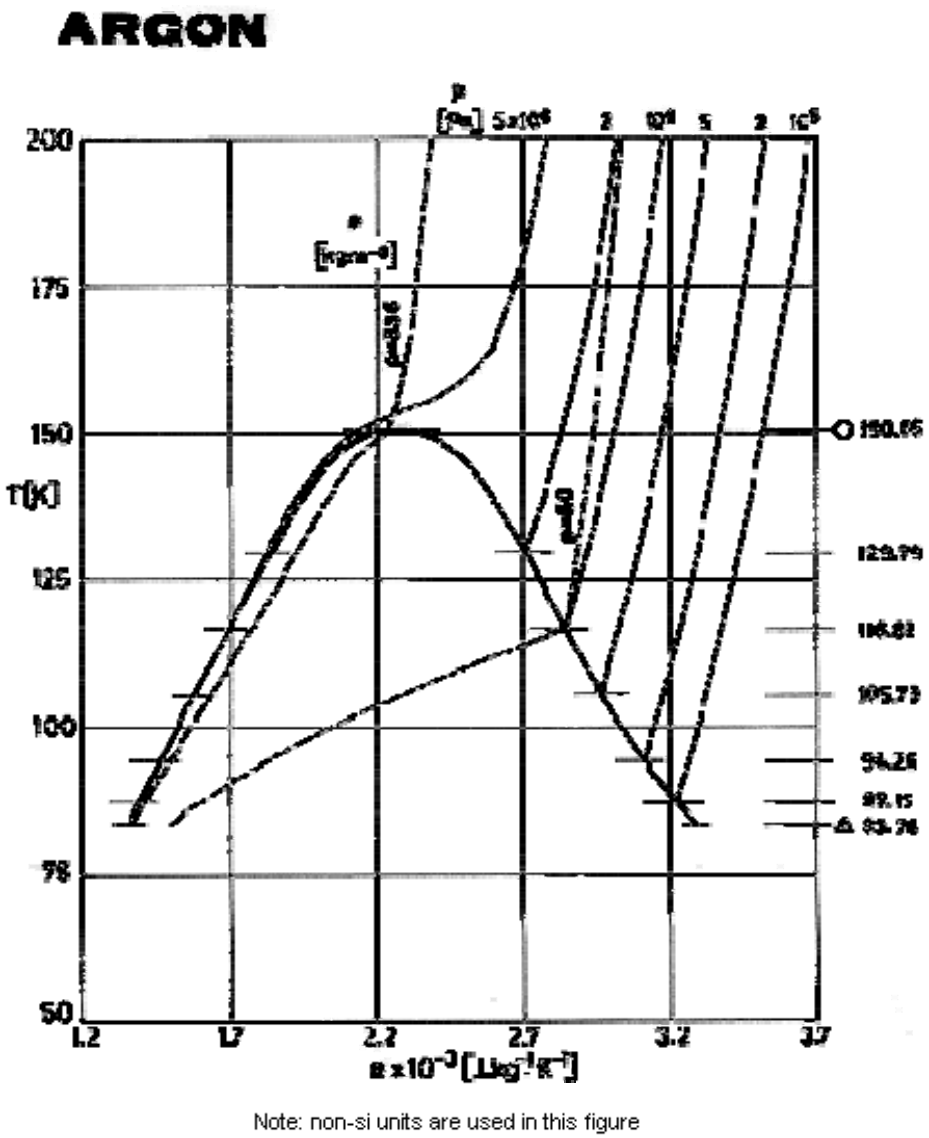

Figure 8-83: Temperature, *T*, entropy, *s*, diagram for Argon. From Vargaftik (1975) [253]. Tabulated values up to *T* = 1300 K and *p* = 10^8 Pa are given in pp. 543 and ff. of the mentioned source. Saturation curve and typical isobars and isochores are shown in the figure.

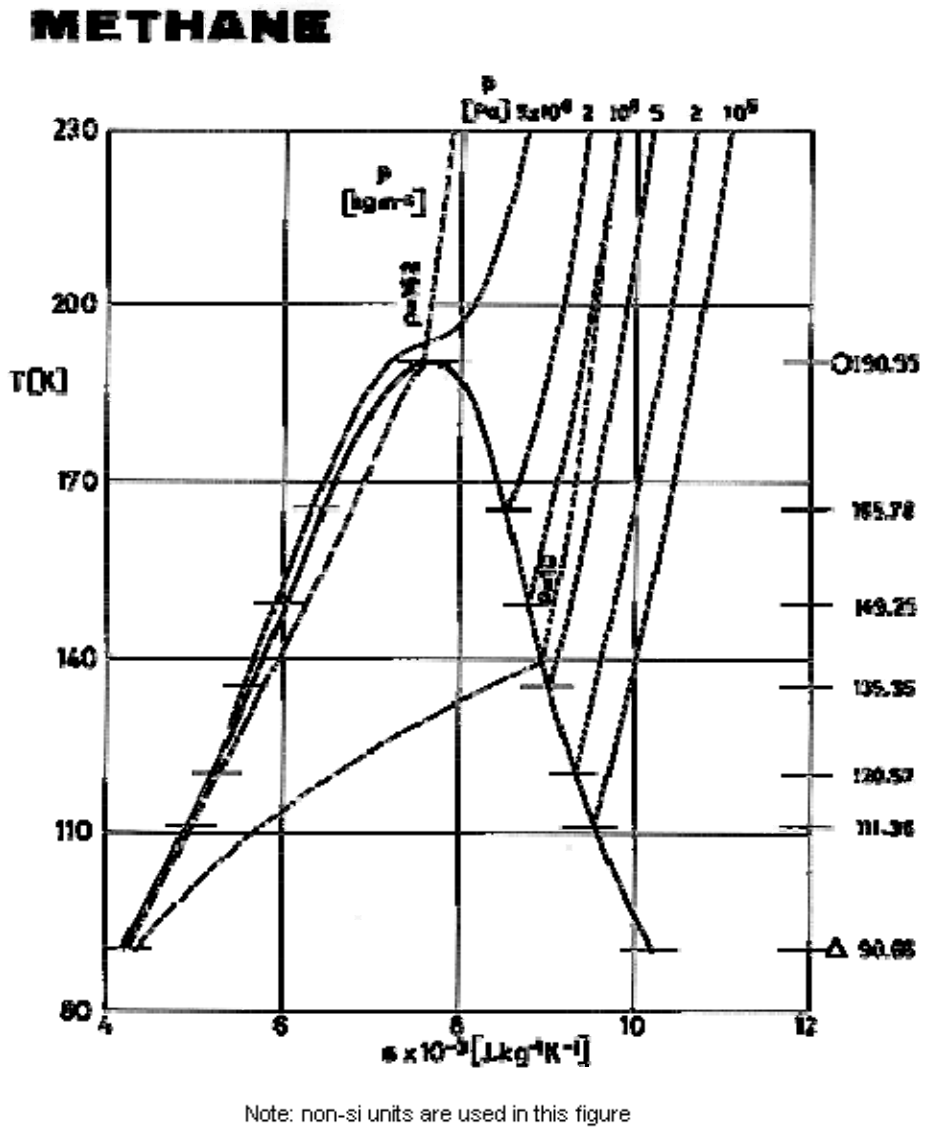

Note: non-si units are used in this figure

Figure 8-84: Temperature, *T*, entropy, *s*, diagram for Methane. From Vargaftik (1975) [253]. Tabulated values up to $T = 1000$ K and $p = 10^8$ Pa are given in pp. 211 and ff. of the mentioned source. Saturation curve and typical isobars and isochores are shown in the figure.

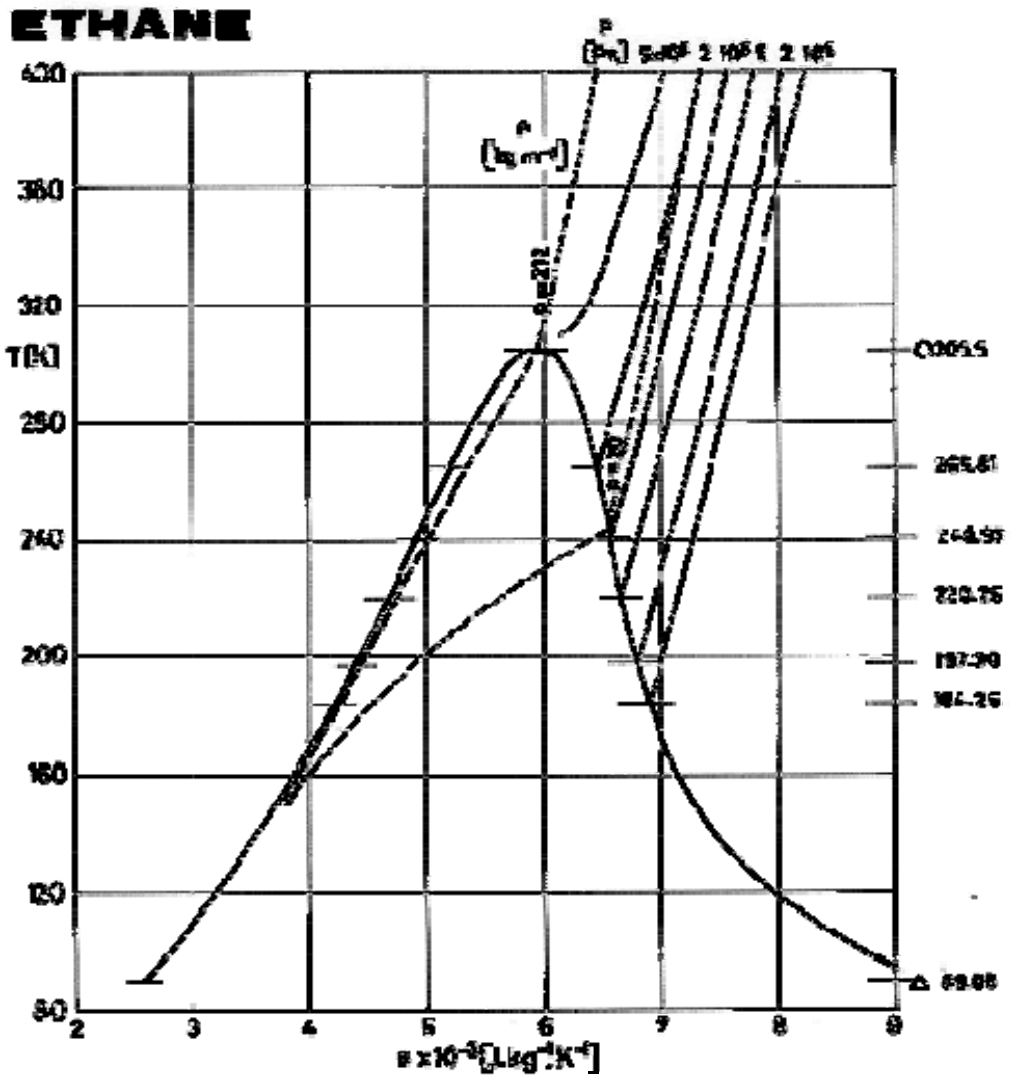

Note: non-si units are used in this figure

Figure 8-85: Temperature, *T*, entropy, *s*, diagram for Ethane. From Vargaftik (1975) [253]. Tabulated values up to *T* = 500 K and *p* = 5x10^7 Pa are given in pp. 225 and ff. of the mentioned source. Saturation curve and typical isobars and isochores are shown in the figure.

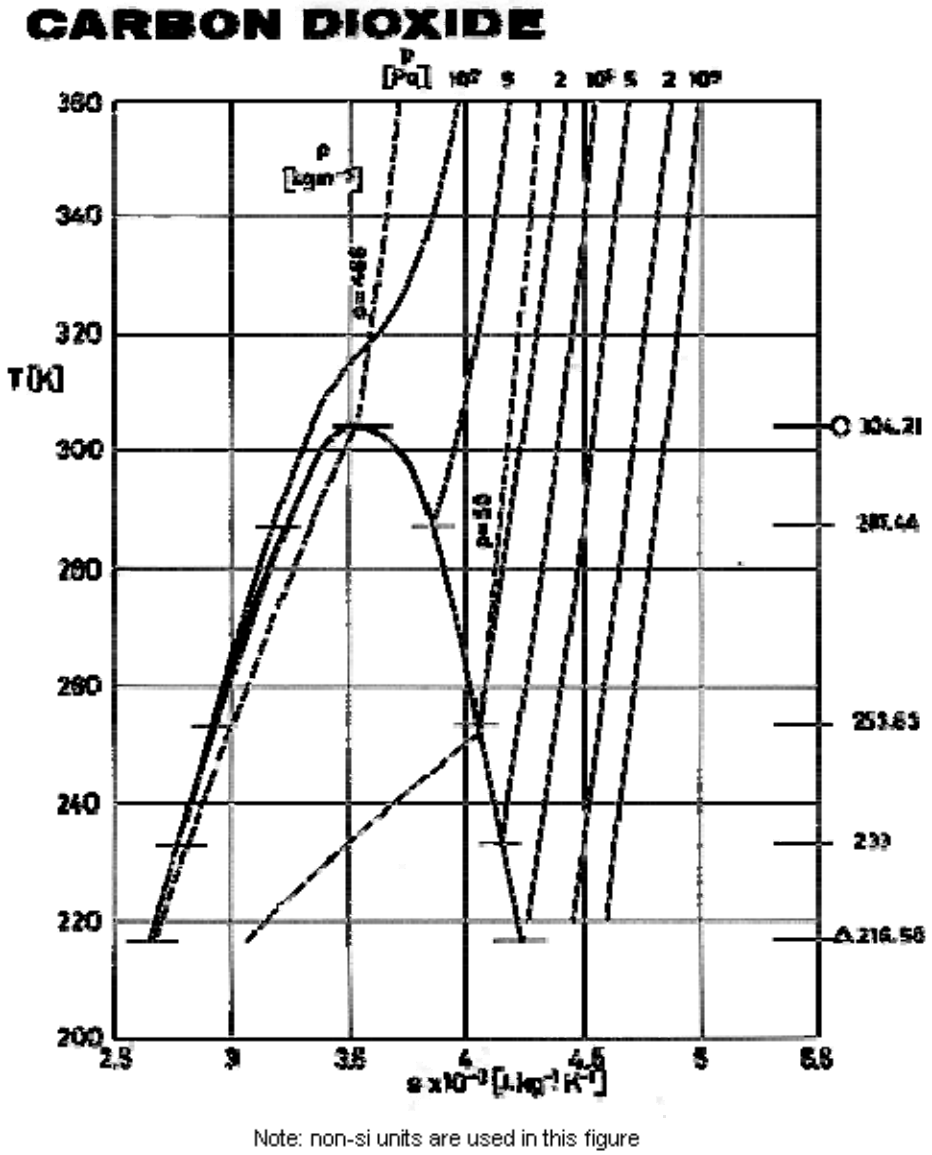

Figure 8-86: Temperature, *T*, entropy, *s*, diagram for Carbon Dioxide. From Angus, Armstrong & de Reuck (1976) [5]. Tabulated values up to *T* = 1100 K and *p* = 10^8 Pa are given in pp. 84 and ff. of the mentioned source. Saturation curve and typical isobars and isochores are shown in the figure.

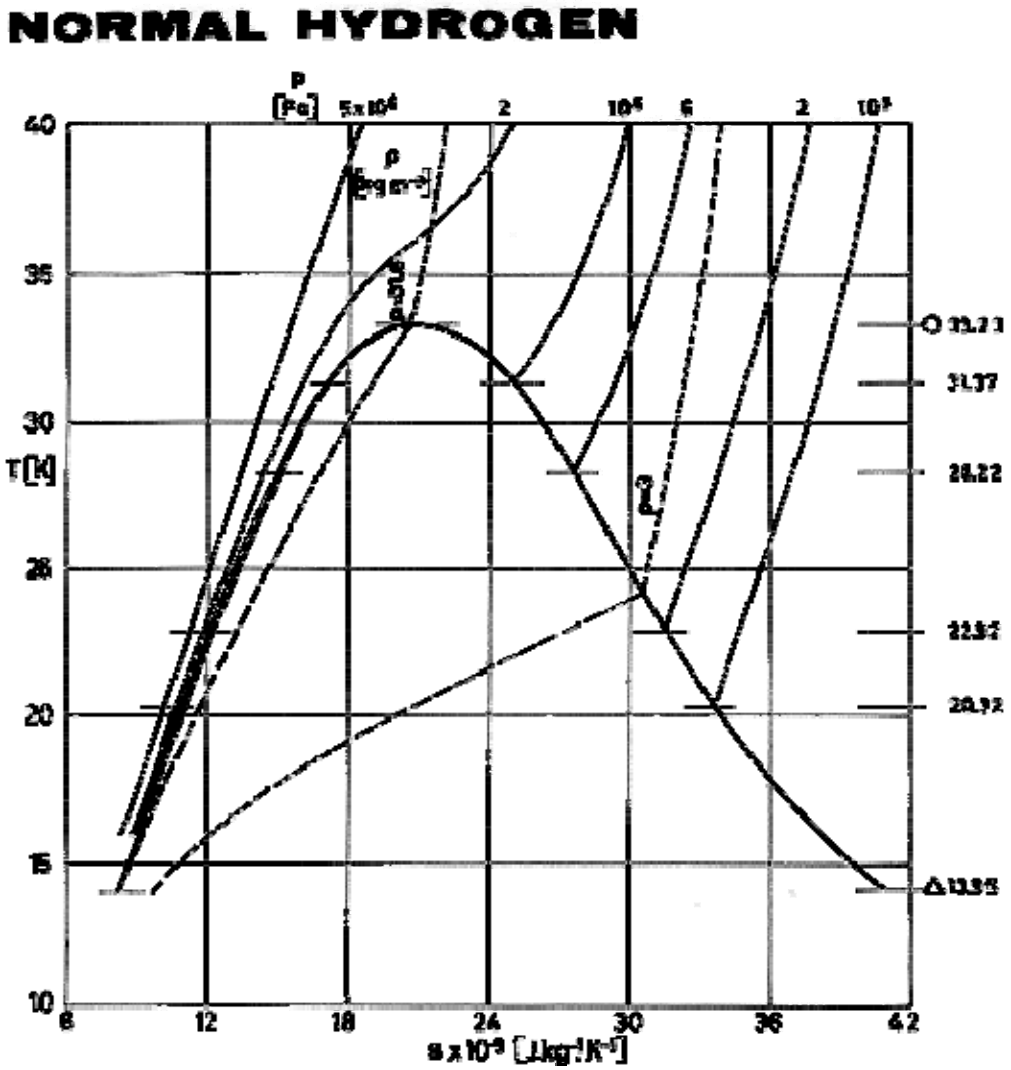

Figure 8-87: Temperature, *T*, entropy, *s*, diagram for Normal Hydrogen. From Vargaftik (1975) [253]. Tabulated values up to $T = 500$ K and $p = 10^8$ Pa are given in pp. 8 and ff. of the mentioned source. Saturation curve and typical isobars and isochores are shown in the figure.

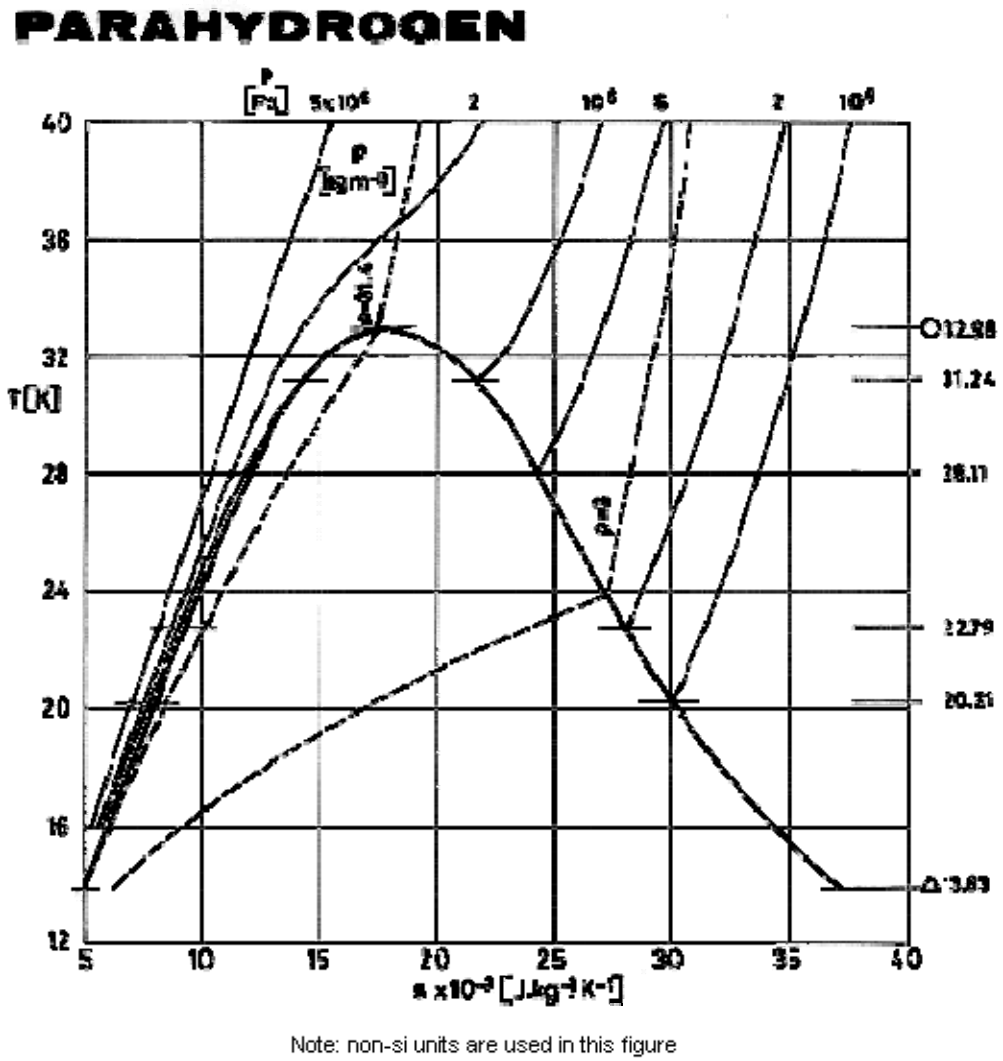

Figure 8-88: Temperature, *T*, entropy, *s*, diagram for Parahydrogen. From Vargaftik (1975) [253]. Tabulated values up to $T = 500$ K and $p = 10^8$ Pa are given in pp. 9, and 16 and ff. of the mentioned source. Saturation curve and typical isobars and isochores are shown in the figure.

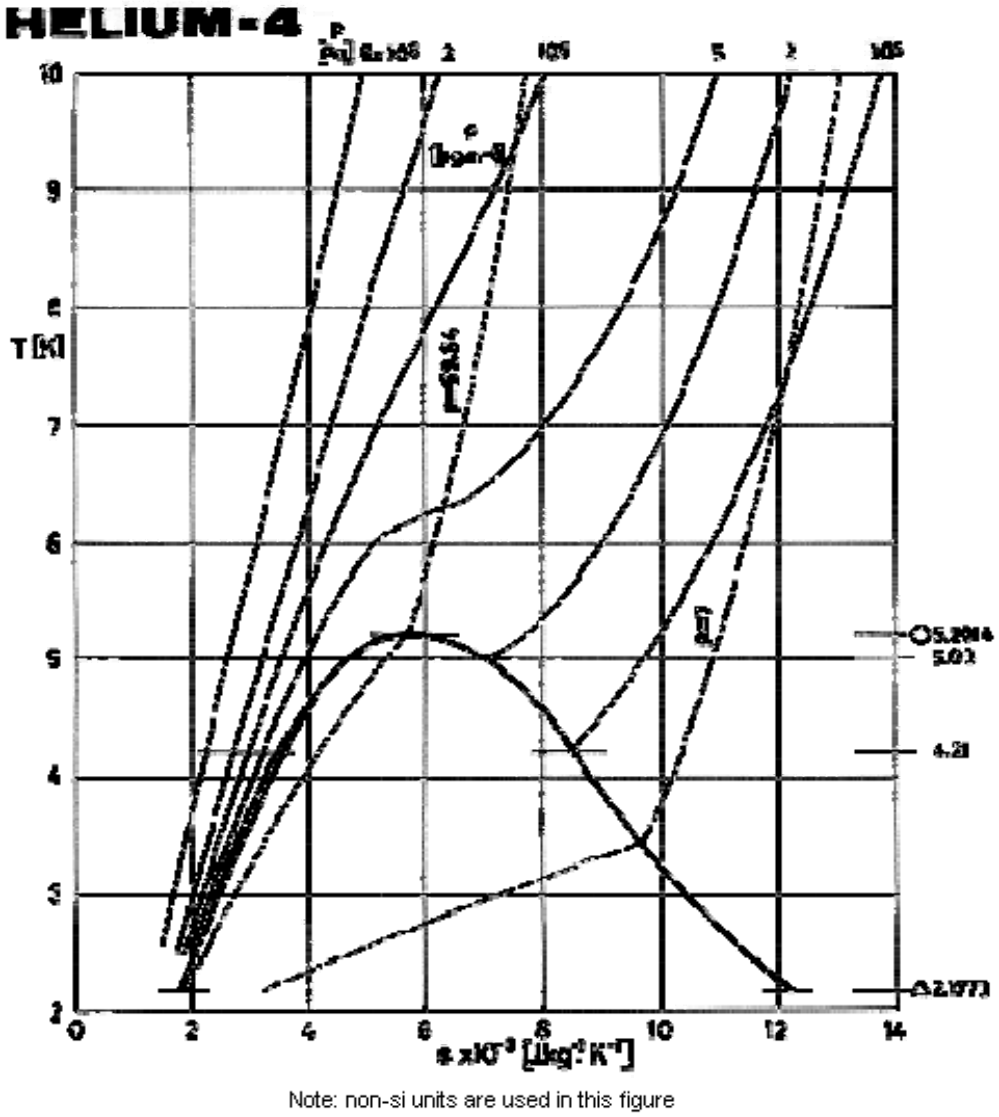

Note: non-si units are used in this figure

Figure 8-89: Temperature, *T*, entropy, *s*, diagram for Helium-4. From Angus & de Reuck (1977) [253]. Tabulated values up to *T* = 1400 K and *p* = 7x10^7 Pa are given in pp. 64 and ff. of the mentioned source. Saturation curve and typical isobars and isochores are shown in the figure.

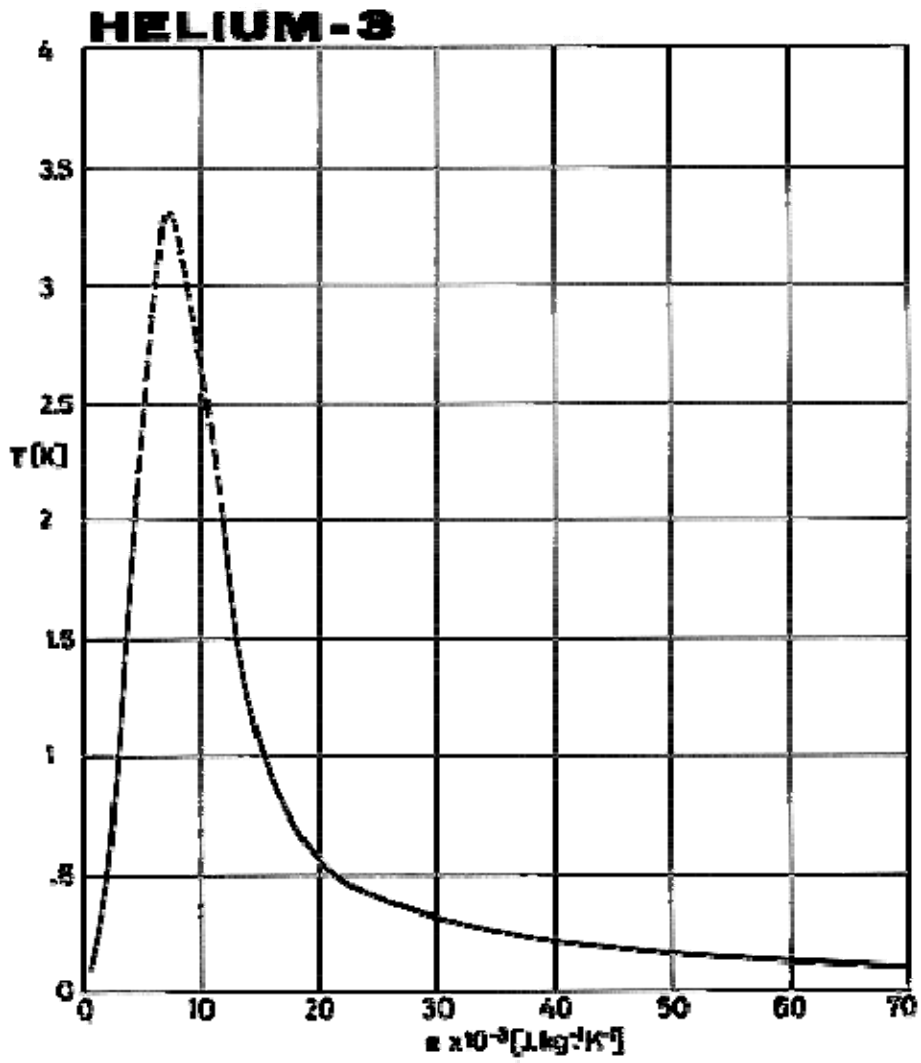

Note: non-si units are used in this figure

Figure 8-90: Temperature, *T*, entropy, *s*, diagram for Helium-3. From Conte (1970) [48]. Only the saturation curve is shown in this figure.

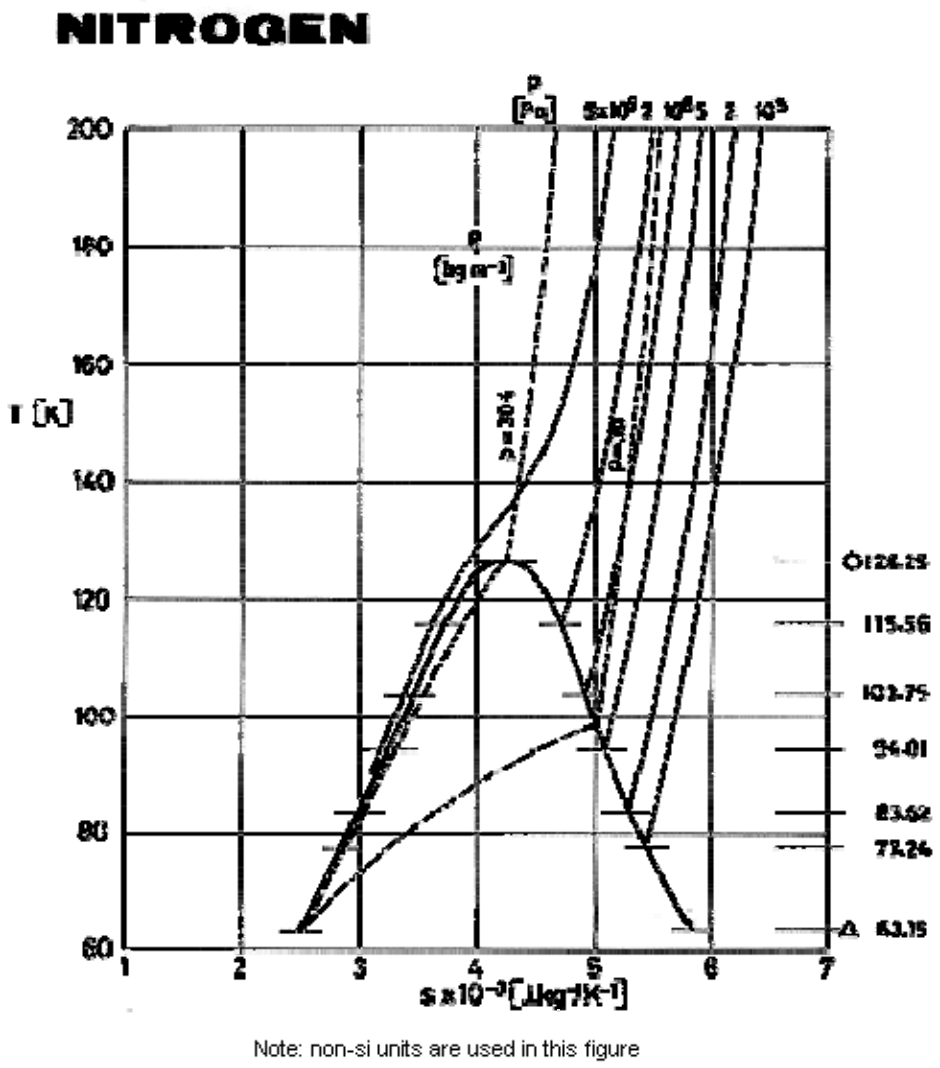

Figure 8-91: Temperature, *T*, entropy, *s*, diagram for Nitrogen. From Vargaftik (1975) [253]. Tabulated values up to *T* = 1300 K and *p* = 10^8 Pa are given in pp. 433 and ff. of the mentioned source. Saturation curve and typical isobars and isochores are shown in the figure.

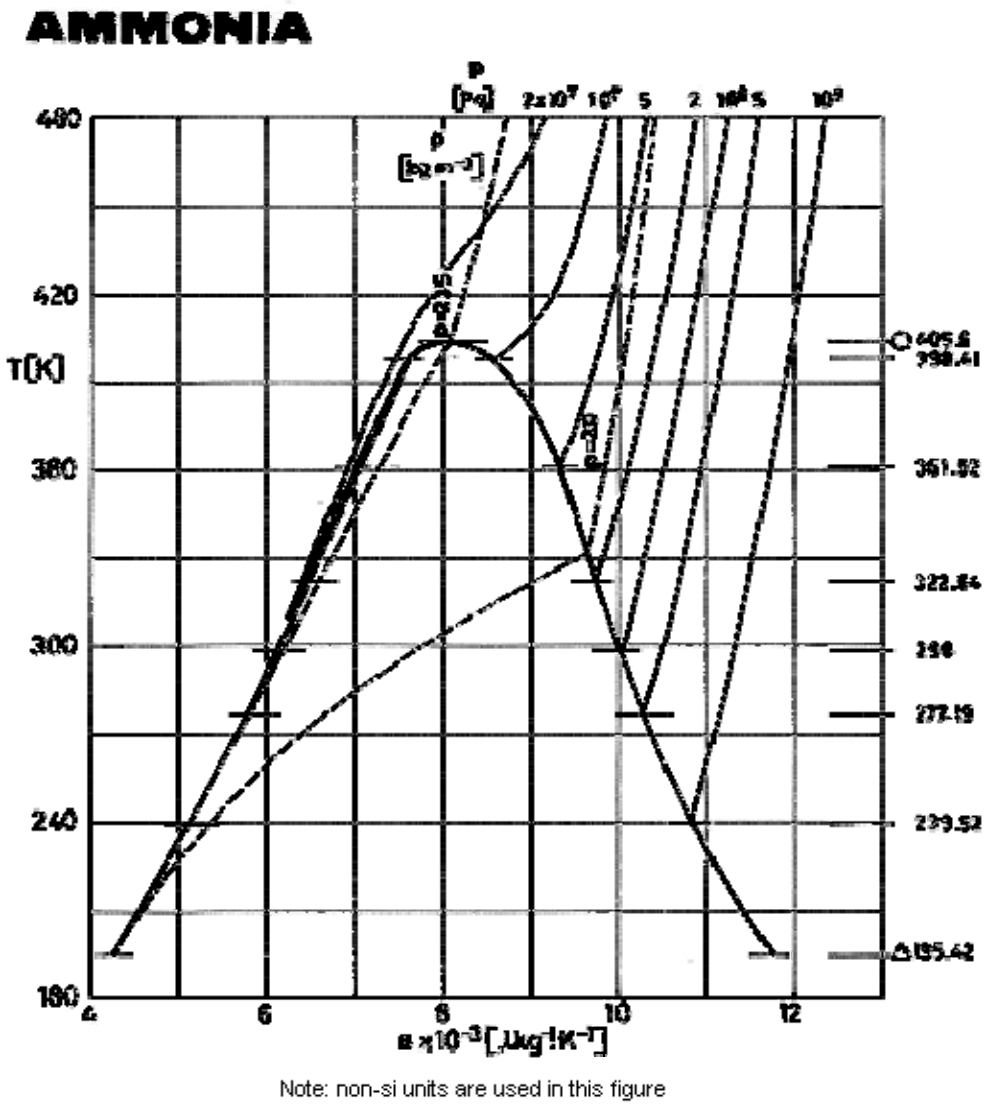

Figure 8-92: Temperature, *T*, entropy, *s*, diagram for Ammonia. From Vargaftik (1975) [253]. Tabulated values up to $T = 560$ K and $p = 1{,}1 \times 10^8$ Pa are given in pp. 464 and ff. of the mentioned source. Saturation curve and typical isobars and isochores are shown in the figure.

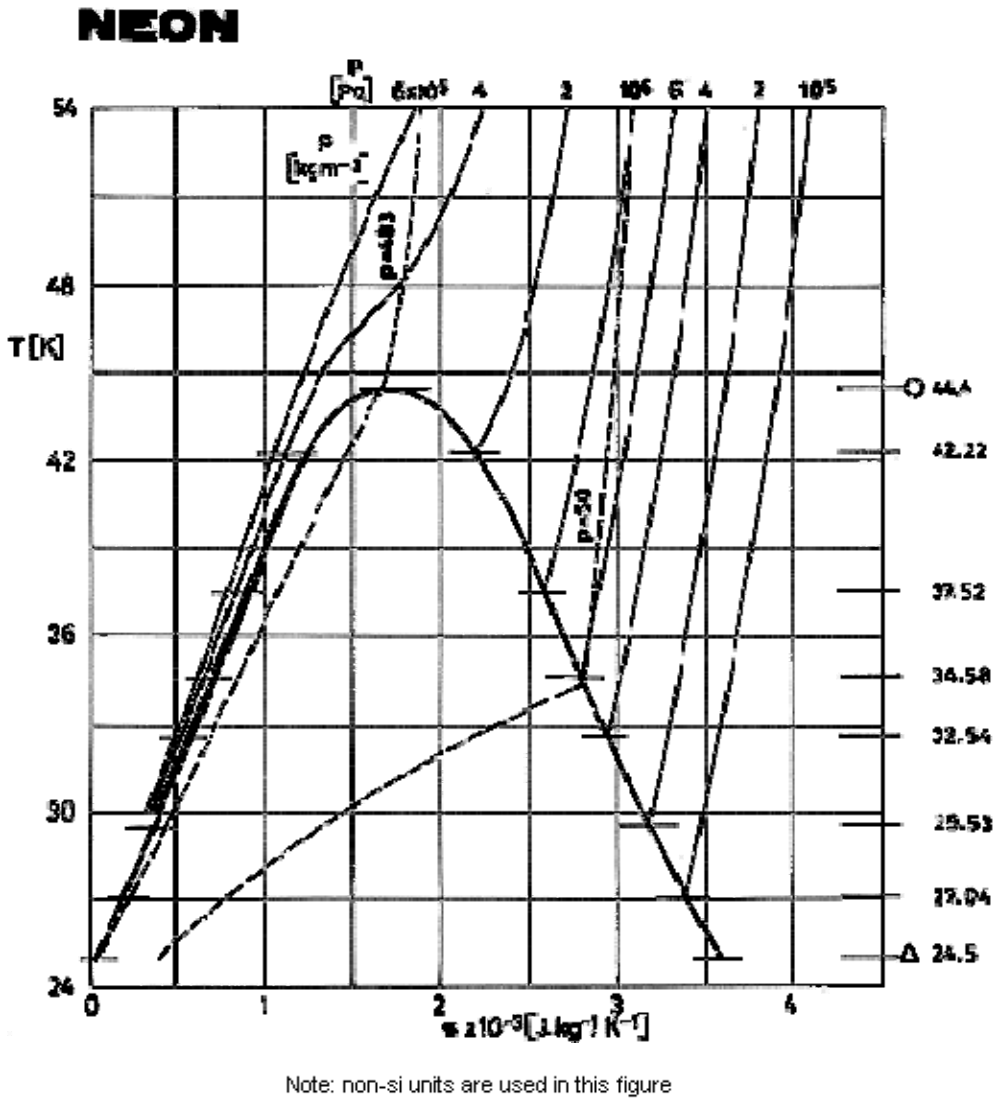

Note: non-si units are used in this figure

Figure 8-93: Temperature, *T*, entropy, *s*, diagram for Neon. From Vargaftik (1975) [253]. Tabulated values up to *T* = 300 K and *p* = 2x10^7 Pa are given in pp. 536 and ff. of the mentioned source. Saturation curve and typical isobars and isochores are shown in the figure.

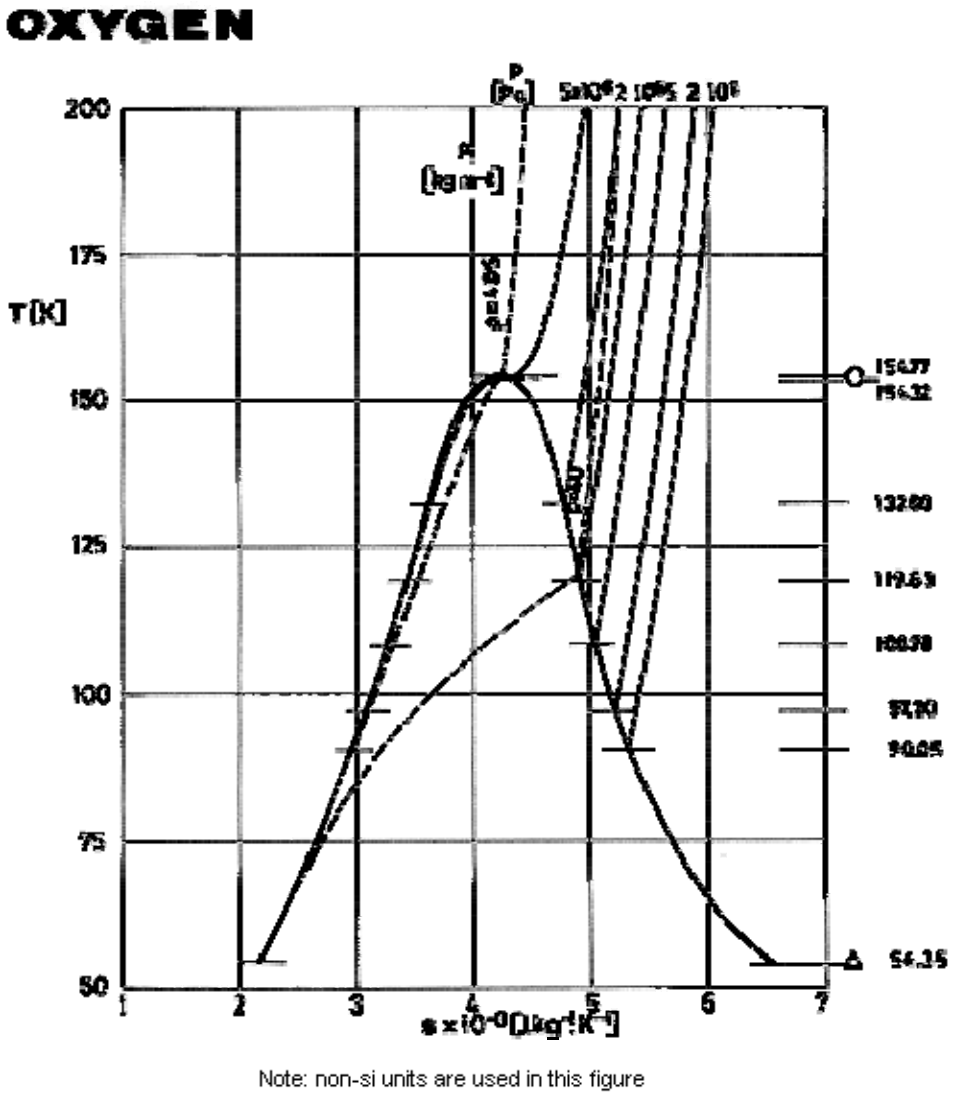

Note: non-si units are used in this figure

Figure 8-94: Temperature, *T*, entropy, *s*, diagram for Oxygen. From Vargaftik (1975) [253]. Tabulated values up to *T* = 1300 K and *p* = 10^8 Pa are given in pp. 477 and ff. of the mentioned source. Saturation curve and typical isobars and isochores are shown in the figure.

8.1.2.1 Entropy departures from perfect gas laws

Corrections for departures from the perfect gas behavior for entropy and enthalpy with pressure can be found in ordinary textbooks on Thermodynamics. For pure, non-polar substances these departures can be estimated once for all by using generalized tables in terms of reduced pressure and temperature ($p_r = p/p_c$, $T_r = T/T_c$) according to the rule of corresponding states (Sonntag & Van Wylen (1981) [226]). This rule, if assumed to hold exactly, would give a single functional relationship between p_r, T_r and ρ_r.

From a systematic analysis of the data from 82 different compounds, Lydersen, Greenkorn & Hougen (see Tribus (1961) [241]) found that gases having the same value of the compressibility factor at the critical point, $Z_c = (p_c/\rho_c)(RT_c/M)$, show approximately the same bahavior.

Here we will be concerned with entropy departures, given in Table 8-4. In this table superscript * indicates perfect gas behavior.

For a perfect gas, the entropy at pressure p and temperature T in terms of that for a reference state, subscript o, is given by

$$s - s_o = \int_o c_p \frac{dT}{T} - \frac{R}{M} \ln \frac{p}{p_o} \qquad [8\text{-}1]$$

Table 8-4: Entropy Departure of Saturated Liquid and Vapor

	$s^*–s$ (liquid) [J.mol^{-1}.K^{-1}]		$s^*–s$ (vapor) [J.mol^{-1}.K^{-1}]	
T_r	Z_c = 0,25	Z_c = 0,29	Z_c = 0,25	Z_c = 0,29
0,50	131,80	93,68	0,0753	0,0586
0,55	116,36	83,05	0,1356	0,084
0,60	102,88	74,31	0,364	0,310
0,65	89,08	66,57	0,736	0,703
0,70	80,58	60,00	1,573	1,339
0,75	71,17	53,81	2,364	2,042
0,80	62,43	48,16	2,925	2,586
0,85	54,52	42,55	4,73	4,44
0,90	46,90	37,32	6,95	6,23
0,92	43,81	35,19	8,16	7,11
0,94	40,67	33,01	9,67	8,28
0,96	37,32	29,37	11,84	9,67
0,98	33,26	25,94	14,98	12,01
1,00	23,68	16,69	23,68	16,69

	$s^*–s$ (liquid) [J.mol^{-1}.K^{-1}]		$s^*–s$ (vapor) [J.mol^{-1}.K^{-1}]	
P_r	Z_c = 0,25	Z_c = 0,29	Z_c = 0,25	Z_c = 0,29
0,05	78,53	64,85	1,519	0,920
0,10	69,50	58,41	2,611	1,494
0,15	63,64	53,93	3,109	2,121
0,20	59,66	50,25	3,699	2,761
0,25	56,32	47,91	4,238	3,117
0,30	53,76	45,65	4,883	3,515
0,35	51,17	43,60	5,577	4,27
0,40	49,25	41,63	6,28	4,77

	$s^*–s$ (liquid) [J.mol^{-1}.K^{-1}]		$s^*–s$ (vapor) [J.mol^{-1}.K^{-1}]	
P_r	Z_c = 0,25	Z_c = 0,29	Z_c = 0,25	Z_c = 0,29
0,45	47,15	39,96	6,99	5,40
0,50	45,27	38,20	7,57	5,94
0,55	43,72	36,69	8,45	6,53
0,60	41,80	35,23	9,04	6,99
0,65	40,58	34,02	9,96	7,70
0,70	38,91	32,80	10,88	8,37
0,75	37,57	31,38	12,01	9,12
0,80	35,82	30,21	13,05	10,00
0,85	34,27	28,95	14,14	11,00
0,90	32,72	27,49	15,90	12,13
0,95	30,00	25,31	17,87	13,72
1,00	23,68	16,69	23,68	16,69

$s^*–s$ [J.mol^{-1}.K^{-1}] for Z_c = 0,27													
P_r T_r	0,1	0,2	0,4	0,6	0,8	1,0	1,2	1,6	2,0	4,0	6,0	10	30
0,60	77,78	72,22	66,73	63,72	62,01	60,38	58,66	56,74	55,02	50,46	48,49	47,49	47,07
0,80	1,67	58,03	52,63	49,54	47,36	45,86	44,69	42,51	41,05	36,82	34,56	32,51	31,00
0,90	1,17	2,30	5,02	42,34	40,25	38,74	37,87	36,74	35,77	32,17	30,29	28,95	28,91
0,94	1,00	1,97	4,23	7,20	36,74	35,52	34,60	33,97	33,39	30,17	28,83	27,32	27,70
0,98	0,88	1,67	3,47	5,82	10,04	30,12	30,50	30,42	30,33	28,12	26,99	26,11	26,57
1,00	0,79	1,55	3,10	5,23	8,58	20,88	27,61	28,62	28,62	26,78	26,15	25,27	25,82
1,02	0,71	1,46	2,85	4,73	7,53	12,84	26,36	26,36	26,94	25,69	25,15	24,35	24,77
1,04	0,67	1,34	2,64	4,35	6,78	10,63	15,82	23,56	24,69	24,60	24,23	23,51	23,93
1,06	0,59	1,21	2,38	4,02	6,11	9,08	12,43	20,08	22,51	23,30	23,14	22,47	23,05
1,08	0,59	1,13	2,18	3,68	5,56	8,03	10,54	15,94	19,71	21,92	21,97	21,42	22,47
1,10	0,50	1,05	2,09	3,39	5,06	7,07	9,25	13,85	16,90	20,59	20,88	20,75	21,63
1,14	0,46	0,92	1,80	2,93	4,31	5,90	7,53	10,96	13,51	18,62	19,16	19,08	20,13
1,18	0,42	0,79	1,55	2,59	3,72	5,02	6,44	9,20	11,55	16,78	17,61	17,66	18,87
1,20	0,381	0,724	1,431	2,418	3,51	4,73	6,02	8,37	10,75	15,86	16,90	16,86	18,07
1,40	0,255	0,381	0,736	1,301	1,97	2,59	3,31	4,44	5,52	9,58	11,13	11,72	13,18
1,60	0,159	0,222	0,444	0,720	1,121	1,46	1,92	2,68	3,31	5,82	7,11	7,95	9,79
1,80	0,092	0,100	0,276	0,490	0,715	0,97	1,26	1,72	2,22	3,68	5,06	6,15	8,03

s^*-s [J.mol^{-1}.K^{-1}] for Z_c = 0,27													
P_r / T_r	**0,1**	**0,2**	**0,4**	**0,6**	**0,8**	**1,0**	**1,2**	**1,6**	**2,0**	**4,0**	**6,0**	**10**	**30**
2,00	0,063	0,042	0,163	0,318	0,510	0,74	0,88	1,17	1,51	3,01	4,06	5,02	6,78
4,00									0,13	0,25	0,04	0,21	1,67
6,00									0,00		0,00	0,25	2,09
10,00									-0,04		-0,29	0,63	1,84

NOTE Reference: Tribus (1961) [241].

8.1.2.2 8.2.1.2.2. Analytical correlations

The optimization of many cryogenic processes by digital computer requires analytical expressions for density, entropy and enthalpy which are uniformly valid in the whole fluid region.

A compilation of relevant formulae for most of the cryogenic fluids listed in Table 8-1 is enclosed in this paragraph.

Possible limitations of the formulae are:

1. Equation for density. Density, ρ, is related to pressure, p, and temperature, T, by the Equation of State. The following remarks, which were made in the past to Van der Waals equation are also relevant to other equations of state.

A sketch of the pressure p as a function of molar volume, v, ($v = 1/\rho$) at different temperatures, T, for a single component system is shown in Figure 8-95.

When $T<T_c$ a kink appears in the isotherms which is unphysical since it implies negative compressibility. This difficulty is overcome by the so-called Maxwell equal area rule. Points 1 and 2, which correspond to the saturation curve, are so placed that areas A and B are equal. In reality, a constant-pressure segment should represent the change 1-2 from liquid to vapor (see Huang (1963) [96]). This simple construction, based on a purely heuristic argument, indicates that for a single component liquid-gas system the Helmholtz potential, A, varies linearly with the molar volume, v, through the phase change ($dA = -sdT - pdV$, and, in the figure, $dT = 0$).

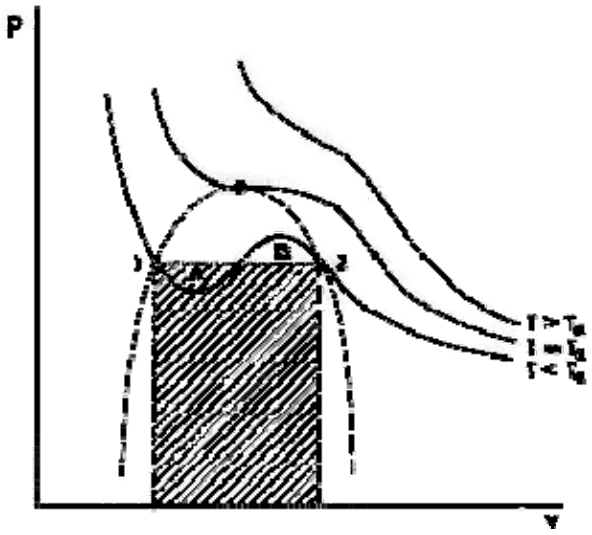

Figure 8-95: *p-v* diagram of a single-component system, illustrating the Maxwell equal area rule.

$$A_1 - A_2 = \int_1^2 pdv = Shadowed\ area\ in\ Fig.\ 4-95 \qquad [8\text{-}2]$$

2. Entropy and Enthalpy equations. These equations do not involve terms for change on evaporation. They can be used directly when calculating changes along a path through the saturation region.

3. Changes on evaporation. These changes can be calculated by inserting the liquid and vapor densities deduced from the equation of state into the equations for the entropy or enthalpy, respectively.

4. Properties along the saturation curve. They are calculated by using the Maxwell equal area rule.

5. Accuracy. In addition to the limits of validity of the different formulae, upper bounds for the errors are given whenever possible. These bounds are different for density (liquid or vapor), enthalpy or entropy and also differ markedly in the different domains of the *p*, *T* diagram, being higher in an area surrounding the critical conditions and in the region of large pressures.

Several authors present very detailed tolerance diagrams, which have not been reproduced here, whereas others merely quote the upper values. The user interested in further details could consult the references given at the end of each data sheet.

ARGON

EQUATION OF STATE

$$p = \rho T\left[\begin{array}{l} R + \rho B + \rho^2 C + \rho^3 D + \rho^4 E + \\ + \rho^5 F + \left(G + \rho^2 H\right)\rho^2 e^{-a_{20}\rho^2} \end{array}\right] \qquad [8\text{-}3]$$

$$B = a_1 - \frac{a_2}{T} - \frac{a_3}{T^2} - \frac{a_4}{T^3} - \frac{a_5}{T^5} \qquad [8\text{-}4]$$

$$C = a_6 + \frac{a_7}{T} + \frac{a_8}{T^2} \quad [8\text{-}5]$$

$$D = a_9 + \frac{a_{10}}{T} \quad [8\text{-}6]$$

$$E = a_{11} + \frac{a_{12}}{T} \quad [8\text{-}7]$$

$$F = \frac{a_{13}}{T} \quad [8\text{-}8]$$

$$G = \frac{a_{14}}{T^3} + \frac{a_{15}}{T^4} + \frac{a_{16}}{T^5} \quad [8\text{-}9]$$

$$H = \frac{a_{17}}{T^3} + \frac{a_{18}}{T^4} + \frac{a_{19}}{T^5} \quad [8\text{-}10]$$

R = 8,3143 J.K^{-1}.mol^{-1}, M = 39,948 x 10^{-3} kg.mol^{-1}, p [Pa], ρ [mol.m^{-3}], T [K]

The coefficients a_i are given in Table 8-5 below.

ENTROPY

$$s^o(T) = (36{,}4256 + 20{,}7857 \ln T)\, J.mol^{-1}.K^{-1} \quad [8\text{-}11]$$

$$\begin{aligned} s_1(\rho,T) = {} & \rho B' + \frac{\rho^2}{2} C' + \frac{\rho^3}{3} D' + \frac{\rho^4}{4} E' + \\ & + \frac{G'}{2a_{20}} \left(1 - e^{-a_{20}\rho^2}\right) + \\ & + \frac{H'}{2a_{20}^2} \left(1 - e^{-a_{20}\rho^2} - a_{20}\rho^2 e^{-a_{20}\rho^2}\right) \end{aligned} \quad [8\text{-}12]$$

$$B' = a_1 + \frac{a_3}{T^2} + 2\frac{a_4}{T^3} + 4\frac{a_5}{T^5} \quad [8\text{-}13]$$

$$C' = a_6 - \frac{a_8}{T^2} \quad [8\text{-}14]$$

$$D' = a_9 \quad [8\text{-}15]$$

$$E' = a_{11} \quad [8\text{-}16]$$

$$G' = -2\frac{a_{14}}{T^3} - 3\frac{a_{15}}{T^4} - 4\frac{a_{16}}{T^5} \quad [8\text{-}17]$$

$$H' = -2\frac{a_{17}}{T^3} - 3\frac{a_{18}}{T^4} - 4\frac{a_{19}}{T^5} \quad [8\text{-}18]$$

$$s = s^o(T) - R\ln\frac{\rho RT}{p_a} + s_1(\rho, T) \quad [8\text{-}19]$$

$s^o(T)$ indicates perfect gas conditions. Based on $c^o_p = (5/2)R$, $p_a = 1$ bar $= 10^5$ Pa.

ENTHALPY

$$h^o(T) = 20{,}7857T \ J.mol^{-1} \quad [8\text{-}20]$$

$$h_1(\rho, T) = T\left[\begin{array}{l} \rho B'' + \frac{\rho^2}{2}C'' + \frac{\rho^3}{3}D'' + \frac{\rho^4}{4}E'' + \\ + \frac{\rho^5}{5}F'' + \left(G + \rho^2 H\right)\rho^2 e^{-a_{20}\rho^2} + \\ + \frac{1}{2a_{20}^2}\left(a_{20}G'' + H''\right) - \\ - \frac{e^{-a_{20}\rho^2}}{2a_{20}^2}\left\{a_{20}G'' + \left(1 + a_{20}\rho^2\right)H''\right\} \end{array}\right] \quad [8\text{-}21]$$

$$B'' = a_1 - 2\frac{a_2}{T} - 3\frac{a_3}{T^2} - 4\frac{a_4}{T^3} - 6\frac{a_5}{T^5} \quad [8\text{-}22]$$

$$C'' = 2a_6 + 3\frac{a_7}{T} + 4\frac{a_8}{T^2} \quad [8\text{-}23]$$

$$D'' = 3a_9 + 4\frac{a_{10}}{T} \quad [8\text{-}24]$$

$$E'' = 4a_{11} + 5\frac{a_{12}}{T} \quad [8\text{-}25]$$

$$F'' = 6\frac{a_{13}}{T} \qquad [8\text{-}26]$$

$$G'' = 3\frac{a_{14}}{T^3} + 4\frac{a_{15}}{T^4} + 5\frac{a_{16}}{T^5} \qquad [8\text{-}27]$$

$$H'' = 3\frac{a_{17}}{T^3} + 4\frac{a_{18}}{T^4} + 5\frac{a_{19}}{T^5} \qquad [8\text{-}28]$$

$$h = h^o(T) + h_1(\rho, T) \qquad [8\text{-}29]$$

$h_o(T)$ indicates perfect gas conditions. Based on $c^o_p = (5/2)R$

Table 8-5: Values of the Coefficient a_i for Argon

a_1	$0{,}31639051 \times 10^{-3}$
a_2	0,13043320
a_3	$-0{,}28370046 \times 10^{1}$
a_4	$0{,}13150788 \times 10^{4}$
a_5	$-0{,}50534111 \times 10^{5}$
a_6	$-0{,}28179523 \times 10^{-8}$
a_7	$0{,}39628356 \times 10^{-5}$
a_8	$0{,}72951535 \times 10^{-4}$
a_9	$0{,}12172661 \times 10^{-11}$
a_{10}	$-0{,}50030773 \times 10^{-9}$
a_{11}	$-0{,}21947285 \times 10^{-16}$
a_{12}	$0{,}16831369 \times 10^{-13}$
a_{13}	$-0{,}11437390 \times 10^{-18}$
a_{14}	$0{,}52614785 \times 10^{-2}$
a_{15}	–0,58356378
a_{16}	$-0{,}11692362 \times 10^{3}$

a_{17}	$-0{,}34445957 \times 10^{-9}$
a_{18}	$0{,}15802557 \times 10^{-6}$
a_{19}	$-0{,}68651100 \times 10^{-5}$
a_{20}	$0{,}55854495 \times 10^{-8}$

NOTE References: Bender (1973) [22], Vargaftik (1975) [253].

METHANE

EQUATION OF STATE

$$p = \rho T \left[\begin{array}{l} R + \rho B + \rho^2 C + \rho^3 D + \rho^4 E + \\ + \rho^5 F + \left(G + \rho^2 H \right) \rho^2 e^{-a_{20}\rho^2} \end{array} \right] \quad [8\text{-}30]$$

$$B = a_1 - \frac{a_2}{T} - \frac{a_3}{T^2} - \frac{a_4}{T^3} - \frac{a_5}{T^5} \quad [8\text{-}31]$$

$$C = a_6 + \frac{a_7}{T} + \frac{a_8}{T^2} \quad [8\text{-}32]$$

$$D = a_9 + \frac{a_{10}}{T} \quad [8\text{-}33]$$

$$E = a_{11} + \frac{a_{12}}{T} \quad [8\text{-}34]$$

$$F = \frac{a_{13}}{T} \quad [8\text{-}35]$$

$$G = \frac{a_{14}}{T^3} + \frac{a_{15}}{T^4} + \frac{a_{16}}{T^5} \quad [8\text{-}36]$$

$$H = \frac{a_{17}}{T^3} + \frac{a_{18}}{T^4} + \frac{a_{19}}{T^5} \quad [8\text{-}37]$$

The external limits of this equation are: 10^4 Pa < p < 10^8 Pa; T_b at 10^4 Pa < T < 573 K.

R = 8,3143 J.K^{-1}.mol^{-1}, M = 16,043 x 10^{-3} kg.mol^{-1}, p [Pa], ρ [mol.m^{-3}], T [K]

The coefficients a_i are given in Table 8-6 below.

ENTROPY

$$s^o(T) = R\left[\sum_{n=0}^{4} \alpha_n T^n + \alpha_5 \ln T\right] \quad [8\text{-}38]$$

$$s_1(\rho,T) = \rho B' + \frac{\rho^2}{2} C' + \frac{\rho^3}{3} D' + \frac{\rho^4}{4} E' + \\ + \frac{G'}{2a_{20}}\left(1 - e^{-a_{20}\rho^2}\right) + \frac{H'}{2a_{20}^2}\left(1 - e^{-a_{20}\rho^2} - a_{20}\rho^2 e^{-a_{20}\rho^2}\right) \quad [8\text{-}39]$$

$$B' = a_1 + \frac{a_3}{T^2} + 2\frac{a_4}{T^3} + 4\frac{a_5}{T^5} \quad [8\text{-}40]$$

$$C' = a_6 - \frac{a_8}{T^2} \quad [8\text{-}41]$$

$$D' = a_9 \quad [8\text{-}42]$$

$$E' = a_{11} \quad [8\text{-}43]$$

$$G' = -2\frac{a_{14}}{T^3} - 3\frac{a_{15}}{T^4} - 4\frac{a_{16}}{T^5} \quad [8\text{-}44]$$

$$H' = -2\frac{a_{17}}{T^3} - 3\frac{a_{18}}{T^4} - 4\frac{a_{19}}{T^5} \quad [8\text{-}45]$$

$$s = s^o(T) - R\ln\frac{\rho RT}{p_a} + s_1(\rho,T) \quad [8\text{-}46]$$

$s^o(T)$ indicates perfect gas conditions. The coefficients α_n are given in Table 8-6 below. $s^o(T)$ [J.mol^{-1}.K^{-1}], p_a = 1 bar = 10^5Pa.

ENTHALPY

$$h^o(T) = RT\sum_{n=0}^{4} \beta_n T^{n-2} \quad [8\text{-}47]$$

This equation is not accurate below 255,4 K and should not be differentiated to obtain heat capacities.

$$h_1(\rho,T)=T\left[\begin{array}{l}\rho B''+\frac{\rho^2}{2}C''+\frac{\rho^3}{3}D''+\frac{\rho^4}{4}E''+\\+\frac{\rho^5}{5}F''+\left(G+\rho^2H\right)\rho^2e^{-a_{20}\rho^2}+\\+\frac{1}{2a_{20}^2}\left(a_{20}G''+H''\right)-\\-\frac{e^{-a_{20}\rho^2}}{2a_{20}^2}\left\{a_{20}G''+\left(1+a_{20}\rho^2\right)H''\right\}\end{array}\right] \quad [8\text{-}48]$$

$$B''=a_1-2\frac{a_2}{T}-3\frac{a_3}{T^2}-4\frac{a_4}{T^3}-6\frac{a_5}{T^5} \quad [8\text{-}49]$$

$$C''=2a_6+3\frac{a_7}{T}+4\frac{a_8}{T^2} \quad [8\text{-}50]$$

$$D''=3a_9+4\frac{a_{10}}{T} \quad [8\text{-}51]$$

$$E''=4a_{11}+5\frac{a_{12}}{T} \quad [8\text{-}52]$$

$$F''=6\frac{a_{13}}{T} \quad [8\text{-}53]$$

$$G''=3\frac{a_{14}}{T^3}+4\frac{a_{15}}{T^4}+5\frac{a_{16}}{T^5} \quad [8\text{-}54]$$

$$H''=3\frac{a_{17}}{T^3}+4\frac{a_{18}}{T^4}+5\frac{a_{19}}{T^5} \quad [8\text{-}55]$$

$$h=h^o(T)+h_1(\rho,T) \quad [8\text{-}56]$$

$h_o(T)$ indicates perfect gas conditions. The coefficients bn are given in Table 8-6 below. $h(T)$ [J.mol^{-1}].

ACCURACY

s^o: 1%, h^o: 1%.

Table 8-6: Values of the Coefficients a_i, α_n and β_n for Methane

a_1	$4{,}42458771 \times 10^{-4}$
a_2	$2{,}22287989 \times 10^{-1}$
a_3	$-6{,}43579378$
a_4	$3{,}22593481 \times 10^{3}$
a_5	$-8{,}79448445 \times 10^{4}$
a_6	$3{,}11845829 \times 10^{-9}$
a_7	$-5{,}00086474 \times 10^{-7}$
a_8	$8{,}48416567 \times 10^{-4}$
a_9	$2{,}14214720 \times 10^{-12}$
a_{10}	$-4{,}10366448 \times 10^{-10}$
a_{11}	$-2{,}72102444 \times 10^{-17}$
a_{12}	$1{,}22818063 \times 10^{-15}$
a_{13}	$4{,}67589592 \times 10^{-19}$
a_{14}	$2{,}04389516 \times 10^{-1}$
a_{15}	$-4{,}93682301 \times 10^{1}$
a_{16}	$3{,}64612970 \times 10^{3}$
a_{17}	$-3{,}37032590 \times 10^{-9}$
a_{18}	$1{,}30738840 \times 10^{-6}$
a_{19}	$-6{,}85462109 \times 10^{-5}$
a_{20}	$9{,}52298031 \times 10^{-9}$
α_0	$6{,}293052 \times 10^{2}$
α_1	$-1{,}181714 \times 10^{-1}$
α_2	$6{,}013609 \times 10^{-4}$
α_3	$-3{,}530733 \times 10^{-9}$
α_4	$7{,}347745 \times 10^{-11}$

α_5	2,212805x10^{2}
β_0	7,170851x10^{5}
β_1	2,095385x10^{4}
β_2	1,853977x10^{2}
β_3	1,818417x10^{-1}
β_4	–6,240077x10^{-6}

NOTE References: API (1952) [8], Bühner, Maurer & Bender (1981) [34].

ETHANE

EQUATION OF STATE

$$p = \rho T\left[\begin{array}{l} R + \rho B + \rho^2 C + \rho^3 D + \rho^4 E + \\ + \rho^5 F + \left(G + \rho^2 H\right)\rho^2 e^{-a_{20}\rho^2} \end{array}\right] \quad [8\text{-}57]$$

$$B = a_1 - \frac{a_2}{T} - \frac{a_3}{T^2} - \frac{a_4}{T^3} - \frac{a_5}{T^5} \quad [8\text{-}58]$$

$$C = a_6 + \frac{a_7}{T} + \frac{a_8}{T^2} \quad [8\text{-}59]$$

$$D = a_9 + \frac{a_{10}}{T} \quad [8\text{-}60]$$

$$E = a_{11} + \frac{a_{12}}{T} \quad [8\text{-}61]$$

$$F = \frac{a_{13}}{T} \quad [8\text{-}62]$$

$$G = \frac{a_{14}}{T^3} + \frac{a_{15}}{T^4} + \frac{a_{16}}{T^5} \quad [8\text{-}63]$$

$$H = \frac{a_{17}}{T^3} + \frac{a_{18}}{T^4} + \frac{a_{19}}{T^5} \quad [8\text{-}64]$$

The external limits of this equation are: 10^4 Pa < p < 10^8 Pa; T_b at 10^4 Pa < T < 573 K.

R = 8,3143 J.K^{-1}.mol^{-1}, M = 30,068 x 10^{-3} kg.mol^{-1}, p [Pa], ρ [mol.m^{-3}], T [K]

The coefficients a_i are given in Table 8-7 below.

ENTROPY

$$s^o(T) = R\left[\sum_{n=0}^{4}\alpha_n T^n + \alpha_5 \ln T\right] \quad [8\text{-}65]$$

$$s_1(\rho,T) = \rho B' + \frac{\rho^2}{2}C' + \frac{\rho^3}{3}D' + \frac{\rho^4}{4}E' + \\ + \frac{G'}{2a_{20}}\left(1-e^{-a_{20}\rho^2}\right) + \frac{H'}{2a_{20}^2}\left(1-e^{-a_{20}\rho^2} - a_{20}\rho^2 e^{-a_{20}\rho^2}\right) \quad [8\text{-}66]$$

$$B' = a_1 + \frac{a_3}{T^2} + 2\frac{a_4}{T^3} + 4\frac{a_5}{T^5} \quad [8\text{-}67]$$

$$C' = a_6 - \frac{a_8}{T^2} \quad [8\text{-}68]$$

$$D' = a_9 \quad [8\text{-}69]$$

$$E' = a_{11} \quad [8\text{-}70]$$

$$G' = -2\frac{a_{14}}{T^3} - 3\frac{a_{15}}{T^4} - 4\frac{a_{16}}{T^5} \quad [8\text{-}71]$$

$$H' = -2\frac{a_{17}}{T^3} - 3\frac{a_{18}}{T^4} - 4\frac{a_{19}}{T^5} \quad [8\text{-}72]$$

$$s = s^o(T) - R\ln\frac{\rho RT}{p_a} + s_1(\rho,T) \quad [8\text{-}73]$$

$s^o(T)$ indicates perfect gas conditions. The coefficients α_n are given in Table 8-7 below. $s^o(T)$ [J.mol^{-1}.K^{-1}], p_a = 1 bar = 10^5Pa.

ENTHALPY

$$h^o(T) = RT\sum_{n=0}^{4}\beta_n T^{n-2} \quad [8\text{-}74]$$

This equation is not accurate below 255,4 K and should not be differentiated to obtain heat capacities.

$$h_1(\rho,T)=T\left[\begin{array}{l}\rho B''+\frac{\rho^2}{2}C''+\frac{\rho^3}{3}D''+\frac{\rho^4}{4}E''+\\+\frac{\rho^5}{5}F''+\left(G+\rho^2H\right)\rho^2e^{-a_{20}\rho^2}+\\+\frac{1}{2a_{20}^2}\left(a_{20}G''+H''\right)-\\-\frac{e^{-a_{20}\rho^2}}{2a_{20}^2}\left\{a_{20}G''+\left(1+a_{20}\rho^2\right)H''\right\}\end{array}\right] \quad [8\text{-}75]$$

$$B''=a_1-2\frac{a_2}{T}-3\frac{a_3}{T^2}-4\frac{a_4}{T^3}-6\frac{a_5}{T^5} \quad [8\text{-}76]$$

$$C''=2a_6+3\frac{a_7}{T}+4\frac{a_8}{T^2} \quad [8\text{-}77]$$

$$D''=3a_9+4\frac{a_{10}}{T} \quad [8\text{-}78]$$

$$E''=4a_{11}+5\frac{a_{12}}{T} \quad [8\text{-}79]$$

$$F''=6\frac{a_{13}}{T} \quad [8\text{-}80]$$

$$G''=3\frac{a_{14}}{T^3}+4\frac{a_{15}}{T^4}+5\frac{a_{16}}{T^5} \quad [8\text{-}81]$$

$$H''=3\frac{a_{17}}{T^3}+4\frac{a_{18}}{T^4}+5\frac{a_{19}}{T^5} \quad [8\text{-}82]$$

$$h=h^o(T)+h_1(\rho,T) \quad [8\text{-}83]$$

$h_o(T)$ indicates perfect gas conditions. The coefficients bn are given in Table 8-7 below. $h^o(T)$ [J.mol^{-1}].

ACCURACY

ρ: 2,12% AAD, s^o: 1%, s-s^o: 0,34% AAD, h^o: 1%, h-h^o: 0,62 % AAD.

Table 8-7: Values of the Coefficients a_i, α_n and β_n for Ethane

a_1	$1{,}24601531 \times 10^{-3}$
a_2	1,02733836
a_3	$-1{,}50606401 \times 10^{2}$
a_4	$3{,}60019215 \times 10^{4}$
a_5	$-2{,}28756697 \times 10^{6}$
a_6	$-8{,}08294382 \times 10^{-8}$
a_7	$7{,}59178750 \times 10^{-5}$
a_8	$-2{,}91069937 \times 10^{-4}$
a_9	$1{,}25678254 \times 10^{-11}$
a_{10}	$-8{,}15974846 \times 10^{-9}$
a_{11}	$-2{,}18811732 \times 10^{-16}$
a_{12}	$1{,}97130389 \times 10^{-13}$
a_{13}	$4{,}47415537 \times 10^{-18}$
a_{14}	−7,50435029
a_{15}	$4{,}86574340 \times 10^{3}$
a_{16}	$-8{,}99282035 \times 10^{5}$
a_{17}	$2{,}81246078 \times 10^{-8}$
a_{18}	$-5{,}44729898 \times 10^{-5}$
a_{19}	$1{,}63714832 \times 10^{-2}$
a_{20}	$2{,}35062004 \times 10^{-8}$
α_0	$5{,}637432 \times 10^{2}$
α_1	$-4{,}230089 \times 10^{-2}$
α_2	$6{,}510299 \times 10^{-4}$
α_3	$-4{,}376264 \times 10^{-7}$

α_4	1,001644x10^{-10}
α_5	1,445599x10^{2}
β_0	6,753591x10^{5}
β_1	4,498516x10^{4}
β_2	7,054210x10^{1}
β_3	2,842253x10^{-1}
β_4	–4,978206x10^{-5}

NOTE References: API (1952) [8], Teja & Singh (1977), Bühner, Maurer & Bender (1981) [34].

CARBON DIOXIDE

EQUATION OF STATE

$$\frac{p}{\rho RT} = 1 + \omega \sum_{i=0}^{9} \sum_{j=0}^{J_i} n_{ij} (\tau - 1)^j (\omega - 1)^i \qquad [8\text{-}84]$$

The external limits of this equation are:

1. At low temperatures, for p < 5,18 x 10^5 Pa, 220 K; for 5,18 x 10^5 Pa ≤p < 10^8 Pa, the melting curve.
2. At high temperatures, for p < 6 x 10^7 Pa, 1100 K; for 6 x 10^7 Pa < p < 10^8 Pa, 700 K.

$R = \boldsymbol{R}/M$; $\boldsymbol{R}$ = 8,3143 J.K^{-1}.mol^{-1}, M = 44,009 x 10^{-3} kg.mol^{-1}, $\omega = \rho/\rho_c$, $\tau = T_c/T$, ρ_c = 0,468 x 10^3 kg.m^{-3}, T_c = 304,2 K.

The coefficients n_{ij} and the dependence of the values of J_i on i are given in Table 8-8 below.

ENTROPY

$$s^o(T) = R \sum_{n=0}^{7} \alpha_n \tau^n \qquad [8\text{-}85]$$

$$s_1(\rho, T) = -R \left[\sum_{i=0}^{9} \sum_{j=0}^{J_i} \frac{n_{ij}}{i+1} (\tau - 1)^j (\omega - 1)^i - \tau \sum_{i=0}^{9} \sum_{j=0}^{J_i} n_{ij} \frac{j}{i+1} (\tau - 1)^{j-1} (\omega - 1)^{i+1} \right]_o^{\omega} \qquad [8\text{-}86]$$

$$s = s^o(T) - R \ln \frac{\rho RT}{p_a} + s_1(\rho, T) \qquad [8\text{-}87]$$

$s^o(T)$ indicates perfect gas conditions. The coefficients α_n are given in Table 8-8 below.

$$\int_{o}^{\omega} \dot{F}(\xi) d\xi = \left[F(\xi)\right]_{o}^{\omega} \qquad [8\text{-}88]$$

p_a = 1 atm = 1,01325 x 10^5 Pa.

ENTHALPY

$$h^o(T) - h^o(0) = RT \sum_{n=0}^{7} \beta_n \tau^n \qquad [8\text{-}89]$$

$$\Delta h^o(0) = 0{,}59647 \times 10^6 \ J.kg^{-1} \qquad [8\text{-}90]$$

$$h_1(\rho,T) = RT\left[\sum_{i=0}^{9}\sum_{j=0}^{J_i} n_{ij}\left(\frac{\omega}{\omega-1} + \frac{j}{i+1}\frac{\tau}{\tau-1}\right)(\tau-1)^j(\omega-1)^{i+1} + \tau\sum_{i=0}^{9}\sum_{j=0}^{J_i}(-1)^i n_{ij}\frac{j}{i+1}(\tau-1)^{j-1}\right] \qquad [8\text{-}91]$$

$$h = h^o(T) + \Delta h^o(0) + h_1(\rho,T) \qquad [8\text{-}92]$$

$h_o(T)$ indicates perfect gas conditions. $h^o(0)$ = 0 corresponds to the perfect crystal at zero temperature. The coefficients β_n are given in Table 8-8 below. $\Delta h^o(0)$ is the enthalpy of sublimation at T = 0 K.

ACCURACY

ρ: 0,5ear the critical point, 0,1% in most of the p,T diagrams, s: 0,1% and better at low pressures, h: 0,2% and better at low pressures.

Table 8-8: Values of the Dimensionless Coefficients n_{ij}, a_n and b_n for Carbon Dioxide

j / i	0	1	2	3
0	–0,725854437	$-0{,}168332974\times10^{1}$	0,259587221	0,37645574
1	0,447869183	$0{,}126050691\times10^{1}$	$0{,}596957049\times10^{1}$	$0{,}154645885\times10^{2}$
2	–0,172011999	$-0{,}183458178\times10^{1}$	$-0{,}461487677\times10^{1}$	$-0{,}382121926\times10^{1}$
3	$0{,}446304911\times10^{-2}$	$-0{,}176300541\times10^{1}$	$-0{,}111436705\times10^{2}$	$-0{,}278215446\times10^{2}$
4	0,255491571	$0{,}237414246\times10^{1}$	$0{,}750925141\times10^{1}$	$0{,}661133318\times10^{1}$
5	$0{,}594667298\times10^{-1}$	$0{,}116974683\times10^{1}$	$0{,}743706410\times10^{1}$	$0{,}150646731\times10^{2}$
6	–0,147960010	$-0{,}169233071\times10^{1}$	$-0{,}468219937\times10^{1}$	$-0{,}313517448\times10^{1}$
7	$0{,}136710441\times10^{-1}$	–0,100492330	$-0{,}163653806\times10^{1}$	$-0{,}187082988\times10^{1}$
8	$0{,}392284575\times10^{-1}$	0,441503812	0,886741970	0
9	$-0{,}119872097\times10^{-1}$	$-0{,}846051949\times10^{-1}$	$0{,}464564370\times10^{-1}$	0

j / i	4	5	6	
0	–0,670755370	–0,871456126	–0,149156928	
1	$0{,}194449475\times10^{2}$	$0{,}864880497\times10^{1}$	0	
2	$0{,}360171349\times10^{1}$	$0{,}492265552\times10^{1}$	0	
3	$-0{,}271685720\times10^{2}$	$-0{,}642177872\times10^{1}$	0	
4	$-0{,}242663210\times10^{1}$	$-0{,}257944032\times10^{1}$	0	
5	$0{,}957496845\times10^{1}$	0	0	
6	0	0	0	
7	0	0	0	
8	0	0	0	
9	0	0	0	

α_0	$0{,}477983597\times10^{2}$	β_0	$0{,}767516488\times10^{1}$	
α_1	$-0{,}103477722\times10^{3}$	β_1	$-0{,}139641330\times10^{2}$	
α_2	$0{,}285920847\times10^{3}$	β_2	$0{,}266614790\times10^{2}$	
α_3	$-0{,}511752178\times10^{3}$	β_3	$-0{,}341840533\times10^{2}$	
α_4	$0{,}570626856\times10^{3}$	β_4	$0{,}289244934\times10^{2}$	
α_5	$-0{,}381060049\times10^{3}$	β_5	$-0{,}153006069\times10^{2}$	
α_6	$0{,}138971347\times10^{3}$	β_6	$0{,}456446566\times10^{1}$	
α_7	$-0{,}212300540\times10^{2}$	β_7	–0,585016654	

NOTE Reference: Angus, Armstrong & de Reuck (1976) [5].

HELIUM-4

EQUATION OF STATE

$$\frac{p}{\rho RT} = 1 + \omega \sum_{i=0}^{8} n_{1i}\tau^{(i-2)/2} + \omega^2 \sum_{i=0}^{7} n_{2i}\tau^{i/2} + \\ + \omega^3 \sum_{i=0}^{3} n_{3i}\tau^{(2i+1)/2} + \omega^4 \sum_{i=0}^{5} n_{4i}\tau^{(i+2)/4} + \\ + \omega^5 \sum_{i=0}^{1} n_{5i}\tau^{i+1} + \omega^2 e^{\gamma\omega^2}\left[\sum_{i=0}^{2} n_{6i}\tau^{i+1} + \omega^2 \sum_{i=0}^{2} n_{7i}\tau^{i+1}\right] \quad [8\text{-}93]$$

Five different regions, I to V, can be identified in the p,T diagram (Figure 8-96 below).

$$p^{I} = p^{A}(\rho,T) \quad [8\text{-}94]$$

$$p^{II} = p^{B}(\rho,T) \quad [8\text{-}95]$$

$$p^{III} = p^{C}(\rho,T) + p^{B}(\rho_b,T) - p^{C}(\rho_b,T) \quad [8\text{-}96]$$

$$p^{IV} = xp^{A}(\rho,T) + (1-x)p^{B}(\rho_b,T) \quad [8\text{-}97]$$

$$p^{V} = xp^{A}(\rho,T) + (1-x) \\ \left[p^{C}(\rho,T) + p^{B}(\rho_b,T) - p^{C}(\rho_b,T)\right] \quad [8\text{-}98]$$

$R = \boldsymbol{R}/M$; $\boldsymbol{R}$ = 8,3143 J.K^{-1}.mol^{-1}, M = 4,0026 x 10^{-3} kg.mol^{-1}, $\omega = \rho/\rho_c$, $\tau = T_c/T$, ρ_c = 0,6964 x 10^{3} kg.m^{-3}, T_c = 5,2014 K.

The coefficients n_{ji} and γ for calculating p^A, p^B and p^C are given in Table 8-9 below.

ρ_b is the boundary densityat the common boundary of regions II and III.

$x = 3 - T/5$, T [K].

ENTROPY

$$s^{o}(T) = \left[1{,}901 + 5{,}1931 \ln T\right] \times 10^{3}\ J.kg^{-1}.K^{-1} \quad [8\text{-}99]$$

$$s_1(\rho,T) = -R\left[\begin{array}{l}\omega\sum_{i=0}^{8}\frac{4-i}{2}n_{1i}\tau^{(i-2)/2} + \frac{\omega^2}{2}\sum_{i=0}^{7}\frac{2-i}{2}n_{2i}\tau^{i/2} + \\ + \frac{\omega^3}{3}\sum_{i=0}^{3}\frac{1-2i}{2}n_{3i}\tau^{(2i+1)/2} + \\ + \frac{\omega^4}{4}\sum_{i=0}^{5}\frac{2-i}{2}n_{4i}\tau^{(i+2)/4} + \frac{\omega^5}{5}\sum_{i=0}^{1}in_{5i}\tau^{i+1} - \\ - \frac{e^{\gamma\omega^2}}{2\gamma}\left(\sum_{i=0}^{2}in_{6i}\tau^{i+1} + \frac{\gamma\omega^2-1}{\gamma}\sum_{i=0}^{2}in_{7i}\tau^{i+1}\right)\end{array}\right]_0^{\omega} \quad [8\text{-}100]$$

Regarding again Figure 8-96 below:

$$s^{I} = s^{o}(T) - R\ln\frac{\rho RT}{p_a} + s_1^{A}(\rho,T) \quad [8\text{-}101]$$

$$s^{II} = s^{o}(T) - R\ln\frac{\rho RT}{p_a} + s_1^{B}(\rho,T) \quad [8\text{-}102]$$

$$s^{III} = s^{o}(T) - R\ln\frac{\rho RT}{p_a} + s_1^{C}(\rho,T) + s_1^{B}(\rho_b,T) - s_1^{C}(\rho_b,T) \quad [8\text{-}103]$$

$$s^{IV} = s^{o}(T) - R\ln\frac{\rho RT}{p_a} + xs_1^{A}(\rho,T) + (1-x)s_1^{B}(\rho,T) \quad [8\text{-}104]$$

$$s^{V} = s^{o}(T) - R\ln\frac{\rho RT}{p_a} + xs_1^{A}(\rho,T) + (1-x)\left[s_1^{C}(\rho,T) + s_1^{B}(\rho_b,T) - s_1^{C}(\rho_b,T)\right] \quad [8\text{-}105]$$

$s^{o}(T)$ indicates perfect gas conditions. Based on $c_{p^o} = (5/2)R$.

$$\int_{o}^{\omega}\dot{F}(\xi)d\xi = \left[F(\xi)\right]_o^{\omega} \quad [8\text{-}106]$$

p_a = 1 atm = 1,01325 x 10^5 Pa.

ENTHALPY

$$h^{o}(T) = 5{,}1931\times10^{3}T\ J.kg^{-1} \quad [8\text{-}107]$$

$$h_1(\rho,T)=RT\left[\begin{array}{l}\omega\sum_{i=0}^{8}\frac{i}{2}n_{1i}\tau^{(i-2)/2}+\frac{\omega^2}{2}\sum_{i=0}^{7}\frac{4+i}{2}n_{2i}\tau^{i/2}+\\+\frac{\omega^3}{3}\sum_{i=0}^{3}\frac{7+2i}{2}n_{3i}\tau^{(2i+1)/2}+\\+\frac{\omega^4}{4}\sum_{i=0}^{5}\frac{18+i}{4}n_{4i}\tau^{(i+2)/4}+\\+\frac{\omega^5}{5}\sum_{i=0}^{1}(6+1)n_{5i}\tau^{i+1}+\\+\frac{e^{\gamma\omega^2}-1}{\gamma}\sum_{i=0}^{2}\frac{i+1}{2}n_{6i}\tau^{i+1}+\\+\omega^2e^{\gamma\omega^2}\sum_{i=0}^{2}n_{6i}\tau^{i+1}+\frac{e^{\gamma\omega^2}(\gamma\omega^2-1)+1}{\gamma^2}\\\sum_{i=0}^{2}\frac{i+1}{2}n_{7i}\tau^{i+1}+\omega^4e^{\gamma\omega^2}\sum_{i=0}^{2}n_{7i}\tau^{i+1}\end{array}\right]_0^{\omega} \quad [8\text{-}108]$$

In the regions of Figure 8-96 below:

$$h^{I}=h^{o}(T)+h_1^{A}(\rho,T) \quad [8\text{-}109]$$

$$h^{II}=h^{o}(T)+h_1^{B}(\rho,T) \quad [8\text{-}110]$$

$$h^{III}=h^{o}(T)+h_1^{C}(\rho,T)+h_1^{B}(\rho_b,T)-h_1^{C}(\rho_b,T) \quad [8\text{-}111]$$

$$h^{IV}=h^{o}(T)+xh_1^{A}(\rho,T)+(1-x)h_1^{B}(\rho,T) \quad [8\text{-}112]$$

$$\begin{array}{l}h^{V}=h^{o}(T)+xh_1^{A}(\rho,T)+\\+(1-x)\left[h_1^{C}(\rho,T)+h_1^{B}(\rho_b,T)-h_1^{C}(\rho_b,T)\right]\end{array} \quad [8\text{-}113]$$

$h_o(T)$ indicates perfect gas conditions. Based on $c_{p^o}=(5/2)R$.

ACCURACY

ρ: > ± 1% near the critical point. Better than 1% in most of the p,T diagram.

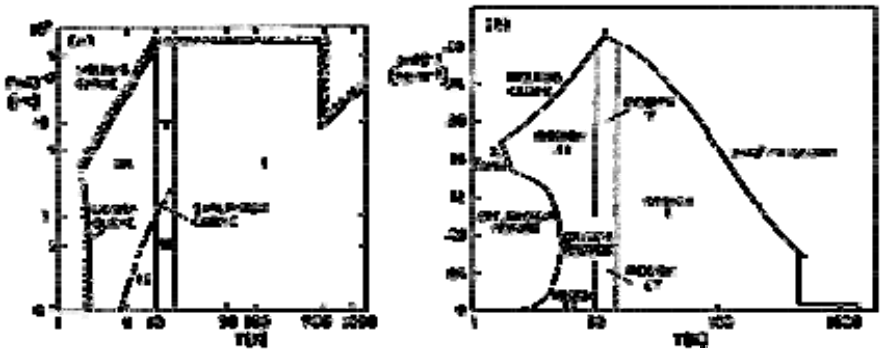

Note: non-si units are used in this figure

Figure 8-96: The five regions I to V. a) in p, T coordinated, b) in ρ, T coordinates.

Table 8-9: Values of the Dimensionless Coefficients n_{ij} and γ for Helium-4

	A	B	C
n_{10}	$-4{,}59869970852 \times 10^{-5}$	$-4{,}59869970852 \times 10^{-5}$	$-4{,}59869970852 \times 10^{-5}$
n_{11}	$-4{,}43178627200 \times 10^{-3}$	$-4{,}43178627200 \times 10^{-3}$	$-4{,}43178627200 \times 10^{-3}$
n_{12}	$2{,}02738009935 \times 10^{-1}$	$2{,}02738009935 \times 10^{-1}$	$2{,}02738009935 \times 10^{-1}$
n_{13}	$5{,}68152317410 \times 10^{-1}$	$5{,}68152317410 \times 10^{-1}$	$5{,}68152317410 \times 10^{-1}$
n_{14}	$-1{,}77764093289$	$-1{,}77764093289$	$-1{,}77764093289$
n_{15}	$-1{,}40448471303$	$-1{,}40448471303$	$-1{,}40448471303$
n_{16}	$2{,}53215569538$	$2{,}53215569538$	$2{,}53215569538$
n_{17}	$-1{,}44853086875$	$-1{,}44853086875$	$-1{,}44853086875$
n_{18}	$2{,}57224547009 \times 10^{-1}$	$2{,}57224547009 \times 10^{-1}$	$2{,}57224547009 \times 10^{-1}$
n_{20}	$-1{,}32911108089 \times 10^{-1}$	$5{,}45717516825 \times 10^{-1}$	$7{,}54851995161 \times 10^{-2}$
n_{21}	$2{,}60105053391$	$-5{,}26218785883$	$2{,}06192112563$
n_{22}	$-1{,}94632822744 \times 10^{1}$	$1{,}38438162246 \times 10^{1}$	$-1{,}43787315035 \times 10^{1}$
n_{23}	$4{,}58381300052 \times 10^{1}$	$-3{,}28771057024 \times 10^{1}$	$2{,}32146598728 \times 10^{1}$
n_{24}	$-5{,}93970872032 \times 10^{1}$	$4{,}52233867349 \times 10^{1}$	$-2{,}34782470378 \times 10^{1}$
n_{25}	$8{,}04044275465 \times 10^{1}$	$-3{,}05702975807 \times 10^{1}$	$3{,}05245092459 \times 10^{1}$
n_{26}	$-4{,}46727519233 \times 10^{1}$	$1{,}04706024245 \times 10^{1}$	$-1{,}05330479443 \times 10^{1}$
n_{27}	$1{,}03755618662 \times 10^{1}$	$-1{,}78805251528$	$3{,}08405355051$

	A	B	C
n_{30}	$5{,}53343739698 \times 10^{-2}$	1,05274082899	$-9{,}04001973585 \times 10^{-1}$
n_{31}	$9{,}26486049266 \times 10^{-1}$	−3,46849108795	$7{,}66114882473 \times 10^{-1}$
n_{32}	$2{,}39789555903 \times 10^{-1}$	1,93273083846	1,53184346013
n_{33}	$-1{,}93125134907 \times 10^{-1}$	$1{,}48012644478 \times 10^{-1}$	$-5{,}23659211353 \times 10^{-1}$
n_{40}	$-1{,}14221631904 \times 10^{-1}$	$2{,}02536392881 \times 10^{1}$	−5,01716678458
n_{41}	$1{,}32468957538 \times 10^{-1}$	$-1{,}22920322279 \times 10^{2}$	$2{,}76430266139 \times 10^{1}$
n_{42}	2,34038221334	$2{,}96428402559 \times 10^{2}$	$-5{,}40258084825 \times 10^{1}$
n_{43}	−7,11715967549	$-3{,}56639003545 \times 10^{2}$	$4{,}67422000131 \times 10^{1}$
n_{44}	$1{,}06499189447 \times 10^{1}$	$2{,}23090549893 \times 10^{2}$	−9,98075965096
n_{45}	−7,81699044091	$-5{,}96732203082 \times 10^{1}$	−6,66243942985
n_{50}	4,03394887953	3,47980556526	5,60781782190
n_{51}	$-1{,}96877124146 \times 10^{1}$	−3,56551573938	$-1{,}21896063466 \times 10^{1}$
n_{60}	$8{,}85278967090 \times 10^{-2}$	$8{,}97149773720 \times 10^{-1}$	−3,95245008176
n_{61}	$2{,}30895686650 \times 10^{-1}$	1,16282299693	$5{,}77174618615 \times 10^{-1}$
n_{62}	−1,86842775250	$-4{,}41170030307 \times 10^{-1}$	−1,39495783311
n_{70}	$3{,}06305701360 \times 10^{-1}$	$-7{,}10142832414 \times 10^{-2}$	$-1{,}94397852603 \times 10^{-1}$
n_{71}	$-5{,}52943290960 \times 10^{-2}$	$-5{,}63950731866 \times 10^{-1}$	$-1{,}57966867600 \times 10^{-1}$
n_{72}	$2{,}99638181518 \times 10^{-1}$	$4{,}64238971532 \times 10^{-1}$	$3{,}19801581443 \times 10^{-1}$
γ	$-1{,}51357 \times 10^{-1}$	$-7{,}56787 \times 10^{-1}$	$-1{,}51357 \times 10^{-1}$

NOTE References: Vargaftik (1975) [253], Angus & de Reuck (1977) [6].

NITROGEN

EQUATION OF STATE

$$p = \rho T\left[\begin{array}{l} R + \rho B + \rho^2 C + \rho^3 D + \rho^4 E + \\ + \rho^5 F + \left(G + \rho^2 H\right)\rho^2 e^{-a_{20}\rho^2} \end{array}\right] \quad [8\text{-}114]$$

$$B = a_1 - \frac{a_2}{T} - \frac{a_3}{T^2} - \frac{a_4}{T^3} - \frac{a_5}{T^5} \quad [8\text{-}115]$$

$$C = a_6 + \frac{a_7}{T} + \frac{a_8}{T^2} \quad [8\text{-}116]$$

$$D = a_9 + \frac{a_{10}}{T} \quad [8\text{-}117]$$

$$E = a_{11} + \frac{a_{12}}{T} \quad [8\text{-}118]$$

$$F = \frac{a_{13}}{T} \quad [8\text{-}119]$$

$$G = \frac{a_{14}}{T^3} + \frac{a_{15}}{T^4} + \frac{a_{16}}{T^5} \quad [8\text{-}120]$$

$$H = \frac{a_{17}}{T^3} + \frac{a_{18}}{T^4} + \frac{a_{19}}{T^5} \quad [8\text{-}121]$$

R = 8,3143 J.K^{-1}.mol^{-1}, M = 28,0134 x 10^{-3} kg.mol^{-1}, p [Pa], ρ [mol.m^{-3}], T [K]

The coefficients a_i are given in Table 8-10 below.

ENTROPY

$$s^o(T) = \left(25{,}7614 + 29{,}1\ln T\right) J.mol^{-1}.K^{-1} \quad [8\text{-}122]$$

$$\begin{aligned} s_1(\rho,T) &= \rho B' + \frac{\rho^2}{2}C' + \frac{\rho^3}{3}D' + \frac{\rho^4}{4}E' + \\ &+ \frac{G'}{2a_{20}}\left(1 - e^{-a_{20}\rho^2}\right) + \frac{H'}{2a_{20}^2}\left(1 - e^{-a_{20}\rho^2} - a_{20}\rho^2 e^{-a_{20}\rho^2}\right) \end{aligned} \quad [8\text{-}123]$$

$$B' = a_1 + \frac{a_3}{T^2} + 2\frac{a_4}{T^3} + 4\frac{a_5}{T^5} \quad [8\text{-}124]$$

$$C' = a_6 - \frac{a_8}{T^2} \quad [8\text{-}125]$$

$$D' = a_9 \quad [8\text{-}126]$$

$$E' = a_{11} \quad [8\text{-}127]$$

$$G' = -2\frac{a_{14}}{T^3} - 3\frac{a_{15}}{T^4} - 4\frac{a_{16}}{T^5} \quad [8\text{-}128]$$

$$H' = -2\frac{a_{17}}{T^3} - 3\frac{a_{18}}{T^4} - 4\frac{a_{19}}{T^5} \quad [8\text{-}129]$$

$$s = s^o(T) - R\ln\frac{\rho RT}{p_a} + s_1(\rho, T) \quad [8\text{-}130]$$

$s^o(T)$ indicates perfect gas conditions. Based on $c_{p^o} = (7/2)R$. Polynomials for c_{p^o} in the range 300 K – 3500 K are given in Karlekar (1983). $p_a = 1$ bar $= 10^5$ Pa.

ENTHALPY

$$h^o(T) = 29{,}1T \ J.mol^{-1} \quad [8\text{-}131]$$

$$h_1(\rho, T) = T\left[\begin{array}{l} \rho B'' + \frac{\rho^2}{2}C'' + \frac{\rho^3}{3}D'' + \frac{\rho^4}{4}E'' + \\ + \frac{\rho^5}{5}F'' + \left(G + \rho^2 H\right)\rho^2 e^{-a_{20}\rho^2} + \\ + \frac{1}{2a_{20}^2}\left(a_{20}G'' + H''\right) - \\ - \frac{e^{-a_{20}\rho^2}}{2a_{20}^2}\left[a_{20}G'' + \left(1 + a_{20}\rho^2\right)H''\right] \end{array}\right] \quad [8\text{-}132]$$

$$B'' = a_1 - 2\frac{a_2}{T} - 3\frac{a_3}{T^2} - 4\frac{a_4}{T^3} - 6\frac{a_5}{T^5} \quad [8\text{-}133]$$

$$C'' = 2a_6 + 3\frac{a_7}{T} + 4\frac{a_8}{T^2} \quad [8\text{-}134]$$

$$D'' = 3a_9 + 4\frac{a_{10}}{T} \quad [8\text{-}135]$$

$$E'' = 4a_{11} + 5\frac{a_{12}}{T} \quad [8\text{-}136]$$

$$F'' = 6\frac{a_{13}}{T} \quad [8\text{-}137]$$

$$G'' = 3\frac{a_{14}}{T^3} + 4\frac{a_{15}}{T^4} + 5\frac{a_{16}}{T^5} \quad [8\text{-}138]$$

$$H'' = 3\frac{a_{17}}{T^3} + 4\frac{a_{18}}{T^4} + 5\frac{a_{19}}{T^5} \quad [8\text{-}139]$$

$$h = h^o(T) + h_1(\rho, T) \quad [8\text{-}140]$$

$h_o(T)$ indicates perfect gas conditions. Based on $c^o_p = (7/2)R$

Table 8-10: Values of the Coefficient a_i for Nitrogen

a_1	$0{,}37713681 \times 10^{-3}$
a_2	0,11808150
a_3	$-0{,}20459519 \times 10^{1}$
a_4	$0{,}10039112 \times 10^{4}$
a_5	$-0{,}23100097 \times 10^{5}$
a_6	$0{,}82438827 \times 10^{-8}$
a_7	$-0{,}11154107 \times 10^{-5}$
a_8	$0{,}31874442 \times 10^{-3}$
a_9	$0{,}88741591 \times 10^{-12}$
a_{10}	$-0{,}14864235 \times 10^{-9}$

a_{11}	$0{,}49951582 \times 10^{-17}$
a_{12}	$-0{,}47638192 \times 10^{-15}$
a_{13}	$0{,}17421249 \times 10^{-18}$
a_{14}	$-0{,}44150312 \times 10^{-1}$
a_{15}	$0{,}95112155 \times 10^{1}$
a_{16}	$-0{,}36302552 \times 10^{3}$
a_{17}	$-0{,}17495594 \times 10^{-9}$
a_{18}	$0{,}81455788 \times 10^{-7}$
a_{19}	$-0{,}20730231 \times 10^{-5}$
a_{20}	$0{,}78475058 \times 10^{-8}$

NOTE References: Bender (1973) [22], Vargaftik (1975) [253].

NEON

EQUATION OF STATE

$$p = \rho RT + \sum_{i=0}^{9} \rho^{i+2} A_i + e^{-\gamma\rho^2} \sum_{i=0}^{6} \rho^{2i+3} A_{i+10} \qquad [8\text{-}141]$$

$$A_0 = a_1 T + a_2 T^{1/2} + \sum_{j=0}^{4} a_{j+3} T^{-j} \qquad [8\text{-}142]$$

$$A_1 = \sum_{j=0}^{3} a_{j+9} T^{1-j} \qquad [8\text{-}143]$$

$$A_2 = \sum_{j=0}^{1} a_{j+14} T^{1-j} \qquad [8\text{-}144]$$

$$A_3 = \sum_{j=0}^{1} a_{2j+19} T^{1-2j} \qquad [8\text{-}145]$$

$$A_4 = a_{24} T^{-1} \qquad [8\text{-}146]$$

$$A_5 = a_{25} T^{-1} \qquad [8\text{-}147]$$

$$A_6 = 0 \quad [8\text{-}148]$$

$$A_7 = a_{29} T^{-1} \quad [8\text{-}149]$$

$$A_8 = 0 \quad [8\text{-}150]$$

$$A_9 = a_{31} T^{-1} \quad [8\text{-}151]$$

$$A_{10} = a_{35} T^{-1} \quad [8\text{-}152]$$

$$A_{11} = 0 \quad [8\text{-}153]$$

$$A_{12} = 0 \quad [8\text{-}154]$$

$$A_{13} = \sum_{j=0}^{1} a_{2(j+20)} T^{-2(j+1)} \quad [8\text{-}155]$$

$$A_{14} = \sum_{j=0}^{1} a_{j+44} T^{-(j+3)} \quad [8\text{-}156]$$

$$A_{15} = \sum_{j=0}^{2} a_{j+46} T^{-(j+2)} \quad [8\text{-}157]$$

$$A_{16} = a_{50} T^{-4} \quad [8\text{-}158]$$

The external limits of this equation are: 8×10^4 Pa < p < 7×10^8 Pa; 26 K < T < 723 K.

R = 8,3143 J.K^{-1}.mol^{-1}, M = 20,179 x 10^{-3} kg.mol^{-1}, p [Pa], ρ [mol.m^{-3}], T [K]. $\gamma = 1/\rho_c^2$, ρ_c = 23,93 x 10^3 mol.m^{-3}.

The coefficients a_i are given in Table 8-11 below.

ENTROPY

$$s^o(T) = 20{,}7857 \ln T \ J.mol^{-1}.K^{-1} \quad [8\text{-}159]$$

$$s_1(\rho, T) = \sum_{i=0}^{9} \frac{\rho^{i+1}}{i+1} A'_i - A'_{10} + e^{-\gamma\rho^2} \sum_{i=0}^{6} \rho^{2i} A'_{i+10} \quad [8\text{-}160]$$

$$A'_0 = a_1 + \frac{a_2}{2}T^{-1/2} - \sum_{j=0}^{3}(j+1)a_{j+4}T^{-(j+2)} \quad [8\text{-}161]$$

$$A'_1 = -\sum_{j=0}^{3}(j-1)a_{j+9}T^{-j} \quad [8\text{-}162]$$

$$A'_2 = a_{14} \quad [8\text{-}163]$$

$$A'_3 = -\sum_{j=0}^{2}(j+1)a_{j+19}T^{-j} \quad [8\text{-}164]$$

$$A'_4 = -A_4T^{-1} \quad [8\text{-}165]$$

$$A'_5 = -A_5T^{-1} \quad [8\text{-}166]$$

$$A'_6 = 0 \quad [8\text{-}167]$$

$$A'_7 = -A_7T^{-1} \quad [8\text{-}168]$$

$$A'_8 = 0 \quad [8\text{-}169]$$

$$A'_9 = -A_9T^{-1} \quad [8\text{-}170]$$

$$A'_{10} = \frac{A_{10}}{\gamma T} + \frac{6\left(a_{40}\gamma^2 + 20a_{46}\right)}{\gamma^6 T^3} + \frac{36\left(a_{44}\gamma + 5a_{47}\right)}{\gamma^6 T^4} + \frac{12\left(a_{42}\gamma^3 + 4a_{45}\gamma^2 + 20a_{48}\gamma + 120a_{50}\right)}{\gamma^7 T^5} \quad [8\text{-}171]$$

$$A'_{11} = \gamma A'_{10} - \frac{A_{10}}{T} \quad [8\text{-}172]$$

$$A'_{12} = \frac{\gamma A'_{11}}{2} \quad [8\text{-}173]$$

$$A'_{13} = \frac{\gamma A'_{12}}{3} \qquad [8\text{-}174]$$

$$A'_{14} = \frac{5a_{46}}{\gamma^2 T^3} + \frac{3\left(a_{44}\gamma + 5a_{47}\right)}{2\gamma^2 T^4} + \frac{2\left(a_{45}\gamma^2 + 5a_{48}\gamma + 30a_{50}\right)}{\gamma^3 T^5} \qquad [8\text{-}175]$$

$$A'_{15} = \frac{a_{46}}{\gamma T^3} + \frac{3a_{47}}{2\gamma T^4} + \frac{2\left(a_{48}\gamma + 6a_{50}\right)}{\gamma 2T^5} \qquad [8\text{-}176]$$

$$A'_{16} = \frac{2A_{16}}{\gamma T} \qquad [8\text{-}177]$$

$$s = s^o(T) - R\ln\frac{\rho RT}{p_a} + s_1(\rho, T) \qquad [8\text{-}178]$$

$s^o(T)$ indicates perfect gas conditions. Based on $c^o_p = (5/2)R$. p_a = 1 bar = 10^5 Pa.

ENTHALPY

$$h^o(T) = 20{,}7857T \ J.mol^{-1} \qquad [8\text{-}179]$$

$$h_1(\rho, T) = \sum_{i=0}^{9} \frac{\rho^{i+1}}{i+1} A''_i - A''_{10} + e^{-\gamma\rho^2} \sum_{i=0}^{7} \rho^{2i} A''_{i+10} \qquad [8\text{-}180]$$

$$A''_0 = a_1 T + \frac{3a_2}{2} T^{-1/2} - \sum_{j=0}^{4} (j+2) a_{j+3} T^{-j} \qquad [8\text{-}181]$$

Note: non-si units are used in this figure

$$A''_1 = \sum_{j=0}^{3} (j+2) a_{j+9} T^{1-j} \qquad [8\text{-}182]$$

$$A''_2 = \sum_{j=0}^{1} (j+3) a_{j+14} T^{1-j} \qquad [8\text{-}183]$$

$$A''_3 = \sum_{j=0}^{1} 2(j+2) a_{2j+19} T^{1-2j} \qquad [8\text{-}184]$$

$$A''_4 = 7A_4 \qquad [8\text{-}185]$$

$$A''_5 = 8A_5 \quad [8\text{-}186]$$

$$A''_6 = 0 \quad [8\text{-}187]$$

$$A''_7 = 10A_7 \quad [8\text{-}188]$$

$$A''_8 = 0 \quad [8\text{-}189]$$

$$A''_9 = 12A_9 \quad [8\text{-}190]$$

$$A''_{10} = \frac{-2A_{10}}{\gamma} - \frac{9\left(a_{40}\gamma^2 + 20a_{46}\right)}{\gamma^6 T^2} - \frac{48\left(a_{44}\gamma + 5a_{47}\right)}{\gamma^6 T^3} - \frac{15\left(a_{42}\gamma^3 + 4a_{45}\gamma^2 + 20a_{48}\gamma + 120a_{50}\right)}{\gamma^7 T^4} \quad [8\text{-}191]$$

$$A''_{11} = \gamma A''_{10} + 3A_{10} \quad [8\text{-}192]$$

Note: non-si units are used in this figure

$$A''_{12} = \frac{\gamma A''_{11}}{2} - \frac{\gamma A_{10}}{2} \quad [8\text{-}193]$$

Note: non-si units are used in this figure

$$A''_{13} = \frac{\gamma A''_{12}}{3} \quad [8\text{-}194]$$

Note: non-si units are used in this figure

$$A''_{14} = \frac{2a_{40}\gamma^2 + 15a_{46}}{2\gamma^2 T^2} - \frac{2\left(a_{44}\gamma + 5a_{47}\right)}{\gamma^2 T^4} + \frac{2a_{42}\gamma^3 - 5a_{45}\gamma^2 - 25a_{48}\gamma - 150a_{50}}{2\gamma^3 T^4} \quad [8\text{-}195]$$

$$A''_{15} = -\frac{3a_{46}}{2\gamma T^2} + \frac{a_{44}\gamma - 2a_{47}}{\gamma T^3} + \frac{2a_{45}\gamma^2 - 5a_{48}\gamma - 30a_{50}}{2\gamma^2 T^4} \quad [8\text{-}196]$$

$$A''_{16} = A_{15} - \frac{5A_{16}}{2\gamma} \qquad [8\text{-}197]$$

Note: non-si units are used in this figure

$$A''_{17} = A_{16} \qquad [8\text{-}198]$$

Note: non-si units are used in this figure

$$h = h^{o}(T) + h_{1}(\rho, T) \qquad [8\text{-}199]$$

$h_o(T)$ indicates perfect gas conditions. Based on $c^o_p = (5/2)R$

ACCURACY

ρ: 0,1% except in the vicinity of the critical pint.

Table 8-11: Values of the Coefficient a_i for Neon

a_1	$0{,}5653412521 \times 10^{-4}$
a_2	$0{,}3492121815 \times 10^{-2}$
a_3	$-0{,}5281123734 \times 10^{-1}$
a_4	$0{,}1511353269 \times 10^{1}$
a_5	$-0{,}7726939279 \times 10^{2}$
a_6	$0{,}1627781825 \times 10^{4}$
a_7	$-0{,}1278521631 \times 10^{5}$
a_9	$0{,}1448956689 \times 10^{-8}$
a_{10}	$0{,}1684992471 \times 10^{-6}$
a_{11}	$-0{,}3161566218 \times 10^{-4}$
a_{12}	$0{,}1681762544 \times 10^{-2}$
a_{14}	$-0{,}9591366803 \times 10^{-14}$
a_{15}	$0{,}1130059075 \times 10^{-10}$
a_{19}	$0{,}2958715965 \times 10^{-18}$
a_{21}	$-0{,}2914091771 \times 10^{-5}$
a_{24}	$-0{,}2884853628 \times 10^{-17}$

a_{25}	$0{,}5087713410 \times 10^{-23}$
a_{29}	$0{,}6838434551 \times 10^{-33}$
a_{31}	$0{,}1316369231 \times 10^{-42}$
a_{35}	0,8654118297
a_{40}	$0{,}437531010 \times 10^{-29}$
a_{42}	$-0{,}5948450789 \times 10^{-26}$
a_{44}	$-0{,}2165033503 \times 10^{-36}$
a_{45}	$0{,}9601308140 \times 10^{-35}$
a_{46}	$0{,}1132387373 \times 10^{-47}$
a_{47}	$0{,}1010428226 \times 10^{-46}$
a_{48}	$-0{,}2580251681 \times 10^{-44}$
a_{50}	$0{,}2140433107 \times 10^{-54}$

NOTE References: Jacobsen, Stewart & Teng (1981) [102].

OXYGEN

EQUATION OF STATE

$$p = \rho T \left[\begin{array}{l} R + \rho B + \rho^2 C + \rho^3 D + \rho^4 E + \\ + \rho^5 F + \left(G + \rho^2 H \right) \rho^2 e^{-a_{20}\rho^2} \end{array} \right] \quad [8\text{-}200]$$

$$B = a_1 - \frac{a_2}{T} - \frac{a_3}{T^2} - \frac{a_4}{T^3} - \frac{a_5}{T^5} \quad [8\text{-}201]$$

$$C = a_6 + \frac{a_7}{T} + \frac{a_8}{T^2} \quad [8\text{-}202]$$

$$D = a_9 + \frac{a_{10}}{T} \quad [8\text{-}203]$$

$$E = a_{11} + \frac{a_{12}}{T} \quad [8\text{-}204]$$

$$F = \frac{a_{13}}{T} \quad [8\text{-}205]$$

$$G = \frac{a_{14}}{T^3} + \frac{a_{15}}{T^4} + \frac{a_{16}}{T^5} \quad [8\text{-}206]$$

$$H = \frac{a_{17}}{T^3} + \frac{a_{18}}{T^4} + \frac{a_{19}}{T^5} \quad [8\text{-}207]$$

R = 8,3143 J.K^{-1}.mol^{-1}, M = 31,9988 x 10^{-3} kg.mol^{-1}, p [Pa], ρ [mol.m^{-3}], T [K]

The coefficients a_i are given in Table 8-12 below.

ENTROPY

$$s^o(T) = (39{,}3639 + 29{,}1 \ln T)\, J.mol^{-1}.K^{-1} \quad [8\text{-}208]$$

Note: non-si units are used in this figure

$$s_1(\rho,T) = \rho B' + \frac{\rho^2}{2} C' + \frac{\rho^3}{3} D' + \frac{\rho^4}{4} E' + \\ + \frac{G'}{2a_{20}}\left(1 - e^{-a_{20}\rho^2}\right) + \frac{H'}{2a_{20}^2}\left(1 - e^{-a_{20}\rho^2} - a_{20}\rho^2 e^{-a_{20}\rho^2}\right) \quad [8\text{-}209]$$

$$B' = a_1 + \frac{a_3}{T^2} + 2\frac{a_4}{T^3} + 4\frac{a_5}{T^5} \quad [8\text{-}210]$$

$$C' = a_6 - \frac{a_8}{T^2} \quad [8\text{-}211]$$

$$D' = a_9 \quad [8\text{-}212]$$

$$E' = a_{11} \quad [8\text{-}213]$$

$$G' = -2\frac{a_{14}}{T^3} - 3\frac{a_{15}}{T^4} - 4\frac{a_{16}}{T^5} \quad [8\text{-}214]$$

$$H' = -2\frac{a_{17}}{T^3} - 3\frac{a_{18}}{T^4} - 4\frac{a_{19}}{T^5} \quad [8\text{-}215]$$

$$s = s^o(T) - R\ln\frac{\rho RT}{p_a} + s_1(\rho,T) \qquad [8\text{-}216]$$

$s^o(T)$ indicates perfect gas conditions. Based on $c_p{}^o = (7/2)R$. Polynomials for $c_p{}^o$ in the range 300 K – 3500 K are given in Karlekar (1983). p_a = 1 bar = 10^5 Pa.

ENTHALPY

$$h^o(T) = 29{,}1T \ J.mol^{-1} \qquad [8\text{-}217]$$

$$h_1(\rho,T) = T\left[\begin{array}{l}\rho B'' + \frac{\rho^2}{2}C'' + \frac{\rho^3}{3}D'' + \frac{\rho^4}{4}E'' + \\ + \frac{\rho^5}{5}F'' + \left(G + \rho^2 H\right)\rho^2 e^{-a_{20}\rho^2} + \\ + \frac{1}{2a_{20}^2}\left(a_{20}G'' + H''\right) - \\ - \frac{e^{-a_{20}\rho^2}}{2a_{20}^2}\left\{a_{20}G'' + \left(1 + a_{20}\rho^2\right)H''\right\}\end{array}\right] \qquad [8\text{-}218]$$

$$B'' = a_1 - 2\frac{a_2}{T} - 3\frac{a_3}{T^2} - 4\frac{a_4}{T^3} - 6\frac{a_5}{T^5} \qquad [8\text{-}219]$$

$$C'' = 2a_6 + 3\frac{a_7}{T} + 4\frac{a_8}{T^2} \qquad [8\text{-}220]$$

$$D'' = 3a_9 + 4\frac{a_{10}}{T} \qquad [8\text{-}221]$$

$$E'' = 4a_{11} + 5\frac{a_{12}}{T} \qquad [8\text{-}222]$$

$$F'' = 6\frac{a_{13}}{T} \qquad [8\text{-}223]$$

$$G'' = 3\frac{a_{14}}{T^3} + 4\frac{a_{15}}{T^4} + 5\frac{a_{16}}{T^5} \qquad [8\text{-}224]$$

$$H'' = 3\frac{a_{17}}{T^3} + 4\frac{a_{18}}{T^4} + 5\frac{a_{19}}{T^5} \qquad [8\text{-}225]$$

$$h = h^o(T) + h_1(\rho, T) \qquad [8\text{-}226]$$

$h_o(T)$ indicates perfect gas conditions. Based on $c^o_p = (5/2)R$

Table 8-12: Values of the Coefficient a_i for Oxygen

a_1	$0{,}35643862 \times 10^{-3}$
a_2	0,14407294
a_3	$-0{,}25661301 \times 10^{1}$
a_4	$0{,}10322523 \times 10^{4}$
a_5	$-0{,}19530479 \times 10^{5}$
a_6	$-0{,}13149946 \times 10^{-9}$
a_7	$0{,}21353195 \times 10^{-5}$
a_8	$0{,}35916916 \times 10^{-3}$
a_9	$0{,}73097410 \times 10^{-12}$
a_{10}	$-0{,}27513075 \times 10^{-9}$
a_{11}	$0{,}64203761 \times 10^{-17}$
a_{12}	$0{,}98687798 \times 10^{-15}$
a_{13}	$0{,}84733604 \times 10^{-19}$
a_{14}	$0{,}63010952 \times 10^{-1}$
a_{15}	$0{,}15107048 \times 10^{2}$
a_{16}	$-0{,}13084843 \times 10^{4}$
a_{17}	$-0{,}19018424 \times 10^{-9}$
a_{18}	$0{,}45774043 \times 10^{-7}$
a_{19}	$0{,}30856640 \times 10^{-5}$
a_{20}	$0{,}55291853 \times 10^{-8}$

NOTE References: Bender (1973) [22], Vargaftik (1975) [253].

8.2 Superfluid Helium-4

The properties of liquid He II (superfluid He^4) which are relevant to the phenomena discussed in Clause 7 are given in this Clause. These phenomena are mainly: Heat exchange through superfluidhelium and vapor formation.

The main body of the clause is Table 8-13 where the following properties are tabulated versus temperature in the range 1,20 K to 2,16 K.

Concentration of superfluid component, ρ_s/ρ.

Entropy per unit mass, s. [$J.kg^{-1}.K^{-1}$].

Density, ρ. [$kg.m^{-3}$].

Gorter & Mellink constant for mutual friction, A. [$m.s.kg^{-1}$].

Dynamic viscosity of the normal component, μ_n. [Pa.s].

Vapor pressure, p_{sat}. [Pa].

Slope of the saturation line, $(dp/dT)_{sat}$. [$Pa.K^{-1}$].

Heat of vaporization, h_{fg}. [$J.kg^{-1}$].

Surface tension, σ. [$N.m^{-1}$].

Four among these properties, (ρ, h_{fg}, p_{sat} and σ) are also presented in this Clause in figures which are somewhat less precise than in Table 8-13.

Table 8-13: Relevant Properties of He II as a Function of Temperature

T [K]	ρ_s/ρ [a]	$s \times 10^{-3}$ [a] [J.kg^{-1}.K^{-1}]	$\rho \times 10^{-3}$ [a] [kg.m^{-3}]	$A \times 10^{-3}$ [a] [m.s.kg^{-1}]	$\mu_n \times 10^{6}$ [b] [Pa.s]	$P_{sat} \times 10^{-3}$ [c] [Pa]	$(dp/dT)_{sat} \times 10^{-3}$ [d] [Pa.K^{-1}]	$h_{fg} \times 10^{-3}$ [e] [J.kg^{-1}]	$\sigma \times 10^{3}$ [f] [N.m^{-1}]
1,20	0,9721	0,0523	0,1451	0,231	1,828	0,0833	0,5883	21,12	0,3601
1,25	0,9629	0,0672	0,1451	0,263	1,682	0,1172	0,7695	21,38	0,3588
1,30	0,9527	0,0853	0,1451	0,298	1,575	0,1611	0,9927	21,63	0,3573
1,35	0,9392	0,1069	0,1451	0,336	1,495	0,2171	1,2549	21,88	0,3557
1,40	0,9233	0,1320	0,1451	0,378	1,460	0,2874	1,5617	22,13	0,3541
1,45	0,9057	0,1620	0,1451	0,423	1,397	0,3741	1,9162	22,37	0,3524
1,50	0,8842	0,1970	0,1451	0,472	1,331	0,4798	2,3211	22,61	0,3506
1,55	0,8594	0,2378	0,1451	0,526	1,319	0,6071	2,7787	22,84	0,3487
1,60	0,8314	0,2840	0,1451	0,584	1,300	0,7586	3,2903	23,07	0,3467
1,65	0,8000	0,3367	0,1451	0,647	1,288	0,9371	3,8576	23,28	0,3446
1,70	0,7645	0,3959	0,1452	0,715	1,274	1,1453	4,4803	23,49	0,3424
1,75	0,7247	0,4617	0,1452	0,791	1,217	1,3860	5,1585	23,68	0,3401
1,80	0,6804	0,5352	0,1453	0,874	1,266	1,6620	5,8896	23,85	0,3377
1,85	0,6310	0,6170	0,1453	0,967	1,390	1,9759	6,6738	24,01	0,3352

T [K]	ρ_s/ρ [a]	sx10^{-3} [a] [J.kg^{-1}.K^{-1}]	ρx10^{-3} [a] [kg.m^{-3}]	Ax10^{-3} [a] [m.s.kg^{-1}]	μ_lx10^{6} [b] [Pa.s]	P_{sat}x10^{-3} [c] [Pa]	$(dp/dT)_{sat}$x10^{-3} [d] [Pa.K^{-1}]	h_{fg}x10^{-3} [e] [J.kg^{-1}]	σx10^{3} [f] [N.m^{-1}]
1,90	0,5757	0,7091	0,1454	1,07	1,411	2,3302	7,5056	24,15	0,3326
1,95	0,5138	0,8122	0,1455	1,20	1,484	2,7272	8,3791	24,27	0,3299
2,00	0,4448	0,9290	0,1456	1,37	1,587	3,1687	9,2858	24,35	0,3271
2,05	0,3678	1,0620	0,1457	1,62	1,787	3,6561	10,213	24,39	0,3237
2,06	0,3510	1,0940	0,1457	1,69	1,793	3,7592	10,398	24,38	0,3222
2,07	0,3330	1,1240	0,1457	1,77	1,839	3,8641	10,585	24,38	0,3207
2,08	0,3150	1,1550	0,1458	1,87	1,866	3,9709	10,772	24,38	0,3192
2,09	0,2960	1,1850	0,1458	2,00	1,899	4,0795	10,958	24,37	0,3178
2,10	0,2769	1,2150	0,1458	2,16	1,941	4,1901	11,146	24,37	0,3164
2,11	0,2550	1,2520	0,1458	2,39	1,982	4,3025	11,332	24,36	0,3150
2,12	0,2318	1,2870	0,1459	2,73	2,030	4,4167	11,516	24,34	0,3136
2,13	0,2068	1,3220	0,1459	3,30	2,093	4,5328	11,698	24,32	0,3123
2,14	0,1782	1,3610	0,1460	4,44	2,178	4,6506	11,878	24,30	0,3110
2,15	0,1442	1,4000	0,1460	7,73	2,282	4,7703	12,054	24,26	0,3097
2,16	0,1044	1,4420	0,1464	33,1	2,351	4,8917	12,226	24,22	0,3085

T [K]	ρ_s/ρ [a]	sx10^{-3} [a] [J.kg^{-1}.K^{-1}]	ρx10^{-3} [a] [kg.m^{-3}]	Ax10^{-3} [a] [m.s.kg^{-1}]	μ_sx10^{6} [b] [Pa.s]	P_{sat}x10^{-3} [c] [Pa]	$(dp/dT)_{sat}$x10^{-3} [d] [Pa.K^{-1}]	h_{fg}x10^{-3} [e] [J.kg^{-1}]	σx10^{3} [f] [N.m^{-1}]
Fig. [g]	Figure 8-97	Figure 8-98			Figure 8-99				

[a] From Dimotakis & Broadwell (1973) [58].

[b] Interpolated by the compiler using experimental results from several sources.

[c] From Mendelssohn (1960) [148].

[d] Calculated by the compiler by numerical differentiation of data from Mendelssohn (1960) [148].

[e] Calculated by the compiler by use of $h_{fg} = (RT^2/Mp_{sat})(dp/dT)_{sat}$ (Clapeyron's formula). R = 8,31432 J.K^{-1}.mol^{-1}, M = 4,0026x10^{-3} kg.mol^{-1}.

[f] Calculated by the compiler after Atkins & Narahara (1965) [13] when $T \leq 2$K, and Magerlein & Sanders (1976) [140].

[g] Numbers in this entry refer to figures in subsequent pages, where additional information on the subject is given.

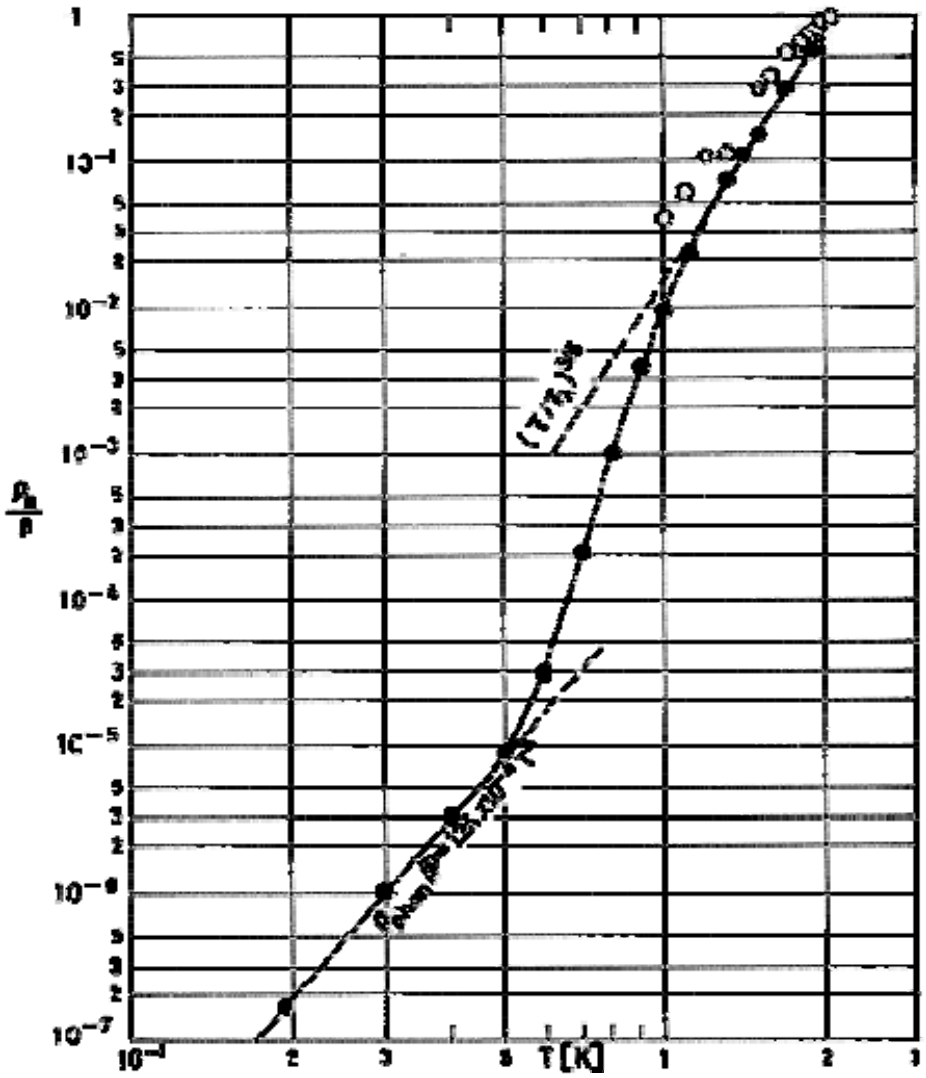

Figure 8-97: Concentration of normal fluid, ρ_n/ρ, as a function of temperature, T, for bulk He II.

● From Andronikashvili (Mendelssohn (1960) [148]).

○ From values of ρ_s/ρ calculated under the assumption the superfluid critical velocity is temperature independent (van Alphen et al. (1969) [246]).

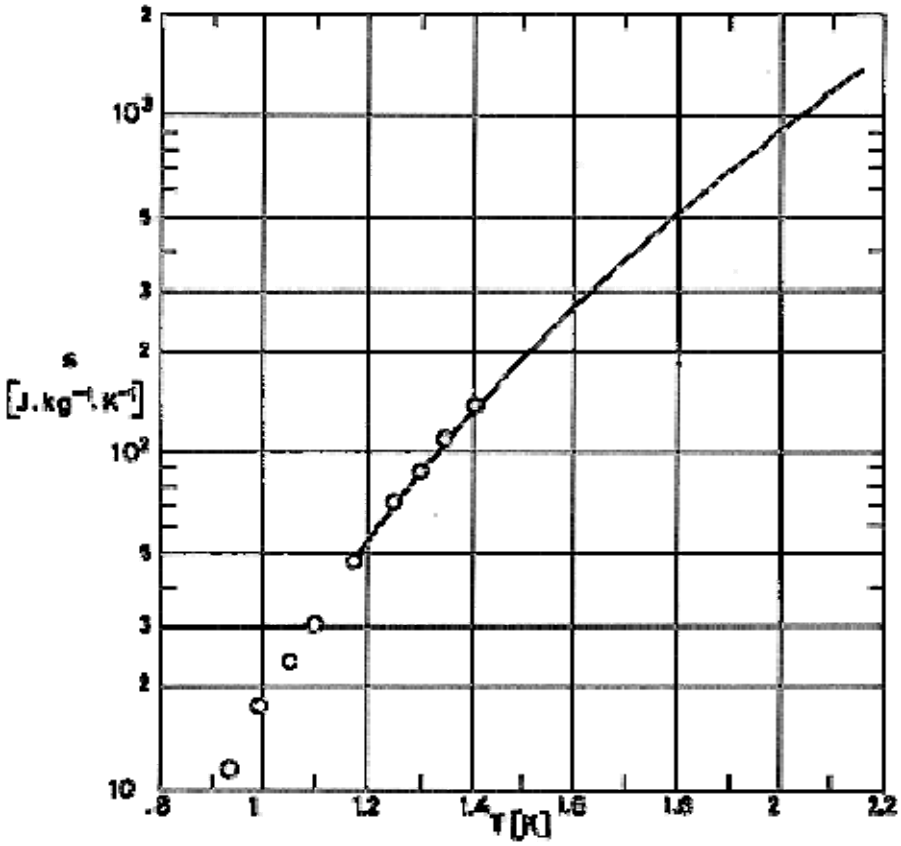

Figure 8-98: Entropy per unit mass, *s*, of liquid Helium II as a function of temperature, *T*.

▬▬ From> Dimotakis & Broadwell (1973) [58].

○ From Broz & Khorana (1976) [31]. From fountain-effect measurements through $5x10^{-7}$ m pore-size filters.

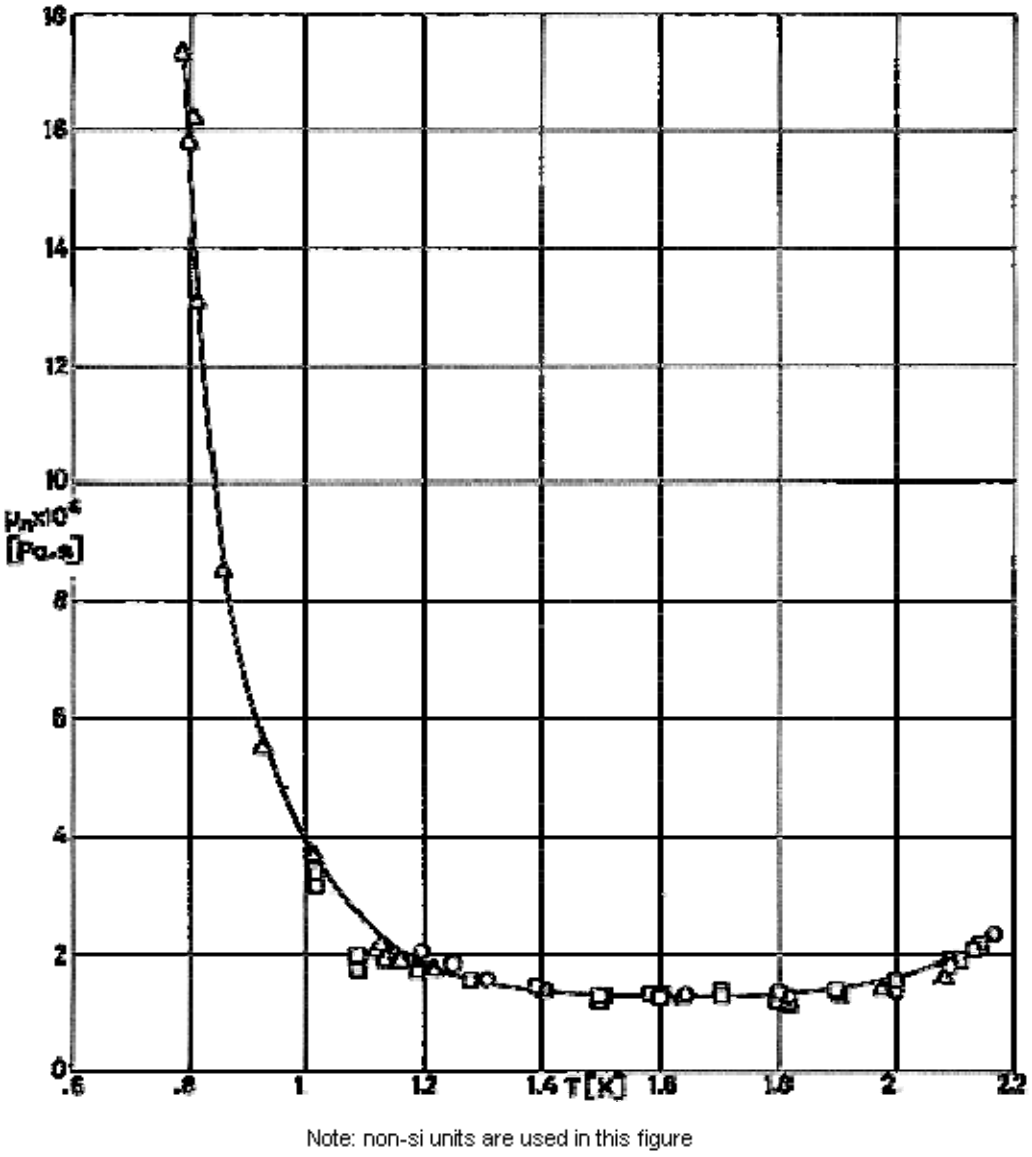

Figure 8-99: Dynamic viscosity, μ_n, of the normal fluid as a function of temperature, T.
○ From Heikkila & Hollis Hallet (1955) [84].
□ From Staas, Taconis & van Alphen (1961) [227].
△ From Woods & Hollis Hallet (1963) [267].

8.3 Normal Helium-3

Helium-3 is the lighter and rarer of the two non-radioactive helium isotopes. Atmospheric helium contains about 1,4 ppm (in volume) of He^3, although this value can be more than five times larger in some rare events (Sano et al, (1984)[206]). The gas from oil wells has only 0,14 ppm of He^3. Like He^4, He^3 is a liquid at ordinary pressure no matter how low the temperature.

He^3 becomes superfluid below 0,0027 K. Evidence of superfluid He^3 is fairly recent (Wheatley (1975) [264], Mermin & Lee (1976) [149]). The three distinct superfluid phases are magnetic and inherently anisotropic.

Although superfluid He^3 is a fascinating fluid, from the basic science point of view, and experiments under reduced gravity are being considered (Kittel & Brooks (1982) [124]), near term spacecraft applications concern temperatures of the order of 0,3 K. The most frequently quoted application is the cooling of long wavelength infrared bolometers.

The operation of infrared bolometers at 0,3 K, through a He^3 system, rather than the 1,5 K, which can be achieved with a pumped He^4 cryostat, results in a reduction of the detector noise equivalent power, NEP, (see clause 8.5), by a factor of 56, and a reduction of the required observation time by a factor of 3000 (Sherman & Figueroa (1980) [220]).

He^4 as delivered by a liquifier is at a temperature of 4,2 K at atmospheric pressure. If the pressure is lowered by pumping on the system, a temperature below 1 K would be reached. In general the practical lowest temperature is 1,2 K to 1,5 K.

When a liquid bath is pumped, the cooling produced per unit of evaporating liquid is approximately equal to its latent heat of vaporization, h_{fg}, which is almost constant for narrow temperature intervals. The evaporating mass flow rate, on the other hand, is proportional to the vapor pressure, which decreases exponentially as an Arrhenius function of T. Thus, the vapor pressure becomes so small that the refrigeration produced by evaporation is entirely compensated by external heat leaks.

For liquid He^3 the lowest achievable temperature is slightly below 0,3 K (instead of 1,5 K), because of two reasons:

1. The vapor pressure of He^3 is, at all temperatures, higher than the vapor pressure of He^4 (Figure 8-100).

2. At temperatures under consideration, He^3 is a normal fluid, no He^3 film exists and there is not increased heat transfer through the film. This advantage presents its drawbacks, however; containment under reduced gravity is easier when phase-separation devices of the superfluid plug type (see clause 7.2) are effective.

   The heat of vaporization of He^3 is less than half that ofHe^4, but this drawback is more than compensated by the favorable, to He^3, vapor pressure ratio.

   He^3 is extremely costly, approximately 500 $ per SPT 1 and, thus closed-cycle coolers should be used.

   Refrigertaors for laboratory use below 1 K have been described by Lounasmaa (1974) [138]. They are bulky and probably not adapted to reduced gravity operation.

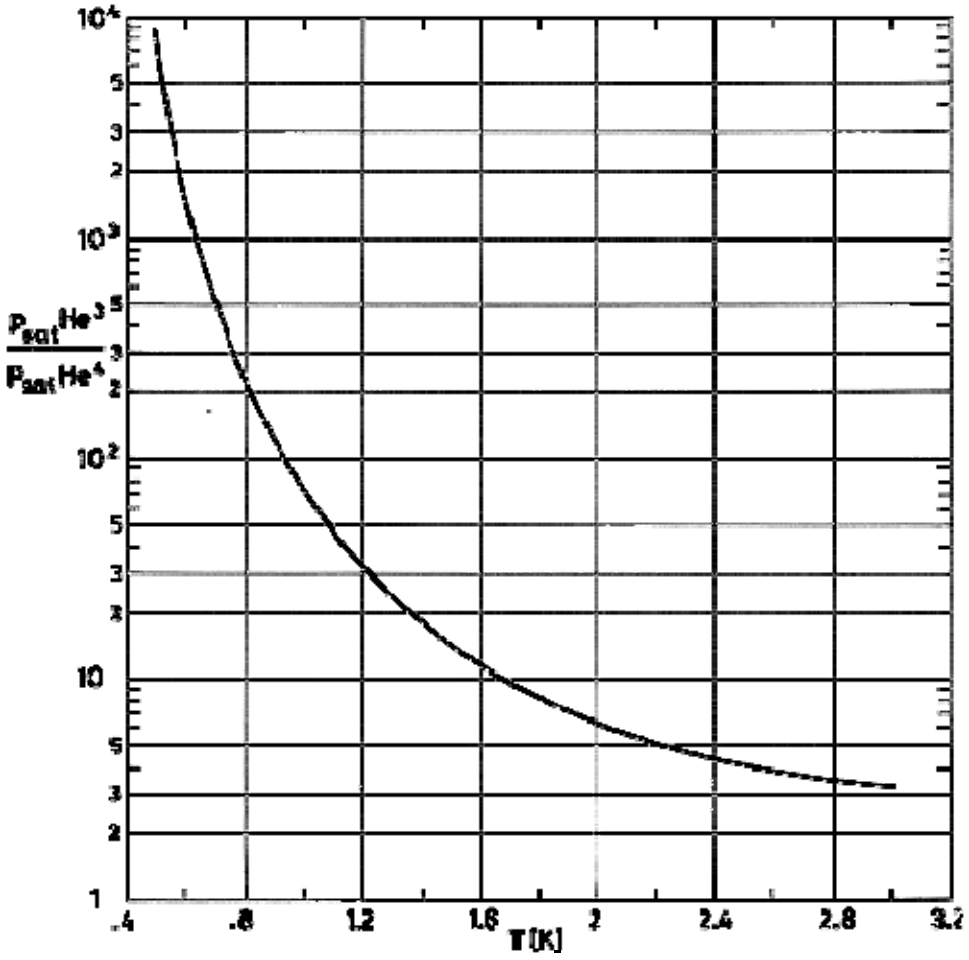

Figure 8-100: He³ to He⁴ vapor pressure ratio, p_{satHe3}/p_{satHe4}, vs. temperature, *T*. Calculated by the compiler after data tabulated in Mendelssohn (1960) .

He³ cryostats for cooling of bolometers detectors have been used (Chanin & Torre (1977) [42]). Work by NASA on spaceborne devices has been reported by Lundholm (1980) [139], Sherman & Figueroa (1980) [220], Vorreiter (1980) [257], Kittel (1982) [123], and Kittel & Brooks (1982) [124].

8.4 Metallic materials

	Specific Heat	Thermal Conductivity	Thermal Expansion	Tensile Strength [b]
Ag	Figure 8-101	Figure 8-103	Figure 8-107	
Al	Figure 8-102	Figure 8-104	Figure 8-107	Figure 8-108
Al Alloys		Figure 8-105		Figure 8-109
Be	Figure 8-101	Figure 8-103		
Cu	Figure 8-102	Figure 8-104	Figure 8-107	Figure 8-108
Cu Alloys		Figure 8-106		Figure 8-110
Ni	Figure 8-101	Figure 8-103	Figure 8-107	
SS [a]	Figure 8-101	Figure 8-103	Figure 8-107	Figure 8-111
Ti	Figure 8-101	Figure 8-103		Figure 8-111
Ti Alloys	-	-	-	Figure 8-111

[a] Stainless Steel.

[b] Additional information on the mechanical properties of alloys used for structural applications at cryogenic temperatures is given in Clause 9.3.

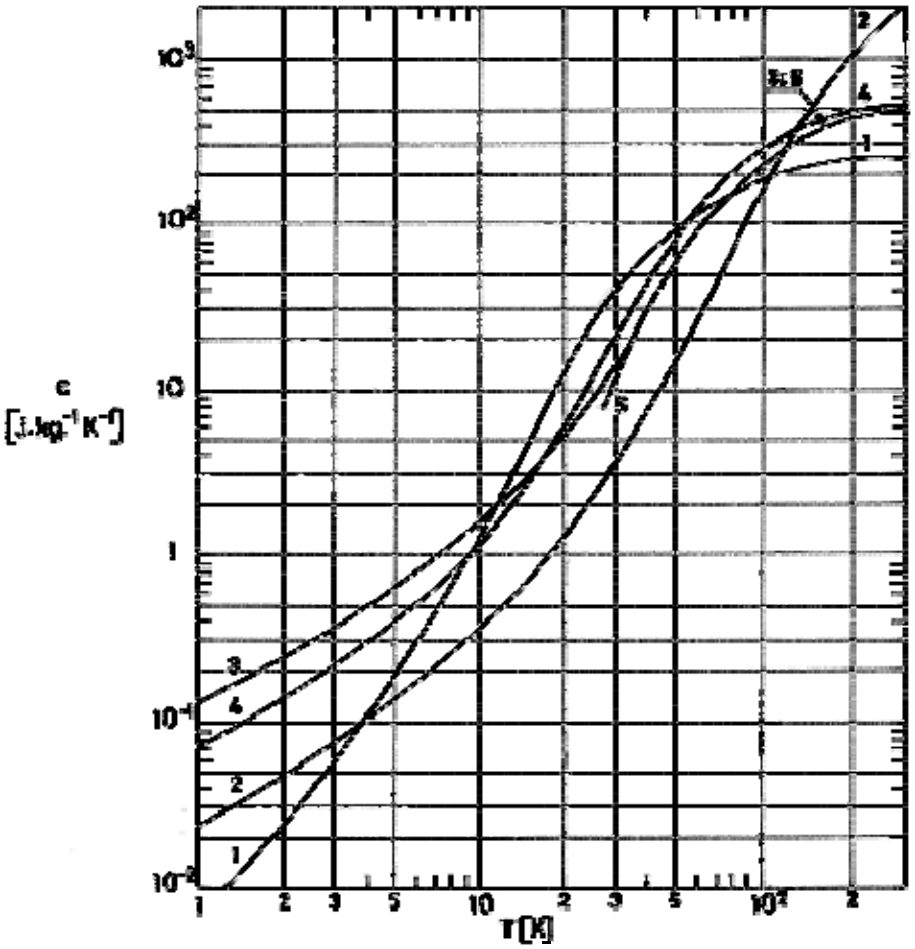

Figure 8-101: Specific heat, *c*, of Silver, Beryllium, Nickel, Stainless Steel and Titanium vs. temperature, *T*. Details concerning these materials are given below.

Explanation of the Figure 8-101

KEY	MATERIAL	COMPOSITION	REFERENCES
1	SILVER	PURE	Johnson (1961) [109]
2	BERYLLIUM	PURE	
3	NICKEL	PURE	
4	TITANIUM	PURE	
5	STAINLESS STEEL	18-8	Gibbons (1971) [74]

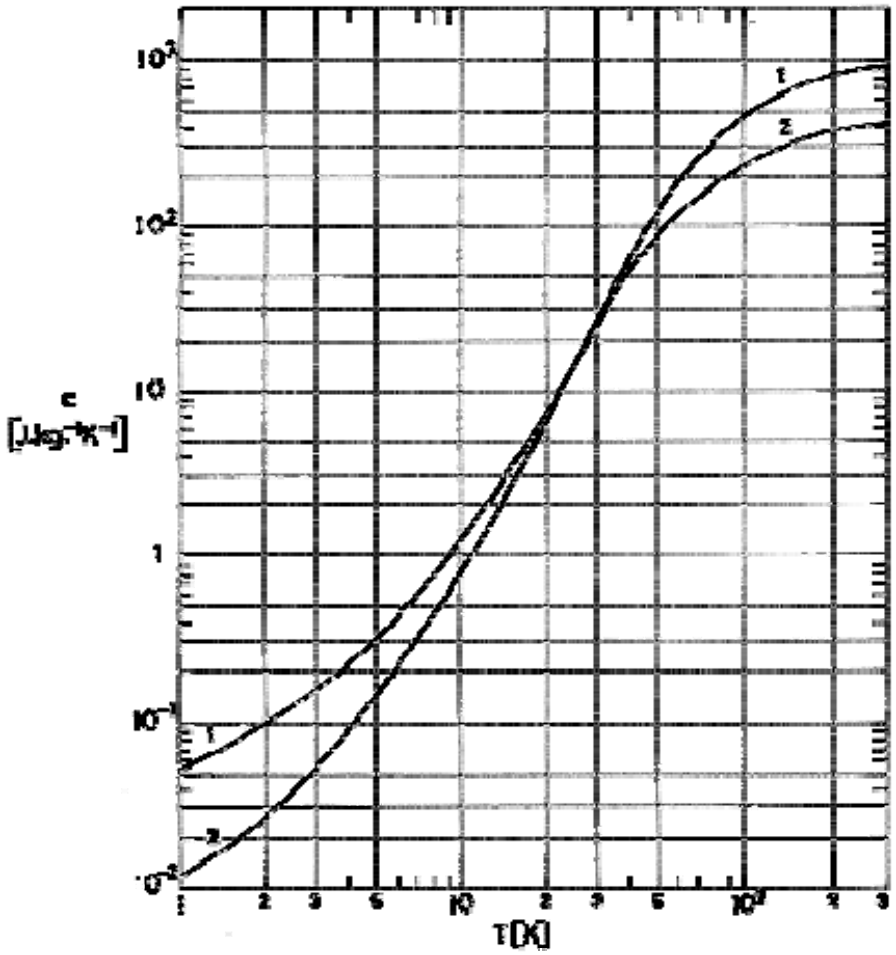

Figure 8-102: Specific heat, *c*, of Aluminium and Copper vs. temperature, *T*. Details concerning these materials are given below.

Explanation of the Figure 8-102

KEY	MATERIAL	COMPOSITION	REFERENCE
1	ALUMINIUM	PURE	Johnson (1961) [109]
2	COPPER	PURE	

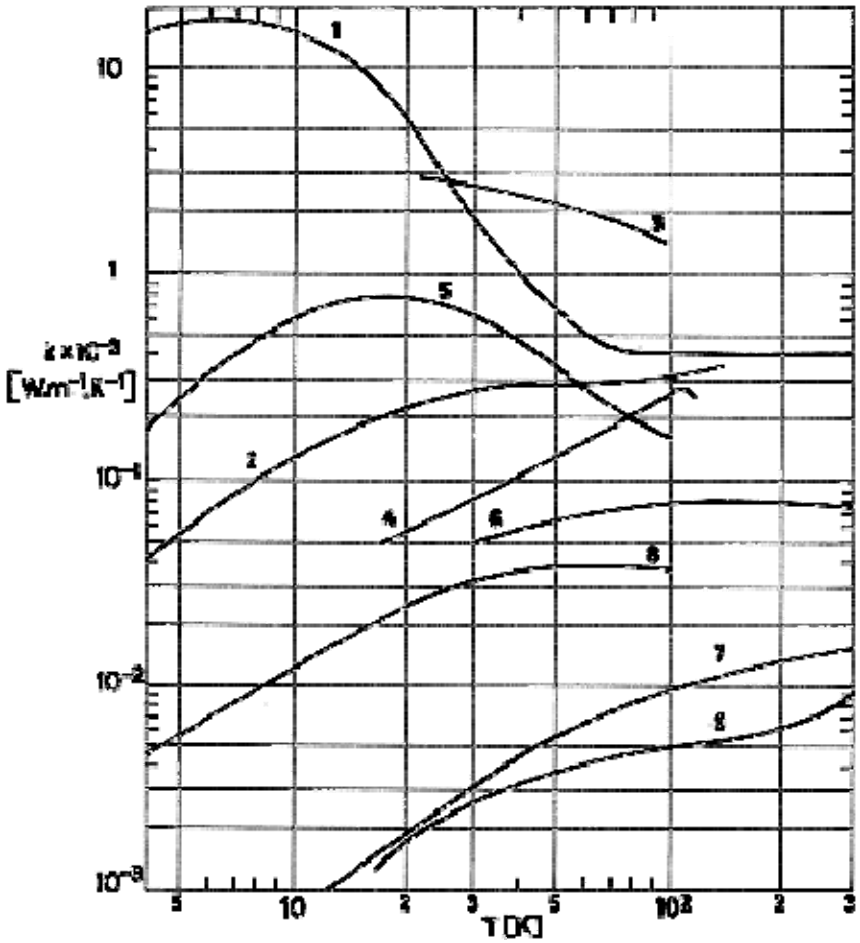

Figure 8-103: Thermal conductivity, *k*, of Silver, Beryllium, Nickel, Stainless Steel and Titanium vs. temperature, *T*. Details concerning these materials are given below.

Explanation of the Figure 8-103

KEY	MATERIAL	COMPOSITION	REFERENCE
1	SILVER	99,9990ure, annealed, and 99,9& pure (Johnson, Matthey).	Johnson (1961) [109]
2		99,999% pure, drawn, (Johnson, Matthey).	
3	BERYLLIUM	"High Purity", single crystal (Degussa).	
4		2% Mg, sintered rod (Brush).	
5	NICKEL	99,99% pure, annealed, (Johnson, Matthey).	
6		99% pure (Int. Nickel).	

7	STAINLESS STEEL	Average value for close curves of types 303, 304, 316, 347, and "stainless" as compiled in N.B.S. Circular 556.	
8	TITANIUM	99,99% pure, (Assoc. Elec. Industries) single crystal.	
9		Rem-Cru, RC130-B, 4,7% Mn, 3,99% Al, 0,14% C.	

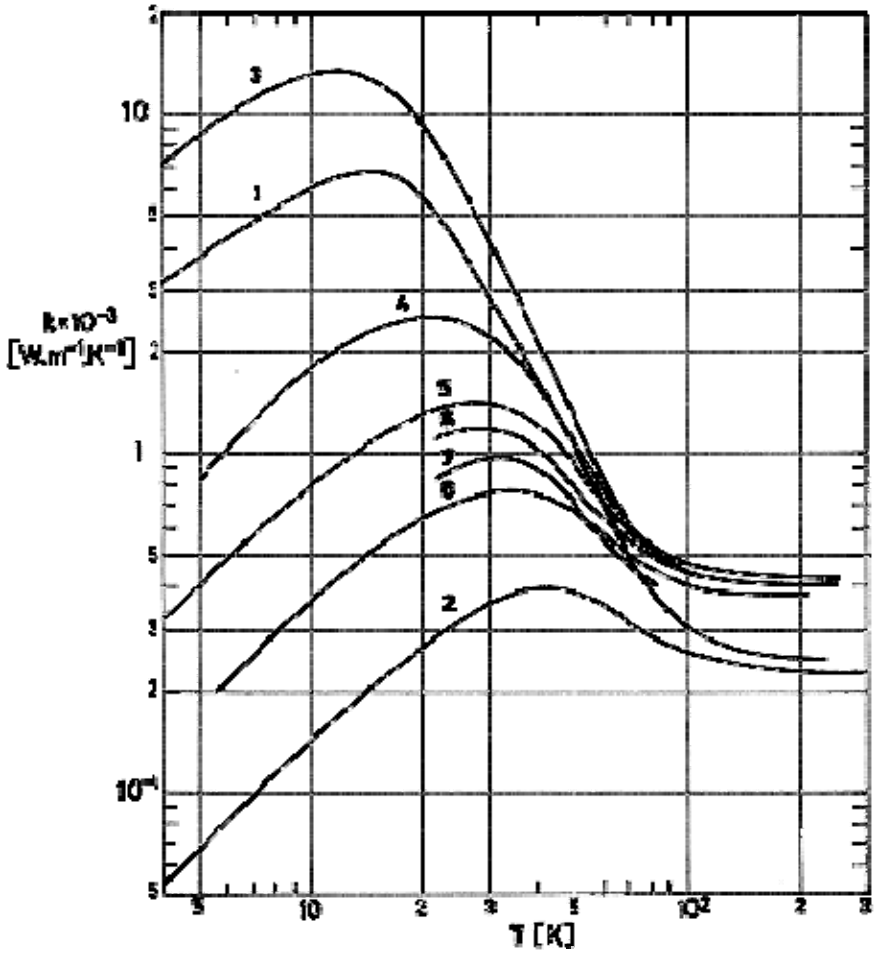

Figure 8-104: Thermal conductivity, *k*, of Aluminium and Copper vs. temperature, *T*. Details concerning these materials are given below.

Explanation of the Figure 8-104

KEY	MATERIAL	COMPOSITION	REFERENCE
1	ALUMINIUM	99,9960ure, single crystal (Alcoa) and 99,99%	Johnson (1961)

		pure, cold drawn (Alcoa).	[109]
2		99% commercial pure, (Alcoa) drawn.	
3	COPPER	High purity; 99,999% pure, annealed, (Am. Smelt Ref.).	
4		Coalesced; 99,98% pure, annealed, (Phelps Dodge).	
5		Electrolytic Tough Pitch; 99,95% pure, annealed.	
6		O.F.H.C.; 99,95% pure; annealed (Oxygen free high conductivity).	
7		(Pb)Cu; 1% Pb, annealed.	
8		(Te)Cu; 0,6% Te, annealed.	

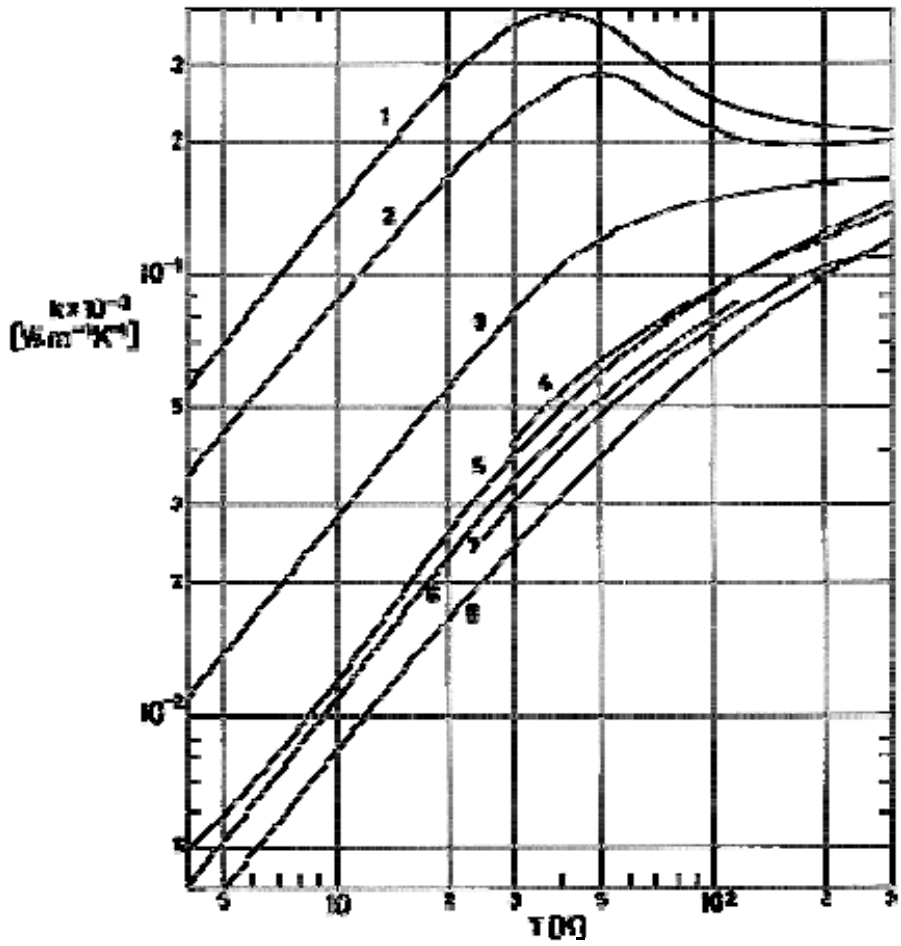

Figure 8-105: Thermal conductivity, *k*, of Aluminium alloys vs. temperature, *T*. Details concerning these materials are given below.

Explanation of the Figure 8-105

KEY	MATERIAL	COMPOSITION	REFERENCE
1	ALUMINIUM ALLOYS	1100-F; Alcoa, 99% Al, as fabricated.	Johnson (1961) [109]
2		6063-T5; Alcoa, 0,4% Si, 0,7% Mg, 98,5% Al as fabricated.	
3		3003-F; Alcoa, 1,2% Mn, 98,5% Al, as fabricated.	
4		4S; 16% Cu, 1,02% Mg, 1,20% Mn, 0,52% Fe, 0,13% Si, 0,02% Cr, 0,02% Ti.	
5		5052-O; 0,25% Cr, 2,5% Mg, 97% Al, annealed.	
6		5154-O; 0,25% Cr, 3,5% Mg, 96% Al, annealed.	

7		75-S; 1,5%Cu, 5,5% Zn, 2,5% Mg, 0,2% Mn, 0,3% Cr.	
8		2024-T4; 0,6% Mn, 1,5% Mg, 4,5% Cu, 93% Al, solution heat treated.	

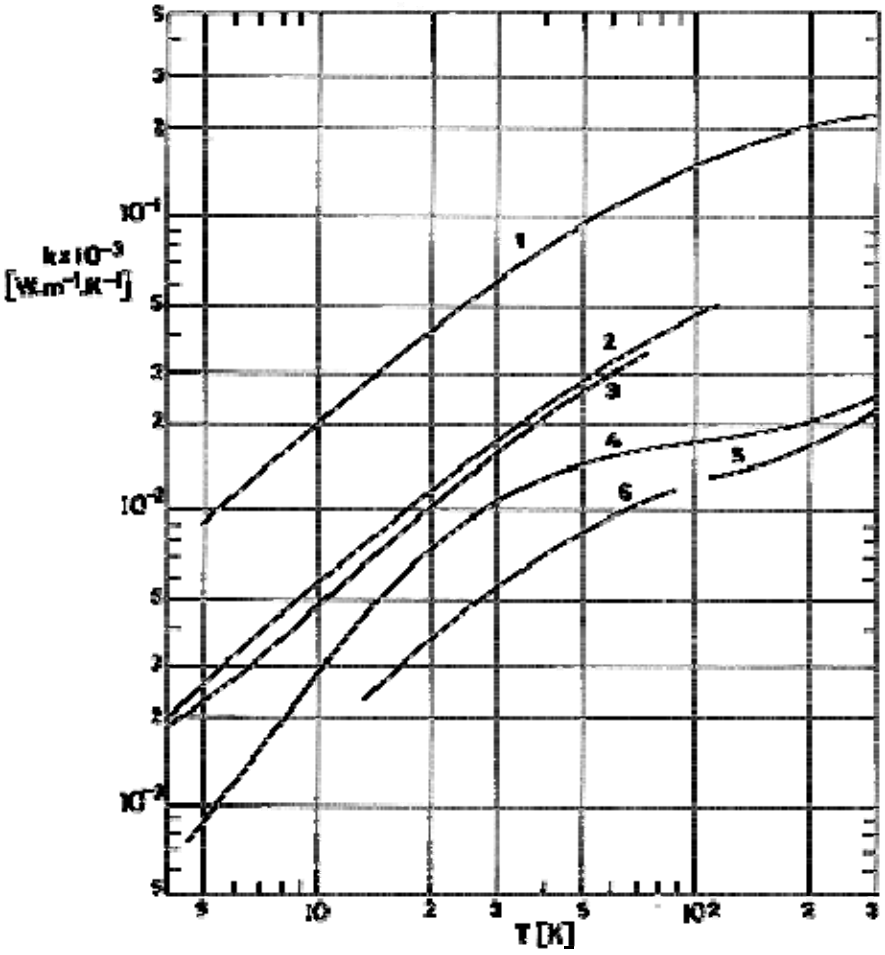

Figure 8-106: Thermal conductivity, *k*, of several Copper alloys vs. temperature, *T*. Details concerning these materials are given below.

Explanation of the Figure 8-106

KEY	MATERIAL	COMPOSITION	REFERENCE
1	COPPER ALLOYS	Phos. Deox. Copper; 0,027% P, 99% Cu, Commercial hard temperature.	Johnson (1961) [109]
2		(Pb) Brass; 35,7% Zn, 3,27% Pb, 1% Sn, 60% Cu,	

		hard temperature.	
3		Beryllium Copper; 2% Be, 98% Cu, held at 573 K for two hours.	
4		German Silver; 47% Cu, 41% Zn, 9% Ni, 2% Pb and 62% Cu, 22% Zn, 15% Ni.	
5		Manganin; 84% Cu, 12% Mn, 4% Ni.	
6		Silicon Bronze; 3,15% Si, 1,13% Mn, 1% Zn, 94% Cu, hard temperature.	

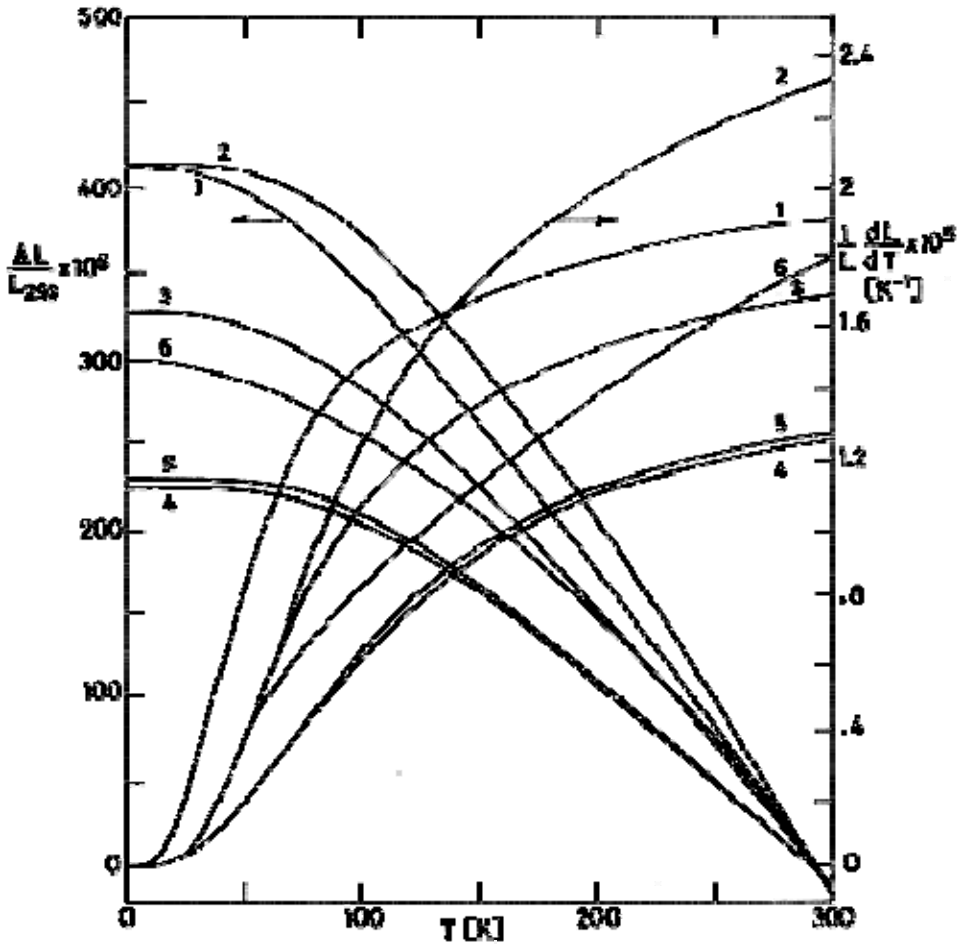

Figure 8-107: Total fractional expansion, $\Delta L/L_{293} = (L_{293}-L)/L_{293}$, and coefficient of expansion, $(1/L)(dL/dT)$, of several metallic materials vs. temperature, T. Details concerning these materials are given below.

Explanation of the Figure 8-107

KEY	MATERIAL	COMPOSITION	REFERENCE
1	SILVER	PURE	Johnson (1961) [109]
2	ALUMINIUM	PURE	
3	COPPER	PURE	
4	NICKEL	PURE	
5		International Nickel Co. Low-carbon nickel, 99,6% pure	
6	STAINLESS STEEL [a]	Stainless Steel 304	Wingley & Halford (1971) [265]

[a] Curve giving $(1/L)(dL/dT)$ for Stainless Steel has been calculated by the compiler after Wingley & Halford (1971) [265].

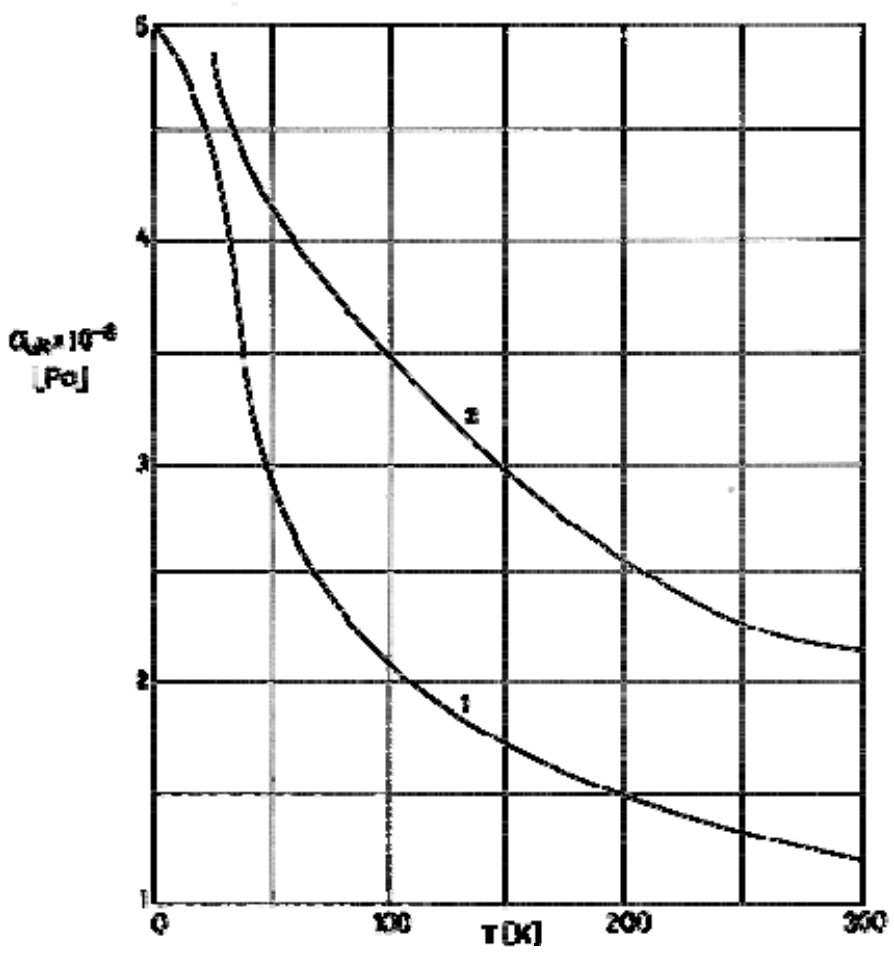

Figure 8-108: Ultimate tensile strength, σ_{ult}, of Aluminium and Copper vs. temperature, *T*. Details concerning these materials are given below.

Explanation of the Figure 8-108

KEY	MATERIAL	COMPOSITION	REFERENCE
1	ALUMINIUM	PURE	Rosenberg (1959)[199]
2	COPPER	PURE	Kropschot (1962) [126]

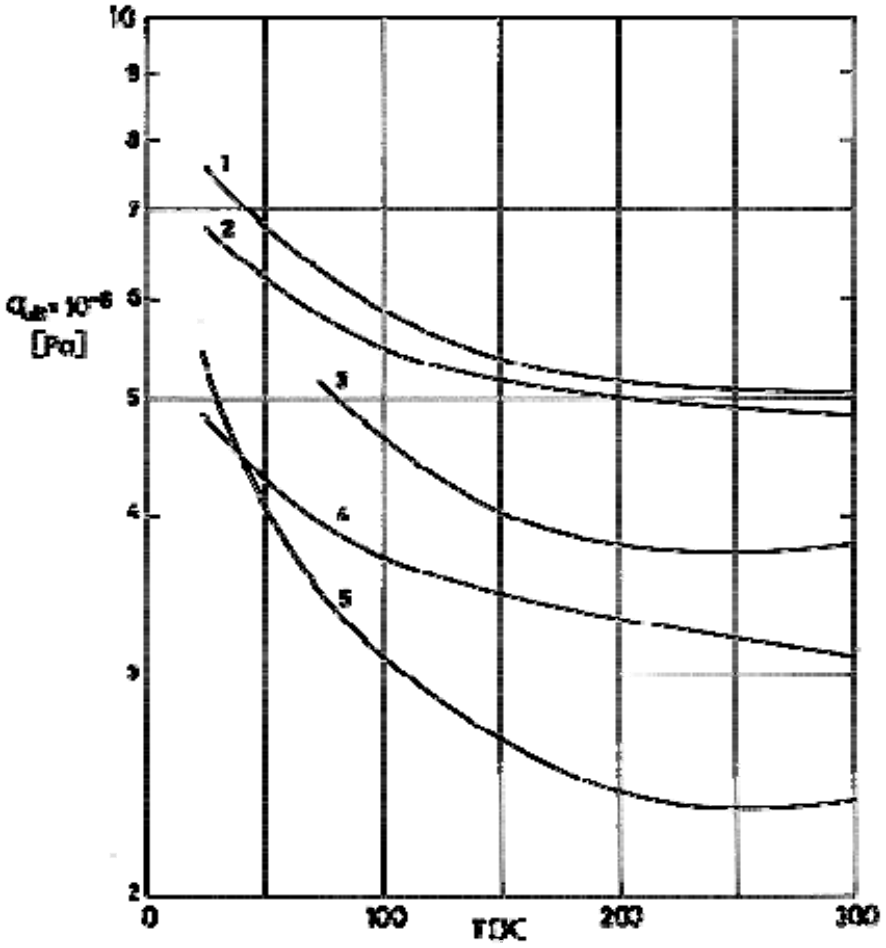

Figure 8-109: Ultimate tensile strength, σ_{ult}, of Aluminium alloys vs. temperature, *T*. Details concerning these materials are given below.

Explanation of the Figure 8-109

KEY	MATERIAL	COMPOSITION	REFERENCE
1	ALUMINIUM ALLOYS	2024-T3	Kropschot (1962) [126]
2		2014-T6	
3		5056-H34	
4		6061-T6	
5		5052-H34	

NOTE T3 Condition: Solution heat treated, cold worked, and naturally aged to a substantially stable condition.

T6 Condition: Solution heat treated and artificially aged.

H34 Condition: Strain hardened (half hard) and then stabilized.

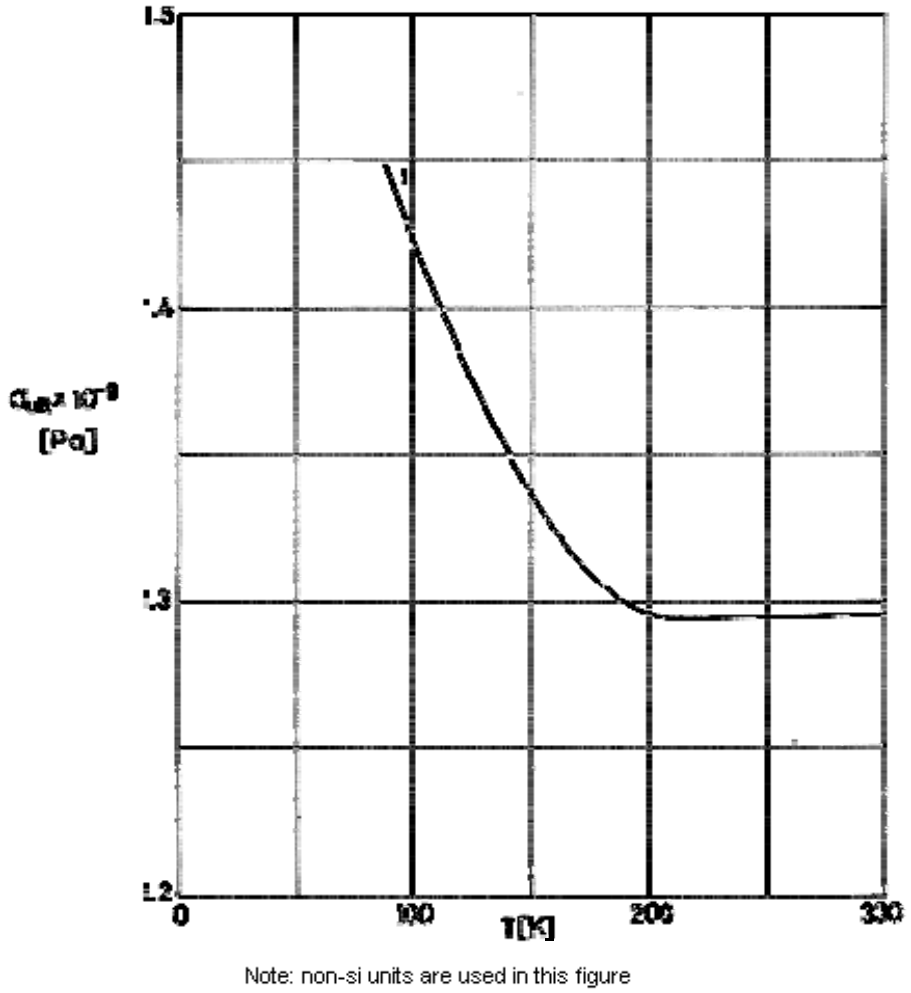

Figure 8-110: Ultimate tensile strength, σ_{ult}, of a representative copper alloy vs. temperature, *T*. Details concerning these materials are given below.

Explanation of the Figure 8-110

KEY	MATERIAL	COMPOSITION	REFERENCE
1	COPPER ALLOYS	Be Cu (Berylco 25)	Kropschot (1962) [126]

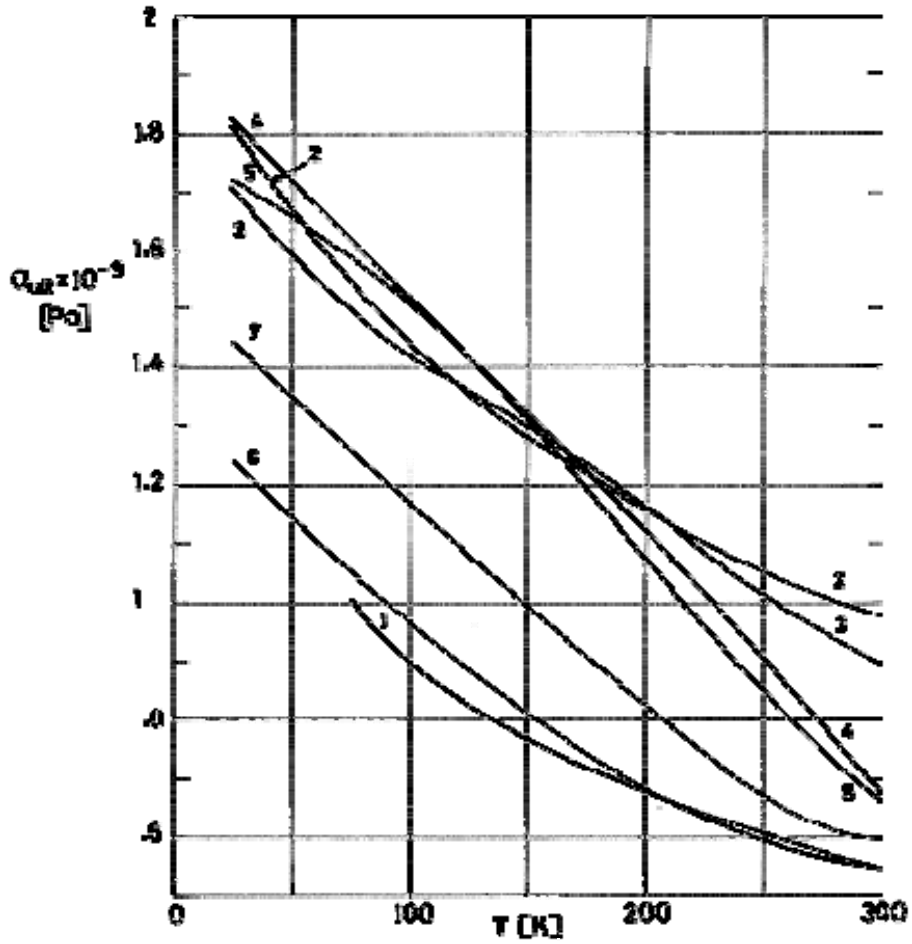

Note: non-si units are used in this figure

Figure 8-111: Ultimate tensile strength, σ_{ult}, of Titanium, Titanium alloys and Stainless Steel vs. temperature, *T*. Details concerning these materials are given below.

Explanation of the Figure 8-111

KEY	MATERIAL	COMPOSITION	REFERENCE
1	TITANIUM	PURE	Kropschot (1962) [126]
2	TITANIUM ALLOYS	6 Al - 4 V annealed	
3		6 Al - 2,5 Sn annealed	
4	ATAINLESS STEEL AISI 300 SERIES	302 annealed	
5		304 annealed	
6		310 annealed	
7		316 annealed	

8.5 Composite materials

			Glass-Reinforced Composites		
			Uniaxial Fiber	Crossply 0°/90°	Cloth
Specific Heat				Figure 8-112	
Thermal Conductivity [a]	Normal				Figure 8-113
	In plane	Longitudinal	Figure 8-114	Figure 8-114	Figure 8-113
		Transverse	Figure 8-114	Figure 8-114	
Thermal Expansion	Normal		Figure 8-115	Figure 8-115	Figure 8-116
	In plane		Figure 8-115	Figure 8-115	Figure 8-117

Tensile Strength	Figure 8-118	Figure 8-118	Figure 8-118
Compressive Strength	Figure 8-119	Figure 8-119	Figure 8-119
Flexural Strength	Figure 8-120	Figure 8-120	Figure 8-120

			Advanced Composites		
			Uniaxial Fiber		
			Graphite-Epoxy	Boron Epoxy	Others
Specific Heat			Figure 8-121	Figure 8-121	Figure 8-121
Thermal Conductivity [a]		Longitudinal	Figure 8-122	Figure 8-122	Figure 8-122
		Transverse	Figure 8-122	Figure 8-122	
Thermal Expansion		Longitudinal	Figure 8-123	Figure 8-123	Figure 8-123
		Transverse	Figure 8-124	Figure 8-124	Figure 8-124

Tensile Strength	In plane	Longitudinal	Figure 8-125	Figure 8-126	Figure 8-126
		Transverse	Figure 8-125	Figure 8-126	Figure 8-126
Compressive Strength	In plane	Longitudinal		Figure 8-127	Figure 8-127
		Transverse		Figure 8-127	Figure 8-127
Flexural Strength	In plane	Longitudinal	Figure 8-128	Figure 8-129	Figure 8-129
		Transverse	Figure 8-128		

	Several Fibers
Cost	Figure 8-130

[a] Thermal conductivities of structural tubes are given in Figure 8-131.

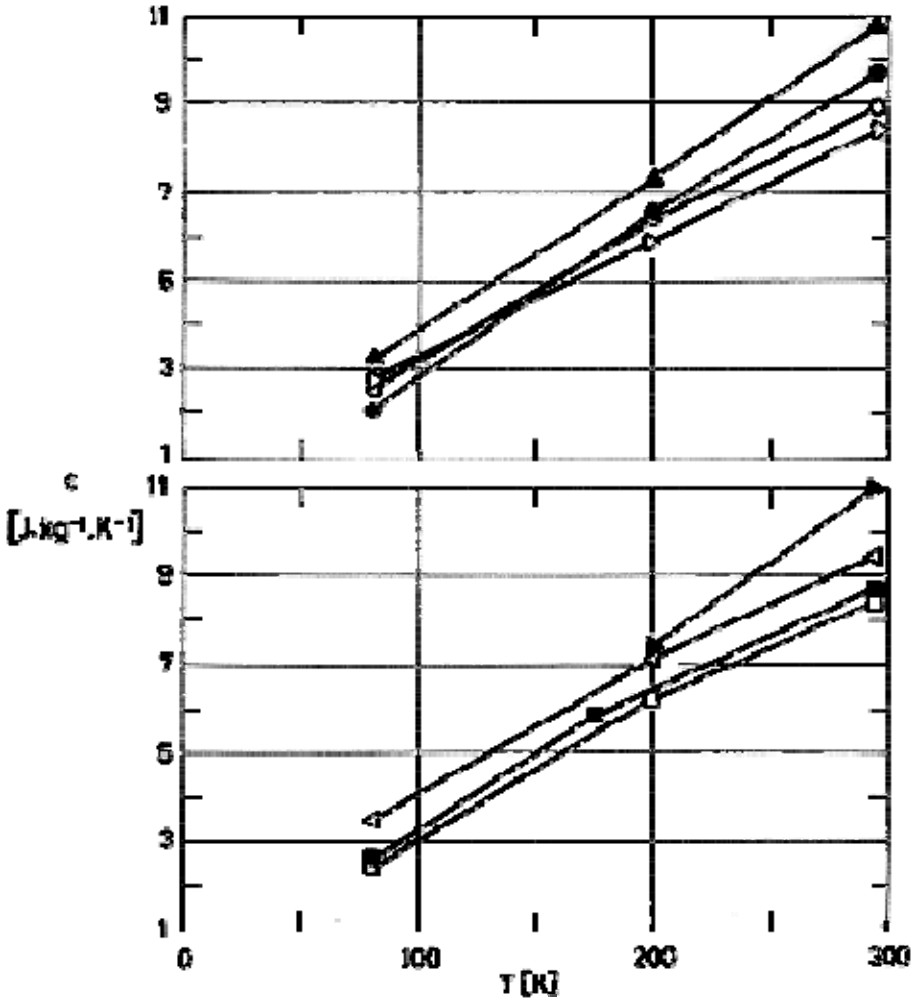

Figure 8-112: Specific heat, *c*, vs. temperature, *T*, of several Glass-Reinforced Composites. From Kasen (1975)a [115].

Explanation of the Figure 8-112.

○	Epoxy	▷	Phenolic	▲	Teflon
□	Silicone	●	Phenyl Silane	▶	Phenyl Formaldehyde
◁	Polyester	■	Polybenzimidazole		

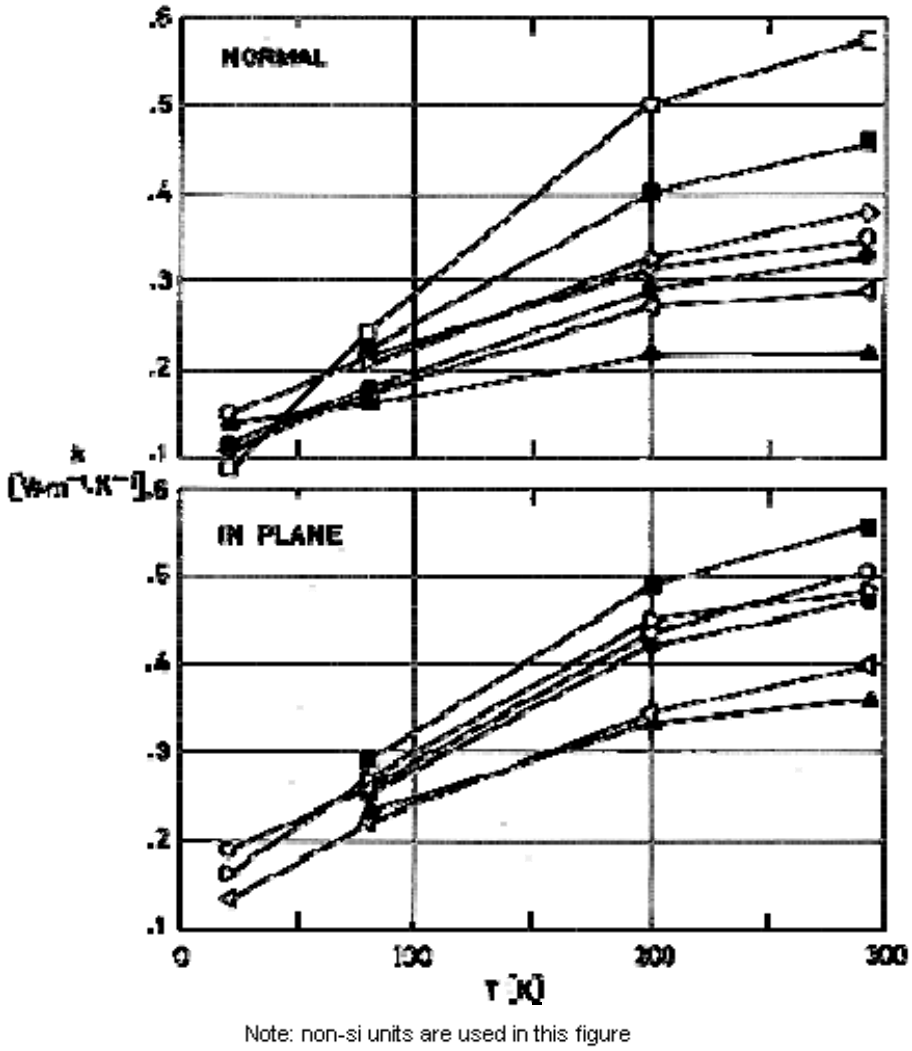

Note: non-si units are used in this figure

Figure 8-113: Thermal conductivity, *k*, vs. temperature, *T*, of several Glass-Cloth Reinforced Composites. From Kasen (1975)a [115].

Explanation of the Figure 8-113.

○	Epoxy	▷	Phenolic	▲	Teflon
□	Silicone	●	Phenyl Silane		
◁	Polyester	■	Polybenzimidazole		

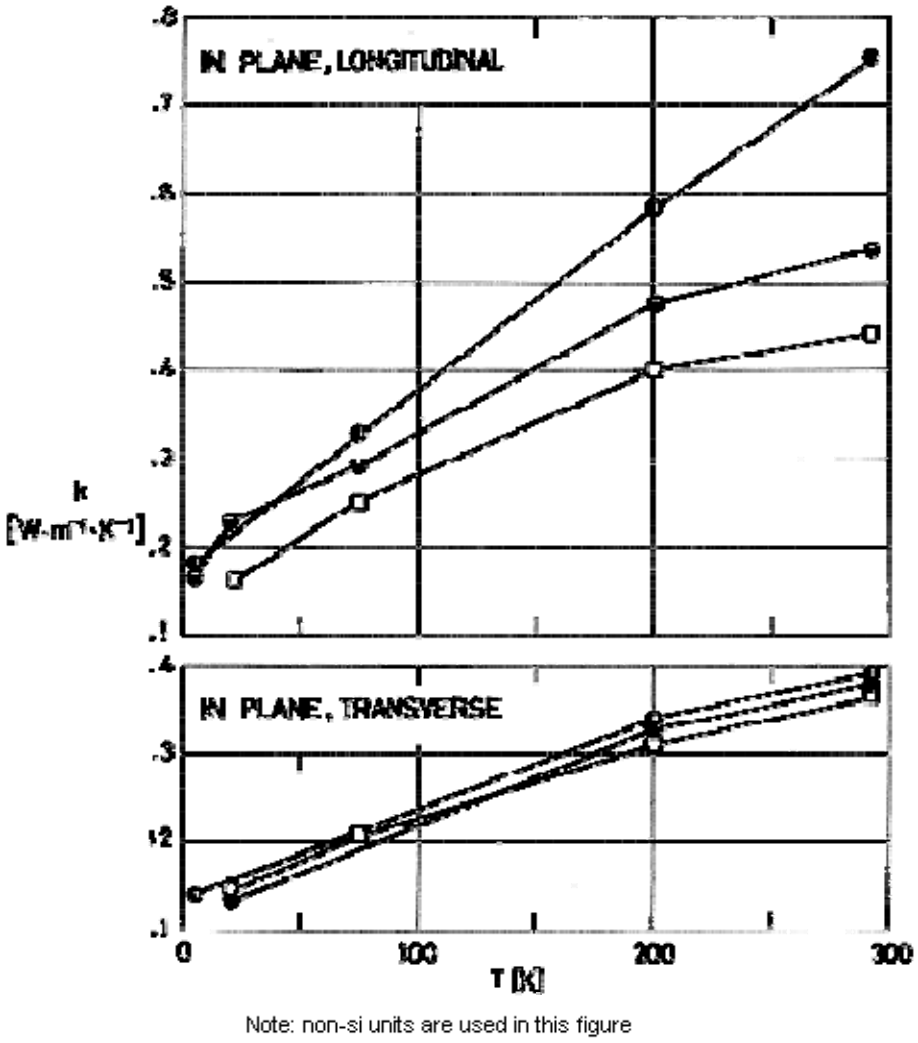

Note: non-si units are used in this figure

Figure 8-114: Thermal conductivity, *k*, in the plane vs. temperature, *T*, of several Glass-Fiber Reinforced Composites. From Kasen (1975)a [115].

Explanation of the Figure 8-114

◐	Epoxy (Uniaxial Fiber)
◓	Epoxy (Crossply 0°/90°)
□	Silicone (Crossply 0°/90°)

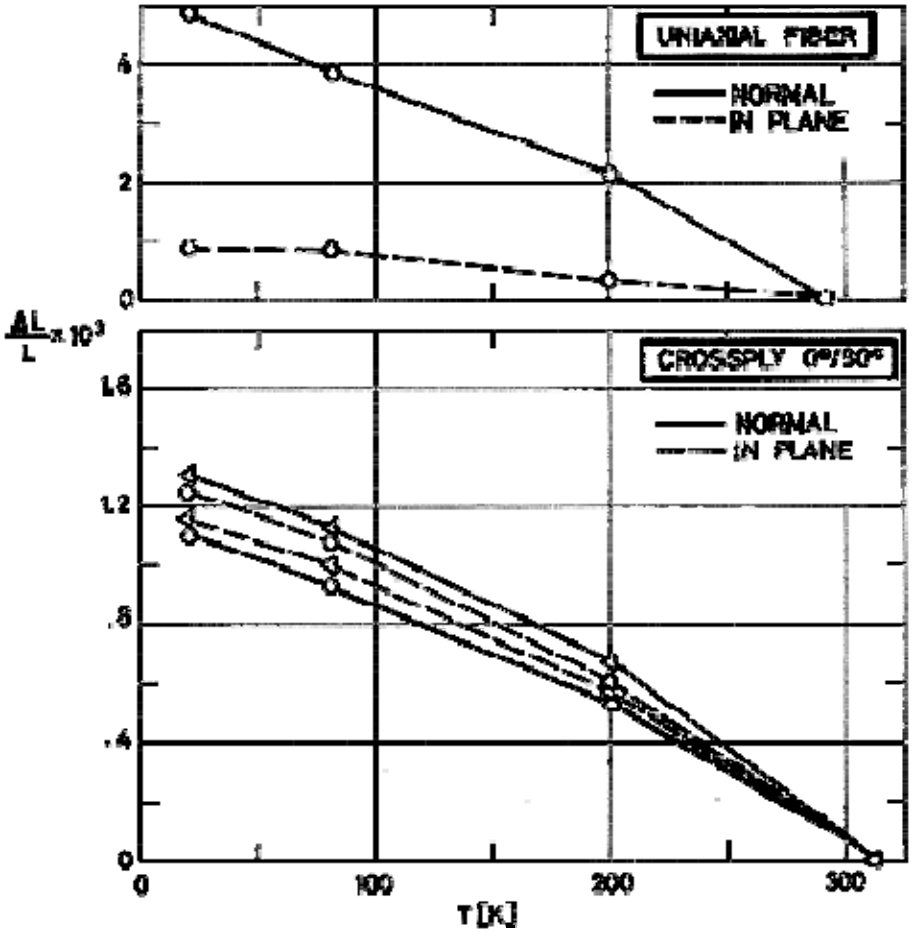

Note: non-si units are used in this figure

Figure 8-115: Thermal expansion, $\Delta L/L$, vs. temperature, T, of several Glass-Fiber Reinforced Composites. From Kasen (1975)a [115].

Explanation of the Figure 8-115.

○	Epoxy
◁	Polyester *

NOTE *Denotes minimal data.

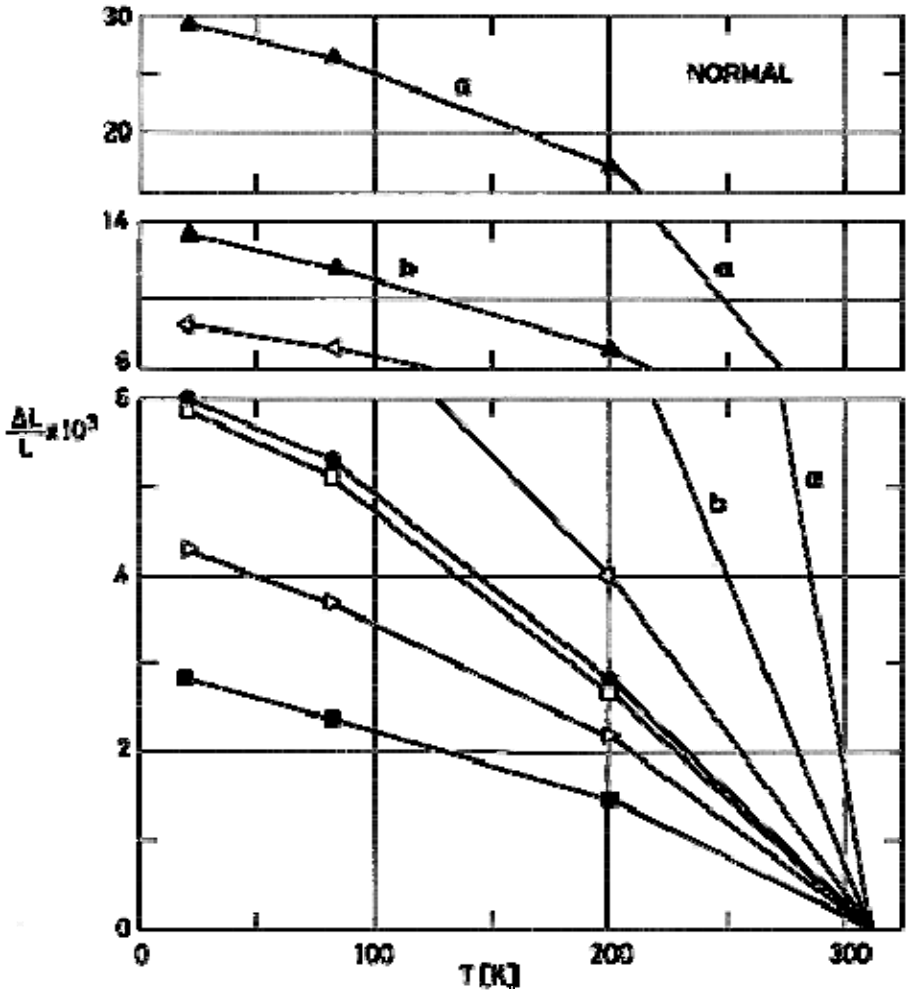

Figure 8-116: Thermal expansion, $\Delta L/L$, normal to the plane, vs. temperature, T, of several Glass-Cloth Reinforced Composites. From Kasen (1975)a [115].

Explanation of the Figure 8-116.

□	Silicone	●	Phenyl Silane	▲(a)	Teflon TFE
◁	Polyester	■	Polybenzimidazole	▲(b)	Teflon FEP
▷	Phenolic				

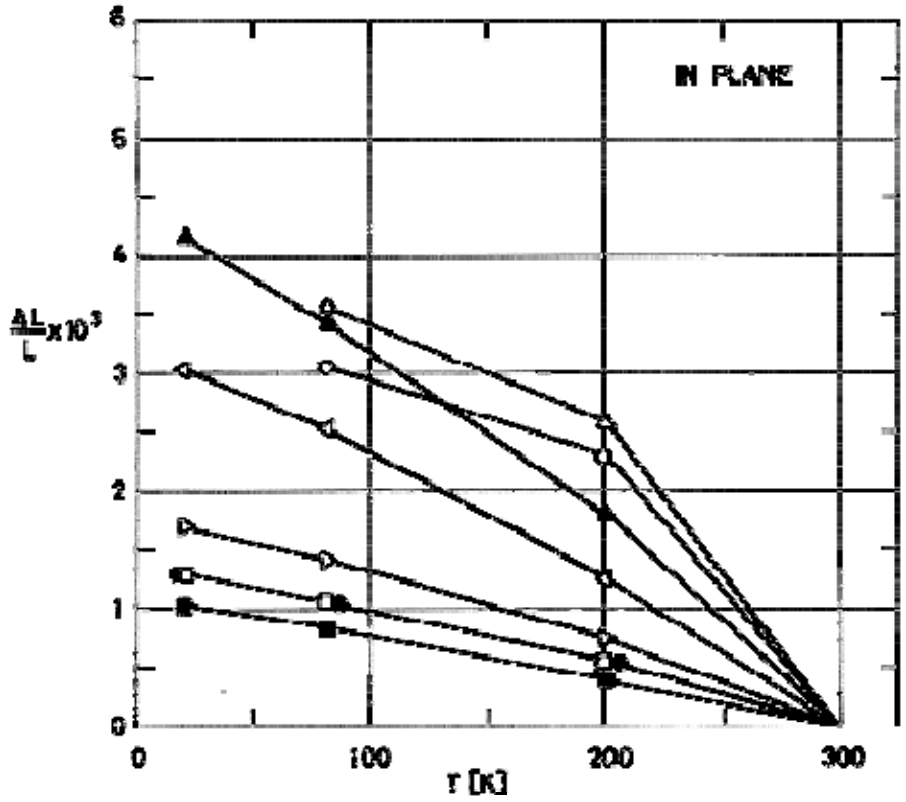

Figure 8-117: Thermal expansion, *ΔL/L*, in the plane, vs. temperature, *T*, of several Glass-Cloth Reinforced Composites. From Kasen (1975)a [115].

Explanation of the Figure 8-117.

○	Epoxy	◁	Polyester	■	Polybenzimidazole
□	Silicone	▷	Phenolic	▲	Teflon
△	Polyurethane	●	Phenyl Silane		

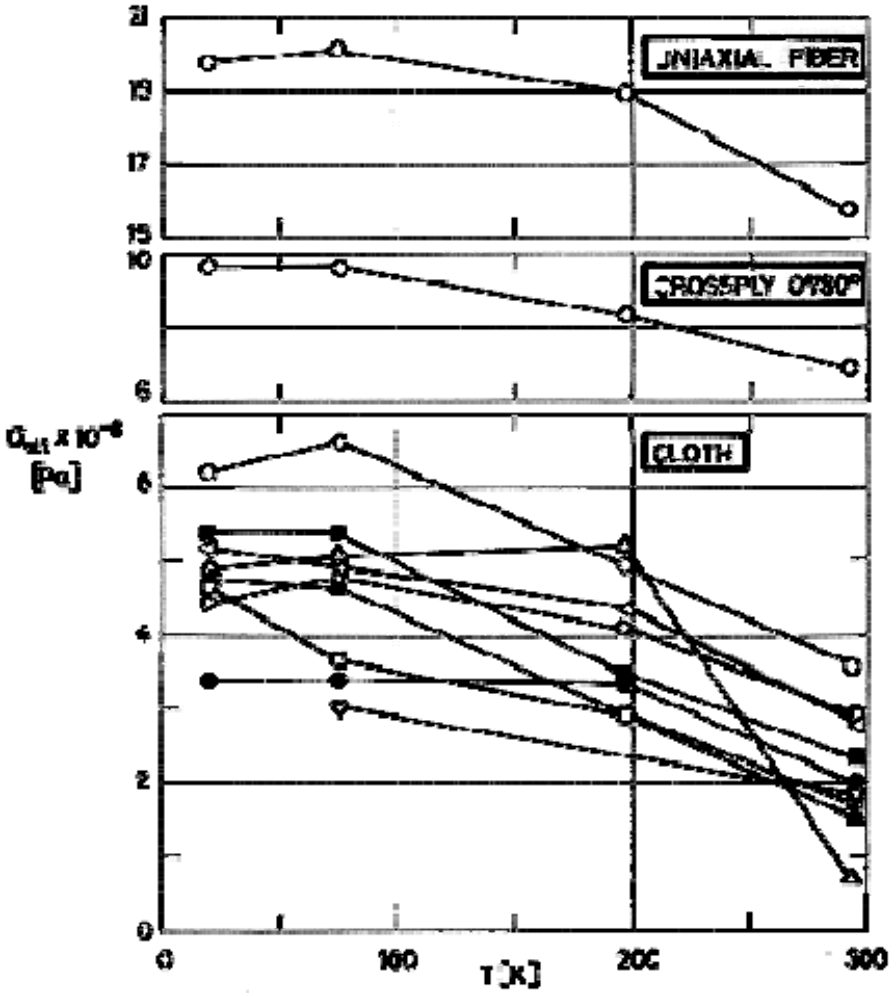

Figure 8-118: Ultimate tensile strength, σ_{ult}, vs. temperature, T, of several Glass-Reinforced Composites. From Kasen (1975)a [115].

Explanation of the Figure 8-118.

○	Epoxy	▽	Polyimide *	●	Phenyl Silane
□	Silicone	◁	Polyester	■	Polybenzimidazole *
△	Polyurethane *	▷	Phenolic	▲	Teflon

NOTE *Denotes minimal data.

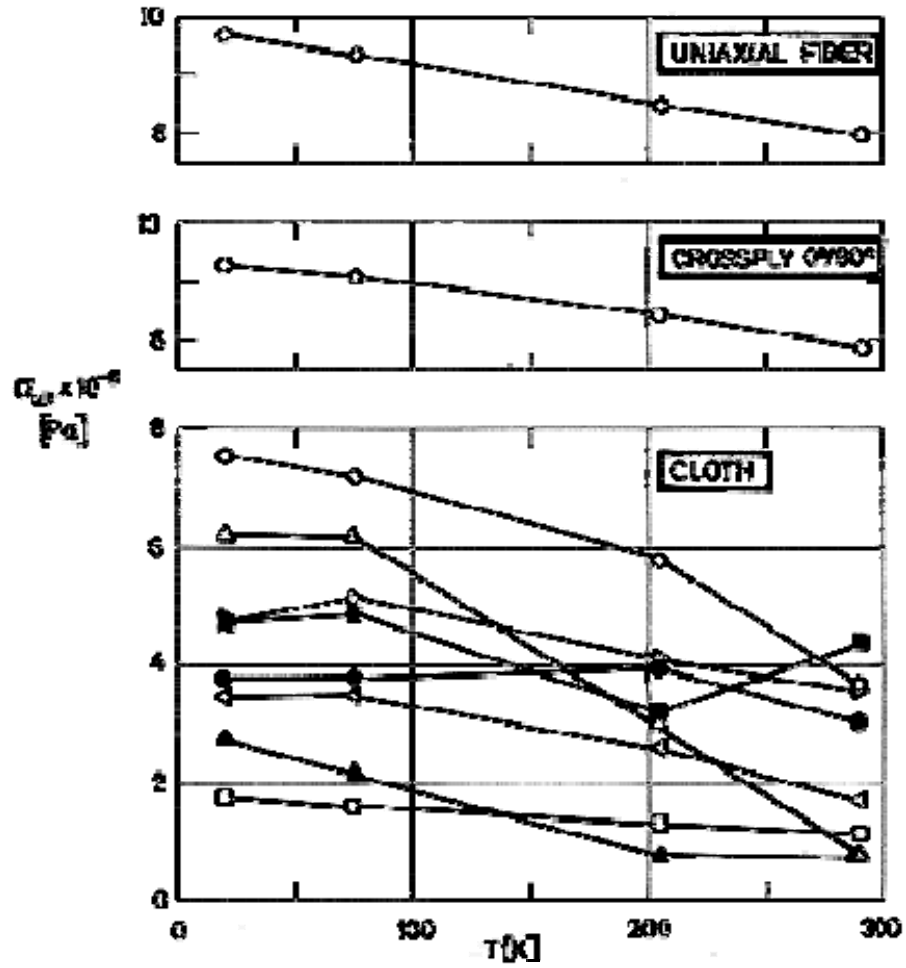

Figure 8-119: Ultimate compressive strength, σ_{ult}, vs. temperature, T, of several Glass-Reinforced Composites. From Kasen (1975)a [115].

Explanation of the Figure 8-119.

○	Epoxy	▽	Polyimide	●	Phenyl Silane *
□	Silicone	◁	Polyester	■	Polybenzimidazole *
△	Polyurethane	▷	Phenolic	▲	Teflon

NOTE *Denotes minimal data.

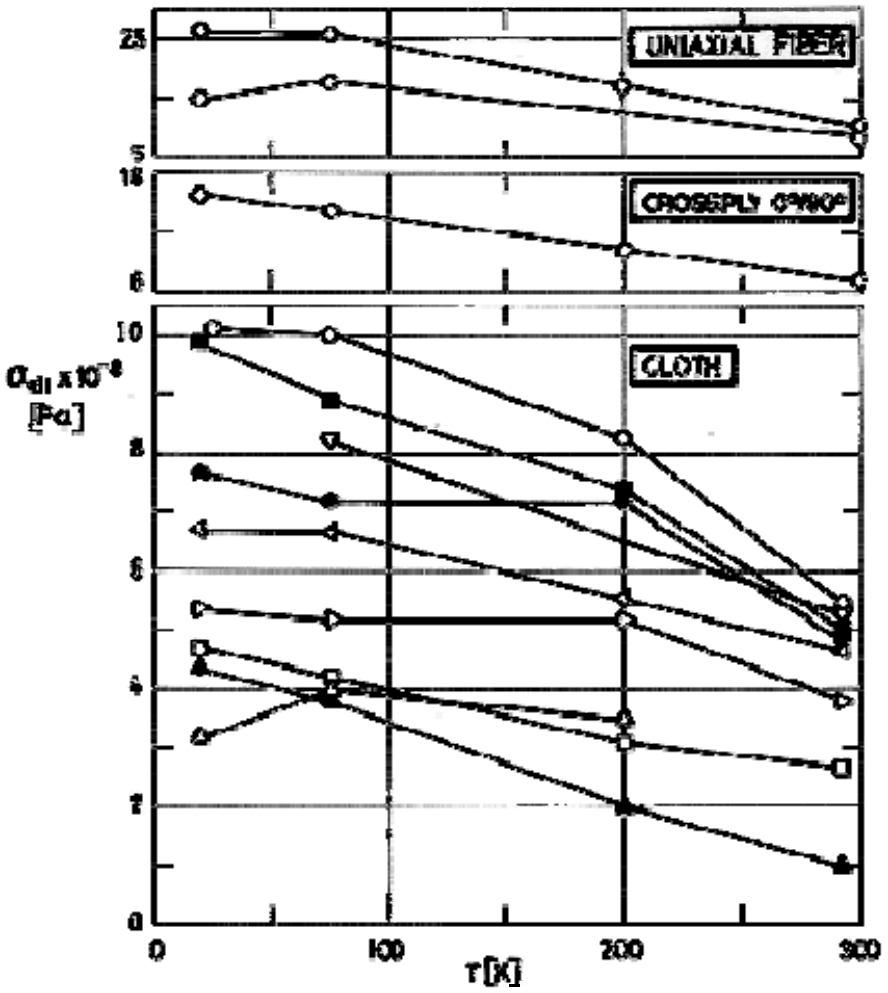

Figure 8-120: Ultimate flexural strength, σ_{ult}, vs. temperature, T, of several Glass-Reinforced Composites. From Kasen (1975)a [115].

Explanation of the Figure 8-120.

○	Epoxy	▽	Polyimide *	●	Phenyl Silane
□	Silicone *	◁	Polyester	■	Polybenzimidazole *
△	Polyurethane *	▷	Phenolic	▲	Teflon

NOTE *Denotes minimal data.

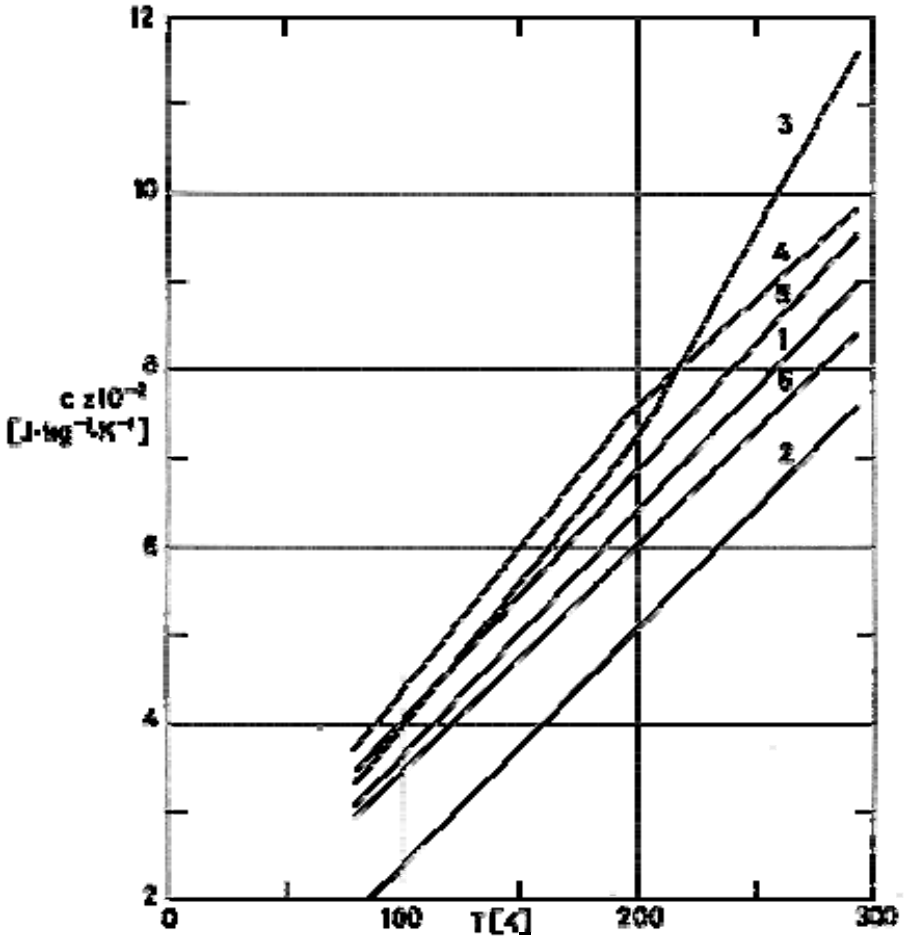

Figure 8-121: Specific heat, *c*, vs. temperature, *T*, of several Advanced Composites. From Kasen (1975)b [116]. Details concerning these composites are given below.

Explanation of the Figure 8-121.

That figure gives the specific heat, *c*, vs. temperature *T*, of several Advanced Composites.

KEY	FIBER		MATRIX	
	NAME	MANUFACTURER	NAME	MANUFACTURER
1	GY-70 [a]	Celanese Corp.	X-904 [a]	Fiberite Corp.
	HT-S [a]	Courtaulds Ltd.		
2	Graphite		Phenolic	
3	Boron [b]		Epoxy [b]	
4	Boron		Aluminium 6061	
5	Borsic[c]-Steel	Hamilton Standard	Aluminium	

6	Borsic[c]-Titanium	Corp.		

NOTE From Kasen (1975)b [116].

[a] Graphite-Epoxy Composites.

[b] Boron-Epoxy composite id SP-272, manufactured by 3 M Co.

[c] Borsic is the trade name of boron fiber coated with a thin layer of silicon carbide.

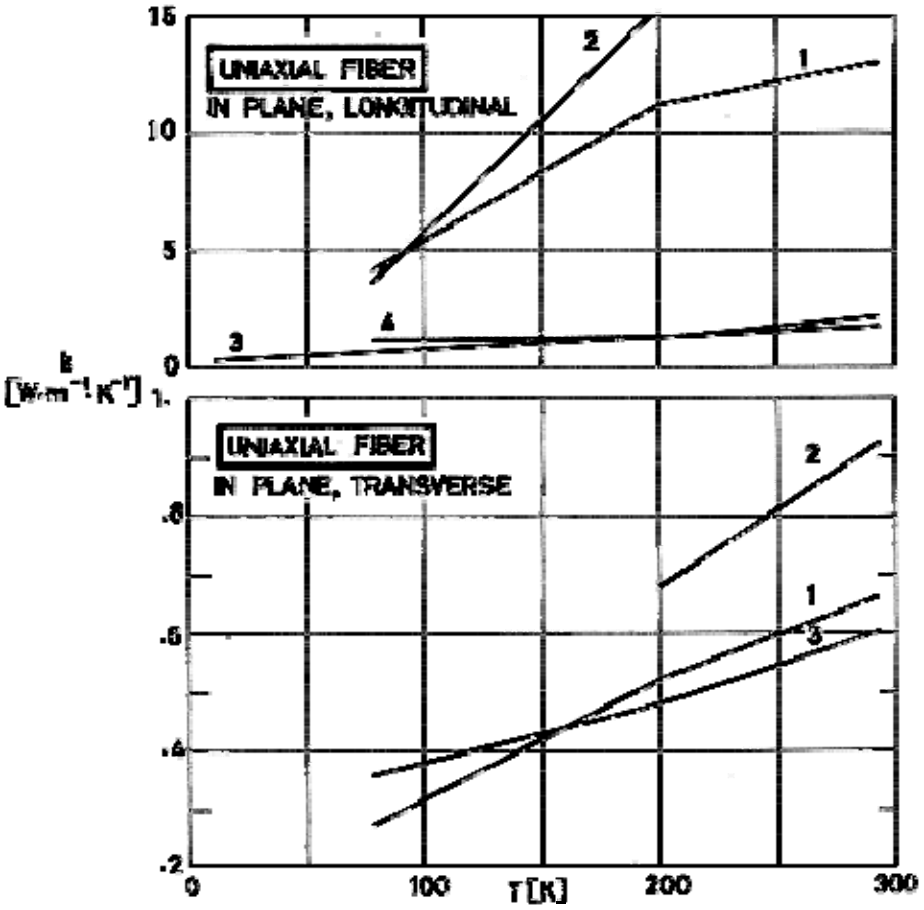

Note: non-si units are used in this figure

Figure 8-122: Thermal conductivity, *k*, in the plane, vs. temperature, *T*, of several Uniaxial Advanced Composites. From Kasen (1975)b [116]. Details concerning these composites are given below.

Explanation of the Figure 8-122.

That figure gives the thermal conductivity, *k*, vs. temperature *T*, of several Uniaxial Advanced Composites.

KEY	FIBER		MATRIX	
	NAME	MANUFACTURER	NAME	MANUFACTURER
1	HT-S [a]	Courtaulds Ltd.	X-904 [a]	Fiberite Corp.
2	Thornel 50 [a]	Union Carbide Corp.	Epoxy [a]	
3	Boron [b]		Epoxy [b]	
4	PRD 49 [c] (Kevlar 49)	E.I. duPont de Nemours Inc.	Epoxy	

NOTE From Kasen (1975)b [116].

[a] Graphite-Epoxy Composites.

[b] Boron-Epoxy composite id SP-272, manufactured by 3 M Co.

[c] PRD 49 (Kevlar 49) is the trade name of an aromatic polyimide fiber.

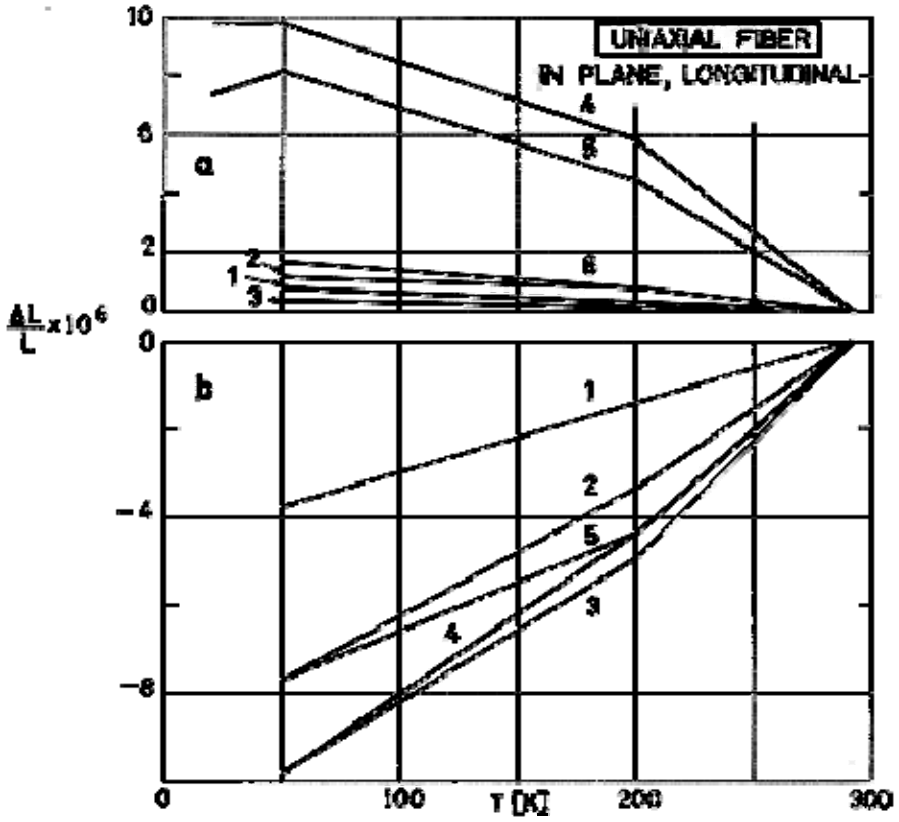

Figure 8-123: In plane, longitudinal thermal expansion, $\Delta L/L$, vs. temperature, T, of several Uniaxial Advanced Composites. From Kasen (1975)b [116]. Details concerning these composites are given below

Explanation of the Figure 8-123.

That figure gives the in plane, longitudinal thermal expansion, $\Delta L/L$, vs. temperature T, of several Uniaxial Advanced Composites. a, Graphite-Epoxy Composites. b,

Boron Composites.

	KEY	FIBER		MATRIX	
		NAME	MANUFACTURER	NAME	MANUFACTURER
a	1	Fibralloy 300	Mosanto Corp.	X-904	Fiberite Corp.
	2	GY-70	Celanese Corp.		
	3	HT-S	Cortlaulds Ltd.		
	4	PRD 49 (Kevlar 49) [a]	E.I. duPont de Nemours Inc.	NASA Resin 2 [b]	
	5	PRD 49		ERLB 4617	Union Carbide Plastics

		(Kevlar 49) [a]			Co.
	6	Thornel 75	Union Carbide Corp.		
b	1	Boron [c]		Epoxy [b]	
	2	Boron		Aluminium 6061	
	3	Borsic [d]	Hamilton Standard Corp.		
	4	Borsic[d]-Steel			
	5	Borsic[d]-Titanium			

NOTE From Kasen (1975)b [116].

[a] Aromatic Polyimide.

[b] NASA Resin 2, developed under NASA sponsorship, consists of:

PRODUCT	NAME	MASS PERCENT	MANUFACTURER
Resin	Epon 828	42,21	Shell Chemical Corp.
Flexibilizers and/or Hardeners	Dodecenyl succinic anhydride	48,92	
	Empol 1040	8,44	Emery Industries Inc.
	Benzyldimethylamine	0,42	

[c] Boron-Epoxy composite is SP-272, manufactured by 3 M Co.

[d] Borsic is the trade name of boron fiber coated with a thin layer of silicon carbide.

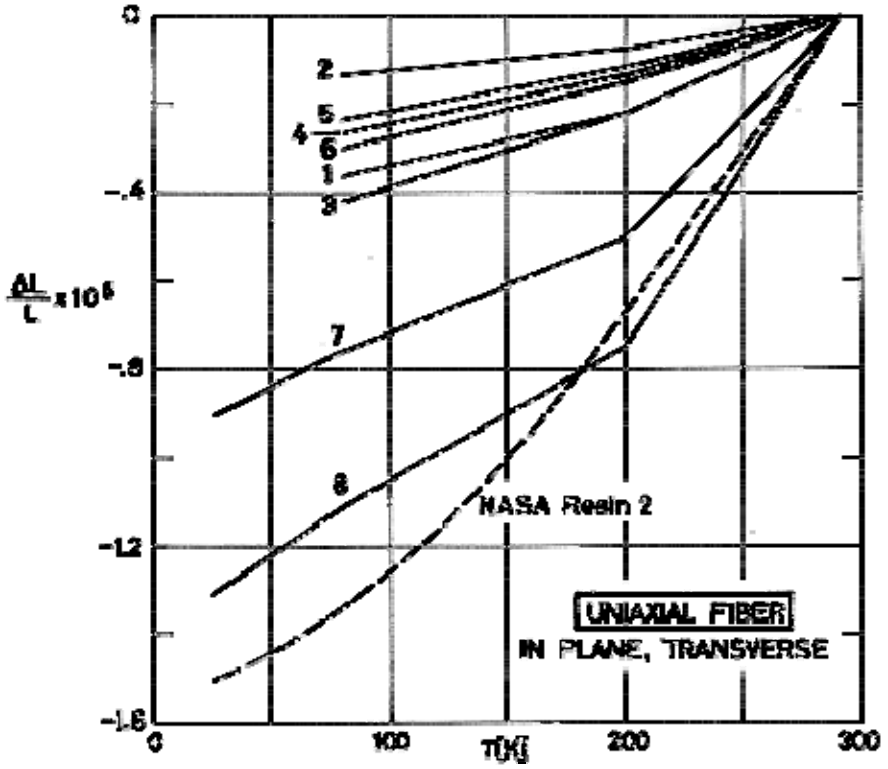

Note: non-si units are used in this figure

Figure 8-124: In plane, transverse thermal expansion, $\Delta L/L$, vs. temperature, T, of several Uniaxial Advanced Composites. From Kasen (1975)b [116]. Details concerning these composites are given below.

Explanation of the Figure 8-124.

That figure gives the in plane, transverse thermal expansion, $\Delta L/L$, vs. temperature T, of several Uniaxial Advanced Composites.

KEY	FIBER		MATRIX	
	NAME	MANUFACTURER	NAME	MANUFACTURER
1	Boron		Aluminium 6061	
2	Boron [a]		Epoxy [a]	
3	Borsic[b]-Steel	Hamilton Standard Corp.	Aluminium 6061	
4	Borsic[b]-Titanium			
5	Fibralloy 320 [c]	Mosanto Corp.	ERLB 4617 [d]	U. Carbide Plastics Co.
6	GY-70 [c]	Celanese Corp.	X-904 [d]	Fiberite Corp.
5	HT-S [c]	Courtaulds Ltd.		

7	PRD 49 [e] (Kevlar 49)	E.I. duPont de Nemours Inc.	ERLB 4617 [d]	U. Carbide Plastics Co.
8	PRD 49 [e] (Kevlar 49)		NASA Resin 2 [f]	

NOTE From Kasen (1975)b [116].

[a] Boron-Epoxy composite id SP-272, manufactured by 3 M Co.

[b] Borsic is the trade name of boron fiber coated with a thin layer of silicon carbide.

[c] Graphite fiber.

[d] Epoxy.

[e] Aromatic polyimide fiber.

[f] NASA Resin 2, developed under NASA sponsorship, consists of:

PRODUCT	NAME	MASS PERCENT	MANUFACTURER
Resin	Epon 828	42,21	Shell Chemical Corp.
Flexibilizers and/or Hardeners	Dodecenyl succinic anhydride	48,92	
	Empol 1040	8,44	Emery Industries Inc.
	Benzyldimethylamine	0,42	

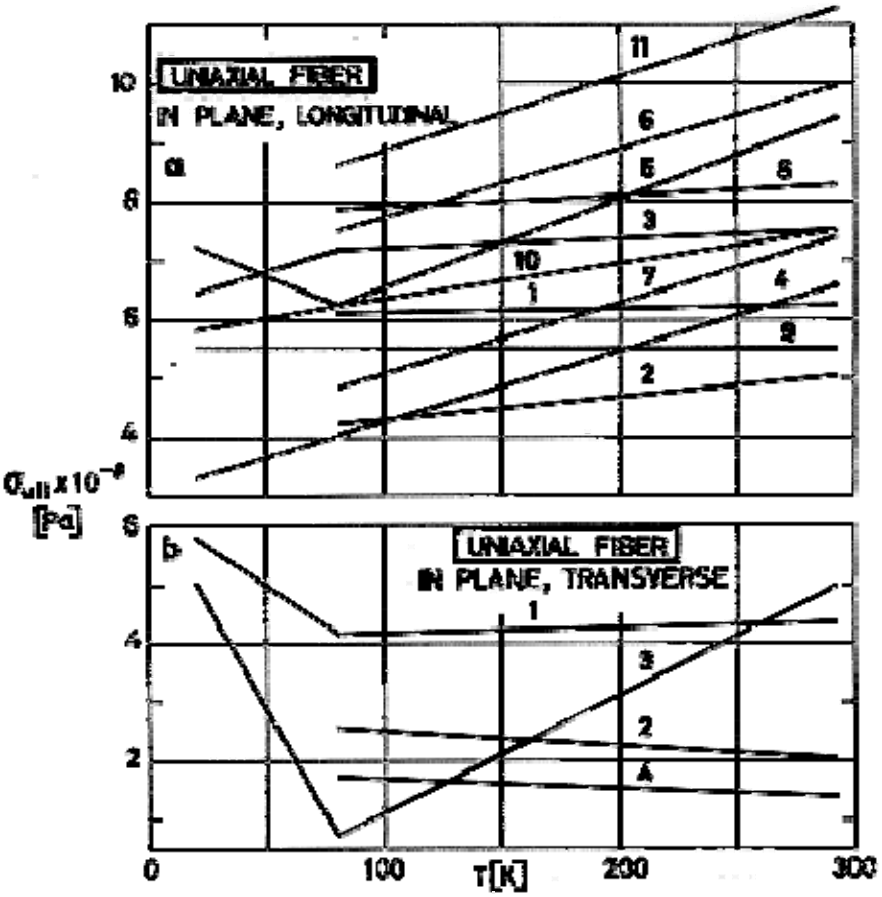

Figure 8-125: Ultimate tensile strength, σ_{ult}, in the plane, vs. temperature, *T*, of several Uniaxial Graphite-Epoxy Composites. From Kasen (1975)b [116]. Details concerning these composites are given below.

Explanation of the Figure 8-125.

That figure gives the ultimate tensile strength, σ_{ult}, in the plane, vs. temperature *T*, of several Uniaxial Graphite-Epoxy Composites.

	KEY	FIBER GRAPHITE		MATRIX EPOXY	
		NAME	MANUFACTURER	NAME	MANUFACTURER
a	1	GY-70	Celanese Corp.		
	2	HMG-25	Hitco Corp.		
	3	HMG-50			
	4	HM-S	Cortlaulds Ltd.		
	5	HT-S		X-904	Fiberite Corp.
	6	Modmor I	Morganite Ltd	ERLB 2256	Union Carbide Plastics Co.

	7	Modmor II			
	8	Samco 320	Samco Corp.	ERLB 2256	Union Carbide Plastics Co.
	9	Thornel 25	Union Carbide Corp.		
	10	Thornel 50			
	11	Thornel 75		ERLB 4617	Union Carbide Plastics Co.
b	1	HT-S	Cortlaulds Ltd.	NASA Resin 2 [a]	
	2	HT-S		X-904	Fiberite Corp.
	3	HT-S		ERLB 4617	Union Carbide Plastics Co.
	4	Thornel 75	Union Carbide Corp.		

NOTE From Kasen (1975)b [116].

[a] NASA Resin 2, developed under NASA sponsorship, consists of:

PRODUCT	NAME	MASS PERCENT	MANUFACTURER
Resin	Epon 828	42,21	Shell Chemical Corp.
Flexibilizers and/or Hardeners	Dodecenyl succinic anhydride	48,92	
	Empol 1040	8,44	Emery Industries Inc.
	Benzyldimethylamine	0,42	

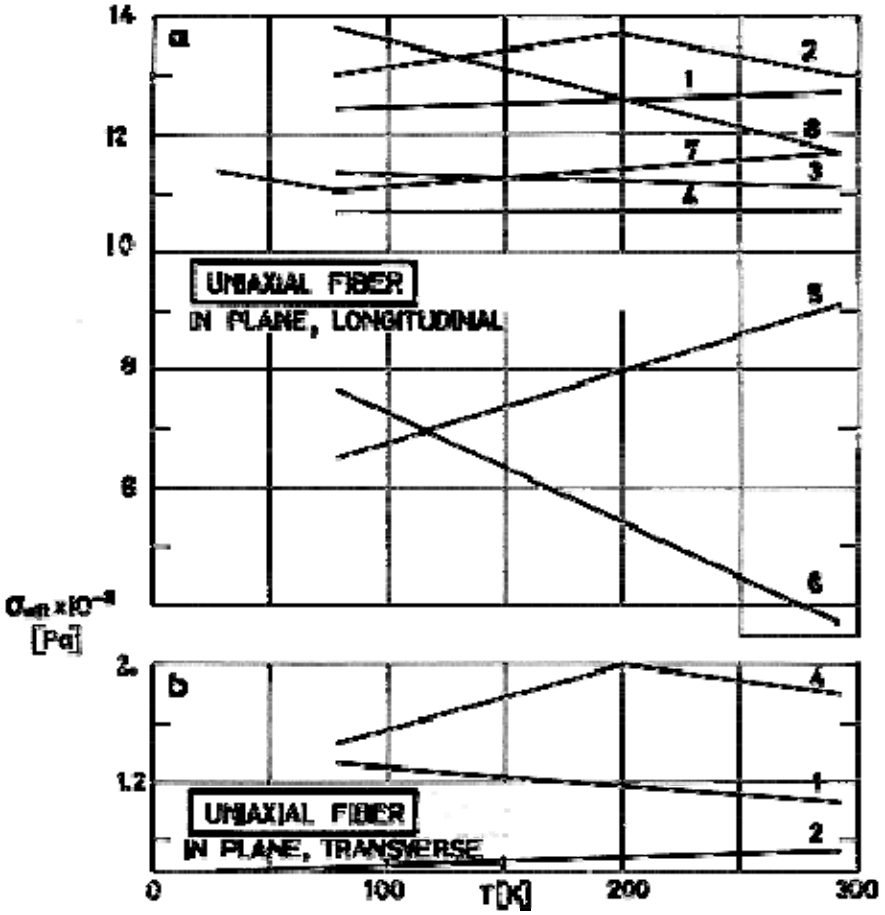

Note: non-si units are used in this figure

Figure 8-126: Ultimate tensile strength, σ_{ult}, in the plane, vs. temperature, T, of several Uniaxial Advanced Composites. From Kasen (1975)b [116]. Details concerning these composites are given below.

Explanation of the Figure 8-126.

That figure gives the ultimate tensile strength, σ_{ult}, in the plane, vs. temperature T, of several Uniaxial Advanced Composites.

	KEY	FIBER		MATRIX	
		NAME	MANUFACTURER	NAME	MANUFACTURER
a	1	Boron		Aluminium 6061	
	2	Boron		Epoxy	
	3	Borsic[a]-Steel	Hamilton Standard Corp.	Aluminium 6061	
	4	Borsic[a]-Titanium			

	5	HT-S [b]	Courtaulds Ltd.	Skybond 703 [c]	Mosanto Corp.
	6	HT-S [b]		HT-424 [d]	American Cyanamid
	7	PRD 49 (Kevlar 49) [e]	E.I. duPont de Nemours Inc.	Epoxy	
	8	Stainless Steel		Aluminium 2024	
b	1	Boron		Aluminium 6061	
	2	Boron		Epoxy	
	3	Borsic[a]-Titanium	Hamilton Standard Corp.	Aluminium 6061	

NOTE From Kasen (1975)b [116].

[a] Borsic is the trade name of boron fiber coated with a thin layer of silicon carbide.

[b] Graphite fiber.

[c] Polyimide matrix.

[d] Epoxy-Phenolic matrix.

[e] Aromatic polyimide fiber.

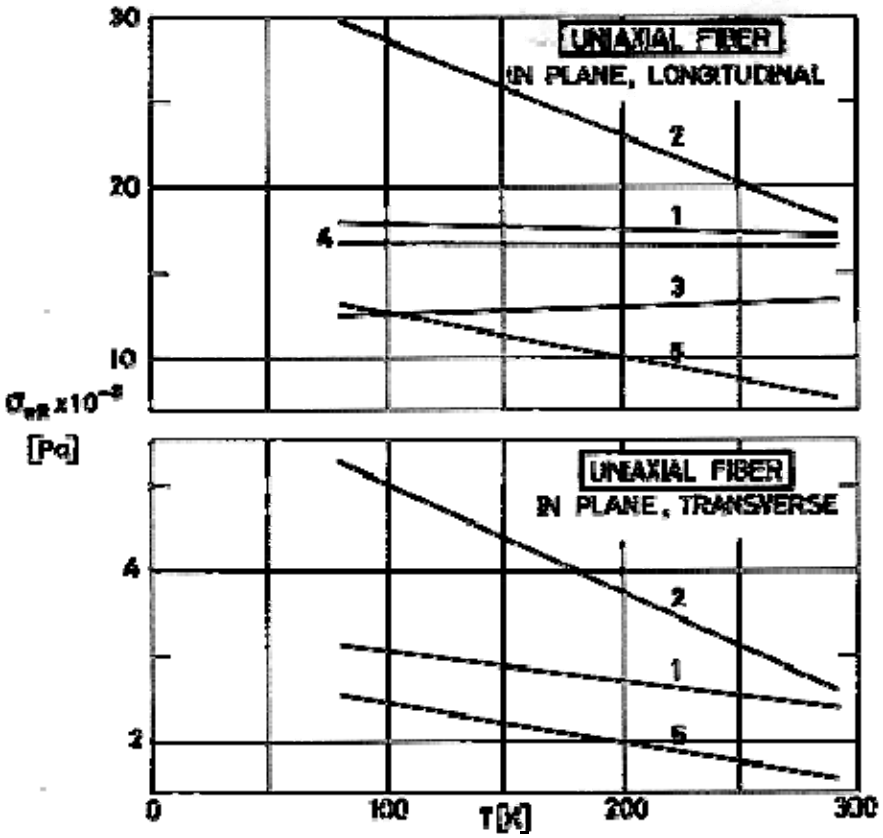

Figure 8-127: Ultimate compressive strength, σ_{ult}, in the plane, vs. temperature, T, of several Uniaxial Advanced Composites. From Kasen (1975)b [116]. Details concerning these composites are given below

Explanation of the Figure 8-127.

That figure gives the ultimate compressive strength, σ_{ult}, in the plane, vs. temperature T, of several Uniaxial Advanced Composites.

KEY	FIBER		MATRIX	
	NAME	MANUFACTURER	NAME	MANUFACTURER
1	Boron		Aluminium 6061	
2	Boron [a]		Epoxy [a]	
3	Borsic[b]-Steel	Hamilton Standard Corp.	Aluminium 6061	
4	Borsic[b]-Titanium			
5	HT-S [c]	Courtaulds Ltd.	X-904 [c]	Fiberite Corp.

NOTE From Kasen (1975)b [116].

[a] Boron-Epoxy composites are: SP-272, manufactured by 3 M Co., and Narmco 5505, manufactured by AVCO Corporation.

[b] Borsic is the trade name of boron fiber coated with a thin layer of silicon carbide.

[c] Graphite-Epoxy composite.

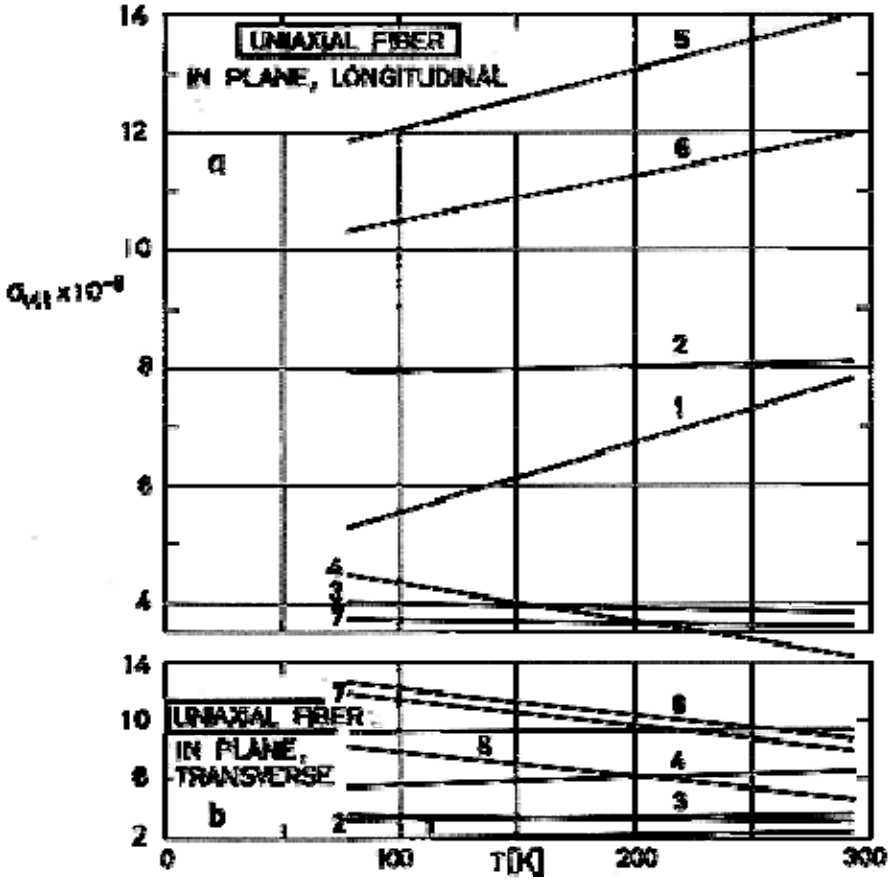

Figure 8-128: Ultimate flexural strength, σ_{ult}, in the plane, vs. temperature, *T*, of several Uniaxial Graphite-Epoxy Composites. From Kasen (1975)b [116]. Details concerning these composites are given below.

Explanation of the Figure 8-128.

That figure gives the ultimate flexural strength, σ_{ult}, in the plane, vs. temperature *T*, of several Uniaxial Graphite-Epoxy Composites.

	KEY	FIBER GRAPHITE		MATRIX EPOXY	
		NAME	MANUFACTURER	NAME	MANUFACTURER
a	1	Fibralloy 300	Mosanto Corp.		
	2	GY-70	Celanese Corp.		

	3	HMG-25	Hitco Corp.		
	4	HM-S	Courtaulds Ltd.		
	5	HT-S			
	6	Modmor II	Morganite Ltd.		
	7	Thornel 50	Union Carbide Corp.		
b	1	GY-70	Celanese Corp.	X-904	Fiberite Corp.
	2	GY-70		E-350 A	
	3	GY-70		1004	
	4	HT-S	Courtaulds Ltd.	3002	
	5	HT-S		X-904	Fiberite Corp.
	6	HT-S		BSP 2401	
	7	HT-S		1004	
	8	Modmor II	Morganite Ltd.		

NOTE From Kasen (1975)b [116].

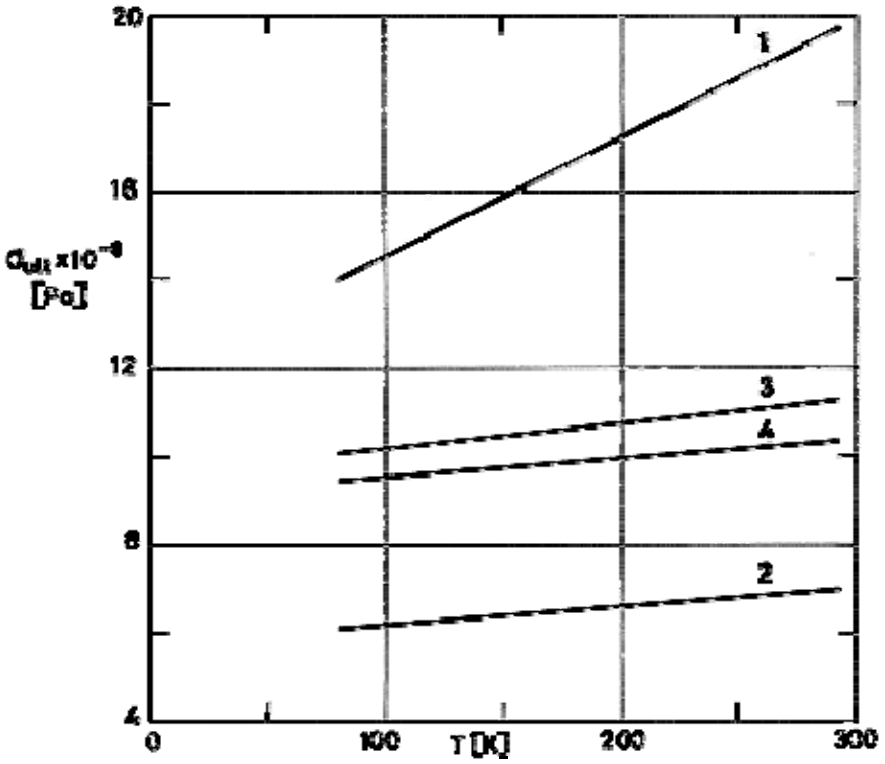

Figure 8-129: Ultimate flexural strength, σ_{ult}, in the plane, vs. temperature, T, of several Uniaxial Advanced Composites. From Kasen (1975)b [116]. Details concerning these composites are given below.

Explanation of the Figure 8-129.

That figure gives the ultimate flexural strength, σ_{ult}, vs. temperature T, of several Uniaxial Advanced Composites.

KEY	FIBER		MATRIX	
	NAME	MANUFACTURER	NAME	MANUFACTURER
1	Boron [a]		Epoxy [a]	
2	GY-70 [b]	Celanese Corp.	Polyimide	
3	HT-S [b]	Courtaulds Ltd.		
4	HT-S [b]		HT-424 [c]	American Cyanamid

NOTE From Kasen (1975)b [116].

[a] Boron-Epoxy composite is SP-272, manufactured by 3 M Co.

[b] Graphite fiber.

[c] Epoxy-Phenolic matrix.

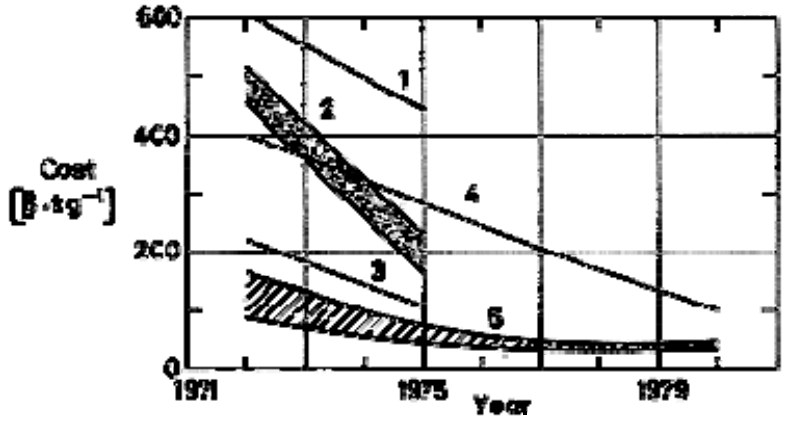

Figure 8-130: Cost of several fibers (for orders above 50 kg). From Greszczuk et al (1975) [78].

Explanation

KEY	FIBER	MANUFACTURER
1	Thornel 75 S	Union Carbide Corp.
2	Thornel 50 S Thornel 400	
3	Thornel 300	
	Modmor II	Morganite Ltd.
4	Boron Fibers [a]	
5	Celion GY 70	Celanese Corp.
	Panex 30 A Fortafil CG-3 Fortafil CG-3 Hitron 201 Hitron 201	

[a] $0{,}142 \times 10^{-3}$ m diameter. Lowest price estimate.

8.5.1 Structural tubes

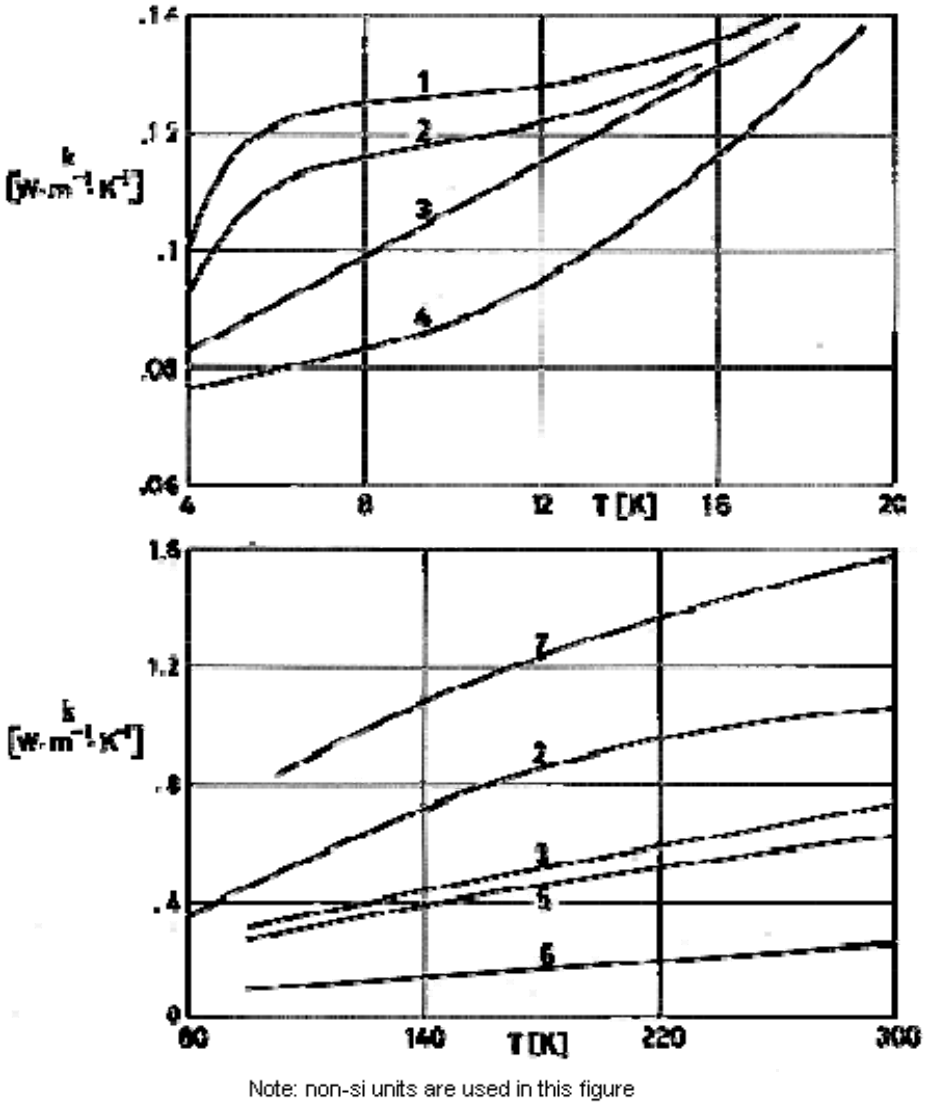

Note: non-si units are used in this figure

Figure 8-131: Thermal conductivity, *k*, vs. temperature, *T*, of several structural tubes. From Foster, Naes & Barnes (1975) [70]. Details concerning these tubes are given below.

Explanation of the Figure 8-131.

That figure gives the thermal conductivity, *k*, vs. temperature *T*, of several structural tubes.

Key	Material	Resin	Outer Diameter Dx10^3 [m]	Thickness tx10^3 [m]	Length Lx10^3 [m]	Density ρx10^{-6} [kg.m^{-3}]	Layer Density N/t [m^{-1}]	% Volume Glass	% Volume Resin
1	Quartz								
2	Glass								
3	1543 S Glass Cloth	U.S. POLYMERIC E 787	55,9	2,5	88,9	1,60	4100	58	32
			66,5	1,52	84	1,60	4100	60	32
4	2112 S [a] Glass Cloth	Unknown	63,5	1,88	84	1,61	4100	38	62
5	1581 S Glass Cloth	U.S. POLYMERIC E 787	54,9	2,00	88,9	1,60	3740	49	42
6		U.S. POLYMERIC E 787							
7	KEVLAR 49 CLOTH 143 Weave	DUPONT 904	58,4	3,80	88,9	1,26	3675	Unknown	Unknown

[a] The tubes made from 1543 and 1581 were hand fabricated. The Kevlar 49 was fabricated using prepreg 143 cloth. The sample No. 4 was purchased from Synthane-Taylor (Synthane-Taylor G-10).

NOTE From Foster, Naes & Barnes (1975) [70].

8.6 Miscellaneous materials

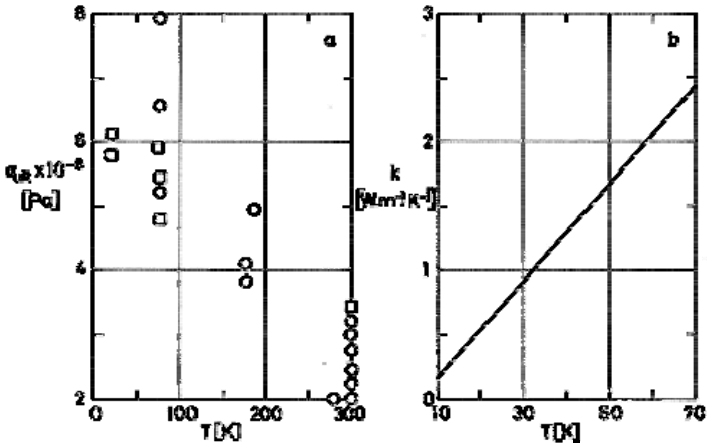

Figure 8-132: Mechanical and thermal properties of Bone. From Wipf & Gibney (1975) [266].
a) Ultimate compressive strength, σ_{ult}, vs. temperature, *T*. ○ Values from Armstrong et al. (1971) [9]. □ Values from Wipf & Gibney (1975) [266].
b) Thermal conductivity, *k*, vs. temperature, *T*.

Tests samples were 6,25x10^{-3} m diameter and 9,4x10^{-3} m length machined with their axis parallel to he fiber, out of compact bone of 2010 ± 50 kg.m^{-3} density (left metacarpal of ruminant animal).

9
Safety with cryogenic systems

9.1 General

The principal hazards in the handling of cryogenic fluids are those associated with the response of the human body and the surrounding to these fluids and their vapors, and those associated with reactions between these fluids and the surroundings. For a fairly recent review of these hazards see Timmerhaus & Flynn (1978). Many relevant data are given by Edeskuty, Reider & Williamson (1971) [62].

The interest in the field of safety with cryogenic systems is obviously not new, but rising fuel costs and the threat of decreasing fuel availability prompted the wide acceptance of LNG for industrial and public use, while liquid hydrogen emerges as a future aircraft or automotive fuel. These reasons, among others, did contribute to the growing interest in the assessment of the potential hazards and means of protection against them.

9.1.1 Physiological hazards

When the human body comes in contact with cryogenic fluids or with cryogenic-cooled surfaces, severe cold burns may result. These are similar to ordinary burns. Because the body is composed mainly of water, low temperature freezes the tissue, damaging or destroying it. Cold gases may not be damaging if the turbulence in the gas is low, since the body can normally tolerate a heat loss of 95 $W.m^{-2}$ for an area of limited exposure. If the heat loss becomes much greater than this, the skin temperature decreases and freezing of the affected area may result. Freezing of facial tissue will occur in about 100 s if the heat loss is 2300 $W.m^{-2}$ (Timmerhaus & Flynn (1978) [236]).

Concern with respiratory and asphyxiation hazards mainly comes from two different reasons: lack of oxygen (the often called nitrogen asphyxiation, see Table 9-6 in clause 9.2.4), and excess of oxygen.

Nitrogen is colorless, odorless, inert, and looks innoxius, but the leakage of nitrogen containers decreases the oxygen content of the atmosphere.

Oxygen gas, on the other hand, produces exhilarating effects when breathed. Nevertheless, lung damage occur when oxygen concentration exceeds 60%, and prolonged exposure to an atmosphere of pure oxygen may cause bronchitis, pneumonia or lung collapse. However, the greatest of highly concentrated oxygen lies in the increased flammability and explosiveness of the materials immersed in oxygen-rich atmospheres (see clause 1.1.1).

9.1.2 Fire and explosion hazards

Fire and explosion hazards come from the coexistence of an oxidant, a fuel and an ignition source.

The oxidant is normally oxygen, although other oxidant -which are used, for example, as propellants- may be handled. Sources of oxygen are: leakage of oxygen containers, condensation of air on

cryogenic-cooled surfaces below 82 K, build-up as a solid impurity in liquid hydrogen, etc. The fuel will be a flammable gas -several among them are used for cryogenic cooling purposes (see clause 9.2.2) or any non-compatible material. The ignition source may be spark, flame, impact, friction, chemical reaction, etc.

Any flammable mixture, between the so called limits of flammability, will support a flame or even a detonation. Beyond the lower or upper limits of flammability the mixture will not maintain its combustion temperature and will automatically extinguish itself. In heterogeneous systems, where solids and/or liquids coexist with gases, and where temperature and concentration gradient exist, the combustion behavior will depend on particle or droplet sizes, heat capacities of components, etc.

All combustible impurities pose a potential hazard in liquid oxygen handling. For the highly soluble impurities, the hazard level is controlled by the combustion behavior of the liquid phase, whereas for the less soluble impurities the dangerous concentration is the saturated solution concentration.

Solution of impurities in liquid hydrogen is very small, nevertheless suspended solids may be carried by the hydrogen to colder portions of the system and deposited there.

Nitrogen does not support combustion, but condensation of the entrapped air (which takes place below approximately 82 K may cause oxygen enrichment of the liquid nitrogen. The composition of the air as it condenses into the liquid nitrogen container is about half oxygen and half nitrogen. This oxygen-rich condensate can cause the same problems associated with the handling of the liquid oxygen.

9.1.3 Pressure hazards

Highly pressurized gases are present, either purposefully or unintentionally, in cryogenic systems. Gas compression during liquefaction or refrigeration, pumping of liquids to high pressures followed by evaporation, and confinement of cryogenic liquid with subsequent evaporation, are three situations where pressure hazards should be taken into account.

Systems containing liquid cryogens can be reach bursting pressures, if not relieved, simply by liquid entrapping in an enclosure. When this liquid vaporizes, pressure in the enclosure can rise very quickly.

Vent lines without appropriate rain traps can collect rainwater, which freezes and plugs the lines.

Overpressures can also result from cool down surges. When a liquid cryogen flows through a warm transfer line, severe pressure surges will occur. These pressure surges can be 10 times the operating or transfer pressure and even can cause backflow into the storage container.

9.1.4 Materials hazards

Low temperatures have the effect of making some structural materials brittle or less ductile than under normal conditions (see clause 9.3.1). Brittle fracture can occur very rapidly, resulting in almost instantaneous failure. Secondary effects of this failure may be, shrapnel damage -if the equipment is under pressure- release of a fluid which can result in fire or explosions, etc.

According to Timmerhaus & Flynn (1978) [236], there are two excellent standards to assess the impact strength of a material. A drop weight test to determine the nil ductility transition (NDT) temperature of a material specimen has been developed by the US Naval Research Laboratory. For brittle fracture to occur, the stress in the material should exceed a certain critical value and the temperature should be below the NDT temperature for a specimen of the same material, hardness, thickness, etc. The Charpy Impact Test, which also uses a drop weight, is routinely accomplished in open air at temperature down to 77 K. At lower temperatures, however, the specimen temperature increases too rapidly

during transfer from the cooling bath, and some insulating procedure should be devised. A simple method for testing at temperature below 6 K has been described by Jin et al. (1974) [105]. These tests have led to the development of codes for the design, fabrication and testing of cryogenic pressure vessels. The ASME Boiler and Pressure Vessel Code (see clause 9.3.3) can be used for these purposes.

Low temperature equipment can fail due to thermal stresses caused by thermal concentration of the material used. Contraction in long pipes can be a serious problem. Provisions should be made for change in length by using bellows, expansion joints, or flexible hose. Pipe anchors, supports, etc., should be carefully designed to allow the concentration to take place.

9.1.5 Safety provisions

A list of provisions for the assurance of personnel safety is given in the following:

1. Direct contact of the skin with a low-temperature fluid or cold surface should be prevented. Protective clothing should be used to this end. Safety goggles, gloves, and boots are required for transferring liquid cryogens.
2. Proper ventilation of the working area is of prime importance. Personnel should work in groups of two or more when handling liquid cryogens. If required to work in confined spaces with uncertain ventilation, the area should be continuously monitored with an oxygen-analyzing device to sound and alarm if the oxygen content of the air becomes too low or too high (16% to 25% is acceptable).
3. Tidiness and cleanliness are important, specially in systems using oxygen because of the increased possibility of fires and explosions.
4. All cryogenic systems should be protected against overpressures due to phase change from liquid to gas.
5. The usual safeguards for handling industrial gases should be observed: avoid gas entrapment between two valves, provide relief on all containers, avoid physical damage to the container, protect gas cylinder valves, anchor gas cylinders securely, and store cylinders in a safe area.
6. Attention should be paid to secondary accidents which can become catastrophic in comparison with the primary accident. For example, a brittle fracture may release sizable quantities of cryogen liquids, causing severe fire or explosion hazards, asphyxiation, further brittle fracture problems or shrapnel damage to other flammable or explosive materials, and so.
7. Corrective action for personnel protection should be planned for those cases where an accident can occur. This requires planning for emergency. Planning for emergency means that personnel know beforehand how to behave in the various foreseeable emergency situations.

9.2 Hazards related to properties of cryogens

Table 9-1: Relevant properties of Cryogen

Property	Numerical Values	Related Physical Phenomena	Related Hazards	Comments
Low Normal Boiling Point, T_B [K]	He: 4,22 H_2: 20,4 Ne: 27,1 N_2: 77,3 F_2: 85,2 Ar: 87,3 O_2: 90,2 CH_4: 111,7	Frost formation.	Line blockage. Seal valve seat erosion. Accumulation of impurities.	Even the highest listed boiling point corresponds to the dew point for a water concentration below 0,01 volume parts per million.
		Freezing of Impurities.	Same as above.	Liquefied cryogens exhibit much higher concentrations of vapor phase impurities than the corresponding gases before liquefaction.
		Air Condensation.	Combustion in an Oxygen rich environment. (See clause 1.1.1)	Liquid He, H_2, Ne and N_2 are cold enough to condense air. Air coming in contact with a surface cooled below 82 K will partially condense with the condensate containing approximately 52% O_2 (by volume) and will continue to condense in this fashion s long as air with 21% O_2 (by volume) is supplied to the surface.
		Direct Contact.	Tissue damage.	Cooling by the fluid takes time. This delay permits flooding the tissue or clothing with water.
Low Heat of Vaporization per Unit Mass, h_{fg}x10^{-3} [J.kg^{-1}]	He: 20,2 H_2: 447,0 Ne: 85,7 N_2: 199,0 F_2: 172,0 Ar: 163,0 O_2: 213,0	Boiling. Pressure build-up. Fluid leakage. Cryogen-air mixing.	Hydrogen and low boiling point hydrocarbons form explosive mixtures with air. (See clause 9.2.2) Oxygen enhances combustion. (See clause 1.1.1) Fluorine is both toxic and	The storage, transfer and handling of the lower-boiling point cryogens pose severe problems. For a given outer temperature the heat transfer to the system is larger the smaller is the normal boiling point. The vaporization index is the ratio of the temperature difference, (300–T_b)K, to the volume heat of vaporization. The larger this number the greater is the difficulty in storing the cryogenic fluid.

Property	Numerical Values	Related Physical Phenomena	Related Hazards	Comments
	CH_4: 508,0		corrosive. (See clause 9.2.3)	Values of the Vaporization Index, $(300-T_B)(\rho h_{fg})^{-1}x10^6$ [$K.m^3.J^{-1}$] He: 118 H_2: 8,8 Ne: 2,6 N_2: 1,39 F_2: 0,83 Ar: 0,93 O_2: 0,86 CH_4: 0,88
Low Heat of Vaporization per Unit Volume, $\rho h_{fg}x10^{-6}$ [$J.m^{-3}$]	He: 2,5 H_2: 31,8 Ne: 104,0 N_2: 160,0 F_2: 260,0 Ar: 228,0 O_2: 243,0 CH_4: 215,0			
High Liquid to Gas Density Ratio, ρ_l/ρ_v (ρ_v at 300 K, 1 atm)	He: 770 H_2: 865 Ne: 1470 N_2: 710 F_2: 975 Ar: 865 O_2: 880 CH_4: 650	Exclusion and/or dilution of air because cryogenic fluid release.	Oxygen enhances combustion. Fluorine is both toxic and corrosive. Others cryogens produce O_2 deficiency (See clause 9.2.4)	ρ_l/ρ_v measures the volume expansion which occurs between liquids at their normal boiling point and the gasses at 300 K and 1 atm.
High Boiling Pressure at 300 K, $p_B x10^{-9}$ [Pa]	He: 0,124 H_2: 0,196 Ne: - N_2: 0,294 F_2: - Ar: - O_2: - CH_4: -	Pressure built-up because of heating.	Bursting.	P_B is the upper pressure that could be attained when cooling is removed from a tightly sealed vessel completely filled with a liquid cryogen. In practice a minimum ullage space of 5-10% is provided in any case and, in addition, suitable pressure relief valves prevent excessive build-up.

NOTE Arranged by the compiler after Edeskuty, Reider & Williamson (1971) [62].

9.2.1 Combustion in an oxygen environment

The presence of highly concentrated Oxygen causes some non-combustibles to become combustible and some combustibles to become explosive.

Compatibility with Oxygen is a relative quality determined by how readily and to what degree a material will react with Oxygen. Incompatibility is usually associated to a violently fast and destructive oxidation process.

Structural materials in pipes, valves, pumps and tanks where Oxygen is present are almost exclusively metallic materials. Organic and plastics have been rejected as being too readily combustible, although some of the more compatible among them could be used non structurally as gaskets, seats, lubricants and the like.

Metal combustion is normally a heterogeneous process where solid, liquid and vapor phase are present. The whole process is controlled by the mass transport of metal and oxidizer into the combustion zone. This mass transport takes place through solid or liquid phases of both the metal and its oxide.

Latent heat of phase change and condensation of the combustion products, as well as the thermophysical properties of these products, are important in metal combustion.

It is generally assumed that the combustion process starts once the temperature exceeds a threshold value called ignition temperature (see Table 9-2). The energy required for ignition is extremely variable and very dependent on the ignition source, kind of energy supplied and rate at which it is applied.

Table 9-2: Several Useful Definitions

Ignition temperature	Minimum temperature at which the combustion process starts.
Flash point	Minimum temperature required to provide a fuel vapor-oxidizer mixture that will propagate a flame.
Limits of flammability	The range of concentrations of gaseous fuel in an oxidizer atmosphere at which the mixture will burn.
Limits of detonability	The range of concentrations of gaseous fuel in an oxidizer atmosphere at which the mixture will detonate, i.e., the flame front will propagate at supersonic speed.
Minimum pressure for combustion	Lower limit of the ambient pressure below which ignition of fuel-oxidizer mixtures is suppressed.
Minimum spark ignition energy in air	The minimum spark energy required to ignite the most easily ignitable concentration of fuel in air.
Quenching distance	The gap between two flat parallel plate electrodes below which ignition of fuel-oxidizer mixtures is suppressed.

Relevant thermal data of several materials in an oxidizing atmosphere are given in Table 9-3.

The ignition temperature of metals decreases when pressure increases as can be seen in Figure 9-1, while the flash point (see Table 9-2) of nonmetals seems to reach an asymptotic value, see Figure 9-2. Nevertheless, the enhancement of existing ignition sources because of pressure increasing is more important than the decreased ignition temperature of materials. Among the causes of ignition which are enhanced by pressure increasing one could mention: adiabatic compression, friction (which depends on the flow rate), availability of Oxygen, possibility of mechanical failures, and the like.

Table 9-4 provides some guidance in the selection of materials to be used in the presence of Oxygen.

9.2.2 Combustible cryogens

Hydrogen and Methane, both of which have outstanding properties as cryogenic coolants, are hazardous materials requiring special handling, which is fairly similar to that of other commonly handled combustibles such as gasoline.

Table 9-5 gives data on those properties of Hydrogen and Methane which are related to their combustion behavior.

Table 9-3: Thermal Data of Relevant Materials in an Oxidizing Atmosphere

Material	Ignition Temp. T_i [K]	Melting Temperature T_M [K]		Boiling Temperature T_B [K]		Thermal Conductivity at 300 K, kx10^{-3} [W.m^{-1}.K^{-1}]	Thermal Diffusivity at 300 K, α x 10^{-3} [m^2.s^{-1}]	Heat of Combustion, h_qx10^{-6} [J.kg^{-1}]	Oxide Volume Ratio [%]
		Metal	Oxide(s)	Metal	Oxide(s)				
Elements									
Aluminium	1000	933	2323	2720	3800	0,22	91,0	31,0	~ 1,3
Beryllium	~ 2500	1356	2820	2750	~ 4300	0,18	44,0	68,0	0,7
Copper	1300	1360	1503-1600	2855	...	0,40	115,0	2,4	1,71
Gold	No Ignite	1336	...	2980	...	0,31	124,0	0,008	...
Iron	1200	1812	1693-1870	3160	...	0,08	23,0	7,0	2,23
Magnesium	900	923	3075	1390	3350	0,16	90,0	25,0	0,81
Manganese	...	1517	2058	2314	3400	0,023	6,3	7,0	1,25
Molybdenum	1023	2890	1070-2880	5100	1530	0,14	63,0	6,1	~ 3,3
Nickel	1730	1730	2230	3110	...	0,06	15,0	4,0	1,64
Silver	No Ignite	1233	...	2450	...	0,40	161,0	0,140	...
Tantalum	1550	3270	2073	5700	...	0,06	26,0	5,6	2,54
Tin	1140	505	1353-2200	2960	...	0,06	39,0	2,4	1,32

Material	Ignition Temp. T_i [K]	Melting Temperature T_M [K]		Boiling Temperature T_B [K]		Thermal Conductivity at 300 K, kx10^{-3} [W.m^{-1}.K^{-1}]	Thermal Diffusivity at 300 K, α x 10^{-3} [m^2.s^{-1}]	Heat of Combustion, h_qx10^{-6} [J.kg^{-1}]	Oxide Volume Ratio [%]
		Metal	Oxide(s)	Metal	Oxide(s)				
Titanium	~ 1600	1950-2070	1920-2400	3550	3000-3300	0,018	7,6	16,0	1,73
Zinc	1170	693	2250	1181	...	0,125	46,0	5,3	1,44
Zirconium	1670	2125	2960	4650	...	0,043	23,0	12,0	1,56
Copper Alloys									
Berylco 25	1133-1144	1144-1255				0,024-0,038	~ 38,0		
Brass 70/30	1273	1183				0,126	39,0	3,6	
Nickel Alloys									
Incoel	1620	1670				0,011	4,0	4,7	
Hastelloy	1600	1640				0,011	4,0	5,0	
Monel	1520	1600				0,025	6,6	3,4	
Iron Alloys									
Cr Steel	1420	1670				0,030	8,5	7,7	

Material	Ignition Temp. T_i [K]	Melting Temperature T_M [K]		Boiling Temperature T_B [K]		Thermal Conductivity at 300 K, kx10^{-3} [W.m^{-1}.K^{-1}]	Thermal Diffusivity at 300 K, α x 10^{-3} [m^2.s^{-1}]	Heat of Combustion, h_qx10^{-6} [J.kg^{-1}]	Oxide Volume Ratio [%]
		Metal	Oxide(s)	Metal	Oxide(s)				
Stainless Steels (300-400)	1400-1670	1670				0,015	4,3	8,0	
Carbon Steel	1370	1780				0,080	23,0	7,5	
Titanium Alloys									
Ti-6Al-4V	~ 1600	1803-1908				0,0066	2,7	16,0	
Ti-8Mn	1610	1775				0,011	5,1	16,0	
Nonmetals									
Teflon TFE	750	~ 600				0,0002	~ 0,1	1,1	
CTFE	700	~ 500				0,0002	~ 0,1	1,5	
Polyethylene	450	~ 400				0,0004	0,2	9,0	
Nylon	475	~ 500				0,0003	0,2	7,0	

NOTE From Clark & Hust (1974) [45].

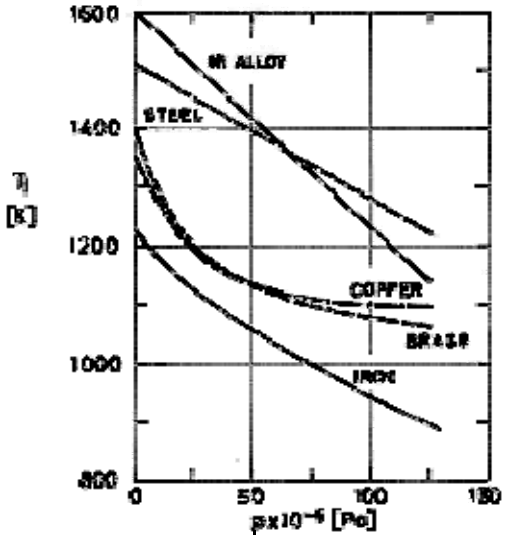

Figure 9-1: Ignition temperature, T_i, of several metals as a function of Oxygen pressure, p. From Clarck & Hust (1974) [45].

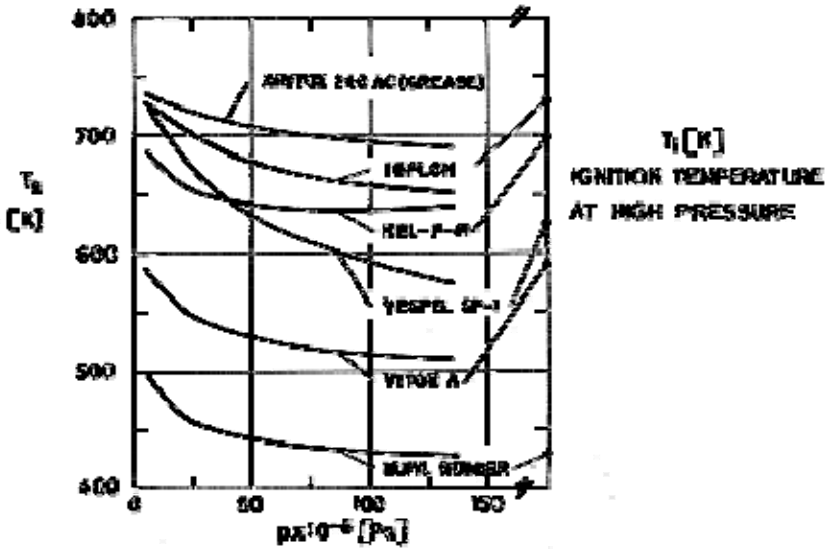

Figure 9-2: Flash point temperature, T_{fl}, of several nonmetals as a function of Oxygen pressure, p. Also shown the ignition temperature, T_i, of the same materials at high pressure. From Clarck & Hust (1974) [45].

Table 9-4: Ranking of Materials for Oxygen Compatibility

Material	Relevant Thermal Property	Comments
Nickel and Copper Alloys.	High thermal diffusivity (heat is carried away rapidly). Low heat of combustion.	The most Oxygen-compatible metals. High Nickel alloys and Nickel-Copper alloys are difficult to ignite and even more difficult to keep burning. Very costly.
Stainless Steels.	Relatively high ignition temperature. Quenchant behavior shown in some tests.	Those with high Nickel content are the best. Austenitic steels are better than martensitic. Low Carbon and low alloy Steels behave like Iron, which is readily ignited and burn fastly. Because their mechanical properties Stainless Steels are the best balance between cost and safety.
Aluminium Alloys.	Melting temperature below ignition temperature. Can flow away from the heat source (which would hinder ignition, although could propagate hot molten masses to another part of the system). Low ignition temperature.	Burning usually ignited by other sources. Violent fragmentation could occur during burning. Widely used in Oxygen systems -with an impressive safety record- because of their low cost and weight per unit strength.
Titanium Alloys.	Low ignition temperature. High heat of combustion.	Incompatible with Oxygen. Their use with Oxygen should be avoided.
Other Metals.	Low ignition temperature.	Incompatible with Oxygen, except noble metals which are highly expensive.
Nonmetals.		Most of them are highly combustible and seldom used structurally when Oxygen is dominant. Polytetrafluoroethylene (TFE) and Polychlorotrifluoroethylene (CTFE) are more compatible than other organic materials because the strong Fluorine-Carbon bond they have. Hydrocarbon impurities should be eliminated by proper cleaning with suitable inert oil-free solvents, followed by drying with oil-free air or a pure inert gas.

NOTE Arranged by the compiler after Clark & Hust (1974) [45].

Table 9-5: Properties of H_2 and CH_4 Related to their Combustion Hazards

Property	H_2	CH_4
Limits of flammability in air. [Vol. %].	4-75	5-15
Limits of flammability in O_2. [Vol. %].	4-96	5-61
Limits of detonability in air. [Vol. %].	20-65	
Limits of detonability in O_2. [Vol. %].	15-90	
Minimum pressure for combustion. [Pa].	6700	6900
Minimum spark ignition energy in air. [J].	$20x10^{-6}$	$300x10^{-6}$
Ignition temperature in air (stoichiometric mixtures). [K].	858	810
Quenching distance at 10^5 Pa (1 atm). [m].	$0,6x10^{-3}$	$2,5x10^{-3}$
Adiabatic flame temperature. [K].	2323	2153
Heat of combustion to form H_2O gas and CO_2 gas. [$J.mol^{-1}$].	$0,242x10^6$	$0,802x10^6$
Flame velocity. [$m.s^{-1}$].	2,70	0,38
Flame emittance.	0,10	
Liquid electrical resistivity. [$\Omega.m^{-1}$].	$\cong 4,6x10^{21}$	
Diffusion coefficient in air at 273 K. [$m^2.s^{-1}$].	$63,4x10^{-6}$	$20x10^{-6}$

NOTE From Edeskuty, Reider & Williamson (1971) [62].

The following considerations will complete the information presented in the above Table

1. The range of concentration for combustibility increases for both H_2 and CH_4 as the pressure is increased. As the pressure is reduced below atmospheric the combustible mixture becomes more difficult to ignite; however, if a suitable ignition source is employed, the limits of flammability are as wide at $2x10^4$ Pa as they are at atmospheric pressure. Figure 9-3 shows the influence of pressure on the limits of flammability of natural gas-air mixtures when an induction coil is used as ignition source. It can be seen that at lowest pressures the range narrows with a pressure being reached below which the mixture will not ignite, at least when using that ignition source.

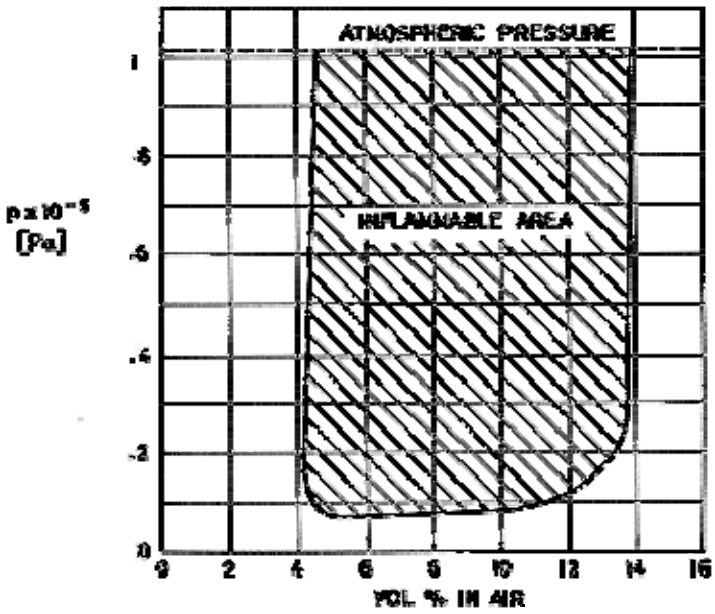

Note: non-si units are used in this figure

Figure 9-3: Effect of pressure in the limits of flammability of natural gas-air mixtures ignited by means of an induction coil. From Lewis & von Elbe (1961) [132].

2. When an electric spark passes through an explosive mixture, a small, more or less spherical, volume of high temperature gas is established. Whether a combustion wave appears or not depends on the size to which the inflamed volume has grown at the time when the temperature at the center has decreased to the order of the normal flame temperature. If the size is too small, the heat transferred from the inner zone cannot balance the heat loss by the outer unburned gas, and the reaction gradually ceases. In any case the minimum ignition energy is a function not only of the characteristics of the combustible mixture but of the configuration of the spark-producing device.

   Notice that the ignition energy for H_2 is very low, so that in most cases of rapid hydrogen release spontaneous ignition results.

3. The quenching distance is the minimum distance between parallel planes which will just allow a flame to pass without cooling to extinction. This distance increases as pressure decreases. For hydrogen at normal pressure, however, the quenching distance is so small that "explosive proof" equipment requires fine manufacturing tolerances.

Figure 9-4 shows minimum ignition energies, *E*, and quenching distances, *D*, for H_2-O_2-inert gas mixtures at atmospheric pressures.

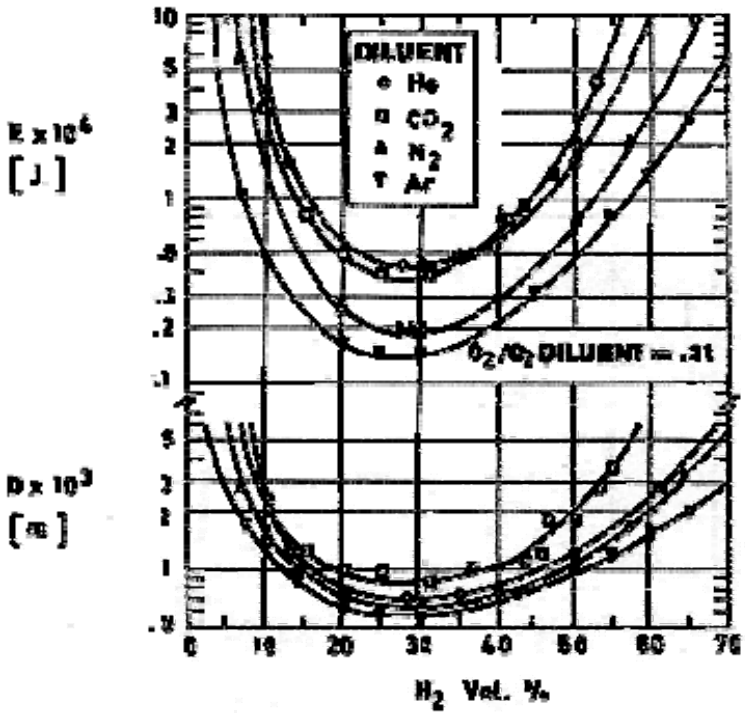

Note: non-si units are used in this figure

Figure 9-4: Minimum ignition energy, *E*, and quenching distance, *D*, for hydrogen-oxygen-inert gas mixtures at atmospheric pressures. From Lewis & von Elbe (1961) [132].

1. Because its very low emittance, hydrogen flame is invisible if impurities are not present.
2. The build up of an electrical charge within a flowing fluid can be a hazard only when its electrical resistance lies between 10^{12} $\Omega.m^{-1}$ and 10^{17} $\Omega.m^{-1}$. Lower resistivity's result in rapid transfer of any charge to the grounded metallic parts of the system, while higher resistivity's, as in the case of hydrogen, require a longer residence time for any significant amount of charge formation. In practice, the existence of either particulate matter in the pipes or two-phase flow, as occurs during system cooldown, can enhance the probability of building up electrostatics charges within the flowing fluid.
3. Large diffusion coefficients result in a rapid contamination of enclosures, but also in a fast decrease of the concentration of combustible when the release takes place outdoors.
4. Commercial Liquefied Natural Gas (LNG) is a mixture, rather than pure CH_4, so that fractionation occurs upon boiling. Effective purging procedures cannot be carried out unless the coldest spot in the container is warmed to at least 273 K.

9.2.3 Fluorine

Fluorine is both extremely reactive and the most toxic gas of cryogenic interest. Because these characteristics Fluorine and Fluorine-Oxygen mixtures are not used for cryogenic cooling purposes. The excellent monography by Schmidt (1967) [207] could be useful to the reader interested in the properties, compatibility and safe handling of these materials.

9.2.4 O_2 deficiency

Healthy subjects can tolerate Oxygen concentrations in the range 13 to 60% volume at total pressure of 1 atm. Symptoms of O_2 deficiency are summarized in Table 9-6 below.

Table 9-6: Symptoms of O_2 Deficiency

O2 Vol % at 10^5 Pa total pressure	At rest, signs and symptoms of O_2 deficiency
12-14	Respiration deeper, pulse faster, coordination poor.
10-12	Giddiness, poor judgment, lips blue.
8-10	Nausea, vomiting, unconsciousness, ashen face.
6-8	8 min, 100% die; 6 min, 50% die and 50% recover with treatment; 4-5 min, all recover with treatment.
4	Coma in 40 sec, convulsions, respiration ceases, death.

NOTE From Edeskuty, Reider & Williamson (1971) [62].

9.3 Change of properties of structural materials

The strength of materials increases as the temperature decreases, but room temperature strength data are used in the design of cryogenic equipment because of the following reasons:

1. Proof testing is performed at ambient temperatures.
2. The equipment may warm up under stress.
3. The temperatures of the system is not uniform.

9.3.1 Temperature embrittlement

The ductility of most structural materials decreases at low temperatures (temperature embrittlement). Figure 9-5 illustrates the dependence of ductility on temperature as measured by several impact methods.

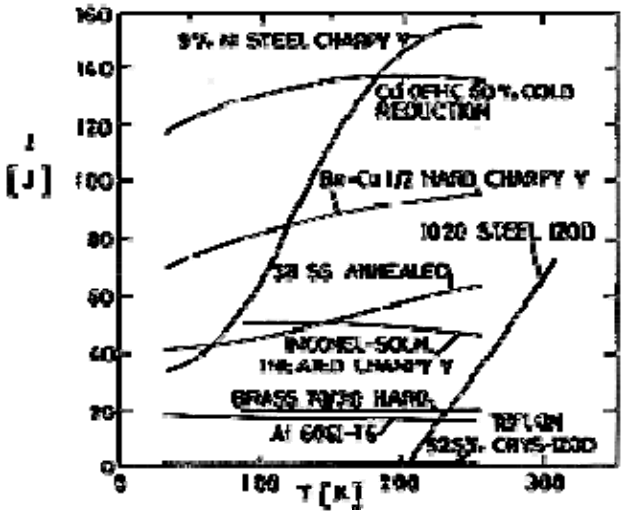

Note: non-si units are used in this figure

Figure 9-5: Dependence of impact energy, *J*, on temperature, *T*, for several materials. From Edeskuty, Reider, Williamson (1971) [62].

Metals which have a face-centered cubic crystal structure, such as Aluminium, Copper, Nickel, Austenitic Stainless Steel, show very little temperature dependence.

Low carbon and 400 series Stainless Steels, which have a body-centered cubic crystal structure, become embrittled at low temperatures. Nevertheless, not all metals possessing a body-centered-cubic crystal structure become brittle, there are some notable exceptions. For example, potassium, lithium and sodium metals, beta brass, and the LA 141 magnesium-lithium alloy retain their ductility down to temperatures near absolute zero.

Two recent review papers concerned with fracture mechanics are those by Hardrath (1974) [82] and by McHenry (1977) [147]. Hardrath's paper provides a brief historical sketch of the discipline and summarizes the current analytical procedures. The paper by McHenry is particularly devoted to fracture at cryogenic temperatures. The basic concepts and their application to the design of cryogenic structures are introduced in this paper. An elementary textbook on the broad field of materials science in that by Ruoff (1972) [204]. Clause 6 and 12 of this book are particularly concerned with mechanical properties of materials.

Table 9-7: Sources of Mechanical Properties of Structural Alloys at Cryogenic Temperatures.

ALUMINIUM ALLOYS	Table 9-8
IRON BASE ALLOYS	Table 9-9
NICKEL BASE ALLOYS	Table 9-10
STAINLESS STEELS. AUSTENITIC	Table 9-11
STAINLESS STEELS. MARTENSITIC	Table 9-12
STEELS	Table 9-13
TITANIUM ALLOYS	Table 9-14

Table 9-8: SOURCES OF MECHANICAL PROPERTIES OF STRUCTURAL ALLOYS (ALUMINIUM ALLOYS) AT CRYOGENIC TEMPERATURES

Alloy	Condition	Temp. [K]	Properties, Base Metal			Properties, Weldments	References (Remarks)
			Tensile	Fracture	Fatigue		
Al-2Cu-2Mg-6Zn (V95)[a] Al-2Cu-2,5Mg-8,5Zn (V96)[a] Al-4Cu-1,5Mg (D16)[a] Al-6,5Cu-Mn-Ti (D20)[a]	QA QA QA QA	4 20 77 293	σ_{ult} $\sigma_{0,2}$ δ				Verkin (1978) [254]
Al-4Cu-1Mn-Mg-Si (AK8)[a] Al-6,5Cu-Mn-Ti (D20)[a]		20 77 200 293	σ_{ult}			σ_{ult}	Yushchenko (1978) [270]
Al-6Cu-Mn (1201[a]~2219)		4 77 293	σ_{ult} (unnotched and notched) $\sigma_{0,2}$ δ RA	J (presumably $J(Cu)$ at 293 K)		σ_{ult} (unnotched and notched)	Ishchenko, Lozovskaya & Sayenko (1978) [99] ([b])
Al-2Mg-Mn (АМГ2)[a] Al-3Mg-Mn-Si (АМГ3)[a] Al-4Mg-Mn-Ti (АМГ4)[a] Al-5Mg-Mn-Ti (АМГ5)[a] Al-6Mg-Mn-Ti (АМГ6)[a] Al-1Mn (АМγ)[a]		20 77 200 293	σ_{ult}			σ_{ult}	Yushchenko (1978) [270]
Al-4,5Mg-0,65Mn (5083) АМГ6[a]	Ann	77 297	σ_{ult} (unnotched and notched) $\sigma_{0,2}$ δ Tear Strength	UPE K_Q K_{max}	$da/dN = c(\Delta K)^n$	Same as for base metal	Kelsey & Nelson (1978) [121]
5083-1 АМГ6[a]		76 111 300	σ_{ult} $\sigma_{0,2}$ δ	$J(C_V)$ J_C δ_c K_c K_D		Same as for base metal	Pense, Stout & Somers (1978) [179]
5083 АМГ6[a]	Ann	(4)	σ_{ult}	J-integral	$da/dN =$		McHenry,

Alloy	Condition	Temp. [K]	Properties, Base Metal			Properties, Weldments	References (Remarks)
			Tensile	Fracture	Fatigue		
		76 295	$\sigma_{0,2}$ δ	J_{IC} $K_{IC}(J)$	$c(\Delta K)^n$		Naranjo, Read & Reed (1978) [145]
5083 АМГ6[a]		77 293	σ_{ult} (unnotched, notched and notched with eccentric tension) $\sigma_{0,2}$ δ	UPE K_Q K_{max}		Same as for base metal	Ishchenko & Novikov (1978) [100]
5083	Ann	4 (unless stated)	σ_{ult} (298 K) $\sigma_{0,2\ (298\ K)}$ δ (298 K)		$da/dN = c(\Delta K)^n$		Tobler & Reed (1977) [238]
5083	Ann	4 76 111			$da/dN = c(\Delta K)^n$		Tobler & Reed (1978) [239]
Al-1,2Mn (3003)	Ann	172 297			$da/dN = c(\Delta K)^n$		Roberts, Wnek & Tafuri (1978) [197] ([c])

[a] USSR designation

[b] Study of welding problems

[c] Study of environmental effects. Atmospheres were Air, H_2O, Ar, N_2.

Table 9-9: SOURCES OF MECHANICAL PROPERTIES OF STRUCTURAL ALLOYS (IRON BASE ALLOYS) AT CRYOGENIC TEMPERATURES

Alloy	Condition	Temp. [K]	Properties, Base Metal			Properties, Weldments	References
			Tensile	Fracture	Fatigue		
Fe-0,05C-25Ni-14Cr-2Ti-1,5Mn-1,3Mo-Si ASTM A453 (A-286)	AnnA	4 76 296	σ_{ult} $\sigma_{0,2}$ δ RA	J-integral J_{IC} $K_{IC}(J)$	$da/dN = c(\Delta K)^n$		Reed, Tobler & Mikessell (1977) [191]
ASTM A453 (A-286)	STA	4 (unless stated)	σ_{ult} (at 298 K) $\sigma_{0,2}$ (at 298 K) δ (at 298 K)		$da/dN = c(\Delta K)^n$		Tobler & Reed (1977) [238]
ASTM A453 (A-286)	STA	4 76 295			$da/dN = c(\Delta K)^n$		Tobler & Reed (1978) [239]
Fe-0,036C-26Ni-15Cr-2,3Ti-1,7Mn-1,3Mo-Si ASTM A453 (A-286)	STQA	4 77 297	σ_{ult} (unnotched and notched) $\sigma_{0,2}$ δ RA	J_{IC} $K_{IC}(J)$	$da/dN = c(\Delta K)^n$	Same as for base metal	Wells, Logsdon & Kossowski (1978) [262]
Fe-36Ni-Cr (Invar 36HX)		4 20 77 293	σ_{ult} $\sigma_{0,2}$ δ	$J(C_U)$		ρ_{ult} $J(CU)$	Yushchenko (1978) [270]
Fe-49Ni		4 76 298	σ_{ult} $\sigma_{0,2}$ δ RA	J-integral J_{IC} $K_{IC}(J)$	$da/dN = c(\Delta K)^n$		McHenry & Schramm (1978) [146]

Table 9-10: SOURCES OF MECHANICAL PROPERTIES OF STRUCTURAL ALLOYS (NICKEL BASE ALLOYS) AT CRYOGENIC TEMPERATURES

Alloy	Condition	Temp. [K]	Properties, Base Metal			Properties, Weldments	References (Remarks)
			Tensile	Fracture	Fatigue		
Inconel 750 Mgf. Proccess VIM-VAR VIM-VAR AAM-VAR VIN HIP HIP (See Remarks)	ST STDA STDA STDA - STDA	4,2 77 297	σ_{ult} (unnotched and notched) $\sigma_{0,2}$ δ RA	J_{IC} K_{IC}	$da/dN = c(\Delta K)^n$	See Wells (1977) [261]. Data given by Wells are: σ_{ult}, σ, δ, RA, J_{IC}, K_{IC}, $da/dN = c(\Delta K)^n$	Logsdon (1977) [136] [a]
Inconel 750	STDA	4 (unless stated)	σ_{ult} (at 298 K) $\sigma_{0,2}$ (at 298 K) δ (at 298 K)		$da/dN = c(\Delta K)^n$		Tobler & Reed (1977) [238]
Inconel 750 Inconel 718	STDA STDA	4 76 295			$da/dN = c(\Delta K)^n$		Tobler & Reed (1978) [239]
Inconel 718 Udimet 718	STDA ST/CW/ST (1255 K)/DA ST/CW/ST (1399 K)/DA ST/CW/DA STDA	4 77 297 77	σ_{ult} $\sigma_{0,2}$ δ RA	J_{IC} K_{IC}	$da/dN = c(\Delta K)^n$		Logsdon, Kossowsky & Wells (1978) [137]

[a] Study of the influence of manufacturing process ad heat treatment on the mechanical properties in a cryogenic environment.

Table 9-11: SOURCES OF MECHANICAL PROPERTIES OF STRUCTURAL ALLOYS (STAINLESS STEELS, AUSTENITIC) AT CRYOGENIC TEMPERATURES

Alloy	Condition	Temp. [K]	Properties, Base Metal			Properties, Weldments	References (Remarks)
			Tensile	Fracture	Fatigue		
Fe-12Cr-22Ni-3Ti-Mo (X12H22T3M)[a] Fe-14Cr-14Mn-3Ni-Ti (X14Г14H3T)[a] Fe-18Cr-9Ni-Ti (X18H9T)[a] Fe-18Cr-10Ni-Ti (X18H10T)[a] Fe-0,03C-20Cr-16Ni-6Mn-0,12N (03X20H16AГ6)[a]	AC/A/AC AC AC AC	4 20 77 293	σ_{ult} $\sigma_{0,2}$ δ	J J_{IC} *UPE*	$\sigma_{0,2}$ vs. Number thermal cycles		Verkin (1978) [254]
Fe-0,03C-15,5Cr-23Ni-9Mn (Kromarc 58) Fe.0,053C-25Cr-29Ni (AISI 319S) Fe-0,018C-20Cr-9,5Mn-7Ni (Pyromet 538)	STWQ STWQ STWQ	4 77 297	σ_{ult} (unnotched and notched) $\sigma_{0,2}$ δ RA	J_{IC} $K_{IC}(J)$	$da/dN = c(\Delta K)^n$	Same as for base metal	Wells, Logsdon & Kossowski (1978) [262]
Fe-17Cr-13Ni-3Mo (X17H13M[a]˜AISI 316) Fe-0,12C-18Cr-10Ni-Ti (12X18H10T[a]˜AISI304) Fe-0,03C-20Cr-16Ni-6Mn-N (03X20H16AГ6)[a]		4 20 77 293	σ_{ult}	$J(C_V)$		Same as for base metal	Yushchenko (1978) [270]
AISI 316 AISI 304 AISI 310	Ann Ann Ann	4 (unless stated)	σ_{ult} (at 298 K) $\sigma_{0,2}$ (at 298 K) δ (at 298 K)		$da/dN = c(\Delta K)^n$		Tobler & Reed (1977) [238]
AISI 304	Several (See Remarks)	6 77	σ_{ult} $\sigma_{0,2}$ δ RA	$J(C_V)$			Jin, Morris & Zackay (1974) [106] ([b])
AISI 316 AISI 304 AISI 304L AISI 310S	Ann Ann Ann Ann	4 76 295			$da/dN = c(\Delta K)^n$		Tobler & Reed (1978) [239]

Alloy	Condition	Temp. [K]	Properties, Base Metal			Properties, Weldments	References (Remarks)
			Tensile	Fracture	Fatigue		
Fe-13Cr-19Mn		77 113 298	σ_{ult} $\sigma_{0,2}$ δ RA	$J(C_V)$ in the range 77K-122K) δ_c		Same as for base metal	Bruner & Sarno (1978) [32]
Fe-13Cr-19Mn		(4) 76 300	σ_{ult} $\sigma_{0,2}$ δ RA	J-integral J_{IC} $K_{IC}(J)$	$da/dN = c(\Delta K)^n$	J-integral J_{IC}, $K_{IC}(J)$ $da/dN = c(\Delta K)^n$	Tobler, McHenry & Reed (1978) [237]
Fe-0,055C-13,5Cr-19Mn-.16N (03K13AI19[a]~Fe-13Cr-19Mn)		77 300	σ_{ult} $\sigma_{0,2}$ δ RA				Morris, Hwang, Yushchenko, Belotzerkovetz & Kvasnevskii (1978) [155]
Fe-0,08C-13Cr-20Mn-0,15N (0X13AG19)[a]		76 111 200 250 300	σ_{ult} $\sigma_{0,2}$ δ	$J(C_V)$ J_C K_c δ_c $_{KD}$		$J(C_V)$ J_C K_c δ_c	Pense, Stout & Somers (1978) [179]
Fe-0,15C-5Cr-25Mn-1Ni-0,1N		77 298	σ_{ult} $\sigma_{0,2}$ δ	$J(C_V)$			Morris, Hwang, Yushchenko, Belotzerkovetz & Kvasnevskii (1978) [155]
Fe-0,056C-21Mn-(06G21)[a] Fe-0,082C-25,5Mn (08G25)[a] Fe-0,057C-32Mn-(06G32)[a] Fe-0,060C-35Mn (06G35)[a] Fe-0,067C-42Mn (07G42)[a] Fe-0,060C-46Mn-(06G46)[a] Fe-0,045C-25Mn (05AG25)[a] Fe-0,054C-30Mn (05AG30)[a] Fe-0,078C-33,5Mn (08AG34)[a]		77 295	σ_{ult} $\sigma_{0,2}$ δ RA				Morris, Hwang, Yushchenko, Belotzerkovetz & Kvasnevskii (1978) [155]

[a] USSR designation
[b] Study of the influence of the heat treatment on the mechanical properties at cryogenic temperatures.

Table 9-12: SOURCES OF MECHANICAL PROPERTIES OF STRUCTURAL ALLOYS (STAINLESS STEELS, MARTENSITIC) AT CRYOGENIC TEMPERATURES

Alloy	Temp. [K]	Properties, Base Metal			Properties, Weldments	References
		Tensile	Fracture	Fatigue		
Fe-0,03C-12Cr-10Ni-Mo-Ti (03X12H10MT)[a]	20 77 293	σ_{ult} $\sigma_{0,2}$ δ	$J(Cu)$		σ_{ult} $J(Cu)$	Yushchenko (1978) [270]

[a] USSR designation.

Table 9-13: SOURCES OF MECHANICAL PROPERTIES OF STRUCTURAL ALLOYS (STEELS) AT CRYOGENIC TEMPERATURES

Alloy	Condition	Temp. [K]	Properties, Base Metal			Properties, Weldments	References
			Tensile	Fracture	Fatigue		
Fe-3,5Ni (ASTM A203E) Fe-5Ni (ASTM A645) Fe-9Ni (ASTM A553)	Q/TEMPER TEMPER/ RevAnn Q/TEMPER	(4) 76 111 (172) (195) 295			$da/dN = c(\Delta K)^n$		Tobler & Reed (1978) [239]
Fe-5Ni (ASTM A645) Fe-9Ni (ASTM A553)	WQ/ TEMPER/WQ WQ/ TEMPER/WQ	4 20 77 (113) 293	σ_{ult} δ	$J(C_V)$ K_c	$\sigma_{f(N)}$	σ_{ult} (base metal 9Ni) $J(C_V)$ K_c (base metal 5Ni) $\sigma_{f(N)}$	Yushchenko, Belotzerkovetz, Starushchenko, Kovalenko & Sitnichenko (1978) [271]
Fe-5Ni (ASTM A645) Fe-9Ni (ASTM A553)	Specially Heat Treated Q/TEMPER	77 113 298	σ_{ult} $\sigma_{0,2}$ δ RA	$J(C_V)$ in the range 77 K-122K) δ_c		Same as for base metal	Bruner & Sarno (1978) [32]
Fe-5Ni (ASTM A645)	Three-Step Heat Treat.	77 103	σ_{ult} (at 298 K)	$J(C_V)$ J_{IC}		Same as for base metal	Muruyama, Pense & Stout

Alloy	Condition	Temp. [K]	Properties, Base Metal			Properties, Weldments	References
			Tensile	Fracture	Fatigue		
Fe-5,5Ni (N-TUP CR-196)[b] Fe-9Ni (ASTM A553)	Three-Step Heat Treat. Q/TEMPER	(298)	$\sigma_{0,2}$	δ_c K_c K_D			(1977) [158]
Fe-5Ni (ASTM A645) Fe-5,5Ni (N-TUP CR-196)[b] Fe-9Ni (ASTM A553)	Three-Step Heat Treat. Three-Step Heat Treat. Q/TEMPER	76 103 300	σ_{ult} $\sigma_{0,2}$ δ	$J(C_V)$ J_{IC} δ_c K_c K_D		J_{IC} δ_c K_c K_D	Pense, Stout & Somers (1978) [179]
Fe-9Ni (ASTM A553)	Q/TEMPER	4 76 295 298	σ_{ult} (at 298 K) $\sigma_{0,2}$ (at 298 K) δ (at 298 K)		$da/dN = c(\Delta K)^n$ (at 4 K, 76 K and 295 K)		Tobler & Reed (1977) [238]
Fe-9Ni (ASTM A553) Fe-12Ni-0,25Ti	Several Several (See Remarks)	6 77	σ_{ult} $\sigma_{0,2}$ δ RA	$J(C_V)$			Jin, Morris & Zackay (1974) [c] [106]
Fe-0,05C-4Mn (05G4)[a] Fe-0,05C-8Mn (05G8)[a] Fe-0,05C-12Mn (05G12)[a]		77 295	σ_{ult} $\sigma_{0,2}$ δ RA				Morris, Hwang, Yushchenko, Belotzerkovetz & Kvasnevskii (1978) [155]
Fe-8Mn-0,2Ti Fe-12Mn-0,2Ti	SA/Thermal cycled SA/ /TEMPER/ /CW/ TEMPER	77	σ_{ult} $\sigma_{0,2}$ δ RA	$J(C_V)$ J_{IC}			Morris, Hwang, Yushchenko, Belotzerkovetz & Kvasnevskii (1978) [155] [d]

[a] USSR designation

[b] Nippon Steel Corporation.

[c] Study of the influence of the heat treatment on the mechanical properties at cryogenic temperatures.

[d] Data on $J(C_V)$ for the 12Mn alloy only.

Table 9-14: SOURCES OF MECHANICAL PROPERTIES OF STRUCTURAL ALLOYS (TITANIUM ALLOYS) AT CRYOGENIC TEMPERATURES

Alloy	Condition	Temp. [K]	Properties, Base Metal			Properties, Weldments	References
			Tensile	Fracture	Fatigue		
Ti Ti-2Al-1,5Cr-Fe-Si Ti-4Al-3Mo-1V Ti-4,5Al Ti-6Al-4V		4 20 77 200 293	σ_{ult} $\sigma_{0,2}$ δ	J			Verkin (1978) [254]
Ti 99,8 (BTI-0)[a] Ti-2,5Zr-1,5Mo (AT-2)[a] Ti-5Al-2,5Sn (BT5-1)[a] Ti-6Al-4V (BT-6C)[a]	Ann Ann	(4) 20 77 293	σ_{ult} $\sigma_{0,2}$ δ	$J(C_V)$		σ_{ult} $J(C_V)$	Yushchenko (1978) [270]
Ti-5Al-2,5Sn Ti-6Al-4V	Ann Ann	4 (unless stated)	σ_{ult} (at 298 K) $\sigma_{0,2}$ (at 298 K) δ (at 298 K)		$da/dN = c(\Delta K)^n$		Tobler & Reed (1977) [238]
Ti-5Al-2,5Sn Ti-6Al-4V	Ann Ann	4 76 (130) 295			$da/dN = c(\Delta K)^n$		Tobler & Reed (1978) [239]

[a] USSR designation

9.3.2 Hydrogen embrittlement

Hydrogen embrittlement is due to a process of permeation of Hydrogen through the metal, which manifests itself by a marked, in some cases dramatic, decrease in the ductility and crack propagation resistance of structural steels under specified conditions of strain rate, temperature, Hydrogen potential, and strength level.

Hydrogen embrittlement should not be confused with Hydrogen attack, which is a chemical process prevailing at elevated temperatures (above 500 K). In contrast to Hydrogen attack, Hydrogen embrittlement is a maximum at about 300 K and is not accompanied by any evidence of microstructural deterioration within the material.

At cryogenic temperatures, cracking due to Hydrogen embrittlement has not been observed. However, in liquid Hydrogen vessels, materials in the ullage space that are near ambient temperature may be susceptible to Hydrogen environment cracking.

Table 9-15 illustrates the effect of Hydrogen embrittlement on several metals which have been subjected to a given hydrogen pressure. Alloys listed in this Table are arranged in order of decreasing susceptibility to tensile tests at ambient temperature. It is to be noted that the Hydrogen environment embrittlement classification o alloys could e different for different types of tests. For instance, alloys found not to be embrittled in tensile tests have been found to be embrittled in other tests.

Table 9-15: Susceptibiliy of Metals to Hydrogen Embrittlement as Measured by Tensile Tests [a]

Material [b]	Strength Ratio, H_2/He		Unnotched Ductility			
			Elongation, δ, %		Reduct. in Area, *RA*, %	
	Notched [c]	Unnotched	He	H_2	He	H_2
18Ni-250 MAR	0,12	0,68	8,2	0,2	55	2,5
410 SS	0,22	0,79	15	1,3	60	12
1042 QTEMPER	0,22	--	--	--	--	--
17-7PH SS	0,23	0,92	17	1,7	45	2,5
Fe-9Ni-4Co-0,2C	0,24	0,86	15	0,5	67	15
H-11	0,25	0,57	8,8	0	30	0
René 41	0,27	0,84	21	4,3	29	11
Electroformed Ni [d]	0,31	--	--	--	--	--
4140	0,40	0,96	14	2,6	48	9
Inconel 718	0,46	0,93	17	1,5	26	1
440 C	0,50	0,40	--	--	3,2	0
Ti-6Al-4V (STA)	0,58	--	--	--	--	--
430 F	0,68		22	14	64	37
Nickel 270	0,70		56	52	89	67
A-515	0,73		42	29	67	35
HY-100	0,73		20	18	76	63
A-372 Class IV	0,74		20	10	53	18
1042 Normalized	0,75				59	27
A-533-B	0,78				66	33
Ti-6Al-4V Ann	0,79		--	--	--	--

Material [b]	Strength Ratio, H_2/He		Unnotched Ductility			
			Elongation, δ, %		Reduct. in Area, RA, %	
	Notched [c]	Unnotched	He	H_2	He	H_2
AISI 1020	0,79				68	45
HY-80	0,80				70	60
Ti-5Al-2,5Sn ELI	0,81				45	39
ARMCO Iron	0,86				83	50
304 ELC SS	0,87				78	71
305 SS	0,89				78	75
Be-Cu Alloy 25	0,93				72	71
310 SS	0,93				64	62
Titanium	0,95				61	61
A-286	0,97				44	43
7075-T73 Al Alloy	0,98				37	35
Incoloy 903 [d]	1,00				50	47
316 SS	1,00				72	75
OFHC Copper	1,00				94	94
NARloy-Z [e]	1,10				24	22
6061-T6 Al Alloy	1,10				61	66
1100-0Al	1,40				93	93

NOTE From Chandler & Walter (1975) [41].

[a] All tests, unless otherwise stated, were made in $6{,}89 \times 10^7$ Pa (10^4 psi) Hydrogen at ambient temperature.

[b] Additional information concerning these materials is given in the following.

[c] $K_t = 8{,}4$. K_t is the stress-concentration factor which is defined as the ratio of maximum stress to net-section stress.

[d] Tested in $4{,}83 \times 10^7$ Pa (7×10^3 psi) Hydrogen.

[e] Tested in 4×10^7 Pa ($5{,}8 \times 10^3$ psi) Hydrogen.

Typical Composition, Percent, of the Alloys which Appear in Table 9-15

18Ni-250 MAR.....:	Fe-18Ni-7,5Co-5Mo-0,4Ti-0,1Al. Maraging.
410 SS.....:	Fe-≤ 0,15C-≤ 1Mn-≤ 1Si-11,5/13,5Cr.
1042 QTEMPER.....:	Fe-0,40/0,47C-0,6/0,9Mn-≤ 0,04P-≤ 0,055. Quenched and Tempered.
17-7PH SS.....:	Fe-0,07C-0,7Mn-0,4Si-17Cr-7Ni-1,15Al.
Fe-9Ni-4Co-0,2C.....:	Nickel Steel for low temperature use.
H-11.....:	Fe-5Cr-1,5Mo-0,4V-0,35C. Medium-Carbon Alloy Steel.
René 41.....:	Ni-1,4/1,6Al-0,003/0,010B-≤ 0,12C-18/20Cr-10/12Co-≤ 5Fe-≤ 0,1Mn-1Mn-9,0/10,5Mo-≤ 0,5Si-0,015S-3,0/3,5Ti. See ECSS-E-HB-31-01 Part 5, clause 4.8.
Electroformed Ni.....:	99,9Ni.
4140.....:	Fe-0,38/0,43C-0,75/1,00Mn-0,04P-0,04S-0-20/0,35Si-0,8/1,1Cr-0,15/0,25Mo.
Inconel 718.....:	52,2Ni-0,04C-18Mn-18,5Fe-0,008S-0,18Si-0,15Cu-19Cr-0,5Al-0,9Ti-3,05Mo-5,13Cb+Ta.
440 C.....:	Fe-0,95/1,20C-≤ 1Mn-≤ 1Si-16/18Cr-≤ 0,75Mo.
Ti-6Al-4V (STA).....:	Ti-5,50/6,75Al-≤ 0,1C-≤ 0,4Fe-≤ 0,015H-≤ 0,07N-≤ 0,3 O-3,5/4,5V. Solution Treated and Aged. See ECSS-E-HB-31-01 Part 5, clause 4.7)
430 F.....:	Fe-≤ 0,12C-≤ 1,25Mn-≤ 1Si-14/18Cr-≤ 15S. Free Machining.
Nickel 270.....:	99,98Ni-0,01C-0,003Mn.
A-515.....:	Fe-0,25C.
HY-100.....:	Fe0,2C-0,1/0,4Mn-2,25/3,50Ni-1,0/1,8Cr-0,2/0,6Mo-0,02Ti-0,02V-0,25Cu.
A-372 Class IV.....:	Fe-0,45C-1,6Mn-0,27Si-0,22Mo.
1042 Normalized.....:	Fe-0,40/0,47C-0,6/0,9Mn-≤ 0,04P-≤ 0,05S.
A-533-B.....:	Fe-≤ 0,25C-1,25Mn-0,52Mo-0,55Ni.
Ti-6Al-4V Ann.....:	Ti-5,50/6,75Al-≤ 0,1C-≤ 0,4Fe-≤ 0,015H-≤ 0,07N-≤ 0,3 O-3,5/4,5V. See ECSS-E-HB-31-01 Part 5, clause 4.7.
AISI 1020.....:	Fe-0,18/0,23C-0,3/0,6Mn-≤ 0,04P-≤ 0,05S.
HY-80.....:	Fe-0,18C-0,1/0,4Mn-2,00/3,25Ni-1,00/1,18Cr-0,2/0,6Mo-

	0,02Ti-0,02V-0,25Cu.
Ti-5Al-2,5Sn ELI.....:	Ti-4/6Al-≤ 0,1C-≤ 0,5Fe-≤ 0,02H-≤ 0,07N-≤ 0,3 O-2/3Sn. Extra Low Interstitial Grade, for low temperature use. See ECSS-E-HB-31-01 Part 5, clause 4.6.
ARMCO Iron.....:	Soft iron containing less than 0,1 impurities. Armco Steel Corp. Trade mark.
304 ELC SS.....:	Fe-≤ 0,03C-19Cr-10Ni. Extremely Low Carbon Stainless Steel.
305 SS.....:	Fe-≤ 0,12C-≤ 2Mn-≤ 1Si-17/19Cr-10/13Ni.
Be-Cu Alloy 25.....:	Cu-2Be-0,25Co. (Brush Beryllium Co.).
310 SS.....:	Fe-≤ 0,25C-≤ 2Mn-≤ 1,50Si-24/26Cr-19/22Ni.
Titanium.....:	99/100Ti.
A-286.....:	Fe-0,08C-15Cr-26Ni-1,25Mo-2Ti. (Allegheny Ludlum).
7075-T73 Al Alloy...:	Al-5,5Zn-2,5Mg-1,5Cu-0,3Cr. Heat Treated and then Stabilized.
Incoloy 903.....:	Henry Wiggin & Company Limited. Trade mark.
316 SS.....:	Fe-≤ 0,80C-≤ 2Mn-≤ 1Si-16/18Cr-10/14Ni-2/3Mo.
OFHC Copper.....:	99,98Cu. Oxygen Free High Conductivity.
NARloy-Z.....:	Rockwell International Corporation. Trade mark.
6061-T6 Al Alloy.....:	Al-0,15/0,35Cr-0,15/0,40Cu-≤ 0,7Fe-0,8/1,2Mg-≤ 0,15Mn-0,4/0,8Si-≤ 0,15Ti-≤ 0,25Zn-≤ 0,15 Others. Solution Heat Treated and then Artificially Aged. See ECSS-E-HB-31-01 Part 5, clause 4.2.)
1100-0Al.....:	99Al. Annealed Recrystallized. See ECSS-E-HB-31-01 Part 5, clause 4.2.

Figure 9-6 shows the effect of Hydrogen pressure on the mechanical propertiesof a typical steel. The figure represents the stress intensity at crack arrest, K_{TH}, as a function of Hydrogen pressure, p. K_{TH} is the threshold stress intensity for sustained load crack growth, and is used instead of the plane strain fracture thoughness, K_{IC}, (the stress intensity at which unstable crack growth occurs) because K_{IC} is generally considered to be a property of a given material and should not be affected by the environment.

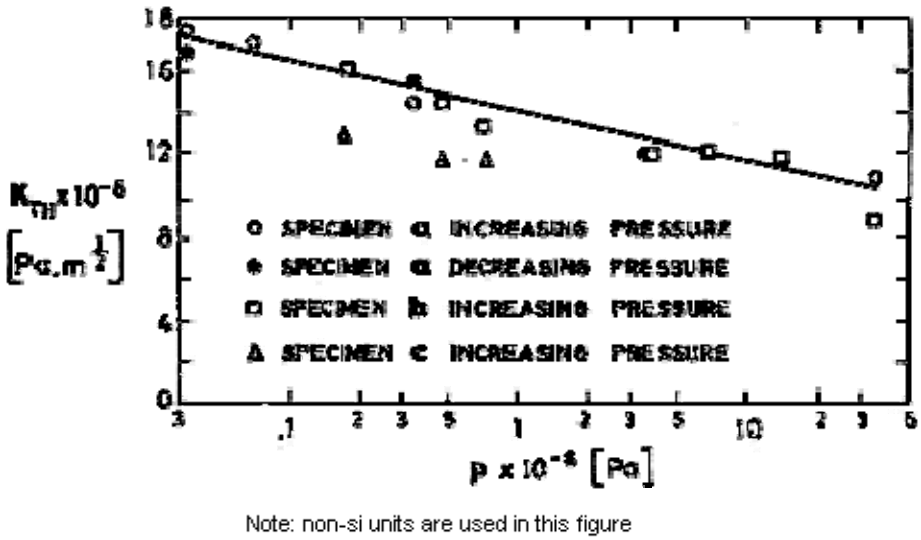

Note: non-si units are used in this figure

Figure 9-6: Stress intensity at crack arrest, K_{TH}, for AISI 4340 in Hydrogen at ambient temperature, as a function of Hydrogen pressure. From Chandler & Walter (1975) [41].

For metals in inert environments, K_{TH} is generally equal to 0,85 to 0,90 K_{IC}. However, K_{TH} is very sensitive to environments as can be seen in Figure 9-6.

Figure 9-7 illustrates in a most dramatic fashion the importance of the strength level in the determination of the susceptibility of structural steels to Hydrogen embrittlement. That figure gives the fracture ductility in tension, measured by means of the tensile reduction in area, *RA*, as a function of the Hydrogen content in the material. CH_2, for several steels, which are identified by the strength level. It can be seen that the susceptibility is much greater for higher strength steels. The same result applies to other mechanical property measurements used to assess hydrogen embrittlement, such as fracture ductility in tension, delayed failure time, threshold stress intensity for crack initiation, and crack growth rate.

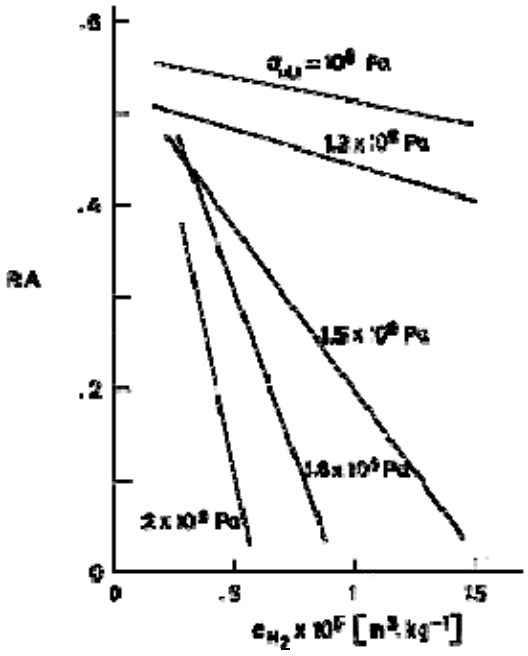

Note: non-si units are used in this figure

Figure 9-7: Fracture ductility, measured by the tensile reduction in area at fracture, *RA*, for several steels, as a function of Hydrogen content, CH_2. From Johnson & Kumnick (1975) [107].

9.3.3 Design codes and acceptance tests

A considerable body of experience on cryogenic structures such as storage tanks and piping systems for non-spatial use is presently available. The ASME Boiler and Pressure Vessel Code (ASME (1977) [11]), comprises the design practices, the fabrication methods, and the type and extent of inspection that have proven to be satisfactory in the past. Section VIII of the mentioned Code is concerned with the rules for construction of pressure vessels. These rules are arranged according to the methods of fabrication, and according to the classes of materials. Additional mandatory requirements for vessels and vessel parts that are to be used at low temperatures are specified when necessary. Although these rules fulfill the end for a fracture control plan, the qualification of materials and welding procedures for fabricating cryogenic structures in accordance with the ASME Pressure Vessel Code is difficult.

Concerning space applications, cryogenic metallic vessels used by NASA for launch vehicles and spacecraft gas containers are designed, fabricated and tested in accordance with an overall fracture control plan. The main aspects of this plan are briefly discussed by McHenry (1977) [147].

Bibliography

[1] Abramowitz, M., Stegun, I.A., "Handbook of Mathematical Functions", 1st ed., Dover Publications, Inc., New York, 1965, Chap. 6, pp. 358-433.

[2] AIR PRODUCTS AND CHEMICALS, "Open Cycle Cryogenic Detector Coolers Variflow Joul-Thomson Cryostats with Automatic Flow Control", Air Products and Chemicals Inc., Advanced Products Department, Allentown, Pennsylvania, 18105.

[3] Alnaimi, A.E., van der Sluijs, J.C.A., "Kapitza Conductance on Molybdenum and Beryllium between 1 and 2 K", Cryogenics, Vol. 15, No. 9, sept. 1975, pp. 509-512.

[4] Alnaimi, A.E., van der Sluijs, J.C.A., "Reduced Kapitza Conductance for Clean Ag Surfaces at Tempertaures between 1 and 2 K", Cryogenics, Vol. 14, No. 11, Nov. 1974, pp. 599-600.

[5] Angus, S., Armstrong, B., de Reuck, K.M., "Carbon Dioxide, International Thermodynamic Tables of the Fluid State", 1st ed., Pergamon Press, Oxford, New York, 1976, pp. 35-55, 78-81, 383-385.

[6] Angus, S., de Reuck, K.M., "International Thermodynamic Tables of the Fluid State Helium-4", 1st ed., Pergamon Press, Oxford, 1977, pp. 35-50, 82-84.

[7] Anon., "Local Cryogenic Cooling with Nonmoving Parts", Aircraft Engineering, Vol. 38, No. 2, Feb. 1966, p. 39.

[8] API, "API Research Project 44, Selected Values of Properties of Hydrocarbons and Related Compounds", Thermodynamic Research Center, Texas A & M Univ. (loose-leaf sheets, extant, 1952).

[9] Armstrong, R.W., Arkayin, B., Haddad, G., "Fracture of Bone Materials in Compression at Temperatures between –200º C and +200º C", Nature, Vol. 232, No. 5312, Aug. 20, 1971, pp. 576-577.

[10] Arp, V., "Heat Transport through Helium II", Cryogenics, Vol. 10, No. 2, April 1970, pp. 96-105.

[11] ASME, "ASME Boiler and Pressure Vessel Code-Section VIII, Rules for Construction of Pressure Vessels - Division 1", with Summer 1977 and Winter 1977 Addenda. The American Society of Mechanical Engineers, New York, July 1, 1977.

[12] Atherton, D.L., Prentiss, P.O., "Multiple Vappour Cooled Shield Position Tolerances", Cryogenics, Vol. 13, No. 5, May 1973, pp. 274-275.

[13] Atkins, K.R., Narahara, Y., "Surface Tension of Liquid He^4", Phys. Rev., A, Vol. 138, No. 2, 19 April 1965, pp. 437-441.

[14] Aydelott, J.C., "Axial Jet Mixing of Ethanol in Cylindrical Containers During Weightlessness", NASA Technical Paper 1487, 1979.

[15] Aydelott, J.C., "Axial Jet Mixing of Ethanol in Spherical Containers During Weightlessness", NASA TM X-3380, 1976.

[16] Balas, C., Leffel, C.S., Wingate, C.A., "The Stirling Cycle Cooler: Approaching One Year of Maintenance-Free Life", in "Advances in Cryogenic Engineering", 1st ed., Vol. 23, K.D. Timmerhaus, Ed., Plenum Press, New York, 1978, pp. 411-419.

[17] Balas, Jr., C., Wingate, Jr. C.A., "An Efficient Long-Life Cryogenic Cooling System for Spacecraft Applications", I.A.F. Paper 75-170. International Astronautical Federation (I.A.F.) XXVIth Congress, Lisbon, 21-27 Sept., 1975.

[18] Barron, R., "Cryogenic Systems", 1st ed., McGraw-Hill Book Company, New York, 1966, Chap. 7, pp. 463-470.

[19] Bear, J., "Dynamics of Fluids in Porous Media", 1st ed., American Elsevier Publishing Company, Inc., New York, 1972, Chap. 5, pp. 118-194, Chap. 10, pp. 579-652.

[20] Bejan, A., "Discrete Cooling on Low Heat Leak Supports to 4,2 K", Cryogenics, Vol. 15, No. 5, May 1975, pp. 290-292.

[21] Bell, G.A., Nast, T.C., Wedel, R.K., "Thermal Performance of Multilayer Insulation Applien to Small Cryogenic Tankage", in "Advances in Cryogenic Engineering", 1st ed., Vol. 22, K.D. Timmerhaus, R.P. Reed & A.F. Clark, Eds., Plenum Press, New York, 1977, pp. 272-282.

[22] Bender, E., "An Equation of State for Predicting Vapour-Liquid Equilibria of The System N_2-Ar-O_2", Cryogenics, vol. 13, No. 1, Jan. 1973, pp. 11-18.

[23] Bennett, M.R., Brown, D.S., Macmichael, D.B.A., Mytton, R.J., Prothero, H., Ross, J.S.H., Sheehan, M., Ward, R., "Study of the Technological Requirements Associated with a Space Infrared Astronomy Survey", International Research & Development Co. Ltd., Newcastle upon Tyne, UK, ESRO CR(P)568, IRD 74/52, ESTEC Contract 2129/73 AK, 1974.

[24] Beran, M.J., "Statistical Continuum Theories", 1st ed., Interscience Publishers, New York, 1968, Chap. 6, pp. 257-268.

[25] Blatt, M.H., Aydelott, J.C., "Capillary Device Passive Thermal Conditioning", J. Spacecraft, Vol. 15, No. 4, July-Aug. 1978, pp. 236-241.

[26] Bob Mardion, G., Claudet, G., Seyfert, P., "Practical Data on Steady Heat Transport in Superfluid Helium at Atmospheric Pressure", Cryogenics, Vol. 19, No. 1, Jan. 1979, pp. 45-47.

[27] Bradshaw, T.W., Orlowska, A.H., "A 4-K Mechanical Refrigerator for Space Applications", ESA SP-288, Dec. 1988, pp. 393-397.

[28] Bradshaw, T.W., Orlowska, A.H., "A Closed Cycle 4-K Mechanical Cooler for Space Applications", ESA SP-324, Dec. 1991, pp. 397-401.

[29] Breckenridge, Jr. R.W., "Cooling Systems for Spaceborne Infrared Experiments", in "Infrared Detection Techniques for Space Research, 1st ed., V. Manno & J. Ring, Eds., D. Reidel Publishing Company, Dordrecht, Holland, 1972, pp. 171-188.

[30] Broadwell, J.E., Liepmann, H.W., "Local Boiling and Cavitation in Heat-Induced Counterflow of He II), Phys. Fluids, Vol. 12, No. 8, Aug., 1969, pp. 1533-1535.

[31] Broz, A.L., Khorana, B.M., "Entropy of Liquid Helium from Fountain-Effect Measurements", Physica, Vol. 81 B, No. 1, Jan. 1976, pp. 84-90.

[32] Bruner, J.P., Sarno, D.A., "An Evaluation of Three Steels for Cryogenic Service", in "Advances in Cryogenic Engineering", 1st ed., Vol. 24, K.D. Timmerhaus, R.P. Reed & A.F. Clark, Eds., Plenum Press, New York, 1978, pp. 529-539.

[33] Budak, B.M., Samarskii, A.A., Tikhonov, A.N., "A Collection of Problems on Mathematical Physics", 1st ed., Pergamon Press, Oxford, 1964, Chap. IV, pp. 425-490.

[34] Bühner, K., Maurer, G., Bender, E., "Pressure-Enthalpy Diagrams for Methane, Ethane, Propane, Ethylene and Propylene", Cryogenics, Vol. 21, No. 3, March 1981, pp. 157-164.

[35] Buller, J.S., "A Miniature Self-Regulating Rapid-Cooling Joule-Thomson Cryostat", in "Advances in Cryogenic Engineering", 1st ed., Vol. 16, K.D. Timmerhaus, Ed., Plenum Press, New York and London, 1970, pp. 205-213.

[36] Caren, R.P., Coston, R.M., "Design and Construction of an Engineering Model Solid Cryogen Refrigerator for Infrared Detector Cooling at 50º K", NASA CR-988, Jan. 1968.

[37] Caren, R.P., Sklenesky, A.F., "Cryogenic Requirements of High Performance Infrared Sensors", ASME Paper 70-HT/SpT-33, Space technology and Heat Transfer Conference, Los Angeles, Calif., June 21-24, 1970.

[38] Carslaw, H.S., "Mathematical Theory of the Conduction of Heat in Solids", 2nd ed., Macmillan and Co., London, 1921, Chap. 7, pp. 113-131.

[39] Challis, L.J., "Some Experiments on the Kapitza Resistance between Metals and Liquid Helium II", Proc. Phys. Soc., Vol 80, Part 3, pp. 759-767, 1962.

[40] Challis, L.J., Dransfeld, K., Wilks; K., "Heat Transfer between Solids and Liquid Helium II", Proc. Roy. Soc., A, Vol. 260, pp. 31-46, 1961.

[41] Chandler, W.T., Walter, R.J., "Hydrogen-Environment Embrittlement of Metals and its Control", in "Hydrogen Energy", Part B, 1st ed., T. Nejat Veziroglu, Ed., Plenum Press, New York, 1975, pp. 1057-1078.

[42] Chanin, G., Torre, J.P., "Operating Performance of He^3 - Cooled Bolometers", in "Advances in Cryogenic Engineering", 1st ed., Vol. 23, K.D. Timmerhaus, Ed., Plenum Press, New York, 1977, pp. 634-639.

[43] Chase, C.E., "Thermal Conduction in Liquid Helium II. II. Effects of Channel Geometry", Phys. Rev., Vol. 131, No. 5, 1 Sept. 1963, pp. 1898-1903.

[44] Childers, R.K., Tough, J.T., "Helium II Thermal Counterflow: Temperature -and Pressure-Difference Data and Analysis in Terms of the Vinen Theory", Phys. Rev., B, Vol. 13, No. 3, 1 Feb. 1976, pp. 1040-1055.

[45] Clark, A.F., Hust, H.G., "A Review of the Compatibility of Structural Materials with Oxygen", AIAA Journal, Vol. 12, No. 4, April 1974, pp. 441-453.

[46] Collier, J.G., "Boiling and Evaporation - II", in "Heat Exchangers", 1st ed., S. Kakac, A.E. Bergles & F. Mayinger, Eds., Hemisphere Publishing Corporation, Washington, 1981, pp. 261-288.

[47] Collins, R.E., "Flow of Fluids through Porous Materials", 1st ed., Reinhold Publishing Corporation, New York, 1961, Chap. 1, pp. 1-21.

[48] Conte, R.R., "Éléments de Cryogénie", 1st ed., Masson & Cie., Editeurs, Paris, 1970, Chap. III, pp. 81-154, Chap. VI, pp. 227-235, 240.

[49] Daniels, A., Gasser, M., Sherman, A., "Magnetically Suspended Stirling Cryogenic Space Refrigerator: Status Report", in "Advances in Cryogenic Engineering", 1st ed., Vol. 27, R.W. Fast, Ed., Plenum Press, New York, 1982, pp. 711-719.

[50] Daniels, A., Stolfi, F., Sherman, A., Gasser, M., "Magnetically Suspended Stirling Space Refrigerator: Test Results", in "Advances in Cryogenic Engineering", 1st ed., Vol. 29, R.W. Fast, Ed., Plenum Press, New York, 1984, pp. 639-649.

[51] Da-Riva, I., Manzano, D.R., Resco, G., Laguna, L., Salsaloni, E., "Características de Medios Porosos Relacionadas con la Transpiración de Gases", ETSI Aeronáuticos, Laboratorio de Aerodinámica, Madrid, Oct. 1972.

[52] Davis, E.J., Anderson, G.H., "The Incipience of Nucleate Boiling in Forced Convection Flow", A.I.Ch.E. Journal, Vol. 12, No. 4, July 1966, pp. 775-780.

[53] De Bruyn Ouboter, R., "review Paper: The Hydrodynamics of Helium II Film", J. Low Temp. Phys., Vol. 12, Nos. 1/2, July 1973, pp. 3-23.

[54] De Gennes, P.G., "Hydrodynamic Dispersion in Unsaturated Porous Media", J. Fluid Mech., Vol. 136, 1983, pp. 189-200.

[55] De Haas, W., van Beelen, H., "A Synthesis of Flow Phenomena in Helium II", Physica, Vol. 83 B, 1976, pp. 129-146.

[56] Denner, H.D., Klipping, G., Klipping, I., Lüders, K., Menzel, J., Ruppert, U., "Mechanism of an Active Phase Separator for Space Applications", in "Advances in Cryogenic Engineering", 1st ed., Vol. 25, K.D. Timmerhaus & H.A. Snyder, Eds., Plenum Press, New York and London, 1980, pp. 783-790.

[57] Denner, H.D., Klipping, G., Klipping, I., Lüders, K., Oestereich, T., Ruppert, U., Schmidtchen, U., Szücs, Z., Walter, H., "Improved Active Phase Separator for He II Space Cooling Systems", in "Advances in Cryogenic Engineering", 1st ed., Vol. 27, R.W. Fast, Ed., Plenum Press, New York, 1982, pp. 1079-1086.

[58] Dimotakis, P.E., Broadwell, J.E., "local Temperature Measurements in Supercritical Counterflow in Liquid Helium II", Phys. Fluids, Vol. 16, no. 11, Nov. 1973, pp. 1787-1795.

[59] Donabedian, M., "Survey of Cryogenic Cooling Techniques", The Aerospace Corporation, El Segundo, California. Air Force Report No. SAMSO-TR-73-74. Aerospace Report No. TR-0073 (3901-01)-1, Oct. 1972.

[60] Doody, R.D., "The High-Capacity, Spaceborne, Vuilleumier Refrigertaor", SPIE Annual Technical Symposium, July 1980. SPIE, Vol. 245, Cryogenically Cooled Sensor Technology, 1980, pp. 108-111.

[61] Dunn, P.D., Reay, D.A., "Heat Pipes", 1st ed., Pergemon Press, Oxford, 1976, Chap. 3, pp. 96-97, Appendix 1, p. 264.

[62] Edeskuty, F.J., Reider, R., Williamson, Jr. K.D., "Safety", in "Cryogenic Fundamentals", 1st ed., G.G. Haselden, Ed., Academic Press, London, 1971, pp. 633-672.

[63] Elsner, A., "Helium Flow through Filters", in "Advances in Cryogenic Engineering", 1st ed., Vol. 18, K.D. Timmerhaus, Ed., Plenum Press, New York, 1973, pp. 141-149.

[64] Enya, S., Kisaragi, T., Ochiai, J., Sasao, Y., Kuriki, K., "Experiments of Surface Tension Separator for Propellant Feed System", J. Spacecraft, Vol. 18, No. 4, July-Aug. 1981, pp. 320-326.

[65] ESDU 68006, "Forced Convection Heat Transfer in Circular Tubes. Part II: Data for Laminar and Transitional Flows Including Free Convection Effects", Engineering Sciences Data Unit, 251-259 Regent Street, London WI, February 1968.

[66] Estermann, I., "Gases at Low Densities", in "Thermodynamics and Physics of Matter", Vol. 1 of High Speed Aerodynamics and Jet Propulsion, F.D. Rossini, Ed., Princeton, New Jersey, 1955, pp. 736-778.

[67] Fester, D.A., "Earth Storable Design, Vol. V, Acquisition/Expulsion System for Earth Orbital Propulsion System Study", NCR-73-79, NAS9-12182, Martin Marietta Corporation, Denver, Colo., Oct. 1973.

[68] Fester, D.A., Eberhardt, R.N., Tegart, J. R., "Space Shuttle Reaction Control Subsystem propellant Acquisition Technology", J. Spacecraft, Vol. 12, No. 12, Dec. 1975, pp. 705-710.

[69] Feyman, R.P., "Application of Quantum Mechanics to Liquid Helium", in "Progress in Low-Temperature Physics", 1st ed., Vol. 1, C.J. Gorter, Ed., Interscience Publishers, Inc., New York, 1955, pp. 17-53.

[70] Foster, W.G., Naes, L.G., Barnes, C.B., "Thermal Conductivity Measurements of Fiberglass/Epoxy Structural Tubes from 4º K to 320º K", AIAA Paper No. 75-711. AIAA 10th Thermophysics Conference, Denver, Colo., May 27-29, 1975.

[71] Fradkov, A.B., Troitskii, V.F., "Helium Cryostats for Physical Studies in Space", Cryogenics, Vol. 15, No. 8, Aug. 1975. Pp. 461-463.

[72] Frederking, T.H.K., Elsner, A., Klipping, G., "liquid Flow Rates of Superfluid Helium II During Thermomechanical Pumping through Porous Media", in "Advances in Cryogenic Engineering", 1st ed., vol. 18, K.D. Timmerhaus, Ed., Plenum Press, New York, 1973, pp. 132-140.

[73] Gaffney, J., Clement, J.R., "Liquid Helium Level-Finder", Rev. Sci. Intr. Vol. 26, No. 6, June 1955, pp. 620-621.

[74] Gibbons, R.M., "Thermophysical Data for Cryogenic Materials", in " Cryogenic Fundamentals", 1st ed., G.G. Haselden, Ed., Academic Press, London, 1971, pp. 673-738.

[75] Glaser, P.E., Black, I.A., Lindstrom, R.S., Ruccia, F.E., Wechsler, A.E., "Thermal Insulation Systems - A Survey", NASA SP-5027, 1967.

[76] Gluck, D.F., "Propellant Position Control by Capillary Barriers during Spacecraft Rotational Maneuvers", J. Spacecraft, Vol. 7, No. 3, March 1970, pp. 242-247.

[77] Gorter, C.J., Mellink, J.H., "On the Irreversible Processes in Liquid Helium II", Physica, Vol. XV, No. 3-4, May 1949, pp. 285-304.

[78] Greszczuk, L.B., Hawley, A.V., White, T., "Advances Composites and their Application to Hydrofoils", J. Hydronautics, Vol. 9, No. 3, July 1975, pp. 81-89.

[79] Haben, R.L., Frederking, T.H.K., "Thermal Boundary Conductance between Graphite and Liquid Helium II", in "Advances in Cryogenic Engineering", Vol. 20, 1st ed., K.D. Timmerhaus, Ed., Plenum Press, New York, 1975, pp. 383-388.

[80] Hall, C.A., Pharo, T.J., Phillips, J.M., Gille, J.P., "Low Thermal Flux Glass-Fiber Tubing for Cryogenic Service", NASA CR-72797, Martin Marietta Corporation, Denver, Colo., March 1971.

[81] Hall, C.A., Spond, D.E., "Low Thermal Flux Glass-Fiber Tubing for Cryogenic Service", in "Advances in Cryogenic Engineering", 1st ed., Vol. 22, K.D. Timmerhaus, R.P. Reed & A.F. Clark, Eds., Plenum Press, New York, 1977, pp. 214-223.

[82] Hardrath, H.F., "Fracture Mechanics", J. Aircraft, Vol. 11, No. 6, June 1974, pp. 305, 312.

[83] Haskin, W.L., Dexter, P.F., "Ranges of Application for Cryogenic Radiators and Refrigerators on Space Satellites", AIAA Paper No. 79-0179. 17th Aerospace Sciences Meeting, New Orleans, La., Jan. 15-17, 1979.

[84] Heikkila, W.J., Hollis Hallet, A,C,, "The Viscosity of Liquid Helium II", Can. J. Phys., Vol. 33, No. 8, Aug. 1955, pp. 420-435.

[85] Heim, J.R., Fast, R.W., "A Low-Heat-Leak, Temperature-Stabilized Support", in "Advances in Cryogenic Engineering", 1st ed., vol. 18, K.D. Timmerhaus, Ed., Plenum Press, New York, 1973, pp. 494-496.

[86] Hellwing, T.M., "Thermal and Fluid Flow Modeling of a Cryostat - Dewar System", AIAA Paper No. 80-0147. 18th Aerospace Sciences Meeting, Pasadena, Calif., Jan. 14-16, 1980.

[87] Henis, J.M.S., Tripodi, M.K., "The Developing Technology of Gas Separating Membranes", Science, Vol. 20, No. 4592, 1 April 1983, pp. 11-17.

[88] Hilal, M.A., McIntosh, G.E., "A Method for Preventing Pressure Oscillations in Tubes Connecting Liquid Helium Reservoirs to Room Temperature", Cryogenics, Vol. 16, No. 2, Feb. 1976, p. 122.

[89] Hill, R.W., Lounasmaa, O.V., "The Thermodynamic Properties of Fluid Helium", Phil. Trans. Roy. Soc., A, Vol. 252. 1013, March 1960, pp. 347-395.

[90] Hilsenrath, J., Beckett, C.W., Benedict, W.S., Fano, L., Hoge, H.J., Masi, J.F., Nuttall, R.L., Touloukian, Y.S., Woolley, H.W., "Tables of Thermodynamic and Transport Properties of Air, Argon, Carbon Dioxide, Carbon Monoxide, Hydrogen, Nitrogen, Oxygen,and Steam", 1st ed., Pergamon Press, Oxford, 1960.

[91] Hirschfelder, J.O., Curtiss, C.F., Bird, R.B., "molecular Theory of Gases and Liquids", 1st ed., John Wiley & Sons, Inc., New York, 1954, pp. 174, 1110-1112.

[92] Hone, D., "Transport Properties of Liquid He^3", Phys. Rev., Vol. 125, No. 5, March 1, 1962, pp. 1494-1495.

[93] Hopfinger, E.J., Altman, M., "A Study of Thermal Transpiration for the Development of a New Type of Gas Pump", ASME Journal of Engineering for Power, Vol. 91 A, No. 3, July, 1969, pp. 207-215.

[94] Hopkins, R.A., Chronic, W.L., "Long-Term Cryogenic Space Storage System", ", in "Advances in Cryogenic Engineering", 1st ed., vol. 18, K.D. Timmerhaus, Ed., Plenum Press, New York, 1973, pp. 486-493.

[95] Horn, S.B., Acord, T.T., Raimondi, P.K., Walters, B.T., "Miniature Cryogenic Coolers", in "Advances in Cryogenic Engineering", 1st ed., Vol 21, K.D. Timmerhaus & D.H. Weitzel, Eds., Plenum Press, New York, 1976, pp. 428-434.

[96] Huang, K., "Statistical Mechanics", 1st ed., John Wiley & Sons, Inc., New York, 1963, Chap. 2, pp. 40-46.

[97] Hughes, J.L., Herr, K.C., "Mariner Mars 1969 Infrared Spectrometer: Gas Delivery System and Joule-Thomson Cryostat", Cryogenics, Vol. 13, No. 9, sept. 1973, pp. 513-519.

[98] Ijsselstein, R.R., de Goeje, M.P., Kramers, H.C., "Combined Measurements on Various Types of Stationary Flow of Superfluid ^4He", Physica, Vol. 96 B, 1979, pp. 312-324.

[99] Ishchenko, A.Ya., Lozovskaya, A.V., Sayenko, M.I., "Metallurgical Problems of Welding 1201 (Al-6Cu-Mn) Alloy", in "Advances in Cryogenic Engineering", 1st ed., Vol. 24, K.D. Timmerhaus, R.P. Reed & A.F. Clark, Eds., Plenum Press, New York, 1978, pp. 175-186.

[100] Ishchenko, A.Ya., Novikov, N.V., "Mechanical Properties of Soviet and American Al-Mg Alloy Plates and Welds for LNG Systems", in "Advances in Cryogenic Engineering", 1st ed., Vol. 24, K.D. Timmerhaus, R.P. Reed & A.F. Clark, Eds., Plenum Press, New York, 1978, pp. 491-504.

[101] Jacob, M., "Heat Transfer", 6th ed., Vol. 1, John Wiley & Sons, Inc., New York, 1958, Chap. 22, p. 461.

[102] Jacobsen, R.T., Stewart, R.B., Teng, J.C.J., "A Thermodynamic Property Formulation for Neon from the Triple Point to 700 K with Pressure to 700 MPa", in "Advances in Cryogenic Engineering", 1st ed., Vol. 27, R.W. Fast, Ed., Plenum Press, New York, 1982, pp. 911-919.

[103] Jewell, C., "An Overview of ESA Cryocooler Activities", ESA SP-324, Dec. 1991, pp. 195-199.

[104] Jewell, C., "Cryogenic Activities at ESTEC", ESA SP-288, Dec. 1988, pp. 381-386.

[105] Jin, S., Horwood, W.A., Morris, Jr., J.W., Zackay, V.F., "A Simple Method for Charpy Impact Testing below 6 K", in "Advances in Cryogenic Engineering", 1st ed., vol. 19, K.D. Timmerhaus, Ed., Plenum Press, New York, 1974, pp. 373-378.

[106] Jin, S., Morris, Jr., J.W., Zackay, V.F., "An Iron-Nickel-Titanium Alloy with Outstanding Toughness at Cryogenic Temperature", in "Advances in Cryogenic Engineering", 1st ed., vol. 19, K.D. Timmerhaus, Ed., Plenum Press, New York, 1974, pp. 379-384.

[107] Johnson, H.H., Kumnick, A.J., "Hydrogen and the Integrity of Structural Alloys", in "Hydrogen Energy", Part B, 1st ed., T. Nejat Veziroglu, Ed., Plenum Press, New York, 1975, pp. 1043-1055.

[108] Johnson, R.C., Little, W.A., "Experiments on the Kapitza Resistance", Phys. Rev., Vol. 130, No. 2, 15 April 1963, pp. 596-604.

[109] Johnson, V.J., "Properties of Materials at Low Temperatures (Phase 1)", 1st ed., Pergamon Press, New York, 1961.

[110] Jones, B.G., Bradshaw, T.W., Orlowska, A.H., Jewell, C., "Development and Pre-Qualification Testing a 20 K Space Cooler", ESA SP-324, Dec. 1991, pp. 411-416.

[111] Jones, E.A., Van der Sluijs, J.C.A., "Some Experiments on the Influence of Surface Treatment on the Kapitza Conductance between Copper and He^4 at Temperatures from 1,2 to 2,0 K", Cryogenics, vol. 13, No. 9, Sept. 1973, pp. 535-542.

[112] Karlekar, B.V., "Thermodynamics for Engineers", 1st ed., Prentice-Hall, Inc., Englewood Cliffs, N.J., 1983, p. 562.

[113] Karr, G.R., Urban E.W., "Superfluid Plug as a Control Device for Helium Coolant", Cryogenics, Vol. 20, No. 5, May 1980, pp. 266-270.

[114] Karr, G.R., Urban, E.W., "Superfluid Plug as a Control Device for Helium Coolant", 71st Annual Meeting, American Institute of Chemical Engineers, Miami, Florida, Nov. 12-16, 1978.

[115] Kasen, M.B., "Mechanical and Thermal Properties of Filamentary-Reinforced Structural Composites at Cryogenic Temperatures. 1: Glass-Reinforced Composites", Cryogenics, Vol. 15, No. 6, June 1975, pp. 327-349.

[116] Kasen, M.B., "Mechanical and Thermal Properties of Filamentary-Reinforced Structural Composites at Cryogenic Temperatures. 2: Advanced Composites", Cryogenics, Vol. 15, No. 12, Dec. 1975, pp. 701-722.

[117] Kays, W.M., "Convective Heat and Mass Transfer", 1st ed., McGraw-Hill Book Company, New York, 1966, Chap. 9, pp. 186-191.

[118] Keller, C.W., Cunnington, G.R., Glassford, A.P., "Thermal Performance of Multilayer Insulations", NASA CR-134477, Lockheed Missiles & Space Company, Sunnyvale, Calif., April 1974.

[119] Keller, W.E., "Helium-3 and Helium-4", 1st ed., Plenum Press, New York, 1969.

[120] Keller, W.E., "Thickness of the Static and the Moving Saturated He II Film", Phys. Rev. Letters, Vol. 24, No. 11, 16 March 1970, pp. 569-573.

[121] Kelsey, R.A., Nelson, F.G., "Mechanical Properties of U.S./USSR Al-Mg Plates and Welds for LNG Applications", in "Advances in Cryogenic Engineering", 1st ed., Vol. 24, K.D. Timmerhaus, R.P. Reed & A.F. Clark, Eds., Plenum Press, New York, 1978, pp. 505-518.

[122] Khalatnikov, I.M., "An Introduction to the Theory of Superfluidity", 1st ed., Benjamin, New York, 1965.

[123] Kittel, P., "Sub-Kelvin Temperatures in Space", in "Advances in Cryogenic Engineering", 1st ed., Vol. 27, R.W. Fast, Ed., Plenum Press, New York, 1982, pp. 745-749.

[124] Kittel, P., Brooks, W.F., "Single Shot Demountable Self Contained ^{3}He Refrigerator", in "Advances in Cryogenic Engineering", 1st ed., Vol. 27, R.W. Fast, Ed., Plenum Press, New York, 1982, pp. 727-734.

[125] Kontorovich, V.M., "Effect of the Rate of Flow of a He II Film on its Thickness", Soviet Phys., JETP, Vol. 3, No. 5, Dec. 1956, pp. 770-771.

[126] Kropschot, R.H., "Mechanical Properties of Materials", in "Applied Cryogenic Engineering", 1st ed., R.W. Vance & W.M. Duke, Eds., John Wiley & Sons, Inc., New York, 1962, pp. 44-59.

[127] Kutateladze, S.S., Borishanskii, V.M., "A Concise Encyclopedia of Heat Transfer", 1st ed., Pergamon Press, Oxford, 1966, pp. 411-441.

[128] Ladner, D.R., Tough, J.T., "Temperature and Velocity Dependence of Superfluid Turbulence", Phys. Rev., B, Vol. 20, No. 7, 1 Oct. 1979, pp. 2690-2701.

[129] Landau, L.D., Lifshitz, E.M., "Fluid Mechanics", 1st ed., Pergamon Press, London, 1959, Chap. XVI, pp. 507-522.

[130] LEFAX, "Thermodynamic Tables and Charts", LEFAX Technical Data Book Library, No. 634, LEFAX, Philadelphia, Pa. 19132.

[131] Lemke, D., Klipping, G., Römisch, N., "Liquid Helium-Cooled Infrared Telescope for Astronomical and Atmospherical Measurements from Space", in "Advances in Cryogenic Engineering", 1st ed., Vol. 23, K.D. Timmerhaus, Ed., Plenum Press, New York, 1978, pp. 628-633.

[132] Lewis, B., von Elbe, G., "Combustion, Flames and Explosions of Gases", 2nd ed., Academic Press, Inc., New York, 1961, Chap. V, pp. 287-346.

[133] Lewis, C.A., "Long-Life Stirling Cycle Coolers for Applications in the 60-110 K Range", ESA SP-288, Dec. 1988, pp. 387-391.

[134] Lizon-Tati, J., Girard, M., "The Helium II Cryostat Facility for Spacelab Payloads", in "Spacecraft Thermal and Environmental Control Systems", M. Khine, B. Battrick & C. Rowley, Eds., ESA SP-139, Nov. 1978, pp. 521-525.

[135] Loeb, L.B., "The Kinetic Theory of Gases", 3rd ed., Dover Publications, Inc., New York, 1961, Chap. V, pp. 166-191.

[136] Logsdon, W.A., "Cryogenic Fracture Mechanics Properties of Several Manufacturing Process/Heat Treatment Combinations of Inconel X750", in "Advances in Cryogenic Engineering", 1st ed., Vol. 22, K.D. Timmerhaus, R.P. Reed & A.F. Clark, Eds., Plenum Press, New York, 1977, pp. 47-58.

[137] Logsdon, W.A., Kossowsky, R., Wells, J.M., "The Influence of Processing and Heat Treatment on the Cryogenic Fracture Mechanics Properties of Incoel 718", in "Advances in Cryogenic Engineering", 1st ed., Vol. 24, K.D. Timmerhaus, R.P. Reed & A.F. Clark, Eds., Plenum Press, New York, 1978, pp. 197-209.

[138] Lounasmaa, O.V., "Experimental principles and Methods below 1 K", 1st ed., Academic Press, London, 1974, Chap. 2, pp. 5-16, Chaps. 3 to 6, pp. 17-139.

[139] Lundholm, Jr. L.G., "NASA Low and Ultralow Temperature Cryogenic Cooler Systems for Space Missions", ISA Transactions, Vol. 19, No. 1, Jan. 1980, pp. 3-14.

[140] Magerlein, J.H., Sanders, Jr., T.M., "Surface Tension of He^4 near T_λ", Phys. Rev. Letters, Vol. 36, No. 5, 2 Feb. 1976, pp. 258-261.

[141] Mason, P., Collins, D., Petrac, D., Yang, L., Edeskuty, F., Williamson, K., "Experiments on the Properties of Superfluid Helium in Zero Gravity", Presented at the Sixth International Cryogenic Engineering Conference, Grenoble, 11-14 May, 1976.

[142] Mason, P.V., "refrigeration for 2º K Sensors in Space: Mechanical or Cryogen?", in "Applications of Cryogenic Technology", 1st ed., Vol. 4, R.W. Vance, Ed., The Cryogenic Society of America, 1972, pp. 372-383.

[143] Matsch, L.C., "Advances in Multilayer Insulations", in "Advances in Cryogenic Engineering", 1st ed., Vol. 7, K.D. Timmerhaus, Ed., Plenum Press, New York, 1962, pp. 413-418.

[144] McCarthy, Jr., J.F. , "Zero-g Propulsion Problems", in "Jet, Rocket, Nuclear, Ion and Electric Propulsion", 1st ed., W.H.T.Loh, Ed., Applied Physics and Engineering, Vol. 7, Springer, Berlin, 1968, pp. 644-727.

[145] McHenry, H.I., Naranjo, S.E., Read, D.T., Reed, R.P., "Low-Temperature Fracture Properties of a USSR Aluminium - 6% Magnesium Alloy", in "Advances in Cryogenic Engineering", 1st ed., Vol. 24, K.D. Timmerhaus, R.P. Reed & A.F. Clark, Eds., Plenum Press, New York, 1978, pp. 519-528.

[146] McHenry, H.I., Schramm, R.E., "Note on the Fracture Propreties of Fe-49 Ni at Cryogenic Temperatures", in "Advances in Cryogenic Engineering", 1st ed., Vol. 24, K.D. Timmerhaus, R.P. Reed & A.F. Clark, Eds., Plenum Press, New York, 1978, pp. 161-165.

[147] McHenry, H.J., "Fracture Mechanics and its Application to Cryogenic Structures", ", in "Advances in Cryogenic Engineering", 1st ed., Vol. 22, K.D. Timmerhaus, R.P. Reed & A.F. Clark, Eds., Plenum Press, New York, 1977, pp. 9-26.

[148] Mendelssohn, K., "Cryophysics", 1st ed., Interscience Publishers, Inc., New York, 1960, Chap. 7, pp. 127-159. Appendix I, pp. 172-173.

[149] Mermin, N.D., Lee, D.M., "Superfluid Helium 3", Scient. Am., Vol. 235, No. 6, Dec. 1976, pp. 56-71.

[150] Metzler, H., Nitzche, D., "Methods of Producing Polished Metallographic Specimens of Porous Iron Green Bodies and Sintered Parts for Fully Automatic Structure Analysis", Practical Metallography, Vol. IX, No. 7, July 1972, pp. 408-411.

[151] Mikesell, R.P., Scott, R.B., "Heat Conduction through Insulating Supports in Very Low Temperature Equipment", Journal of Research of the National Bureau of Standards, Vol. 57, No. 6, Dec. 1956, pp. 371-378.

[152] Mitchell, R.C., Stark, J.A., White, R.C., "Zero-g Hydrogen Tank Venting Systems", in "Advances in Cryogenic Engineering", 1st ed., Vol. 12, K.D. Timmerhaus, Ed., Plenum Press, New York-London, 1967, pp. 72-81.

[153] Mittang, K., "Kapitza Conductance and Thermal Conductivity of Copper, Niobium and Aluminium in the Range from 1,3 to 2,1 K", Cryogenics, Vol. 13, No. 2, Feb. 1973, pp. 94-99.

[154] Molnar, W., "Insulation", in "cryogenic Fundamentals", 1st ed., G.G. Haselden, Ed., Academic Press, London, 1971, Chap. 4, pp. 199-235.

[155] Morris, Jr., J.W., Hwang, S.K., Yushchenko, K.A., Belotzerkovetz, V.I., Kvasnevskii, O.G., "Fe-Mn Alloys for Cryogenic Use: A Brief Survey of Current Research", in "Advances in Cryogenic Engineering", 1st ed., Vol. 24, K.D. Timmerhaus, R.P. Reed & A.F. Clark, Eds., Plenum Press, New York, 1978, pp. 91-102.

[156] Moses, R.A., Gluck, D.F., "Cryogenic Thermal Stratification and Interfacial Phenomena for Heated Tanks During Prolonged Orbital Flight", in "Advances in Cryogenic Engineering", 1st ed., K.D. Timmerhaus, Ed., Plenum Press, New York, 1973, pp. 81-91.

[157] Müller, M., Seidel, A., Lizon-Tati, J., "Design and Test of a Cryogenic Phase Separator for Zero-G Environment", in "Environmental and Thermal Control Systems for Space Vehicles", T.D. Guyenne & J.J. Hunt, Eds., ESA SP-200, Dec. 1983, pp. 191-196.

[158] Murayama, N., Pense, A.W., Stout, R.D., "The Fracture Toughness of Cryogenic Steels", ", in "Advances in Cryogenic Engineering", 1st ed., Vol. 22, K.D. Timmerhaus, R.P. Reed & A.F. Clark, Eds., Plenum Press, New York, 1977, pp. 27-34.

[159] Nachtsheim, P.R., Swigert, P., "Satisfaction of Asymptotic Boundary Conditions in Numerical Solution of Systems of Nonlinear Equations of Boundary-Layer Type", NASA TN D-3004, Oct. 1965.

[160] Naes, L.G., Nest, T.C., "Long-life Orbital Operation of Stirling Cycle Mechanical Refrigerators", SPIE Annual Technical Symposium, July 1980. SPIE, Vol. 245, Cryogenically Cooled Sensor Technology, Part 23, 1980, pp. 126-135.

[161] Nast, T.C., Barnes, C.B., Wedel, R.K., "Development and Orbital Operation of a Two-Stage Solid Cryogen Cooler for Infrared Detector Cooling", AIAA Paper No. 76-475, AIAA 11th Thermophysics Conference, San Diego, Calif., July 14-16, 1976.

[162] Nayfeh, A.H., "Perturbation Methods", 1st ed., John Wiley & Sons, New York, 1973, Chap. 4, pp. 110-158.

[163] Neeper, D.A., Dillinger, J.R., "Thermal Resistance at Indium-Sapphire Boundaries between 1,1 and 2,1 K", Phys. Rev., A, Vol. 135, No. 4, 17 Aug. 1964, pp. 1028-1033.

[164] Neeper, D.A., Pearce, D.C., Wasilik, R.M., "Kapitza Resistance of Mercury between 1,1 and 2,1 K", Phys. Rev., Vol. 156, No. 3, 15 April 1967, pp. 764-768.

[165] Nekrasov, B., "Hydraulics for Aeronautical Engineers", 1st ed., MIR Publishers, Moscow, 1969, Chap. VI, pp. 80-84.

[166] Neu, J.T., Good, R.J., "Equilibrium Behavior of Fluids in Containers at Zero Gravity", AIAA Journal, Vol 1, No. 4, April 1963, pp. 814-819.

[167] Neugebauer, G., "Future Prospects of Infrared Observations of Active Nuclei", Phys. Scripta, Vol. 17, March 1978. pp. 325-326. Symposium on Quasars and Active Nuclei of Galaxies, Copenhagen, Denmark, June 27-July 2, 1977.

[168] Nicol, J., Bohm, H.V., "Continuous Refrigeration between 4,2° K and 1° K", in "Advances in Cryogenic Engineering", 1st ed., Vol. 5, K.D. Timmerhaus, Ed., Plenum Press, New York, 1960, pp. 332-337.

[169] Niendorf, L.R., Choksi, S.C., "Ultra-Efficient Insulation System for Solid Cryogen Coolers", in "Advances in Cryogenic Engineering", 1st ed., Vol. 12, Timmerhaus, Ed., Plenum Press, New York, 1967, pp. 286-299.

[170] Niinikoski, T.O., "Construction of Sintered Copper Heat Exchangers", Cryogenics, Vol. 11, No. 3, June 1971, pp. 232-233.

[171] Norris, R.H., Buckland, F.F., Fitzroy, N.D., "Heat Transfer Data Book", General Electric Company, Schenectady, New York, Section G 513,1, p. 3, June 1967.

[172] Olijhoek, J.F., van Alphen, W.M., de Bruny Ouboter, R., Taconis, K.W., "Adiabatic Superfluid Flow at Supercritical Velocities through Capillaries", Physica, Vol. 35, pp. 483-486, 1967.

[173] Olijhoek, J.F., Van Beelen, H., de Bruyn Ouboter, R., Taconis, K.W., "The Role of Gorter-Mellink Mutual Friction in Cooling by Forced Superfluid Flown", Physica, Vol. 69, pp. 38-48, 1973.

[174] Olijhoek, J.F., van Beelen, H., de Bruyn Ouboter, R., Taconis, K.W., Koops, W., "Thermal Effects in Adiabatic Flow of He II - The Role of Mutual Friction and the Influence of Pressure on the Limit for Cooling", Physica, Vol. 72, pp. 355-380, 1974.

[175] Oren, A., Gutfinger, C., "Analysis of a Joule-Thomson Cryogenic Detector Cooling", Isr. J. Technol., Vol. 17, Part 4, 1979, pp. 194-200.

[176] OXFORD INSTRUMENTS, "Cryogenic Desing for Space Missions", The Oxford Instrument Company, Osney Mead, Oxford. Prepared under ESTEC Contract number 2596/75PP, 1976.

[177] Paivanas, J.A., Roberts, O.P., Wang, D.I-J., "Multishielding - An Advanced Superinsulation Technique", in "Advances in Cryogenic Engineering" 1st ed., Vol. 10, K.D. Timmerhaus, Ed., Plenum Press, New York, 1965, pp. 197-207.

[178] Patullo, A.W., van der Sluijs, J.C.A., "The Kapitza Conductance of Clean Copper Surfaces between 0,3 K and 1,3 K", Cryogenics, Vol. 23, No. 11, Nov. 1983, pp. 587-598.

[179] Pense, A.W., Stout, R.D., Somers, B.R., "Fracture Toughness of Cryogenic Alloys", in "Advances in Cryogenic Engineering", 1st ed., Vol. 24, K.D. Timmerhaus, R.P. Reed & A.F. Clark, Eds., Plenum Press, New York, 1978, pp. 548-559.

[180] Peterson, E.W., Wurtz, Jr., H.P., Winner, M.R., "Joule-Thomson Cryostat Cooled Infrared Cell Having a Built-in Thermostat Sensing Element", Patent No. 3,942,010. US Patent Gazette, Vol. 944, No. 1, March 1976.

[181] Petrac, D., "Superfluid Porous Plug as Liquid-Vapor Separator in Low Gravity Space Flights", Proceedings of the 14th International Low Temperature Physics Conference, Helsinki, Aug. 1975. Vol. 4, North Holland/American Elsevier, Amsterdam, 1975, pp. 33-36.

[182] Petrac, D., Mason, P.V., "Evaluation of Porous-Plug Liquid Separators for Space Superfluid Helium Systems", in "Proc. 7th Intern. Cryogenic Engineering Conference", IPC Science and Technology Press, Guilford, England, 1978, pp. 120-125.

[183] Petrac, D., Mason, P.V., "Temperature Control of Superfluid Helium in Zero G by a Porous Plug", Proc. International Cryogenic Engineering Conference, IPC Science and Technology Press, Geneva, 1980, pp. 97-101.

[184] Petrash, D.A., Nussle, R.D., Otto, E.W., "Effect on the Acceleration Disturbances Encountered in the MA-7 Spacecraft on the Liquid-Vapor Interface in a Baffled Tank During Weightlessness", NASA TN D-1577, Jan. 1963.

[185] Philip, J.R., "Flow in Porous Media", in "Annual Review of Fluid Mechanics", Vol. 2, 1st ed., M. van Dyke, W.G. Vincenti & J.V. Wehausen, Eds., Annual Reviews Inc., Palo Alto, Calif., 1970, pp. 177-204.

[186] Pope, W.L., Smoot, G.F., Smith, L.H., Taylor, C.E., "Superconducting Magnet and Cryostat for Space Application", in "Advances in Cryogenic Engineering", 1st ed., Vol. 20, K.D. Timmerhaus, Ed., Plenum Press, New York, 1975, pp. 47-60.

[187] Probert, S.D., "Thermal Insulation in Relation to Cryogenics", H.M.S.O. Publication, TRG Report 1455(R/X), 1967.

[188] Quayle, O.R., "The Parachors of Organic Compounds", Chem. Revs., Vol. 53, 1953, pp. 439-489.

[189] Rae, W.J., Dunn, M.G., "Gasdynamics of the Cryogenic Cooler of the Nimbus F Spacecraft", J. Spacecraft, Vol. 13, No. 12, Dec. 1976, pp. 732-739.

[190] Ranzjevic, K., "Tables et Diagrammes Thermodynamiques", 1st ed., Editions Eyrolles, Paris, 1970, p. 240.

[191] Reed, R.P., Tobler, R.L., Mikesell, R.P., "The Fracture Toughness and Fatigue Crack Growth Rate of an Fe-Ni-Cr Superalloy at 298, 76 and 4 K", ", in "Advances in Cryogenic Engineering", 1st ed., Vol. 22, K.D. Timmerhaus, R.P. Reed & A.F. Clark, Eds., Plenum Press, New York, 1977, pp. 68-79.

[192] Reivari, P., "Dependence of Nuclear Polarized Fe^{57} Mössbauer Spectra on the Magnitude and Sign on the Hyperfine Field", Phys. Rev. Letters, Vol. 22, No. 5, 3 Feb., 1969, pp. 167-169.

[193] Reynolds, Jr., C.L., Anderson, A.C., "Kapitza Resistance to Solid He^4 below 1K", Cryogenics, Vol. 17, No. 12, Dec. 1977, pp. 709-710.

[194] Reynolds, Jr., C.L., Anderson, A.C., "Thermal Boundary Resistance to Solid Helium, Hydrogen, Deuterium and Neon, Phys. Rev., B, Vol. 14, No. 9, 1 Nov. 1976, pp. 4114-4120.

[195] Richter, R., Mahefkey, E.T., "Developments of Thermal Energy Storage Units for Spacecraft Cryogenic Coolers", AIAA Paper No. 80-0145. 18th Aerospace Sciences Meeting, Pasadena, Calif., Jan. 14-16, 1980.

[196] Roberts, P.H., Donnelly, R.J.., "Superfluid Mechanics", in "Annual Review of Fluid mechanics", 1st ed., Vol. 6, M. Van Dyke, W.G. Vincenti & J.V. Wehausen, Eds., Annual Reviews Inc., Palo Alto, Calif., 1974, pp. 179-225.

[197] Roberts, R., Wnek, K., Tafuri, J.C., "Environmental-Assisted Fatigue Crack Propagation in 3003-O Aluminium", in "Advances in Cryogenic Engineering", 1st ed., Vol. 24, K.D. Timmerhaus, R.P. Reed & A.F. Clark, Eds., Plenum Press, New York, 1978, pp. 187-196.

[198] Rolfo, A., Prost, R., "Spaceborne Solid Cryogen Cooler for IR Detectors", in "Spacecraft Thermal and Environmental Control Systems", M. Khine, B. Battick & C. Rowley, Eds., ESA SP-139, Nov. 1978, pp. 527-530.

[199] Rosenberg, H.M., "The Measurement of Mechanical Properties of Metals at Low Temperatures", in "Progress in Cryogenics", 1st ed., Vol. 1, K. Mendelssohn, Ed., Heywood & Co., Ltd., London, 1959, pp. 119-136.

[200] Rott, N., "Damped and Thermally Driven Acoustic Oscillations in Wide and Narrow Tubes", Journal of Applied Mathematics and Physics (ZAMP), Vol. 20, Fasc. 2, 25-3-1969, pp. 230-243.

[201] Rott, N., "Thermally Driven Acoustic Oscillations. Part II: Stability Limit for Helium", Journal of Applied Mathematics and Physics (ZAMP), Vol. 24, Fasc. 1, 25-1-1973, pp. 54-72.

[202] Rott, N., "Thermally Driven Acoustic Oscillations. Part III: Second Order Heat Flux", Journal of Applied Mathematics and Physics (ZAMP), Vol. 26, Fasc. 1, 25-1-1975, pp. 43-49.

[203] Runck, R.J., "Compatibility of Materials with Rocket Propellants and Oxidizers", DMIC Memorandum 201, Batelle Memorial Institute, Columbus, Ohio, Jan. 29, 1965.

[204] Ruoff, A.L., "Introduction to Materials Science", 1st ed., Prentice-Hall, Inc., Englewood Cliffs, N.J., 1972, Chap. 2, pp. 59-93, Chap. 12, pp. 511-565.

[205] Sample, H.H., "The Heat Capacity of Solid Helium-3", Iowa State University of Science and Technology, 1966. Available from University Microfilms, Inc., Ann Arbor, Michigan.

[206] Sano, Y, Nakamura, Y., Wakita, H., Urabe, A., Tominaga, T., "Helium-3 Emission Related to Volcanic Activity", Science, Vol. 224, No. 4645, 13 April 1984, pp. 150-151.

[207] Schmidt, C., "Influence of the Kapitza Resistance on the Thermal Conductivity of Filled Epoxies", Cryogenics, Vol. 15, No. 1, Jan. 1975, pp. 17-20.

[208] Schorre, U., "He II Phase Separation with Slits and Porous Plugs for Space Cryogenics", Cryogenics, Vol. 24, No. 10, Oct. 1984, pp. 536-548.

[209] Schotte, U., "Flow States and Heat Transfer Properties of He II Phase Separators", in "Advances in Cryogenic Engineering", 1st ed., Vol. 27, R.W. Fast, Ed., Plenum Press, New York, 1982, pp. 421-430.

[210] Schwarz, K.W., "Turbulence in Superfluid Helium: Steady Homogeneous Counterflow", Phys. Rev., B, Vol. 18, No. 1, 1 July 1978, pp. 245-262.

[211] Scull, S.R., Jewell, C., "Pre-Qualification Level Testing of an 80 K Stirling Cycle Cooler", ESA SP-324, Dec. 1991, pp. 201-207.

[212] Seidel, A., "Design and Thermal Control Concept of a He II Cryostat for Space Application (GIRL)", in "Spacecraft Thermal and Environmental Control Systems", M. Khine, B. Battick & C. Rowley, Eds., ESA SP-139, Nov. 1978, pp. 517-519.

[213] Seidel, A., "Liquid-Vapour Phase Separator for a Cryogenic Liquid in a Zero-g Environment", MBB-Report No. UR-571/82, Ottobrunn, Sept. 1982.

[214] Selzer, P.M., Fairbank, W.M., Everitt, C.W.F., "A Superfluid Plug for Space", in "Advances in Cryogenic Engineering", 1st ed., Vol. 16, K.D. Timmerhaus, Ed., Plenum Press, New York, 1971, pp. 277-281.

[215] Shelpuk, B., Crouthamel, M.S., Cygnarowicz, T.A., "ICICLE: Integrated Cryogenic Isotope Cooling Engine System", ASME Paper 7-HT/SpT-30, Space Technology and Heat Transfer Conference, Los Angeles, Calif., June 21-24, 1970.

[216] Sherman, A., "Cryogenic Cooling for Spacecraft Sensors, Instruments, and Experiments", Astronautics & Aeronautics, Vol. 16, No. 11, Nov. 1978, pp. 39-47.

[217] Sherman, A., "History, Status and Future Applications of Spaceborne Cryogenic Systems", in "Advances in Cryogenic Engineering", 1st ed., Vol. 27, R.W. Fast, Ed., Plenum Press, New York, 1982, pp. 1007-1029.

[218] Sherman, A., "Mathematical Analysis of a Vuilleumier Refrigerator", ASME Paper 71-WA/HT-33, ASME Winter Annual Meeting, Washington D.C., Nov. 28-Dec. 2, 1971.

[219] Sherman, A., Brennan, P., "Cryogenic and Low Temperature Heat Pipe/Cooler Studies for Spacecraft Application", J. Spacecraft, Vol. 13, No. 5, May 1976, pp. 288-293.

[220] Sherman, A., Figueroa, O., "A Portable ^{3}He Cryostat for Studies in Astrophysics", in "Advances in Cryogenic Engineering", 1st ed., Vol. 25, K.D. Timmerhaus & H.A. Snyder, Eds., Plenum Press, New York, 1980, pp. 775-782.

[221] Sherman, A., Gasser, M., Goldowsky, M., Benson, G., McCormick, J., "Progress on the Development of a 3 to 5-Year Lifetime Stirling Cycle Refrigerator for Space", in "Advances in Cryogenic Engineering", 1st ed., Vol. 25, K.D. Timmerhaus & H.A. Snyder, Eds., Plenum Press, New York, 1980, pp. 791-800.

[222] Slegtenhorst, R.P., "On the Flow of Helium II under the Influence of a Heat Current", Leyden University, Oct. 1981.

[223] Slegtenhorst, R.P.,Private Communication, Oct. 22nd 1981.

[224] Slegtenhorst, R.P., van Beelen, H., "A Survey of Experimental Data on Capillary Flow of Helium II in the Temperature Range between 1 K and 2 K", Physica, Vol. 106 B, pp. 200-212, 1981.

[225] Snyder, N.S., "Heat Transport through Helium II: Kapitza Conductance", Cryogenics, Vol. 10, No. 2, pp. 89-95, April 1970.

[226] Sonntag, R.E., van Wylen, G., "Introduction to Thermodynamics, Classical & Statistical", 2nd ed., John Wiley & Sons, New York, 1982, Chap. 12, pp. 413-415.

[227] Staas, F.A., Taconis, K.W., van Alphen, W.M., "Experiments on Laminar and Turbulent Flow of He II in Wide Capillaries", Physica, Vol. 27, No. 10, Oct. 1961, pp. 893-923.

[228] Straty, G.C., "Thermodynamic Properties of Solid Helium", University of Florida, Dec. 1996. Available from University Microfilms, Inc., Ann Arbor, Michigan.

[229] Streed, E.R., Murphy, D.W., Brna, T.J., "Refrigeration Systems for Space Telescopes", in "Applications of Cryogenic Techology", 1st ed., Vol. 3, R.W. Vance, Ed., The Cryogenic Society of America, 1971, pp. 204-230.

[230] Strogin, M., Zimmerman, G.O., Fairbank; H.A., "Specific Heat in Liquid ^{3}He", "Proceedings of the Eight International Conference on Low Temperature Physics", R.O. Davies, Ed., Butterworths, London, 1963, pp. 29-30.

[231] Svhmidt, H.W., "Fluorine and Fluorine-Oxygen Mixtures in Rocket Systems", NASA SP-3037, 1967.

[232] Tegart, J.R., Fester, D.A., "Space Storable Propellant Acquisition System", J. Spacecraft, Vol. 12, No. 9, Sept. 1975, pp. 544-551.

[233] Tegart, J.R., Uney, P.E., Anderson, J.E., Fester, D.A., "Space Storable Propellant Acquisition System", NASA CR 114493, Contract NAS 2-6548, Martin Marietta Aerospace, Ect. 1972.

[234] Telschow, K., Rudnick, I., Wang, T.G., "An Experiment on the Bernoulli Thinning Effect in Unsaturated Superfluid Films", J. Low Temp. Phys., Vol. 18, Nos. 1/2, Jan. 1975, pp. 43-63.

[235] Thring, M.W., "Pulsating Combustion. The Collected Works of F.H. Reynst", 1st ed., Pergamon Press, Oxford, 1961.

[236] Timmerhaus, K.D., Flynn, T.M., "Safety with Cryogenic Systems", in "Advances in Cryogenic Engineering", 1st ed., Vol. 23, K.D. Timmerhaus, Ed., Plenum Press, New York, 1978, pp. 721-729.

[237] Tobler, R.L., McHenry, H.I., Reed, R.P., "Fracture Mechanics Parameters for an Iron - 13% Chromium - 19% Manganese Stainless Steel and its Welds at Cryogenic Temperatures", in "Advances in Cryogenic Engineering", 1st ed., Vol. 24, K.D. Timmerhaus, R.P. Reed & A.F. Clark, Eds., Plenum Press, New York, 1978, pp. 560-572.

[238] Tobler, R.L., Reed, R.P., "Fatigue Crack Growth Rates of Structural Alloys at 4 K", in "Advances in Cryogenic Engineering", 1st ed., Vol. 22, K.D. Timmerhaus, R.P. Reed & A.F. Clark, Eds., Plenum Press, New York, 1977, pp. 35-46.

[239] Tobler, R.L., Reed, R.P., "Fatigue Crack Growth Resistance of Structural Alloys at Cryogenic Temperatures", in "Advances in Cryogenic Engineering", 1st ed., Vol. 24, K.D. Timmerhaus, R.P. Reed & A.F. Clark, Eds., Plenum Press, New York, 1978, pp. 82-90.

[240] Torre, J.P., Chanin, G., "Test Flight Results of a Balloon-Borne He^3 Cryostat", in "Advances in Cryogenic Engineering", 1st ed., Vol. 23, K.D. Timmerhaus, R.P. Reed & A.F. Clark, Eds., Plenum Press, New York, 1978, pp. 640-643.

[241] Tribus, M., "Thermostatics and Thermodynamics", 1st ed., Van Nostrand Company, Inc., Princeton, 1961, Chap. 9, pp. 243-270.

[242] Tsao, Chi K., "Temperature Distribution and Power Loss of a Gas-Cooled Support for a Cryogenic Container", Cryogenics, Vol. 14, No. 5, May 1974, pp. 271-275.

[243] Urbach, A.R., Herring, R.N., "A Liquid Helium Dewar for Space Experiments", AIAA Paper No. 76-476, AIAA 11th Thermophysics Conference, San Diego, Calif., July 14-16, 1976.

[244] Urban, E., Katz, L., Hendricks, J., Karr, G., "Cryogenic Helium II Systems for Space Applications", in "Spacecraft Thermal and Environmental Control Systems", M. Khine, B. Battick & C. Rowley, Eds., ESA SP-139, Nov. 1978, pp. 507-515.

[245] Urban, E.W., Katz, L., Karr, G.R., "Helium II Flow through and Vapor Separation by Porous Plugs", Proceedings of the 14th International Low temperature Physics Conference, Helsinki, Aug. 1975, Vol. 4, North Holland/American Elsevier, Amsterdam, 1975, pp. 37-40.

[246] Van Alphen, W.M., de Bruny Ouboter, R., Olijhoek, J.F., Taconis, K.W., "The Critical Flow Rate of Superfluid Helium through Narrow Capillaries", Physica, Vol. 40, No. 4, 20 Jan. 1969, pp. 490-496.

[247] Van der Heijden, G., van der Boog, A.G.M., Kramers, H.C., "Forces in the Flow of Liquid He II - III. Flow with v_n and v_s Unequal Zero", Physica, Vol. 77, 1974, pp. 487-513.

[248] Van Dyke, M., "perturbation Methods in Fluid Mechanics", Annotated Edition, The Parabolic Press, Stanford, Calif., 1975.

[249] Van Sciver, S.W.,, "Kapitza Conductance of Aluminium and Heat Transport from a Flat Surface through a Large-Diameter Tube to Saturated Helium II", in "Advances in Cryogenic Engineering", 1st ed., Vol. 23, K.D. Timmerhaus, Ed., Plenum Press, New York, 1978, pp. 340-348.

[250] Van Sciver, S.W.,, "Kapitza Conductance of Aluminium and Heat Transport through Subcooled He II", Cryogenics, Vol. 18, No. 9, Sept. 1978, pp. 521-527.

[251] Van Spronsen, E., Verbeek, H.J., de Bruyn Ouboter, R., Taconis, K.W., van Beelen, H., "Experimental Proof that a Moving He II Film Can be Thinner than a Static Film", Phys. Letters, A, Vol. 45, No. 1, 27 Aug. 1973, pp. 49-50.

[252] Van Spronsen, E., Verbeek, H.J., van Beelen, H., de Bruyn Ouboter, R., Taconis, K.W., "Investigations on the Saturated Moving He II Film with a Length of up to 200 m", Physica, Vol. 77, 1974, pp. 570-608.

[253] Vargaftik, N.B., "Tables of the Thermophysical Properties of Liquids and Gases", 2nd ed., Hemisphere Publishing Corporation, Washington, 1975.

[254] Verkin, B.I., "The Development of Cryogenic Materials Science in the USSR", in "Advances in Cryogenic Engineering", 1st ed., Vol. 24, K.D. Timmerhaus, R.P. Reed & A.F. Clark, Eds., Plenum Press, New York, 1978, pp. 37-51.

[255] Vinen, W.F., "Mutual Friction in a Heat Current in Liquid Helium II. III. Theory of the Mutual Friction", Proc. Roy. Soc., A, Vol. 242, pp. 493-515, 1957.

[256] Von Karman, Th., "Sorbonne Lectures 1951-1952". See also "Fundamental Equations in Aerothermochemistry", Proc. 2nd AGARD Combust. Colloq., Liège, Belgium, December 1955.

[257] Vorreiter, J.W., "Cryogenic Systems for Spacecraft", Contemp. Phys., Vol. 21, No. 3, May-June 1980, pp. 201-217.

[258] Wang, T.G., Petrac, D., "Thickness of an Accelerating Superfluid Film", Phys. Rev., B, Vol. 11, No. 11, 1 June 1975, pp. 4221-4223.

[259] Ward-Smith, A.J., "Internal Fluid Flow", 1st ed., Clarendon Press, Oxford, 1980, Chap C, pp. 192-194.

[260] Weast, R.C., "Handbook of Chemistry and Physics", 57th ed., CRC Press. Inc., Cleveland, 1976, p. F-47.

[261] Wells, J.M., "Evaluation of Incoel X750 Weldments for Cryogenic Applications" in "Advances in Cryogenic Engineering", 1st ed., Vol. 22, K.D. Timmerhaus, R.P. Reed & A.F. Clark, Eds., Plenum Press, New York, 1977, pp. 80-90.

[262] Wells, J.M., Logsdon, W.A., Kossowsky, R., "Evaluation of Weldments in Austenitic Stainless Steels for Cryogenic Applications", in "Advances in Cryogenic Engineering", 1st ed., Vol. 24, K.D. Timmerhaus, R.P. Reed & A.F. Clark, Eds., Plenum Press, New York, 1978, pp. 150-160.

[263] Wey-Yeng, K., "An Investigation of the Temperature Discontinuity at the Boundary between a Solid and Superfluid Helium", Soviet Phys., JETP, Vol. 15, No. 4, pp. 635-645, Oct. 1962.

[264] Wheatley, J.C., "Experimental Properties of Superfluid ^{3}He", Rev. Mod. Phys., Vol. 47, No. 2, April 1975, pp. 415-470.

[265] Wigley, D.A., Halford, P., "Materials of Construction and Techniques of Fabrication", in Cryogenic Fundamentals", 1st ed., G.G. Haselden, Ed., Academic Press, London, 1971, Chap. 6, pp. 321-325.

[266] Wipf, S.L., Gibney, R.B., "Properties of Bone at Low Temperatures and its Potential as Cryostat Support Material", Cryogenics, Vol. 15, No. 11, Nov. 1975, pp. 645-648.

[267] Woods, A.D.B., Hollis Hallet, A.C., "The Viscosity of Liquid Helium II between 0,79º K and the Lambda Point", Can. J. Phys., Vol. 41, No. 4, April 1963, pp. 596-609.

[268] Yang, L.C., Mason, P.V., "Superfluid Helium Film in Zero Gravity", Cryogenics, Vol. 20, No. 2, Feb. 1980, pp. 91-97.

[269] Yazaki, T., Tominaga, A., Narahara, Y., "Stability Limit for Thermally Driven Acoustic Oscillation", Cryogenics, Vol. 19, No. 7, July 1979, pp. 393-396.

[270] Yushchenko, K.A., "Low Temperature Weldable Steels and Alloys" in "Advances in Cryogenic Engineering", 1st ed., Vol. 24, K.D. Timmerhaus, R.P. Reed & A.F. Clark, Eds., Plenum Press, New York, 1978, pp. 120-128.

[271] Yushchenko, K.A., Belotzerkovetz, V.I., Starushchenko, T.M., Kovalenko, L.V., Sitnichenko, G.Ya., "Investigation of Steels for their Application in LNG Transportation and Storage Welded Systems", in "Advances in Cryogenic Engineering", 1st ed., Vol. 24, K.D. Timmerhaus, R.P. Reed & A.F. Clark, Eds., Plenum Press, New York, 1978, pp. 540-547.

[272] Zemansky, M.W., "heat and Thermodynamics", 5th Ed., McGraw-Hill Book Company, New York, 1968, Chap. 11, pp. 275-334, Chap. 12, pp. 335-346.